europhysics conference abstracts

23rd European Physical Society Conference on

Controlled Fusion and Plasma Physics

Kiev, 24-28 June,1996

Editors: D.Gresillon, A.Sitenko and A.Zagorodny

Contributed Papers, Part III

Published by: The European Physical Society

Series Editor: Prof. R.Pick, Paris

Managing Editor: G.Thomas, Geneva

Volume 20C

Part III

23rd European Physical Society Conference on

Controlled Fusion and Plasma Physics



Max-Planck-Institut für Plasmaphysik
19. Jan. 1998
Bibliothek

Bogolyubov Institute for Theoretical Physics, Kiev, Ukraine

24-28 June 1996

Editors: D Gresillon, A.Sitenko and A.Zagorodny

98-9829



europhysics conference abstracts

23rd European Physical Society Conference on

Controlled Fusion and Plasma Physics

Kiev, 24-28 June,1996

Editors: D.Gresillon, A.Sitenko and A.Zagorodny

Contributed Papers, Part III

Published by: The European Physical Society

Series Editor: Prof. R.Pick, Paris

Managing Editor: G.Thomas, Geneva

Volume 20C

Part III

EUROPHYSICS CONFERENCE ABSTRACTS is published by the European Physical Society © 1996

Reproduction rights reserved

This volume is published under the copyright of the European Physical Society. We wish to inform the authors that the transfer of copyright to the EPS should not prevent an author from publishing an article in a journal quoting the original first publication or to use the same abstract for another conference. This copyright is just to protect EPS against using the same material in similar publications.

PREFACE

The 23rd EPS Conference on Controlled Fusion and Plasma Physics was organized on behalf of the European Physical Society by the National Academy of Sciences of Ukraine, State Committee on Science, Technologies, and Industrial Policy of Ukraine, and the Bogolyubov Institute for Theoretical Physics (BITP) in Kiev, Ukraine.

The 1996 Conference included the topics: A - Tokamaks, B - Stellarators, C - Alternative Magnetic Confinement, D - Plasma Edge Physics, E - Plasma Heating and Current Drive, F - Diagnostics, G - Basic Collisionless Plasma Physics, H - High Intensity Laser Produced Plasmas and Inertial Confinement, I - Astrophysical and Geophysical Plasmas, J - Low-Temperature Plasmas.

The Conference Proceedings are published in three parts, including:

Part I - Topic A; Part II - Topics B,C,D,E;
Part III - Topics F,G,H,I,J, and postdeadline papers.

The four-page papers are arranged within topical groups in the ascending order of file numbers. An exception is made for 24 contributions which were selected for oral presentation at the Conference. Such papers are presented at the beginning of each topical group.

According to EPS Plasma Physics Division regulations, the Conference Proceedings contain the four-page papers of all those contributions for which at least one author was a registered participant at the Conference. There are 371 papers which satisfy this condition. The three parts of the proceedings will be mailed to all registered participants of the Conference.

The papers of five Review Lectures and 21 Topical Lectures will be published in a special issue of the journal "Plasma Physics and Controlled Fusion", which will also be mailed to all registered participants.

D.Gresillon, A.Sitenko, A.Zagorodny

July 1996

Program Committee

D.Gresillon	(Ecole Polytechnique, CNRS, Palaiseau France - *Chairman*)
G.Fussmann	(MPI fur Plasmaphysik, Bereich Berlin, Germany)
X.Garbet	(CEA, Cadarache, France)
C.Hidalgo	(CIEMAT Fusion, Madrid, Spain)
L.Kovrizhnykh	(General Physics Institute, Moscow, Russia)
S.Prager	(University of Wisconsin, Madison USA)
A.Sitenko	(BITP, Kiev, Ukraine)
F.Sluijter	(Eindhoven University, The Netherlands - *Chairman of the EPS PlasmaPhysics Division*)
M.Tendler	(Royal Institute. of Technology, Stockholm, Sweden)
P.Thomas	(JET Joint Undertaking, Abingdon, UK)
H.Weisen	(CRPP-EPFL, Lausanne, Switzerland)
J.Winter	(KFA, Juelich, Germany)

Local Organizing Committee

A.Sitenko	*Chairman*
A.Zagorodny	*Vice-Chairman*
O.Pavlichenko	*Vice-Chairman*
I.Goutych	*Scientific Secretary*
G.Bugrij	
Yu.Chutov	
S.Fomina	
O.Kocherga	
Ya.Kolesnichenko	
V.Krol'	
A.Polozov	
P.Schram	
P.Sosenko	
K.Stepanov	
I.Yakimenko	

CONTENTS

PART I

Topic A TOKAMAKS 1

Oral Presentations 3

a002 (OP1)	**A.Zeiler**	Electron Temperature Fluctuations in Drift-Resistive Ballooning Turbulence	3
a102 (OP2)	**P.C.de Vries**	Temperature Profile Perturbations Measured by High Resolution ECE-Diagnostics	7
a154 (OP3)	**F.Ryter**	Perturbative Transport from Sawtooth Propagation and ECRH Modulation in ASDEX Upgrade	11
a008 (OP6)	**V.Mertens**	High Density Operation in Auxiliary Heated ASDEX Upgrade Discharges	15
a124 (OP7)	**G.T.Hoang**	Transport and Density Fluctuations in Non-Inductive Current Drive Experiments in Tore Supra	19
a176 (OP8)	**S.Briguglio**	Particle Simulation of Alpha-Particle-Driven Modes in Tokamaks	23
a035 (OP13)	**J.-M.Moret**	How the Shape Influences the TCV Plasma Properties	27
a137 (OP14)	**T.C.Hender**	Stability of TFTR Reverse Shear Discharges	31
a043 (OP19)	**V.V.Parail**	Numerical Analysis of the Heat Pulses in JET	35
a141 (OP20)	**M.Valovic**	H-Mode Confinement Scaling and ELMs on COMPASS-D	39

Poster Contributions 43

a001	**H.Zohm**	Beta-Limiting Phenomena in ASDEX Upgrade	43
a004	**W.Suttrop**	The Role of Edge Parameters for L-H Transitions and ELM Behaviour on ASDEX Upgrade	47
a005	**B.Scott**	Three Dimensional Computation of Collisional Drift Wave Turbulence and Transport in Tokamak Geometry	51
a010	**L.Zakharov**	Occurrence of Sawteeth in ITER and their Effects on Alpha Particles and Stability	55
a011	**R.E.Bell**	Transport Barrier Formation in TFTR Reversed Magnetic Shear Plasmas	59
a012	**M.P.Petrov**	Aspects of Trapped Confined Alpha Physics on TFTR	63
a014	**L.Zakharov**	Triggering Disruptions in TFTR at High β	67

a015	**R.J.Goldston**	TF Ripple Loss of Alpha Particles from the ITER Interim Design: Simulation and Theory	71
a016	**G.L.Schmidt**	Extension of TFTR Enhanced Reversed Shear Regime to Larger Core Volume and Higher Current	75
a019	**T.Kass**	The Fishbone-Instability in ASDEX Upgrade	79
a020	**A.Kallenbach**	Optimization of Radiative H-Mode Operation	83
a021	**P.Franzen**	Online Confinement Regime Identification for the Discharge Control System at ASDEX Upgrade	87
a022	**W.Feneberg**	Bootstrap Current Derived from Different Model Collision Operators	91
a023	**R.Dux**	Measurement and Modelling of Impurity Transport in Radiating Boundary Discharges in ASDEX Upgrade	95
a024	**H.J.de Blank**	Radial Current Balance in ASDEX Upgrade Discharges in the L- and H-Mode Phases	99
a026	**M.Alexander**	Transport Investigations Using "Dimensionless Similar" Discharges in ASDEX Upgrade	103
a029	**T.C.Hender**	Error Fields, Low Collisionality and High Beta on COMPASS-D	107
a030	**H.Weisen**	Measurement and Modelling of Light Impurity Behaviour in TCV	111
a032	**Z.A.Pietrzyk**	Electron Density Profiles during Ohmic H-Modes in TCV	115
a033	**Y.Martin**	Shape Dependence of Ohmic H-Mode Accessibility in TCV	119
a034	**J.-M.Moret**	Breakdown in a Continuous Low Resistivity Vessel in TCV	123
a036	**F.Hofmann**	On the Possibility of Creating Doublet-Shaped Plasmas in TCV	127
a038	**D.H.Liu**	Scalings of Resistive Mode of Finite Pressure	131
a040	**P.Galli**	Nonlocal Response of JET H-Mode Discharges to Temperature Perturbations Induced by Impurity Injection	135
a041	**R.A.M.Van der Linden**	Ballooning Instabilities in the Scrape-off-Layer of Diverted Tokamaks as Giant ELM Precursors	139
a042	**D.Borba**	Linear and Nonlinear Dynamics of Alfven Eigenmodes in JET Plasmas	143
a044	**B.Balet**	MHD Related Transport Analysis in JET	147
a045	**H.P.L.de Esch**	Simulations of JET Hot-Ion H-Modes with a Predictive Code	151

a046	**A.Taroni**	Transport Modelling with a Combined Core and Edge Code	155
a049	**A.Rossi**	First Measurements of Gas Balance and Chemical Composition in the MK I Pumped Divertor Phase of JET Using the Gas Collection System	159
a051	**R.D.Gill**	Strong Asymmetries in Impurity Distributions of JET Plasmas	163
a052	**R.D.Gill**	Properties of Giant ELMs	167
a054	**M.G.O'Mullane**	Monitoring of Detachment and the Edge Using VUV/XUV Impurity Spectra from the Mark I Divertor Phase of JET	171
a055	**S.Clement**	Effects of Density and Plasma Configuration on the Divertor Asymmetries	175
a056	**S.Ali-Arshad**	Plasma Movement at ELMs in JET	179
a057	**T.C.Hender**	Monte-Carlo Simulations of Fast Particle Confinement during a Sawtooth Crash	183
a058	**M.de Benedetti**	Effect of the Error Fields on Plasma Stability in JET and ITER	187
a059	**M.de Benedetti**	Identification of the Physical Mechanisms of Low-m, n=1 MHD Mode Control in JET	191
a060	**G.A.Cottrell**	ICRH in Hot-Ion H-Modes in JET	195
a061	**A.Cherubini**	A Description of ELM-Free H-Modes in Terms of a Neoclassical Edge Barrier and a "Mixed" Model for Energy and Particle Transport	199
a062	**M.G.O'Mullane**	Variation of Impurity Transport during ELMy H-Modes in JET Plasmas	203
a063	**R.Sanchez**	Simulation Model for Runaway Electron Diffusion in the JET Tokamak	207
a064	**C.C.Petty**	Nondimensional Transport Experiments on DIII-D and Projections to an Ignition Tokamak	211
a065	**M.S.Chu**	Resistive Instabilities in Advanced Negative Central Shear Tokamaks With Peaked Pressure Profiles	215
a070	**K.N.Sato**	Characteristics of Ice Pellet Ablation and its Effect on Plasma Potential in the JIPP T-IIU Tokamak	219
a071	**V.B.Minaev**	Spherical Tokamak GLOBUS-M	223
a073	**O.A.Silivra**	Coherent Magnetoacoustic Cyclotron Instability in Plasmas with High Energy Ions	227
a074	**V.A.Yavorskij**	Results of 3D Fokker-Planck Simulation of Ripple-Induced Loss of Alpha Particles in TFTR	231

a075	**V.Goloborod'ko**	On Distribution Function of Fast Fusion Products in Tokamak Plasma	235
a078	**V.I.Poznyak**	Investigation of the Current-Kinetic Instability in the T-10 Tokamak	239
a080	**V.I.Ilgisonis**	Shear Flow Steady State of Tokamak Plasma with Anisotropic Pressure	243
a082	**S.V.Soldatov**	Numerical Simulations of Density Fluctuations in T-10 SOL	247
a083	**S.V.Soldatov**	Investigation of Three Types of Core Small Scale Density Fluctuations, Identified in T-10 Experiments	251
a084	**Yu.V.Gott**	On the Models of Heat Transport in a Turbulent Magnetized Plasma	255
a085	**Yu.V.Gott**	Neoclassical Ion Heat Transport in a Plasma with High Gradients in Parameters	259
a087	**V.A.Shurygin**	Temporal Evolution of Chromium Line Emission during Argon Puffing in T-10	263
a088	**Yu.I.Gott**	Effect of a Finite Plasma Pressure on the Neoclassical Ion Heat Transport	267
a090	**Yu.N.Dnestrovskij**	Fast Processes within the Canonical Profiles Transport Model	271
a091	**N.T.Besedin**	Neutral Atom Distribution Function Behavior in Nonmaxwellian Plasma	275
a092	**I.M.Pankratov**	Runaway Electrons Secondary Generation	279
a093	**M.R.Wade**	Characterization of Core Impurity Transport and Accumulation in Various Operating Regimes in DIII-D	283
a094	**A.W.Hyatt**	Magnetic and Thermal Energy Flow during Disruptions in DIII-D	287
a095	**C.M.Greenfield**	Transport in High Performance Weak and Negative Central Shear Discharges in DIII-D	291
a096	**T.A.Casper**	Modeling of Current Profile Evolution and Equilibria in Negative Central Shear Discharges in the DIII-D Experiment	295
a097	**B.Coppi**	Thermal Transport Coefficient for Ohmic and ICRF Plasmas in Alcator C-Mod	299
a099	**F.Bombarda**	Rationale for Ignition Experiments and the Ignitor Program	303
a100	**P.Detragiache**	Global Stability and Operational Regimes of Ignition Experiments	307

a101	**A.H.Kritz**	Transport Simulations of Tokamak Parameter Scans Using the Weiland Ion Temperature Gradient Model	311
a103	**J.H.Chatenet**	Self-Sustainment of Magnetic Islands	315
a104	**L.Krlin**	Nonlinear and Stochastic Interaction between TAE and Alpha Particles	319
a106	**S.V.Mirnov**	Evolution of Edge Plasma Parameters during L-H Transition in T-11M	323
a109	**Yu.V.Yakovenko**	Post-Crash Relaxation of the Space and Velocity Distributions of Fast Ions	327
a110	**V.V.Lutsenko**	Effect of Sawtooth Crashes on Fast Ions with Various Energies and Pitch Angles	331
a111	**Ya.I.Kolesnichenko**	Rapid Cyclotron Instabilities in Plasmas with Fast Ions	335
a112	**H.Shirai**	Analyses of Electron and Ion Transport Properties in JT-60U H-Mode Plasmas with Improved Core Confinement	339
a115	**S.G.Kalmykov**	Relation of the Toroidal Current to the Radial Plasma Flux in Tokamaks. Possible Manifestation of This Relation in L-H Transition in the TUMAN-3 Device	343
a116	**J.P.Goedbloed**	Profile Dependent Signature of the Linear MHD Spectrum	347
a117	**J.P.Goedbloed**	MHD Stability Analysis of the KT-2 Plasma	351
a118	**A.A.M.Oomens**	Development of Double Double-Tearing Modes in Reversed Shear Tokamak Plasmas	355
a119	**C.P.Tanzi**	Influence of Magnetic Reynolds Number on Internal Disruptions in the RTP Tokamak	359
a122	**M.Ghoranneviss**	Modification of Plasma Confinement Using Resonant Helical Field on IR-T1 Tokamak	363
a123	**J.de Kloe**	Pellet Disturbed Plasmas in the RTP Tokamak	368
a125	**T.Wijnands**	Feedback Control of the Current Profile on Tore Supra	372
a126	**X.L.Zou**	Parametric Analysis of Internal Magnetic Fluctuations in the TORE SUPRA Tokamak	376
a127	**J.Johner**	Global Energy Confinement Time Scaling Derived from the Local Rebut-Lallia-Watkins Transport Model	380
a128	**X.Garbet**	Scaling Laws of Turbulence in Tokamaks	384
a129	**J.H.Misguich**	Diffusion Processes in Stochastic Magnetic Fields	388

a130	**X.L.Zou**	Similarity Experiments in Tore Supra	392
a131	**A.L.Pecquet**	Impurity Content and Sustainment of the Tore-Supra Snakes	396
a132	**B.G.Hong**	Time-Dependent Transport Simulation Study for Advanced Tokamak Mode in KT-2 Tokamak	400
a133	**P.Buratti**	Sawtooth Studies on the FTU Tokamak	404
a134	**P.Micozzi**	Correlation among Plasma Rotation, Magnetic Configurations and Improved Confinement Regimes in Present Large Tokamak Experiments	408
a135	**K.G.McClements**	Modelling the Dependence of Sawtooth Stability on ICRH Power in Tokamak Plasmas	412
a136	**R.J.Buttery**	Study of Internal Reconnection Events on the START Tokamak	416
a139	**G.G.Castle**	Halo Currents and VDEs in COMPASS-D	420
a140	**M.J.Walsh**	First Results of Neutral Beam Heating in START Spherical Tokamak Plasmas	424
a142	**E.Haddad**	Impurity Content of TdeV Plasmas from Simulations of VUV Lines, SXR and Radiation Profile Measurements	428
a143	**R.Raman**	Enhanced Plasma Confinement after Compact Toroid Fuelling	432
a156	**A.V.Melnikov**	HIBP Measurements of the Plasma Electric Potential on T-10	436
a157	**A.Jarmen**	Toroidal η_i Mode Stability at Large Temperature Gradients	440
a163	**V.Rozhansky**	Formation of Transport Barriers	444
a164	**I.Kaganovich**	Transverse Current in a Braided Magnetic Field	448
a168	**I.Garcia-Cortes**	Studies of Turbulence in the JET Divertor Plasmas	452
a171	**X.Litaudon**	Nonlinear Evolution of MHD Instabilities in Tokamak Plasmas with Hollow Current Profiles	456
a173	**A.Geraud**	Analysis of Pellet Fuelling Efficiency from the International Pellet Ablation Database	460

PART II

Topic B STELLARATORS 465

Oral Presentations 465

b005 (OP15)	**E.Holzhauer**	Edge Turbulence and Transport Barrier Associated with the H-Mode in the W7-AS Stellarator	467
b031 (OP21)	**E.D.Volkov**	Review of Experimental Investigations on the U-3 and U-3M Torsatrons	471

Poster Contributions 475

b001	**A.V.Zolotukhin**	Guiding Center Motion of Collisionless Alpha-Particles in a Helias Reactor Configuration	475
b002	**H.Maassberg**	Neoclassical Transport in High-Mirror Advanced Stellarators	479
b003	**F.-P.Penningsfeld**	3MW Neutral Injection into the Stellarator Wendelstein 7-AS. Heating Efficiency at High-Beta Operation	483
b004	**H.Maassberg**	Neoclassical Transport Predictions for Stellarators in the Long-Mean-Free-Path Regime	487
b007	**J.Geiger**	Stability of W7-AS Configurations with Reduced Vacuum Magnetic Well	491
b008	**R.Brakel**	Radiative Boundary Studies in the Wendelstein 7-AS Stellarator	495
b009	**G.Cattanei**	Ion Cyclotron Resonance Heating Experiments on the Stellarator W7-AS	499
b010	**A.Ardelea**	Global Stability of n=1 External Modes for Plasmas with Helical Boundary Deformation and Net Toroidal Current	503
b012	**K.Watanabe**	Superposition of ECH on NBI Plasma in Heliotron E	507
b013	**K.Watanabe**	Parameter Study of 106GHz Second Harmonic ECH Plasma in Heliotron-E	511
b014	**Zh.Andrushchenko**	Effect of High-Energy Particles on GAE Modes in a Stellarator	515
b016	**A.A.Subbotin**	Highest Beta in Quasisymmetric Stellarator	519
b018	**E.L.Sorokovoj**	Electrostatic Fluctuations and Their Contribution to Particle Losses at the Plasma Boundary in the U-3M Torsatron	523

b019	**V.V.Nemov**	Mercier Criterion Investigation in the Region of the Island Magnetic Surfaces of Stellarators	527
b020	**M.S.Smirnova**	Confinement of Charged Particles in Torsatrons and Heliotrons with Additional Toroidal Magnetic-Field Ripple	531
b021	**V.I.Tyupa**	Analytical Calculations of the Average Magnetic Well in the Uragan-2M Torsatron with Different Profiles of Plasma Pressure	535
b022	**A.Ya.Omel'chenko**	Investigation of Plasma Stability Relatively to the Development of Quasi Flute Resistive Modes (G-modes) in Stellarators	539
b023	**V.A.Rudakov**	New Modular Helical System with Properties Close to a Continuous Helical Trap	543
b025	**G.G.Lesnyakov**	Studies of Magnetic Surfaces in the "Uragan-2M" Torsatron	547
b026	**A.A.Shishkin**	Progress in Reactor Heliotron/Torsatron Physics Study	551
b027	**I.N.Sidorenko**	Particle Orbits in Quadrupole Large Helical Device Configurations	555
b028	**S.V.Kasilov**	Application of Mapping Techniques for the Kinetic Equation in the Weak Collisions Regime	559
b029	**S.F.Perelygin**	Calculation of Electron Drift in a Magnetic System of the DRAKON type	563
b030	**K.Y.Watanabe**	Study of Magnetic Configuration of Heliotron Produced by Sectored Modular Coils	567
b032	**E.D.Volkov**	Radial Distribution of Electron Temperature in RF Discharge Plasma in Torsatron Magnetic Configuration with Island Structure	571
b034	**S.Morimoto**	Studies of Electron Confinements in Heliotron DR Using Stellarator Tetrode Method	575
b035	**R.Sanchez**	Resistive Stability Studies in the TJ-II Flexible Heliac	579
b036	**R.C.Wolf**	Study of the Power Balance in the W7-AS Stellarator by Means of 2-Dimensional Limiter Thermography and Bolometry	583
b038	**F.Medina**	Generation of Several Non-Thermal Electron Populations in TJ-I Upgrade Torsatron	587
b039	**E.De la Luna**	Electron Cyclotron Emission Measurements in the TJ-I Upgrade Torsatron	591
b040	**C.Hidalgo**	Energy Distribution of Charge Exchange Neutral Particles and Vertical Asymmetries in the TJ-IU Torsatron	595
b041	**V.Tribaldos**	Polarization Effects on ECRH in TJ-II Stellarator	599

b042	**B.Zurro**	Observation of Topological Structures and Asymmetries in Impurity Radiation Profiles in a Torsatron	603
b043	**J.Qin**	Equilibrium Beta and Diamagnetic Beta in Stellarators	607
b044	**F.Castejon**	Plasma Collapsing Mechanisms in Stellarators	611
b048	**S.E.Grebenshchikov**	The Peculiarities of Breakdown and Plasma Heating in the Stellarator L-2M by EM Waves on the Second Harmonic of Electron Cyclotron Resonance Frequency (ECRH)	615
b049	**S.E.Grebenshchikov**	Plasma Confinement in L-2M Stellarator	619

Topic C ALTERNATIVE MAGNETIC CONFINEMENT 623

Oral Presentation 625

c022 (OP4)	**S.Hokin**	Reversed-Field Pinch Operation with a Resistive Shell and Graphite Wall in Extrap T2	625

Poster Contributions 629

c001	**A.Buffa**	Recent Results of RFX	629
c002	**T.Bolzonella**	Effects of Shell Gap Modifications on RFX Plasma Behaviour	633
c003	**T.Bolzonella**	First Results of Hydrogen Pellet Injection in the RFX Experiment	637
c004	**T.Bolzonella**	Study of the Dependence on Density Control of the RFP Setting-up Phase in RFX	641
c005	**A.Murari**	Total Radiation Emissivity Distributions in RFX	645
c006	**M.Valisa**	Studies of the Ion Heating in RFX	649
c009	**V.I.Krauz**	Some Features of Neutron Radiation and Deutron Beams Generation in a Plasma Focus with the Flat Electrode Geometry	653
c013	**V.D.Yegorenkov**	Resonant Diocotron Instability of a Wide Electron Layer in Magnetic Gaps of Magnetoelectrostatic Traps	657
c015	**A.N.Lyakhov**	Principles of D-3He Fusion	660
c016	**A.N.Lyakhov**	Kinetic Stability of D-3He Plasma in the Central Cell of Tandem Mirror	664
c017	**V.I.Davydenko**	Characteristics and Mechanisms of Hot Initial Plasma Creation in the End System of AMBAL-M	668

c023	**P.Hoerling**	Impurity Ion Temperature and Flow Velocity Measurements at the Extrap-T2 Reversed-Field Pinch	672
c024	**O.A.Lavrent'ev**	Investigation of the Fundamental Processes of Plasma Accumulation, Heating and Confinement in the Multislit Electromagnetic Traps	676
c026	**O.A.Lavrent'ev**	Modeling of Processes of Plasma Accumulation, Heating and Confinement in the Multislit Electromagnetic Trap	680
c030	**A.A.Ivanov**	The Plasma Neutron Source Simulations In the GDT Experiment	684
c031	**P.A.Bagryansky**	Studies of Plasma Axial Confinement and Transverse Transport in the GDT Experiment	688
c033	**D.G.Solyakov**	Steady-State Electrodischarge Magnetic Trap - GALATEYA	692

Topic D PLASMA EDGE PHYSICS 697

Oral Presentations 699

d020 **(OP9)**	**G.D.Porter**	Divertor Characterization Experiments and Modeling in DIII-D	699
d054 **(OP16)**	**G.Mank**	Physical Prospects of the Dynamic Ergodic Divertor	703

Poster Contributions 707

d001	**D.Desideri**	First Measurements of Electron Energy Distribution In RFX Edge Plasma	707
d002	**R.Guirlet**	Analysis of VUV Ne Radiation in the JET Divertor during Ne Injections	711
d003	**M.Weinlich**	Electron Temperature In Front of the Target Plates in Various Divertor Scenarios in ASDEX Upgrade	715
d004	**J.Schweinzer**	Scaling of Edge Parameters for High Confinement, High Density ASDEX Upgrade Discharges	719
d005	**J.-M.Noterdaeme**	Mutual Influence between the ICRF Antennas and the Edge Density on ASDEX Upgrade	723
d006	**G.Theimer**	The Edge Turbulence in the W7-AS Stellarator: 2 d Characterization by Probe Measurements	727
d007	**O.P.Heinrich**	Edge Ion Temperature Profiles in L- and H-Mode Discharges of ASDEX	731
d009	**W.van Toledo**	Observation of ELM-Induced Neutral Particle Charge Exchange Fluxes in TCV	735

d011	**K.Uehara**	Ion Behavior and Electron Energy Distribution Function Observed by Electrostatic Probes in Tokamak Boundary Plasma	739
d012	**A.S.Usenko**	Thermal Radiation of Semibounded Plasma with Transition Layer	743
d013	**G.Igonkina**	Wall Conditioning in T-15. Investigation of Wall Surface State by WASA II	747
d014	**G.Sergienko**	Spectroscopy of Molecular Hydrogen in TEXTOR Edge Plasmas	751
d015	**G.G.Lesnyakov**	On Application of Plasma Chemical Reaction for Particle Removal by Cryopumped Divertor of Thermonuclear Device	755
d016	**G.P.Glazunov**	Experiments with Edge-Plasma and a Biased Movable B_4C-Limiter Interaction: Possible Use for Boronization and Pumping during Discharge Cleaning in Uragan-3M Torsatron	759
d017	**R.D.Wood**	Measurements of Divertor Impurity Concentrations on DIII-D	763
d019	**W.P.West**	Modeling of Impurity Spectroscopy in the Divertor and SOL of DIII-D Using the 1D Multifluid Model NEWT1D	767
d022	**V.P.Budaev**	Control of Plasma Edge via Biasing in Tokamak TF-2	771
d025	**L.M.Bogomolov**	Classic-Like I-V Characteristics of Swept Langmuir Probe and Measuring Edge Plasma Electron Temperature	775
d028	**S.I.Lashkul**	Scrape-off Layer Plasma Measurements in Lower Hybrid Heating Experiments on FT-2 Tokamak	779
d029	**M.Goniche**	Acceleration of Electrons in the Near Field of Lower Hybrid Frequency Grills	783
d030	**W.R.Hess**	Impurity Production & Radiation Properties of the Tore Supra Ergodic Divertor Configuration with RF-Heating	787
d031	**V.O.Girka**	Ion Surface Cyclotron Waves in Edge Plasma of the Fusion Devices	791
d036	**R.Marchand**	Finite Element Modelling of TdeV Edge Plasma and Beyond	795
d037	**H.Kastelewicz**	Interpretation of the Carbon Line Emission in the ASDEX-Upgrade Divertor	799
d038	**H.Kastelewicz**	B2 - Eirene Simulations for a Deuterium Plasma at PSI-1	803
d039	**A.Herrmann**	Characterization of the Power Deposition Profiles in the Divertor of ASDEX Upgrade	807

d040	**V.Rohde**	Scrape-off Layer Behavior in ASDEX Upgrade Ohmic L-Mode Density Scan	811
d041	**G.Mank**	Investigation of the Removal Efficiency for D_2, He, and Ne in the ALT-II Limiter Throat	815
d043	**J.Rapp**	Characteristics of the Impurities Mo and W in Discharges with Neon Edge Radiation Cooling in TEXTOR-94	819
d045	**R.Simonini**	A Predictive Study of the JET Mark II Gas Box Divertor	823
d046	**M.A.Pedrosa**	Statistical Properties of Turbulent Transport and Fluctuations in Tokamak and Stellarator Devices	827
d050	**I.Rogal'**	Charged-Particle Density Profiles near the Wall in the Presence of Strong Electric Fields	831
d051	**V.A.Kurnaev**	Unstable Plasma-Surface Interaction as Edge Turbulence Driving Mechanism	835
d052	**I.E.Garkusha**	Investigation of the Erosion Coefficients of Boron Carbide and Tungsten Irradiated by the High Power Plasma Streams	839

Topic E PLASMA HEATING AND CURRENT DRIVE 841

Oral Presentations 843

e010 **(OP5)**	**S.J.Gee**	Current Amplification in the SPHEX Spheromak Operated as a Helicity Injected Tight Aspect Ratio Tokamak	843
e007 **(OP22)**	**H.P.Laqua**	Resonant and Non-Resonant Electron Cyclotron Heating at Densities Above the Plasma Cut-off by O-X-B Mode Conversion at W7-AS	847

Poster Contributions 851

e001	**A.G.Peeters**	Extension of the Ray Equations of Geometric Optics to Include Diffraction Effects	851
e003	**V.V.Bulanin**	Microturbulence Behaviour Study during LH-Heating in FT-2 Tokamak by CO_2-Laser Scattering	855
e004	**V.V.Dyachenko**	Investigation of the Decay Waves at $f=f_0-n \cdot f_{ci}$ in LH Experiments on the FT-2 Tokamak	859
e005	**G.T.Hoang**	Investigation of Lower Hybrid Wave Damping	863
e006	**M.Rome**	Effect of the Radial Drift of Trapped Suprathermal Electrons on the ECRH Power Deposition Profile	867

e008	**A.G.Peeters**	First ECRH Experiments in ASDEX-Upgrade	871
e011	**K.M.Rantamaki**	Simulations of Fast Particle Generation by LH Waves near the Grill	875
e012	**A.I.Lyssoivan**	A Study of ICRF Plasma Production for Tokamak Start-up and Wall Conditioning Purposes in TEXTOR-94	879
e013	**O.Tudisco**	Electron and Ion Temperature Response to Localized ECRH at 140GHz, 0.5MW, Fundamental Resonance, in the FTU Tokamak	883
e017	**Ph.Bibet**	Numerical Simulation of the Coupling Properties of Advanced Lower Hybrid Wave Launchers	887
e018	**I.N.Rosum**	Turbulent Heating of Magnetized Inhomogeneous Plasma by Lower Hybrid Radiation	891
e020	**V.V.Olshansky**	Modelling of Electron-Ion Parametric Turbulence for Ion Bernstein Waves	894
e021	**V.I.Lapshin**	Splitting the Eigen Frequencies of Fast Magnetosonic and Alfven Waves with Bumpy Magnetic Field	898
e023	**A.I.Pyatak**	Quasilocal Cherenkov Absorption of MHD Waves by Electrons in a Tokamak	902
e024	**N.Marushchenko**	Suprathermal Ion Generation at Fundamental Minority Cyclotron Resonance Heating	906
e025	**C.B.Forest**	Fast Wave Heating and Current Drive in Tokamak Plasmas with Negative Central Shear	910
e026	**Yu.V.Petrov**	Efficient ICRF Heating of D^+-H^+ Plasma Containing Small Boron Admixture on T-11M Tokamak	914
e027	**A.A.Kabantsev**	Effect of a Nonuniform Radial Electric Field on Sheared Toroidal Rotation and Bootstrap Current	918
e028	**V.E.Moiseenko**	Localized Global Eigenmodes and Mode Conversion Zones in ICRF	922
e029	**V.V.Plyusnin**	Plasma Production Below the Ion Cyclotron Frequency with Crankshaft Type Antenna	926
e031	**S.K.Sipila**	Bipolar Modification of Bootstrap Current Density by Localized RF Heating	930
e032	**E.Westerhof**	ECCD Experiments in RTP	934
e033	**E.Westerhof**	Propagation of a Wave Beam through Cyclotron Resonance	938
e036	**Y.Peysson**	Study of the 2D Fast Electron Momentum Dynamics during Lower Hybrid Current Drive	942

e040	**R.Cesario**	Study of the Waveguide Antenna Coupling of the Ion Bernstein Wave Experiment on FTU	946
e041	**N.Marushchenko**	Bounce Averaged Fokker-Planck Code for the Simulation of ECRH at W7-AS	950
e042	**P.Brooker**	Characterization of LHCD Suprathermal Electron Distributions on TdeV	954
e043	**V.S.Marchenko**	Efficient Impurity Extraction with Moderate Power Off-Axis ICRF Heating in a Rippled Tokamak	958
e044	**K.N.Sato**	Cold Front Propagation and Fast Non-Local Temperature Response in Pellet Injected Heliotron E Plasma	961
e049	**S.Heuraux**	Self-Consistent Currents on ICRH Antenna and Screen Parts Taking into Account Magnetic Shielding	965
e050	**A.Ekedahl**	Profile Control in JET with Off-Axis Lower Hybrid Current Drive	969
e051	**J.A.Heikkinen**	Dynamics of ECRH Current Drive in the Presence of Source Frequency Tuning	973
e053	**Yu.M.Voitenko**	Anomalous Resistivity and Energy Release in the Low-Beta Electromagnetoplasma	977
e055	**J.J.Martinell**	On Plasma Rotation Driven by Ponderomotive Forces	981

PART III

Topic F DIAGNOSTICS 985

Oral Presentations 987

f036 (OP10)	**D.Voslamber**	Determination of the D/T Fuel Mixture Using Two-Photon Laser Induced Fluorescence in Combination with Neutral Beam Injection	987
f052 (OP17)	**L.Krupnik**	An Advanced Heavy Ion Beam Diagnostic for the TJ-II Stellarator	991
f054 (OP23)	**A.V.Krasilnikov**	TFTR D-T Neutron Spectra Investigation Using Natural Diamond Detectors	995

Poster Contributions 999

f002	**A.N.Veklich**	The Fast Scanning Interferometry of High Density Plasma	999
f004	**T.Geist**	Frequency Shift of Reflectometry Signals due to Rotation of Density Turbulence in W7-AS	1003

f005	**S.Fiedler**	Investigation of the Neutral Gas Distribution on W7-AS Using the Monte-Carlo Code EIRENE in Combination with the Li-Beam Diagnostic	1007
f006	**W.Suttrop**	Measurement of Fast Density Profile Changes by FM Broadband Reflectometry on ASDEX Upgrade	1011
f007	**J.Gafert**	Investigation of Ion Dynamics in the ASDEX Upgrade Divertor by High Resolution Spectroscopy: First Results on Ion Drift Velocities	1015
f009	**P.T.Lang**	On the Possibility of q-Profile Measurement by Observation of Pellet Ablation by a Fast-Framing Camera at ASDEX Upgrade	1019
f010	**J.Stober**	Profiles of Ion Temperature and Neutral Density from the Simulation of Charge Exchange Measurements and Additional Experimental Data	1023
f011	**M.Schittenhelm**	Interpretation of Mirnov Measurements in ASDEX Upgrade	1027
f012	**V.Johnson**	Measurements of Impurity Transport in SPHEX Spheromak and START Tokamak	1031
f013	**H.Weisen**	X-Ray Tomography on TCV	1035
f014	**V.I.Afanassiev**	He^+ Halo Formation during Neutral Beam Injection into Magnetically Confined Plasma	1039
f015	**V.I.Afanassiev**	Possibility of Using Li^+ Fraction of Lithium Atomic Beam for Fusion Alpha-Particle Diagnostics	1043
f018	**K.N.Sato**	Development of a Spatially Resolved, Steady-State Bolometer for LHD Core and Divertor Plasmas	1047
f021	**V.K.Kiseliov**	Submillimeter Laser Interferometer-Polarimeter for Plasma Diagnostics	1051
f022	**V.K.Kiseliov**	A Set of Quasioptic Submillimeter-Wave Devices for Thermonuclear Plasma Diagnostics	1055
f023	**O.A.Bashutin**	Three-Mirror Laser Interferometer for Diagnostics of Thermonuclear Plasma	1059
f025	**G.P.Ermak**	High-Stable Millimeter-Wave Vector Analyzer	1063
f026	**G.P.Ermak**	Ultrafast Millimeter Wave Amplitude Modulator for Reflectometry of Plasma	1066
f027	**E.Z.Gusakov**	Plasma Current Profile Diagnostics on FT-2 Based on the Correlation Reflectometry Measurements of MHD Modes	1068
f028	**O.Tudisco**	Two Colour Interferometer for Density Measurements on FTU	1072
f029	**D.Pacella**	A Comprehensive Analysis of Impurity Transport in FTU Plasmas	1076

f030	**K.G.McClements**	Interpretation of Measurements of ICRF-Heated Minority Proton Distributions in JET	1080
f031	**A.G.Koval**	The Research of Charged Component of Controlled Fusion Installation Constructive Materials Sputtering Products	1084
f034	**M.N.Beurskens**	Double Pulse Thomson Scattering at RTP: First Results	1088
f035	**V.Basiuk**	Fast Ion Losses during Neutral Beam Injection on Tore Supra: Experiments and Simulations	1092
f037	**Y.Peysson**	Fast Electron Bremsstrahlung Tomographic System on Tore Supra	1096
f039	**M.Yu.Kantor**	Photon Recycling Thomson Scattering Diagnostics for Precise Measurements of Electron Temperature Evolution at Fast Transient Processes in Plasma of FT-2 Tokamak	1100
f040	**P.Sosenko**	Electromagnetic Wave Scattering from Turbulent Density Fluctuations in Fusion Plasma	1104
f041	**D.L.Grekov**	Propagation of the Microwave Beams in Magnetized Inhomogeneous Plasmas	1108
f044	**Yu.Dnestrovskij**	The Sensitivity of Algorithm of Charge Exchange Neutrals Spectra Elaboration to Various Perturbations	1112
f046	**V.A.Bryzgunov**	X-Ray Spectroscopic Set Study for ITER	1116
f047	**V.L.Berezhnyj**	Effect of Plasma, Neutron Irradiation and Heating on the Carbon Graphites Elements of mm and sub-mm Diagnostics for a Fusion Plasma	1120
f048	**A.I.Skibenko**	Density Fluctuation Studies for the "Uragan-3M" Torsatron via Microwaves	1124
f049	**W.Bohmeyer**	Test of Mirrors for Optical Diagnostics in ITER	1128
f051	**I.P.Zapesochny**	Laboratory Modeling of Elementary Processes in Plasma	1132
f053	**E.Z.Gusakov**	The Two-Dimensional Theory of Reflectometry Diagnostics of Plasma Fluctuations	1136
f055	**K.J.McCarthy**	A Temporal Study of CV Line Ratio Variations Across the TJ-IU Torsatron	1140
f056	**M.Sadowski**	Application of CR-39 and PM-355 Nuclear Track Detectors for Measurements of Fast Ions from High-Temperature Plasmas	1144
f057	**G.Leclert**	One-Dimensional Fluctuation Reflectometry: Enhanced Cut-off Response due to Large Amplitude Localized Fluctuations	1148

f058	**G.Leclert**	Spectral Effects in 1-D Fluctuation Reflectometry: Analytical and Numerical Investigation of the Phase Shift due to Small Amplitude Localized Fluctuations	1152
f059	**F.A.Karelse**	Current Density Profile Evolution Measured with the Triple Laser Polarimeter at RTP	1156
f061	**V.Zdrazil**	Determination of the Temperature of Non-Homogeneous and Non-Stationary Plasma	1160
f067	**V.F.Gubarev**	Plasma Boundary Determination from Magnetic Measurements in Eddy Currents Presence for Tokamak	1164

Topic G BASIC COLLISIONLESS PLASMA PHYSICS 116

Oral Presentations 1171

g013 (OP11)	**J.H.Misguich**	Percolation Scaling Law for Turbulent Diffusion	1171
g015 (OP18)	**T.J.Schep**	Geometrical Approach to Hamiltonian Fluids	1175

Poster Contributions 1179

g001	**Yu.I.Chutov**	Relaxation of Electron Oscillations in Bounded Non-Neutral Plasmas with Dust Particles	1179
g002	**A.Yu.Kravchenko**	Some Properties of Plasmas with Dust Particles	1183
g004	**T.A.Davydova**	Shortwavelength Langmuir and Upper Hybrid Solitons	1187
g006	**S.Medvedev**	External Kink Mode Stability of Tokamaks with Finite Edge Current Density in Plasma Outside Separatrix	1191
g008	**N.A.Azarenkov**	Mechanisms of Self-Interaction of Magnetoplasma Surface Waves at the Plasma-Metal Interface	1195
g011	**V.Lapshin**	Global Strongly Nonlinear Structures in Bounded Plasma-Relativistic Beam System	1199
g012	**S.K.Kim**	Observation and Control of a Steady-State, Non-Monotonic Double Layer in a Triple Plasma Machine	1203
g014	**E.Westerhof**	Numerical Studies of Dipole Drift-Vortices	1207
g016	**C.Riccardi**	Drift Waves Destabilization in a Toroidal Plasma	1211

g017	**C.Riccardi**	Experimental Analysis of Waves Modifications in Presence of Ponderomotive Effects	1215
g018	**K.Akimoto**	Interaction of Ultra-Short Electromagnetic Pulses with Plasmas	1219
g020	**V.L.Selenin**	Study of the Two-Plasmon Decay of Lower Hybrid Waves by Enhanced Scattering Techniques	1223
g022	**Zh.Andrushchenko**	Ballooning Vortices in a Plasma with Hot Particles	1227
g032	**A.Atipo**	Experimental Control of Chaos in a Glow Discharge Using Spatial Autosynchronization	1231
g034	**D.A.Keston**	Bernstein Modes in a Weakly Relativistic e^-e^+-Plasma	1235
g036	**V.A.Buts**	Development of Dynamical Chaos under Nonlinear Interaction of Waves in Magnetized Beam-Plasma Systems	1239
g037	**A.P.Tolstoluzhsky**	Development of Dynamical Chaos under Nonlinear Interaction of Waves in Unbounded Unmagnetized Plasma	1242
g038	**O.V.Manuilenko**	Development of Dynamical Chaos under Nonlinear Interaction of Waves in Bounded Magnetized Plasma	1246
g040	**I.Onishchenko**	Radiation Spectrum Broadening in Beam-Plasma Interaction, Caused by Induced Scattering	1249
g043	**L.N.Vyacheslavov**	Manifestation of Wave Collapse in Developed Strong Langmuir Turbulence in a Magnetic Field	1253
g044	**V.Grimalsky**	Nonlinear Surface Waves in Electronic Plasma	1257
g046	**T.A.Davydova**	Nonlinear Structures Near Marginal Stability Boundary in Tokamaks	1261
g047	**V.M.Lashkin**	Influence of Small-Scale Fluctuations on Coherent Structures in Ion-Temperature-Gradient-Driven Turbulence	1265
g051	**V.I.Karas'**	2,5-Dimensional Numerical Simulation of Propagation of the Finite Sequence of Relativistic Electron Bunches (REB) in Tenuous and Dense Plasmas	1269
g053	**S.M.Zinevych**	Fluctuations and Collective Wave Scattering in Collisional Plasma	1273
g054	**A.Zagorodny**	Diffusion Influence on the Electron Density Fluctuations in Turbulent Magnetoactive Plasmas	1277
g055	**A.E.Kobryn**	The Solution of Enskog-Landau Kinetic Equation Using Boundary Conditions Method	1281

g057	**I.P.Yakimenko**	Hydrodynamic Interactions and Fluctuations in Suspensions in Compressible Fluids	1285
g058	**T.Chmyr**	Fluctuation Theory of Bremsstrahlung in a Plasma with Fluid-Like Random Motions	1289
g062	**Yu.M.Voitenko**	Kinetic Alfven Turbulence Excitation by the External Electric Field $E_0 \parallel B_0$ in a Low-β Magnetoplasma	1293

Topic H HIGH INTENSITY LASER PRODUCED PLASMAS AND INERTIAL CONFINEMENT 1298

Poster Contributions 1299

h001	**G.N.Burlak**	Nonlinear Modulation of Strong Electromagnetic Wave in Weakly Inhomogeneous Plasma	1299
h003	**A.D.Suprun**	Determination of Appearance and Development Conditions for Plasmas Plume-Source Produced by High Intensity Laser: Theory and Numerical Experiment	1303
h005	**J.S.Bakos**	Investigation of the Expansion of an Aluminum Micro-Pellet Cloud in a Hot Plasma	1307
h008	**V.I.Karas'**	High-Current Ion Beam Acceleration and Stability in Two Accelerating Cusps of Induction LINAC	1311

Topic I ASTROPHYSICAL AND GEOPHYSICAL PLASMAS 1317

Oral Presentation 1317

i001 (**OP24**)	**T.Shcherbinina**	To the Theory of Decameter Jovian Radioemission S-Bursts with Positive Drift	1317

Poster Contributions 1321

i002	**E.P.Kontar**	Propagation of Electron Beams in Solar Magnetic Loops	1321
i005	**A.K.Yukhimuk**	Nonlinear Mechanism of Electromagnetic Radiation Generation in Space Plasmas	1325
i006	**I.K.Konkashbaev**	Interaction of the Inherent Atmosphere of the Spacecraft Moving in the Vicinity of the Sun with Solar Wind	1329
i007	**A.V.Chechkin**	Generation of Large-Scale Structures in Gradient-Drift and Rossby Wave Turbulence	1333
i008	**A.A.Boeva**	A Nonsteady Magnetic Lateral Shock Wave in Cosmic Plasma	1337

i009	**O.Verkhoglyadova**	Large-Scale Structure Formation in the Cometary Ionosphere due to Plasma Streams	1341
i018	**E.H.Farshi**	On the Possible Generation of Gamma-Bursts in the Plasma Pinches	1345
i019	**E.H.Farshi**	"Semi-relativistic" Model of the Cosmic Ray Generation in a Plasma Pinch	1349
i020	**I.O.Anisimov**	Radioemission of the Modulated Electron Beam in the Accidentally Inhomogeneous Plasmas	1353
i021	**I.O.Anisimov**	On the Possibility to Observe the Whistler Modes Transitional Radiation in the Beam-Plasma Experiments in the Ionosphere	1357
i024	**A.N.Kryshtal**	To the Problem of Generation Mechanism of Solar Type III Bursts	1361
i025	**Yu.V.Khotyaintsev**	Nonlinear Low-Frequency Waves in Magnetized Space Plasma	1364
i026	**V.Kubaichuk**	Plasma-Current-Produced Charging of a Dust Particle	1368
i027	**O.Bystrenko**	Effective Forces in Dusty Plasmas and Colloidal Suspensions	1372
i033	**D.A.Dziubanov**	Cyclical Variations of the F2 Region Parameters from the Incoherent Scatter Radar Data	1376
i034	**Yu.I.Podyachy**	The Phase Relationships of Electron Density and Ionospheric Plasma Temperature Variations in the Gravitational Wave Propagation	1380
i035	**T.G.Zhivolup**	The Role of Excited Molecular Ions in the Variation of the E-Layer Peak Height with Changeable Solar Activity	1384

Topic J LOW-TEMPERATURE PLASMAS 1389

Oral Presentation 1391

j019 (**OP12**)	**M.Kraemer**	Experimental Sudy and Modeling of a Pulsed Helicon Discharge	1391

Poster Contributions 1395

j002	**P.L.Dan'ko**	Electron Emission from Materials Processed by Pulsing Gas-Discharge Plasmas	1395
j003	**V.S.Yakovetsky**	Computer Modeling of a Plasma Jet Expanding into Vacuum Vessel	1399

j005	**O.I.Gerasimov**	Elastic Charged Particle Scattering by Centers with Coulomb and Short-Range Potentials	1403
j006	**V.M.Yakovenko**	Surface Helicons in Plasma-Like Media and their Collisionless Damping	1407
j009	**K.P.Shamrai**	Excitation and Absorption of Waves in a Helicon Plasma Source	1411
j010	**V.B.Taranov**	Wave Spectra and Impedance of Antennas Driving Helicon Plasma Sources	1415
j011	**P.V.Poritsky**	On Fractal Dimension of Plasma Leader Channel under Electrical Breakdown	1419
j012	**S.K.Kim**	Frequency-Resonant Behaviours of Plasma Density in the Helicon RF Plasma	1422
j014	**V.D.Yegorenkov**	Analytical Model of Electric Field Pattern in a Collisional Low Pressure RF Discharge	1426
j015	**V.D.Yegorenkov**	Determination of Electron Transport Coefficients from Breakdown Curves of RF and Combined Discharges	1430
j016	**V.Levandovskii**	The Effect of Slightly Excited Electron Plasmas on Phase Transitions in Solids	1434
j021	**I.O.Anisimov**	Evolution of the Space Charge Waves of the Electron Beam in the Overcritical Plasma Barrier	1438
j026	**V.V.Kulish**	Acceleration of Quasi-Neutral Plasma Bunches in Crossed EH-Undulated Fields	1442
j030	**V.I.Golota**	Investigations of High-Pressure Glow Discharge with High-Speed Pumping	1446
j032	**V.V.Chebotarev**	Investigation of the Quasistationary Plasma Flow in the Axial Magnetic Field and Modeling Experiments on the Current Disruption	1450

POSTDEADLINE PAPERS 1455

Oral Presentation 1457

pd022 (**OP8a**)	**M.J.Walsh**	Record Central Beta Produced by NBI in the START Spherical Tokamak	1457

Poster Contributions 1461

pd003	**A.Glushkov**	Resonances in Strong External Fields in Atomic Spectra Autoionization Resonances in Tm	1461
pd004	**A.Glushkov**	Spectroscopy of the Atom in Laser Field: Deformation of Radiation Atomic Lines. Multi-Photon Processes. Absorption Spectra of Dense Nonideal Plasma: QED Approach	1466

pd005	**A.Glushkov**	Spectroscopy of Ne-Like Multicharged Ions and Ne-Like Plasma as an Active Medium for X-Ray Lasing: Atomic Data	1471
pd011	**L.V.Poperenko**	Ellipsometrical Investigations of Stainless Steel Mirrors Irradiated by Chromium Ions	1473
pd013	**M.Tunklev**	Spectroscopic Investigation of Carbon IV	1477
pd016	**V.M.Malnev**	Influence of the Earth Electrostatic Field on Sodium Atoms Emission from the D-Ionosphere	1481
pd017	**V.N.Malnev**	Formation of a New Phase Nucleus in an Excited Dipole Plasmas	1485
pd019	**H.Abbasi**	The Influence of Electron Trapping on the Propagation of the Electrosound Waves in Plasma	1489
pd020	**C.M.Greenfield**	Improved Fusion Performance in Low-q, Low Triangularity Plasmas with Negative Central Magnetic Shear	1493
pd023	**J.A.Heikkinen**	On Channeling of ICRF Minority Tail Energy	1497

F

DIAGNOSTICS

Determination of the D/T fuel mixture using two-photon laser induced fluorescence in combination with neutral beam injection

D. Voslamber and W. Mandl

Ass. EURATOM-CEA, DRFC-SPPF, CEN Cadarache, F-13108 St. Paul-lez-Durance

Introduction

In nuclear fusion experiments which use a D/T fuel mixture and in future fusion reactors the control and therefore the measurement of the D/T density ratio is indispensable for the optimisation of the fusion rate. For complete information, isotope-specific knowledge is required on the ion density profiles in the plasma bulk as well as on the neutral density profiles in the plasma edge. For the isotope-selective determination of neutral densities (H,D,T) a method based on Doppler-free two-photon induced laser resonance fluorescence (in Ly-α) has been suggested previously [1,2]. This diagnostic is local and time-resolved but requires fairly high neutral densities which, at least in large tokamaks, are only found in edge and divertor regions. In the present contribution we address the question whether this method can be extended farther into the plasma bulk by using a neutral diagnostic beam and exploiting the thermal neutrals that are created by charge exchange between the beam neutrals and the plasma ions.

Doppler-free two-photon spectroscopy

Two-photon excited laser resonance fluorescence can be made isotope-selective by an (approximate) elimination of linear Doppler broadening in the excitation process. This is achieved by the use of two counter-propagating laser beams, each having half the selected atomic resonance frequency and providing one photon to an atomic excitation. The linear Doppler shifts of the two photons have then opposite sign and cancel each other in the sum of the two frequencies. Hence all atoms, irrespective of their velocity, are in resonance with the two laser beams. While the two-photon absorption lines are thus Doppler-free, the fluorescence lines are not; these, however, can be separated by introducing a short time delay between the two laser shots for D and T.

For a quantitative treatment of the excitation process one has to account for the Stark-Zeeman effect caused by the external fields $\vec{B}$ and $\vec{v}\times\vec{B}$. Among the various possible schemes we consider here the case where excitation and fluorescence occur in the Lyman-α line. Only the central component of the upper (n=2) hydrogen level triplet can be excited efficiently, because its position is nearly unperturbed by the external fields and gives thus rise to a narrow peak in the two-photon absorption profile. The same is not true for the outer components of the triplet whose dependence on the atomic velocity leads to a large thermal spread of their positions and to corresponding large wings of the absorption profile.

Figure 1 shows some spectral profiles of the central component of the two-photon absorption line for D and T atoms in a plasma with equal portions of D and T. The normalisation is such that the surface under the curves is proportional to the frequency-integrated two-photon transition strength and to the probability of fluorescence emission perpendicular to the magnetic field. The shapes of the spectral profiles are influenced by several broadening mechanisms: quadratic (relativistic) Doppler broadening, motional Stark broadening (arising from the effect of the electric $\vec{v}\times\vec{B}$ field on the fine-structure components), plasma Stark broadening (predominantly due to atom-ion collisions) as well as

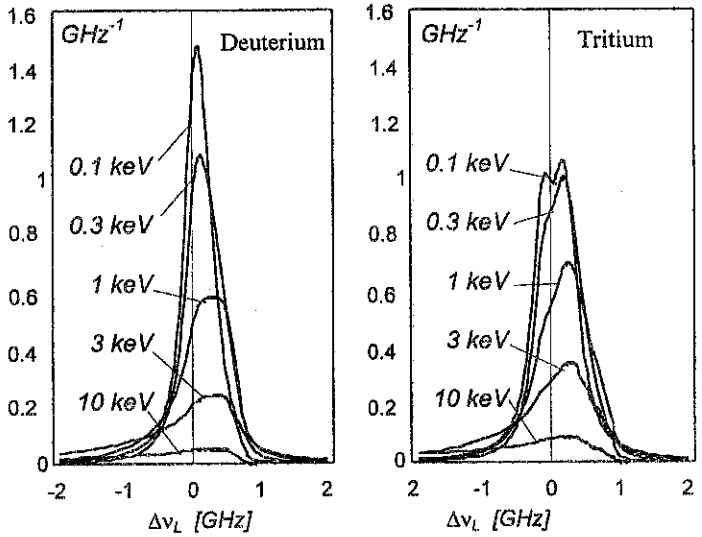


Fig.1. Profiles (as functions of laser detuning) of central component of D and T atoms in a D/T plasma for various temperatures. *(B=4T, n_e=3 $10^{19}m^{-3}$, n_{D+}/n_{T+}=1, Z_{eff}=1)*

distorting effects arising from the influence of fine and hyperfine structure. Not included in the profiles of Fig.1 is the residual linear Doppler broadening originating from the finite angle divergence of the laser beams and the additional broadening introduced by the finite laser bandwidth. From Fig.1 the total line width is seen to be at most a few GHz. This is much smaller than the 113 GHz in laser frequency which separate the deuterium and tritium lines.

The peak intensities of the profiles are seen to decrease noticeably with increasing temperature. The reason is that for larger temperatures one has both a lowering of the two-photon transition strength and an enlargement of the quadratic Doppler width. In contrast to the peak intensities themselves, their ratios I_D/I_T taken from deuterium and tritium profiles at identical plasma conditions depend only weakly on the plasma parameters. Therefore, rough knowledge of these parameters from independent diagnostics suffices for the determination of the fuel mix n_{D0}/n_{T0}. Determining density ratios rather than absolute densities has also the advantage of avoiding absolute calibration.

Detection limit and required laser performance

To establish the detection limit for the neutral densities n_{D0} and n_{T0}, the following assumptions have been made: (a) the signal-to noise ratio is dominated by the shot noise of the detector, (b) the detected photon numbers obey Poisson statistics, (c) the background radiation at the Lyman-α wavelength is of the order of $10^{19}m^{-2}s^{-1}sr^{-1}$. This number is characteristic of the cool edge emission and is relatively independent of the size of the tokamak. It is usually much larger than the Bremsstrahlung, even in a tokamak like ITER. In case a neutral beam is used, background radiation by excited beam-created neutrals has also to be considered. For neutral densities near the detection limit this contribution turns out to be much smaller than the cool edge emission. For high neutral densities it may become more

intense, but then the signal-to-noise ratio is so large that the background radiation does no harm.

On the basis of the assumptions mentioned and with the use of customary optical parameters, the neutral density detection limit n_{crit} is found to be of the order of 10^{14} m^{-3}. While n_{crit} is relatively independent of the plasma parameters, the laser characteristics that are required for producing sufficient fluorescence signals (when n_{D0}, $n_{T0} \geq n_{crit}$) strongly depend on them. This is particularly the case for the pulse energy which has to increase with temperature (roughly scaling as $T^{3/2}$) so as to compensate for the decreasing peak intensities of the two-photon absorption profile (see Fig.1). Up to about *1-2 keV*, *30-50 mJ* pulse energy suffice to attain signal-to-noise ratios of the order of two (when n_{D0}, $n_{T0} = n_{crit}$). However, to achieve the same at *15 keV* the required laser energy approaches the order of *1 J*.

At PTB Berlin [3] a laser spectrometer has been developed which is tunable at 243 nm (which corresponds to half the Ly-α frequency), has bandwidth $\leq$ *0.5 GHz* and delivers pulses of *2.5 ns* duration with energies up to *50 mJ*. The beam divergence (typically *0.3 mrad*) is sufficiently small for residual Doppler broadening to be negligible. With these performances the diagnostic should be applicable in edge and divertor regions of large tokamaks, such as ITER; it should further be applicable in the main plasma up to temperatures of *1-2 keV* if there is some way to create neutral densities in excess of n_{crit}.

Use of a diagnostic neutral beam

The objective of using a neutral beam in the present context is the creation of thermal neutrals (with n_{D0}, $n_{T0} \geq n_{crit}$) via charge exchange (CX) between the beam neutrals and the plasma ions. In addition to the benefit of probing regions deeper in the bulk, this has also the advantage that the information obtained from the fluorescence actually concerns the ion density ratio, which appears still more relevant than the isotopic neutral density ratio.

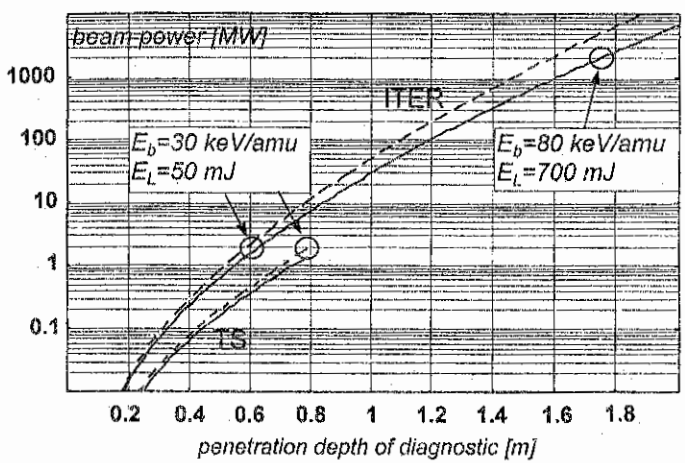


Fig.2. Required neutral beam power as a function of the penetration depth of the diagnostic. The plasma parameters correspond to those of TS shot 14317@5s in the lower curves and to an ITER model in the upper curves. The solid lines are for Z_{eff}=*1*, the dashed lines for Z_{eff}=*2*. The beam particle energy E_b and the laser pulse energy E_L are indicated for three experimental situations.

In order to study the possible performance of such a technique, we have done a model calculation for a D beam penetrating a D plasma that may contain some C^{6+} impurities (Z_{eff}=1 and 2). The calculation consists of four steps. First the beam attenuation is evaluated as a function of the plasma radius r, accounting for ionising collisions with electrons and ions and for CX. Second the density profile $n_{D0}(r)$ of thermal D atoms is calculated from their birth rate due to CX and their loss rate due to ionisation and diffusion out of the neutral beam. Third the optimal beam particle energy (the one leading to the highest $n_{D0}(r)$) is calculated as a function of r. The existence of an optimum results from an opposite dependence of beam penetration and CX cross section on the beam energy. Fourth, the beam power required for attaining n_{crit} is calculated as a function of r. In steps 1 and 2, the cross sections for beam attenuation have been taken from ADAS [4], those for ionisation by ion collisions from Aladdin [5].

Choosing a beam radius of *10 cm*, the calculation has been applied to two cases of different plasma conditions, one corresponding to an ohmic discharge of TS (#14317@5s, flat n_e profile with $n_e(0)=5.7\ 10^{19} m^{-3}$, $T_e(0)=1.8\ keV$, plasma radius $a=0.8m$), the other to an ITER model ($n_e(r)=1.4\ 10^{20}\ (1-(r/a)^2)^{1/2}\ m^{-3}$, $T_e(r)=20\ (1-(r/a)^2)^2\ keV$, $a=3m$). The results are shown in Fig.2, which presents the beam power required for attaining the detection limit as a function of the penetration depth of the diagnostic (distance from the edge). It is seen that with a beam power of e.g. *2 MW* the diagnostic might be applied to the total outer plasma radius of a tokamak like TS (right lower circle) and covers about *60 cm* of the outer plasma radius of the ITER model (left lower circle). In both situations the beam particle energy and the required laser pulse energy are about *30 keV/amu* and *50 mJ*, respectively. As an example of a short-pulse ($\approx$ *1* μs) multi-GW beam (under development, but not yet accomplished [6]) we also consider a beam power of *2 GW* and find that with such a beam the diagnostic would cover *1.6 - 1.8 m* of the outer plasma radius of a tokamak like ITER (upper circle). In this case the beam particle energy and the required laser pulse energy would be about *80 keV/amu* and *700 mJ*, respectively.

We note that further diagnostic output, besides the isotope mix, can in principle be obtained by tuning the laser over the atomic resonances (assuming sufficiently narrow laser bandwidth) and also by exciting the fast beam atoms in addition to the atoms generated by charge exchange. Information on the ion temperature *or* Z_{eff} (according to whether quadratic Doppler or plasma Stark broadening prevails) can in principle be obtained from the line profiles (Fig.1). By crossing the two laser beams under a small angle, the ion velocity distribution (implying the temperature) and the plasma rotation velocity component perpendicular to the laser beam direction can in principle be inferred from the linear Doppler broadening thus introduced. Excitation of the fast beam neutrals (in the outer π components of the Stark triplet) would induce fluorescence lines displaced by a large Doppler shift from that of the CX-created neutrals. Their polarisation (perpendicular to the electric $\vec{v} \times \vec{B}$ field) would yield information on the q-profile analogously to the classical MSE experiments, while their intensity would be a measure of the beam attenuation.

References

[1] D. Voslamber, report EUR-CEA-FC-1387 (1990)

[2] D. Voslamber, in Spectral Line Shapes, Vol.8 (AIP Conf. Proc. 328), Ed. A.D.May, J.R.Drummond, E.Oks, AIP Press, New York 1995

[3] K. Grützmacher et al, in Diagnostics for Experimental Thermonuclear Fusion Reactors, Ed. P.E.Stott et al, Plenum Press, New York 1996

[4] Atomic Data Analysis Structure of JET, files adf02, adf07

[5] Aladdin data base, ORNL-6086/V1

[6] D.J. Rej et al, Rev. Sci. Instrum. 63, 4934 (1992)

AN ADVANCED HEAVY ION BEAM DIAGNOSTIC FOR THE TJ-II STELLARATOR

L. Krupnik[1], I. Nedzelskij[1], Yu. Trofimenko[1], C. Varandas [2], A. Malaquias[2], A.Melnikov[3], C. Hidalgo [4], I. Garcia-Cortes[4]

[1] *Institute of Plasma Physics, NSC "KhIPT", Kharkov, Ukraine*

[2] *Associacion EURATOM/IST, Centro de Fusao Nuclear, Lisbon, Portugal*

[3] *Institute of Nuclear Fusion, RRC "Kurchatov Institute", Moscow, Russia*

[4] *Associacion EURATOM/CIEMAT, para Fusion, Madrid, Spain*

1. INTRODUCTION.

The Heavy Ion Beam Probe (HIBP) diagnostic is known as a powerful tool for the investigations of transport processes in plasmas of thermonuclear devices with magnetic confinement. It is able to measure the plasma potential, density, electron temperature and poloidal magnetic field profiles as well as their fluctuations with high temporal and spatial resolution [1].

Two different approaches of HIBP were developed based on two secondary ions detection schemes. We classify these schemes as the "classic" and "direct". In "classic" scheme the detector grid is formed by changing the beam energy and injection angle with arrangement of the detector in one distinct point [2]. The "direct" scheme uses a multiple cell array (MCA) detector which collects the secondary ions created along primary beam trajectory [3]. The "classic" detection scheme is more convenient for the measurements of plasma potential with electrostatic energy analyzer while plasma density, electron temperature and poloidal magnetic field measurements are easier to conduct by "direct" detection.

This paper presents an advanced HIBP diagnostic that has been developed for TJ-II stellarator based on the simultaneous utilization of both detection systems. TJ-II is a medium size stellarator with 4 periods, 1.5 m major radius and 1 T nominal magnetic field [4]. The effective radius of the plasma can vary from 0.1 to 0.2 m, depending on operational mode.

2. HIBP GEOMETRY OPTIMIZATION.

The HIBP design is based on the trajectory calculations of probing particles in the magnetic field of plasma device and simulation of beam attenuation effect.

2.1. Ions trajectory calculations.

The complexity of the TJ-II magnetic configuration defines a strong three dimensional

nature of beam trajectories that requires a special consideration to determine the optimum geometrical arrangement of the HIBP installation. The main problem of HIBP geometry optimization arises from the high flexibility of TJ-II operational modes. The search of the best location of the energy analyzer shows the impossibility to obtain only one collection point for all the modes without degradation of the detector grids. However, a regime dependent distribution of the collection points along a distinct collection line was found. Fig.1 presents the sets of optimized detector grids covered the plasma cross section in different operational modes of TJ-II. These grids are formed by the detector lines of constant energy (horizontal) and constant injection angle (vertical). The energies and injection angles for Cs^+ ions are in the range of 80-200 keV and $\pm$ 7.5^0. Note that the detector grids are three dimensional also with maximal deviation in the toroidal direction of $\pm$7 cm.

The effect of possible overlapping of secondary Cs^{2+} ions by tertiary Cs^{3+} ions in MCA detector, imposes another requirement to the optimization procedure. Fig.2 presents the Cs ions trajectories in optimized arrangement of MCA detector for the regime of TJ-II with moderate value of hard core currents I_h = 75 kA, I_c = 250 kA (HREF2 operational mode). The part of Cs^+ trajectory along which Cs^{2+} ions are created presents the effective detector line for MCA detector.

The comparison of Figs.1,2 shows that the proposed combine version of HIBP allows to conduct simultaneous measurements of plasma parameters in two different detector lines.

2.2. Simulations of the diagnostic beam attenuation.

A computational code was elaborated to estimate the secondary ion currents on the MCA detector and energy analyzer considering the attenuation effect of the plasma. This code includes the real electron density and temperature profiles as well as the experimental cross sections for the electron impact ionization processes $Cs^+ \rightarrow Cs^{2+}$, $Cs^+ \rightarrow Cs^{3+}$ and $Cs^{2+} \rightarrow Cs^{3+}$. The results of these calculations for the regimes with 800 kW ECRH ($n_e(0) = (1.5\text{-}2) \times 10^{13}$ cm^{-3}, $T_e(0)$ = 1 keV) and 2 MW NBI ($n_e(0) = 1.2 \times 10^{14}$ cm^{-3}, $T_e(0)$ = 350 eV) are shown in Fig.3. A strong attenuation of primary and secondary beams occurs in the NBI regime limiting the capabilities of HIBP measurements to electron density up to 2×10^{14} cm^{-3}.

3. THE TJ-II HIBP INSTALLATION.

The scheme of TJ-II HIBP installation is shown in Fig.2. It consists of Cs^+ injector, MCA detector electrostatic energy analyzer and a VME based control and data acquisition system (CDAS). The injector includes the thermoionic Cs+ ion source, accelerating tube and primary beam line with electrostatic plates and beam monitors. The self consistent active beam

control by two groups of the electrostatic plates is utilized in primary and secondary beam channels. It allows to minimize the dispersion of the entrance angles into analyzer [5].

The number of cells in MCA detector, their configuration and distribution can be chosen in order to obtain the plasma density and temperature measurements in radial and/or toroidal directions with the desirable spatial resolution. A special slit (5×15 cm^2) is foreseen in the detector assembly for the simultaneous operation of both detection systems.

The secondary beam energy analyzer is the most crucial part of the HIBP diagnostic. We shall use a standard 30^0 Proca-Green electrostatic plate analyzer [2]. The design of TJ-II HIBP analyzer was based on computer simulations which allowed to obtain optimum geometry from the point of view of minimization of the electric field nonuniformity. The operation with two entrance slits is foreseen for the potential correlation measurements.

The CDAS is composed by a 20 bit ADC, 110 ADC acquisition channels (512 kb, 1.2 Mhz) and 8 DAC control channels (512 kb, 1 MHz).

4. CONCLUSIONS.

An advanced HIBP diagnostic was developed for TJ-II stellarator based on the utilization of two different detector schemes: MCA detector and 30^0 Proca-Green electrostatic energy analyzer. This innovative design aims to spread and improve the HIBP capabilities in simultaneous measurements of plasma potential, density and electron temperature profiles as well as their fluctuations.

REFERENCES.

[1] T.P. Crowley and RPDL Team, "Rensselaer HIBP Diagnostic Methods and Techniques", IEEE Transactions on Plasma Science, vol.22, No 4, p.291, 1994.

[2] Yu. N Dnestrovskij, A.V. Melnikov, L.I. Krupnik, I.S. Nedzelskij, "Development of HIBP Diagnostics, ibid, p.310.

[3] J.A.C. Cabral, A. Malaquias, A. Praxedes, W.van Toledo, C.A.F. Varandas, "The Heavy Ion Beam Diagnostic for the Tokamak ISTTOK", ibid, p.350.

[4] C. Alejaldre et al, "TJ-II Project: A Flexible Heliac Stellarator", Fusion Technology, vol. 17, p. 131, 1990.

[5] A. Fujisawa, H.Iguchi, M. Sasao, Y. Hamada, J. Fujita, "Active Beam Control of Beam Trajectories for HIBP on Heliac Magnetic Configurations", Rev. Sci. Instrum., vol. 63, p. 3694, 1992

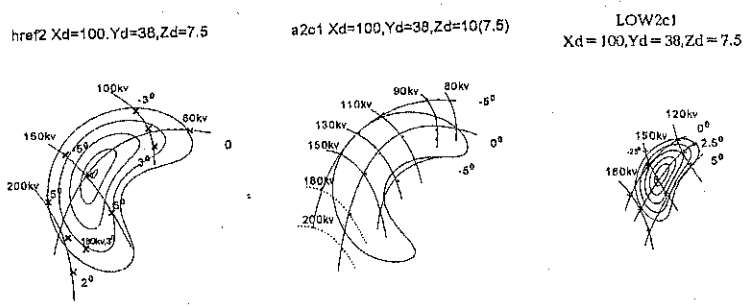


Fig. 1. Detector grids for different modes of TJ-II operation.

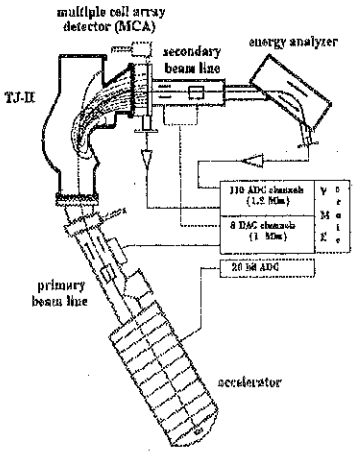


Fig. 2. TJ-II HIBP installation.

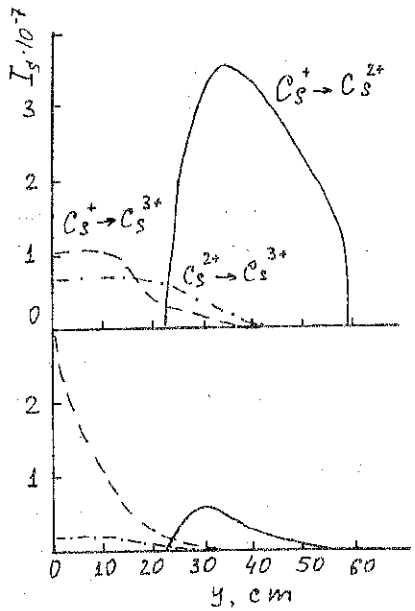


Fig.3. Results of attenuation effect simulation: ECRH regime (a), NBI regime (b).

TFTR D-T Neutron Spectra Investigation Using Natural Diamond Detectors

A. V. Krasilnikov,[1] N. N. Gorelenkov,[1] R. V. Budny, L. C. Johnson and A. L. Roquemore
Princeton Plasma Physics Laboratory, P.O.Box 451, Princeton, NJ , 08543-0451, USA
[1]Troitsk Institute of Innovating and Fusion Researches, 142092 Troitsk,
Moscow region, Russia

1. INTRODUCTION The high flux of 14 MeV neutrons during high power Deuterium - Tritium (D-T) Neutral Beam Injection (NBI) experiments on the Tokamak Fusion Test Reactor (TFTR) has made it possible to use neutron spectrometry to study the ion distribution under reactor-like conditions. During the 1995-96 experiments, discussed below, up to six NBI sources were aimed in the counter-direction and six in the co-direction, with a total power of up to 30 MW of 105 keV D-T injection. The TFTR ion distribution function during NBI as calculated by the 2-dimensional transport code, TRANSP [1], is non-Maxwellian and anisotropic. This anisotropy is directly reflected in the D-T neutron energy distribution so that a measure of its dynamics provides information about the ion energy distribution, transport and slowing down time of high energy particles and alpha-particle birth energy distribution.

2. DIAGNOSTIC ARRANGEMENT Natural diamond detectors (NDD) [2,3] were developed in Russia to be used as D-T neutron spectrometers [4]. Three of these spectrometers, with energy resolution 2-3 % and varying detection efficiency, have been placed in a variety of locations around the TFTR [5]. The sensitivities of the detectors and the speed of the signal processing electronics drive the location and shielding required for each detector [5]. The first detector (NDD1) was placed inside a central channel (R=268cm) of the TFTR vertical neutron collimator during the 1995 campaign to provide a view perpendicular to the plasma current axis. During the 1996 experiments NDD1 was moved to another collimator location closer to the plasma core with a larger aperture, (see Fig. 1) which increased the flux to the detector by ~20 times. The second detector (NDD2) was placed inside a small specially designed shielding enclosure in the TFTR test cell and provided measurements of the spectral broadening of 14 MeV neutrons having angles of emission of 60-120° with respect to the plasma current (see Fig. 2). This detector was placed 11m from the plasma axis, 2.6 m below the TFTR equatorial plane, and without collimation. During the 1995 experiments a third (NDD3) detector was placed in an open area near the test cell floor ~5 m from plasma axis (see Fig. 2) and provided measurements of neutrons with emission angles of 0-180°. In 1996 this detector was placed inside the TFTR fusion gamma shield with a viewing cone tangential to the plasma current axis in the TFTR midplane (see Fig. 2) and measured neutrons with emission angles in the range of 110-180° (counter direction) with respect to plasma current.

3. D-T NEUTRONS ENERGY DISTRIBUTION Examples of NDD pulse height spectra measured by three NDDs during 28 MW NBI heating in 1996 are shown in Fig 3. The full width at half-maximum (FWHM) of the $^{12}C(n,\alpha)^{9}Be$ line of the spectrum is a measure of the broadening of the energy distribution of the D-T neutrons that leave the plasma along the detector viewing cone and contains information about the corresponding mean effective ion temperature T_{eff}.

In the lab system the kinetic energy of the neutrons is given by [6]

$$E_n = \frac{1}{2}m_n V^2 + \frac{m_\alpha}{m_n+m_\alpha}(Q+K) + V\mu\sqrt{\frac{2m_n m_\alpha}{m_n+m_\alpha}(Q+K)} \qquad (1)$$

where V - is the center -of-mass velocity, Q - nuclear energy release of the reaction, K - relative kinetic energy, μ - is the cosine of the angle between V and neutron velocity in the center-of-mass system, m_n and m_α - neutron and alpha-particle masses.

For a Maxwellian plasma with ion temperature T, the analytical calculations [6] yield a D-T neutron spectrum in the Gaussian shape:

$$f(E_n) = \frac{1}{\sqrt{2\pi}\,\sigma_E} \times \exp\left(-(E_n - \langle E_n \rangle)^2 / 2\,\sigma_E{}^2\right) \quad (2)$$

where $\sigma_E{}^2$ is the standard deviation. The FWHM is given by

$$\Delta E_n = \sqrt{8 \ln 2}\,\sigma_E = \sqrt{\frac{16\, m_n T_i \langle E_n \rangle \ln 2}{m_n + m_\alpha}}, \quad (3)$$

where the average neutron energy is

$$\langle E_n \rangle = \frac{1}{2} m_n \langle V^2 \rangle + \frac{m_\alpha}{m_n + m_\alpha} (Q + \langle K \rangle). \quad (4)$$

For plasmas with ion temperatures in the range 30-50 keV,

$$\Delta E_n = 180 \sqrt{T_{eff}} \text{ (where } \Delta E_n \text{ and } \sqrt{T_{eff}} \text{ in keV).} \quad (5)$$

The ion component in TFTR contains both thermal and hot beam ions. The sources of thermal ions are gas puffing, recycling (few % T from the walls) and thermalization of beam ions. The emitted neutrons result from three interactions: beam-plasma (60-80%), beam-beam (~10%) and thermal neutrons (10-30%). To model the D-T neutron spectra measured by each of the three NDD's the Neutron Source post TRANSP (NST) code was developed. This code utilized TRANSP [1] to calculate deuterium and tritium plasma densities and temperatures as well as D and T beam distribution functions and applies fusion cross sections to derive the neutron emission spectra. This formulation is well known (see for example [7]). As seen below, reasonable agreement with measurement is obtained with this model. Spectral broadening of D-T neutrons escaping from the TFTR plasma with emission angles of 90°, $60\text{-}120^o$ and $0\text{-}180^o$, was observed during the 1995 experimental campaign by the NDD1, NDD2 and NDD3 respectively. These measurements were made with NBI power of between 10 - 30 MW and demonstrated for the first time the anisotropy of the ion distribution function in TFTR during high power NBI experiments. Because of the large momentum of T ions transferred to the center-of-mass of reacting nuclei, the FWHM of the beam-plasma neutron energy distribution is higher for the reaction of beam tritons with plasma deuterons than for the reverse case. The results are shown in Fig. 4 along with calculated points from NST code. Another comparison between the dynamics of the $T_{eff,\perp}$ as measured by NDD1 during 22 MW NBI and as modeled by NST code, is shown in Fig. 5. The FWHM of perpendicular as well as tangential (with respect to plasma current axis) neutrons are different due to the anisotropy of the hot beam ions since the majority of the neutrons from TFTR are from beam-plasma and beam-beam interactions [1]. The FWHM is a function not only of the plasma ion temperature but also of the average energy of the beam ions along the detector viewing cone which is a function of electron density. The dynamics of $T_{eff,\perp}$ is illustrated in Fig. 5 where the time evolution of the electron density during NBI changes the penetration of beam ions and thus changes the effective perpendicular temperature with time.

Another example of the measurements versus modeling is shown in Fig. 6. In this case, 18 MW of balanced tritium only, NBI, was injected into a deuterium plasma. The tangential detector showed large broadening of the neutron spectra due to the momentum of beam tritons in the tangential direction. NST calculates the total contributions from beam-plasma and plasma-plasma interactions and fits the resulting data with a Gaussian. Good agreement is seen between measurements and NST model.

The D-T neutron spectrum of the plasma with anisotropic deuteron and triton distribution functions is also anisotropic. The distribution function can be approximated at different angles ($\arccos\chi$) between the direction of the neutron emission and plasma current, by a Gaussian (see equation (2)) with the standard deviation:

$$\sigma_E{}^2 = \frac{4\, m_n \langle E_n \rangle}{m_n + m_\alpha} \frac{T_\parallel T_\perp}{(\sqrt{T_\parallel} + \chi^2(\sqrt{T_\perp} - \sqrt{T_\parallel}))^2} \quad (6)$$

where: $T_{\parallel} = T_{\parallel ij} = \frac{m_D T_{\parallel Di} + m_T T_{\parallel Ti}}{m_D + m_T}$ and $T_{\perp} = T_{\perp ij} = \frac{m_D T_{\perp Di} + m_T T_{\perp Ti}}{m_D + m_T}$) (7)

$T_{\parallel Di} = \langle E_{\parallel Di} \rangle$, $T_{\perp Di} = \langle E_{\perp Di} \rangle / 2$, $T_{\parallel Ti} = \langle E_{\parallel Ti} \rangle$, $T_{\perp Ti} = \langle E_{\perp Ti} \rangle / 2$. (8)

The D-T neutron average energy for such anisotropic plasma also depends on χ:

$$\langle E_n \rangle = \frac{m_\alpha}{m_n + m_\alpha} Q + \frac{3}{2} \left(\frac{m_n}{m_n + m_\alpha} T + \frac{m_\alpha}{m_n + m_\alpha} \frac{m_D T_T + m_T T_D}{m_n + m_\alpha} \right) +$$

$$\frac{m_\alpha}{m_n + m_\alpha} \Delta E_{\parallel} + \sqrt{2} \frac{m_D \langle v_{\parallel Di} \rangle + m_T \langle v_{\parallel Tj} \rangle}{m_n + m_\alpha} \sqrt{\frac{m_n m_\alpha Q}{m_n + m_\alpha}} \chi \quad (9)$$

where: $T_{D,T} = T_{\parallel D,T} + T_{\perp D,T}$, $\Delta E_{\parallel ij} = \frac{(\langle v_{\parallel Di} \rangle - \langle v_{\parallel Tj} \rangle)^2 m_D m_T}{m_D + m_T}$,

and $\langle v_{\parallel Di} \rangle$ and $\langle v_{\parallel Tj} \rangle$ are averaged over the distribution function velocities of deuterons and tritons, and i and j refer to beam and plasma.

This semi-analytical model, based on equations (6)-(9) was applied to the neutron spectra in Fig. 6 and the derived spectrum is shown by the dashed curve. The values of $T_{\parallel Di}$, $T_{\perp Di}$, $T_{\parallel Ti}$, $T_{\perp Ti}$, $\langle v_{\parallel Di} \rangle$ and $\langle v_{\parallel Tj} \rangle$ were determined by averaging over deuteron and triton distribution functions calculated by TRANSP. Fusion reactivity $\langle \sigma v \rangle$ was calculated in accordance with reference [7]. Corresponding values of the neutron sources in the case of anisotropic plasma are:

$$S_{nij} = f_n(E) \langle \sigma\, v \rangle \left(\frac{m_D T_T + m_T T_D}{m_n + m_\alpha} + \frac{2}{3} \Delta E_{\parallel ij} \right) n_{Di}\, n_{Tj} \quad (10)$$

4. CONCLUSION AND DISCUSSION Natural Diamond Detectors have successfully measured both perpendicular and tangential D-T neutron spectra during TFTR high power experiments. These measurements demonstrate for the first time the anisotropy of the ion distribution function of TFTR plasma during NBI. Simulation of the measured spectra using NST code and semi-analytical model yields information about the ion temperature, averaged perpendicular and tangential beam ion energies, and averaged ion tangential velocity for balanced as well as for unbalanced beam injection. The excellent energy resolution, high radiation resistance ($5 \times 10^{14}/cm^2$) and a very small sizes (detector housing ~ $1 cm^3$) of NDDs make them one of the best choices for neutron spectrometry in future burning plasma experiments such as the International Thermonuclear Experimental Reactor (ITER).

ACKNOWLEDGMENT We are grateful to Drs. E.A.Azizov, V.S.Khrunov and K.M.Young for useful discussions, and for the support for this work which was done as part of the PPPL-TRINITI collaboration.

REFERENCES

[1] R.V.Budny, *et al.*, Nuclear Fusion **35**, p. 1497 (1995).

[2] E.A.Konorova, S.F.Kozlov, Sov.Phys.Semiconductors **4**, 1600 (1971)

[3] A.E.Luchanskii, *et al.*, Sov. Atomic Energy **63**, 639 (1987).

[4] A.V.Krasilnikov, "Diamond detector based D-T neutron spectrometer for ITER" in "Diagnostics for Experimental Thermonuclear Fusion Reactor" ed. by P.E.Stott, *et. al.* p.435, Plenum Press, New York and London (1995).

[5] A.V.Krasilnikov, A.L.Roquemore, E.A.Azizov, V.S.Khrunov, K.M.Young, to be published in Rev. Sci. Instrum. (1997).

[6] H.Brysk, Plasma Physics, **15**, p.611 (1973).

[7] S.V.Putvinskij, Reviews of Plasma Phys. **18**.

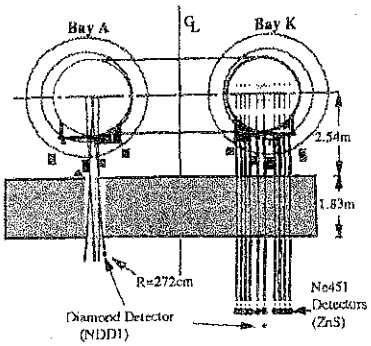


Fig. 1. Vertical viewing locations in TFTR Multichannel Neutron Collimator

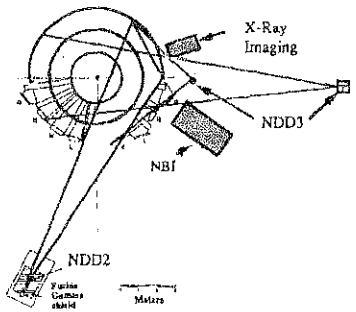


Fig.2. Diamond detector positions inside fusion gamma shielding (NDD2), in compact shielding enclosure(NDD3), and in open space (NDD3) in TFTR test cell.

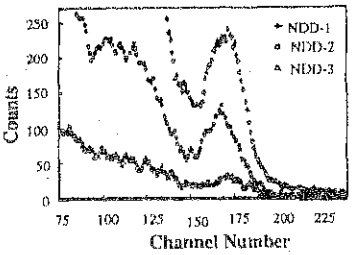


Fig. 3. NDD pulse height spectra from five 28 MW TFTR DT discharges accumulated for 400 ms.

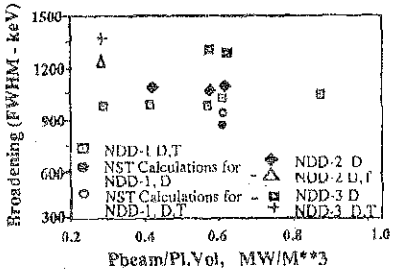


Fig. 4. Broadening of the neutron spectra as a function of NBI power (10 to 30 MW) and emission angle for D and D/T injection. The results are compared to the NST calculation.

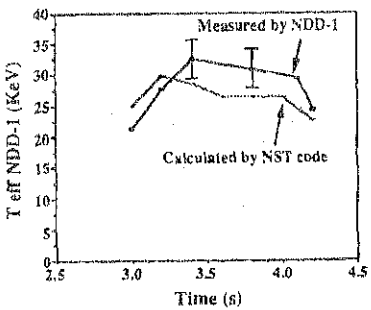


Fig. 5. Comparison of measured and calculated effective perpendicular temperature for 22MW DT injection.

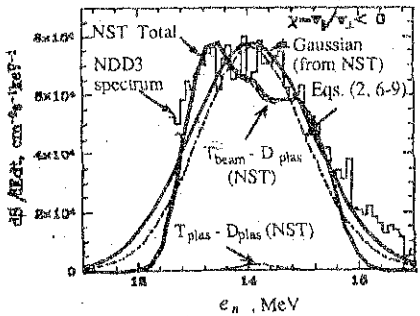


Fig. 6. Comparison of the measured tangential spectra with models using NST and semianalitical codes for 18 MW tritium beam injection.

The Fast Scanning Interferometry of High Density Plasma

I.L. Babich, A.N. Veklich, V.A. Zhovtyansky
Radiophysics Dept., Taras Shevchenko Kiev University, 252033, Kiev, Ukraine

1. Introduction

It is well known a Fabry-Perot interferometer (FPI) makes it possible to measure the width of plasma radiated spectral lines. It yields a high spectral resolution. The preliminary monochromatization of radiation in this case is need. As a rule for this propose the compact monochromator is used. The combination of above-mentioned spectral devices coupled with an image dissector tube allows to carry out the fast scanning (~1 μs) of the spatial distribution of spectral line shapes [1].

For determination of spectral lines profiles it is necessary to evaluate the instrumental contour of the experimental set-up [2]. The result of measurements I (ξ) is represented by product of the monochromator transfer function Φ(ξ) and convolution of a true spectral profile of an investigated line J (ξ) and total instrumental contour W (ξ):

$$I(\xi) = \Phi(\xi) \int_{-\infty}^{+\infty} W(\xi - \xi')J(\xi')d\xi', \qquad (1)$$

where ξ - the proportional to spectral coordinate λ dimensionless quantity; and W (ξ) - the convolution of the FPI's instrumental contour S (ξ) and the image dissector tube D (ξ):

$$W(\xi) = \int_{-\infty}^{+\infty} D(\xi - \xi')S(\xi')d\xi'. \qquad (2)$$

The instrumental contour S (ξ) of an FPI, as shown in Fig.1 a, can be presented as a superposition of equidistant profiles of the dispersion form with identical intensities [3]. Practically, width of the FPI's instrumental contour should not exceed 0.1 ÷ 0.2 from value of its free spectral range Δλ. The instrumental contour D (ξ) of the image dissector tube with a reading hole in slit form can be presented by a Gaussian curve (Fig.1 b), and for image dissector tube DI-04 its width is 0.075 mm [2]. As it is visible from expression (1), observable profile of a line I (ξ) depends from the relationship between a true spectral profile J (ξ) and total instrumental contour W (ξ).

Two limiting cases will be considered.

i) A true spectral profile J (ξ) is compared with a total instrumental contour W (ξ)

As is known [4], the monochromator transfer function F (ξ) can have trapezoidal or triangular form. It is desirable in this case to select it trapezoidal, as shown in Fig.1 c. The monochromator influence has an effect thus only for wings of a spectral line on distance about half of free spectral interval Δλ of its centre. Therefore in the equation (1) function Φ (ξ) can with a certain degree of accuracy be replaced by a constant (for example, one). The observable

profile of a line I (ξ) in this case represents Voigt function and for determination of a true profile of the spectral line J (ξ) one can use the results of paper [2].

ii) A true spectral profile J (ξ) much wider a total instrumental contour W (ξ)

Such case may be realized in dense plasma (for example, in plasma accelerators [5] or Z-pinch plasma [6]), when the spectral lines are strongly broadened and their profiles are considerably in excess of a set-up instrumental contour. Thus an observable profile of a spectral line I (ξ) will not essential differ from a true spectral profile J (ξ).

2. Interferometry of High Density Plasma

In actual practice the maximum width of spectral line which is able to measure is limited by the free spectral range of the FPI (Δλ). Beginning with some value of spectral line width δλ comparable to Δλ (δλ ~ Δλ), the ratio I_{min}/I_{max} becomes grater than 0.5 (see Fig. 2). It makes the determination of spectral line width difficult.

In this paper the method of the determination of spectral line width δλ comparable to Δλ is proposed. The range enhancement of recording widths will allow to measure parameters of high density plasma, such as plasma of free-burning electric arc as well as laser produced plasma.

We consider two neighbouring interference maxima of different intensity and width ($\delta\lambda_1$ and $\delta\lambda_2$). Stark broadening of spectral lines is supposed i.e. Lorentzian profile is realized: $I_\lambda = I_0 / (\lambda^2 + \delta\lambda^2 / 4)$. $I_\Sigma(\lambda)$ - is the total profile (Fig.3).

We take into account also the preliminary monochromator transfer function Φ(ξ), which should have in this case the triangular form with half-width equal to FPI's free spectral range Δλ, i.e. $\Phi(\xi) = \Phi_0[1 - (|\xi / \Delta\lambda|)]$ at $0 \le \xi \le \delta\lambda$ (Fig.1 d) [4]. We write down obvious system of the equations for various points of the interferogram:

- in minimum ($\xi = \lambda_1$):

$$I_\Sigma(\lambda_1) = \frac{I_{o1}}{(\lambda_1^2 + \delta\lambda_1^2 / 4)} \frac{\Delta\lambda - \lambda_1}{\Delta\lambda} + \frac{I_{o2}}{(\Delta\lambda - \lambda_1)^2 + \delta\lambda_2^2 / 4} \frac{\lambda_1}{\Delta\lambda}, \qquad (3)$$

- in maxima ($\xi = 0$ and $\xi = \Delta\lambda$, accordingly):

$$I_\Sigma(0) = I_{o1} / (\delta\lambda_1^2 / 4), \qquad (4)$$

$$I_\Sigma(\Delta\lambda) = I_{o2} / (\delta\lambda_2^2 / 4). \qquad (5)$$

From a condition of an function $I_\Sigma(\xi)$ extremum for a point λ_1 we obtain:

$$I_{o1} \frac{2\lambda_1\Delta\lambda - \lambda_1^2 + \delta\lambda_1^2 / 4}{(\lambda_1^2 + \delta\lambda_1^2 / 4)^2} = I_{o2} \frac{\Delta\lambda^2 - \lambda_1^2 + \delta\lambda_2^2 / 4}{((\Delta\lambda - \lambda_1)^2 + \delta\lambda_2^2 / 4)^2}, \qquad (6)$$

where $I_{o1} = 4I_1 / \delta\lambda_1^2$; $I_{o2} = 4I_2 / \delta\lambda_2^2$.

Knowing from experiment $I_\Sigma(\lambda_1)$, $I_\Sigma(0)$, $I_\Sigma(\Delta\lambda)$, λ_1 and $\Delta\lambda$, it is possible to solve system of the equations (3) - (6) in a numerical kind and to obtain the values $\delta\lambda_1$ and $\delta\lambda_2$.

In case of homogeneous plasma for adjacent interference maxima it is possible to assume approximate equality of intensities $I_1 \sim I_2$ and of widths $\delta\lambda_1 \sim \delta\lambda_2$. Thus $\xi = \lambda_1 = \Delta\lambda/2$ and system of the equations (3) - (6) is reduced to the ratio:

$$I_\Sigma(\lambda_1) / I_\Sigma(0) = I_{min} / I_{max} = \gamma, \qquad (7)$$

where

$$\gamma = \delta\lambda^2 / (\Delta\lambda^2 + \delta\lambda^2). \qquad (8)$$

In Fig. 4 (the curve 1) the spectral line width (normalized to the FPI's free spectral range) versus dimensionless parameter γ is presented. Having determined for each interference maximum the value γ and using the given graphics dependence, one can determine width of a spectral line for various sections of investigated plasma, and with it the spatial distribution of such plasma parameters.

We evaluate the error of the offered method in the line width $\delta\lambda$ determination. We consider, that relative error in the intensity determination both in a maximum and in minimum of interferogram does not exceed 5 %. That is $\Delta I_\Sigma(\lambda_1) / I_\Sigma(\lambda_1) = \Delta I_\Sigma(0) / I_\Sigma(0) = 0.05$. Taking into account the relations (7) and (8), it is possible to obtain the expression for a relative error δ of the width $\delta\lambda$ determination:

$$\delta = \frac{d(\delta\lambda)}{\delta\lambda} 100\% = \frac{1}{2(1-\gamma)} \sqrt{\left(\frac{\Delta I_\Sigma(\lambda_1)}{I_\Sigma(\lambda_1)}\right)^2 + \left(\frac{\Delta I_\Sigma(0)}{I_\Sigma(0)}\right)^2}\, 100\% \qquad (9)$$

In fig. 4 (the curve 2) the dependence $\delta(\gamma)$ is shown.

3. Conclusions

Thus, in this paper an express technique of the high spectral and spatial resolution diagnostics of wide plasma objects class (including dense) is offered. The offered method of measurement of spectral line width is characterized by sufficient accuracy. As is seen from Fig. 4, at the value $\gamma = 0.8$ the percentage error of the width measurement may not exceed 20.

References

1. Veklich A.N., Zhovtyansky V.A. *J. Appl. Spectroscopy* (Traslate from Russian) **50** 359 (1989)

2. Andreeva L.I., Zhovtyansky V.A., Kaydalov S.A., et al. *Фотоэлектронные приборы для исследования быстропротекающих процессов* 97 (1979)

3. Rautian S.G. *Успехи физических наук* **66** 475 (1958)

4. Malyshev V.I. *Введение в экспериментальную спектроскопию* 1979

5. Volkov Ya.F., Marinin V.V., Mitina N.I. *J. Appl.Spectroscopy* (in Russian) **56** 451 (1992)

6. Rantsev-Kartinov V.A., Stepanenko M.M., Trofimovich E.E. *22nd EPS Conf. on Contr. Fusion and Plasma Physics. Abstracts of Inv. and Contr. Papers. United Kingdom* 195 (1995)

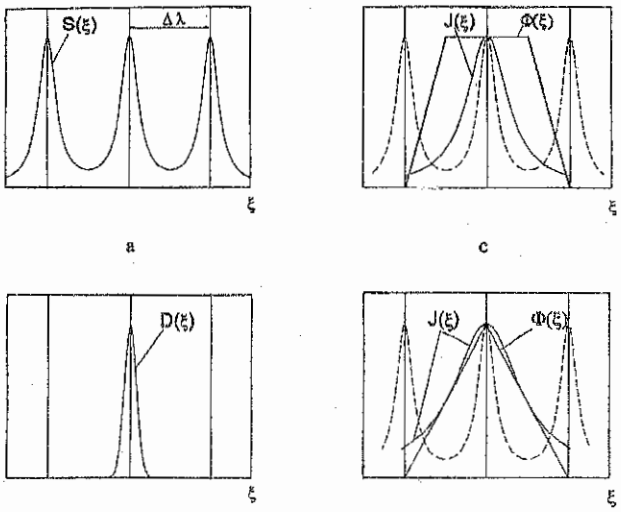


Fig. 1

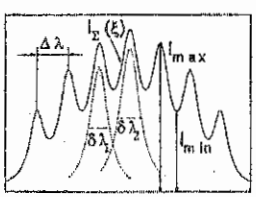


Fig. 2

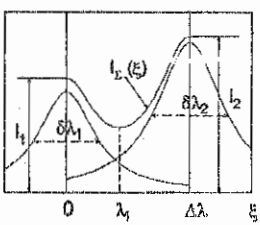


Fig. 3

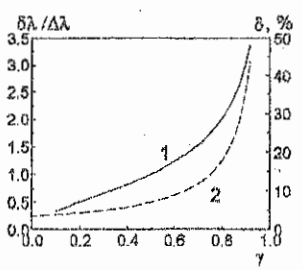


Fig. 4

Frequency shift of reflectometry signals due to rotation of density turbulence in W7-AS

B. Brañas*, M. Hirsch, J. Baldzuhn, T. Estrada*, T. Geist ,
H.J. Hartfuss, J. Sánchez*, V. Zhuravlev*
Max-Planck Institut für Plasmaphysik, EURATOM Ass., D-85748 Garching, FRG
**Asociación EURATOM-CIEMAT, 28040 Madrid, Spain*

Introduction

Reflectometry provides information about density fluctuations from a measurement of the phase changes of a mm-wave reflected at the cut-off layer in the plasma. Under turbulent plasma conditions an unidirectional drift of the measured phase is observed which cannot be explained by a realistic movement of the cut-off layer due to density changes. An understanding of this phase drift is essential for the interpretation of phase and amplitude of the reflected wave in terms of density turbulence. To clarify the situation two-dimensional simulations of the interaction between the mm-wave and the turbulent plasma have been performed[1,2]. They show that if parts of the wavefront reflected from different regions in the plasma interfere destructively at the receiving antenna sudden phase changes appear in combination with a drop in the signal amplitude. A preferential direction of this changes - i.e. a phase drift - results, if the density structures are rotating with the plasma. In addition some asymmetry between the reflecting structures and the wavefield must exist. The validity of such a model based on plasma rotation has been investigated experimentally with the reflectometer at W7-AS.

Experiments

The **reflectometer system**[3,4] at W7-AS combines heterodyne detection, a high dynamic range and bandwidth with operation at small wavelengths (X-mode propagation). The two poloidally separated antennas (θ=+6° and -6°) for launching and receiving the signal use Gaussian beams focused to a beam waist of 2cm in the plasma. The symmetry axis between the antennas is in the equatorial plane oriented towards the torus center at a toroidal position with elliptically elongated flux surfaces. The cut-off surfaces are almost perpendicular (87.4°) to the probing direction. An Amplitude Modulation system integrated into the reflectometer provides a time delay measurement which is used to obtain density profile information. All signals, carrier phase, time delay and signal amplitude, are sampled at 10 MHz. These characteristics make the system suitable for a detailed analysis of the reflectometer response to plasma density perturbations. From a previous study[1] instrumental reasons, e.g. insufficient sampling or an intermittent loss of signal power, can be excluded as the origin of the observed drift.

The observed phase drift strongly depends on plasma conditions. The most pronounced effect is its sudden disappearance in the H-mode[1]. Under typical L-mode conditions the magnitude of the phase drift shows a **characteristic radial profile**: it is

positive for positions outside the separatrix and negative within the confinement region with a maximal red shift of a few 100 kHz. This red shift decreases towards the plasma center. If the drift is strong the phase spectrum has a 1/f dependence and the measured amplitude and phase signals show low coherence. In contrast, if the unidirectional phase drift is negligible in comparison with the symmetric phase fluctuations, the spectra differ from a 1/f dependence. In this case for frequencies f > 50 kHz amplitude and phase signals are coherent with a phase shift between them very close to $\pi/2$.

In order to test the **influence of the antenna geometry** on the observed drift transmitting and receiving antenna have been interchanged on a shot to shot basis using a variety of different plasma conditions (toroidal magnetic field of 1.25 / ±2.5 T, heating with 400/800 kW ECRH and 0.5 MW NBI, average density between 2 and 14 10^{19} m^{-3}, rotational transform 0.34 and 0.53): The observed phase drift does not change significantly when transmitting and receiving antenna are interchanged.

The **correlation between the phase drift and poloidal plasma rotation** has been investigated for two types of ECRH heated discharges which display different rotation profiles (Fig.1) : (1a) ECRH heating 400 kW off axis + 400 kW on axis and (1b) ECRH 400 kW off axis only. The poloidal rotation profile of the plasma is obtained as a sum of ExB and pressure driven rotation. The radial electric field is measured from the Doppler shift of impurity emission lines (B IV). As can be seen in Fig.1, for the two plasma conditions the radial profile of the phase drift qualitatively corresponds with the poloidal plasma rotation profile. For pure off-axis heating (Fig. 1b) the electron temperature and its gradient have very low values inside the heating location (r_{eff}~10 cm). Therefore the diamagnetic contribution to plasma rotation is very low at these positions, a feature that is also observed in the values of the phase drift.

An **inversion of plasma rotation** has been archieved by inverting the magnetic fields of the stellarator. All other plasma parameters are kept constant: Density and temperature profiles measured with Thomson scattering, Li-beam, reflectometry and ECE respectively show no variation as the magnetic field is reversed. Impurity rotation (BIV) changes sign confirming the inversion of the ExB velocity. An example of the observed phase drift is given in Fig. 2 : For all probed radial positions the drift is inverted as the plasma rotation is reversed. In some discharges the absolute value of the drift measured for positive and negative magnetic fields nevertheless differs by up to a factor of 2.

A **detailed analysis of the phase changes** shows that the inversion of the drift is related to the shape of the measured phase fluctuations. Figs. 3 gives a detail of the phase and amplitude of a reflected signal for two corresponding discharges with positive and negative magnetic field. For example with positive B (Fig. 3b) during a fluctuation the measured phase increases faster than it decreases and the minima in the amplitude occur during the phase increase. This observation that the amplitude minima correlate with the bigger rates of phase change is consistent with the simulations. A coherency analysis shows that the coherence

between phase and amplitude is high for frequencies 50 kHz < f < 2 MHz and the phase shift between both signals is $\pm\pi/2$ for positive and negative magnetic field respectively.

As during this period the phase does not always recover to its previous value, in the long term a drift in negative direction is obtained. This **intermittent behaviour** can be explained taking into account that the phase responds non linearly to changes in the local density gradient induced by the fluctuations. This local gradient is a function of the average one, the amplitude and the wavelength of the fluctuations. An intermittent phase drift appears if for certain time intervals, the turbulent structures are such that the microwaves reflected at them interfere destructively at the antenna. During the rest of the time the amplitudes of the density turbulence are lower or their wavelengths are larger therefore all power received at the antenna is reflected at a smoother surface i.e. at the same distance to the horn. Another explanation would be that the intermittence occurs due to small turbulence structures, that appear and disappear.

Discussion

The experimental results obtained with the reflectometer at W7-AS are compatible with an explanation of the observed phase drift based on density structures rotating with the plasma. As the direction of the drift can be inverted by inverting plasma rotation radially propagating density bursts can be excluded to be the main origin of the phase drift.

For the origin of the asymmetry in the reflected wavefield necessary to explain a net phase drift some experimental clues can be given : A vertical displacement of the plasma larger than 2-3 mm with respect to the antenna axis can be excluded from the lack of profile change as the magnetic field is reversed. Following the 2D WKB code calculations this small displacement can not produce the required asymmetry unless the turbulent structures have very high amplitude or very short poloidal wavelengths. The same holds for the small 2.6° misalignment of the horn axis from the normal to the cut-off surfaces. According the 2D simulations[2] the poloidal separation of emitting and receiving horns could introduce the required asymmetry. Nevertheless the experiments show that the phase drift does not change significantly as the horns are interchanged. Therefore the experimental results would be consistent with an explanation of the phase drift based mainly on an asymmetry in the turbulent structures themselves. As the observed phase drift direction is inverted when inverting the magnetic fields in this case the asymmetry must be independent on the rotation direction. In order to obtain more conclusive results 2D full-wave simulations are currently under way.

References

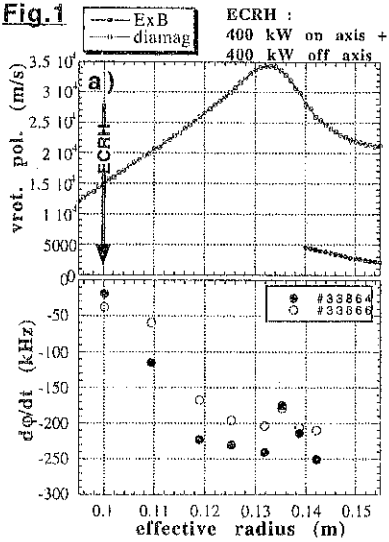
[1] B. Brañas, M. Hirsch, V. Zhuravlev, J. Sánchez, E. de la Luna, T. Estrada, T. Geist, H. J. Hartfuß, Proc. of the 22nd EPS Conference, Bournemouth, UK, 3-7 July 1995, Vol. 4, p 161.

[2] J. H. Irby, S. Horne, I. H. Hutchinson, P. C. Stek, Plasma Phys. Control. Fusion. 35, 601 (1993).

[3] H. J. Hartfuss, T. Estrada, M. Hirsch et al., Rev. Sci. Instrum 65(7), 2284 (1994).

[4] M. Hirsch, H.J. Hartfuß, T. Geist, E. de la Luna, Rev. Sci. Instrum. 67(5), p1807 (1996)

Fig.1



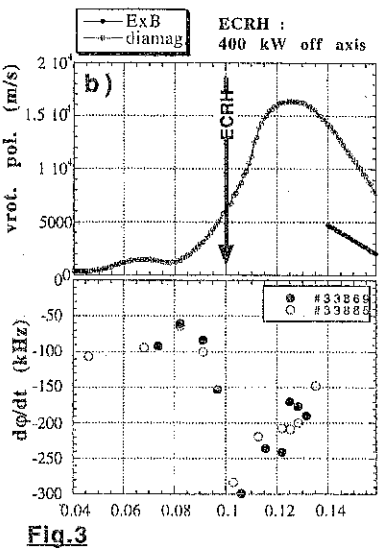


Fig. 1: Radial profiles of poloidal plasma rotation (ExB-component obtained from spectroscopy and diamagnetic drift) and of the phase drift for two types, a), b) of ECRH heated discharges.

Fig. 2: Frequency shift of the reflected signal as a function of cutoff layer position for discharges with normal and inverted magnetic fields. Plasma rotation changes as B is inverted while all other plasma parameters are kept constant.

Fig.3: Time traces of reflectometer phase and amplitude for positive and negative B-fields. The asymmetry of phase and amplitude signals changes sign as the magnetic field is reversed.

Fig.2

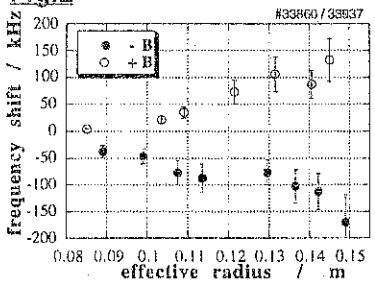
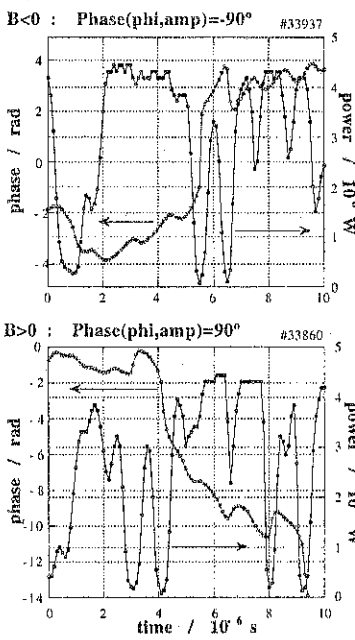


Fig.3



Investigation of the Neutral Gas Distribution on W7-AS Using the Monte-Carlo Code EIRENE in Combination with the Li-Beam Diagnostic

S. Fiedler, O. P. Heinrich, J. Das, K. McCormick and the W7-AS-Team
Max-Planck-Institut für Plasmaphysik, EURATOM Association,
D-85748 Garching, Germany

1. Introduction

The Li beam diagnostic on W7-AS /1/ allows the measurement of neutral density n_0 outside the plasma column as well as electron density profiles of the main plasma by observation of the collisionally induced LiI line radiation (671nm) from an injected high energy neutral Li-beam (20-66keV/0.5-3.0mA). Central profiles for higher densities are achieved by incorporating line integrated data from the HCN interferometer /2/. Thus highly accurate density profiles from the plasma middle to the walls are available. Using n_e-profiles and n_0 derived from the Li-beam in combination with H_α intensities measured at several points around the vessel, the Monte-Carlo code EIRENE is implemented to determine the important neutral sources as well as the absolute neutral density distribution.

2. Density profile reconstruction

For peak densities $n_{e0} < 4 \cdot 10^{19}$ m^{-3} profiles spanning the entire outer radius can be reconstructed by the Li beam diagnostic. Central profiles for higher densities are achieved, under the assumption of flat profiles, by incorporating data from HCN interferometry.
The HCN interferometer on W7-AS measures line densities along three parallel lines of sight in the φ=29° plane (approximate elliptical plasma cross section, cf. fig. 2.1). At low densities these data can be used to cross check the Li beam data. To this end the reconstructed Li density profiles are mapped along the magnetic surfaces using the TRANS-database to the plane of the HCN interferometer, integrated along the line of sights, and directly compared. Using the electron temperature profile as measured by Thomson scattering in the Li beam density reconstruction algorithm /3/ and a central beta consistent with the derived profile for the field line mapping, excellent agreement is found, cf. fig. 2.2. For higher central densities $n_0 \leq 1 \cdot 10^{20}$ m^{-3} the entire gradient region is still accessible by the Li beam diagnostic. The effective plateau value of the density profile can be calculated by subtracting the contribution of the plasma edge from the central HCN channel. A cubic spline approximation is used to construct a smooth transition between the edge density profile and the derived plateau value. To take into account possible uncertainties in the Li beam density profile, the plateau value is varied in such a way that the line integral of the smoothed density profile fits the line density of the HCN interferometer to within a tolerance of less then 2%. The outermost channel of the HCN interferometry is used to check the field line mapping. For the EIRENE calculation below a low iota (ι_a=0.34, no islands at the plasma edge), medium density (small beta effects) shot (#33359) is chosen. The derived density profile for this shot together with the edge density profile measured by the Li beam diagnostic is shown in fig. 2.3. Measurements of this quality can be routinely carried out on a ms time scale.

3. Neutral density measurements

The neutral density is registered in the injection port by observing the Li_{2p} line radiation from the Li beam induced by collisions between Li beam atoms and neutral particles. The observation volume is at a point 0.55 m from the plasma surface, thereby minimizing any interference from background light at the Li(2p) wavelength while maintaining a good vacuum conductance to the main vessel. The signal is calibrated by injection of the Li beam into the discharge chamber at known molecular gas pressure and applied magnetic field. Since EIRENE calculations indicate that molecules make up 99% of the neutral density within the injection port, this calibration may be directly applied to measurements performed during plasma discharges. For the discharge under investigation, see the EIRENE calculation below, the neutral density is determined to be $n_0 = 3.6 \cdot 10^{17}$m^{-3} ($1.5 \cdot 10^{-5}$ mbar).

4. H_α measurements

H_α intensities are recorded at different toroidal positions (cf. fig. 5.5): (1) spatially resolved by a diode array at the inner limiter, (2) at φ=10°, (3) at φ=18°, the position of the Li beam diagnostic and (4) at φ=23°. Data for positions 2-4 are absolutely calibrated via an Ulrich sphere (e.g. $H_\alpha(\varphi=18°) = 1.8 \cdot 10^{18}$ photons $m^{-2}s^{-1}sr^{-1}$) and used in the EIRENE calculations.

5. EIRENE simulation of H_α and n_o measurements

The neutral gas distribution plays a crucial role for source terms entering into the particle balance of the plasma edge and hence is an important component of edge investigations. To determine the absolute neutral density in the module of the Li beam, the neutral density distribution is calculated with the 3D Monte-Carlo code EIRENE /4/, using $n_e(r)$ profiles and n_o from the Li beam as well as the H_α intensity measured at 4 positions including the Li beam port and the poloidal H_α distribution at an inboard limiter. With these independently measured quantities n_o and H_α a consistency check of the EIRENE modelling of the neutral source locations is also possible. To properly accommodate the n_o measurement located deep inside a port, the Li beam port is also simulated as shown on the computational grid in fig. 5.1. Periodicity is assumed in the toroidal direction, i.e. each of the 5 modules is treated identically.

For clear conditions concerning neutral sources a discharge without islands (i_a=0.34) is considered, where the plasma has been shifted towards the inboard limiters (B_z=18mT) so that they comprise the main neutral source. The neutral source distribution is taken to be the same as the H_α intensity profile measured along the plasma-facing side of an inboard limiter.

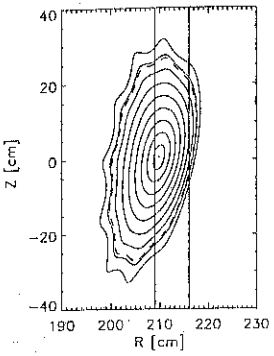
This assumption yields self-consistent results: in fig. 5.3 the comparison between experimental and calculated H_α profiles shows good agreement over the entire limiter. Fig. 5.4 illustrates the corresponding lower inboard limiter and H_α line of sights, together with the neutral atom distribution. Since the distance of the Li beam to the inboard limiter is about 0.5 m toroidally and 150° poloidally, it is not clear a priori, which source dominates the local neutral density, i.e. the limiters or the global plasma-wall interaction. The scaling of the neutral particle distribution from the limiter source to its absolute H_α intensity shows that at the Li beam plane this source strength is too low for the corresponding H_α signal. This becomes clear from the toroidal variation of the neutral density shown in fig. 5.5: Between the limiter and Li beam plane the atomic density decays by 2 decades. Therefore a second source at the wall is introduced, which for simplicity is assumed to be a point source in the Li beam plane. It turns out that one has to put its location at the upper part of the so-called helical edge (corresponding to the upper tip of the plasma in fig. 5.1), which is expected to be the principal plasma-wall interaction area away from limiters. By scaling the point source neutral distribution with the H_α signal at the Li beam, n_o in the Li beam port and the next further H_α are predicted by the calculation to within 50%, whereas with other source locations the differences are more than an order of magnitude, if a reasonable solution exists at all. This shows that the helical edge defines the dominant region for the global plasma-wall interaction. In fig. 5.2 the toroidally and poloidally averaged atomic densities of the two sources are compared: inside the limiter the limiter source dominates the neutral density by a factor of 10, but outside the wall source is even higher than the latter.

6. Conclusions

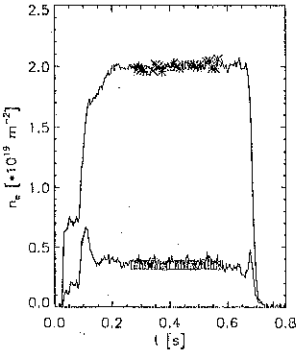
Employing the Li beam $n_e(r)$ profiles and H_α intensities it has been possible to find a self-consistent 3D neutral source distribution in EIRENE showing that on the limiter the source profile corresponds roughly to the H_α intensity profile and that the helical edge is mainly responsible for the global plasma-wall interaction. In addition the neutral density in the Li beam port could be modelled for the first time, giving agreement within 50% to the experimental n_o value from the Li beam.

References:
/1/ K. McCormick, 21st EPS International Conference on Plasma Physics, Europhysics Conference Abstracts Vol. **18B**, Part III (1994) 1268
/2/ S. Fiedler, IPP-Report III/209 (October 1995)
/3/ J. Schweinzer, et al., Plasma Physics and Controlled Fusion, **34** (1992) 1173
/4/ D. Reiter, report of KFA-Jülich, Institut für Plasmaphysik, Nr. 2599 (1992)

2.1



2.2



2.3

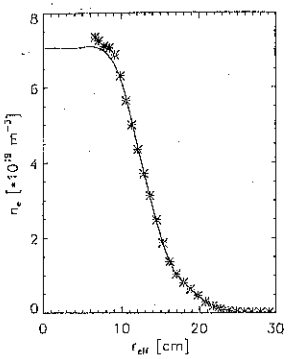


Fig. 2.1 Magnetic flux surfaces for discharge #34540 with line of sights for the HCN interferometer.

Fig. 2.2 Line densities of the HCN channels indicated in fig. 2.1 (solid lines) compared to the line integrals calculated from the Li beam data (symbols) for discharge #34540.

Fig. 2.3 Reconstructed profile using Li-beam edge density profile (symbols) and the central HCN chord for discharge #33359.

Fig. 5.1 Computational grid and diagnostics at the Li beam phi plane. The Li-beam n_e profile along the beam line is directly mapped onto the grid flux surfaces. Toroidally the grid has a resolution of 50 cells per module.

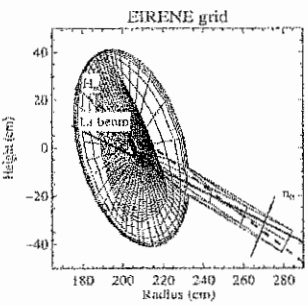
Fig. 5.2 Globally averaged atom density profile of the inboard limiter and the helical edge wall source with the Li beam n_e and Thomson temperature profile. The shadow line indicates the limiter position.

Fig. 5.3 Experimental and calculated H_α profiles at the lower inboard limiter. The tile index varies from bottom to top.

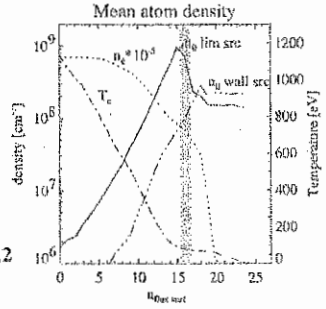
Fig. 5.4 Atomic density at the lower inboard limiter. The H_α intensity profile is used as the neutral source distribution.

Fig. 5.5 Toroidal atom density distribution of the limiter source on the flux surface in front of the inboard limiter for the half of one module. Higher values correspond to brighter colours. The upper picture shows along the poloidally averaged atomic density the toroidal positions of the inboard limiter (1), the Li beam plane (3) and two other H_α locations (2,4).

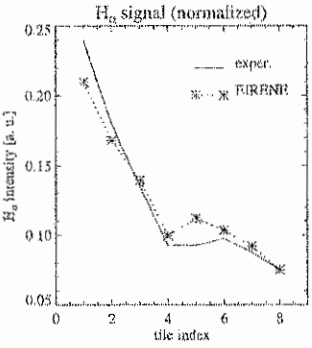
5.1


EIRENE grid
Height (cm)
Radius (cm)
180
200
220
240
260
280
40
20
0
−20
−40
La beam

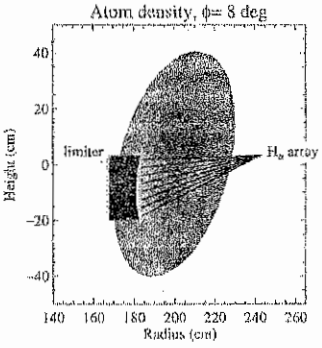
5.2


Mean atom density
density [cm⁻³]
Temperature [eV]
lim src
wall src
0
5
10
15
20
25
200
400
600
800
1000
1200

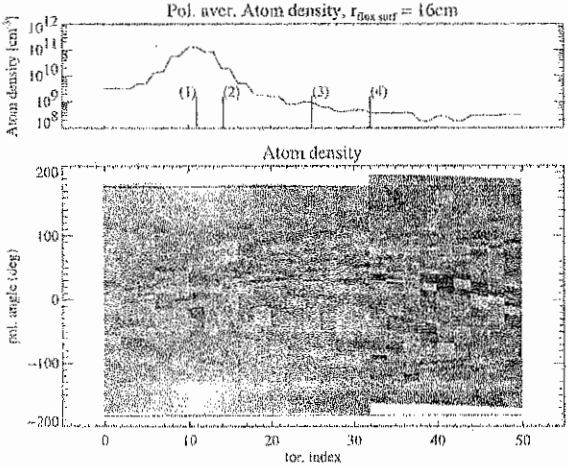
5.3


H_α signal (normalized)
exper.
EIRENE
H_α intensity [a. u.]
tile index
0.25
0.20
0.15
0.10
0.05
0
2
4
6
8

5.4


Atom density, ϕ= 8 deg
limiter
H_α array
Height (cm)
Radius (cm)
40
20
0
−20
−40
140
160
180
200
220
240
260

5.5


Pol. aver. Atom density, $r_{flux\ surf}$ = 16cm
Atom density [cm⁻³]
(1)
(2)
(3)
(4)
Atom density
pol. angle (deg)
tor. index
200
100
0
−100
−200
0
10
20
30
40
50

Measurement of Fast Density Profile Changes by FM Broadband Reflectometry on ASDEX Upgrade

B. Kurzan, M. Maraschek, A. Silva‡, P. Varela‡, I. Nunes‡, M. E. Manso‡, F. Serra‡, W. Suttrop, H. Zohm, ASDEX Upgrade Team
IPP Euratom Association, Boltzmannstr. 2, 85748 Garching, Germany
‡ Centro de Fusão Nuclear, EURATOM / Instituto Superior Técnico, P-1096 Lisboa, Portugal

1 Introduction

Plasma discharges near the density limit show fast electron density profile changes which are studied with microwave reflectometry: Near the density limit the discharge becomes MHD unstable leading to growing magnetic tearing modes. These magnetic islands strongly modulate the shape of the electron density profile. From the form of the profile the modes present can be determined. After the density limit marfes, which are cold and dense plasma clouds, occur, leading to a fast steepening of the density profile on the High-Field side of the tokamak.

2 Method

The results presented here were obtained with the Frequency Modulated (FM) broadband reflectometry system on ASDEX Upgrade in O-mode polarization [1]. The microwave frequencies launched to the plasma were swept between 16 and 72 GHz in 100 μs (20 μs are possible) corresponding to probed cut-off densities of $0.3 - 6.4 * 10^{19}\ \mathrm{m}^{-3}$. The density profiles are determined by calculating the distance $\Delta R(f)$ between the cut-off layer and the beginning of the plasma, depending on the microwave frequency f, by

$$\Delta R(f) = \frac{c}{2\pi^2} \int_0^f \frac{d\varphi}{df'} \frac{df'}{\sqrt{f^2 - f'^2}} \qquad (1)$$

(c: speed of light in vacuum, f': integrating variable). φ is the phase difference between the microwave reflected from the plasma and a reference signal. The group delay $d\varphi/df'$ of the results presented here is calculated with an algorithm determining in a first step the zero crossings of the interference pattern, obtained by correcting the raw signal for the internal reflections and then symmetrizing around zero, combined in a second step with a statistical analysis to improve signal quality (fig. 1). This analysis can be combined with other algorithms for determining the group delay, as the minimum-maximum method [2], or the digital frequency discriminator [3]. In order to remove fringe count errors, the zeroes found in a first step are analysed concerning their statistical significance. The criterium used here is given by the Poisson statistics describing the noise of the detector system. If the standard deviation $\sigma_{\Delta f}$ of the frequency distances Δf_i of neighbouring zeroes (labeled with the index i) is bigger than their mean distance $\overline{\Delta f}$, they are detected as noise and removed. For the calculation of

$$\overline{\Delta f} = < \frac{\Delta f_i}{\Delta f_r} >, \qquad \sigma^2_{\Delta f} = < \left(\frac{\Delta f_i}{\Delta f_r} - \overline{\Delta f} \right)^2 > \qquad (2)$$

(< . > denoting the average over a group of typically 7 neighbouring zeroes) the frequency resolution Δf_r determined by the number of acquired microwave frequencies per sweep must be specified. This algorithm seems to have great potential to determine the group delay in case of low signal to noise ratio: Since it principally analyses only small parts of the whole frequency sweep for good signal quality the noisy parts in a sweep are cut out. The gap in the data is closed by interpolating from the neighbouring valid data points. For flat profiles where there is no interference pattern at the higher frequencies, the point where the signal disappears below the noise level is determined and the profile evaluation ends (see fig. 1).

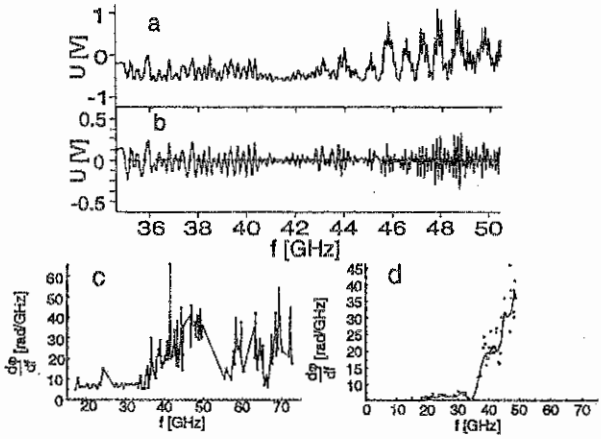


Fig. 1: Correcting the raw data of a frequency sweep with plasma (a) for the internal reflections (obtained without plasma) and then symmetrizing around zero, the interference pattern from the plasma is obtained (b). The group delay $d\varphi/df$ *shown in (c), is calculated from the signals (b). The noise in* $d\varphi/df$ *stems from the fringes of small amplitude. These parts are removed after the application of the statistical analysis. The result, which is also corrected for delays between the reflected and the reference signal, is shown in (d). This group delay is used for the evaluation of the electron density profile.*

The initialization of the electron density profile is based on the measured group delay of the microwaves with the lowest frequencies [4]: Here, the distance of the plasma from the antennas, which can vary during a discharge, is estimated in this way. The group delay corrected for the vacuum distance is then used for calculating the profile.

3 Electron Density Profiles for a Density Limit Discharge

In the following, electron density profiles for an Ohmic density limit discharge on ASDEX Upgrade (plasma current 600 kA, toroidal magnetic field – 2 T), showing the occurence of a marfe and fast changes due to MHD activity, are studied.

3.1 Occurence of a Marfe

A marfe [5] starting after the density limit in the divertor and moving up to the equatorial plane of the plasma on the High-Field side of the tokamak can be clearly identified by the steepening of the density profile: the profile of the pre-marfe phase shows within milliseconds

a strongly increased particle content and a steepening of the gradient outside the separatix (fig. 2). This coincides with an increase of the Bremsstrahlung intensity in the near infrared, viewing the equatorial plane of the plasma. After this, the marfe is moving to the inside of the plasma (time 1.93805 s) in accordance with an increase in the Bremsstrahlung intensity, due to the higher density of the marfe.

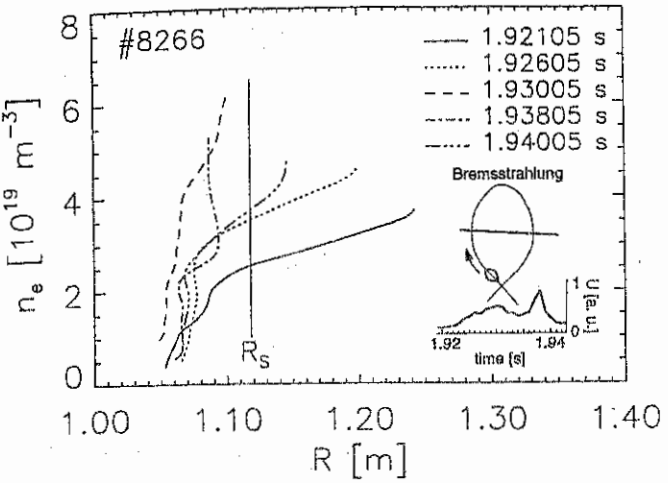


Fig. 2: A marfe occurs on the High-Field side in the equatorial plane of the plasma between the times 1.923 s and 1.941 s, as seen in the Bremsstrahlung intensity U, plotted in the insert picture. The electron density profiles measured with the reflectometry system on the High-Field side shows an increase of the gradient of the electron density profile outside the separatrix, positioned at R_s, compared to the pre-marfe profile at 1.92105 s. The marfe is at the centre of the sightline at 1.930 s (steepest density gradient) in accordance with Bremsstrahlung. After this the marfe is moving to the inside of the plasma (1.93805 s) reflected in the peaking of the Bremsstrahlung intensity due to higher density of the marfe. At around 1.94005 s the marfe is leaving the region of observation, leading to a flattening of the density profile.

3.2 Identification of m=4 and m=5 Modes

After the density limit mode locking occurs at the time 1.858 s. From analysing the magnetics data in the phase before locking the m=2 and m=3 modes were found to be present. When the island widths are growing nonlinear coupling of the modes gives rise to the generation of modes of higher poloidal wave number (m=4, m=5). After mode locking has occured, the mode structure can not be inferred by the magnetics. The m=4 and m=5 modes are, however, detected in the electron density profiles, when the mode structure starts moving around its locked position (fig. 3): The earliest profile in the following series (fig. 3) at the time 1.85905 s (now termed 1. profile) is still unperturbed. The 2. and 3. profile shows a flattening at the q=5 flux surface shifting the steep gradient zone to the q=4 surface (the q-profile used here was reconstructed from magnetic measurements). The flattening is extended up to the q=4 flux surface in the 4. and 6. profile. The 5. profile shows an unperturbed shape similar to the 1. profile. So the fast flattening and steepening of the profiles is observed

repetitively. From the varying shapes of the electron density profiles the m=4 and m=5 modes are identified to be present.

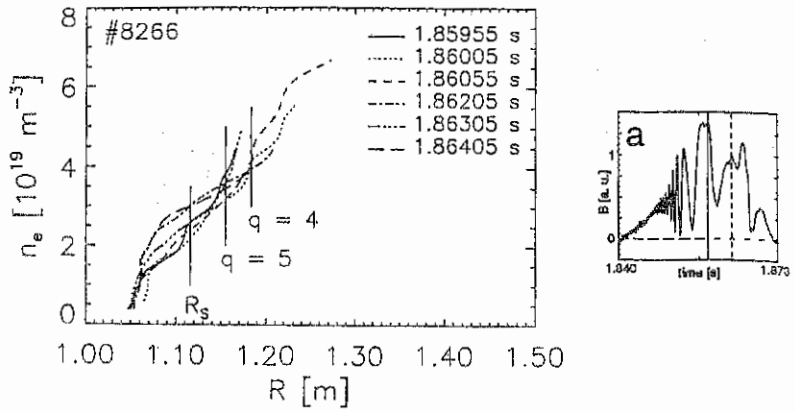


Fig. 3: Mode locking occurs at the time 1.858 s as can be seen in the perturbed poloidal magnetic field (a). After this the coupled mode structure is moving around its locked position. In the electron density profiles (shown until 1.86405 s corresponding to the broken line in (a)) the m=4 and m=5 modes can be detected after mode locking: the earliest (1.) density profile is still unperturbed followed by a flattening of the density profile around the q=5 surface (2. and 3. profile), extending in the 4. and 6. profile also up to the q=4 surface, interrupted by the 5. profile showing the unperturbed form. So the flattening and steepening of the profile is repetitive. The position of the magnetic separatrix is denoted by R_s. The q-profile was reconstructed from magnetic measurements.

4 Conclusion

The applied algorithm for the determination of density profiles is flexible enough to resolve density profiles of different shape. It has great potential to recover profiles also from noisy signals. It is presently used for fast automatic routine evaluations on ASDEX Upgrade. The time history of the position and the density gradient of a marfe occuring on the inboard side of the tokamak is presently directly measured only by the microwave diagnostic installed there. After the locking of tearing modes, a flattening and steepening of the electron density gradient can be observed at rational q-surfaces, ascribed to a movement of the modes around their locked positions.

References

[1] A. Silva, et al., Fusion Technology, Vol. 1, 747 (1993); A. Silva, et al., to be submitted to Rev. Sci. Instr.

[2] M. E. Manso, et al., Proc. IAEA Techn. Com. Meet. on Reflect., Abingdon (1992)

[3] A. Silva, et al., 22nd EPS Conference on Controlled Fusion and Plasma Physics, Bournemouth, 19C, IV-413 (1995)

[4] P. Varela, et al., Rev. Sci. Instr. 66 (10), 4937 (1995)

[5] G. B. Field, The Astrophysical Journal 142, 531 (1965); J. Neuhauser, et al., Nucl. Fus. 26, 1679 (1986), H. Capes, et al., Phys. Fluids B 4 (5), 1287 (1992); V. Mertens, et al., Plasma Phys. Contr. Fusion 36, 1307 (1994)

Investigation of Ion Dynamics in the ASDEX Upgrade Divertor by High Resolution Spectroscopy: First Results on Ion Drift Velocities

J. Gafert, M. Niethammer, K. Behringer†, D. Coster†, C. Dorn†, K. Hirsch, S. de Peña-Hempel†, U. Schumacher, ASDEX Upgrade- and NI-Team

Institut für Plasmaforschung, Universität Stuttgart, Pfaffenwaldring 31
D-70569 Stuttgart, Germany

† MPI für Plasmaphysik, EURATOM Association, D-85748 Garching, Germany

1 Introduction

Divertor physics studies turn out to be one of the most important tasks in fusion research using magnetically confined plasmas. The divertor is necessary for dispersion of the plasma power, for fuel gas and helium ash control, for reduction of impurity production at the boundary and for screening these impurities from the plasma core. Hence detailed investigations of the plasma parameters and of the ion dynamics in the divertor region and their modelling have high priority.

Optical spectroscopy with high spectral, temporal and spatial resolution in different directions to the magnetic field lines is a key to deducing a variety of these important divertor parameters and mechanisms. The highly resolved emission spectra are dominated by Doppler shift and broadening as well as by the Zeeman pattern, integrated along the line of sight. Hence, measured with high resolution, the spectra are — in terms of ion temperature and ion drift velocity distributions — a sensitive probe for the ion dynamics.

2 Experimental

In ASDEX Upgrade the emission profiles of several spectral lines are measured using high resolution spectroscopy. There are 30 lines of sight in a poloidal plane [1] and 44 lines of sight viewing tangentially to the toroidal magnetic field, half of them in the field direction and half of them opposite to it. This scheme of sight lines is illustrated in Fig. 1a as viewed from the top and in Fig. 1b as a projection into a poloidal plane (for some selected chords in Sector 14 of ASDEX Upgrade). The various lines of sight viewing from opposite directions cover the area from the outer divertor tiles beyond the X-point and thus allow for probing of both sides of the X-point region. This special matrix-like arrangement of the chords was chosen to diagnose the ion dynamics in the outer as well as in the inner divertor fan.

Quartz lenses and optical quartz fibers are used to couple the light collected along the lines of sight into the 1.5 m Echelle spectrometer, whose spectral resolution is about 10^5. The spectra are recorded by an intensified 2D CCD camera. For simultaneous data acquisition up to 32 chords can be selected via fiber coupling out of the 74 chords available. For an unambiguous determination of line shifts selected poloidal chords are always taken as an internal reference.

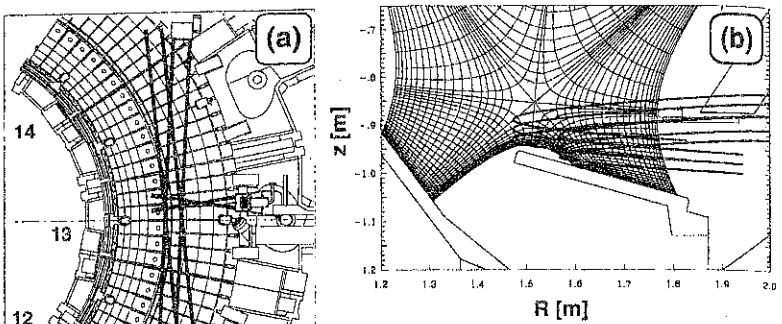


Fig. 1: Schematic representation of the poloidal and toroidal lines of sight in ASDEX Upgrade seen from the top (a) and as a projection into a poloidal plane (b, selected toroidal chords in Sector 14)

3 Zeeman Effect of Spectral Lines

As an example for a measurement we show the HeI singlet line at 667.815 nm, which has a simple Zeeman pattern and thus is suitable for demonstrating some characteristic features. In Fig. 2 the profile of the HeI-line for a radial (poloidal) chord (a) is compared to a profile measured with a tangentially oriented (toroidal) chord viewing in the direction of the toroidal magnetic field (b). While for the poloidal case the π-component clearly dominates, the tangential orientation is governed by the two σ-components. There is no significant Doppler shift observable for these HeI-spectra. The fit curves overlayed on the spectra were obtained by non-linear least squares fits to a convolution of the theoretical Zeeman-pattern with the instrumental function and a Gaussian describing the thermal broadening. Fig. 3 gives the results for the parameters of interest in this context as a function of time. The wavelength positions (relative to the poloidal case) shown in Fig. 3a for the poloidal and toroidal sight lines from Fig. 2 are the same within the error margin which is mainly given by the pixel resolution of the CCD camera. Similar results of the dependence on the chord direction are obtained for the magnetic field strength B (Fig. 3b) and for the ratio of the π- and σ-components (Fig. 3c). The magnetic field strength values are in very good agreement with the magnetic measurements. These values and the π/σ-ratio are used for calculating the

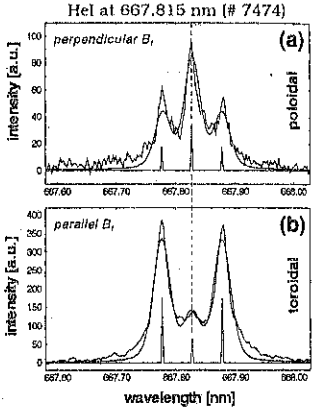


Fig. 2: Example of the HeI singlet line spectra for a chord viewing in the poloidal direction (a) and parallel to the toroidal magnetic field (b)

Zeeman-profiles of the other (ionic) lines observed for the identical lines of sight in similar discharge scenarios. As this procedure is only justified if the (spatial) emission profiles along the lines of sight are similar, this situation is checked by additional measurements with the boundary layer spectrometer [2] and the divertor spectrometer [3] at ASDEX Upgrade.

4 Drift Velocities of Ions

In contrast to the atomic line HeI the ionic spectral lines of all impurities in the plasma boundary show pronounced Doppler shifts for the toroidal observation. These ionic lines are, e.g., CII (doublet at $\lambda \approx 658$ nm), CIII (triplet at $\lambda \approx 465$ nm and singlet at $\lambda = 229.687$ nm), BII (singlet at $\lambda = 345.141$ nm), BIV (triplet line at $\lambda = 282.168$ nm) and HeII (doublet at $\lambda \approx 468.6$ nm).

Fig. 4 shows the CIII-singlet line spectra that were recorded under high recycling conditions (2 time ranges in # 8057: $P_{NI} = 2.0$ MW/7.5 MW, $\overline{n}_e \approx 6{\cdot}10^{19}$ m^{-3}/$8{\cdot}10^{19}$ m^{-3}) for the poloidal (b) and two toroidal chords (a, c) viewing into opposite directions. The shifts (relative to the average poloidal position λ_{pol}) deduced from these spectra are plotted as a function of time in Fig. 5a, clearly demonstrating the opposite Doppler shifts for the parallel and antiparallel (to $\vec{B}$) toroidal observation. These Doppler shifts result in (sight line averaged) drift velocities v_D of the order of $1.1{\cdot}10^4$ m/s that are given in Fig. 5b. Taking a C^{2+}-ion temperature of about 6 eV obtained from the Doppler width of the CIII-spectra the corresponding Mach numbers are in the range of 0.4 - 0.5. It should be noted that the observation volume is well above the high recycling region which is located close to the divertor plates. As to compare these experimental results with model calculations the distribution of C^{2+}-drift velocities along the appropriate lines of sight (for a typical L-mode discharge with $\overline{n}_e = 6{\cdot}10^{19}$ m^{-3}) was calculated using the B2-EIRENE code [4]. The v_D-values obtained from this simulation and from the spectroscopic data presented here (chord integrated) agree within about 50 %.

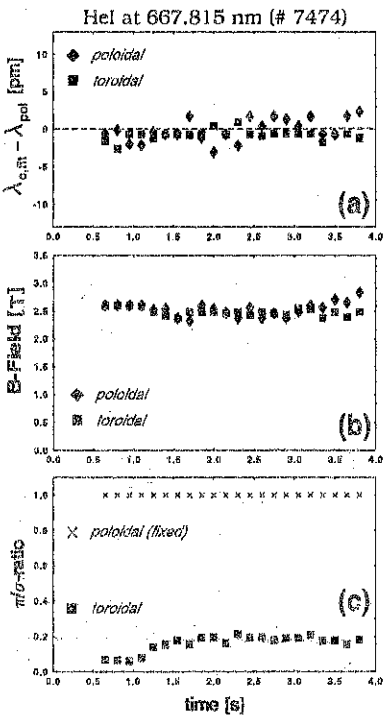


Fig. 3: Time dependence of (a) line shifts (relative to λ_{pol}), (b) magnetic field strength and (c) π/σ-ratio determined by fits to the HeI spectra of # 7474

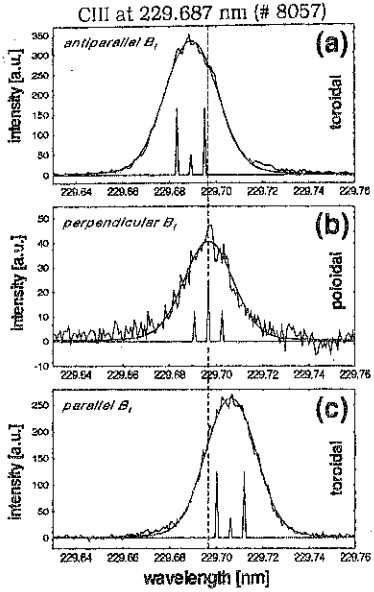


Fig. 4: Example of the CIII singlet line spectra for a poloidal (b) and two toroidal chords, one viewing in the direction of (c) and one opposite to (a) the toroidal magnetic field

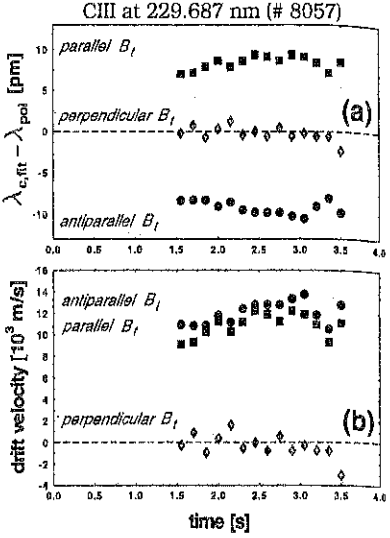


Fig. 5: (a) Doppler shifts (relative to the averaged poloidal position λ_{pol}) determined by non-linear least squares fits to the CIII spectra of # 8057 and (b) the resulting drift velocities towards the outer divertor plates as a function of time

Due to the matrix-like arrangement of the lines of sight mentioned above, the spectra are measured as a function of the radial position and thus yield information on drift velocities in both the outer and the inner divertor. By choosing appropriate chords it is possible to deduce ion drift speeds to the outer as well as to the inner divertor plates. This allows for a comparison of the ion dynamics in both divertor areas. As an example, the BII-spectra (λ = 345.141 nm) of an ohmic discharge (# 7193, $\bar{n}_e \approx 3.7 \cdot 10^{19}$ m^{-3}) yield v_D-values of about $1.1 \cdot 10^4$ m/s (towards the outer divertor) and of about $1.5 \cdot 10^4$ m/s for the drift of B^+ towards the inner divertor well above the divertor plates.

These first experimental results clearly demonstrate that the determination of drift velocities via the Doppler shift of emission lines is a suitable technique for investigating the drift dynamics of impurities in the ASDEX Upgrade divertor.

References

[1] Lieder, G. et al., Europhys. Conf. Abstr. **19C**, Part III, 409–412 (1995).

[2] Field, A. et al., Rev. Scient. Instrum. **66** (1995) 5433.

[3] Lieder, G. et al., Europhys. Conf. Abstr. **17C**, Part II, 579–582 (1993).

[4] Schneider, R. et al., J. Nucl. Mater. **196–198** 810 (1992).

ON THE POSSIBILITY OF q-PROFILE MEASUREMENT BY OBSERVATION OF PELLET ABLATION BY A FAST-FRAMING CAMERA AT ASDEX UPGRADE

H.W. Müller, P.T. Lang, K. Büchl, M. Kaufmann, P. McCarthy, V. Mertens, J. Miroshnikov, W. Schneider, H. Zohm, ASDEX Upgrade Team*
Max-Planck-Institut für Plasmaphysik, EURATOM-Assoziation
** Technical University St. Petersburg*

INTRODUCTION

Knowledge and control of the current density distribution and/or the profile of the safety factor q is of great importance for controlled thermonuclear fusion research on tokamaks. Mechanisms of transport processes and different instabilities are assumed to base on the connection between such processes and the q-profile. Interpretation and future active control of improved stability and confinement as well as control of bootstrap current with respect to advanced and possible continuous tokamak operation consequently requires information on the q-profile. Unfortunately, this plasma property is one of the most difficult to measure.

The method applied for the studies at ASDEX Upgrade is based on multiframe photography of cold plasma clouds near an ablating pellet. When injecting a deuterium pellet for particle refuelling into a hot plasma, the ablating material fills a spatial sequence of flux tubes following the magnetic field lines. Inside the flux tube, a cold, dense, high collisional plasma, containing a small fraction of neutrals, emits visible light after undergoing collisional excitation. Therefore, it is possible to observe the flux tubes passed by the pellet by means of a fast-framing camera. From these pictures the inclination angle of the magnetic field may be determined with respect to the torus midplane. Due to the application of a photographic camera for the investigations presented here, an adequate data analysis is very time consuming. A novel cooled 2D CCD camera detector that is currently developed[1], will greatly improve the performance of this experiment.

EXPERIMENTAL ARRANGEMENT AND DATA ANALYSIS TECHNIQUE

A scetch of the experimental arrangement is given in figure 1. Pellets are injected by means of a centrifuge injector horizontally near the midplane of the torus. By variation of pellet mass and/or velocity the pellet penetration depths into the plasma, which determines the radial range for the q-profile measurement, can be adjusted. Since pellet velocity is measured accurately, a precise localization $\mathbf{R}(t)$ of the pellet is possible at each time.

Via a window directly above the pellet injection port, nearly the whole injection path can be observed by the fast-framing camera: the camera's line of sight is slightly tilted with respect to the pellet injection path. The light is emitted inside the ablation cloud, passes through the observation window and is then directed via mirrors onto the cameras entrance lens. The image is further directed via a constantly rotating mirror onto one of 72 circular arranged lenses and finally focussed on the film. The ablation cloud image passes one lens within 4 μs; when the recording is finished, a series of up to 72 ablation cloud pictures has been imaged on the film. The total sequence covers a period of about 280 μs with each frame averaging the evolution within 4 μs. The light flux is controlled by a shutter mounted just behind the entrance lense.

For the analysis, the exposed film is developed and scanned to yield a digitized 2D intensit distribution of each frame. The inclination angles of the ablation clouds are determined b processing the digitized intensity distribution using two different methods. The first method fi a straight line to the points of maximum intensity, the second method calculates the principa axis of the intensity distribution. A check is performed by comparing results obtained by bot methods. A good coincidence of the inclination angles using both analysis methods was found This indicates correct determination of the angle. For each frame, the mean value of both value is adopted as α_M. Using it's recording time, the frame's radial position can be determined an hence the experimental values $\alpha_M(\mathrm{R})$ are obtained.

RESULTS AND DISCUSSION

With the knowlege on the radial profile of the magnetic field line inclination angle, the purpos is to determine the safety factor profile. It is easy to obtain q(R) from a given $\alpha_M(\mathrm{R})$ profil for example in the case of circular, concentric flux surfaces, where it can be calculated directl to be

$$q = \frac{r}{R_0} \times cot(\alpha_M)$$

However, since

$$q = \frac{1}{2\pi} \oint_{\psi_p} \frac{B_t}{R \cdot B_p} ds_p$$

is a global parameter and $\alpha_M(\mathrm{R})$ is a local value, the problem shows growing complexity with additional plasma shaping efforts. For an elongated plasma with triangularity as in ASDEX Upgrade, detailed knowledge on the plasma geometry is required for the q(r) reconstruction. Although there have been efforts to derive equations for an approximate calculation[2], the accuracy when using the analytic expressions for a direct calculation of q(R) decreases rapidely with increasing complexity of the plasma geometry. In our case, results were not satisfactory when using these analytic expressions. Consequentely, we determined the field line inclination angle $\alpha_{EC}(\mathrm{R})$ using a plasma equilibrium code and compared the results with the measured values $\alpha_M(\mathrm{R})$. The result is plotted in figure 2, where the triangles represents the $\alpha_{EC}(\mathrm{R})$ values, the crosses result from the camera measurements. Error bars indicate the uncertainty of each data point. The maximum possible error resulting from the error in the penetration depth of the pellet is identical to the uncertainty in the radial position of the whole measurement. This error is represented by the bar in the lower left corner. As can be recognized from figure 2, the measured field line inclination angles are in good agreement with those from the plasma equilibrium reconstruction at the plasma edge but show a growing discrepancy with increasing distance from the separatrix towards the plasma centre. This means the q-profile obtained by the equilibrium code is in agreement with the real field line inclination near the seperatrix but drops too rapid; the measured field line inclination in the plasma centre indicates higher q values there. In figure 3 the q-profile from the equilibrium code is plotted as solid line. The dashed line refers to a equilibrium estimated from the performed measurement of $\alpha_M(\mathrm{R})$.

The discrepancy between the equilibrium code and the camera measurements however can be due to the equilibrium code's decreasing accurancy towards the plasma centre. For the calculation of the equilibrium, the applied algorithm tries to find the most likely equilibrium plasma configuration which reproduces measurements of coils mounted at the tokamaks vacuum vessel. These signals are dominated by the magnetic conditions near the plasma surface. As the distance to the coils is greater and the volume is smaller, the plasma central region signal contribution is small compared to that one of the edge region. Consequentely, the equilibrium reconstructer

is more accurate for the edge region where its reliability drops with decreasing distance to the plasma centre.

CONCLUSION

We found that the ablation clouds of evaporating pellets injected for the purpose of plasma refueling can be used to visualize magnetic field lines. For the plasma boundary region the measured inclination angles are in excellent agreement with those obtained using the equilibrium code based on the magnetic coil data. As for the plasma boundary the code is most accurate we consider the cameras measurement determines the inclination angle correctly. For the plasma regions closer to the plasma centre, the discrepancy is most probably caused by the decreasing sensitivity of the equilibrium code to this region. Whereas the accuracy of the q values strongly decreases for the equilibrium code analysis, it remains almost constant for the $\alpha_M(\mathbf{R})$ measurement with decreasing distance to the plasma centre. Moreover, the q-profile deduced from the $\alpha_M(\mathbf{R})$ data is supposed to be more accurate than the q-profile from the equilibrium code. Figure 4 shows the reduction of the normalized experimental error margin $\frac{\Delta j}{\Delta j_{axis}}$ and $\frac{\Delta q}{\Delta q_{axis}}$ when including the $\alpha_M(\mathbf{R})$ data to the code input data (stars) in comparison with magnetic coil data only.

Thus, although it cannot yield a satisfactory determination of q-profiles on its own in complex plasma configurations, the technique of measuring field line inclination angles by observation of pellet clouds with a fast framing camera can significantly improve the accuracy of a q-profile reconstruction when combined with another method. As shown here, combination of the local measurement of the inclination angles with the equilibrium code analysis can improve the result obtained substantially.

ACKNOLEDGEMENT

We hereby acknowledge financial support of this joint project by the Bundesministerium für Bildung und Forschung in the context of the Russian-German Science and Technology cooperation 'Gesteuerte Kernfusion und Plasmaphysik'.

REFERENCES

[1] I.V. Miroshnikov, Rev. Sci. Instrum. **66**, 389 (1994).
[2] TFR Group, Europhys. Lett., **2**, 267, (1986).
TFR Group, Nucl. Fusion, **27**, 1975 (1987).
S.M. Egorov et al., JETP Lett., **46**, 180 (1987).
R.D. Durst et al., Rev. Sci. Instrum. **59**, 1623 (1988).

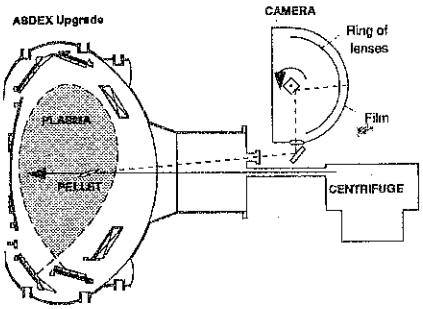


Figure 1

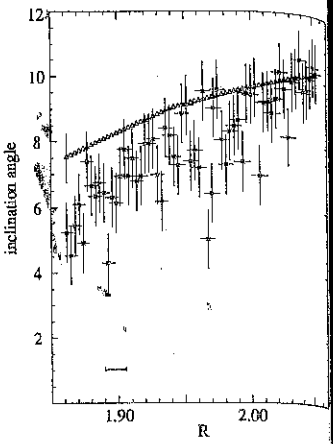


Figure 2

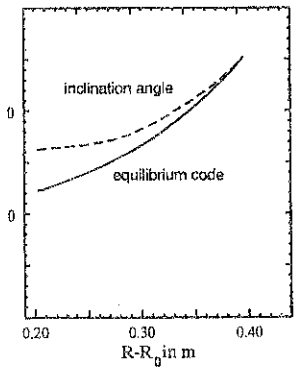


Figure 3

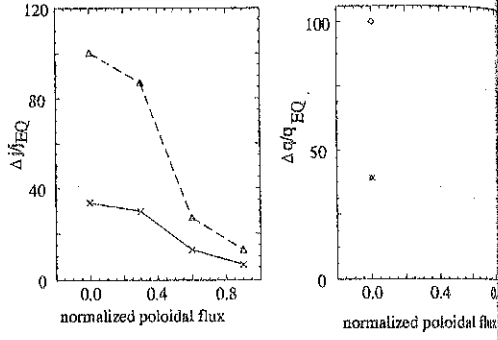


Figure 4

Fig 1: *Experimental setup*
Fig 2: α_M *compared to* α_{EC}.
Fig 3: *The solid line shows the q-profile calculated by the equilibrium code, the dashed line an estimation for the q-profile based on* α_M.
Fig 4: *Reduction of error in current density (j) and q when including* α_M *to the equilibrium code (stars) with respect to the errors in j and q calculated without* α_M *measurements.*

Profiles of Ion Temperature and Neutral Density from the Simulation of Charge Exchange Measurements and Additional Experimental Data.

J. Stober, D. P. Coster, H.-U. Fahrbach, R. Fischer, G. Haas, W. Herrmann, O. Kardaun, A. Khutoretsky †, S. de Peña Hempel, D. Reiter‡, R. Schneider, H. Verbeek, the ASDEX-Upgrade team, and the NBI team
Max-Planck-Institut für Plasma-Physik, EURATOM-Association,
D-85748 Garching, Germany
† RRC "Kurchatov-Institute", 123182, Moscow, Russia
‡ IPP, Forschungszentrum Jülich GmbH, EURATOM-Association,
D-52425 Jülich, Germany

1 Introduction

At ASDEX-Upgrade a method to evaluate the ion temperature profile has been developed by fitting the measured energy spectra of the neutral hydrogen and deuterium fluxes varying the parameters of the T_i profile. Two detection principles are used to cover the extremely wide energy range [15 eV, 20 keV]. It turned out that a reasonable accuracy at the separatrix can only be obtained when measurements of the total neutral flux are included in the fit as well [1]. In addition to the T_i profile, the neutral density along the lines of sight and a spatially constant H/D-ratio are determined. The method can also be used during neutral beam injection (NBI) so that comparison with local T_i measurements from charge exchange recombination spectroscopy (CXRS) is possible. The results are also compared to classical logarithmic slope evaluation. Finally, the problem of the parameterization-dependent results is addressed and we present first results of a Bayesian approach to determine the necessary degree of regularization.

2 Experimental

The energy spectra of the neutral fluxes are measured with two methods. One is based on the reionization in a gas cell and an energy and mass separation of these ions in parallel electric and magnetic fields [2]. The lowest detectable energy is normally set to 500 eV. At ASDEX-Upgrade, there are two analysers of this type which both view the plasma from the outer midplane. One is fixed and views the plasma center (CXA I), the other is turnable to vary its poloidal and toroidal direction (CXA II). The other method is a time-of-flight analysis of the neutrals without isotope separation (LENA) [3]. Its energy range is between 15 eV and 1 keV. The total neutral flux is measured directly with an ion gauge at the outer vessel wall [4]. Additionally an H_α measurement has been set up with a line of sight close to the one of LENA (horizontal, 20 cm above the magnetic axis). For the T_i evaluation further experimental data are used: n_e from interferometry combined with lithium beam, T_e from Thompson scattering or ECE, and the proton density from spectroscopy [5]. These quantities, as well as T_i, are assumed to be constant on flux surfaces.

3 Fitting procedure

To model the energy-resolved neutral fluxes $S(E_0)$, we assume that the velocity distribution of the ions has Maxwellian form:

$$S(E_0) = \frac{1}{2\pi^{3/2}} \int_0^L < \sigma_{cx} v_{rel} > (x) \cdot n_0(x) \cdot n_i(x) \cdot \frac{\exp(-E_0/T_i(x))}{T_i^{3/2}(x)} \cdot E_0^{\frac{1}{2}} \cdot \exp\left(- \int_0^x \frac{ds}{\lambda_{tot}(s)} \right) dx$$

The neutral density is obtained with the EIRENE Monte-Carlo code [6], using only the experimental data and the T_i parameters of the corresponding iteration step as input for the plasma background. The positioning of an assumed source of neutrals at the outer plasma-facing structures (outer source), which is required by the code, turned out to be of minor importance. For very low densities inner-wall sources also play a role, but only for the central plasma. Volume recombination as source of neutrals must not be neglected. For the T_i profile a linear spline parameterization is used. Parameters to be fitted are the T_i values at the knots. Additional parameters are the spatially constant H/D-ratio and the strength of the outer source. We use a χ^2-type minimization, which takes experimental errors into account. The number of time consuming neutral density calculations could be reduced to 3 or even less by a two step algorithm, which optimizes the parameter values for a fixed neutral density which is recalculated only in an outer loop. Parameter errors are estimated from the curvature at the minimum of χ^2. In the following graphs error bars refer to one standard deviation.

4 Comparison with T_i from other diagnostics

In the case of NBI heated plasmas, local T_i-data are available from CXRS [7] also. Figure 1 shows a comparison of the two methods. The agreement is quite good in this case.

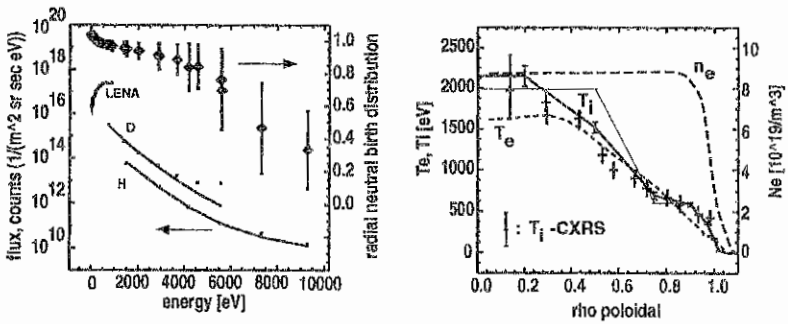


Figure1: Analysis of a NBI-heated plasma (I_p = 1.0 MA, B_t = -2.5 T, 5 MW NBI). Left: data with errors, fit (solid lines) and birth regions of the neutrals. Since deuterium is injected, this isotope deviates from the fit at higher energies. Only the 3 lowest points are used for χ^2. Note that LENA data are given as uncalibrated count rates $1/(m^2\ sr\ sec)$ since isotopes cannot be separated. Right: temperature and density profiles. The thin solid line refers to a fit of the fluxes alone. The thick solid line is the result when the deviation from the CXRS values is included in χ^2 ($\rho_{pol} = \sqrt{\frac{\Psi - \Psi_{axis}}{\Psi_{sep} - \Psi_{axis}}}$, Ψ = pol. Flux).

Inclusion of the CXRS data improves the fit in the central plasma.
With the movable CXA II analyser, a series of similar shots was used to obtain the maximum T_i on different lines of sight from the logarithmic slope at high energies [8]. For the analysed scenario (ohmic, $n_e = 3 \cdot 10^{19} m^{-3}$) the agreement was good and, as with CXRS, the fit could be improved including the additional data.

5 Ohmic density scan

As an application, an ohmic density scan is shown in figure 2:

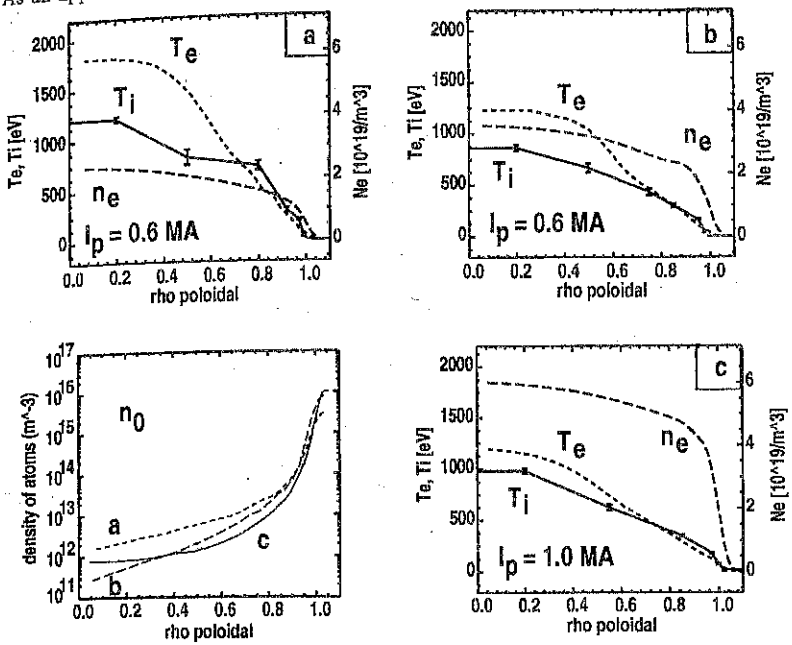


Figure 2: Comparison of ohmic discharges with different plasma densities.

The increased coupling between the primarily heated electrons and the ions with increased density leads to a decrease of the relative difference between T_e and T_i. In the analysed density range, the dominant source of neutrals in the center changes: In the low density case (a), only wall neutrals are important. As n_e increases (reduction of neutral mean free path), n_0 decreases (b). Here, wall and volume sources are of equal importance for the center. With further increasing n_e (and nearly the same T_e), the volume source dominates (c) and leads to a rather constant n_0 over a wide radial range.

6 Bayesian Regularization

A problem of the procedure discussed so far, is the choice of the knot configuration of the linear spline for T_i. In practice, a trial configuration is accepted, if the resulting T_i-profile

has no oscillations and if χ^2 is reasonably low. Often several trials are necessary. Since several configurations are acceptable, the choice is somewhat arbitrary. Alternatively, one can choose "many" knots and use a regularization, for example by adding $\lambda \int d\rho\, f(T^{(k)}(\rho))$ to the minimization functional. The choice of the weight λ, or even several weights for separate radial intervals, is often made manually (as is the choice of the intervals) and is to some extent arbitrary also.

Here, we present the results of a procedure that automatically determines its local degree of regularization combining an adaptive kernel method with Bayesian statistics [9]. The parameterization is $T_i(\rho) = \sum_{j=1}^{N} h_j \cdot \exp(-\frac{(\rho-\xi_j)^2}{2b_j^2})/\sqrt{2\pi}b_j$ with N "large enough" (here N = 37) and ξ_j fixed and spaced "narrowly enough". The regularization enters via a Bayesian prior distribution for $\vec{b}$: $p(\vec{b}) = \Gamma(N_p/2)/(2\pi \sum_{j=1}^{N} b_j)^{N_p/2}$, $N_p = \sum_{j=1}^{N} \frac{1}{b_j}$ being called the generalized dimension of the parameterization. The posterior distribution is analysed, and its maximum (MAP), its mean, and its variance are determined. As a first step, the method has been implemented with fixed neutral densities, that were obtained from the manual linear spline method. Figure 3 shows a comparison of both methods.

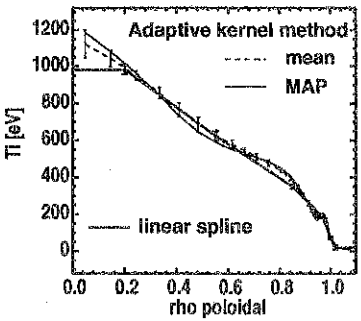


Figure 3: Comparison of the optimized linear spline (3rd trial, same as fig. 2c) with the result of the Bayesian adaptive kernel method. The error bars of the dashed curve represent the corresponding standard deviations of the posterior distribution. The T_i values and their errors agree well over a large radial range. The intuitive positioning of the knots seems to be sensible.

References

[1] Stober J. et al., *Proc. of the 22nd EPS Conference on Controlled Fusion and Plasma Physics, Bournemouth, 1995*, **19C,III**, 249 (1995), EPS

[2] Bartiromo et al., *Rev. Sci. Instrum.*, **58**, 788 (1987)

[3] Verbeek H., *J. Phys.*, **E19**, 964 (1986),
Verbeek H., Schiavi A., *IPP-Report*, **9/103**, (1994)

[4] Haas G. et al., *J. Nucl. Mater.*,**121**, 151 (1984),
Klepper C. C. et al., *J. Vac. Sci. Technol.*, **A 11**, 446 (1993)

[5] Dux R. et al., *IPP-Report*, **10/1**, (1996)

[6] Reiter D., *KFA Jülich reports*, **Jül-1947**, (1984), **Jül-2599**, (1992)

[7] Boileau A., *Plasma Phys. Controlled Fusion*, **31**, 779, (1989)

[8] Wagner F., *J. Vac. Sci. Technol.*, **20**, 1211 (1982)

[9] Fischer R. et al., to be published

Interpretation of Mirnov Measurements in ASDEX Upgrade

M. Schittenhelm, H. Zohm, ASDEX Upgrade - Team

Max-Planck-Institut für Plasmaphysik - EURATOM Association, D-85740 Garching

Most MHD instabilities are connected with perturbations of the equilibrium field. The evaluation of the perturbation field would be one of the directest methods to investigate the mode structure. Unfortunately, in a hot fusion plasma, measurements of the perturbation fields using pick-up coils (Mirnov probes) [1] are only possible outside the plasma without any resolution in the radial direction. Due to this reason, the analysis of complex mode structures is difficult.

In the ASDEX Upgrade tokamak [2], the modulation of the poloidal field due to a rotating mode structure is measured by a poloidal array of 30 pick up coils and by 4 coils in a toroidal plane. For a detailed analysis of the modes, the Mirnov probe measurements are compared with simulations of the perturbation field at the probe locations. In the simulation, the current flows along the equilibrium field lines on the resonant flux surface and, to ensure $\nabla \cdot j = 0$, the current density is proportional to the magnetic field. The location of the resonant surface and the field line geometry are computed from equilibrium analysis. The induced screening currents in vacuum vessel and in conducting structures close to the Mirnov probes are taken into account while computing the perturbation field. Results of this new Mirnov Interpretation Code (MIC) are presented in the following section.

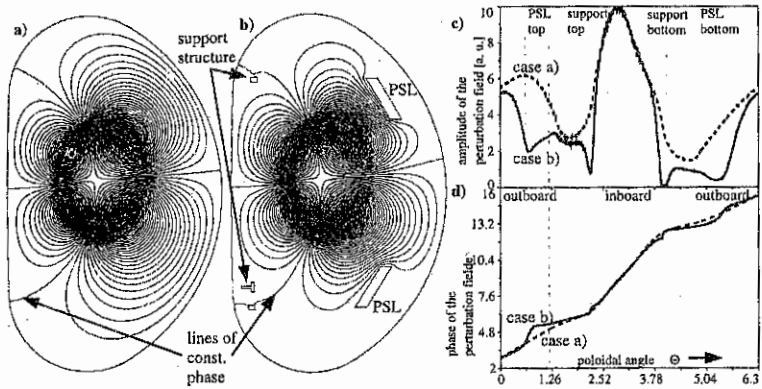


Figure 1: *Influence of the screening currents on the perturbation field. a) Simulation of the perturbation flux for a typical m=2 mode considering screening currents only in the vessel. b) Simulation with additional screening currents of in-vessel components. c), d) Amplitude and phase of the perturbation field parallel to the vessel at the probe position (2.5 cm inside the vessel) in the cases a and b.*

For the discussion of the influence of the screening currents, Fig. 1 shows the computed perturbation flux function, which results from an $m = 2$ perturbation on the $q = 2$

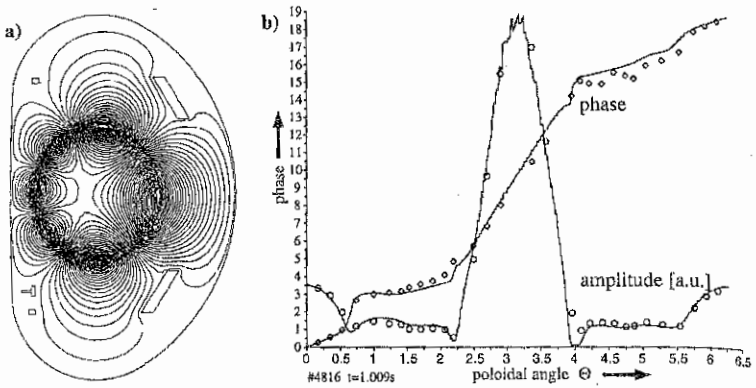


Figure 2: *Comparison of the calculation and the measurements of a $m = 3$ mode in a limiter plasma with circular cross-section. a) Calculated perturbation flux. b) The amplitude and the phase of the mode vs. the poloidal angle of the probe position. The simulated perturbation field is in good agreement with the measurements.*

surface (the edge q of the plasma is $q_{95} = 5.0$). Due to screening currents, the flux function vanishes at the vessel wall and the contour lines nestle to the wall. The phase at a given poloidal angle Θ depends on the radial distance from the resonant surface. Points of equal phase can be found along the lines of vanishing flux (Fig. 1a). Away from the midplane, points of equal phase have a clear divergence from a straight line. Ignoring this 'vessel effect', the reduction of the wave length on the high field side due to toroidicity, shaping and β-effects would be overestimated.

Fig. 1c,d shows the influence of the in-vessel components on the perturbation fields. The amplitude and phase are computed 2.5 cm inside the vessel (position of the Mirnov probes) versus the poloidal angle Θ. Close to the in-vessel components, the screening effect reduces the amplitude up to a factor of 10. The amplitude in the midplane shows a small influence. The influence on the phase is only noticeable outboard in the region of the Passive Stabilisation Loop (PSL) which is formed like a saddle coil (m=1; n=0 structure) to slow down the vertical plasma movement [3]. Together with their support structure, the conductors of the PSL result in an effective n=8 screening loop in front of the outboard probes at usual mode frequencies of several kHz.

The new method for the interpretation of Mirnov measurements can be demonstrated for a circular limiter plasma in a fast current ramp up scenario. Due to the decreasing edge safety factor q, a ($m = 3$, $n = 1$) kink mode can develop when the $q = 3$ surface leaves the plasma. The simulation assuming a perturbation current on this surface shows a good agreement with the measurements (Fig. 2).

On the contrary to the circular limiter plasma discussed before, a dominant ($m = 2$, $n = 1$) mode always occurs before disruptions in elongated divertor plasmas. In this case, the simulated amplitude of the modulation is in disagreement with the measurements. The measured and simulated ratio between the amplitudes of outboard and inboard midplane probes differs by a factor of two. Another experimental fact is that the ratio between these

amplitudes is not constant during the growth of the modes. Especially in a density limit discharge with high $q_{95} = 5$ at the edge, the amplitude of the perturbation field increases by a factor of 10 in a few ten milliseconds before the first minor disruption. In this short time interval, the equilibrium of the plasma does not change, but the ratio between the inside and the outside amplitude decreases, as shown in Fig. 3a. The variation of the

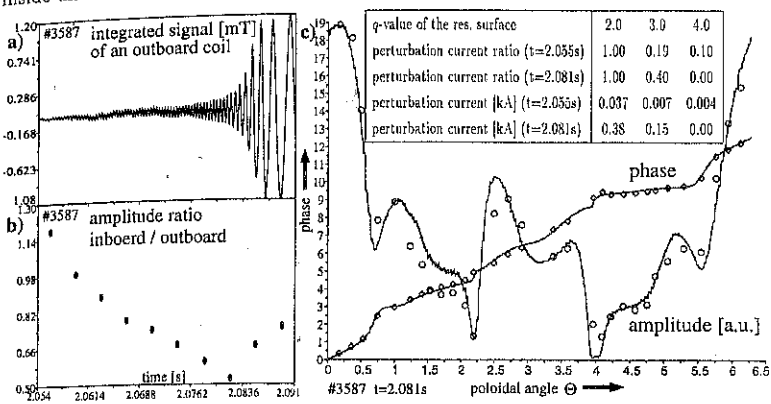


Figure 3: *Before the density limit is reached, a MHD mode develops. a) In the high q case, the amplitude increases by a factor of 10 in few ten milliseconds. b) The measured amplitude of the low field side increases more than two times faster compare to the high field side although there is no change of the position or the equilibrium of the plasma. By assuming mode coupling, the simulation fits the measurements very well.*

amplitude ratio indicates the development of coupled modes on neighbouring resonant surfaces. Assuming perturbation currents on those surfaces, the perturbation field is computed for every surface alone in the described way. To superpose the fields for the final result, it is necessary to find the correct ratio between the perturbation currents on the different surfaces. Using complex amplitudes for the specification of the simulated and measured field (i. e. also allowing for a vaying phase angle), the value of the currents on the different surfaces can be computed by a least square fit. To get a good agreement with the measurements in the case shown in Fig. 3c, perturbation currents are assumed on the $q = 2$, $q = 3$ and $q = 4$ surfaces. The amplitudes of the assumed sheet currents are summarised in Fig. 3c for two time points at the begin and the end of the mode growth. Comparing the two time points, it becomes clear that the coupled $m = 3$ mode grows twice as fast as the dominant $m = 2$ mode. In spite of the strong contribution of the $m = 3$ mode at $t = 2.081$s, the phase is dominated by the $m = 2$ mode. Only the consideration of the amplitude *and* phase can give the contribution of coupled modes in the presented way.

Fig. 4a shows the time traces of a representative, high q density limit discharge (q_{95}=5) [4] 150 ms before the final disruption. Approximately 10 ms before the density limit, a rotating MHD-mode occurs and grows exponentially. The rotation frequency decreases from 2.4 kHz to 0.72 kHz at the saturation point. At first, no mode locking occurs

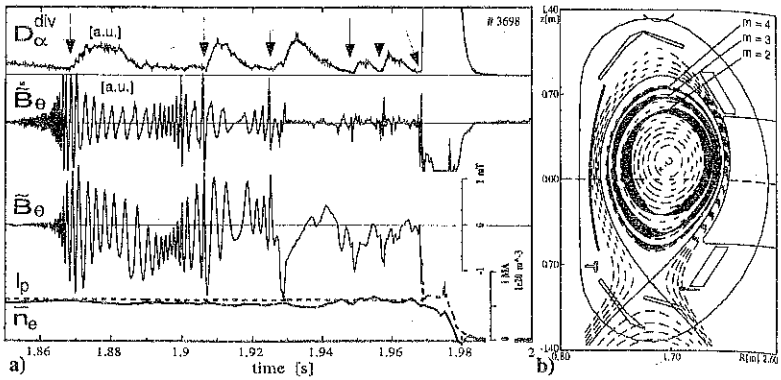


Figure 4: *a) Time traces of a density limit discharge at high q. The arrows mark the begin of an increased transport of particles and energy on the divertor plate at the occurrence of a minor disruption or the terminating major disruption. b) The reconstructed island structure at t=1.869s*

and the islands decrease their amplitudes. At lower amplitude, the islands accelerate their rotation until the perturbation increases again. The islands saturate at the same amplitude as before. This cycle is repeated two or three times until the mode locks. After 30 to 50 ms the major disruption terminates the discharge.

Using the analysis presented before, the saturation amplitudes of perturbation currents are (t=1.869s): q=2 : 4.3kA; q=3 : 1.9kA; q=4 : 0.43kA. By superposing the helical equilibrium flux and the computed perturbation flux, the resulting islands can be illustrated. Although this linear treatment does not give the new consistent equilibrium with all perturbation currents, it allows to illustrate the island structure and to give an estimate for the island width (Fig. 4b). This analysis confirms that the minor disruptions start when the growing islands on the different surfaces come close together [5, 6]. Because of the mode locking before the major disruption such an exact analysis of the measurements is not possible for the major disruption.

To summarize, it should be pointed out that the phase and amplitude of the perturbation field must be considered to reconstruct complex mode structures. By a comparison of the simulated perturbation field with the measurement, the contribution of coupled modes on different surfaces and of the induced screening currents can be distinguished. The induced screening currents have a noticeable influence on the measured perturbation field.

References

[1] S. Mirnov and I.V. Semenov. *Plasma Phys. Contr. Fusion Research*, 2:22, 1971.

[2] W. Köppendörfer et. al. In *Fourteenth internationel conference on plasma physics and controlled nuclear fusion resaerch, Würzburg, Germany.* IAEA, Wien, 1992.

[3] O. Gruber et al. *Plasma Phys. Contr. Fusion*, 35:B191, 1993.

[4] V. Mertens et al. *Plasma Phys. Contr. Fusion*, 36:1307, 1994.

[5] A. Bondeson et. al. *Nuclear Fusion*, 31:1695, 1991.

[6] H. Zohm et al. *Plasma Phys. Contr. Fusion*, 37:A313, 1995.

Measurements of Impurity Transport in SPHEX Spheromak and START Tokamak.

V. Johnson, K. J. Gibson, G. Cunningham.
Dept. of Physics,
UMIST, P.O. Box 88, Manchester, M60 1QD.

Introduction

The study of particle transport in magnetically confined plasmas is an important element in the understanding of global power and particle balance. To facilitate these studies a number of diagnostics based on the introduction of transient bursts of impurities have been developed. Principal amongst these are fast gas puffing and laser ablation [1]. Here we report on a further development of an additional technique [2] based on the release of impurities from the electrodes of an arc discharge.

The "spark plug" probe described in this paper overcomes the problems of cost and lack of spatial control encountered with the more traditional techniques. The probe allows the introduction of a short ($< 10\mu s$), spatially localised ($\sim$ 0.5cm) burst of high or low Z impurities. We report on the application of the diagnostic to two separate devices, the UMIST spheromak, SPHEX [3], and START [4], the low aspect ratio tokamak at Culham Laboratory. In both cases values of particle confinement obtained are in good agreement with values estimated by other techniques. In addition, we demonstrate the potential for the diagnostic to be used to study particle trajectories along field lines, particularly at the plasma edge.

The impurity injection system

The experimental setup consists of a concentric electrode tip (4cm long) (see Figure 1), mounted at the end of a vacuum sealed, insertable probe housing. The central electrode connects via an ignitron to a 60μH, 3μF, 1.5mΩ LCR circuit producing a damped oscillating signal capable of delivering a maximum of 150 joules in a $10\mu s$ burst. From arc discharge data this corresponds to an injection of 1×10^{18} ions; for the chosen impurity this implies a density perturbation of $< 10\%n_e$.

The choice of electrode material is a compromise between having sufficiently high electrical conductivity and being suitable for transport studies. This is largely determined by the need to have an extrinsic impurity (to minimise the effect of recycling) and by the available spectroscopic instrumentation. In practice, on

smaller devices, it is not always possible to reconcile these criteria and the data reported here was taken with electrodes manufactured from graphite.

Results

The probe was initially designed for transport studies on the UMIST spheromak, SPHEX. The device is a gun injected spheromak similar in design to the CTX device which was operated at the Los Alamos Laboratories, New Mexico.

Figure 2 shows the temporal decay of CIII and CIV after on-axis impurity injection during the non-driven phase (i.e. when the there is no voltage applied on the Marshall gun electrodes). ($T_e \approx 25$eV, $n_e \approx 5 \times 10^{19}$m^{-3}). Analysis of the CIV decay returns a τ_p of 250μs. The data is modelled using the 1D impurity transport code, STRAHL, commonly used for the interpretation of spectroscopic measurements on other machines. A comparison of the experimental and modelled data is also shown in Figure 2. The density and temperature profiles required by the code were determined from previous Langmuir probe data [5]. The results shown are fitted for a $D_\perp$ 80-100m^2 s^{-1} throughout the plasma; there is no pinch term included in this analysis. The value obtained is in good agreement with previous estimates based on studies of decreases in plasma rotation in decaying spheromaks [6].

A similar analysis of impurity injection carried out during driven SPHEX operation suggests a degradation in confinement properties. This may be related to increased global magnetic fluctuation levels, associated with the current drive process, but requires further work for confirmation.

In addition to the SPHEX results, this technique has now been applied for the first time to a high temperature plasma on the START tokamak ($T_e = 300$eV, $n_e \approx 2 - 8 \times 10^{19}$m^{-3} for the data considered here), providing the first direct measurement of impurity confinement in a tight aspect ratio tokamak. Raw data from a typical discharge in which impurities were injected is shown in Figure 3, showing clearly the burn through of the ionisation states CII-CV. Analysis of CV decay (representative of core confinement for these conditions) suggests a value for τ_p of around 3-5 ms, a factor of 2-3 greater than the energy confinement time.

Of special interest on START is a series of studies made of the edge plasma and the injection process. Figure 4 is a CCD image of the START plasma during the firing of the probe. The colour COHU 8390 CCD camera used has a framing time of 0.1ms producing one image per $\approx$ 20ms shot. The exceptionally good optical access of the device has allowed the trajectory of the injected impurity ions to be studied in some detail. On the START machine, determination of the magnetic equilibrium is complicated by the lack of any field measurements on the outboard side of the plasma. On the assumption that the ionised carbon is

streaming initially along the field, it has been possible to make a good fit of the equillibrium from the reconstruction of the local pitch of the field lines [7].

This analysis gives some indication of the potential of the probe for other studies of particle trajectories. In particular, the possibility of installing a modified version of the probe in both the START and COMPASS-D divertor regions is being studied.

Conclusion

In this paper we have described a technique for impurity particle injection for use on transient tranport analyses. The "spark plug" probe provides a cheap, compact diagnostic offering high spatial and temporal resolution. The probe has been used successfully on both high and low temperature plasma devices and the values of particle confinement time are in good agreement with those obtained by other techniques. The probe has also allowed the study of impurity ion trajectories at the edge of the START tokamak; in the future it is planned to use a similar technique for studies of particle transport in the divertor.

Acknowledgements

The work on START was funded in part by the UK Department of Trade and Industry and EURATOM. One of the authors (VJ) is grateful to the Engineering and Physical Sciences Research Council (EPSRC) for studentship support.

References

[1] E. S. Marmar, J. L. Cecchi, S. A. Cohen, Rev. Sci. Instrum **46**, 1149 (1975).

[2] F. M. Levington and D. D. Meyerhofer, Rev. Sci. Instrum **58**, 8 (1987).

[3] P. K. Browning, G.Cunningham et al, Phys. Rev. Lett **68**, 1718 (1992).

[4] A. Sykes *etal* Plas. Phys. & Contr. Fus. **35** (8) 1051 (1993)

[5] S. J. Gee, UMIST, Private Communication (1995)

[6] K. J. Gibson, S. J. Gee and M. G. Rusbridge Plas. Phys. & Contr. Fus. **37** (1) 31 (1995)

[7] R. Buttery, UKAEA Fusion, Private Communication (1996).

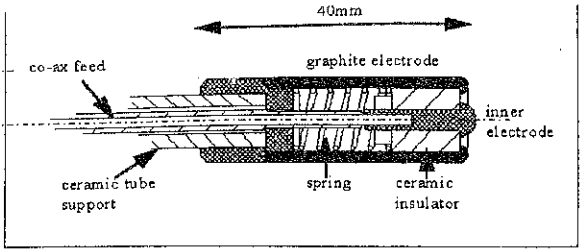


Fig. 1: Schematic of spark plug tip

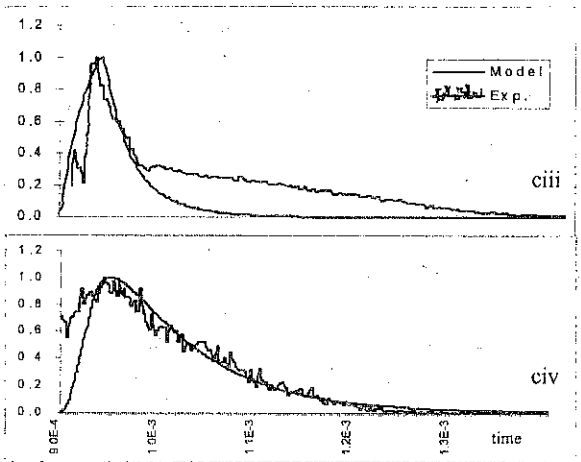


Fig. 2 Raw SPHEX data with model data overlaid

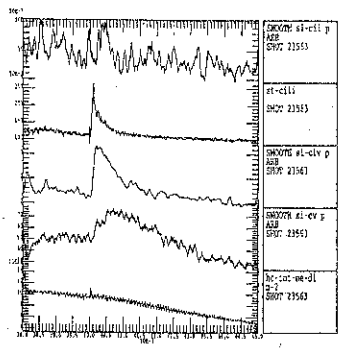


Fig. 3 START shot 23568 showing temporal history of C ionisation states. Injection occurs at 40ms.

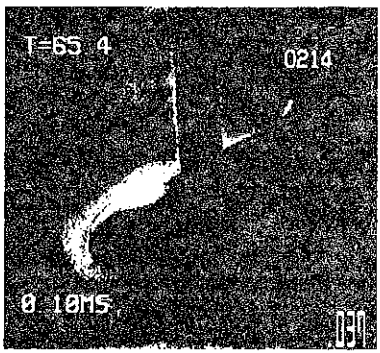


Fig. 4: CCD image from START showing carbon emission localised to field line.

X-Ray Tomography on TCV

M. Anton, H. Weisen, M. J. Dutch, W. Von der Linden, I. Furno,

F. Bühlmann, R. Chavan, B. Marletaz, P. Marmillod, P. Paris

Centre de Recherches en Physique des Plasmas

Association EURATOM - Confédération Suisse

Ecole Polytechnique Fédérale de Lausanne, 1015 Lausanne, Switzerland

Abstract

The TCV tokamak ($B_T \leq 1.5$ T, R = 0.88 m, $a \leq 0.25$ m, $\kappa \leq 3$) is equipped with a soft X-ray tomography system consisting of 10 pin-hole cameras with 20-element planar Si diode arrays arranged around the plasma cross section. The aim of the diagnostic is to provide an independent measurement of the shape of the flux surfaces in the plasma core, to study MHD phenomena and to assist in the evaluation of the impurity content of the plasma. Successful commissioning of the system was dependent on the accurate determination of the actual camera geometries, the dimensions of which deviate within tolerances of ~0.1mm from their nominal values. It was also necessary to take account of the effect of the inactive 'dead' layer at the PIN diode surface causing angle- and spectrally dependent additional absorption, as discussed previously [1]. Several different pixel methods, including a novel method based on Fisher information, have been tested, both on simulated and on experimental data. The method based on Fisher information provides the most accurate reconstructions of both the overall emissivity profile and of small perturbations due to MHD modes. It has been used in investigations of the effect of plasma shape on sawtooth behaviour, showing a dramatic reduction at negative triangularity, of sawtooth amplitude, determined by application of the method of Biorthogonal Decomposition on the inverted data. The sawtooth inversion radius, determined using the same method, exhibits no significant dependence on triangularity [2].

Experimental determination of system geometry

Even small mechanical errors (0.1-0.2mm) can lead to substantial error in the reconstructions due to the small detector to aperture distances (~14 mm) and element separations (1 mm). Since it was impossible to achieve finer tolerances in the camera setup, which also has too satisfy severe constraints of vacuum tightness and thermal insulation, the departures of the actual geometry from the nominal one had to be determined experimentally. This was achieved by comparing the detected signals and simulated signals for several plasmas created at different positions in the elongated TCV vacuum chamber. The position and shape of these was obtained using the inverse equilibrium code LIUQE which uses external magnetic measurements. Once adjusted, no further geometrical corrections were necessary and reliable reconstructions using the initially determined geometry have now been obtained for more than one operational year.

Comparison of Pixel Methods

The poloidal cross section of the TCV has been divided into n_{pix} square pixels (3.8×3.8 cm^2) with emissivity $\mathbf{g}_i$ the contribution of which to the detected signals ($\mathbf{f}_j$) is described by a a tranfer matrix **T**:

$$\mathbf{f}=\mathbf{T}\mathbf{g}$$

Since the problem is underdetermined and the transfer matrix can be badly conditioned, we find a unique and sensible solution looking for a minimum of

$$\phi = \frac{1}{2}\chi^2 + \alpha R$$

where R is a regularizing functional and a is a positive number which determines the weighting between the goodness-of-fit, represented by χ^2, and the requirements imposed on the solution by R. The performance of different methods have been tested: First and Second Order Linear Regularization [3], Maximum Entropy [4] and a new method [5] relying on the Fisher Information (fig.1). In the case of the Minimum Fisher Information $R = |\nabla^2 g/g|$, as compared to First Order Regularization for which $R = |\nabla g|^2$. Computationally the Minimum Fisher Information reconstruction has been implemented as an iterative weighted first order regularization method, abbreviated MFR [2]. Independently of the noise affecting the data, the most faithful reconstruction are obtained with MFR (fig.1). Both linear regularization methods yield emissivity distributions which are too broad and Bayesian Maximum Entropy is too noisy. The good performance of the MFR is due to the fact that the smoothing is less strong where the Soft X-Ray emissivity is highest, i.e. at the plasma center.

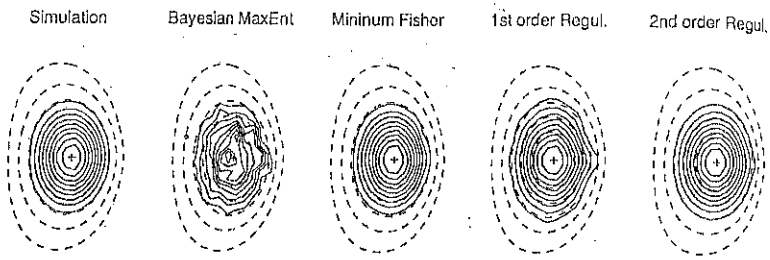


FIG. 1. Reconstruction of the simulated emissivity using different methods of inversion.

Dependence of sawtooth amplitude on plasma triangularity

For the analysis of sawteeth and MHD activity, we use the Biorthogonal Decomposition or SVD, applied to a time series of tomographic reconstructions. Let **X** be a matrix whose lines contain the time series of the different pixel emissivities, then the results of SVD is:

$$\mathbf{X} = \mathbf{U}*\mathbf{S}*\mathbf{V}^T$$

where the columns of the matrix **U** represent the spatial "eigenmodes", called *topos* , while the corresponding temporal information is contained in the columns of **V** or *chronos* [6].The pairs of *topos* and *chronos* are coupled by the elements of the diagonal matrix **S**, their corresponding singular values. The elements of **S** are stored in descending order, so that the first *topos /chronos* pair contains the most important features (fig. 2, top right). The contributions of different features is the relative signal energy

$$p_k = S_k^2/E_x$$

where S_K is a singular value and E_X is the sum of the squares of the diagonal elements of **S**.

In the example of fig. 2, from a reconstruction with 10 kHz time resolution, the most important *topos* (top, from left to right) have the appearances of an average emissivity profile (*topos* #1), an inversion profile (*topos* #2), and a pair of perturbations (#3 and #4) the sum of which corresponds to a rotating m=1 mode. The corresponding *chronos* shows that the inversion

profile changes sign at the sawtooth crash, when also the short burst of m=1 activity occurs. M=1 modes modulated by sawteeth are frequently observed on TCV.

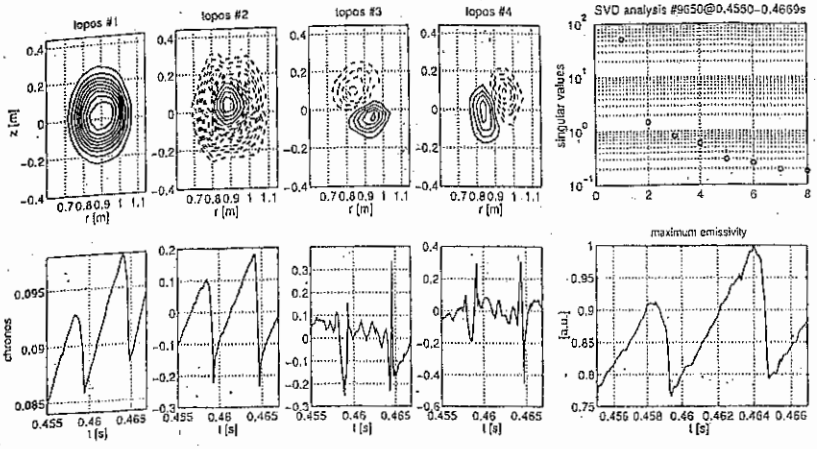


FIG. 2. SVD analysis of a reconstructed time series from TCV discharge #9650.

In TCV a strong correlation is observed between sawtooth amplitude and plasma triangularity. We investigated several time intervals during discharges where the triangularity was ramped down, using MFR and SVD as above. Fig. 3 shows that the relative sawtooth energies, determined from the corresponding singular values, decrease dramatically as plasma triangularity decreases. At negative triangularity the m=1 mode activity can become permanent, leading sometimes to mode locking and disruptions. Despite the reduction in sawtooth amplitude there is no significant dependence of sawtooth inversion radius on triangularity (fig.4). Discharges with negative triangularity have better confinement than discharges with positive triangularity [7]. The reduction in sawtooth amplitude with triangularity is consistent with the reduced ohmic heating power necessary to sustain discharges with negative triangularity.

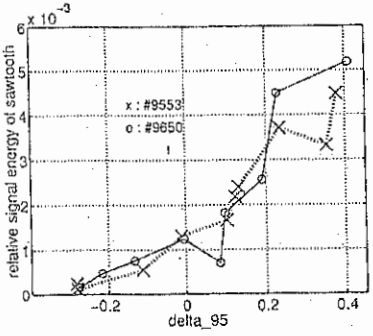


FIG. 3. Relative signal energy of the topos/ chronos pair representing sawtoothing as a function of the plasma triangularity.

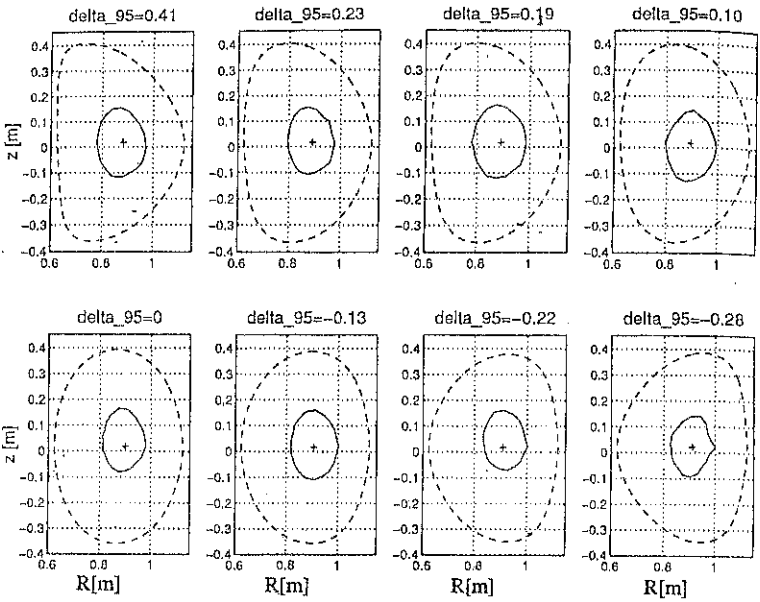


FIG. 4. Inversion radius deduced from the topos are shown with the last closed flux surface for different time intervals of TCV discharge #9650.

Acknowledgements

This work was partly funded by the *Fonds National Suisse de la Recherche Scientifique.*

References

[1] ANTON M, DUTCH M J and WEISEN, H: Rev. Sci. Instrum. 66 7 p3762 (1995)

[2] ANTON M et al., X-Ray Tomography on TCV, submitted to PPCF

[3] PRESS, W H TEUKOLSKY, S A , VETTERING, W T, and FLANNERY, B P:

" Numerical Recipes in FORTRAN: The Art of Scientific Computing"

[4] VON der LINDEN, W:Appl. Phys. A **60** p155 (1994)

[5] FRIEDEN B R, Journal of Modern Optics Vol **35** 8 (1988)

[6] DUDOK DE WIT T, PECQUET A L, VALLET J C and LIMA R: Phys. Plasmas 1 (10)

[7] J M MORET, M ANTON, R BEHN et al, this conference

He^+ halo formation during neutral beam injection into magnetically confined plasma.

A.V.Khudoleev, V.I.Afanassiev, M.I.Mironov
A.F.Ioffe Physical-Technical Institute, 194021, St.Petersburg, Russia

High energy neutral particle diagnostics has been recently implemented on several large tokamaks for measurements of fast hydrogen or helium atoms escaping from plasma [1]. To infer distribution function of the fast ions inside plasma from out coming atomic fluxes accurate modeling of neutralization processes in plasma is required. It has been experimentally found that fast protons are mostly neutralized by H-like ions created during neutral beam injection [2,3]. The correct calculation of the H-like ion density distribution around the torus is also important for spectroscopic diagnostics [4]. In present paper we concentrated on the modeling of He^+ population during hydrogen neutral beam injection. This problem is especially important in view of prospects of the diagnostics mentioned above for ITER were helium ash concentration can be as high as 2.5 10^{13} cm^{-3}.

As it has been noticed before in [4] He^+ ions originating from reaction

$$He^{2+} + H^0 \rightarrow He^+ + H^+ \quad (\sigma_{1ex}) \qquad (1)$$

inside the beam area can leave it and travel along magnetic field lines. This was called "plume" effect. Schematically it is shown in Fig.1a for ions moving in positive direction from the beam. Due to probability of re-excitation of these ions before their ionization He^+ plume ions can corrupt both absolute level and spatial localization of spectroscopic helium density measurements. It was indicated that ionization and charge-exchange eq.(1) are the dominant atomic processes for He^+ density formation in plasma. For typical plasma parameters ratio $\lambda_{ion}/2\pi R_{tor}\, q$ is small, where λ_{ion} is ionization mean free path, R_{tor} is the plasma major radius and q is the safety factor. For this reason He^+ ions cannot travel around the torus. In this case plume attenuation factor becomes $\xi(x) \sim \exp(-x/\lambda_{ion})$, where x is displacement from the beam center along a magnetic field line.

In present paper we consider specific mechanism of He^+ density formation in the plasma containing substantial number of helium ions. Considered process can be called "ion halo" of neutral beam. It is related with the significant influence of charge-exchange reaction

$$He^{2+} + He^+ \rightarrow He^+ + He^{2+} \quad (\sigma_{2ex}) \qquad (2)$$

on He^+ density in the vicinity of the beam. This process is schematically shown in Fig.1b. Since for the energy range of interest E ~ 10^2-10^4 eV/amu charge-exchange cross-section of process eq.(2) is high enough: σ_{2ex} (E) ~ (7-4) 10^{-16} cm^2 [5], He^+ ions can change direction of their motion to the opposite and reappear in the beam area without traveling around the torus. If He^{2+} concentration in plasma is sufficiently high so that charge-exchange mean free path $\lambda_{ex} \ll 2\pi R_{tor} q$, He^+ ions will participate in the diffusion-like process similar to the relay charge-exchange of hydrogen neutrals. For typical plasma parameters it takes place when $N_{He^{2+}} \gg 1/(2\pi R_{tor} q \sigma_{2ex}) \sim 10^{12}$ cm^{-3}. Magnitude of this effect can be found from rather simple estimates.

Near the beam axis ratio of ion halo to plume density can be approximately expressed as $\lambda_{ion}/(\lambda_{cx}+\lambda_{ion})$. For plasma with temperatures $T_i = T_e = 5keV$ $\sigma_{2cx} = 5\ 10^{-16}\ cm^2$, $<\sigma_{ion} v_e> = 2.6\ 10^{-9}\ cm^3/s$, $v_i = 5\ 10^7\ cm/s$ and this ratio is about $\sim\ 1/(1 + 0.1/\alpha)$, where $\alpha = N_{He2+}/N_e$. To define spatial distribution of ion halo density we need to come to more accurate calculations. It can be found from solution of the kinetic equation for He^+ ion distribution function which takes into account both ionization and charge-exchange processes. Physical similarity between this problem and neutral hydrogen penetration into plasma from the wall allows to use the results from [6] where analytic solution for neutral hydrogen density was obtained. Following [6] we can write down initial equation for He^+ ion distribution function in the form :

$$\upsilon_x\, \partial f(x,\upsilon)/\partial x = -\nu(\upsilon) f(x,\upsilon) + \varphi(\upsilon) N_{He+}(x) \nu_{ex}(x,\upsilon) \qquad (3)$$

where x is the coordinate along a magnetic field line, $f(x,\upsilon)$ and N_{He+} are distribution function and density of He^+, $\varphi(\upsilon)$ is He^{2+} normalized distribution function, ν_{ex}, ν_{ion} - charge-exchange and ionization collision frequencies with cross-sections corresponding to He^+ ions, $\nu=\nu_{ex}+\nu_{ion}$. For generality it is necessary to include some other elementary processes into eq.(3) such as proton impact ionization and charge-exchange with helium but for plasma parameters of interest their cross-sections are small and can be neglected. Both plasma temperature and density assumed to be constant along x coordinate. Eq.(3) can be integrated analytically to find $N_{He+}(x)$ under assumption that $\varphi(\upsilon)$ can be approximated by one-dimensional δ-function:

$$\varphi(\upsilon)=1/2\{\delta(\upsilon+\upsilon_{Ti}) + \delta(\upsilon-\upsilon_{Ti})\} \qquad (4)$$

The integration gives following spatial dependence of He^+ density:

$$N_{He+}(x) \sim \{\exp(-x/\lambda)+\exp(-(L-x)/\lambda)+\eta[\exp(-x/\kappa)+\exp(-(L-x)/\kappa)]\} \qquad (5)$$

where $L = 2\pi R_{tor}\, q$, $\lambda=(1/\lambda_{ex}+1/\lambda_{ion})^{-1}$, $\kappa=\sqrt{\lambda\lambda_{ion}}$ and η is certain function of the mean free paths $\eta=\eta(\lambda,\lambda_{ion})$. The first two terms describe absorption factors for the first generation of He^+ ions moving in positive and negative direction around the torus respectively. The second two terms correspond to the sum over all generations of He^+ ions expired charge-exchange in plasma. Since usually in the experimental conditions L/λ, $L/\kappa >> 1$ eq.(5) may be finally reduced to the form:

$$N_{He+}(x) \sim [\exp(-x/\lambda)+\eta\exp(-x/\kappa))] \qquad (6)$$

Since $\lambda_{ion} > \kappa > \lambda$ one can easily see from eq.(6) that charge-exchange process eq.(2) do not just increases He^+ density inside the beam area but also makes dependence $N_{He+}(x)$ steeper.

The results obtained are correct for sufficiently narrow neutral beam, i.e. for the case when $L_{beam} << \lambda_{cx}, \lambda_{ion}$. To check the analytic model eq.(3)-(6), to keep option to calculate $N_{He+}(x)$ for broader beam with arbitrary distribution of neutral density across its injection line and to avoid unnecessary limitation applied by approximation eq.(4) numeric code based on Monte-Carlo method was developed. The results of numeric calculations are presented in Fig.2-Fig.4. All variants were calculated with following common input parameters: $T_i=T_e=5keV$, $L_{beam}=40$ cm and for uniform neutral density distribution across the beam. Results were normalized to the flux

$\Gamma=N_{beam}\ N_{He2+}<\sigma_{1ex}\ v_i>L_{beam}$, where $<\sigma_{1ex}\ v_i>=2\ 10^{-7}$ cm^3/s corresponds to E_{beam} =20 keV. In Fig.1 calculated variants for pure helium plasma are shown. Curve 1 was calculated with $\sigma_{2ex}=0$ corresponding to plume ions. Curve 2 was calculated without inversion of particle motion to obtain first generation of ion halo. Curve 3 is ion halo as a sum over all generations. Comparing these curves one can see a good agreement between numerical and analytical results eq.(6): ion halo gives higher density which decays faster along magnetic field line. In Fig.3 we presented results of modeling of helium density scan at the same electron density. Ion halo obviously increases near the beam with He^{2+} density increase and decays faster in accordance with eq.(6). Behavior of ion halo substantially differs from neutral hydrogen penetration into plasma. It happens mainly for the following reasons. Ion halo is truly one dimensional object because ions cannot cross magnetic field lines and they can move only to and from their origin place. Distribution function of the initial ion flux (first generation) is the same as He^{2+} distribution function.

The results in Fig.3 show some sign of non linearity: while ion density rises by 5 times halo density increases by factor 8. It can be interpreted as follows: for low N_{He2+} halo mechanism plays minor role which steadily increases with helium density. Above certain level of N_{He2+} nearly all of He^+ ions coming out from the beam area are returned back through charge-exchange process. It is clearly demonstrated in Fig.4 where we modeled density scan in pure helium plasma. Ion halo is directly proportional to the ion density in vicinity of the beam center for sufficiently wide range of density variation. Increase of plasma density affects only spatial distribution.

Conclusions.

Effect of He^+ ion halo of neutral beam related with charge-exchange of helium ions can be substantial for plasma containing more then 5-10% of helium ions.

The effect reveals itself in two ways: it causes the increase of He^+ density in the vicinity of the beam axis and contracts its spatial distribution along magnetic field line. Underestimation of these features may lead to misinterpretation of the experimental data both in high energy neutral particle and spectroscopic diagnostics.

Ion halo is especially important in plasma with high helium concentration. There are some experimental evidences [7] that in He-beam fueling discharges CHERS measures higher helium density than it can be expected from alternative data.

According to our calculations even for ITER plasma with $T_{e,i}$=20keV, $N_e=1.310^{14}$ cm^{-3}, $N_{He2+}=2.5\ 10^{13}$ cm^{-3} ion halo will enhance He^+ population by factor of 1.5.

References

[1] A.I.Kislyakov et. al., to be published in *Fusion Engineering and Design*

[2] M.P.Petrov et al., *19th EPS Conf. on Contr. Fus. and Plasma Phys.*, **16C(II)** 1034 (1992)

[3] A.A.Korotkov et al., *21st EPS Conf. on Contr. Fus. and Plasma Phys.*, **18B(I)** 266 (1994)

[4] R.J.Fonk et al., *Phys.Rev. A*, 29 3288 (1984)

[5] C.F.Barnett,editor, *Atomic data for fusion* , ORNL-6086 **1** (1990)

[6] O.V.Konstantinov,V.I.Perel, *Zh. Tehn. Fiz.*, XXX, 1485 (1960)

[7] A.C.Maas, Ph.D. theses, JET (1995)

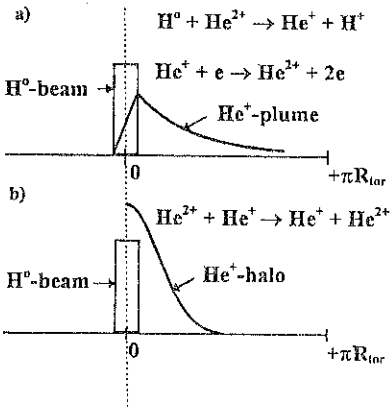


Fig.1. Schematic drawing of relative densities for: a) plume ions moving in one direction; b) ion halo due to charge-exchange reactions.

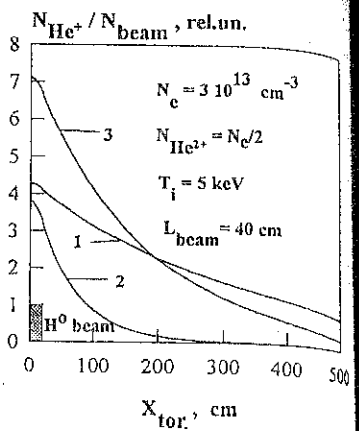


Fig.2. Spatial distribution of He^+ density. 1- plume density with ionization only as in [4]; 2- first generation of ion halo; 3- ion halo as a sum over all generations.

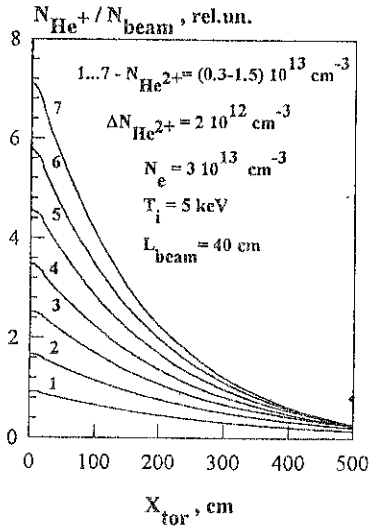


Fig.3. Spatial distribution of ion halo densities for different He^{2+} content in plasma.

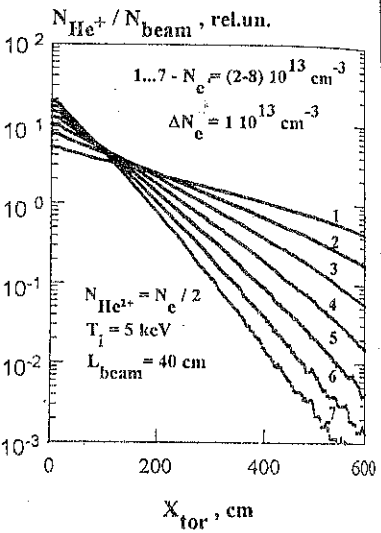


Fig.4. Spatial distribution of ion halo densities for different plasma concentrations.

Possibility of using Li^+ fraction of lithium atomic beam for fusion alpha-particle diagnostics.

M.I.Mironov, V.I.Afanassiev, A.V.Khudoleev
A.F.Ioffe Physical-Technical Institute, 194021, St.Petersburg, Russia

Introduction

Several years ago a fusion alpha-particle diagnostics based on double charge-exchange of alphas on fast Li and He neutral beams was proposed [1]. Using the beam of MeV-energy range and observation of neutralized alphas at a small angle to beam injection were considered as necessary conditions to benefit by high charge-exchange cross-section at small relative velocities of alphas and beam atoms. Experimental realization of such approach on tokamaks meets some difficulties caused mainly by absence of convenient ports placed opposite to each other or leads to large both beam and cx-flux absorption because injection and observation are possible to carry out only at long plasma size [2,3]. In the case of Li beam, however, there is another possibility to neutralize alphas by means of charge-exchange on fraction of Li^+ beam ions produced by ionization of atomic lithium beam. Since velocity vector of these ions is isotropically distributed in the plane passing through the beam injection line and perpendicular to the magnetic field line, it is possible to measure flux of neutralized alphas in any direction of the observation laying at the same plane. Besides of easy arrangement of experimental layout in this case, it allows also to optimize beam and cx-flux absorption and improve spatial resolution of the method. In the paper a model used for Li^+ density calculation and expected charge-exchange alpha particle fluxes produced by this ion beam fraction are estimated for ITER and JET plasma parameters.

Model Calculations

In the model calculation we consider experimental layout where atomic lithium beam is injected into the center of plasma and beam line is perpendicular to magnetic axis (see Fig.1). Li^+ ions arised from ionization of initial atomic beam are followed by Larmour orbit trajectories and confined by magnetic field near the "birth" place of the ions. We assume that plasma volume observed by neutral particle analyzer (NPA) is large enough to neglect an effect of escaping Li^+ ions along magnetic field lines due to divergence of the beam. Magnetic field is assumed to be uniform, so toroidal shift of Li^+ ions is also not taken into account in the model. Velocity vector of produced Li^+ ions will be isotropically distributed in the plane perpendicular to the magnetic field axis. Since double charge-exchange cross-section between Li^+ ions and alphas is sharply reduced at relative velocities $v_{rel}>3\cdot10^8$ cm/s [4] (see Fig.2), flux of resulted $_4He^0$ atoms will be mainly formed at the same plane. If line of sight of the NPA lays in this plane, the

counting rate of $_4He^0$ atoms detected at NPA channel (in frames of mentioned above assumptions) can be written as:

$$dN/dt = V\,2\pi R_l \Sigma n_k \sigma_k^{Li0\to Li^+} / \{1-\exp(-2\pi R_l \Sigma n_k \sigma_k^{Li^+\to Li^{++}})\} n_b k_b n_\alpha k_\alpha \langle\sigma v\rangle_{dex} \qquad (1)$$

where V is volume determined by intersection of beam and line of sight of the NPA, R_l is Larmour radius of Li^+ ion, $\Sigma n_k \sigma_k^{Li0\to Li^+}$ is sum of processes which lead to Li^+ production, $\Sigma n_k \sigma_k^{Li^+\to Li^{++}}$ is sum of processes which lead to Li^+ ionization, n_b is beam density and $k_{b,\alpha}$ are absorption coefficients of beam and flux of $_4He^0$ atoms; $n_\alpha = f_\alpha(E)\Delta\Omega E\delta E$, where $\Delta\Omega$ and δE are solid angle and energy resolution of the NPA, respectively. Energy distribution function of alphas $f_\alpha(E)$ is assumed to be classical and isotropic [5] and described by formulas:

$$\begin{aligned} f_\alpha(E) &= f_1(E) = 0.5 n_i n_d R_{dt} \tau_s\, E^{1/2}/(E_{cr}^{3/2}+E^{3/2}), && E\le E_0 \\ f_\alpha(E) &= f_1(E_0)\exp\{-(E^{1/2}-E_0^{1/2})^2/2T_i\}, && E>E_0 \end{aligned} \qquad (2)$$

where $n_{i,d}$ is density of deuterium and tritium, R_{dt} is rate of d-t fusion reaction, E_{cr} and E_0 are critical and birth energy for alphas and τ_s is slowing down time. Rate of double charge-exchange $\langle\sigma v\rangle_{dex}$ between Li^+ ions and alphas in eq.(1) is averaged over Larmour circle and defined as:

$$\langle\sigma v\rangle_{dex}) = (2\pi)^{-1}\int_0^{2\pi} \exp\{-R_l\varphi\ \Sigma n_k \sigma_k^{Li^+\to Li^{++}}\}\ \sigma_{dex}(v_{rel})\ v_{rel}\ d\varphi \qquad (3)$$

where v_{rel} is relative velocity of Li^+ ions and alphas.

Results and Discussion

The described model was applied to estimate possibilities of this alpha-particle diagnostics on ITER [6] and JET [7] tokamaks for plasma parameters given in the Table.

Tokamak	ITER	JET
Major plasma radius, m	8.14	3.07
Minor plasma radius, m	2.8	1.0
Plasma elongation.	1.6	1.6
Toroidal field, T	5.68	2.8
Electron density, cm^{-3}	$10^{14}[1-(r/a)^{20}]$	$3.6\cdot10^{13}[1-(r/a)^2]^{0.2}$
Deuterium/Tritium ratio	0.5/0.5	0.9/0.1
Electron temperature, keV	$22[1-(r/a)^6]^6$	$10[1-(r/a)^2]^{1.5}$
Ion temperature, keV	$20[1-(r/a)^6]^6$	$20[1-(r/a)^2]^{1.5}$
Effective charge	1.5	2.4
Beam of Li^0 atoms, MeV/mA	7/10	4/10
NPA solid angle, cm^2st	$2\cdot10^{-5}$	$1.5\cdot10^{-4}$
Efficiency of NPA neutron shield	100	-

Since absorption of Li^0 atoms is expected to be higher then of $_4He^0$ cx-flux, the experimental layout with lithium beam injection at horizontal plane of tokamaks (along small plasma size) and observation of cx-flux in vertical direction is considered as more preferable. Dependencies of absorption coefficients on distance from plasma center for ITER and JET conditions are shown in Fig.3 and Fig.5, respectively. Calculations with taking into account an enhancement of absorption due to ionization of excited states [7,8] are presented in the figures by dotted curves. It is seen that role of this effect can be substantial in Li^0 case.

Dependencies of counting rate of $_4He^0$ atoms at 10% energy window of the NPA on alphas energy for ITER and JET parameters (see Table) are presented in Fig.4 and Fig.6, respectively. Calibration data for sensitivity of the NPA detectors to neutrons and γ-rays [9] were used to estimate the corresponding counting rates produced by the radiation in d,t plasma operation. For alphas energy >1MeV the counting rate of alphas is within 10^3-10^4 counts/s and exceeds (n,γ) noise background. It allows to study the behavior of fusion alphas with 100ms time resolution within 10% of statistics accuracy.

Note that in the case of low absorption of Li^+ ion fraction (JET), the model can give overestimates since a life time of the ions determined by ionization process becomes comparable with time of escaping these ions from NPA observed volume due to ion drift effects and this ion trajectory analysis should be taken into account for more accurate calculations.

Summary

Using Li^+ ion fraction of MeV-energy atomic lithium beam is proposed for fusion alpha-particle diagnostics. The approach allows to arrange experimental layout using perpendicular tokamak ports and optimize beam and cx-flux absorption in the plasma. Simplified model is developed to estimate expected charge-exchange fluxes of $_4He^0$ atoms for ITER and JET (supershot with 10% of tritium) parameters. It is shown that injection of Li^0 beam with energy of several MeV and current up to10 eq.mA can provide the measurements with 10% energy and 100ms time resolution within 10% statistics accuracy.

References

[1] D.E.Post et. al., *Journal of Fusion Energy*, 1(2) 129 (1981).
[2] V.I.Afanassiev et al., *ITER Diagnostics Meeting*, ITER-IL-PH-79510, 1989.
[3] J.M. McChesney et al, *General Atomic Report*, GA-A21958 (1995).
[4] S.V.Putvinskii, *in Reviews of Plasma Physics*, 18 239 (1993).
[5] ITER Engineering Design Activities, S55RE1 95-07-11 F1 (1995).
[6] The JET Team, *Technical Report*, JET-P(91)66 (1991).
[7] A.A.Korotkov, *Nucl.Fusion A+M Supplement* 3 79 (1992).
[8] A.A.Korotkov and M.S.Samsonov, *Preprint PTI*, 1351 (1989).
[9] A.B.Izvozchikov et al, *Technical Report*, JET-R(91)12 (1991).

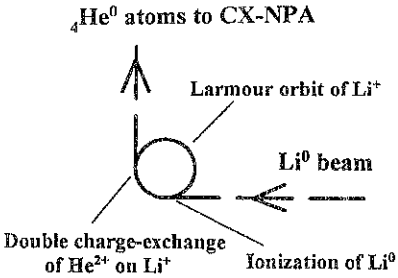


Fig.1 Schematic diagram of experimental layout of active CX alpha-particle diagnostics with use of Li^+ fraction of Li^0 beam.

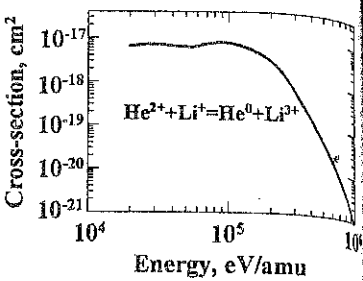


Fig.2 Double charge-exchange cross-section of alpha particles on Li^+ beam ions.

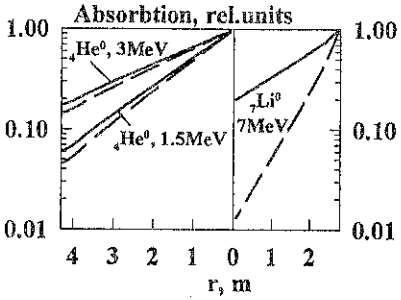


*Fig.3 **ITER**: Absorbtion of $_7Li^0$-beam and $_4He^0$-flux versus distance from the plasma center (solid and dotted curves are corresponded to calculation with and without enhancement of absorbtion due to ionization of excited states, respectively).*

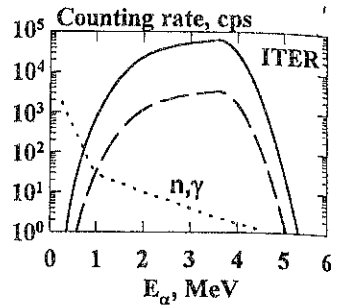


Fig.4 Alphas and n,γ-background counting rates at NPA energy window $\Delta E/E=0.1$ (detection efficiency is 100%, solid angle $\omega s=2 \cdot 10^{-5}$ $cm^2 st$, neutron shield efficiency is 100 and lithium beam of 7MeV/10mA).

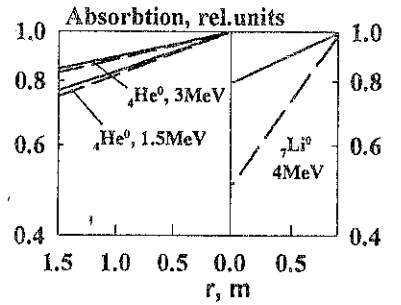


*Fig.5 **JET**: Absorbtion of $_7Li^0$-beam and $_4He^0$-flux versus distance from the plasma center (solid and dotted curves mean as in Fig.3).*

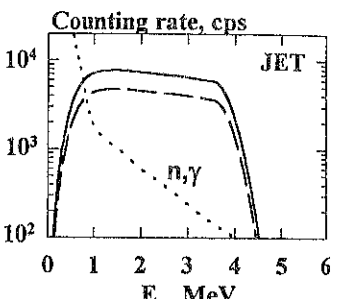


Fig.6 Alphas and n,γ-background counting rates at NPA energy window $\Delta E/E=0.1$ (detection efficiency is 20%, solid angle $\omega s=1.5 \cdot 10^{-4}$ $cm^2 st$, without neutron shield, lithium beam of 4MeV/10mA).

Development of a Spatially Resolved, Steady-State Bolometer for LHD Core and Divertor Plasmas

B. J. Peterson, S. Sudo and K.N. Sato

National Institute for Fusion Science, Nagoya 464-01, Japan

Abstract

Bolometer diagnostic development activities at the National Institute for Fusion Science are directed towards the realization of a spatially resolved (in two dimensions) steady state (30 minute) bolometer for use on the Large Helical Device (LHD) which is currently under construction in Toki-shi, Japan. LHD is a heliotron/stellarator device having a major radius of 3.9 m and a minor radius of 0.5 - 0.65 m. Superconducting helical and poloidal coil sets will be used to provide a 3 - 4 T confining magnetic field. Heating power up to 30 MW for short pulse (10 seconds) and 3 MW for long pulse (30 minutes) operation will result in maximum power densities of 10 W/cm^2 and 1 W/cm^2 respectively at the the detector radius. Taking these high heat loads into consideration, research and development is being carried out on bolometer cameras capable of making continuous measurements of the radiated flux during long pulse measurements. Details of this camera design will be shown, demonstrating how they can be used for reactor-relevant steady-state detection. In addition, plans will be shown for arrays measuring the radiation profile along the divertor leg and measuring the two dimensional distribution of the radiation from the core plasma.

1. Introduction

Bolometers have played an important role in fusion research by providing information on the total radiated power for power balance studies[1, 2]. Recent application of arrays of bolometers has provided information on the spatial distribution of the source of the radiation from the core and divertor plasmas[3]. In the Large Helical Device (LHD) our goal is to develop a spatially (in two dimensions) and time resolved measurement of the the radiation from the core and divertor regions of the plasma during long pulse (30 minute) operation. We plan to achieve this objective through the use of arrays of conventional metal film bolometers[4, 5] and XUV diodes[6] as well as with a newly proposed IR imaging bolometer[7].

2. The Large Helical Device and Expected Plasma and Radiation Parameters

LHD is an l=2, m=10 continuous winding torsatron/heliotron currently under construction in Toki, Japan, with a major radius of 3.9 m and an average minor plasma radius of 0.6 m. Superconducting helical and poloidal field coils will be used to provide a magnetic field from 3 - 4 T. Operational plans for LHD include both short pulse (5 seconds) and near steady-state,

long pulse (30 minutes) scenarios[8]. During long pulse operation a maximum of 3 MW of electron cyclotron heating (ECH) power is expected. For short pulse operation a maximum input power of 30 MW from a combination of neutral beam injection (NBI), ion cyclotron heating (ICH) and ECH is planned. Electron temperatures will range from 3 to 10 keV. In most scenarios where electron temperatures will be on the order of 3 keV, the 4 micron foil used for the ASDEX type bolometer will be adequate for stopping a majority of the photons. We may consider sacrificing some sensitivity for a thicker absorbing layer on a set of detectors to be used for the higher temperature plasmas expected in the short pulse mode of operation. Neutron radiation is expected to be negligible until Deuterium beams come on line in the fourth year of operation with a neutron rate of $2x10^{16}$/sec for 10 keV electrons[9]. At that time silicon photodiode detectors may need to be replaced with more neutron-resistant metal foil bolometers.

3. Plans for Bolometer Arrays on LHD

Our planned bolometer arrays can be classified into 3 categories according to their purpose. Flanges at 7 of the 10 outboard mid-plane ports will be used to measure the total power radiated by the plasma and any toroidal variation in the radiated power. Each flange would host a 2π bolometer and a horizontal (toroidal) array of XUV photodiodes viewing the plasma through a vertical slit. Six flanges (two at an upper vertical port, two at the corresponding lower vertical port, and two at an outboard mid-plane port) will use one-dimensional, 16 channel, metal foil bolometer arrays to measure radiation from the divertor regions of LHD. An example of the views obtained from the upper and lower vertical ports is shown in Fig. 1. Using a semi-toroidal plane through the machine a three point view of the plasma from upper and lower vertical and outboard mid-plane ports can be achieved as shown in Fig. 2. These views, each consisting of a 32 channel metal foil bolometer array and a 64 channel photodiode array, will be used to reconstruct the two dimensional radiation profile using tomographic techniques. As can be seen in Figs. 1 and 2, it is impossible in LHD to have a view of the core plasma without looking through the helical divertor legs. This presents a problem in the ability to differentiate the core radiation from the divertor radiation. If the divertor radiation is not too dominant, comparison of views of the divertor only with those which include the core may be used to distinguish the two sources of radiation. In the future we would like to consider installing bolometer arrays inside the vacuum vessel in order to add more views for tomographic purposes and to provide a view of the core plasma which does not look through the divertor region.

4. Bolometer Array Pinhole Camera Design

A bolometer camera holding a 32 channel array of ASDEX type metal foil bolometers and a 64 channel array of XUV photodiodes has been design as shown in Figs. 3 and 4. This camera is

designed to fit on a 152 mm conflat flange, which is the standard size envisioned for LHD bolometer arrays. Current plans utilize two gate valves with silicon rubber seals in order to avoid problems related to the degradation of viton seals when exposed for long periods to high-powered microwaves. For the outboard mid-plane port shown in Fig. 2 and for an input power of 3 MW the power density at the pinhole in the total radiating case would be 0.5 W/cm^2. Water cooling on the order of 10 ml/sec would be necessary to keep the change in the temperature to within 1 °C. The size of the pinhole is 8 mm for a resolution at the magnetic axis of 4 cm for the 32 channel metal foil bolometer array and 2 cm for the 64 channel XUV diode array. Time resolution for the metal bolometers is typically 1 ms, and 1 μs for the photodiodes. Considering the collimation by the pinhole, the detector sees a power density of 100 $\mu W/cm^2$, which is 100 times the typical sensitivity of the ASDEX type metal foil bolometers[5]. At this power level cooling of the detector or its mount would not be necessary. A shutter and filter wheel would be used to protect the detectors during carbonization or boronization, and provide the means of inserting filters to differentiate the contributions of photons in various spectral ranges.

5. Conclusion

We have described preliminary plans for bolometric diagnostics on LHD including toroidal, divertor and two dimensional arrays. A camera design utilizing a filter/shutter wheel and a water-cooled pinhole have also been shown. Ongoing development work includes detector examination and calibration and camera prototype fabrication and testing.

References

[1] H. Hsuan, K. Bol and R.A. Ellis, Measurement of the energy balance in ATC tokamak, Nucl. Fusion 15 (1975) 657-661.

[2] J. Schivell, G. Renda, J. Lowrance and H. Hsuan, Bolometer for measurements on high-temperature plasmas, Rev. Sci. Instrum. 53 (1982) 1527-1534.

[3] A.W. Leonard, W.H. Meyer, B. Geer, D.M. Behne and D.N. Hill, 2D tomography with bolometry in DIII-D, Rev. Sci. Instrum. 66 (1995) 1201-1204.

[4] E.R. Mueller and F. Mast, A new metal resistor bolometer for measuring vacuum ultraviolet and soft x radiation, J. Appl. Phys. 55 (1984) 2635 - 2641.

[5] K.F. Mast, J.C. Vallet, C. Andelfinger, P. Betzler, H. Kraus and G. Schramm, A low noise highly integrated bolometer array for absolute measurement of VUV and soft x radiation, Rev. Sci. Instrum. 62 (1991) 744-750.

[6] R.J. Maqueda, G.A. Wurden and E.A. Crawford, Wideband "silicon bolometers" in the LSX field reverse configuration experiment, Rev. Sci. Instrum. 63 (1992) 4717-4719.

[7] G. A. Wurden, A Rad-Hard, Steady-State, Digital Imaging Bolometer System, in the Proceedings of the 7th International Toki Conference on Plasma Physics and Controlled

Nuclear Fusion, Toki, Japan, to appear in Fusion Engineering and Design.
[8] O. Motojima, N. Ohyabu, A. Komori, N. Noda, K. Yamazaki, H. Yamada, A. Sagara, S. Yamaguchi, K.Y. Watanabe, N. Inoue, H. Suzuki, Y. Kubota, J. Yamamoto, M. Fujiwara and A. Iiyoshi, Long pulse operations scenario of LHD, Proc. 6th International Toki Conference on Plasma Physics and Controlled Nuclear Fusion, Toki, Japan 27 (1995) 123-130.
[9] M. Sasao, M. Isobe, M. Osakabe, A. Taniike, T. Iguchi, H. Takada, T. Iida and M. Wada, Preparation for fusion product measurement on LHD, Proc. 7th International Toki Conference on Plasma Physics and Controlled Nuclear Fusion, Toki, Japan, to appear in Fusion Engineering and Design.

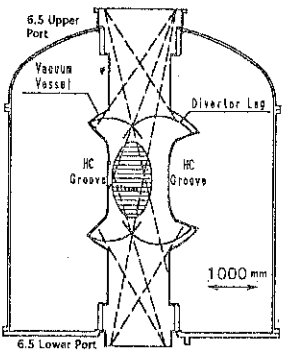


Figure 1. Divertor bolometer arrays.

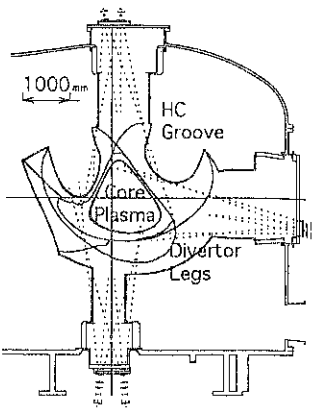


Figure 2. Two-dimensional bolometer arrays.

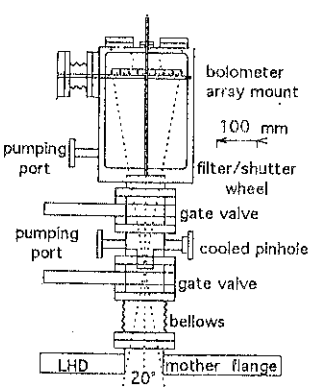


Figure 3. Bolometer array pinhole camera.

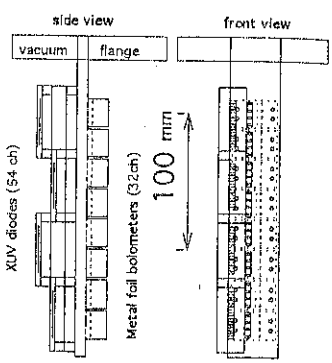


Figure 4. Bolometer array mount.

Submillimeter Laser Interferometer - Polarimeter for Plasma Diagnostics

Yu.E.Kamenev, V.K.Kiseliov, E.M.Kuleshov, B.N.Knyaz'kov,
V.K.Kononenko, P.K.Nesterov, M.S.Yanovsky

Institute of Radiophysics and Electronics of the National Academy of Science of Ukraine
12 Acad. Proskura st., Kharkov, 310085, Ukraine

Abstract

There are presented the results of investigation of the gomodyne laser interferometer-polarimeter $\lambda = 0{,}195$ mm made on the quasioptical element basis. The interferometer -polarimeter is combined with Tokamak-15 multychannel interferometer and provides the synchronous determination of the plasma electron density n_e and poloidal magnetic field B_p across anyone of the seven vertical probing channels without disturbance for working of the others channels. The electron density responce threshold is $3{,}4 \cdot 10^{11} cm^{-3}$, the polarization resolution is not worse than 0,1° and the phase difference measurement error is ±4°.

The determination of the plasma parameter such as the mean electron density n_e and the poloidal magnetic field B_p induced by plasma cord current is great importance for the investigation of the high temperature plasma of the experimental thermonuclear mountings. One of the well-known methods of the electron density determination consist in the measuring of the plasma shift of the electromagnetic wave probing the plasma relative to the wave passing over the free space. It is necessary to keep condition $\omega >> \omega_0$ (where ω is the radiation frequency and ω_0 is the plasma frequency) in order to avoid influence of refraction. So that phase shift φ stipulated by change of electron density can be determinated by the formula

$$\varphi = L\omega_0^2 / 2c\omega , \qquad (1)$$

where L is the path length of the electromagnetic wave passed across the plasma, c is the light speed.

The phase shifts are convenient for measuring when $n_e = 10^{12} - 10^{14} cm^{-3}$ and the plasma is probed by the waves with $\lambda = 0{,}1 - 0{,}3$ mm.

For determination of the poloidal magnetic field induced by plasma cord current [1] there are used the Faraday effect which consists in the rotation of the polarization plane of the probing radiation when radiation is passed along of the magnetic field lines of force. If cyclotron frequency $\omega_H^2 << \omega^2$ then Faraday rotation angle Ψ may be determinated by the formula

$$\Psi = 9{,}3 \cdot 10^5 B_p n_e L / \omega^2 . \qquad (2)$$

One of the factors causing Faraday angle measurement error is the Cotton-Mouton effect caused by linear birefringence when the wave is passed across of the magnetoactive plasma. In order to avoid influence of this effect it is expedient to use shortwave part of the submillimeter wave range since the Faraday rotation scales with λ^2, whereas linear birefringence increases as λ^3.

With a glance to above in the IRE NAS of Ukraine the laser submillimeter interferometer-

polarimeter with λ = 195 μm have been developed. The interferometer-polarimeter provides the synhronous determination of the plasma electron density n_e and the poloidal magnetic field B_p and have been intended for using in Tokamak-15 mountings.

The Faraday rotation measurement method and corresponding to it principle of interferometer-polarimeter construction are chosen on the base of experimental comparison of the following quasioptical methods of the polarization plane rotation angle measurement:

a) amplitude measurement method by the level of signal reflected from the polarizing wire grating mounted orthogonally to the initial polarization of the wave [2];

b) method of measurement of the angular phase difference between orthogonally polarized signal components selected by polarizing grating after transformation of the signal to the signal with circular polarization [3].

The experiment showed [4] that the phase measurement method have the best polarization sensitivity. However, in the condition of refraction of the MW radiation the measurement error arises owing to disalignment of the difference phase section transforming polarization. Therefore amplitude method was chosen as main and phase method - as subsidary.

It is to be noted that a some transformation of polarization takes place when signal passes along the beamguide and sircuit elements. To reduce influence of this transformation the analyzing and polarizing gratings are mounted directly near at the antennas of the plasma chamber.

The combination of the interferometer-polarimeter (λ = 195 μm) with the Tokamak-15 multichannel interferometer (λ = 337 μm) is one of the main features of the device. It provides synhronous determination of the plasma electron density and the poloidal magnetic field across anyone of the seven vertical probing channels without disturbance for working of the other channels.

The MW part of the interferometer-polarimeter is completely realized on the basis of the hollow dielectric beamguide and quasioptical functional devices with butt joints. This allows to reduce influence of plant vibrations on measurement results.

The interferometer-polarimeter operates with homodyne frequency conversion using the Doppler shifter [5] providing frequency shift of 106 kHz. The submillimeter RF-pumped gas DCN laser is used as radiation source of the interferometer-polarimeter. The laser resonator contains the discharge tube of the length of 2 m and inner diameter of 44 mm. The one-dimensional wire grating with the period of 30 μm and the wires of 8 μm in diameter is used as output mirror. The radiation power is 10 mW, the power of a pumping being 800 W.

The photoreceiver based on impurity-electron cyclotron resonance effect in n-InSb at 4,2 K was used for heterodyne detection of the laser radiation. The sensing element of receiver 1,5 x 1,5 x 1,0 mm was placed in the 2 mm airgap of SmCo magnet which provides the magnetic field of 7,5 kGs. Radiation is coupled into the sensing element with the metal beamguide and the circular tapered transition of output aperture of 2 mm diameter . The noise equivalent power in heterodyne mode detection was 5 x 10^{-16} W/Hz for the estimated 38 μW power of local oscillator .

The polarimeter is calibrated in the absence of the plasma by polarization calibrator designed for introdusing of the angle discrete succession of the polarization plane turn scale on the oscillograph screen. The polarization plane of the output linearly polarized wave is installed with the help of the turn polarizer containing two tilted wire gratings. The turn polarizer is connected with the stepping motor controlled by a computer. With the its help the regimes of the polarization plane turn are realized with the step of 0,25°, 0,5° and 1°. A time between the steps is regulated from 10 ms to 300 ms. The system provides the cyclical reiteration of the calibration process in any interval of angles being the limits of ±10°.

While testing the interferometer-polarimeter the influence of the metal antennas on the polarization measurement results was being investigated in detail [6]. It was shown that accessory probing radiation polarization change is observed by refraction, which is increased when the antennas are present. This effect substantially increases errors of measurement. In the connection, the open beamguide ends with the fused quartz windows are used as antennas. To determine the polarization resolution of interferometer-polarimeter the registration of the calibration characteristics was being carried out by photographing of the oscillogram of the polarimeter signal when the polarization plane is turned by step with the aid of calibrator. The results of experiment demonstrated that polarization was not worse than 0,1°, the lock-in amplifier of 10 ms time constant using when power of laser was 30 mW and the total length of the measuring channel was 12 m.

The phase noise is the important characteristic of interferometer-polarimeter when the interferometer measurements are carried out. The phase noise determine the density response threshold and is caused by various causes such as defects of the shifter disk, plant vibrations et al. Value of plasma electron desity corresponding to the phase noise may be determinated by the formula

$$n_{eN} = 6{,}86 \cdot 10^{-11} \varphi_N c^2 / L\lambda \qquad (3)$$

where φ_N is swing of the phase noise, degree. The phase noise value is about 15°. This coresponds to the electron density of $3{,}4 \cdot 10^{11}$ cm^{-3}. Thus, the responce threshold is 0,2% from the expected plasma density.

The phase shift error $\Delta\varphi$ was estimated by comparison of the phase shift φ_{if} measured on the intermediate frequency with phase shift φ_{MW} intoduced by the calibrated MW phaser, the plase shift φ_{MW} was taken as a true value. The experimentally obtained discrepancy is less than ±4°.It corresponds to the electron density of 10^{11} cm^{-3}. The electron density measurement total error is 0,3%.

Thus, the interferometer-polarimeter with operating wavelength of 195 μm have been developed, which was combined with Tokamak-15 multychannel interferometer (λ = 337 μm) and provides the synchronous determination of the plasma electron density and the poloidal magnetic field across anyone of the seven vertical probing channels without disturbance for working of the other channels. In contrast to existing similar devices the interferometer-polarimeter operates in

the short wave part of the submillimeter range. This allows to decrease the refraction of radiation and the mistake provoked by plasma birefringence. The MW part of the interferom polarimeter is completely realized on the basis of the hollow dielectric beamguide quasioptical functional devices with butt joints. This allows to reduce influence of plant vibrat on measurements results without of the subsidiary optical interferometers, screening contriva and special frame for functional element fastening using in the devises on mountings TFR, J and others. The experimental results allow to draw a conclusion, that it is expedient to refuse f metal antennas. This allows to obtain the polarization resolution not worse than 0,1°.

References

1. H.Soltwish. Experimental test of far-infrared polarimetry for Faraday rotation measuremen the TFR 600 Tokamak. Infrared Physics, vol. 21, 1981, pp. 287-298.

2. H.Soltwish. Current distribution measurement in a tokamak by FIR polarimetry. Rev. Instrum., vol. 57, N8, 1986, pp.1939-1944.

3. N.I.Malyh, A.G.Nagorny, E.S.Yampol'sky.. Homodyne polarimeter for plasma diagnos Heads of a report of 4 All-Unior conference on hightemperature plasma diagnostics (in Russian)

4. P.K.Nesterov, V.A.Scherbov. Model investigations of MW part of one-channel submilli interferometer-polarimeter designed for Tokamak plasma diagnostics. Physical research with of radio waves of millimeter and submillimeter band. Ed. V.K.Kiselyev et al. Kiev, IRE NA Ukraine, 1991, pp. 82-87 (in Russian).

5. P.K.Nesterov, V.A.Scherbov. Doppler frequency shifters of the submillimeter band. Ph and techniques of millimeter and submillimeter waves. Ed. V.P.Shestopalov et al. Kiyev, N Dumka, 1983, pp. 251-256 (in Russian).

6. P.K.Nesterov. Investigation of influence of metal antennas and MW radiation refraction o characteristics of one-channel submillimeter interferometer-polarimeter. Scientific instru making of millimeter and submillimeter wave range. Ed. V.K.Kiselyev et al. IRE NAS Ukr 1992, pp. 50-55 (in Russian).

A Set of Quasioptic Submillimeter-Wave Devices for Thermonuclear Plasma Diagnostics

V.I.Bezborodov, Yu.E.Kamenev, V.K.Kiseliov, B.N.Knyaz'kov, V.K.Kononenko, E.M.Kuleshov, P.K.Nesterov, V.N.Polupanov, M.S.Yanovsky

Institute of Radiophysics and Electronics of the Academy of Sciences of Ukraine
12 Acad, Proskura st., Kharkov, 310085, Ukraine

Abstract - The research and development results in the design of quasioptic submillimeter-wave measuring devices and systems for diagnostics of high - temperature magnetoactive plasma in contemporary machines for thermonuclear fusion are presented here.

Attained in the modern experimental mountings of the guided thermonuclear synthesis (GTS) with magnetic holding (TOKAMAKS, stellarators, mirror traps) values of the hot plasma and prospects of the its obtaining in the large volumes stipulate use of submillimeter (SMM) wave ranges for purposes of the plasma radio wave diagnostics together with reguirements of maximal reduction of influence of refraction and mechanical vibrations on measurement accuracy [1]. In this wave ranges quasioptical (QO) principles of forming, transmission and transformation of electromagnetic wave beams using in devices with characteristic dimensions which to a great extent exceed operating wavelength are extremely effective.

The element basis of the QO radiomeasuring instruments and devices of a short wave part of the millimeter and submillimeter wavelength ranges ($0,2...2,0 mm$) using hollow dielectric and metal-dielectric waveguides as transmission line has designed in IRE NAS of Ukraina [2].

There are designed intricate radiomeasuring complexes for plasma diagnostics of large tokamaks and stellarators made on the basis of the designed QO measuring methods, element basis, SMM lasers and high sensitive low temperature receivers [3-6].

For determination of the electron density profile on the Tokamak-15 have been designed and created the multichannel homodyne HCN-laser interferometer allowed to determine values of the plasma electron density about $2 \cdot 10^{14} cm^{-3}$. The main regime of the interferometer work consists in the measuring of the phase shift of the ordinary

electromagnetic wave probing of the plasma cross section along the nine cho relative to the wave passing along the reference channel. The submillimeter waveguid gas HCN laser was used as the radiation source [7]. The radiation power was abo $60mW$. The interferometer operate using homodyne frequency conversion. T conversion was realized by QO Doppler frequency shifter. Reception of SM radiation and its conversion in radiation with intermediate frequency of $106KHz$ a carried out by QO low temperature receiver based on impurity-electron cyclotr resonance effect in n - $InSb$. The noise equivalent power was $2 \cdot 10^{-15} W/Hz$ heterodyne mode detection. The phase noise of the interferometer was less than 5^0.

There have been designed the SMM interferometer-polarimeter for t synchronous determination of the mean plasma electronic density and the azimuth current of the plasma in "Tokamak-15" mounting [4, 8]. The RF pumped DCN las ($\lambda = 195mm$) has been used as SMM radiation source. The plasma azimuthal curre was determined by synchronous measurement of the Faraday rotation angle of t polarization plane of the wave in the poloidal magnetic field induced by this curre and mean plasma electronic density along chosen direction of the probing. T determination of Faraday angle is made by amplitude method being consisted measuring of the level of the cross-polarized component of the signal. This compone is caused by Faraday rotation respect to calibration level given by QO calibrator polarization. The calibrator is made on the basis of the wire gratings with ste changing of the turn angle given by the step drive with computer control. The to measured electron density is $10^{15} cm^{-3}$. The phase shift measurement error is less tha 4^0. The polarization angle resolution is not worse than $0,1^0$ when measured Farad rotation angle is within $0...7^0$. Structure of the designed interferometer-polarimet allows its unification with the above-mentioned multichannel interferomet $\lambda = 337\mu m$working on the Tokamak-15 long ago without mutual disturbances. Th interferometer-polarimeter provides possibility of the synchronous determination of th electronic density radial profile and azimuthal plasma current when channels of th multichannel interferometer ($\lambda = 337\mu m$) are used together with interferomete polarimeter.

The QO circuit of the superheterodyne receiver with superhigh intermedia frequency has been carried out in the wavelength range of $1...2mm$ for measurement o the local electron temperature on the GTS mountings by determination of the cyclotro radiation spectrum [9]. The receiver have been realized on the basis of the quarte wave and half-wave QO polarization interferometers with tracking tuning system. I provides the upper and lower side band separate reception, calibration, heterodyn noise filtration and side band suppression. For measurement of the electro temperature profile on the Tokamak-15 the multichannel frequency separator of th

cyclotron plasma radiation has been realized on the basis of the cascade of the tunable polarization interferometers. There have been measured the frequency of the radiation from the nine plasma volumes disposed along of the large radius of the torus [10].

The QO quadrature mixers of the homodyne analyzers of the asymmetrical spectra have been made for measurement of the spectral distributions which arise while scattering SMM wave on the plasma density fluctuations. This mixers provide separate production of the spectra of the upper and lower side bands of the scattered signal and compensation of the influence of the frequency component of the initial radiation in the spectrum of a signal arriving on the mixer input on the measurement results [11]. Heterodyne signals given on the quadrature mixer are formed from the orthogonal components of the branched circularly polarized wave. The mixer frequency range is 140...600GHz.

On the basis of the metal-dielectric wavequide (MDW) of $14 \times 14mm$ cross-section there have been designed and created set of the radiomeasured equipment of the wide employment and superwideband circuit of the low temperature Josephson's receiver of the plasma radiation covering spectrum part from 60GHz to 600GHz [12].

REFERENCES

1. C.H.Ma, D.P.Hutchinson, P.A.Staats, K.L.VanderStuls. *Measurements of electron dencity and plasma current distributions in TOKAMAK plasm.* - Intern. J. of IR and MM Waves. - 1982, pp. 263 - 267.

2. A.Y.Usikov (Ed.), *Electronics and Radiophysics of mm and submm Waves.* Kiev; Naukova dumka, 1986 (in Russian).

3. Y.E.Kamenev, V.K.Kiseliov, E.M.Kuleshov et al. *Submillimeter Laser Interferometer for High Density Plasma Diagnostic. Intern. J. of IR and MM Waves.* vol.16, N6, June 1995, pp. 999 - 1007.

4. Yu.E.Kamenev, V.K.Kiseliov, E.M.Kuleshov et al. *Submillimeter Laser Interfero-meter - Polarimeter for Plasma Diagnostics. Int. Conf. on Millimeter and Sub-millimeter Waves and Applications,* 10 - 14 January 1994, San Diego, USA, Proc. SPIE 2250, pp. 326 - 328 (1994).

5. Yu.E.Kamenev, V.K.Kiseliov, E.M.Kuleshov et al. *Submillimeter Laser Interfero-meter for High Density Plasma Diagnostics. Int. Simp. "Physics and Engineering of Millimeter and Submillimeter Waves"*, June 7 - 10, Kharkov, Ukraine, Conf. Proc., vol.3 p. 650 (1995).

6. Е.П.Горбунов, Е.М.Кулешов, П.К.Нестеров и др. *Применение многоканального интерферометра вертикального зондирования для измерения профиля плотности плазмы на Токамаке Т-15*. *Физика плазмы* (Москва). вып. 2, с. 162 -165, 1992г.

7. Ю.Е.Каменев, Е.М.Кулешов. *Газоразрядные субмиллиметровые лазеры непрерывного излучения. III Всес. симп. по миллиметровым и субмиллиметровым волнам.* Т.*1* , Горький, 1980, с. 18 - 19.

8. Y.E.Kamenev, V.K.Kiseliov, E.M.Kuleshov et al. *Submillimeter Laser Interfero-meter - Polarimeter for Plasma Diagnostics. 18th Int. Conf. on Infrared and Millimeter Waves*, James R.Birch, Jerence I.Parker, Editors. SPIE 2104, pp. 252 - 253 (1993).

9. В.И.Безбородов, Б.Н.Князьков, Е.М.Кулешов, М.С.Яновский. *Квази-оптический тракт супергетеродинного приемника с раздельным приемом полос.* Изв.вузов "Радиоэлектроника", 1989, т.33, N3, с. 29 -33.

10. М.С.Яновский, В.И.Безбородов, Б.Н.Князьков. *Квазиоптический частотный разделитель.* Изв.вузов "Радиоэлектроника", 1991, т.34, N11, с. 76 -78.

11. М.С.Яновский, Б.Н.Князьков, Е.М.Кулешов, В.И.Безбородов. *Квазиоптические смесительные устройства гомодинного анализатора асимметричных спектров.* Изв.вузов "Радиоэлектроника", 1990, т.33, N11, с. 46 - 51.

12. V.I.Bezborodov, Yu.E.Kamenev, V.K.Kiseliov et al. *Quasi-Optical and Waveguiding Radio-Measuring Devices of Millimeter and Submillimeter Wave Range. Int. Symp. "Physics and Engineering of Millimeter and Submillimeter Waves"*, June 7 - 10, Kharkov, Ukraine, Conf. Prof., vol.3, pp 643 - 645 (1995).

Three-mirror laser interferometer for diagnostics of thermonuclear plasma

O.A. Bashutin, E.D. Vovchenko, G.I. Kozin, A.S. Savjolov
Moscow State Engineering Physics Institute (MEPhI), 115409, Moscow, Russia

Introduction

Progress in controlled fusion researches is connected, first of all, with experiments on large tokamaks, where plasma has parameters close to those in future thermonuclear reactor. That makes demands concearning development of laser interferometers for plasma diagnostics. First, when heavy hydrogen isotopes are used as a working substance, the diagnostics must be placed outside the biological shield of the thermonuclear installation. In this case, the path of the measuring beam increases and influence of vibrations becomes stronger. Second, increase of electron density up to 10^{15} cm^{-3} makes necessary to substitute infrared probing wavelenghts for the submillimeter ones. Unfortunately quality of mirrors, must be better in this case while they quickly degrade due to neutron irradiation. Moreover, sensitivity of the interferometer to external vibrations is higher in the infrared range. This is why the classical types of diagnostic interferometers can not be used for these purposes. Multi-pass interferometers are very sensitive to minor changes of the mirror reflection. One-pass and two-pass interferometers are more stable to degradation of mirrors, but contrast of the interference pattern becomes less then the detection threshold of the system because of low sensitivity of such a sceme.

Construction of the interferometer

To overcome the problems mentioned, it is proposed to use an original three-mirror two-mode laser interferometer (λ=3.39 μm), that has been developed at MEPhI. This interferometer combines stability of the two-pass sceme with the high sensitivity of the multi-pass design. The schematic drawing of the interferometer is shown in fig.1.

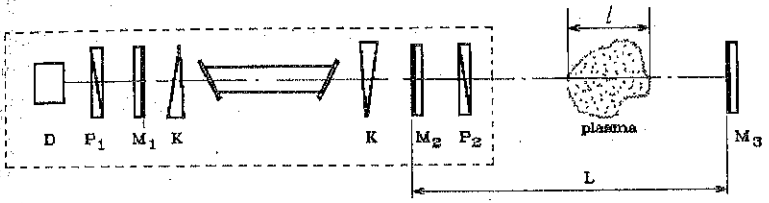


Fig.1. Schematic drawing of the three-mirror two-mode interferometer elements

The principle of the device operation is based on the effect of influence of intrinsic radiation, reflected from an external reflector M_3, on parameters of the two-mode He-

Ne laser (λ=3.39 μm) with anisotropic resonator M_1-M_2, which works in a regime o
"soft" competition of modes having orthogonal polarizations. The optical wedges K a
used as anisotropy elements. The polarizer P_2 divides the laser radiation into signal an
reference modes. The signal mode of radiation passes P_2 and goes to the extern
reflector M_3 while the reference mode is absorbed by the polarizer. The main element
of the interferometer, except the external reflector, are located in a compact unit, tha
can be placed far from the plasma object under investigation.

Rate equations

It is know [1] that the radiation, reflected back from M_3 into resonator of th
laser, changes its amplitude and frequency characteristics. The analysis shows [2], that
a reflecting surface (M_3 in Fig.1) with effective amplitude factor of reflection ρ
placed on distance L from the laser, the amplitude P and the frequency ν of the las
generation formed by the three-mirror resonator changes relative to the amplitude P
and frequency ν_0 of the primary two-mirror resonator as follows:

$$P - P_0 = A \cdot \frac{\eta}{\eta - 1} \cdot \frac{1}{S} \cdot \rho \cdot Cos\left(\frac{4 \cdot \pi \cdot L}{\lambda}\right) \qquad (1)$$

$$\nu - \nu_0 = A \cdot \Gamma \cdot \rho \cdot Sin\left(\frac{4 \cdot \pi \cdot L}{\lambda}\right) \quad , \qquad (2)$$

where A - the coefficient, charactirizing the mirrors of the laser; η - th
magnitude of excess the amplification over the losses in resonator; S - the factor o
connection between modes (S=1 for one-mode laser ; S – 10^{-2} for two-mode He-N
laser with λ=3,39 μm); Γ - the bandwidth of resonator: λ - the wavelength of the las
radiation.

The plasma, placed in the cavity M_2-M_3 between the laser and the reflecti
mirror changes the length of the optical path L of this interval. As a result, the power o
generated radiation and the frequency of the three-mirror resonator are changed an
can be measured by appropriate methods. Change in the optical path L by λ/
corresponds to introduction of the plasma with linear density of ~ $2*10^{16}$ cm^{-2} in th
resonator cavity. The maximum change of both the power and the frequency does no
depend on L and diminishes when the mirror M_3 degrades. Therefore, the lower lim
of measured densities is determined by the background noice of the detection system.

Experimental results

Measurements of the variation in power of the mode selected by the polarizer
can be performed by a relatively simple and reliable equipment. When the cooled
photodiode was used as a detector, the sensitivity of the interferometer was as hig
as $(N_e \bullet l)_{min} \approx 5 \bullet 10^{12}$ cm^{-2} if the reflectivity of the mirror M_3 was 100% (ρ=1). Th
sensitivity was limited only by the noise of the detection system. This method was use

in investigations of a high-current and low pressure quasistationary volume discharge [3] with plasma density of about 10^{15} cm^{-3}. A plate of nonpolished aluminium alloy, placed at 2 m from the main block of the interferometer was used as a reflector. Results of the interferometer measurements agree with probe measurements, as shown in fig.2.

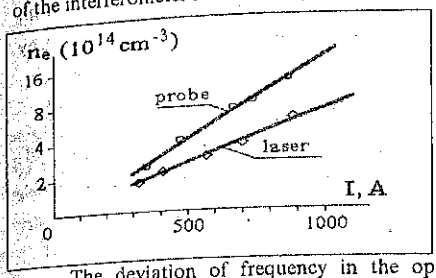


Fig.2. Electron density in a high-current quasistationary volume discharge as a function of current.

° - Langmuir probe measurements

◊ - interferometer measurements

The deviation of frequency in the optical range is measured with a high sensitivity by use of additional reference radiation having a frequency in depend of the measured parameter. The basic mode of a phase anysotropic resonator can be used as a reference.

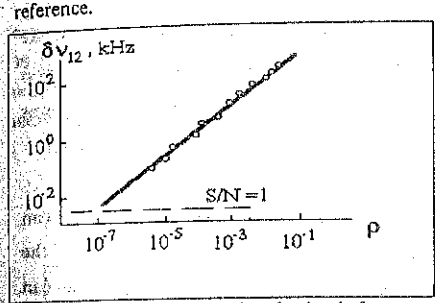


Fig.3. Deviation $\delta\nu_{12}$ of the beat frequency as function of the reflection coefficient ρ from an external mirror.

Information on plasma is obtained from measurements of changes of the beat frequency formed due to mixing of the signal and reference modes in the polarizer P_1. The plasma density is estimated as being proportional to the change of the beat frequency. This method requires a more complex equipment. It was used for study of influence of reflecting properties of an external mirror M_3 on the parameters of the interferometer. The effective factor of reflection ρ was changed by using a set of glass attenuators installed between the polarizer P_2 and the mirror M_3. Influence of plasma was simulated by longitudinal scanning of the mirror M_3, fixed on piezoelectric ceramic vibrating with an audial frequency. The beat frequency of the modes was recorded by a cooled photodiode. The dependence of the beat frequency deviation $\delta\nu_{12}$ on ρ_3 is shown in fig.3. It is a linear function in the measured range of ρ. Extrapolation of this dependence up to the level of noise of our instrumentation gives the value

ρ_{min}~10^{-7} in the bandwidth of 1 Hz. It corresponds to sensitivity $(N_e \cdot l)_{min} \approx 10^{11}$ cm^{-2}. Using a diffusive reflector (with the scattering indicatriss shown in fig.4) made of berillium deposited on a metal substrate and placed 0.7 m from the laser, one can measure the change of the optical length L even measuring the change of radiation power of the signal mode. When the change of beat frequency of radiation reflected by a nonpolish alluminium plate removed 56 m from the laser was used for measurements, the ratio of signal to noise was as high as $(7\text{-}12)\cdot 10^3$.

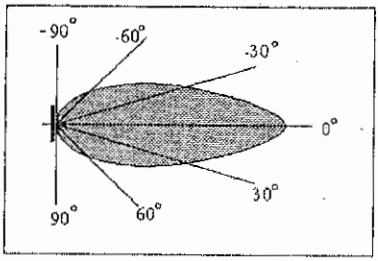


Fig.4. The scattering indicatriss of berillium deposited on a metal substrate for normal incidence of radiation .

To control influence of vibrations on the results of measurements, one can use the laser radiation with λ=0,63 μm reflected by the same external mirror M_3. It was found that the radiation power of the He-Ne laser LGN-302 (λ=0.6328 μm) was changed by 70% when receiving the refflected radiation.

Conclusion

The measurements show, that the three-mirror two-mode interferometer can work with low reflecting or even with diffusive external reflectors. Degradation of the surface of the reflector changes only the sensitivity of this interferometer. This effect can be taken into consideration by calibration from time to time. The use of a diffusive reflector reduces influence of mechanical vibrations. These facts give rise to suggestion, that the surface of the tokamak first wall can be used as a reflector for this interferometer. The base unit of the interferometer can be placed outside the biological shield of the thermonuclear installation.

References

1. I.L. Bershtein . Izvestiya Vuzov. Radiofizika. , 1973, v.16, p. 525

2. G.I Kozin, V.V. Petrov, E.D. Protchenko. Kvantovaya Electronica , 1991,v.18, №3, pp. 391-393.

3. O.A. Bashutin, E.D. Vovchenko, D.V. Mozgrin et al. Proc. of XXII ICPIG, Hoboken, New Jersey, 1995, v.2, pp. 97-98.

High-Stable Millimeter-Wave Vector Analyzer

G.P. Ermak, I.D. Revin, M.Yu. Demchenko, B.K. Skrunnik
Institute of Radiophysics and Electronics NAS of Ukraine
12 Ak. Proskura Str., 310085 Kharkov, Ukraine
e-mail: ermak@ire.kharkov.ua

A number of microvawe plasma diagnostics working in the short part of millimeter wave range require the high stable sources with output power more then 1 Watt and the high resolution receiving system. New opportunities for the collective scattering and interferometry of plasma can provide a new type of electrovacuum devices - Diffraction Radiation Oscillators (DRO) and locked measuring systems based on the DROs.

The high-resolution high stable Vector Analyzer of the superheterodyne type with coherent heterodyne was developed and investigated in a short part of mm band. The source of mm wave radiation is the DRO locked by PLL-system with frequency standard. That allowed to increase the long-time instability up to 5×10^{-10}.

The DRO is the source of high-stable electromagnetic oscillations of the average level of the output power of the EHF band. A series of the small-sized packetized DROs in the frequency band 30-250 GHz with output power 50-0.5 Watt and with the frequency instability up to 10^{-7} has been designed. High frequency stability and high output power of the DRO allow to design the precision measuring systems for researches of materials and devices having great losses in mm wave band.

The scheme of the Vector Analyzer is shown on Fig.1.

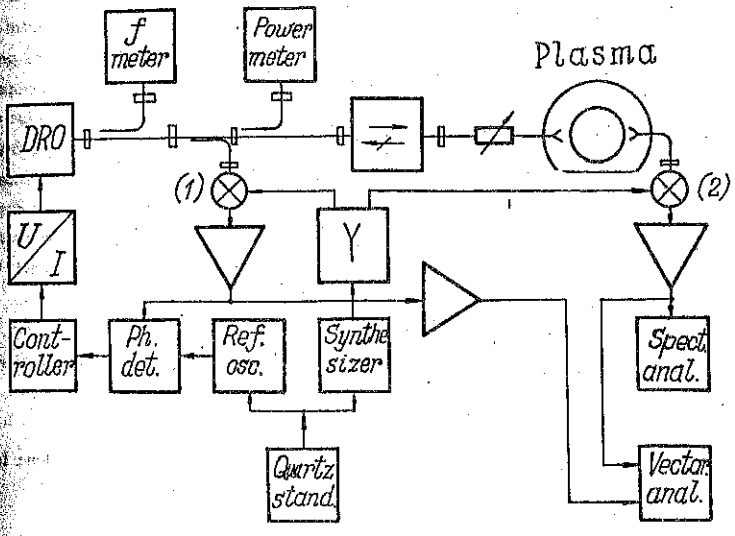


Fig.1

The output signal of DRO downconverets by the PLL harmonic mixer (1). The signal bo
sent to the phase detector containing in PLL-system and is used as a heterodyne signal. PLL-sys
contains the elements which are necessary to stabilize a DRO, that works in the frequency range
75 GHz. The frequency synthesizer locked by quartz reference oscillator is used as a reference si
for PLL harmonic mixer. The signal from the PLL harmonic mixer contained in the PLL-syste
directed to the reference channel of the vector receiver. The probing signal passed through
plasma or investigated devices is mixed in the receiving mixer (2) with the signal coming from
coherent heterodyne. Then the probing signal is sent to the measuring channel of the vector recei
The Vector Analyzer measures the transmitted and reflected signals by the simultane
measurement of amplitude and phase of the probing signal.
The deep heterodyne decoupling, that rules out the signal leakage from the heterodyne into the IF
channel, is carried out in the spectrometer. The measurement of the probing signal is carried out
an intermediate frequency by spectrum analyzer with a transmission band 3 Hz or by vec
voltmeter. The analyzer has electrical frequency tuning with a frequency step of 1 Hz. The sensitiv
of the receiving system is 90 dBmW, and the dynamic range is 120 dB.
Phase-locked spectrum of the DRO measured with an audio spectrum analyzer after do
converting the phase-lock IF to 20 kHz is presented in Fig 2. The frequency span is 5 Hz/divis
and the bandwidth is 3 Hz.

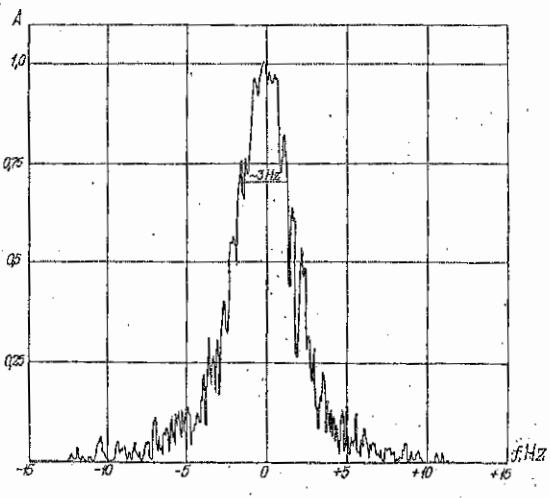


Fig. 2.

In figure 3 the long term stability of the DRO for locked and unlocked conditions is done. In th
locked mode a long term error of +/- 5 Hz in frequency range 60-75 GHz is achieved.

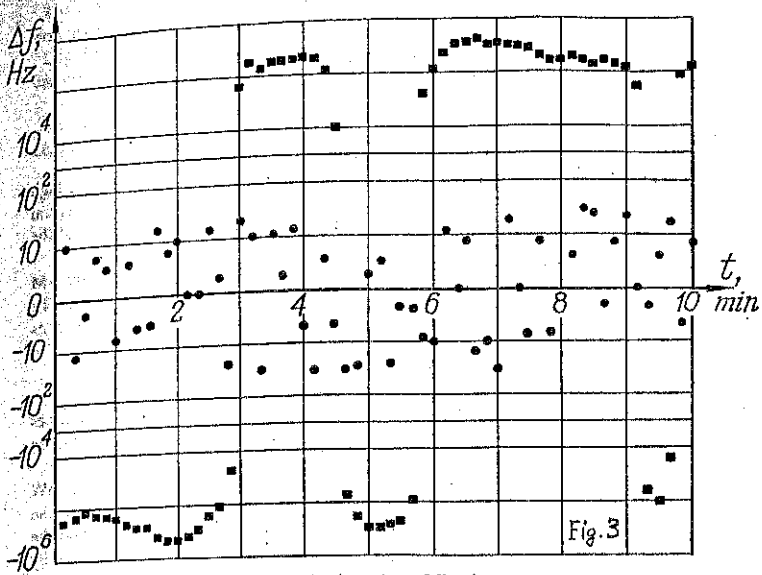


Fig.3

The main specification of the Vector Analyzer is as following:

- long-time instability	$> 5\times10^{-10}$
- frequency range	30-75 (150)GHz
- output power	10 -1 W
- sensitivity	10^{-10} W
- electrical frequency tuning	15-30 MHz
- resolution	3 Hz
- phase noise at 100 kHz detuning.	>80 dB

The Analyzer is well- suited not only for diagnostics, but for measuring of components, antennas, cavities and other objects at wide range of parameters change as well.

ULTRAFAST MILLIMETER WAVE AMPLITUDE MODULATOR FOR REFLECTOMETRY OF PLASMA

G.P. Ermak
Institute of Radiophysics and Electronics NAS of Ukraine,
12 Ak. Proskura Str., 310085 Kharkov, Ukraine.
E-mail: ermak@ire.kharkov.ua

In modern pulsed radar /1,2/ and amplitude modulation reflectometry /3/ of fusion plasma the high speed PIN switches and PIN attenuators are used . They provide the amplitude modulation to several hundred MHz and pulses with a pulse duration of 1-3 ns. The resolution in the measurement of the distances to the plasma strongly depend on the speed of the modulators.

An ultrafast varactor amplitude modulator has been designed for the use in pulsed radar and AM reflectometry in a millimeter band. The modulators are available in the 18-150 GHz range. The modulator provides the speed of the amplitude modulation up to 5 GHz and pulses up to 0.25 ns with ON/OFF ratio of 25-30 dB for a single diode and 35-40 dB for the two diodes modulator. The insertion loss of the single diode modulator is 1.5-2 dB over 0.5 GHz band.

It can operates with a sources which have got an output in CW mode up to 1- 3 Watts.

The modulator has an operating band < 1 GHz, but in reflectometres which use the sources working at the fixed frequencies it is not regarded as a disadvantage, because each source can be supply with an individual modulator.

The results of testing of the Ultrafast modulator in the pulse mode with 57 GHz , 200 mW IMPATT oscillator are presented in Fig 1, where the curve 1 is a RF pulse, generated by the modulator, and the curve 2 is the driving pulse. The duration of the driving pulse is 150 ps and the amplitude is 15 Volt. The duration of the RF pulse is about 250 ps. The driving pulse is measured by a detector with a negative output. For comparison, the driving and RF pulses are shown in the same polarity.

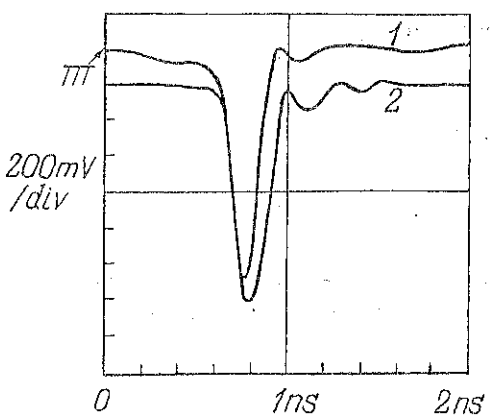


Fig.1

The modulator match well with pulse drivers which work on 50 Ohm load and have adjustment of bias in the range of (-0.5...+0.5) Volt.

Logic level "0" corresponds to isolation and logic "1" corresponds to transmission. This condition can be changed to opposite.

The modulator provides the linear change of the output signal in changing of the bias voltage from zero to 15 Volts and can be used as an electrical tuning attenuator (see Fig. 2).

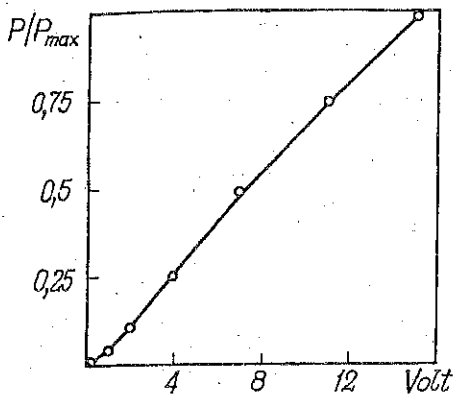


Fig.2

The further investigation of the modulator will be involve to broadening of the operating bandwidth.

Author expresses his gratitude to Dr. A. Hugenholts and Dr.S. Heijnen from Institute of Plasma Physics Rijnhuzen, the Netherland for the assistance in testing of the modulator.

References

1. O.S. Pavlichenko, A.I. Skibenko, and I.V. Yasin, ITER-IL-Ph-07-0-15 (1990).

2. C.A.J. Hugenholtz and S.H. Heijnen, Rev. Sci. Instrum. 62 (1991) 1100-1101.

3. J. Sanchez, B. Branas, T. Estrada, and de la Luna, "Research Proposal on Amplitude Modulated Reflectometry System for the JET Divertor", CIEMAT 685 (1992).

PLASMA CURRENT PROFILE DIAGNOSTICS ON FT-2 BASED ON THE CORRELATION REFLECTOMETRY MEASUREMENTS OF MHD MODES.

A.Yu.Stepanov, V.N.Budnikov, **E.Z.Gusakov**, L.A.Esipov, E.R.Its, V.Yu.Shorikov.
IOFFE Physico-Technical Institute, St. Petersburg, Russia

1. Introduction. The problem of the current profile diagnostics is very important for reactor plasmas. However, this problem has not yet been solved completely. It should be pointed out to the difficulties like access restrictions and high radiation levels. In this respect the microwave diagnostics should be highly attractive. The most advanced one is the reflectometry which is commonly used for density profile and density small-scale fluctuations measurements. Moreover, it is known that the reflectometry diagnostics can register signals from MHD oscillations [1,2]. The purpose of this study was to demonstrate the possibility of plasma current profile estimation by the correlation reflectometry. The method is based on the determination of the MHD mode oscillations localized in the vicinity of resonant magnetic surfaces by the correlative analysis of multichannel reflectometry signals.

2. Principle. We propose to use at least two reflectometers situated at different poloidal and toroidal angles in the manner similar to the magnetic Mirnov's coils for the correlative analysis of MHD modes. The data are processed by correlative and spectral techniques [3,4]. Normalized crosscorrelation function $S_{n12}(\tau)$, autopower $G_i(\omega)$ (i=1, 2) and crosspower $G_{12}(\omega)$ spectra, coherence $\gamma(\omega)$ and cross-phase $\Phi(\omega)$ spectra are calculated. Analysis of time evolution of these functions should give information on the location of resonant magnetic surfaces, which allows one to derive q −profile data. The essential difference between reflectometry and Mirnov's coils correlative method is that one can scan locally in the plasma core in the reflectometry case.

3. Scheme of the FT-2 Correlation Reflectometry. MHD density perturbations are studied by fixed frequency O-mode reflectometry on the FT-2 tokamak. Two reflectometers operate simultaneously at the same frequency 35 GHz, corresponding to cut-off density $n_e = 1.5 \cdot 10^{13}$ cm^{-3}. Experiments are carried out at two different configurations of the emitting-receiving systems which are referenced below as "poloidal" and "toroidal".

Fig.1 shows the scheme in the poloidal case where the reflectometers are located in the same poloidal cross-section ($\Psi_p = 0^\circ$) and separated poloidally by $\phi_p \approx 18^\circ$. The same 10 mW probing oscillator and the same emitting antenna A_i are used for both reflectometers . Two reflected signals are received by the antennae A_{s1} and A_{s2} and registered by the direct detection schemes. The amplitude modulation of the signals carries the information on MHD density oscillations. After the amplification in frequency band up to 500 kHz the signals enter the analogy-digital converter with the sampling step of 1 mks. In the toroidal case the toroidal separation is $\Psi_t = 180^\circ$ and the poloidal one is $\phi_t \approx 72^\circ$. The probing power is divided into two channels and enters two emitting antennae. The receiving part is identical to that of the poloidal case.

4. Experimental Results. Fig.2 presents FT-2 oscillograms of the plasma current I_p, electron density n_e and magnetic field B. The calculated minor radial positions of the cut-off r_c and magnetic surfaces r_q for different $q = m/n$ are also shown in the plot. The scan of the r_c along the minor radius is performed by the variation of the electron density during tokamak pulse and from discharge to discharge. The experiments are carried out at plasma currents ~20 and ~30 kA providing the accessibility of the magnetic surfaces $q = 1.5 \sim 4.0$. Intersection of the curves r_c and r_q determines expected radius and time when the reflectometry signals reflect from a given magnetic surface.

4.1. Poloidal Reflectometry. Fig.3a demonstrates 3-D function $S_{n12}(\tau, t)$ for this case. The dark grayscales indicate positive correlation (the darker, the higher). First of all a distinct maximum is observed at $\tau \sim -3$ mks over a period of measurement. The crosscorrelation function of this type is consistent with the one of noise signal with delay of $\tau \sim -3$ mks between the channels. Probably this delay is related to poloidal rotation velocity of the plasma electron component (about $0.5 \cdot 10^6 cm/s$).

Then, it is seen from Fig.2 that one can expect reflectometry signals from $q = m/n = 3$ at point in time $t \sim 15$ ms. According to the diagram in Fig.3a noticeable peaks at $\tau \sim -3$, 8 and 19 mks are observed just at $t \sim 15$ ms. This effect is seen clearly in the plot of the time evolution of S_{n12} (Fig.3b). Moreover, the regularity arises also at $t \sim 15$ ms. At this time the reflectometry signals have high regular structure at high correlation.

It is notable that delays between two channels $\tau \sim -3$ mks derived from the noise signals and the signals from magnetic surfaces $q = 3$ accord closely suggesting that the MHD modes and electron component rotate with the same poloidal velocity.

Fig.4 gives coherence and cross-phase spectra at $t = 14$ ms. Two multiple frequencies ~90 and ~180 kHz with high coherence level are observed. For rotating MHD modes the cross-phase must increase linearly with mode number (or frequency) in the poloidal case $\Phi = \phi_p \cdot m$. One can see that the cross-phases for these frequencies are on the same line (dashed) for which $m' = 6$ and 12 (m' is the mode number measured by the reflectometry). A factor of 2 difference of the mode numbers measured by the reflectometry and evaluated from the q-profile $m' = 2 \cdot m$ is probably explained by the detection scheme used, only sensitive to the amplitude modulation. The maximum amplitude of the reflected signal is expected to occure when the cut-off surface is perpendicular to the line of sight of the reflectometer. The number of such positions is twice a mode number.

The best results are observed for the magnetic surface $q = m/n = 2$. We also register coherence peaks when the reflectometers probe the region of $q = 2$. The coherence and cross-phase spectra at $t = 11$. ms are shown in Fig.5. Three multiple frequencies ~40, ~80 and ~120 kHz with high coherence are clearly distinguished. The experimental cross-phase data agree well with the calculated linear function just at these frequencies. The linear dependence of phase on frequency gives $m' = 4$, 8 and 12 respectively at mentioned frequencies and the modes m = 2, 4 and 6 are registered.

We also register high coherence spectra at the magnetic surfaces q = 1.5, 2.5 and 4.0 However, the agreement between observed and expected cross-phase data for these modes is poor.

Fig.6a. gives the obtained data on q−profile for different plasma currents. For each plasma current the data are obtained during the same discharge. For comparison, calculated q−profiles for quadratic parabola current density are shown. The magnetic coils data on the plasma periphery are also plotted. For both cases the q−profiles are similar and agree well with the calculated dependences. The drawback of these measurements is that the data are obtained at different moments in time. The experimental data allow to obtain radial profiles of the linear (and angular) velocities of MHD perturbations, Fig.6b. In spite of the similarity of q−profiles for different plasma currents, the profiles of the rotation velocity differ essentially on the plasma periphery. The rotation velocity of MHD modes coincides with the electron diamagnetic drift direction.

4.2. Toroidal reflectometry. In the toroidal case selected plasma current 27 kA permits the reflectometry probing of the magnetic surfaces q = 1.5, 2.0, 2.5. Detectable peaks are observed only for q = 2.0, 2.5. A good agreement between the cross-phase data and expected values is observed only for calculated magnetic surface q = 2.5: the cross-phase in this region at fundamental MHD frequency passes zero. This result agrees well with the fact that in the toroidal case the magnetic line goes directly from the first to the second reflectometer for $q \sim 2.5$. The width of the spectral lines of the fundamental MHD modes is larger than the one in the poloidal case at least by a factor of 1.5. A smaller number of the MHD harmonics (only fundamental and the first) are observed in the toroidal configuration.

5. Conclusions. The above results are obtained in spite of several complexities typical for small FT-2 tokamak. The q−profile and cut-off positions are unsteady during time of analysis (512 mks). The radial resolution of the O-mode reflectometer is quite poor for FT-2 parameters. The poloidal and toroidal resolutions are not high enough because of too wide beam patterns. It should be stressed that these complexities are not essential in devices with longer discharge time and larger scales, where the profile scan can be performed by the frequency sweep of the reflectometer.

Thus, the described diagnostic technique allows one to make estimation of the location of different magnetic surfaces, which can provide information on the plasma current profile. Besides, the diagnostics gives frequency spectra and poloidal rotation velocities of the MHD perturbations on rational magnetic surfaces.

This work was supported in part by INTAS grant 94-2236 and RFBS grant 96-02-17913.

References.

[1] P.J.Cripwell, Extraordinary Mode Reflectometry at JET, Ph.D.Thes., ICSTM University, London (1992).

[2] M.E.Manso, F.Serra, A.Silva et. al., Measurements of MHD Activity with Reflectometry on ASDEX, Coll. of Papers IAEA Tech. Com. Meeting "Microwave Refletometry for Fusion Plasma Diagnostics", Vienna, 1992, pp.123-132.

[3] J.S.Bendat and A.G.Piersol, Random Data: Analysis and Measurement Techniques, Witey, 1971.

[4] S.H.Marple, Digital Spectral Analysis With Applications, Prentice-Hall, 1987.

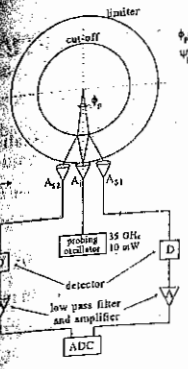


Fig. 1. Scheme of FT-2 poloidal cross-correlation reflectometer.

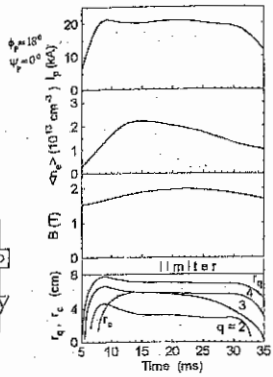


Fig. 2. Typical oscillograms of the FT-2 tokamak. r_c - position of the cut-off, r_q - position of magnetic surfaces.

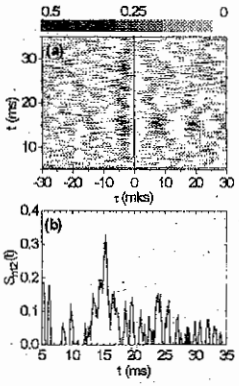


Fig.3. (a): 3-D normalized cross-correlation function $S_{n12}(\tau, t)$.

(b): Time evolution of S_{n12} at $\tau = 6$ mks.

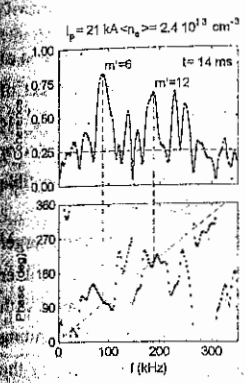


Fig. 4. Coherence and cross-phase spectra for $q = 3$ at $t = 14$ ms. Dashed line in the phase plot is the calculated curve for $\phi_p = 18°$.

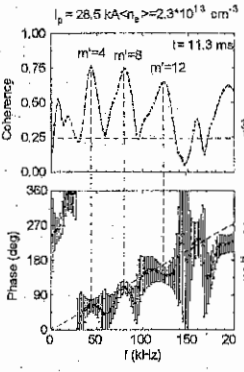


Fig.5. Coherence and cross-phase spectra for $q = 2$ at $t = 11.3$ ms.

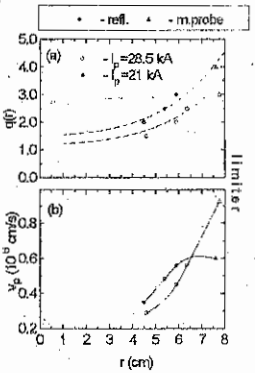


Fig.6. (a): Obtained and calculated (dashed curve) data on q −profiles for different plasma currents.

(b): Radial profiles of the linear velocity of the MHD perturbations for different plasma currents.

Two colour interferometer for density measurements on FTU

D. Frigione, **O. Tudisco,** L. Acitelli+ , A.A. Petrov*, V. G. Petrov*
Associazione EURATOM-ENEA sulla Fusione - C.E. Frascati, CP 65, 00044 Frascati (Roma), Italy

Introduction

Plasma density is currently measured on FTU by a five channel DCN (λ=195 μm) interferometer [1] that successfully works at almost all the densities of the FTU operation range. Some problems arise at densities larger than 2 x 10^{20} m^{-3} due to refraction. Furthermore, during pellet injection, fringes are lost during the fast density perturbation.

In order to get more reliable measurements also in these extreme conditions, we have developed and tested a single channel two colour interferometer employing a CO_2 laser (λ = 10.6 μm) as main wavelength and a visible HeNe one (λ=0.63 μm) for compensating the vibrations.

The phase shift suffered by a light beam crossing the plasma has two contributions: one proportional to λ due to the plasma itself and the other, inversely proportional to λ, due to the vibrations of the mechanical structures:

$$\frac{\phi}{2\pi} = \frac{\phi_p}{2\pi} + \frac{\phi_{vib}}{2\pi} = 4.48 \times 10^{-16} \lambda L \bar{n} + \frac{\delta_{vib}}{\lambda} \qquad (1)$$

Here L is the chord length, $\bar{n}$ is the line average density and δ_{vib} is the total excursion of the optical path due to vibrations. Long wavelengths minimize the disturbing effect of vibrations with respect to the plasma effect. On the other hand, refraction effects due to the plasma density gradient increase with λ^2 and eventually may bend the beam outside the detector view field. The optimal wavelength for a conventional interferometer is the longest compatible with refraction: for instance, for FTU, it is in the range of a few hundreds microns.

For a shorter wavelength, say 10.6 μm, the disturbing effect of vibration is several times larger than the plasma one: however this contribution can be compensated by introducing another interferometer, with a different wavelength, that shares almost all the optical components with the first interferometer. If λ_1 and λ_2 are the two wavelengths and ϕ_1 and ϕ_2 the corresponding phase shifts then the plasma density can be obtained applying eq. (1) and eliminating the vibrations, provided that δ_{vib} be identical for both interferometers:

$$\bar{n} = \frac{3.55 \times 10^{14}}{L} \frac{\phi_1 \lambda_1 - \phi_2 \lambda_2}{\lambda_1^2 - \lambda_2^2} \qquad (2)$$

+ ENEA Guest
* Troisk Institute of Innovation and Thermonuclear Research, TRINITI, 142092 Troisk, Moscow Region, Russia

Another important feature of an interferometer for plasma density measurements is the frequency shift that must be introduced in one beam in order to apply the heterodyne detection technique. A rotating grating (Veron wheel [1]) is employed for the DCN laser (λ=193 μm) on FTU that gives a shift of 10 kHz, while for the CO_2 laser (λ=10.6 μm) an opto-acoustic Bragg cell is used to introduce a frequency shift of 40 MHz [3,4,5].

This frequency shift f_s determines the maximum rate of variation of the density that can be detected by the system without loosing fringes. In fact, in order to be unambiguously identified, the phase variation must satisfy the condition:

$$\left|\frac{d}{dt}\frac{\phi_p}{2\pi}\right| \le \frac{f_s}{2} \qquad (3)$$

that gives an upper limit for the density variation rate of

$$\left|\frac{d\bar{n}}{dt}\right| \le 1.12\times10^{15}\frac{f_s}{\lambda L} \qquad (4)$$

For comparison, we report in Table I, together with other relevant quantities, this limit for DCN and CO_2 that must be compared with density rise rate of 1.3 x 10^{24} m^{-3} s^{-1}, estimated for FTU when a pellet with an equivalent density of 1x$10^{20}$$m^{-3}$ is injected with a speed of 2000 m/s.

Table I

	DCN	CO2	HeNe
One fringe density ($X10^{19}m^{-3}$). L=0.6 m	1.91	35.1	-
Density resolution ($X10^{19}m^{-3}$). Min $\Delta\phi=10^{-2}$ rad	0.003	0.056	-
Beam deflection (rad). $\bar{n}=2X10^{20}$ m^{-3}; Parabolic profile	0.01	3X10^{-5}	-
Diffraction limit density($X10^{20}$ m^{-3})	1.2	22	-
Number of fringes due to vibration δ_{vib}= 50 μm	0.26	4.7	79.4
Vibration equivalent density ($X10^{19}$ m^{-3}). δ_{vib}= 50 μm	0.49	160	-
Max. fringes rate due to vibrations (fringes/sec). δ_{vib}=50μm in 50 ms	5.2	100	1600
*Maximum detectable density rate (m^{-3} s^{-1}) f_s(DCN)=10 kHz; f_s(CO2)=40MHz**	9.6X10^{22}	7.0X10^{27}	-
*Max rate due to pellet injection (fringes/sec)**	5.2X10^4	2850	120

**Typical plasma density rise rate when pellet is injected is of $1.x10^{24}$ $m^{-3}s^{-1}$*

Experimental lay-out and preliminary results.

A schematic lay -out of a two colour interferometer is shown in Fig 1. The Bragg cell (BC) splits the laser beam into two parts and introduce a frequency shift in the diffracted beam. The two wavelengths are put together by means of a dichroic mirror that totally reflects wavelength 1 whilst it is transparent to wavelength 2. One part of each wavelength (probe beam)

crosses the plasma and is then mixed with the other beam (reference beam) by a beam sp
(BS). Another dichroic mirror separates the two wavelengths before arriving at the detect
is important to note that the only elements, not shared by the two wavelengths, are mirro
and M2 that, for this reason, are made as stable as possible.

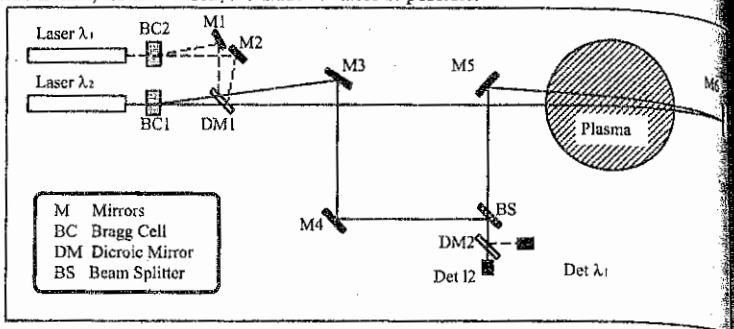


Fig 1. *Schematic lay-out of the two colour interferometer.*

A Mach-Zender scheme has been mounted and tested in laboratory on a granite bench
x 2.5 m) that holds all the optics apart those (two mirrors) that will deviate the beam into
plasma [6]. In order to reduce the vibrations, this two mirrors will be fixed to the anti-vibrat
structure that holds the optics of the DCN interferometer. Two ZnSe windows, with AR coat
for both CO_2 and HeNe, will be used for the FTU vacuum insulation. The total optical path
about 23 m long. Only two focusing elements have been used: the first concave mirror (f=
m) makes a waist of 6 mm of diameter around the plasma centre and the second (f=3 m)
placed on the top of the tokamak and reflects the beam back with approximately the same size
the same place. The first mirror is also used to focus the return beam onto the detectors. T
diameter of the CO_2 beam is kept below 20 mm along the whole path and mirrors with
diameter of 50 mm are employed to avoid diffraction. The HeNe beam diameter, however,
kept below 7 mm by means of an additional lens (f = 0.4 m) placed before the Bragg cell. F
symmetry the same optics has been used in the reference beam.

The power of the CO_2 laser is 7 W whilst that of the HeNe one is 12 mW. The C
detector is a HgCdTe room-temperature photoresistor, while the HeNe one is a PIN photodio
The signal is amplified by an AGC amplifier and compared with the LO signal, taken from t
Bragg cell driver, by a phase comparator giving the sine and cosine of the phase difference.
fast ADC Camac module has been used to acquire the phase comparator outputs.

In the laboratory test, the equalization of the two arms lengths within few centimeters h
proven to be crucial in order to get an interference signal as clean as possible: this effect
possibly due to the presence of more than one longitudinal mode in the HeNe laser emissio

Figure 2 shows the interference signal at the detector together with the superimposed disturbance when varying the path length of the reference beam. Close to the zero path difference the noise becomes about 2%.

After this optimization, data are elaborated in order to correct the systematic errors introduced by the phase comparators, in particular the different amplitudes and offsets of the sine and cosine outputs and a small periodic phase error. These errors are measured and then almost totally eliminated by introducing a path variation of few CO_2 fringes on the reference beam [7]. As these systematic errors vary slowly, this correction will remain valid, during the plasma measurements, provided that the correction parameters are obtained immediately before the tokamak pulse.

The final result of the vibration compensation with and without the correction of the error introduced by the phase comparator is shown in fig 3. Data are relative to a linear excursion of 70μm. Spontaneous and induced vibrations have been compensated with a residual error of 0.02μm corresponding to a line plasma density of about 4×10^{17} m^{-2}.

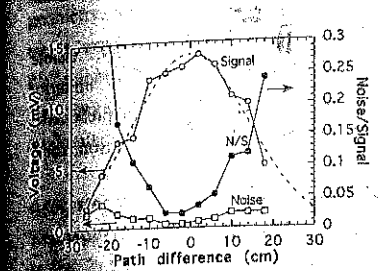


Fig 2. Interference signal at the detector versus the path difference with the superimposed disturbance when varying the path length of the reference beam.

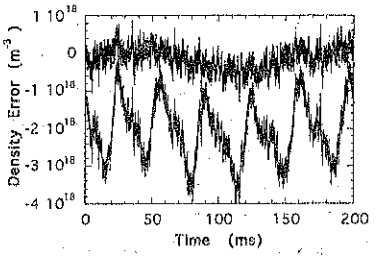


Fig 3. *Density error due to vibration compensation with and without the phase error correction*

Acknowledgement

We are indebted to P. Innocente and S. Martini of the Padua RFX group, for helpful discussions and suggestions deriving from their experience in the field and for providing most of the components that have been employed in the prototype apparatus.

References

[1] D. Veron, *Diagnostic for fusion reactor condition*, Vol 1, Varenna 1982, EUR8351-IEN
[2] S.M. Wolfe et al, Appl. Opt. **15** (1976),2645
[3] H. Irby et al, Rev. Sci. Instrum. **59** (1988), 1568
[4] D.N. Carlstrom et al, Rev. Sci. Instrum **59** (1988), 1063
[5] P. Innocente and S. Martini, Rev. Sci. Instrum. 63 (1992) 4996
[6] D. Brigione and O. Tudisco, Enea report **RT/ERG/FUS/94/20**
[7] P. Innocente et al, Rev. Sci. Instrum. **61** (1990) 2285

A Comprehensive Analysis of Impurity Transport in FTU Plasm

D. Pacella*, M. Mattioli°, R. Bartiromo*, K.B. Fournier†, M. Finkenthal•

* Associazione EURATOM- ENEA sulla Fusione, Centro Ricerche Frascati, C.P. 65 - 00044 Frascati, Rome , Italy
° EURATOM - CEA Association , Cadarache, France
† Lawrence Livermore National Laboratory, USA
• Johns Hopkins University , Baltimore, USA

Introduction

An absolutely calibrated, wide range soft X-ray (SXR) spectrometer [1] has been used measure simultaneously the central content of all metallic impurities and to assess the ionisa equilibrium of the central molybdenum charge states [2]. Information from the periph plasma is obtained with a SPRED U.V. spectrometer, which has also been used to evaluate light impurity content of the plasma.

Comparing the experimental data of the SXR-UV spectrometers, bolometry, vis bremsstrahlung emission and X-ray tomography with the simulations from an impu transport code, it is possible to study the impurity transport processes. This comprehens analysis has been done in detail for a discharge in the flat-top phase and, for comparison, fo similar one having the sawtooth activity.

Soft X-ray Spectrometer

This spectrometer, planned and built at the Frascati Tokamak Upgrade [1], uses Bragg diffraction on six flat rotating crystals. The detector is formed by three stacked Multi Wire Proportional Chamber, each with different absorption efficiencies. It has a wide energy range, an high counting rate capability, operates with simultaneously different crystals and allows resolution of the different orders of diffraction. In the present case mosaic graphite crystals have been used. The acquired X spectra (fig. 1) cover energy range 2.3-12 keV with low resolving power (about 200) and with time resolution of 33 ms per spectrum [2].

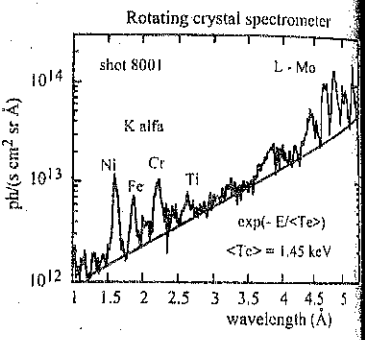


Fig.1 - Soft X ray spectrum acquired with the rotati crystal spectrometer

Discharge Characteristic

The plasma parameters (shot 8001) are: current I_p = 600 kA, toroidal field B_T = 6 T, minor radius a = 30 cm (R = 93 cm), central electron temperature and density $T_e(0)$ = 2 keV, $n_e(0) = 1.3 \times 10^{14}$ cm^{-3}, a molybdenum poloidal limiter and a stainless steel vacuum chamber. The central content of Ni, Fe, Cr, Ti is given by the code and the Kα emission, measured with the XKR spectrometer (fig. 1). Each of these features is a blend of the Kα emission of the He-like, H-like and Be-like charges states [3]. For molybdenum we look at the 2p-3d transitions labelled '3D' and '3C' and related satellites of Mo 32+, Mo 31+, Mo 30+, all of which are excited mainly from the ground state and are sensitive to the ionisation balance in the plasma. The central density of molybdenum has been estimated with the line '3D' $2s^22p^6$-$2s^22p^53d$ (Mo 32+) of Mo 32+. A more detailed analysis of the ion charge state of Mo will be described in the following.

The impurity transport simulation code [4] describes, for a given atomic species, in cylindrical geometry, ionisation, recombination and radial transport, given by diffusive and convective terms, expressed by diffusion coefficient D (cm^2/s) and inward velocity V (cm/s). S=aV/2D (a: minor radius) is the peaking parameter of the Gaussian impurity radial profile. The code then computes the most intense X-ray and U.V. lines and, summing all over the impurities, the total radiated power, the mean effective charge and the continuous soft X emissions.

Assessment of Central Molybdenum Ionisation Equilibrium and Impurity Transport Coefficients

In fig. 2a the experimental spectrum of Mo [2], limited to the features 3C, 3D (4.5-5 Å) is shown, acquired by the low resolution X-ray spectrometer. A detailed , quasi steady state, collisional radiative model, developed at Lawrence Livermore National Laboratories and Johns Hopkins University, has been applied to the FTU spectra [2]. It uses fully relativistic atomic structure data and distorted wave approximation collisional excitation rates. In fig 2a the individual lines coming from this model are shown to explain very well the low resolution acquired spectra. The model provides a synthetic spectrum for each ion "i" (i= Mo 33+, Mo 32+, Mo 31+, Mo 30+, Mo 29+) at a given electron temperature and density T_e^0,N_e^0. To reproduce the experimental spectrum, obtained by emission integrated along the central line of sight, radial temperature and density profiles have to be taken into account.

Since we are considering lines excited by the ground state, we can scale the line emissivity ε as function of T_e, N_e, N_z along the line of sight, following the relation $\varepsilon = N_e \times N_z \times Q(T_e)$.

The total spectrum is then a sum of single ion spectra, each one weighted by a factor P_i given by:

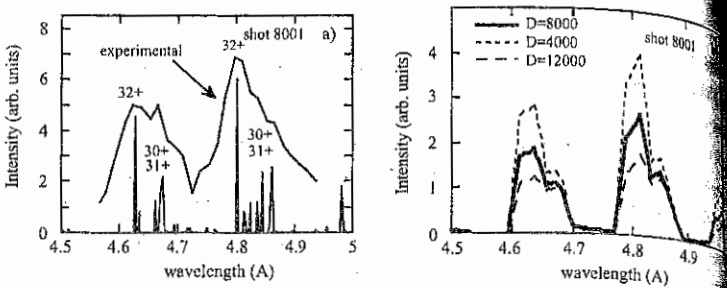


Fig.2 2p - 3d transitions of Mo 32+ , Mo 31+ , Mo 30+ a) low resolution experimental spectrum and high resolution; b) simulated spectra with different diffusion coefficient D (cm^2/s)

$$P_i = \int_0^{r_c} \frac{N_e}{N_e^0} \cdot N_i^z(r) \cdot \frac{Q(T_e(r))}{Q(T_e^0)} dr$$

where $Q(T_e)$ is the excitation rate coefficient of a line, provided by the LLNL model, N_i^z is radial profile of the molybdenum ion with charge "i" from the code and r_c is the radius at wh the density of the considered charge states goes to zero (in the present case $r_c \approx 12$ cm). In F 2b three different low resolution synthetic spectra are shown, obtained using different choi of the weights P_{30+}, P_{31+}, P_{32+} (normalised at P32+); curve "1" is obtained using fracti abundance profiles calculated by the code, with impurity diffusion coefficient D = 4000 cm curve "2" with D = 8000 cm^2/s and curve "3" with D = 12000 cm^2/s. It is evident that the c 2 (D = 8000, P_{32+}=1, P_{31+}=0.75, P_{30+}=0.45) reproduce well the experimental spectrum (2a); while other simulations have shown that $N_i^z(r)$ distributions for Mo32+, Mo31+

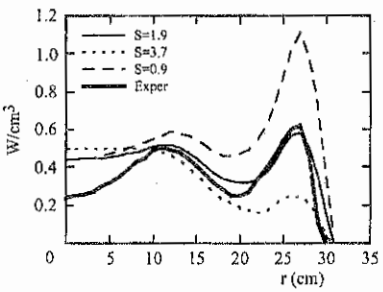


Fig.3 - Comparison between total radiated power measured by bolometry and simulated curves with different peaking parameter S

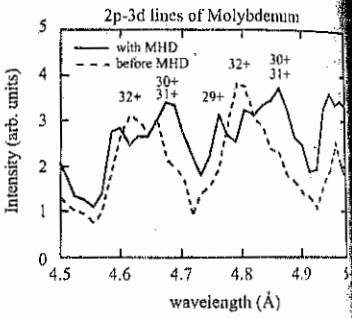


Fig.4 - Molybdenum experimental spectra for a discharge with sawtooth, before and during MHD activity

Tab I - Central impurity densities (cm^{-3})

N (Ni) = 4.8×10^{10}	N (Fe) = 1.3×10^{10}	N (Cr) = 6×10^{9}
N (Mo) = 1×10^{10}	N (Ne) = 4.4×10^{11}	N (O) = 1×10^{11}

Mo30+ are insensitive to the inward velocity V. To infer the V value and consequently the peak parameter S, we used the SPRED spectroscopy and the bolometric signals. In fig. 3 the experimental Abel-inverted profile of the radiated power is plotted, together with three different simulations from the code, corresponding to S=0.5, S=1.9, S= 3.8. Agreement is satisfactory with S=1.9. The SPRED gives supplementary information on the impurity profile peaking; for example the simulated brightness of Mo XIII at λ = 341 Å is of the order of the background level with S=1.9, but with a less peaked (S=0.5) profile it should be easily detected. Having chosen the transport parameters D and V_A, the code simulates the most important lines in X-UV range, in particular **Ni (292 Å), Ni (247 Å), Cr (390 Å), Mo (374 Å), O (630 Å), Ne (465 Å)**, and achieves good agreement with the measured lines. In table I the resulting central impurity densities are given.

Continuous soft X emission , simulated by the code using these central impurity densities, agrees with the value measured by the spectrometer (continuous line of fig. 1) in the range 2-12 KeV. This comparison provides a further global check on the validity of the above analysis.

Discharge with Sawtooth Activity

For a plasma discharge with sawtooth activity, the weights P_i which reproduce the experimental molybdenum spectrum (fig. 4) are P_{32+}=1, P_{31+}=2, P_{30+}=2, indicating an increase of the Mo30+ and Mo31+ abundance relative to Mo32+. Suitable abundance curves of the central molybdenum charge states can be obtained by the impurity transport code by increasing the diffusion coefficient in the central region ($0 < r < 12$ cm), thus producing a central flattening of the impurity profile.

The present work was performed in part under the auspices of U.S. D.O.E. by the L.L.N.L. under contract No. W - 7405 - ENG - 48 .

References

[1] R. Bartiromo et al., Phy. Res. **B 95** (1995) 537
[2] K. B. Fournier et al., Phys. Review **E 53** , 1 January 1996
[3] TFR Group et al., Phys. Review **A 32** , 4 October 1985
[4] TFR Group, Nucl. Fusion **25** (1985) 981

Interpretation of Measurements of ICRF–Heated Minority Proton Distributions in JET

KG McClements[1], RO Dendy[1] and A Gondhalekar[2]

[1] UKAEA, Fusion, Culham, Abingdon, Oxfordshire, OX14 3DB, UK
(UKAEA/Euratom Fusion Association)

[2] JET Joint Undertaking, Abingdon, Oxfordshire, OX14 3EA, UK

1. Introduction

Measurements made using a neutral particle analyzer (NPA) in JET have yielded i perpendicular velocity distribution of protons in the MeV energy range. The techni involves detection of hydrogen atoms formed by neutralization of the protons via cha exchange with hydrogen–like impurity ions [1,2]. The protons, a minority species in t plasma, are heated by waves in the ion cyclotron range of frequencies (ICRF) and a anisotropic. The energy range of the measurements is 0.3 MeV – 1.1 MeV. The measur quantity is $\tilde{\Gamma}$, the flux of atoms arriving at the NPA per unit area per unit energy. is proportional to the line integral of the proton energy distribution F_h, weighted wi respect to the neutralization probability per unit time P_ν. Thus, we have

$$\tilde{\Gamma}(E) = \int_{-b}^{b} P_\nu(E,Z) F_h(E,Z) dZ, \qquad (1)$$

where E is the energy of a proton moving towards the NPA, Z is vertical distance, and is the height of the plasma along the NPA line–of–sight. We can define a line–integrat distribution

$$\tilde{F}_h(E) \equiv \frac{\tilde{\Gamma}(E)}{P_\nu(E,0)} = \frac{1}{P_\nu(E,0)} \int_{-b}^{b} P_\nu(E,Z) F_h(E,Z) dZ. \qquad (2)$$

The radial profiles of the parameters upon which $P_\nu(E,Z)$ depends all have sca lengths of the order of b, whereas the scale length of F_h is smaller than the widt of the ICRF power deposition profile, which is much smaller than b. Thus, we ma set $P_\nu(E,Z)$ equal to $P_\nu(E,0)$ in Eq. (2), so that $\tilde{F}_h(E)$ is simply the line integral $F_h(E,Z)$. Korotkov and Gondhalekar [1,2] assumed a Maxwellian energy distributio $\tilde{F}_h \propto E^{1/2} \exp(-E/\tilde{T}_\perp)$, and deduced best–fit temperatures $\tilde{T}_\perp$ lying between 100 an 300 keV for ICRF powers in the range 2–10 MW. Our purpose here is to deduce physical interpretation of $\tilde{T}_\perp$, and to check the consistency of that interpretation wit independent measurements of the total ICRF–heated proton energy.

2. Local Proton Energy Distribution

We adopt a bi–Maxwellian model for the local proton velocity distribution, i.e.

$$f_h(\mathrm{v},Z) = \frac{n_h(Z) m_p^{3/2}}{(2\pi)^{3/2} T_\parallel(Z)^{1/2} T_\perp(Z)} \exp\left(-\frac{m_p(v_x^2+v_y^2)}{2T_\perp(Z)} - \frac{m_p v_z^2}{2T_\parallel(Z)} \right), \qquad (3)$$

where n_h is proton density, m_p is proton mass, and $T_\parallel$, $T_\perp$ are local temperatures parallel and perpendicular to the magnetic field, which lies in the x–direction. We assume that the poloidal component of the field can be neglected, so that one of the velocity space directions (z) can be identified with the vertical coordinate space direction Z. Only atoms with $v_x/(v_x^2+v_y^2)^{1/2} \geq 200$ can enter the NPA, and the velocity vector of a proton is not changed by the capture of an electron. In these circumstances, the velocity distribution of protons which, if neutralized, can be detected by the NPA is given by

$$\tilde{f}_h(v_x, Z) = \int\int dv_x dv_y f_h(\mathbf{v}) = \frac{v_x^2 n_h(Z) m_p^{3/2}}{200^2 2^{3/2} \pi^{1/2} T_\parallel(Z)^{1/2} T_\perp(Z)} \exp\left(-\frac{m_p v_x^2}{2T_\perp(Z)}\right). \quad (4)$$

Using the fact that $E \simeq m_p v_x^2/2$, and writing $F_h(E,Z)dE = \tilde{f}_h(v_x,Z)dv_x$, we infer that the local energy distribution of protons which can be detected by the NPA is

$$F_h(E,Z) = \frac{C_0 E^{1/2}}{T_\perp(Z)} \exp\left(-\frac{E}{T_\perp(Z)}\right), \quad (5)$$

where $C_0 \propto n_h(Z)/T_\parallel(Z)^{1/2}$. Stix [3] predicted that ICRF–heated ions would have a tail distribution of this form, the energy density $n_h T_\perp$ being approximately equal to $\rho_{RF}\tau_s$ where ρ_{RF} is the ICRF wave power density coupled to minority ions and τ_s is the slowing–down time.

Ray–tracing and full wave calculations for JET indicate that ρ_{RF} has a centrally–peaked, Gaussian radial profile [4]. In such cases $n_h T_\perp \sim \rho_{RF}\tau_s$ yields

$$T_\perp(Z) = \frac{\rho_0 \tau_s(Z)}{n_h(Z)} \exp\left(-\frac{Z^2}{D^2}\right) \simeq T_\perp(0) \exp\left(-\frac{Z^2}{D^2}\right), \quad (6)$$

where ρ_0, D and $T_\perp(0)$ are constants. The second equality in Eq. (6) follows from the fact that τ_s/n_h has a scale length of the order of $b \gg D$. For similar reasons, C_0 may be treated as a constant in Eq. (5).

3. Line–Integrated Proton Energy Distribution

With F_h given by Eq. (5) and $T_\perp$ given by Eq. (6), the integral in Eq. (2) is tractable analytically. We consider the equivalent integral

$$\tilde{F}(\mathcal{E}) = \mathcal{E}^{1/2} \int_0^\infty \exp\left(\xi^2 - \mathcal{E}e^{\xi^2}\right) d\xi. \quad (7)$$

Here, $\mathcal{E} = E/T_\perp(0)$ and $\xi = Z/D$. The fact that $D \ll b$ makes it possible to replace the finite interval of integration in Eqs. (1) and (2) with a semi–infinite interval in Eq. (7). Setting $e^{\xi^2} \simeq 1 + \xi^2 + \xi^4/2$, we obtain

$$\tilde{F}(\mathcal{E}) \simeq \frac{\sqrt{\pi}}{2} e^{-\mathcal{E}} \left\{1 + \frac{1}{8\mathcal{E}}\right\}. \quad (8)$$

Except in the limit $\mathcal{E} \ll 1$, Eq. (8) provides an extremely good approximation to $\tilde{F}(\mathcal{E})$

Korotkov and Gondhalekar [1,2] obtained a set of best–fit temperatures $\tilde{T}_\perp$ correspond ing to various levels of applied ICRF power in a single discharge. For each power le in the range 2–10 MW, they fitted a single Maxwellian to the line–integrated prot distribution over the entire energy range of the measurements. The distribution giv by Eq. (8) is not a single temperature Maxwellian, since it does not have a simp $\mathcal{E}^{1/2}e^{-\mathcal{E}}$ dependence. Such a dependence would imply $\tilde{T}_\perp = T_\perp(0)$, since $\mathcal{E} = E/T_\perp(0)$ and $\tilde{T}_\perp$ is defined by $\tilde{F}_h \propto E^{1/2}\exp(-E/\tilde{T}_\perp)$. One can define an energy–depende temperature $\bar{T}_\perp$ by writing

$$\bar{T}_\perp(\mathcal{E}) \equiv -\frac{T_\perp(0)}{d\ln(\tilde{F}/\mathcal{E}^{1/2})/d\mathcal{E}}. \qquad (9)$$

The mean value theorem requires that $\bar{T}_\perp[E/T_\perp(0)]$ equal the measured temperatur $\tilde{T}_\perp$ at an energy $E = E_*$ lying within the 300–1100 keV range of the measurements: w set E_* equal to the median energy of 650 keV.

The function defined by Eq. (9) is plotted in Fig. 1. Using Eq. (8) to evaluate th derivative in Eq. (9), and recalling that $\mathcal{E} = E/T_\perp(0)$, we obtain a quadratic equati for $T_\perp(0)$. With $E = E_*$ and $\bar{T}_\perp = \tilde{T}_\perp$, the appropriate solution is

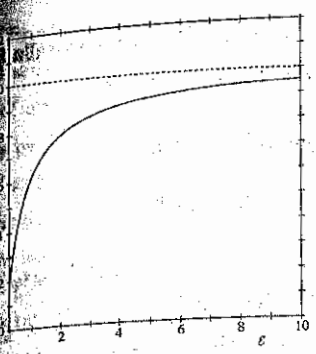
$$T_\perp(0) = 4E_*^2\left[\frac{1}{\tilde{T}_\perp} - \frac{1}{2E_*} - \left(\frac{1}{\tilde{T}_\perp^2} - \frac{1}{E_*\tilde{T}_\perp} - \frac{1}{4E_*^2}\right)^{1/2}\right] \simeq \tilde{T}_\perp\left(1 + \frac{\tilde{T}_\perp}{2E_*}\right). \qquad (10)$$

In the case of the distribution function data presented in Refs. [1,2], the best–fit valu of $\tilde{T}_\perp$ range from 80 keV for 2 MW ICRF heating power, to 265 keV for 10 MW ICR heating power. Setting $E_* = 650$ keV, we find that Eq. (10) gives $T_\perp(0) \simeq 85.4$ ke when $\tilde{T}_\perp = 80$ keV, and $T_\perp(0) \simeq 344.5$ keV when $\tilde{T}_\perp = 265$ keV. The Stix model implies that $T_\perp(0) \propto P_{\rm RF}$. Using Eq. (10) to obtain a set of values of $T_\perp(0)$ fro observed values of $\tilde{T}_\perp$ [2], we find that $T_\perp(0) \propto (P_{\rm RF})^{0.89\pm0.06}$: this compares wi $\tilde{T}_\perp \propto (P_{\rm RF})^{0.77\pm0.06}$. In this respect, the Stix model is in good agreement with th corrected tail temperature.

We can now calculate the total anisotropic proton energy content $W_{\rm p}$ for comparis with values obtained from diamagnetic measurements [5]. The energy density of a bi Maxwellian proton distribution with $2T_\perp \gg T_\parallel$ is $u = n_h T_\perp$. We assume, for simplici that u is only weakly dependent on poloidal angle: this is justified when $T_\parallel/T_\perp$ is greate than the local inverse aspect ratio [6]. The total proton energy content is then

$$W_{\rm p} = \int u d^3r \simeq 4\pi^2 R_0 \int_0^a u(r) r dr \simeq 2\pi^2 R_0 D^2 n_h T_\perp(0), \qquad (11)$$

where R_0 is major radius, a is minor radius and r is minor radial distance. We hav set $T_\perp = T_\perp(0)\exp(-r^2/D^2)$ and assumed that n_h has a flat spatial profile. Using Eq (11), we have calculated $W_{\rm p}$ for eleven ICRF–heated JET pulses, with $T_\perp(0)$ obtaine from NPA measurements of $\tilde{T}_\perp$ at times when no sawteeth had occurred for several slowing–down times. n_h was deduced from separate measurements [7]. Fig. 2 show $W_{\rm p}$ versus $W_{\rm fast}$, the proton energy content deduced from diamagnetic measurement Within the limits of experimental uncertainty, $W_{\rm p} = W_{\rm fast}$.



$T_\perp/T_\perp(0)$ *as a function of* $\mathcal{E}$.

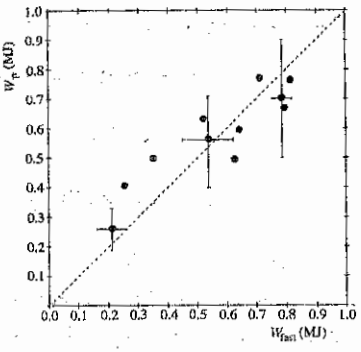


Fig.2: W_p *given by Eq. (11) versus* W_{fast} *deduced from diamagnetic measurements.*

Conclusions

We have deduced a physical interpretation of new line-integrated NPA measurements of ICRF-heated proton distribution functions in JET. Assuming that the perpendicular velocity distribution of the protons is locally Maxwellian, with a temperature which has a Gaussian radial profile, we have shown that the peak proton tail temperature $T_\perp(0)$ has a dependence on ICRF power which is approximately linear: this is consistent with the model of ICRF heating developed by Stix [3]. Moreover, our inferred values of $T_\perp(0)$ are consistent with estimates of the total ICRF-heated proton energy content deduced from diamagnetic measurements. These results validate a model of impurity-induced neutralization of MeV protons developed by Korotkov and Gondhalekar [1,2], and are encouraging for the development of the NPA as a diagnostic of fusion products in forthcoming deuterium–tritium experiments in JET.

Acknowledgments

This work was funded by the UK Department of Trade and Industry and Euratom.

References

[1] AA Korotkov & A Gondhalekar, Proc. 21st Eur. Conf. on Contr. Fusion and Plasma Physics, Montpellier (1994), I, p.266
[2] AA Korotkov & A Gondhalekar, *Nucl. Fusion* submitted (1996)
[3] TH Stix, *Nucl. Fusion* **15** 737 (1975)
[4] LG Eriksson & T Hellsten, *Phys. Scr.* **52** 70 (1995)
[5] DA Boyd et al., Nucl. Fusion **29** 593 (1989)
[6] KG McClements et al., *Phys. Plasmas* in press (1996)
[7] K Günther et al., *J. Nucl. Materials* in press (Proc. 12th Int. Conf. on Plasma Surface Interactions in Controlled Fusion Devices, St. Raphaël, 1996)

The research of charged component of controlled fusion installation constructive materials sputtering products

A. G. Koval, V. A. Litvinov, S. V. Gritzaenko

Kharkov State University, 310077, Kharkov, Ukraine

The present work is devoted to the study of differential and integral characteristics of secondary ion emission from stainless steel, beryllium and boron samples surface. The results of such researches can be of the interest as for studying of surfaces erosion effect of inverted to plasma chambers and various devices, as for studying of effect of plasma parameters deterioration with impurity particles penetration in plasma.

It is necessary to emphasize, that we imply the studying of true secondary ions sputtered in charged state directly from surface of studied material, instead of particles ionized (after sputtering) in boundary areas of plasma.

The studied materials samples were bombarded by the primary ions of inert gases under 60° to the normal and with density $3 \cdot 10^{-5}$ A/cm^2 that corresponds $2 \cdot 10^{13}$ part./sm^2 flux. The He^+ and Ar^+ were used as primary ions. The ions Ar^+ were studied so that to simulate the sputtering by heavy impurity particles, such as carbon, oxygen, various metal atoms and ions. The secondary ions, sputtered in normal direction were subjected to analysis. Before measurements the samples were subjected to long clearing by ion beam, during clearing were removed several thousands of monatomic layers.

The results of energy spectra measurement of the secondary atomic matrix ions (which are the main part of sputtered ions flux) from metals surface at residual atmosphere in target chamber, i.e. at enough pure conditions have shown following. The spectra of atomic ions take rather the wide energy interval. At sputtering of stainless steel sample both the He^+ and Ar^+ ions the principal structural feature of secondary ions spectra of main components is high-energy maximum at 100–300 eV. The spectra of matrix ions sputtered from beryllium and boron surface along with high-energy maximun have low-energy — at 10–20 eV. The average energy of atomic matrix ions is several hundreds eV.

As far as in real conditions the constructive elements can be subjected to impact of chemical active particles, such as the oxygen or hydrogen, it have measured the energy spectra of atomic ions at simultaneous influence on surface high-energy He^+ or Ar^+ sputtering particles, as well as chemical active particles O_2 or H_2 with thermal energies. The results of measurements in the case of stainless steel surface sputtering by Ar^+ and He^+ ions at various partial pressures of oxygen in target chamber are adduced on fig. 1, 2, and spectra of ions from beryllium and boron surfaces sputtered by ions Ar^+ are shown on fig. 3, 4. The adduced data testify that for metal surfaces the oxygen effect results in rather significant modifications. First of all, the total amount of secondary ions grows significantly, and degree of growth depends on their energy. The amount of low-energy ions grows in several orders, the amount of high-energy ions increases in considerably

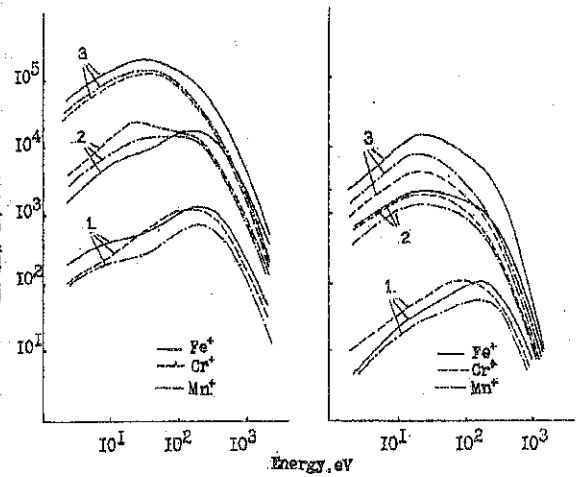


Fig.1. Energy spectra of atomic matrix secondary ions sputtered from stainless steel surface by Ar^+ ions at different oxygen partial pressures:

$1 - 7 \cdot 10^{-7}$, $2 - 1.3 \cdot 10^{-4}$, $3 - 1.3 \cdot 10^{-3}$ Pa.

Fig.2. Energy spectra of atomic matrix secondary ions sputtered from stainless steel surface by He^+ ions at different oxygen partial pressures:

$1 - 7 \cdot 10^{-7}$, $2 - 1.3 \cdot 10^{-5}$, $3 - 1.3 \cdot 10^{-4} \div 1.3 \cdot 10^{-3}$ Pa.

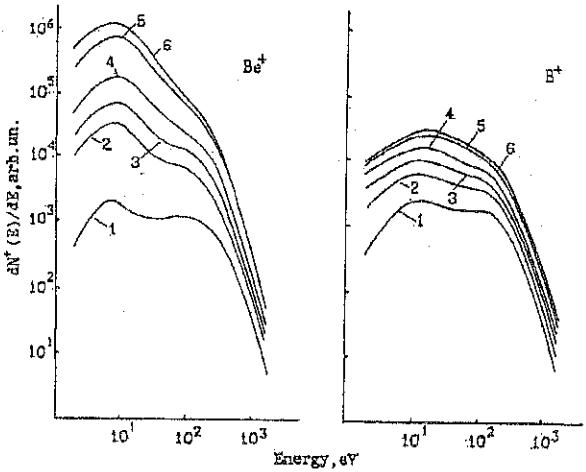


Fig.3. Energy spectra of atomic matrix secondary ions sputtered from beryllium surface different oxygen partial pressures:

1 – $7\cdot10^{-7}$, 2 – $2.7\cdot10^{-5}$, 3 – $6.7\cdot10^{-5}$, 4 – $1.3\cdot10^{-4}$,
5 – $6.7\cdot10^{-4}$, 6 – $1.3\cdot10^{-3}$ Pa.

Fig.4. Energy spectra of atomic matrix secondary ions sputtered from boron surface different oxygen partial pressures:

1 – $7\cdot10^{-7}$, 2 – $2.7\cdot10^{-5}$, 3 – $6.7\cdot10^{-5}$, 4 – $1.3\cdot10^{-4}$,
5 – $6.7\cdot10^{-4}$, 6 – $1.3\cdot10^{-3}$ Pa.

smaller degree. It results in significant transformation of spectra form. The main structu feature becomes the low-energy maximum. Naturally, value of average energy is reduc and, for example for beryllium the average energy decreases with 300 eV for cl conditions to 90 eV for completely oxidized surface.

In boron case the oxygen effect is displayed considerably less. The total of seconda ions grows whole in 7 times, average energy is reduced only to 230 eV.

At hydrogen effect on studied surfaces basically the same tendencies in change energy spectra that in case of oxygen are observed. However general growth of seconda ions amount and change of spectra form are displayed in considerably smaller degree. T

Differences in results of sputtering by primary Ar^+ and He^+ ions consists first of all that in result of greater sputtering coefficient by Ar^+ ions, at other equal conditions, on studied surface the smaller effective covers by oxygen or hydrogen realized, than during sputtering by He^+ ions.

The experience of work with various metals and oxides, semi-conductor and dielectric materials permits to make some assumptions concerning to ionization mechanisms of atoms, sputtered from surface. As for clean surfaces of one-element solids, ionization of sputtered atoms happens as a result nonadiabatic electronic exchanges between levels of atom and substrate [1, 2]. In this connection, it is considerable role of the electronic structure of solid, as well as position of valence level relative to the electronic zones. Also it is significant role of ionized atom neutralization processes on range of from surface [3].

At occurrence on studied surface chemical active particles (the oxygen, hydrogen) the polarization of chemical bonds between matrix and adsorbed atoms happens. In these conditions the determining role for ionization of sputtered atoms the breakage of polarized bonds plays. The efficiency of ionization at breakage of polarized bond considerably higher than as a result nonadiabatic electronic exchanges. Besides neutralization probability of flying off ions is significantly decreased, first, because of reduction of free electrons amount in substrates and secondly, because of is possible formation of forbidden zone [4].

The presented researches have given the definite information concerning to energy characteristics of secondary ion emission from various materials surface. Besides the changes of energy characteristics in dependencies on amount of chemical active particles on studied surface are investigated. The obtained information can be useful at choosing of materials for manufacturing of constructive elements of controlled fusion reactors.

1. V. A. Litvinov, B. M. Fizgeer, A. G. Koval, Izv. Akad. Nauk SSSR, Ser.Fiz. 54 (1990) 1334.

2. I. A. Bandos, A. G. Koval, Yu. V. Slusarenko, A. Yu. Sobolev, Surf. Sci. 296(1993) 97.

3. P. Williams, Surf. Sci. 90 (1979) 588.

4. A. G. Koval, Radiotechn. Electron. 37 (1992) 2051.

Double Pulse Thomson Scattering at RTP: First Results

M.N.A. Beurskens, C.J. Barth, C.C. Chu, N.J. Lopes Cardozo, H.J. van der Meiden, F.J. Pijper and the RTP-team.

FOM-Instituut voor Plasmafysica 'Rijnhuizen', Associatie Euratom-FOM, P.O. Box 1207, 3430 BE Nieuwegein, The Netherlands

Abstract

At RTP, a double pulse multiposition Thomson scattering diagnostic (resolution $2.5\,mm$) has been developed and installed. First measurements show interesting dynamics of small scale structures such as rotating islands and filaments and gradients in a sawtoothing ECH plasma.

Introduction

The research program of the Rijnhuizen Tokamak Project (RTP; $R/a = 0.72/0.1$, $B_T \leq 2.3\,T$, $I_p \leq 150\,kA$, $q_a \geq 2$) is concentrated on transport physics[1]. For a typical Ohmic plasma ($100\,kA$) the central electron temperature (T_e) is $\sim 1\,keV$ at a density of $5 \times 10^{19}\,m^{-3}$. Additional heating of the plasma is performed by Electron Cyclotron Heating (ECH) at 60 and 110 GHz.

One of the research goals is to study small-scale structures on the T_e profile. These structures have been demonstrated with a single pulse high resolution ($2.5\,mm$ in a range of $-125\,mm < z < 175\,mm$) multiposition Thomson scattering system[2]. In Ohmic n_e plasmas, clear steps on T_e and n_e with a typical size of $10\,mm$ appear near rational q-surfaces. When central ECH is applied, high T_e peaks, and steep edges show up. These peaks, called filaments, have a width of 5-10 mm. Analysis of many shots has confirmed the statistical significance of these structures [3]. The steps in Ohmic discharges and the steep edges in ECH plasmas are likely to affect the heat transport[4] in the tokamak. A closer study of the shape and the dynamics is required to quantify their effect on transport. For this reason a double pulse multiposition Thomson scattering diagnostic has been developed and installed. This diagnostic measures two T_e and n_e profiles with a temporal separation (Δt) in the range of 10–800 μs. A schematic is shown in Fig. 1.

In this paper the first double pulse Thomson scattering measurements are presented. Firstly, the consistency of the system is checked by measuring with $\Delta t = 0 \mu s$. Next two examples with $\Delta t = 100 \mu s$ are given for an Ohmic and an ECH discharge.

Description of the system

A double pulsed ruby laser beam (max. $2 \times 12.5\,J$) is injected vertically through the centre of the plasma. Scattered light is collected by a viewing doublet, guided to a Littrow polychromator and subsequently detected by two ICCD (Intensified Charge Coupled Device) cameras which gate at the first, respectively the second laser pulse. Both ICCD cameras view the same image intensifier via a beamsplitter. The optical system has been optimised, so that the total noise of the system is fully determined by the photon statistics at the first detection (i.e. at the GaAsP cathode of the first image intensifier, effective quantum efficiency $\approx 20\,\%$). The spatial resolution of the system is $2.5\,mm$ and its spectral resolution is $3.6\,nm$. Computer simulations[5] of the system have shown that the error at $T_e \approx 1\,keV$ is of the order of 2-3 % for $n_e \approx 10^{20} m^{-3}$.

Double pulse measurements

To demonstrate that measurements by both cameras give consistent results, Fig. 2 shows a measurement of T_e and n_e in which the cameras are gated at the same moment, $\Delta t = 0\mu s$. It concerns an Ohmic plasma discharge with $I_p = 60\,kA$ and $n_e(0) \approx 6.5 \times 10^{19} m^{-3}$. The figure shows that both measured profiles are very similar. Most striking is the jump in both T_e and n_e around $z = -30\,mm$, moreover several small scale structures on both T_e and n_e can be identified in both pictures. Camera 2 yields 5-10 % higher T_e due to a calibration deviation.

Fig. 3 gives an example with $\Delta t = 100\mu s$ of a measurement of a similar plasma. Now the first laser pulse plateaux at -70 $mm < z <$ -50 mm and 50 $mm < z <$ 70 mm are observed, while at the second pulse the profiles are rather smooth. Also the reversed case has been observed; a smooth first profile and plateaux in the second. The plateaux are interpreted as rotating m=2 islands. Note that the excellent resolution of the system allows access to the profiles inside the islands. The measurements are consistent with the rotation frequency of about 15 kHz usually observed in Ohmic discharges in RTP.

Application of ECH (60 GHz, 140 kW) to a low density plasma ($I_p = 60\,kA$, $n_e(0) \approx 2 \times 10^{19} m^{-3}$) leads to profiles as shown in Fig. 4. The first pulse shows large filaments in the plasma center. In the second recording, after $\Delta t = 100\mu s$, there are no filaments anymore and the T_e gradient near z = -30 and 30 mm becomes steeper. Central electron cyclotron emission measurements show that the first laser pulse is just before and the second just after the sawtooth crash. Most probably the sawtooth crash is the cause of the disappearance of the filaments. Other measurements without a sawtooth crash between the two laser pulses showed filaments on both T_e profiles.

Conclusions

We have shown first double pulse Thomson scattering measurements, proving the proper operation of the system. The two cameras yield the same T_e and n_e profiles for $\Delta t = 0\mu s$. When the ICCD cameras are gated at two different laser pulses, separated by 100 μs, the measurements show rotation of islands in an Ohmic discharge, and the dynamics of filaments in ECH plasmas. Further measurements with a scan of Δt, allow a study of the dynamics of small scale structures.

Acknowledgements

Many thanks are due to the technical staff of RTP for very efficient operation of the machine. This work was performed under the Euratom-FOM association agreement, with financial support from NWO and Euratom.

References

1. N.J. Lopes Cardozo, *et al.*, Phys Rev. Letters **73** (1994) 256-259.

2. M.N.A. Beurskens, *et al.*, Proc. 22nd EPS Conf. on Contr. Fusion and Plasma Phys., Bournemouth (1995) Vol. II. 129-132

3. N.J. Lopes Cardozo, *et al.*, Plasma Phys. Control. Fusion **36** Suppl (12)B (1994) B133-142.

4. M.N.A. Beurskens, *et al.*, 'Double Pulse Thomson Scattering system at RTP', submitted to Rev. Sci. Instrum.

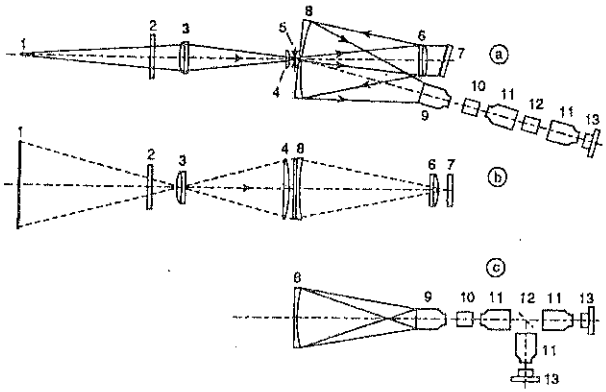


Fig. 1 Schematic of the double pulse multiposition Thomson scattering system: (a) top view and side views of the system (b) and of the detector branch (c).

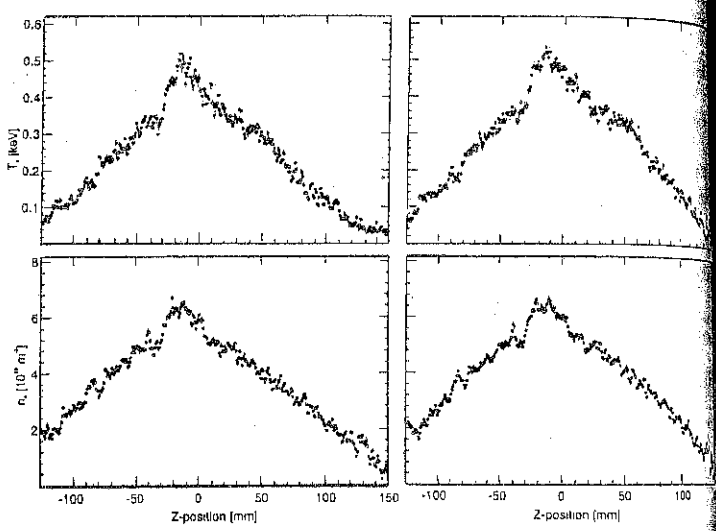


Fig. 2 T_e and n_e profiles measured with two camera's with $\Delta t = 0$ μs of an Ohmic (0 kA plasma.

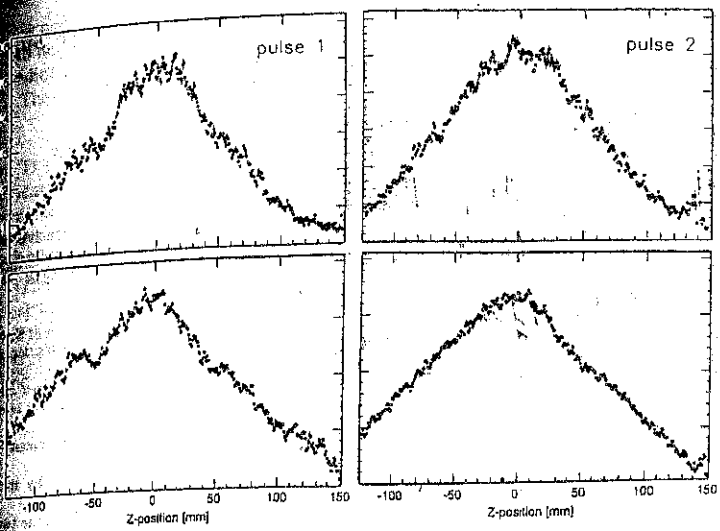


Fig. 3 T_e and n_e profiles with Δt = 100 μs for a similar Ohmic plasma as in Fig. 2.

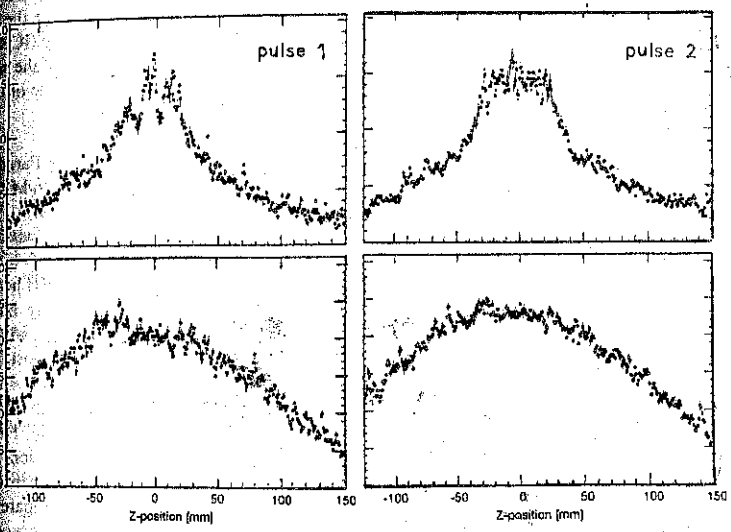


Fig. 4 T_e and n_e profiles with Δt = 100 μs for an ECH heated plasma.

Fast ion losses during neutral beam injection on Tore Supra : experiments and simulations

V. Basiuk, Ph. Lotte, G. Martin, R. White#
DRFC, CE Cadarache, F-13108 Saint-Paul-Lez-Durance, France.
PPPL, Princeton University, NJ 08543

Abstract : Tore Supra is well equipped to understand and predict ripple related phenomena, which is an impo issue for next generation of tokamaks. Direct losses of fast ions trapped in the toroidal field ripple of TO SUPRA, during neutral beam injection (NBI, up to 1.5 MW) and Fast Wave minority heating (FCI, up MW) were studied, using two diagnostics (electric probes):

- one collects directly the flux of fast ion entering a vertical port (DRIPPLE I)[1],
- the second (DRIPPLE II)[2] is a Faraday cup positioned in a vertical port and filtered to select fas by their Larmor radius (thus their energy). The energy range (100 keV -> MeV) of the detector depends on parameters: the magnetic field and the injected fast ion mass (D^0 or H^0). For low magnetic field (toroidal fi = 2.2 T), the D^0 beam energy injection (Einj = 70 keV) is accessible. Preliminary results give access t energy spectrum of lost fast ions. It allows a direct calibration of that type of collector which was construct study fast ion losses during ICRF heating.

The fast ion losses (direct or stochastic losses) and the shine-through are calculated by means of:

-a Fokker Planck code which simulates the neutron flux,

-a Monte-Carlo code which simulates quite well the current collected by the coll DRIPPLE I during NBI experiments and the energy spectrum.

The estimation of the ripple losses rate during NBI experiments is quite similar with the two code gives confidence in these codes which can be used to calculate the heat flow of lost fast ions on inner or wall, limiters... and to design a new type of protection against ripple losses on Tore Supra.

I) Introduction

The aim of the diagnostic DRIPPLE II[2] is to study the time evolution (≈ 2 ms) o energy spectrum of fast ion trapped in the toroidal magnetic field ripple during the mo sawteeth regime. This regime, achieved with ion cyclotron resonance frequency (ICRF) s an unusual burst of fast ion, correlated with a stabilization or even a decreasing of the electr temperature (figure I-1). The use of neutral beam injection (NBI) at different value of magn field allows a calibration in energy and validates the diagnostic.

II) The diagnostic DRIPPLE II

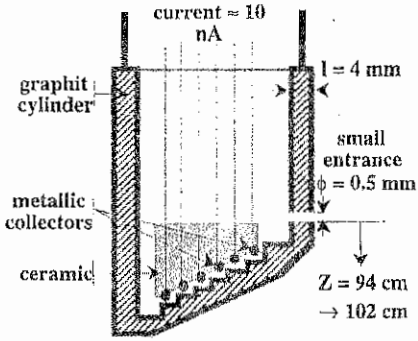


Figure II-1 : Schematic view of DRIPPLE II.

Dripple II (figure II-1) is a Faraday c positioned in a vertical port and filtered select fast ions by their Larmor rad (thus their energy). It was constructed support the high flux of lost io observed during ICRF or NBI heating ≈ 100 W cm^{-2}, estimated by means DRIPPLE[1], which has no ene resolution and collects all the lost fast entering the port). The collector is mad a hollow graphite cylinder with a sl entrance slot. Thus, it provides two ki of selection in the flux of fast ions:

-an area selection, as the aperture (≈ 7.9 10^{-7} m^{-2}) is small compared to 2.8 10^{-3} m^{-2} area collection of a collec of DRIPPLE I, which give an expected ratio in the current between the two diagnosti 3600.

-a pitch angle selection. Simulations show that all fast ions whose $|v_{//} / v|$ is greater than 0.02 will not enter the cylinder. Almost 10 % of the fast ions which reach the pinhole, fulfilled that condition.

The estimated current for such a diagnostic is then:

$$I_{dripple\ II} \propto \frac{I_{dripple\ I}}{3600 \times 10} \propto 30 \times \left(\frac{I_{dripple\ I}(mA)}{1} \right) nA$$

The low value of this current imposed an amplification by a factor 10^6, 10^7. This amplification is responsible for the high level of noise that often occurs during ICRF experiments and prevents quantitative analysis.

A small polarisation (+ 10 V) is applied on each metallic collector to avoid the emission of secondary electrons[2].

The diagnostic can move vertically (from 0.94 to 1.04 m) between shots in a way to have a spatial resolution, as it intercepts different iso-B. The energy range depends both on the level of the magnetic field at the collectors and on the ion mass. For B_T = 3.4 T (figure II-2), the energy threshold, calculated by means of the Monte Carlo "ORBIT"[4], is about 30 keV (D^0) and decreases linearly with B_T.

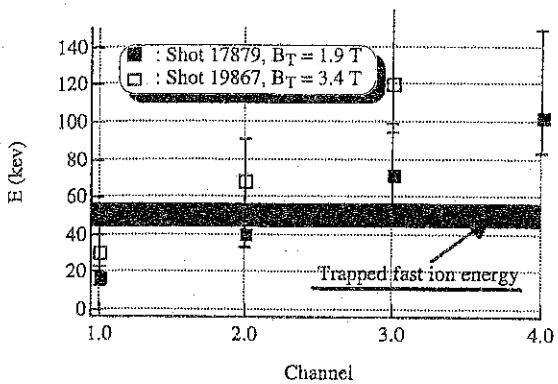


Figure : II-2 Energy resolution during NBI (D^0) for channel 1 to 4 at two different magnetic fields

III) Simulations

The simulations, during NBI, were undertaking with two types of codes:

-a Fokker Planck code[5], which allows, by means of the distribution functions, the prediction of the neutron flux as well as the global losses.

-a Monte Carlo code[4], "ORBIT". This code reproduces quite well the Fokker Planck estimation of ripple losses and the total level and the profile of the current measured by the diagnostic DRIPPLE I. It allows an estimation of the local heat flux per MW injected on the outer wall ($\phi \approx$ 30-40 W/cm^2/MW) or inside a vertical port ($\phi \approx$ 100-120 W/cm^2/MW).

IV) Experimental results

IV-1) Neutral Beam Injection

Neutral beam injection (D^0) has been carried out on Tore Supra[6] with three of the six sources (source 1,2 → co-injection, source 3 → counter injection) at a level of 1.7 MW.

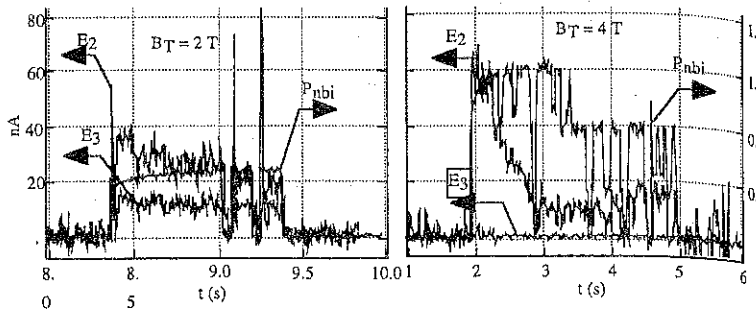


Figure IV-1: Time evolution of the collector 2 and 3 for two magnetic fields a) shot 17879, B_T = 1.9 T, (E_2 = 40 ± 15 keV, E_3 = 72 ± 20 keV) b) shot 19868, B_T = 3.4 T, (E_2 = 70 ± 20 keV, E_3 = 120 ± 30 keV). Unfortunately, the collector 1 did not work during that day.

Figure IV-1 show the current measured by the DRIPPLE II for two different magnetic fields (1.9 T and 3.4 T):

-For 1.9 T, the signal of DRIPPLE II is correlated with the signal of neutral beam power. The energy is in good agreement with the injection energy (E_{inj}), if we consider that the fast ions are rapidly lost in the ripple. Monte Carlo Simulations show that almost 80 % of lost ions have an energy greater than $0.8*E_{inj}$. The collector 2 (E=40 ± 15 keV) and the collector 3 (E=72 ± 20 keV) shows a small signal whose the ratio r23 is around the prediction of the simulation for the injected energy (for E_{inj} = 55 keV → $r23_{simulation} \approx 1.8$, $r23_{experiments} \approx 2$). The altitude of the probe is 98 cm (z). It is at the same location as the collector two of DRIPPLE I, which is located at the adjoining port and received about 2 mA current. The expected current, by means of code "ORBIT", is then around 60 mA, not far from the measured current (sum of the six currents).

-For 3.4 T, the collector 2 shows a signal whose variations are due to the fact that NBI is applied during the current ramp-up and the profile of density (so the deposit profile) changes. The main point is that the collector 3 does not show any signal at all, as it was predicted, since its energy range is upper than 90 keV.

These two experiments validate the diagnostic DRIPPLE II, and give confidence on the method to measure the energy.

IV-2) Application : Monster sawteeth regime

During monster sawteeth regime, achieved with ICRF (power = 4.5 MW, dipole configuration), a burst of fast ions (Figure IV-3) is surimposed on the usual fast ion signal of DRIPPLE I[3]. It is correlated with a flatness of the electronic temperature. First results of DRIPPLE II, show that the mean energy of fast hydrogen ion involved in that burst, is higher than fast ions lost in the sawteeth crash or during the so-called usual fast ion signal:

$$\langle E \rangle = \frac{\int_{E_a}^{E_b} E\, f(E)\, dE}{\int_{E_a}^{E_b} E\, dE}, \text{ with } E_a = 120 \text{ keV}, E_b = 700 \text{ keV} \Rightarrow \begin{matrix} \langle E \rangle_{t_1} \approx 200 \text{ keV} \\ \langle E \rangle_{t_2} \approx 160 \text{ keV} \\ \langle E \rangle_{t_3} \approx 150 \text{ keV} \end{matrix}$$

These values are comparable to those obtained by calorimetry measurements[3], it implies a minority concentration around 10%, and the experimental value is around 5 %.

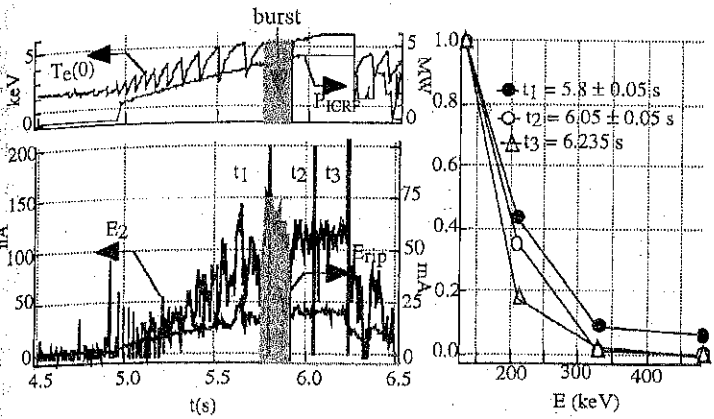


Figure : IV-3 a) Time evolution of collector 2 (E = 130 keV) during a monster sawteeth, compared to the electronic temperature at the center of the plasma and the current measured by DRIPPLE I. b) Energy spectrum (collectors 2,3,4 and 5) at three different times: $t_1 \rightarrow$ during the fast ion burst correlated with the stabilization of Te, $t_2 \rightarrow$ after the burst, $t_3 \rightarrow$ at the crash of the sawteeth.

V) Conclusions

The diagnostic DRIPPLE II begins to give useful results on the energy distribution of fast ions. It is validated by means of neutral beam injection and gives its main results concerning the time energy evolution during sawteeth stabilization. It will be used in the next campaign to have more statistic and to study the effect of Lower Hybrid wave on fast ions created by ICRH.

References

[1] Basiuk V. et al, 19th EPS Conference on controlled Fusion and Plasma Physics, Innsbruck, Vol. 16C, part I, p 175-178

[2] Basiuk V. et al, Fusion Technology, vol. 26, 222, (Nov. 1994)

[3] Basiuk V. et al., Nuclear Fusion, vol. 35, No 12 (1995)

[4] White R.B., Phys Fluids B2, 845 (1990)

[5] M. Tuszewski, J.P. Roubin, Nuclear fusion, vol. 28, N°3 (1988)

[6] P. Bayetti et al, 17th SOFT, Rome, p. 437 (1992)

FAST ELECTRON BREMSSTRAHLUNG TOMOGRAPHIC SYSTEM ON TORE SUPRA.

Y. Peysson

DRFC, CE Cadarache, F-13108 St-Paul-Lez-Durance, France

1. Introduction

The non-thermal bremsstrahlung emission observed during Lower Hybrid (LH) experiments provides a quite direct insight of the fast electron distribution in real and momentum spaces in tokamak plasmas. It is therefore a stringent test on the validity of models describing propagation and absorption of the LH wave, a critical issue for current density profile control experiments in relation with the advanced tokamak concept. Furthermore, the dynamics of these electrons enables to probe the level of stochasticity of the magnetic topology, which could be responsible for the anomalous electron energy transport in tokamaks. For this purpose, a new fast electron bremsstrahlung tomographic system is designed for the tokamak TORE SUPRA in order to study the hard x-ray (HXR) photon energy range between 20 and 200 keV. Performances of detectors as well as shielding capabilities against the noise induced by fast thermonuclear neutrons are discussed. Simulations of profile reconstruction are also presented for relevant operating conditions.

2. Physical objectives

The achievement and control of steady state fusion plasmas with economically relevant performances is one of the major challenge in the next decades for tokamak physics [1]. With superconducting toroidal coils, active heat and particle control systems, and a large available choice of plasma heating methods, the TORE SUPRA tokamak is especially well designed for this type of studies, so-called "advanced tokamak scenarios". High-density steady state tokamak operation with active control of heat, particles, impurity influxes and current density profiles raise several questions on the route to achieve such plasmas, their stability and performances, and their ability to be driven by external feedback control systems. Among all possible scenarios, stationary states with magnetic shear reversal are probably the most attractive, as the shape of the off-axis current density profile required to achieve such high-β_p regimes is grossly consistent with the expected one from the bootstrap current fraction (80-90%) [2]. Therefore, power requirements to sustain such self-organised discharges may be low enough for a competitive reactor scheme, with a reduced recycled power fraction to be foreseen. Such scenarios, which require a fine control of the plasma current density profile are investigated on TORE SUPRA, by launching quasi-electrostatic Lower Hybrid waves, in order to drive a fast current carrying electron population. Among various suitable methods to diagnose these high-energy electrons, the non-thermal bremsstrahlung emission is one of the most efficient, as it offers a quite direct insight on the build-up of the tail electron distribution function [3]. It allows to recover not only the energy range of fast electrons, but also their whole dynamics in momentum space. As the launched wave power spectrum lies mainly between $n_{//} = 1.4$ and 2.5, where $n_{//}$ is the parallel refractive index with respect to the local magnetic field direction, the expected energy of resonant electrons with waves by Landau damping ranges between 20 and 200 keV. Therefore, the interesting plasma bremsstrahlung emission falls into the hard x-ray energy domain for which numerous tested spectrometry techniques are well known [4].

The choice of the most appropriate type of x-ray detectors, as well as their geometrical arrangement around the tokamak is a trade off between the primary requirement of a high spatial resolution, and the capability to get valuable details on the fast electron temporal dynamics [5]. The main difficulty relies to the fact that local bremsstrahlung emission may be recovered only by Abel inversion of noisy line-integrated data. Even if efficient numerical inversion techniques may be used, like linear regularisation or maximum entropy, it turns out that a large redundancy in the spatial measurement, which acts as a local radial averaging, is highly recommended for an accurate image reconstruction especially in the core of the plasma, a critical region for shear reversal scenarios, when the hard x-ray emission may be off-axis during this regime. As plasma

emissivity is low in the interesting photon energy range ($\lesssim 10^{+7}$ photon.keV^{-1}.cm^{-3}.s^{-1}), the adequate number of detectors is only determined by the available place for the camera near the tokamak, so that the photon flux on each detector surface fulfils time resolution requirements, of the order of Δt = 3-5ms. Indeed, the lowest timescale (collisional slowing-down) ranges between 5 and 10 ms for 100 keV electrons at current operating electron plasma densities, $n_e \approx 3 - 5 \cdot 10^{19}$ m^{-3}. Because of the dependence in energy of most physical mechanisms which are involved in the build-up of the non-thermal electron tail, the knowledge of the photon energy spectrum is also necessary. However, as the bremsstrahlung emission is a continuous function of the photon energy, only a coarse multichannel analysis is necessary, in contrast to most usual needs in nuclear radiation spectroscopy.

3. Detectors and shielding

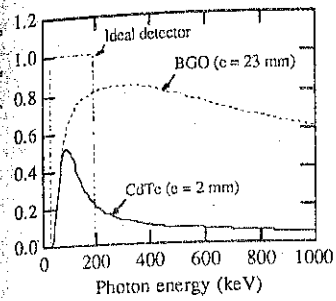


Fig. 1. Comparative x-ray detector efficiencies

Besides physical requirements, severe additional constraints may contribute to the choice of the most suitable detector for HXR measurements on a tokamak: high ambient varying magnetic field level (up to 0.1 T), high neutron and γ fluxes due to thermonuclear D-D fusion reactions (up to $R_n = 10^{+14}$ neutron.s^{-1} on TORE SUPRA, between thermal energies and 2.5 MeV), lack of place in the vicinity of the machine (reduced size of ports, large number of diagnostics and heating systems). Among most current X/γ ray detectors which may be foreseen for the design of the new HXR tomographic system, it turns out that cadmium telluride CdTe semiconductor operating at room temperature is one of the best candidate for highly resolved HXR measurements both in time and space [6]. Indeed, the high stopping efficiency in the energy range of interest - 60% at 122 keV for a 2 mm thick detector - which falls down rapidly above 200 keV allows to use very small size crystals, a critical condition not only for the design of compact cameras but also for operating in a noisy n/γ environment without a dedicated radiation shielding (Fig.1). Moreover, CdTe detectors exhibit several nice additional properties: no sensitivity to magnetic field, short pulse rise time (0.05 - 0.5 µs) which enables high counting rates up to 1-2×10^5 count/s/line-of-sight. This latter point is especially important to reduce statistical fluctuations at an acceptable low level for an accurate determination of profiles and time evolutions of the plasma HXR emission. Indeed, on the basis of a 10% relative deviation to the mean HXR intensity value, and considering only 4 energy channels, the estimated counting rate to achieve a time resolution of 5 ms on the full photon energy range is close to 100 kHz. In order to avoid tail pileup, which may distort recorded energy spectra, the width of shaped pulses must be as small as possible. Considering as a rule of thumb that this should not be less than 10 times detector pulse rise time, it is clear that the required counting rate of 100 kHz is compatible with CdTe time performances.

The x-ray measurement under high neutron and γ-ray fluxes without a specific shielding is usually a very difficult task, owing to the large number of events which could appear and corrupt the signal. Indeed, as neutrons may travel several centimeters of matter without any type of interaction, the size of an efficient n/γ shielding is always very large, and therefore incompatible with the prospect of a compact HXR camera. From test experiments which have been carried out with the present day camera, it has been shown that the noise level inside the lead shielding box, which is 10 cm thick, is independent of the direct n/γ flux through collimating apertures, and is moreover nearly isotropic. It is therefore likely that most neutrons or γ-rays impinging HXR detectors are resulting from inelastic scattering in the tokamak structure or/and in the lead box

itself. In this case, reducing the detector volume may strongly increase the signal to noise ra and lead to much larger margins for the diagnostic operating conditions. The use of a thin detector with a very high x-ray stopping efficiency like CdTe, and which exhibits in addition a cut-off-like behaviour above the interesting photon energy range is thus very attractive. Indeed, most of prompt γ-rays resulting from neutron interactions in common materials have an energy larger than 200 keV [7].

In order to validate the use of CdTe for HXR measurements on a tokamak, test experiments have been carried out, by replacing a BGO scintillator (e = 23 mm, V ≈ 45 cm^3) of the former HXR diagnostic by a CdTe semiconductor (e = 2mm, V ≈ 5×10^{-2} cm^3) [3]. It is therefore possible to compare at the same time, the behaviour of two neighbouring lines-of-sight viewing a similar plasma region with different detectors. All detectors are placed in the same lead box, with 1 mm thick aluminium and iron absorber foils. Due to the large thickness of the BGO detectors, their stopping efficiency is close to 0.8 up to 500 keV, while the CdTe one falls off very rapidly above 200 keV as shown in Fig.1. From both size effect and x-ray stopping efficiency level, BGO detectors are expected to be much more sensitive to the ambiant noise than CdTe, when thermonuclear reactions occur. To give a clear evidence of the difference of behaviour between detectors, and to separate the non-thermal bremsstrahlung signal from the n/γ noise, plasma density has been increased during LH heating, by adding deuterium gas during the discharge in helium target plasma. The rise in density is expected to lower the bremsstrahlung signal, while the increase of the thermonuclear D-D fusion reactions leads simultaneously to a growth of the noise level. The photon energy spectra measured by the two detector types, and recorded in 256 channels during 200 ms, are displayed in Fig.2, at two different times. It is interesting to notice that despite the very small size of the CdTe detector, as compared to BGO scintillators, both give similar signal levels between 20 and 200 keV, at a counting rate of 15 kHz. In this photon energy range, the signal for both detectors may be ascribed to bremsstrahlung emission, as it decreases when plasma density increases, due to a much higher fast electron collisionality. At higher energies, large differences are observed between the two detectors. While no signal is detected with CdTe, a clear increase of the background noise is measured with BGO. The broad peak close to 511 keV is likely the signature of all recombinations of electron-positron pairs created by interactions of high-energy γ-rays in the lead shielding. The noise level below 500 keV is nearly constant and merge with the bremsstrahlung signal at 130 keV, while for CdTe, no evidence of noise is found at the same energy value. So, even if the BGO detectors have a better x-ray stopping efficiency, noise prevents their use at a quite low level neutron rate. Hence, for high temperature plasma conditions corresponding to $R_n \approx 10^{+14}$ $n.s^{-1}$, the noise level is estimated to $5\times10^{+3}$ $count.keV^{-1}.s^{-1}$ for present day used BGO, far above the bremsstrahlung signal, while it is expected to remain only at 5 $count.keV^{-1}.s^{-1}$ for CdTe by just considering the volume effect. Finally, it is worth noting that no evidence has been found of a specific noise in the studied photon energy range which could be ascribed to the very large n-γ capture cross section of thermal neutrons by cadmium, even for pure D_2 discharge without fast electron bremsstrahlung. This confirms that the "slow" neutron population, whose energy is less than 0.5 eV, is much lower than the "fast" one [8].

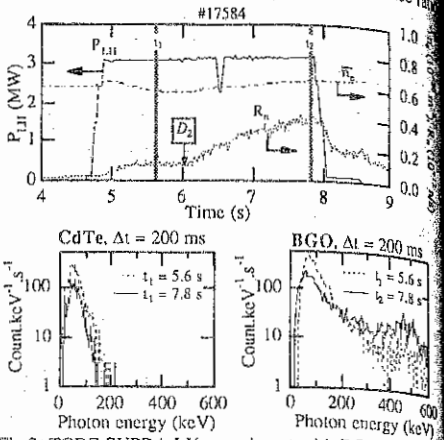


Fig.2. TORE SUPRA LH experiment with BGO and CdTe

3. Instrumental configuration and profile reconstruction

The HXR tomographic system is made of two different pine-hole cameras, with 21 and 38 detectors for the horizontal and vertical one respectively (Fig.3). For each chord, a coarse spectrometry is carried out with 8 energy channels. Geometrical characteristics of each camera are very similar in view to reduce as much as possible large artificial differences between signal levels. In particular, distances between collimating apertures and supports of detectors are the same for both cameras and equal to 50 cm. For similar reasons, arrays of detectors are placed on a ring shaped support which avoid large variations of the geometrical extend from chord to chord, because of the rather small detector-aperture distances. A wide domain of the plasma is scanned wich ranges from $(R+R_0)/a \approx -0.88$ to $(R+R_0)/a \approx +0.79$. All detectors are shielded against n/γ noise by a 2 cm thick lead box.

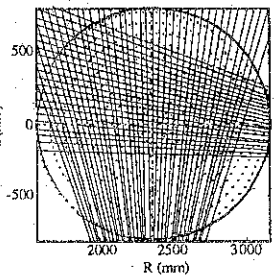
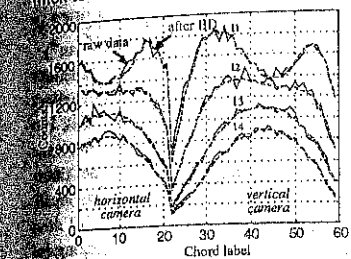


Fig.3 HXR tomographic system



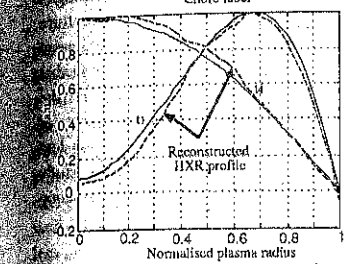


Fig.4 Simulated profile reconstruction

The profile reconstruction technique used for data processing is based on standard procedures which have been carefully benchmarked with the former HXR camera installed on TORE SUPRA. Taking advantage of the large redundancy of signals, raw data are first filtered using the well known biorthogonal decomposition (BD) method [9]. It is therefore possible to estimate consistently from time and space evolutions all averaged signal levels and corresponding error bars according to the Poisson statistic. Local profile of the HXR emissivity are then determined from processed line integrated data using linear regularisation or maximum entropy inversion techniques. To illustrate the profile reconstruction capability of the new tomographic system, a simulation of a diffusive relaxation as a function of time of an initial hollow emission profile has been considered. Simulated raw line-integrated data, and data processed using the BD method are reported for all chords at different times in Fig. 4. The local emissivity is then determined by an Abel inversion based on a second order linear regularisation for two different values of the time. From Fig. 4, it is shown that accurate profile reconstruction may be obtained, either for peaked or hollow profiles. It is interesting to notice that in the case of an hollow profile, the level of the local HXR emissivity in the core of the plasma is fairly well reproduced.

References

[1] L.Laurent, Int. Work. on "Tokamak Concept Improvement", Varenna, Italy, (1994).
[2] D.Moreau, Ibid.
[3] J.P.Bizarro, et al., Phys. Fluids B 5 (1993) 3276.
[4] G.Knoll, Radiation Detection and Measurement, 2nd Edition (John Wiley & Sons, 1989).
[5] Y.Peysson, Plasma Phys. Control. Fusion 35 (1993) 253.
[6] Y.Peysson and R.Arslanbekov to be published in Nucl. Instr. and Methods.
[7] M.A. Lone et al., Atomic Data and Nucl. Data Tables, 26 (1981) 511.
[8] P.Joyer, G.Martin, Reactor Dosimetry ASTM STP (1994) 1228.
[9] T.Dudok de Wit, et al., Phys. Plasmas 1 (1994) 3288.

PHOTON RECYCLING THOMSON SCATTERING DIAGNOSTICS FOR PRECISE MEASUREMENTS OF ELECTRON TEMPERATURE EVOLUTION AT FAST TRANSIENT PROCESSES IN PLASMA OF FT-2 TOKAMAK

M.Yu.Kantor, D.V.Kouprienko, S.I.Lashkul, V.M.Zavadsky.
Ioffe Physical-Technical Institute, RAS, Saint-Petersburg, Russia

ABSTRACT

New approach to high precision Thomson scattering diagnostics based on the laser multipass and intraresonator plasma probing is presented in the work. The approach is tested with TS system developed for FT-2 tokamak. The system provides laser probing energy to be increased up to 1600 J and ensures the laser to operate at multipulse mode with repetition rate up to 10-15 kHz. This is particularly attractive for the investigation of fast transient processes in low dense plasmas.

1. INTRODUCTION

Thomson scattering has proved to be a direct and reliable method for the local measurements of plasma electron temperature under dense plasma conditions ($n_e > 10^{13}$ cm^{-3}). There are well-developed approaches that provide a wide range of diagnostic capabilities including multiple temperature measurements during a single plasma discharge. Such approaches appear to be much less effective under low dense plasma conditions because of the lack of scattered photon flux. Higher rate of plasma transient processes at low dense plasma presents additional difficulties for the measurements of temperature evolution. At the same time alternative diagnostics (SXR and ECE, for instance) do not provide reliable information on local electron temperature at low density and auxiliary heated non-maxwellian plasma.

From this point of view the significant increase of the accuracy of Thomson scattering is of importance in the study of low dense plasma. Of special interest are multiple temperature measurements with high repetition rate of laser pulses. In recent years a number of efforts were made in this field of research [1-4]. The work presents new approach to Thomson scattering that ensures a substantial progress in these directions. The approach was used as the basis for the diagnostic system developed for FT-2 tokamak. The system allows the precise measurements of electron temperature evolution at plasma density from 10^{12} cm^{-3} with temporal resolution less then 0.1 ms. The detailed data on the electron temperature evolution are necessary for the study of the transition to plasma improved confinement and the mechanism of plasma-wave interaction under LH heating and CD in FT-2 tokamak..

2. NEW APPROACH TO LASER PROBING

The new approach to Thomson scattering is based on multipass and intraresonator plasma probing [1,2]. Multipass plasma probing is performed by means of optical system consisting of two spherical mirrors with vacuum vessel of plasma machine placed between them. The multipass system forces the laser beam to traverse many times the plasma volume and ensures the beam to come back to laser rod. Then amplified laser beam comes again to plasma probing. So, the laser rod and plasma volume are placed inside common resonator cavity several dozen meters in length. Photon recycling inside the resonator is considered as intraresonator laser probing if round-loop light losses are compensated by light amplification.

Multipass and intraresonator probing change considerably the laser operation mode and require to revise the laser probing scheme. Instead of normally used multistage laser (oscillator

multiamplifiers) a single rod appears to be the most efficient in this case. Effective conversion of stored inversion into the laser radiation is provided by low light losses.

This offers considerable scope for the development of probing laser. We realized this advantage to get the multipulse laser operation. To provide the most rapid pulsing the laser is forced to yield a number of pulses during a single flash lamp discharge. For these purposes Q-switch of the laser is performed with a saturable absorber placed in the resonator cavity.

The layout of the laser system is shown in fig. 1. The main components of the system are laser rod (2), saturable absorber (3) and elongated resonator cavity formed by rear mirror (1) and multipass system. There are low reflectance glass plates installed near the absorber to form auxiliary resonator cavity. This cavity provides fine laser operation tuning. In the case of low light losses the plates may be replaced from the system, if necessary. High light losses result in the increase of pumping threshold, disturb the laser operation mode and make it to be unreproducible. Under these conditions the plates get to be of considerable importance. The auxiliary resonator cavity facilitates the start of laser pulse and ensures a stable laser oscillation.

3. EXPERIMENTAL RESULTS

The new approach was realized in Thomson scattering of FT-2 tokamak. A ruby rod 240 mm in length, 21 mm in diameter and 0.012% Cr_2O_3 dopant concentration has been used in the system. The beam diameter was limited down to 16 mm by a diaphragm aperture placed near the rod. The multipass system consists of two spherical mirrors of 1000 mm in curvature radii spaced at 2 meters from each other. The circulating beams form a fan region between the mirrors with caustic at plasma center. About 80% of input laser energy come back to the ruby rod after 30 passes providing the probing energy to be 27 times as greater as laser output. Color glass with CdSe centers was used as saturable absorber for laser Q-switching. To ensure prolonged laser oscillation the flash lamp discharge was extended up to 2 ms.

Fig. 2 and 3 present a laser oscillations with 70% and 55% absorbers. Pulse energy and power is related to the probing volume. The total probing energy in plasma exceeds 1500 J. The probing power is about 100 MW that is typical for Thomson scattering. Thus, laser pulse is about 1 μs in duration. The oscillation is controlled with laser pumping, saturable absorber and glass plates, if any. The oscillation parameters of interest are pulse probing energy and peak power, the number of pulses in a train and temporal interval between them. The number of pulses and pulse energy rises with laser pumping. This results in linear increase of total probing energy with stored pump energy. Laser operation is high sensitive to absorber transmission as well. The higher the absorber transmission the more the number of laser pulses in train but the less the pulse power. The experimental data presented in fig. 4 and 5 demonstrate that the laser system is good controlled with pumping voltage and absorber transmission in a wide range of parameters.

The ruby rod used in our experiments does not suffer high enough light load. We had to keep laser beam intensity at ruby no more than 5 MW/cm^2 while capacitor bank allowed to increase laser pumping much more. The system supplied with ruby of higher quality could provide considerably more probing energy and power even as compared with attained parameters.

4. SCATTERED LIGHT COLLECTION AND DATA ACQUISITION

The cross-section of irradiated volume ranges from 2*12 mm at plasma center to 3*18 mm at plasma edge. The spatial resolution of the measurements is determined by the height of

observed plasma volume that was chosen to be 1 cm. Scattered light is collected from a
spatial point within 0.01 ster solid angle by f/2.4 objective of 260 mm focus length. Temper
spatial profile is measured by shifting spectrometer along the probing beam axis shot by
The light is spectrally resolved by f/4.8 spectrometer of 15 A/mm reciprocal dispersion
distributed among 12 spectral channels with a set of lightguides. The spectral width of
channel is 45 A. Overall light transmission of the collection system is 25%. Scattered signa
measured by means of eight photomultipliers with multialkai photocatodes of 2% quan
efficiency. The dynamic range of temperature measurements ranges from 50 eV to 1 keV.

Each photomultiplier is followed by amplifier and integrator gated by two sequ
pulses of equal duration. Scattered and background signals are integrated within first
Second gate picks up background light only. Gate duration is 3 μs and corresponds to
pulse duration at zero level. Time interval between the end of first gate and start of next on
taken to be 0.2 μs. Test measurements show that subtruction of plasma background
integrated within neighboring gates is performed with accuracy determined by photoelec
statistics. Thus, scattered signal and plasma background are evaluated correctly.

Digitizing time of the signal must be less then 60 μs to ensure time resolved temper
measurements. To provide rapid digital conversion our data acquisition system is based on 10
successive approximation ADCs of 1 μs digitizing time. The ADCs are trice triggered at
laser pulse. First triggering is performed just before laser pulse to measure a noise. The o
ones are performed just after first and second gates. All the signals are written in ADC bu
memory and readout in PC after each laser oscillation. Thus, the digitizing cycle is about 8
that is much less then laser repetition rate.

5. EXPECTED ACCURACY OF TEMPERATURE MEASUREMENTS

The accuracy of temperature measurements is determined by both the number
collected scattered photons and the number of plasma background photons. Taking into acco
overall light losses the expected number of collected scattered photons within scattered spectr
at 10^{13} cm^{-3} plasma density and 75 J laser pulse is about $5*10^5$. High laser probing power rema
the ratio between scattered and background light to be typical for Thomson scattering. T
means that the accuracy of temperature measurements is mainly determined by photoelectr
statistics. Under these conditions used photomultipliers of 2% quantum efficiency allow
expect 3% error of temperature measurements at a single laser pulse and 10^{13} cm^{-3} plas
density.

Thus, the diagnostic system provides the measurements of electron temperat
evolution with better than 10% accuracy at plasma density upper 10^{12} cm^{-3}. Under steady-st
plasma conditions scattered signals may be stored over all laser oscillation train. This rai
additionally the sensitivity of the diagnostics more than ten-fold and ensures 10% accuracy
temperature measurements in plasma of 10^{11} cm^{-3} density.

REFERENCES

1. T.Yu. Akatova, D.G.Bulyginsky *et al*: Proc. of the 17th Conf. on Contr. Fusion and Plasma Heating,
Amsterdam, 1990, v. IV, p. 1684.
2. M.Yu.Kantor, G.T.Razdobarin, 6th Intern. Sympos. on Laser Aided Plasma Diagnostics, Bar Harbor,
USA, , 1993, p. 267.
3. R.E.Stockdale, T.N.Calstrom *et al*, Rev. Sci. Instrum., v. 66, 1, p. 490, 1995.
4. C.J.Barth, C.C.Chu, A.J.H.Donne, Rev. Sci. Instrum., v. 66, 1, p. 501, 1995.

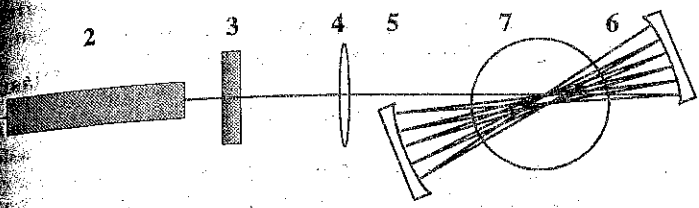


Fig.1. Layout of laser probing system
1 - rear mirror, 2 - ruby rod, 3 - saturable absorber, 4 - focusing lens
5, 6 - spherical mirrors, 7 - plasma volume

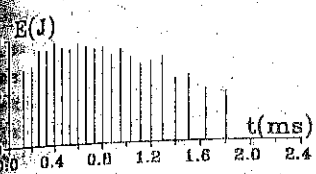


Fig.2 Laser oscillation with 70% absorber.
N_{pulse}=21, E_{total}=1625 J, E_{pulse}=77 J, P_{pulse}=50 MW, $T_{interval}$=70 μs, T_{train}=1.7 ms

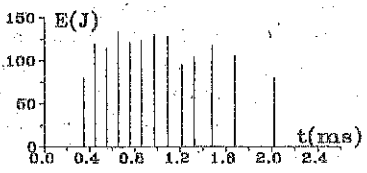


Fig.3 Laser oscillation with 55% absorber.
N_{pulse}=13, E_{total}=1500 J, E_{pulse}=117 J, P_{pulse}=115 MW, $T_{interval}$=110 μs, T_{train}=1.7 ms

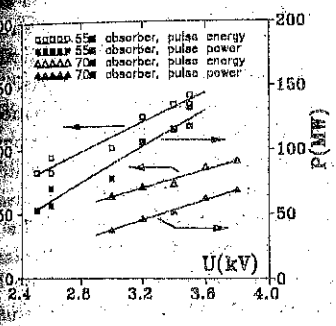


Fig.4. Pulse energy and pulse power versus pumping voltage.

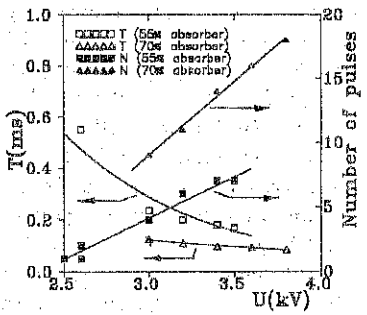


Fig.5. Time interval and number of pulses versus pumping voltage.

Electromagnetic Wave Scattering from Turbulent Density Fluctuations in Fusion Plasma

P. Sosenko*, A. Sitenko* and D. Grésillon**

* International Centre of Physics & M.M. Boholiubov Institute for Theoretical Physics, 252130, Kyiv, Ukraina;
** LPMI, École Polytechnique, Palaiseau F 91128, France

1. Introduction.

Electromagnetic wave scattering is routinely and successfully used for diagnosing both fusion and space plasmas, in particular thermal plasmas [1, 2]. However experiments (for instance tokamak microwave and infrared scattering, or radar backscattering in ionosphere and magnetosphere) reveal frequently non-thermal and low-frequency features in plasma fluctuations [3]. This means that real plasmas can be in turbulent states, possibly with fluid-like random motion. Such a motion, associated with large-scale and low-frequency electromagnetic fields, can be produced by internal non-equilibrium factors or by external sources. Thus, the spectrum of electromagnetic wave scattering is of considerable value for measuring turbulent plasma properties in a non-perturbative way [3, 4]. It is especially worth interpreting the "collective scattering" signal since it might directly show the plasma diffusion and loss of confinement across the magnetic field.

This report studies the electromagnetic wave scattering from density fluctuations in the magnetized plasma, which arise in turbulent plasma convection across the magnetic field. The stationary spectrum of density fluctuations in a strongly turbulent plasma state is calculated by means of the renormalized statistical approach [4, 5], and related to the spectrum of the fluctuations of the convective-cell type electric field in the plasma. The spectral shape in frequency is governed by the anomalous diffusion coefficient. Therefore, the latter can be deduced from the "collective scattering" signal. The anomalous diffusion coefficient is calculated in a self-consistent way, unlike in the model [3, 4], from the turbulent convective-cell spectrum. Conditions for the spectral shape to be Loretzian or Gaussian are analyzed. The anisotropy of the spectral intensity is determined. The spectral intensity is found to be $\langle(\delta n)^2\rangle_k/\bar{n}^2 \sim 1/L_n^2 k^4$, which corresponds to the mixing length level for the integral intensity. (Here $\bar{n}$ is the mean plasma density, δn is the fluctuation of the electron density, L_n is the characteristic length scale of plasma inhomogeneity across the magnetic field).

2. Fluctuation Spectral Distributions.

We start from the continuity equation for electrons in a macroscopically agitated plasma,

$$\partial_t n + \vec{\nabla} \cdot (n\vec{V}) = 0 \ , \tag{1}$$

with a turbulent velocity field $\vec{V}$. Such a fluid-like motion is associated with anomalous plasma transport across the magnetic field $\vec{B} \equiv B\vec{h}$, $\vec{V} \approx \vec{V}_\perp$. The electron density n is represented as a sum of a statistical mean value $\bar{n} \equiv \langle n \rangle$ and a fluctuation δn. One can distinguish the case of strong density fluctuations, $\delta n \sim \bar{n}$, and the case of weak density fluctuations, $\mid \delta n/\bar{n} \mid << 1$. Let us analyze the latter taking account of nonlinear effects, which can be important for small-scale fluctuations, $\vec{\nabla}\delta n \sim \vec{\nabla}\bar{n}$, and for weakly compressible velocity fluctuations, $\delta n\vec{\nabla}\cdot\delta\vec{V} \sim \lambda\delta\vec{V}\cdot\vec{\nabla}\delta n$, with $\lambda << 1$. From (1):

$$(\partial_t + \delta\vec{V}\cdot\vec{\nabla})\delta n + \vec{\nabla}\cdot(\delta n\langle\vec{V}\rangle) = -\delta\vec{V}\cdot\vec{\nabla}\bar{n} + \langle\delta\vec{V}\cdot\vec{\nabla}\delta n\rangle \ . \tag{2}$$

The interest is in the density fluctuations induced by the velocity fluctuations in the presence of equilibrium density gradients, $\vec{\nabla}\bar{n} \neq 0$: $\delta n \equiv \delta\tilde{n} + \delta n_{ind} \approx \delta n_{ind}$, where passive density fluctuations $\delta\tilde{n}$ convected by the turbulent velocity field are disregarded. The induced fluctuations are found by means of the (retarded) Green function $w(\vec{r},t;\vec{r}',t')$ ($w = 0$, when $t < t'$):

$$\partial_t w + \vec{\nabla}\cdot(w\vec{V}) = \delta(t-t')\,\delta(\vec{r}-\vec{r}') \ , \tag{3}$$

$$\delta n = -\int d\vec{r}'dt' w(\vec{r},t;\vec{r}',t')\delta\vec{V}(\vec{r}',t')\cdot\vec{\nabla}'\bar{n}(\vec{r}',t') \ . \tag{4}$$

The system is assumed to be weakly non-stationary and non-uniform: $\bar{n}(\vec{r},t) \approx \bar{n}(\vec{r})$, $\langle w(\vec{r},t;\vec{r}',t')\rangle \approx W_F(\vec{r}-\vec{r}',t-t')$, $\langle\delta\vec{V}(\vec{r},t)\delta\vec{V}(\vec{r}',t')\rangle \approx \langle\delta\vec{V}\delta\vec{V}\rangle_{\vec{r}-\vec{r}',t-t'}$, then for small-scale fluctuations $\langle\delta n(\vec{r},t)\delta n(\vec{r}',t')\rangle \approx \langle(\delta n)^2\rangle_{\vec{r}-\vec{r}',t-t'}$ with fixed density gradient.

The spectral distribution $\langle(\delta n)^2\rangle_K$, $K \equiv (\vec{k},\omega)$, of the electron density fluctuations (which is the space-time Fourier transform of $\langle(\delta n)^2\rangle_{\vec{r},t}$) is related to the spectrum $W_F(K)$ of the Green function and to the spectral distribution $\langle\delta\vec{V}\delta\vec{V}\rangle_K$ of the velocity fluctuations by means of (4). This is achieved by neglecting the fluctuations of the Green function (which also corresponds to the independence approximation [6]):

$$\langle(\delta n)^2\rangle_K = \mid W_F(K)\mid^2 \langle(\delta\vec{V}\cdot\vec{\nabla}\bar{n})^2\rangle_K \ . \tag{5}$$

The spectrum of density fluctuations differs from the spectrum of velocity fluctuations and it can be both broader and narrower than the latter depending on the spectrum of the Green function. In the case of convective-cell turbulence [5], associated with fluctuating potential electric fields $\vec{E} = -\vec{\nabla}\Phi$, $\vec{V} = c\vec{h}\times\vec{\nabla}\Phi/B$ is the electric drift velocity:

$$\langle(\delta n)^2\rangle_K = \mid W_F(K)\mid^2 \langle(\delta\vec{V})^2\rangle_K(\vec{h}\times\vec{k}\cdot\vec{\nabla}\bar{n}/k_\perp)^2 \ . \tag{6}$$

This spectrum has an anisotropic dependence on the wavevector even for an isotropic spectrum of the electric field fluctuations.

3. Green Function Spectrum.

The Green function is related to the probability density $P(\vec{r},t;\vec{r}',t')$ for a te particle transition from a space point $\vec{r}'$ where it is a a time instant t' to anot point $\vec{r}$ during the time $t-t'$:

$$w(\vec{r},t;\vec{r}',t') = \vartheta(t-t')\ P(\vec{r},t;\vec{r}',t')\ ,$$

where $\vartheta(t)$ is the Heavyside step function, and P satisfies the continuity equati $\partial_t P + \vec{\nabla}\cdot(P\vec{V}) = 0$, with the initial condition $P = \delta(\vec{r}-\vec{r}')$. In the approximati of the unbounded plasma, P can be represented as an orbit delta-function,

$$P = \delta(\vec{r}-\vec{R}_F(t))\ ,\quad \frac{d\vec{R}_F}{dt} = \vec{V}(\vec{R}_F,t)\ ,\quad \vec{R}_F(t') = \vec{r}'\ ,$$

where $\vec{R}_F(t)$ is a trajectory of a test particle. Plasma agitation is associated wi fluid-like flows across the magnetic field, characterized by a random displacem $\vec{R}_F$.

In the case of a weakly non-stationary and non-uniform system,

$$\langle P\rangle \approx P_F(\vec{r}-\vec{r}',t-t')\ ,\quad W_F(\vec{r},t) = \vartheta(t)\ P_F(\vec{r},t)\ .$$

The space Fourier transform $S_F(\vec{k},t)$ of $P_F(\vec{r},t)$ is the characteristic function turbulent motion:

$$S_F(\vec{k},t)\ =\ \langle e^{-i\vec{k}\cdot\vec{R}_F}\rangle\ ,\quad S_F(K) = \int dt e^{i\omega t}\langle e^{-i\vec{k}\cdot\vec{R}_F(t)}\rangle\ .$$

Its spectrum $S_F(K)$ determines the Green function spectrum:

$$W_F(K) = \frac{i}{2\pi}\int d\omega' \frac{S_F(\vec{k},\omega')}{\omega-\omega'+i0}\ .$$

The shape of the characteristic function spectrum can be Gaussian or Lorentzia depending on a turbulence correlation length [3] and statistics of a turbulent veloci field.

4. Convective-Cell Turbulence.

In this case the frequency dependence of $\langle(\delta\vec{V})^2\rangle_K$ and $S_F(K)$ can be taken i the form of a Lorentzian profile [5] with decorrelation rates $\gamma_{N\vec{k}}$ and $\gamma_{F\vec{k}}$ respectivel Then (6) integrated over the frequency yields the spectral intensity of fluctuations

$$\langle(\delta n)^2\rangle_{\vec{k}}\ =\ (\vec{h}\times\vec{k}\cdot\vec{\nabla}\bar{n}/k_\perp)^2\frac{\langle(\delta\vec{V})^2\rangle_{\vec{k}}}{\gamma_{F\vec{k}}(\gamma_{F\vec{k}}+\gamma_{N\vec{k}})}\ ,$$

with $\langle(\delta\vec{V})^2\rangle_{\vec{k}}$ the spectral intensity of the velocity fluctuations. When one can mea sure the spectral distributions for the density and velocity fluctuations by differen experimental methods, (6) and (10) can be used to check theoretical models for th transition probability and decorrelation rates.

Let us consider the situation of inverse energy cascade in the convective-cell turbulence [5], with

$$\langle(\delta\vec{V})^2\rangle_{\vec{k}} \sim k^{l_V} \ , \quad \gamma_{F\vec{k}} \sim \gamma_{N\vec{k}} \sim k^{l_F} \ , \tag{11}$$

$$l_V = 2l_F - 4 \ . \tag{12}$$

The latter equation takes into account the assumtion that large convective cells carry smaller convective cells without distorting them. Then from (10),

$$\langle(\delta n)^2\rangle_{\vec{k}} \ = \ C(\vec{h}\times\vec{k}\cdot\vec{\nabla}\bar{n}/k)^2 \ k^{-4} \ , \tag{13}$$

where C is a numerical constant. That is $\langle(\delta n)^2\rangle_{\vec{k}} \sim k^{-4}$, which corresponds to experimental observations. The spectral intensity (13) is independent of the magnetic field and energy input rate.

One can average (13) over the angle to get

$$\langle(\delta n)^2\rangle_k \ = \ \frac{C\bar{n}^2}{2L_n^2k^4} \ \rightarrow \ \langle(\frac{\delta n}{\bar{n}})^2\rangle \ = \ \frac{\pi C}{2L_n^2k_{min}^2} \ . \tag{14}$$

Here $L_n \equiv 1/\mid\vec{\nabla}\bar{n}\mid$ is a characteristic scale of density inhomogeneity, k_{min} is a characteristic value of k from the energy containing range. Equation (14) justifies the mixing-length estimate.

The decorrelation rate $\gamma_{N\vec{k}}$ can be related to the anomalous diffusion coefficient D [6], $\gamma_{Nk_{min}}/k_{min}^2 \sim D$. Therefore, the spectrum width is governed by the anomalous diffusion coefficient, $\gamma_{N\vec{k}} \sim Dk^2(k_{min}/k)^{4/3}$, and the latter can be deduced from the scattering signal.

References

[1] I. Hutchinson, *Principles of Plasma Diagnostics*, Cambridge Univ. Press, Cambridge etc. (1987).

[2] A. Sitenko, *Electromagnetic Fluctuations in Plasmas*, Academic Press, New York London (1967).

[3] D. Grésillon, B. Cabrit, J.P. Villain, C. Hanuise et al. Collective Scattering of Electromagnetic Waves and Cross-B Plasma Diffusion. Plasma Phys. Contr. Fusion 1992. 34(13) 1985-1991.

[4] P.P. Sosenko, D. Grésillon. Collective Scattering from Plasmas: Effects of Particle and Fluid Motions. In *Proc. 20th EPS Conf. on Contr. Fusion and Plasma Phys. (26-30 July 1993, Lisboa, Portugal), Contr. Papers*, 17C(III), 1239.

[5] A. Sitenko, P. Sosenko. The Renormalized Theory of Nonlinear Fluctuations and Plasma Turbulence. In *Proc. 1984 Int. Conf. on Plasma Phys. (Lausanne, Switzerland), Invited Papers*/Ed. by M.Q. Tran, and R.J. Verbeek (CRPP, Ecole Polytechnique Federale de Lausanne, 1984), 2, 921.
A.G. Sitenko, P.P. Sosenko. Kinetic Description of Convective Excitations in a Plasma. Sov. J. Plasma Phys. 1985. 11(8) 557-560.

[6] J. Weinstock. Lagrangian-Eulerian Relation and the Independence Approximation. Phys. Fluids. 1976. 19(11) 1702-1711; Analytical Approximations in the Theory of Turbulent Diffusion. Phys. Fluids. 1978. 21(6) 887-890.

PROPAGATION OF THE MICROWAVE BEAMS IN MAGNETIZED INHOMOGENEOUS PLASMAS

D.L.Grekov

Institute of Plasma Physics,
National Science Center "Kharkov Institute of Physics and Technology",
310108, Kharkov, Ukraine

Previously the propagation of the microwave beams in vacuum have been carried o intensively in connection with the problems of the transmission lines, the resonators and laser beams [1].

At the moment the microwave beams are widely used as for diagnostics (reflectom and interferometry), and for RF plasma heating. The propagation of microwaves in plasma usually analyzed with application of the ray tracing technique.

The main objects of the paper presented are

-analytical study of peculiarities of RF frequency band (10-200 GHz) microwave bea propagation in magnetized inhomogeneous plasma;

-elucidation of influence of a low density scrape-off layer plasma on distribution antenna-emitted fields in ITER-scale devices and construction of starting conditions for r tracing.

Let introduce the Cartesian coordinate system (X,Y,Z) : $OZ \parallel \nabla n_e$, $OX \parallel \vec{B}$ (n_e - electr density, $\vec{B}$ - confining magnetic field). The OX axis is the main direction of the bea propagation. Antenna is located in the YZ plane. For the ordinary wave $E_x >> E_y, E_z$ and f the extraordinary wave $E_y >> E_z >> E_x$. Taking into account $\frac{\partial E_i}{\partial z} >> \frac{\partial E_i}{\partial x}, \frac{\partial E_i}{\partial y}$ we obta from the Maxwell equation for the ordinary (o-) wave $(E_x \equiv E_o)$

$$\frac{\partial^2 E_o}{\partial z^2} + \frac{\omega^2}{c^2}\varepsilon_3 E_o + \frac{\partial^2 E_o}{\partial y^2} + \varepsilon_3 \frac{\partial^2 E_o}{\partial x^2} = 0 \qquad (1)$$

and for extraordinary (e-) wave $\left(E_y \equiv E_e\right)$

$$\frac{\partial^2 E_e}{\partial z^2} + \frac{\omega^2}{c^2}\frac{\varepsilon_1^2 - \varepsilon_2^2}{\varepsilon_1} E_e + \frac{\partial^2 E_e}{\partial y^2} + \left(1 + \frac{\varepsilon_2^2}{\varepsilon_1^2}\right)\frac{\partial^2 E_e}{\partial x^2} = 0, \qquad (2)$$

where

$$\varepsilon_1 = 1 - \frac{\omega_p^2}{\omega^2 - \omega_c^2}, \quad \varepsilon_2 = \frac{\omega_c}{\omega}\frac{\omega_p^2}{\omega^2 - \omega_c^2}, \quad \varepsilon_3 = 1 - \frac{\omega_p^2}{\omega^2}.$$

The solutions of the Eqs. (1,2) are obtained using the parabolic approximation [2]. They are written as $(\alpha = o, e)$

$$E_\alpha(x,y,z) = -\frac{iA_\alpha}{2\pi}\sqrt{\frac{c}{\omega k_\alpha(z)}}\left[\psi_{1\alpha}(z)\psi_{2\alpha}(z)\right]^{-1/2} exp\left[i\int_0^z k_\alpha(z)dz\right]\times$$

$$\int\int E(\xi,\eta)\, exp\left\{\frac{i}{2}\left[\frac{(y-\xi)^2}{\psi_{2\alpha}(z)} + \frac{(x-\eta)^2}{\psi_{1\alpha}(z)}\right]\right\} d\xi d\eta. \qquad (3)$$

Here

$$k_o(z) = \frac{\omega}{c}\varepsilon_3^{1/2}(z), \qquad k_e(z) = \frac{\omega}{c}\left[\frac{\varepsilon_1^2(z) - \varepsilon_2^2(z)}{\varepsilon_1(z)}\right]^{1/2},$$

$$\psi_{1o}(z) = \frac{c^2}{\omega^2}\int_0^z k_o(z')dz', \qquad \psi_{2o}(z) = \int_0^z dz' / k_o(z'),$$

$$\psi_{1e}(z) = \int_0^z \frac{\varepsilon_1^2(z') + \varepsilon_2^2(z')}{\varepsilon_1^2(z')}\frac{dz'}{k_e(z')}, \qquad \psi_{2e}(z) = \int_0^z \frac{dz'}{k_e(z')}.$$

At $n_e = 0$ the integrals (3) are expressed in the terms of the Fresnel function For vacuum we have $\psi_{1\alpha}(z) = \psi_{2\alpha}(z) = z\,c/\omega$, i.e. $z = \omega\psi_{1,2\alpha}/c$. The influence of the plasma can be characterized by the effective change of z, viz., for the X-axis z changes into $z_\parallel = \omega\psi_{1\alpha}(z)/c$, and for the Y-axis z transforms into $z_\perp = \omega\psi_{2\alpha}(z)/c$. As calculations show the presence of a scrape-off layer plasma has no effect on the e-wave field distribution. But for o-wave especially in the long wavelength part of the range this effect is noticeable. The o-wave amplitude distribution is not symmetrical relative to the toroidal direction. This deviation from symmetry is caused by the action of the low density plasma.

With the purpose of the more detailed analysis of the o-wave propagation let us search for the solution of the Eq. (1) in the form

$$E_o = \sqrt{\frac{c}{\omega k_o(z)}}\, exp\left[-i\int_0^z k_o(z')dz'\right] A(x,y,z)$$

Then for $A(x,y,z)$ we have

$$\frac{c^2 k_o^2(z)}{\omega^2}\frac{\partial^2 A}{\partial x^2}+\frac{\partial^2 A}{\partial y^2}-i2k_o(z)\frac{\partial A}{\partial z}=0 \qquad (4)$$

The solution of the diffusion equation (4) may be written as

$$A(x,y,z)=A_0 H_m\left(\frac{\sqrt{2}x}{w_{\parallel}(z)}\right)H_n\left(\frac{\sqrt{2}y}{w_{\perp}(z)}\right)exp\left\{-i\left[P(z)+k_o(z)\left(\frac{x^2}{2q_{\parallel}}+\frac{y^2}{2q_{\perp}}\right)\right]\right\} \qquad (5)$$

where $H_n(x)$ - Hermitian polynomials. Further we shall analyze the propagation of the princi mode - m = n = 0. By writing q_α as

$$\frac{1}{q_\alpha}=\frac{1}{R_\alpha(z)}-\frac{2i}{k_o(z)w_\alpha^2(z)},$$

where R_α - radiuses of curvature of wave front in the direction of X or Y, and w_α dimensions of a beam in these directions, we obtain

$$w_{\perp}(z)=w_{\perp 0}\left\{1+\left[\frac{2}{w_{\perp 0}^2}\int_0^z\frac{dz'}{k_o(z')}\right]^2\right\}^{1/2}, \qquad (6)$$

$$R_{\perp}(z)=k_o(z)\int_0^z\frac{dz'}{k_o(z')}\left\{1+\left[\frac{2}{w_{\perp 0}^2}\int_0^z\frac{dz'}{k_o(z')}\right]^{-2}\right\}, \qquad (7)$$

$$w_{\parallel}(z)=w_{\parallel 0}\left\{1+\left[\frac{2c^2}{\omega^2 w_{\parallel 0}^2}\int_0^z k_o(z')dz'\right]^2\right\}^{1/2}, \qquad (8)$$

$$R_{\parallel}(z)=\frac{c^2 k_o(z)}{\omega^2}\int_0^z k_o(z')dz'\left\{1+\left[\frac{2c^2}{\omega^2 w_{\parallel 0}^2}\int_0^z k_o(z')dz'\right]^{-2}\right\}, \qquad (9)$$

$$iP(z) = \frac{1}{2}\int_0^z \frac{1}{i\frac{w_{\perp 0}^2}{2} + \int_0^{z'} \frac{dz''}{k_o(z'')}} \frac{dz'}{k_o(z')} + \frac{1}{2}\int_0^z \frac{k_o(z')dz'}{\frac{i\omega^2 w_{\parallel 0}^2}{c^2} + \int_0^{z'} k_o(z'')dz''} \quad (10)$$

Separating in expression for $iP(z)$ real and imaginary part we get the deference in a phase and amplitude of a bounded microwave beam and plane wave

$$A(z, x=0, y=0) = A_0 \left\{1 + \frac{4}{w_{\perp 0}^4}\left[\int_0^z \frac{dz'}{k_o(z')}\right]^2\right\}^{-1/4} \left\{1 + \frac{4c^4}{\omega^4 w_{\parallel 0}^4}\left[\int_0^z k_o(z')dz'\right]^2\right\}^{-1/4} \times$$

$$\exp\left\{arctg\left[\frac{2}{w_{\perp 0}^2}\int_0^z \frac{dz'}{k_o(z')}\right] + arctg\left[\frac{2c^2}{\omega^2 w_{\parallel 0}^2}\int_0^z k_o(z')dz'\right]\right\} \quad (11)$$

Let us analyze the distinctions in a bounded wave beam propagation in vacuum and in plasma using Eqs. (6)-(9) in approximation of low density plasma ($\omega_p^2(z) << \omega^2$). From them it follows

- plasma results in narrowing, in comparison with vacuum, beam dimension in a direction parallel an external magnetic field and ones broadening in perpendicular to a magnetic field direction;
- penetrating into plasma curvature of beam phase front, in comparison with vacuum decreases; for a direction, parallel to magnetic field this effect is more pronounced in "far" zone ($D = \frac{2\lambda z}{w_{a0}^2} >> 1$), than in "near" ($D<<1$), and for perpendicular direction - vice versa;
- plasma presence results in the beam amplitude increase as compared to vacuum; this effect doesn't depend on the plasma density profile.

It is interesting to point out that plasma presence results in the ordinary and extraordinary wave astigmatism, the ordinary wave astigmatism doesn't depend on plasma gyrotropy value.

REFERENCES

1. H.Kogelnik , T.Li Applied Optics, 5, (1966) 1550.

2. V.A.Fock Electromagnetic Diffraction and Propagation Problems. Pergamon Press. New York (1965) 320.

THE SENSITIVITY OF ALGORITHM OF CHARGE EXCHANGE NEUTRALS SPECTRA ELABORATION TO VARIOUS PERTURBATIONS

Yu.N. Dnestrovskij, A.V. Khutoretsky
Institute of Nuclear Fusion, Russian Research Centre "Kurchatov Institute"
A.O. Verbitskij, A.P. Smirnov
Moscow State University, Moscow, Russia

1. Introduction

The algorithm for ion temperature determination by charge exchange neutrals spe... was described in [1]. To check its sensitivity to various perturbations, we carried out ... numerical experiments consisted of two steps. At the first step, referred as a "quasi experim... the particle flux outgoing from the plasma is calculated for some chosen temperature profi... and other plasma parameters. At the second step we try to find a temperature profile wh... results in a closest fit with the quasi experimental one.

2. The Numerical Experiment

The first step of the algorithm [1] consists of the model calculation of the particle flu... outgoing from the plasma. The ion temperature profile $T(x)$ is a parametrized unkno... function. The flux from the plasma seen by the analyzer (omitting the recombination) is

$$F = F(E) = \frac{2E}{m^2}\int \sigma_{cx}(E)N(x)f(x,E)\Psi dl \tag{1}$$

$$\Psi(M,E) = \exp\left[-\int\left(\sigma_{cx}(E)+\sigma_i(E)+\frac{<\sigma_e u>}{v_E}\right)ndl'\right] \tag{2}$$

$$f(x,E) = n(x)\pi^{-3/2}(2T(x)/m)^{-3/2}\exp(-E/T(x)) \tag{3}$$

where x is the dimensionless magnetic surface coordinate ($0 < x < 1$), a_s is the minor pla... radius, $N(x)$ is the density of the bulk wall neutrals, integrals are taken along the view chords.

We introduce the following discrepancy functional J as a measure of proximity of ... model and experimental spectra:

$$J = \sum_i \int_{E_{min}}^{E_{max}} dE\rho_i(E)\left(\frac{F_i^{exp} - A_i F_i}{F_i}\right)^2 \tag{4}$$

where F_i^{exp} and F_i are the experimental and computed spectra, A_i are constants to be found, ... index i numerates chords. For $T^{calc}(x)$ we assume

$$T(x) = T_0(1-x^{2\alpha})^{2\beta}/(1+Cx^2) \tag{5}$$

where T_0, α, β, C are free parameters to be found. The level lines of the functional J in the space of parameters (T_0, α, β, C) looks like the multidimensional ravines (curved elongated valleys). Therefore we developed a special method of minimization of the functional J.

The measurements of $F^{exp}(E)$ along the each chord are carried out in the energy range $E^i_{min}<E<E^i_{max}$. As a quasi experimental temperature profile, we take

$$T^{exp}(x) = (1\ \mathrm{keV})\,[2/3(1-x^{2\alpha_1})^{\sigma} + 1/3(1-x)^5] \qquad (6)$$

This profile with two inflation points is designated by stars in Figures.

The profiles of bulk cold neutrals are calculated by slightly corrected diffusive model [2]

$$N(x) = N_0 \exp(-l(x)); \quad l(x) = Da_s \int_x^1 \frac{ss_3}{v_i}\, dx' \qquad (7)$$

where $l(x)$ is an optical length, v_i is the ion thermal velocity, $s_3 = (<\sigma_i u>+<\sigma_{ex} u>)n$, $ss_3 = s_3(1+<\sigma_{ex} u>n$; $D=3$, if other is not stated.

The proximity of the $T^{exp}(x)$ and $T^{calc}(x)$ profiles can be described by the following two parameters

$$DT = (T^{calc}(0)-T^{exp}(0))/T^{exp}(0), \quad L_1 = \left(\int_0^1 |T^{exp}(x) - T^{calc}(x)|dx\right)\cdot\left(\int_0^1 T^{exp}(x)dx\right)^{-1} \qquad (8)$$

Similar parameters DT^* and L_1^* are obtained by replacing $T^{exp}(x)$ with $T^{im}(x)$, where $T^{im}(x)$ are the temperature profiles reconstructed with "wrong" bulk neutral density, but without a noise. The calculations were carried out for the circular plasma with $a_s = 0.4$ m, along five chords with shooting parameters $p_i = (0,\ 0.2,...0.8)a_s$; $E^i_{min} = 2T^i_{max}$, $E^i_{max} = 6T^i_{max}$, $\Delta E^i = 0.5T^i_{max}$ (totally 9 energies), where $T^i_{max} = T(p_i)$ is the maximal ion temperature on the i-th chord. For the density $(n_e = n)$ we take $n(x) = n(0)\cdot(0.8(1-x^2) + 0.2)$, where $n(0)$ is a varying parameter (in 10^{19} cm^{-3}).

3. The sensitivity of $T(x)$ reconstruction to the spectra perturbations

A small flux of particles in the high energy channels of the analyzer is a main source of errors. Its amplitude is proportional to the square root of the signal. To simulate it, we introduce an artificial error into spectra

$$\tilde{F}_i^{exp}(E) = F_i^{exp}(E) + \Delta\cdot\eta\cdot\left(F_i^{exp}(E^i) / F_i^{exp}(E^i_{max})\right)^{1/2} \qquad (9)$$

where Δ is the noise amplitude at the high energy tail, η is a random variable uniformly distributed in the range $-1<\eta<1$. Then the perturbed spectra are used as input data for restoring of the temperature profile. This restoring is repeated several (typically 5) times with various random additions to find out the statistical properties of restored $T(x)$ profiles. A bar above a

variable denotes the mean value, and σ denotes the standard deviation. Fig.1 and Table 1 that the accuracy of the reconstruction of $T(x)$ is quite reasonable in all variants.

4. The sensitivity to non-consistency of the bulk neutrals profiles

To calculate $F(E)$, we need in the spatial distribution of the bulk neutrals, but it well known. To check the sensitivity of the reconstruction, we introduce two parameters D_0= 3 and D_1, and two neutral densities according to (3), the former being used calculations of $F_i^{exp}(E)$ and F_i^{exp}, the latter for $F_i(E)$. The coefficient D_1 is varied difference in the bulk neutral densities is characterized by the parameter $\gamma=N^{calc}(0)/N^{exp}(0)$ results of calculations are shown in Fig. 2 and Table 2. One can see that the errors are mo even for large γ.

5. Conclusion

Reconstruction of the ion temperature profile from known charge exchange neu spectra relates to the ill posed problems. The used method of the regularization is based on supposition that the unknown function belongs to a some bounded class. The chosen class to be rather wide for good approximation of the expected functions, but have not to be wide to provide a good stability of reconstruction. The class (5) satisfies both requirem Even for the high plasma density $n(x)$ and considerable perturbations of neutrals spectra accuracy of $T(x)$ reconstruction remains admissible.

References

[1] Yu.N. Dnestrovskij, A.V. Melnikov, A.P. Smirnov, A.V. Khutoretsky. The algorithm for Ion Temperature Determination by Charge-exchange Neutral Spectra. Moscow, 1994, Kurchatov Institute preprint IAE-5780/6

[2] Yu.N. Dnestrovskij and D.P. Kostomarov. Mathematical Modeling of Plasmas. Springer, Berlin, 1986.

Table 1

Δ	δ_T %	$\sigma(T(0))$ %	δ_{T_i} %	δ_T %	$\sigma(T(0))$ %	δ_{T_i} %
	n(0)=2			n(0)=10		
0	2.9	-	1.4	1.3	-	1.2
25	3.4	1.7	1.7	0.4	2.8	2.5
50	4.9	3.2	2.9	2.2	4.7	3.7

Table 2

γ	δ_T %	δ_T^* %	$\sigma(T(0))$ %	δ_{T_i} %	$\delta_{T_i}^*$ %
1	7.8	4.2	3.3	4.5	3.4
5	-14.0	1.0	1.6	11.2	2.2

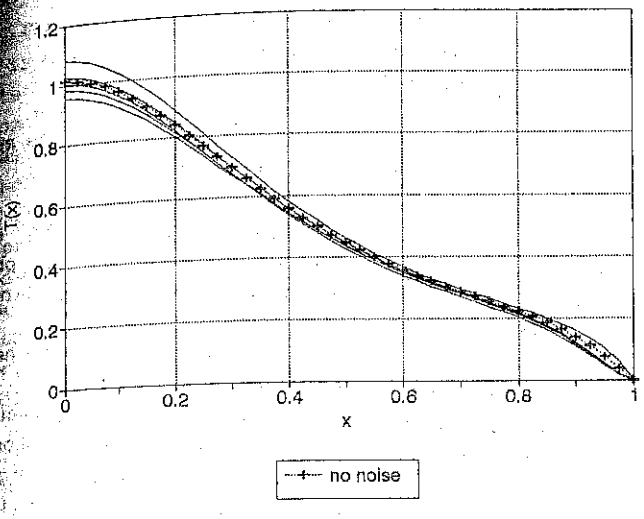


Fig. 1 . The restored T(x) profiles.
$n(0) = 10$, $\Delta = 0.5$, 5 realizations of "noise"

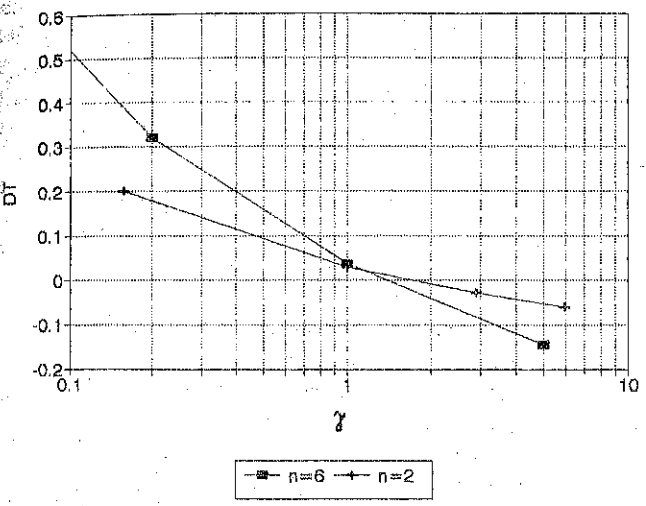


Fig. 2. The dependence *DT* versus γ.

X-Ray Spectroscopic Set Study for ITER

V.A.Bryzgunov, A.B.Gil'varg*

Kurchatov Institute RRC, Moscow, 123182 Russia

*Shubnikov Institute of Crystallography, Moscow, 117333 Russia

As known, the radial T_i-profiles are decided to be measured by x-ray techniques at ITER [1]. The precise measurement of the Doppler broadening in spectral lines of heavy impurities will require a high throughput of a spectrometer and an effective shielding against intense neutron and γ-ray radiation from the tokamak.

It is proposed to extract the plasma radiation through an extremely-norrow channel in the ITER shield and then, if possible, to separate the x-ray radiation from a foreign one with an additional mirror. The calculations have shown that a spectrometer with the spherically-bent quartz crystal and a concave graphite mirror will allow one to determine T_{i_o} by the measurement of x-ray Kr^{34+} line profile [2].

The spherically-bent crystal focusses the radiation at a sagittal plane (Fig.1). The focal length of the analyzing crystal depends on the Bragg angle, θ, being equal $f_s = R/2\sin\theta$, where R is a radius of a bend. In the diagram, according to the Johann geometry, $b = R\sin\theta$ and, as a result, the distance of a virtual entrance slit from the crystal is equal $a_s = -R\sin\theta/\cos2\theta$. The slit is $H_s = H_{det}a_s/b$ - high. It is evident that the x-rays have the least angular divergence at $\theta = 45^o$. The divergence of rays is determined by the detector height, H_{det}. When $H_{det} = 0$, the sagittal divergence is absent.

In the proposed optical scheme (Fig.2) the "mirror" and the "crystal" have the crossed dispersions. They are optically conjugated and form a focussing 2D-spectrometer. The resolving power of graphite is considerably worse than that of quartz. As a result, the graphite mirror will slightly modulate the intensity along a spectral line only.

From the geometrical consideration it follows that the optimal radius of a mirror is equal: $R_{Gr} \approx d_{Gr}/d \cdot R/\cos2\theta$, where d_{Gr} and d are interplanar spacings in graphite and in

For the spherically-bent crystal at $\theta < 45^\circ$ a concave mirror is needed, but at $\theta > 45^\circ$, a convex one. At $\theta = 45^\circ$, the graphite mirror should be flat. In these cases, the spectrometer uses the radiation reflected by the mirror with the least deviation from the Bragg angle, θ_{Gr}.

The optics, Fig.2, can be applied to the chord measurement with different impurities. When each detector is located in a focal plane of its own analyzing crystal, one flat mirror can be used (Fig.3). It is hard to satisfy the condition $b = f_s$ for a spherically-bent crystal because of restricted opportunities to select the required interplanar spacing. However, for conjugation with a flat mirror one can use a toroidally-bent crystal or an asymmetric spherically-bent one, where the diffraction planes form an angle α with the crystalline plate surface (See, Table I).

Table I. Geometrical parameters of focussing crystals

Crystal bend	Meridional radius	Sagittal radius	Sagittal focal length, f_s	b Johann geometry
Cylindrical	R	∞	∞	$R \sin\theta$
Spherical	R	R	$R/2\sin\theta$	$R \sin\theta$
Spherical asimmetric cut	R	R	$R/2\sin\theta\cos\alpha$	$R\sin(\theta+\alpha)$
Toroidal	R	R_s	$R_s/2\sin\theta$	$R \sin\theta$

The characteristics of some quartz crystals for different plasma impurities are given in Table II. The majority of the chosen atomic planes has already been used in spectral measurements at JET [3].

Table II. Two-fold bent crystals for the ITER spectrometer

Impurity	λ_w, Å	hkl	2d, Å	θ,(°)	R_s/R	α,(°)
Ar	3.949	110	4.9130	53.49	1.292	-13.68
Ti	2.611	103	3.3178	51.90	1.239	-11.4825
Cr	2.182	$20\bar{3}$	2.7496	52.52	1.260	-12.3541
Fe	1.851	$20\bar{3}$	2.7496	42.31	0.906	6.0121
Ni	1.588	$22\bar{3}$	2.0296	51.48	1.224	-10.8807
Cu	1.478	$22\bar{3}$	2.0296	46.74	1.061	- 3.2908
Kr	0.9454	$50\bar{2}$	1.624	35.60	0.878	-

The analytical consideration of the x-ray path from extended source has allowed us to calculate geometric aberrations in the spectrometer. For the toroidally-b crystal the tangential shift of a monochromatic ray is equal the arc of the Rowland circle:

$$\Delta s \approx \frac{h_{det}^2}{R\sin 2\theta} - \frac{l^2}{2R\,tg\theta} + \left(1 - \frac{R_s}{R}\right)\left(\frac{h^2}{2R}\,tg\theta - \frac{h^2 R_s/R - 2hh_{det}}{R\,\sin 2\theta}\right)$$

where l and h are the coordinates of the point, where the strikes the crystal, h_{det} is the height of the line respecti to the mid plane of the spectrometer. When $l = h = h_{det} = 0$ i.e. for the rays which are reflected at the crystal poi (central point) and pass in the mid plane of the spectrome the ray shift is $\Delta s = 0$.

For the spherically-bent crystal the shift is equal:

$$\Delta s \approx \frac{h_{det}^2\,tg\theta}{2R\sin^2(\theta+\alpha)} - \frac{l^2}{2R\,tg(\theta+\alpha)} - \frac{\sin\alpha\,\cos(\theta+\alpha)}{\sin^2(\theta+\alpha)\cos\theta}\left(\frac{h^2\cos^2(\theta+\alpha)}{2R} - \frac{hh_{det}}{R}\right)$$

Some numerical estimates have shown that the expecte Doppler broadening in the x-ray lines considerably exceeds th response broadening (See, also [2]).

There is an original glue-free technology for the two-fold bent crystal production [4]. A thin crystalline plate is pressed to a concave surface of the glass backing and retaine on it due to adhesion. At such a joint to the backing, no loca mechanical stresses emerge in the plate and initially-hig resolving power of a crystal is retained.

R E F E R E N C E S:

1. R.BARNSLEY, R.M.GIANNELLA, K.D.LAWSON, N.J.PEACOCK. Warenn Diagnostic Workshop, 1995.

2. V.A.BRYZGUNOV, A.B.GIL'VARG. ITER-IL-PH-07-0-54, July 1990 V.A.BRYZGUNOV, A.B.GIL'VARG, A.N.SVETCHKOPAL. Fizika Plazmy, 1994, **20**, 596. [Plasma Physics Reports, 1994, **20**, 536].

3. R.BARTIROMO, F.BOMBARDA, R.M.GIANNELLA at al. Rev. Sci Instrum., 1989, **60**, 237.

4. A.B.GIL'VARG. USSR Patent 570111. Izobretenia, promyshlennye obraztsy, tovarnye znaki, 1977, 31, 185. V.A.BRYZGUNOV, A.B.GIL'VARG, S.A.CHUVATIN. Fizika Plazmy, 1987, **13**, 242. [Sov. J. Plasma Physics, 1987, **13**, 137]

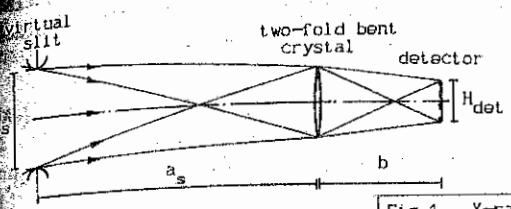


Fig.1. X-ray focussing with the two-fold bent crystal in the sagittal plane of the Johann spectrometer.

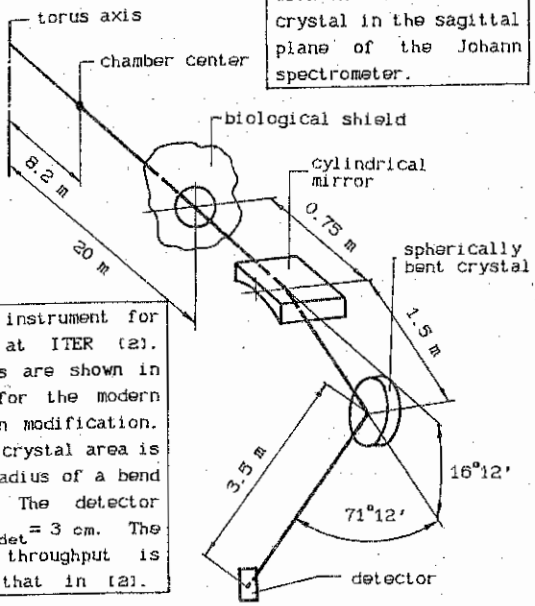
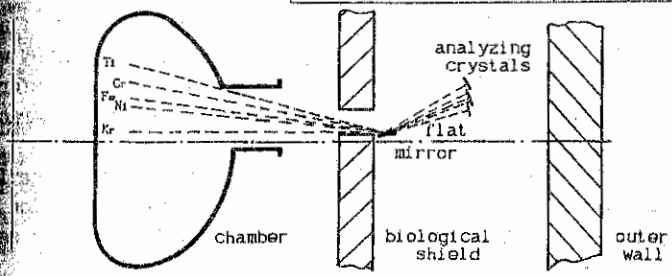


Fig.2. X-ray instrument for measurements at ITER [2]. The dimensions are shown in the drawing for the modern tokamak design modification. The analyzing crystal area is $6^2 \times 8$ cm^2, radius of a bend is R = 6 m. The detector height is H_{det} = 3 cm. The spectrometer throughput is the same as that in [2].

Fig.3. Schematic drawing of an X-ray compact instrument set with a common mirror at the ITER-midplane port.



EFFECT OF PLASMA, NEUTRON IRRADIATION AND HEATING ON THE CARBON GRAPHITES ELEMENTS OF MM AND SUB-MM DIAGNOSTIC FOR A FUSION PLASMA

V.L.Berezhnyj, V.V.Chebotarev, I.P.Fomin, V.L.Ocheretenko, A.I.Skibenko, V.S.Voitsenya
Institute of Plasma Physics, NSC KPTI, Kharkov, 310108, Ukrai

To measure main plasma parameters in ITER, several metho of diagnostics in MM and sub-MM wave ranges are being planne ECE, interferometry, polarimetry and reflectometry. Antenna wavequides and reflectors of these diagnostics can be expose directly by plasma streams, neutral and charged particles an wide spectrum of electromagnetic radiations. All these facto can result in change of the working properties of diagnosti elements as well as parameters of a plasma, as a result of flux of heavy impurities to the plasma volume. Earlier proposed diagnostic elements in MM and sub-MM wave range (antennas, wavequides, reflectors) made of carbon graphite mat rials (CGM) as an alternative to metal ones [1]. In this pape results are presented on the influence of plasma, neutron irra diation and heating on working characteristics of diagnosti elements from CGM.

Pulsed power plasma streams were generated by quasistatio nary plasma accelerator QSPA Kh-50 (the energy flux varied fr 1 to 15 MJ/m^2) and produced the conditions, that can be met b diagnostic components during the disruption instability. Plan reflectors of various types of graphites were subjected to pla sma stream impact and reflectivity at different frequencies wa measured. After exposure to plasma there was observed a smal enhancement of reflectivity of graphite plates. The reason o graphite plate reflectivity enhancement is the decrease of mi crorelief value. Exposure of graphite antenna by plasma flux showed the some increase of the emitted energy flux for MM wav range. At the same times the metallic one showed some deforma tion of antenna surface and the deterioration of its characte ristics.

The fluence of neutrons ~ $3\cdot10^{22}$ cm^{-2} is supposed for ITE therefore its value ~ $2\cdot10^{22}$ cm^{-2} was used for irradiation o the samples of CGM of GR-280, RGT-91 and UAM-91 type. The depe

dencies of thermal conductivity K, being one of main exploitation characteristic OGM, of RGT-91 and UAM-91 are presented on Fig.1. The fundamental results are that K very decrease after the irradiation by neutrons of the investigated samples. The thermal conductivity of nonirradiated samples decreases with the increase of the measurement temperature too. The thermal conductivity K increases for RGT-91 and UAM-91 with the irradiation temperature increase from 400 to 700°C of the same fluence of neutrons ~ $2 \cdot 10^{22}$ cm^{-2}, but remains significantly smaller then for nonirradiated samples. The radiotechnical characteristics of antennae, wavequides, mirrors depend on the electroconductivity σ and reflectivity of the matherials. The alteration of these characteristics, that depend from the irradiation conditions, is presented in Fig.2. The reflectivity coefficient was measured on λ=337 μm at an angle 45°. At the neutron fluence $2 \cdot 10^{22}$ cm^{-2} and T_{irr}=400°C the relative reflection coefficient decreased from initial value 90% to 82% at same fluence, but at T_{irr}=700°C it decreased up to 80%. At the irradiation by fast neutrons (E>0.2 MeV) at fluence $3.5 \cdot 10^{21}$ cm^{-2} coefficient R for GR-280 graphite decreased from initial value 81% to 78% at T_{irr}=700°C. For UAM-91 sample at F=$2 \cdot 10^{22}$ cm^{-2} value of R decreased from 77% to 68% at T_{irr}=400°C and to 66% at T_{irr}=700°C. In Fig.2 the electroconductivity is presented by dark points at the same conditions for direct current also. The measured value of σ is in accord one with the calculated from the measured coefficient of reflection.

For the elucidation of the heating influence on the radiotechnical characteristics of UHF diagnostic elements they were heated by the electric current to 1000°C in the vacuum vessel with pressure ~ 50-60 mtorr. The temperature was measured by pyrometer and termel. The temperature dependencies of travelling wave amplitude in circular graphite (type MPG) wavequide (diameter 6.2 mm, length 200 mm, thickness of walls 6 mm) were investigated for the frequencies 37, 52, 75 and 105 GHz. Heated graphite conic antenna (inner diameters 10 mm and 40 mm, external diameter 20 mm and 50 mm, length 150 mm) was explosed at frequencies 37 and 75 GHz, for which it had the directivity diagram width 9° and 4° respectively. The dependencies of heated graphite plates (40×110 mm) the reflectivities were examined at the incidence angle 9°, for frequency 75 GHz. Each element was

subjected to 15-20 heat-stroke but the surface quality deteri oration was not observed. The temperature dependencies of rela tive amplitudes of the waves travelling in wavequide, radiated by antenna and reflected by graphite plate are presented in Fig.3 for the frequency 75 GHz. The relative amplitudes for fre quencies 37.5, 55, 75 and 105 GHz at T=900°C are equal to 0.77, 0.83, 0.67 and 0.58 with respect to their values at T=20°C. The temperature dependencies of electroconductivity for different frequencies were measured at the same time. As σ is increasing with temperature the enhancement of amplitude could be expected. However the amplitude was decreasing with temperature. This is not connected with electroconductivity, but this effect can be explain of by the change of surrounding property in the wavequi ide, antenna space and near the reflector, for example with appearance of slight graphite dust in this space. The analysis of dust, that were collected near wavequide showed, that dust particles had dimensions from several μm to 70 μm. Using the expression for effective cross-section of for coal-graphite par ticles absorption[2] and taking dimension of particles $a=10^{-5}$ m and $\sigma=5\cdot10^{4}$ 1/Ohm·m, we obtain the wave amplitude as

$$A/A_0 = \exp\left[-\frac{3\cdot10^{-17}\ N\ L}{\lambda^2}\right].$$

Here L, N, λ are the wave path length, particle density and the wavelength respectively. The comparison of experimental and calculated data (with $N=10^{13}$ m^{-3}) for wavequide temperature 800°C showed, that attenuation due to graphite dust is a probab ly reason. For example at f=55, 75 and 105 GHz the experimental and calculated values of relative amplitude were equal to 0.85 and 0.82, 0.68 and 0.67, 0.73 and 0.50 respectively.

So, the effects of exposure to pulsed plasma streams with energy-flux density up to 15 MJ/m^2, of neutron irradiation with a fluence $2\cdot10^{22}$ cm^{-2} and of the heating up to the temperature 1000°C are not critical for a using of the graphite antennas, wavequides and reflectors in the devices with thermonuclear plasma parameters.

1. A.I.Skibenko, V.L.Berezhnyj, V.V.Chebotarev et al. 7th Inter national conference on Fusion Reactor Materials. 1995, Obninsk, Russia, 1995, Abstracts, p. 47.

2. A.E.Basharinov, V.M.Poljakov. Radiotechnika i electronika, N6, 1967, p. 984-988, in Russian.

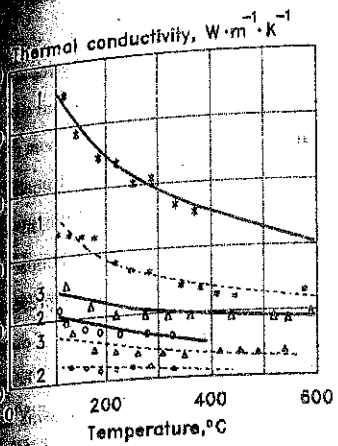


Figure 1

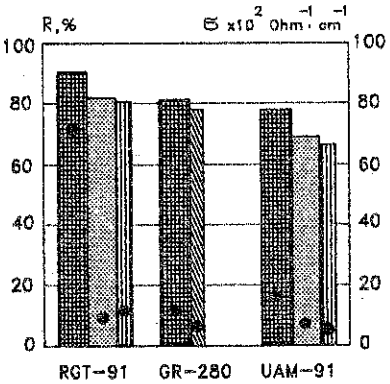


Figure 2

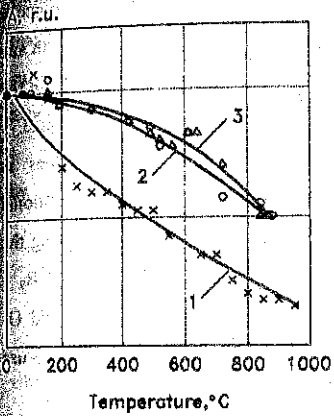


Figure 3

Fig.1. The dependencies of thermal conductivity of RGT-91 (solid) and UAM-91 (dashed) graphite on the temperature of measurements for nonirradiated (1) and irradiated with $F=2\times10^{22}$ n·cm^{-2} at $T_{irr}=400°C$ (2) and $T_{irr}=700°C$ (3).

Fig.2. The change of reflectivity coefficient CGM with irradiation : ▦ – nonirradiated; ▧ – $T_{irr}=700°C$, $F=3.5\times10^{21}$ n·cm^{-2}; ▨ – $T_{irr}=400°C$, $F=2\times10^{22}$ n·cm^{-2}; ▥ – $T_{irr}=700°C$, $F=2\times10^{22}$ n·cm^{-2}; and conductivity σ (dark points).

Fig.3. The dependencies of wave relative amplitude on the temperature for frequency f=75 GHz :
1 – passing through graphite waveguide;
2 – radiated by graphite conic antenna;
3 – reflected by graphite plates.

Density Fluctuation Studies for the "Uragan-3M" Torsatron via Microwaves.

A.I.Skibenko, O.S.Pavlichenko, R.O.Pavlichenko, I.P.Fomin
Institute of Plasma Physics, National Science Center "Kharkov Institute of Physics and Technology, Kharkov, Ukraine.

The microwave methods of diagnostics (interferometry, reflectometry, "resonancemetry") are commonly used on the U-3M torsatron for reconstruction of the temporary and spatial characteristics of electron density and their fluctuations in the confinement region and in the divertor fluxes as well. In this report we present results of studies of electron density fluctuations with emphasis on capabilities of dual polarisation multifrequency reflectometry and microwave Fabry-Perot resonator. These studies were performed during experiments on RF creation and heating of plasma in the U-3M torsatron using two types of RF antennae [1].

The layout of experiment for the electron density and their fluctuation measurements in the confinement region is presented on Fig.1 . Taking into account definiteness of a configuration of a vacuum magnetic field in torsatron, weak influence of plasma on it and assuming that density is constant on given magnetic surface in any section of torus, the plasma crossection was divided into number of layers equal to the number of probing beams and average density for any of such layers was determined.

The range of electron density and confining magnetic field values in experiments on U-3M torsatron ($n_e(0) < 8 \cdot 10^{12}$ cm^{-3}, $B_0 < 1.2$ T) gives some additional possibilities for dual polarisation reflectometry. They are seen from Fig.2 showing the cut-off layer positions for O-wave (1) and X-wave at $n_e(0) = 5 \cdot 10^{12}$ cm^{-3} and $B_0 =$ 0.46T (2), 0.7T (3), 1.2T (4). One can see that cut-off frequencies for X- and O-modes at large part of plasma radius differ on more than 10 GHz . This allows to use quite different probing frequencies for dual polarisation correlation reflectometry.

Signals of a reflected wave represent a superposition of phase oscillations, caused by a motion of a reflecting layer and by fluctuations of density near to this layer. However at reflection of a wave in a peripheral layer the regular phase shift that exceeding one, produced by a reflecting layer motion, by a factor 3-4 is observed. This

so called "phase run-away"[3] is being explained as a manifestation of a plasma rotation with poloidal linear velocity of $1 \div 3 \cdot 10^4$ cm/s.

Comparison of spectra of phase fluctuations for O- and X- waves of same frequency show, that spectra of a X-wave are more rarefied than that of O-waves, as the reflection of these waves occurs on greater depth and contribution of a transit layer is more significant. Using measured phase shifts of passing and reflected waves and the fluctuation spectra of waves of various frequency, radial profiles of electron density, amplitude and frequency of their fluctuations were determined during experiments on RF plasma creation and heating with single frame type antenna [2] at B_0=0.46T and RF power up to 200 kW (Fig.3).

For studies of divertor plasma flows, bending around helical windings, a resonator method was applied. The Fabry-Perot resonator with spherical mirrors by a diameter of 85 mm , curvature radius of 100mm and distance between them of 86 mm ($Q=5 \cdot 10^4$), was placed from the external part of a winding. It was excited on the frequency F_0=36,75 GHz, that was swept with the period of 0,05÷2 ms and the sweep range of $\Delta F_0 \approx 100$ MHz. At unperturbed plasma flow a resonance displacement without change of its form is observed. When the plasma density in resonator is fluctuating and if the fluctuation period is less than the sweep period T, the resonance curve is broadening and splitting. Fig. 4 illustrates this feature for the U-3M experiment.

The amplitude δ and frequency Ω of the electron density pulsation $\tilde{n}$ described by $\tilde{n} = n\delta \sin 2\pi\Omega t$ can be determined from the formulas:

$$\delta = (\eta - 1)\sqrt{\frac{1-\beta}{\beta}}\,Q^{-1}\,\frac{n_c l_m}{\bar{n} l_p}$$

$$\Omega = \frac{\eta_2\,\Delta F_0\,n_c l_m}{\delta\,\mathrm{T}\,F_0\,\bar{n} l_p}$$

where l_p , l_m , $\bar{n}$ and n_c are the plasma thickness , distance between mirrors, average plasma density and critical density correspondingly. $\eta = \Delta f_\beta' / \Delta f$, $\eta_2 = \Delta f_\beta'' / \Delta f_\beta$, Δf - the width of a unperturbed resonance, $\Delta f_\beta'$ - the width of a splitted resonance, $\Delta f_\beta''$ - the width of individual peak of a splitted resonance, β - the level on which width of a resonance is measured.

The measurements of the electron density and their fluctuations in the confinement region and in the divertor flows were carried out in experiment on RF plasma creation in the U-3M with the help of two frame antennas (Fig.5). The first two half-turn - antenna effectively created plasma of rather low density ($\bar{n} \leq 6 \cdot 10^{}$ cm^{-3}); at increase of density the localisation of the RF field is moved on the plasma periphery and the growth of density was limited. Switching-on of the second - third half-turn - antenna provides further increase of density at smaller RF power input. The electron density in divertor flows also increased and the density fluctuation level was decreasing.

At conclusion we want to emphasise some advantages of dual polarisation reflectometry for the electron density and fluctuation profile reconstruction:

1) X-wave probing needs narrower range of frequencies as compared to O-wave probing for given density profile;
2) an opportunity to receive the information on local density on an internal slope of profile with X-wave probing;
3) reduction of indefiniteness of a reflecting layer position at X-wave probing;
4) an opportunity to receive reflection from adjacent plasma layers at considerably larger frequency difference at dual polarisation probing in correlation reflectometry.

REFERENCES

1. Volkov E.D. et al.. In Plasma Physics and Controlled Nuclear Fusion Research (Proc. 14th Int. Conf. , Wurzburg, 1992), vol.2, IAEA, Vienna, 1993, 679.
2. А.И.Скибенко, О.С.Павличенко, Р.О.Павличенко, И.П.Фомин. Физика плазмы, 1994, т.20, №1, 13-14.
3. В.В.Буланин, Д.О. Корнеев, Физика плазмы, 1994, т.20, №1, 18-21.

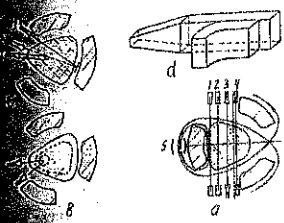


Fig. 1

Layout of microwave diagnostics on the U-3M tokamak: *a*) interferometers λ=1 mm (1,2,4), λ=2 mm (3,5), Fabry-Perot resonator (5); *b*) reflectometer; *c*) interferometer (1,2), interferometer λ=4 and 8 mm (3,4), *d*) waveguide device for input-output of dual polarization waves.

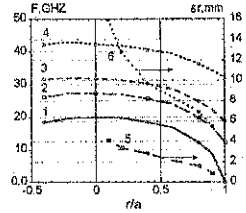


Fig. 2

Radial distribution of cut-off frequencies at $n(0)=5.10^{12}$ cm^{-3}: 1) O-wave; 2),3),4) X-wave at B_0=0.46, 0.7, 1.2 T correspondingly and indefiniteness of radial positions of cut-off layers: 5)X-wave, 6) O-wave.

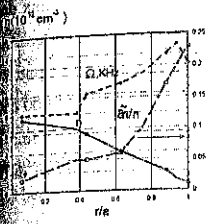


Fig. 3

Radial distribution of electron density, frequency and amplitude of fluctuations at

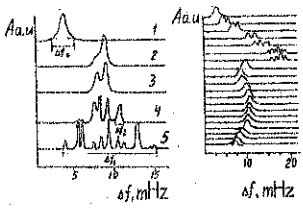


Fig. 4

Response of Fabry-Perot resonator with plasma on density fluctuations: on the left - calculations at 1) nl=0, 2) 3) 4) 5) at nl $=5.10^{16}$ cm^{-2} and $\frac{\delta(nl)}{nl}$=0.05, 0.1, 0.3, 0.8 correspondingly; on the right - experiment

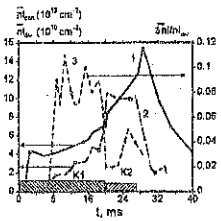


Fig.5

Time behaviour of electron density in plasma core (1) and divertor (2) and fluctuations in divertor (3) in the U-3M.

Test of mirrors for optical diagnostics in ITER

W. Bohmeyer, G. Fussmann, P. Kornejew, H.D. Reiner, H. Grote
Max-Planck-Institut für Plasmaphysik, Berlin Branch, EURATOM Association, Germany

Introduction

Optical diagnostics play an important role for all fusion devices. For ITER the access to the plasma is restricted because no direct view to the plasma is allowed. Therefore all diagnostics have to use mirrors. Especially the first mirror will be influenced by the plasma (neutrons, neutrals, deposition). Requirements for these elements and results of theoretical and experimental investigations are summarized in /2, 3, 4/.

From /5/ it is known that an important interaction between the plasma and the mirror is the bombardment by fast neutrals generated by charge exchange. The energy and the flux density depend on the position of the mirror. For the divertor region typical flux densities of 10^{19} atoms/cm²s and particle energies between 2 and 20 eV are expected. For the core region flux densities of $2 \cdot 10^{15}$ atoms/cm²s are typical; here the particle energy can rise up to 1000 eV.

Behrisch et al. /6/ have studied the erosion and deposition problem in JET by inserting small polished graphite test targets at various locations. They found, that deposition of different species is dominant for some position.

Assuming that the interaction of solids with fast neutrals is determined in the first place by the impact energy this process can be simulated by the bombardment with ions of the same mass and energy. In this paper we investigate the influence of D^+ bombardment on the optical parameters of different mirror materials.

Experimental setup

For the experiments we used the quasineutral plasma generated in the PSI-1 by a stationary arc discharge in an axial magnetic field /1/. Different mirrors (Tab. 1) were inserted into the target chamber using a movable water cooled target holder (Fig. 1). All mirrors were biased to -200 V to enable proper comparison between different mirrors the ion flux density was also kept fixed. The mirrors were located at the edge of the plasma column where the ion density gradient is large.

All mirrors were exposed for 3.5 hours. Electron temperature (2-3 eV) and density (10^{10} cm^3) were set as low as possible in order to avoid i) ionization and hence redeposition of the sputtered

...material and ii) sputtering by heavy ions eroded from the mirror surface.

surface material	bulk material	technology	diameter/ thickness [mm]
Cu	Cu	diamond turning	41 / 10
Al	Al	diamond turning	41 / 10
Mo	Mo	polishing	32 / 7
Mo	Mo	diamond turning	38 / 7
Au(~1 µm)	Cu (diamond turned)	coating	41 / 10
Rh(~500 nm)	Cu (diamond turned)	coating	41 / 10

Tab. 1: Investigated mirror materials

...the saturation current was determined for each mirror. Additionally a profile of the ion saturation current was determined by a flat Langmuir probe one-side-insulated. During all experiments about 1 cm² of the mirror surface was protected by a molybdenum plate for providing a reference area. The temperature of the backside of the mirrors was measured by means of a thermocouple; it always was less than 60° C.

During the experiments a He-Ne-laser beam (having a TEM_{00}-profile, broadened by a telescope) irradiated an area of ~1 cm² in the centre of the test mirror where the ion flux density was maximum. Behind a second telescope that was used to reducte the laser beam diameter the reflected beam was analysed by means of a CCD-detector system with respect to reflectivity and beam profile quality.

Finally after plasma exposure the regular and diffuse reflectivity were determined at three different wavelength using a Hg-lamp (Fig. 2). Additionally the topology of some mirrors was analysed by means of a scanning electron microscope. For all mirrors the shape of the surface profile was determined using an optical profilometer.

Results

For the evaluation of the mirrors we determined the light intenstity regulary and diffuse reflected from the mirror surface relativ to the incident one. The total diffuse reflectivity was calculated taking into accout the apperture of the detector. In Fig. 3 the regular and total diffuse reflectivity for the different mirrors are shown. Important is the strong decrease of the regular reflectivity for Al, Cu and Au especially for short wavelengths. Mirrors made of Mo and Rh showed the best results. This is in general a confirmation of the results predicted in /4/. For the comparison the diffuse erosion of an uneroded Al-mirror is included in the right picture of Fig. 3. It is obvious that for all mirrors the degradation is connected with an increase of the diffuse reflectivity. In

comparison to a new mirror these values increase by some orders of magnitude after a fluence of $1.5 \cdot 10^{21}$ D^+/cm^2.

After a 3.5 hour exposure to 200 eV D^+-ions the 1 µm Au-coating was destroyed in the region of high ion flux density, whereas under same conditions the 0.5 µm Rh-coating was not damaged significantly. The scanning electron microscope showed a structure of the eroded and uneroded Rh-surface which is similar to the typical pattern of recristallization of Cu.

Sufficient cooling of the mirrors is very important. First tests showed for surface temperatures ≥200°C the properties of Cu-mirrors change drastically due to recrystallization. this sensitivity can be reduced by adding some percent Ag. The critical temperature is thus increased to ≥300°C. Mo-mirrors show a similar behaviour but at higher temperatures (≥500°C).

Summary

It has been found that a fluence of $1.5 \cdot 10^{21}$ D^+/cm^2 leads to a substancial reduction of the regular reflectivity for Cu, Al, Au surfaces. Such fluences of CX-neutrals at energies around 100 eV are expected for ITER within 210 hours near the vessel wall. A better resistance with respect to surface damaging was found for Rh and Mo in particular. In all cases sufficient cooling is essential to avoid recristallization processes.

Acknowledgement

The autors thank Mrs. G. Weinberg from the Fritz-Haber Institut Berlin for carrying out the REM measurements.

Literature

/1/ H. Behrendt, W. Bohmeyer, L. Dietrich, G. Fußmann, H. Greuner, H. Grote, M. Kammeyer, P. Kornejew, M. Laux, E. Pasch, 21st EPS Conference on Controlled Fusion and Plasma Physics, Montpellier, 1994, p. 1328

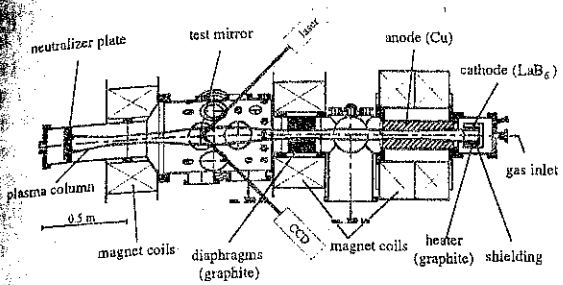
/2/ C.I. Walter, L. de Kock, Proceedings of the International Workshop on Diagnostics for ITER, Varenna 1995, p. 39

/3/ D.V. Orlinski, dito p. 51

/4/ V.S. Voitsenya, dito p. 61

/5/ M. Mayer, L. de Kock, IPP-Report, in press

/6/ M. Mayer, R. Behrisch, V. Prozesky, P. Andew, A. T. Peacock, 22nd EPS Conference on Controlled Fusion and Plasma Physics, Bournemouth, 1995, p. 301



Principle of the plasma generator PSI-1 with in-situ reflectivity measurements

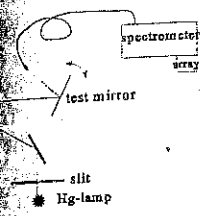


Fig. 2: Optical setup for the reflectivity measurements at different wavelength

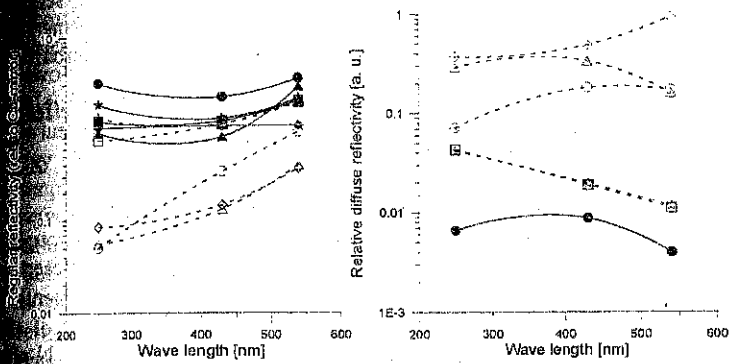


Fig. 3: Regular and diffuse reflectivity of various mirror surface materials eroded by deuterium ions; closed symbols: before and open symbols: after plasma exposure (fluence: $\approx 2.10^{21} D^+/cm^2$); ■ - rhodium, ★ - molybdenum, ▲ - gold, ● - aluminium, ♦ - copper

LABORATORY MODELING OF ELEMENTARY PROCESSES IN PLASMA

I.P.Zapesochny
Institute for Electron Physics, Ukr.Nat.Acad.Sci.
294016, Uzhgorod, Ukraine

Elementary processes occuring at collisions of atomic particles (atoms, simplest molecules, electrons, ions, photons), such as ionization, excitation, charge-exchange recombination, elastic scattering etc. take place in natural, laboratory and plasma of different technical devices (including thermonuclear setups). They essentially affect the electrical, magnetic, thermal and radiant properties of plasma. Hence, it is evident that for deep understanding of phenomena in plasma the knowledge of cross-sections of such elementary processes is required.

In the experimental physics of collisions of atomic (plasma) particles these processes can be simulated in their pure form. The main idea consists in creation of such experimental conditions for pair collisions, by means of which a certain elementary process can be observed isolated from the others. In most cases such case can be realized by observing the single-collision condition for the interacting particles in limited volume. Meanwhile, the secondary processes should be negligibly small. So, in the case of studying the process of energy levels excitation and photon spectra of plasma particles these latter would be stepwise excitation and second order impact. Finally reliable simulation of some separate elementary process is achieved, when sufficiently low densities of both bombarding particles, and the particles of target being used.

The working formula at the experimental studies of total effective cross-section of an elementary process is given by:

$$\sigma(v) = \frac{Z}{N n_0 v l}$$

obtained from the known law of the particles beam transmision through a target, the interacting particles single-collision condition being observed ($\lambda >> l$). Here $\sigma(v)$ is the effective cross-section of a certain elementary process at the given velocity v (or the corresponding energy E) of the interaction $N = N_0 v$ - the density of the bombarding particles beam, N and N_0 - concentrations of the target particles layer and bombarding particles respectively, l - length (thikness) of the target particles layer; Z - the number of interaction (scattering) acts, corresponding to this elementary process; λ - the average free path lenth of the bombarding particles in the target.

While studying process of atom (or ion) energy levels excitation it is convenient to determine the number of excitation acts for this level z from the number of photons (or intensity) of the corresponding spectral line, emitted by the excited target particle under the effect of electron impact. Under the stationary conditions the number of excitation acts for a certain level of the given particle is equal to the number of its de-excitation acts. A simple procedure enables one to conclude, that in order to determine the cross-section of the level excitation by means of photon spectroscopy one should take into account the role of cascade transitions (from the higher excited levels). Then the effective cross section of the level excitation can be determined from

$$\sigma_k(\upsilon) = \sum_{m=0}^{k-1} \sigma_{km}(\upsilon) - \sum_{l=k+1}^{\infty} \sigma_{lk}(\upsilon),$$

where σ_{km} and σ_{lk} being so-called excitation cross-sections of the lines, corresponding to the given level de-excitation (transition k→m), and cascade transitions (l→k). In the second sum are can restrict to several terms, since with the increase of the main quantum number of the given series their sections decrease very sharply.

In the experimental studies of pair collisions of plasma particles two ways of putting target particles into the zone of interaction with the bombarding beam are used: chamber technique (or the one-beam technique) and crossing beams technique. In the first case a vacuum chamber, in which sourse, former and detector of sharply directed bombarding particles beam are located is fully filled with the target particles. In the second case in the chamber the same devices are located for two beams, which intersect in deep vacuum (in most cases the angle is equal to 90^0).

In last decades perfect devices are created to obtain stable, unform in energy electron, ion atomic beams since major elementary processes are accompanied by emission, which generally covers a relativly bread range of wavelength (from near infrared to soft X-ray), then in order to select specific lines different spectral devices are used, including rarions kinds of vacuum monochromators and spectral filters.

In precise experiments, studying the dependence of given persent effective cross-sections on the energy (speed) of pair interactions of particles high unformity of the bombarding particles in enrgy is extremally important, especially for electron beams, in collisions with atoms and ions. Perfect monochromators and electron-ion analisers created by scientists, provided high level of electron beams uniformity in energy (~0,01eV) in the range of the particle interaction energy of about 1 to 10eV.

Up to the present time a great number of data on the effective cro sections of inelastic processes at pair collisions of electrons, ions a atomes (atoms and ions of groups I, II, III of the periodic table and no gases) have been obtained. The cross-sections of excitations, ionizatio autoionizing, dielectronic recombination of atoms and ions by electr impact have been measured in the energy range from the process tresho to the hundred of eV. And the cross-sections of resonant and no resonant charge-exchange excitation at collisions of heavy particles ha been measured in the energy range from zero to several KeV.

Absolute values of the effective cross-sections of e.g. atom leve excitation cover a considerable range of energies from 10^{-21} cm^2 to 10^{-14} cm^2. The energy dependence of the absolute cross-section of excitation of N resonance level by electron impact is shown as an illustration in Fig.1. It compared with the theoretical calculation in the first approximation o Born (the energy range from 0 to 300 eV) and by close-coupli calculation (from 0 to 30 eV). The examples of cascade transitions ro and resonant, autoionizing, interferential phenomena in the cross-sectio of inelastic proccesses are given in Fig.2 to.4.

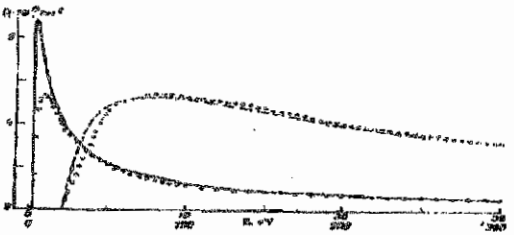


Fig.1. The excitation cross-section of resonant 2 p-level of sodium atom by electron impact [1].

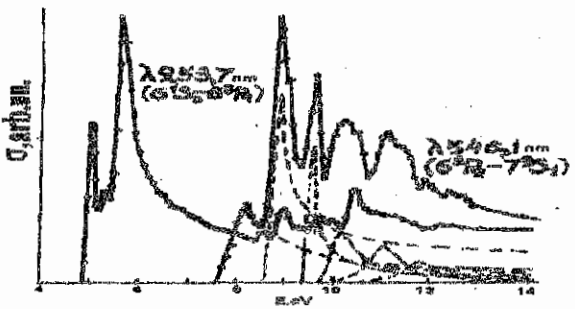


Fig.2. Energetic dependences of excitation cross-sections of resonant lines of Hg atom [2].

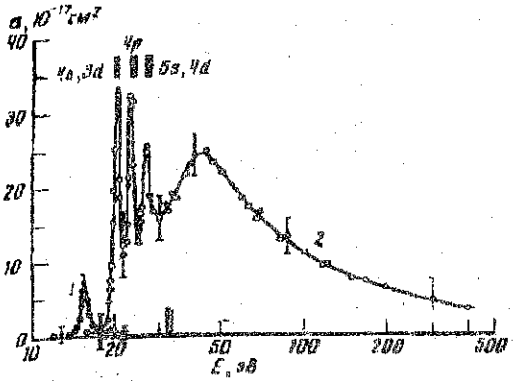


Fig.3.The excitation cross-sections of sodium ion resonant line (60.1+60.8+61.3)nm (curve2) and dielectronic recombination radiation 72.3nm (curve1) [3].

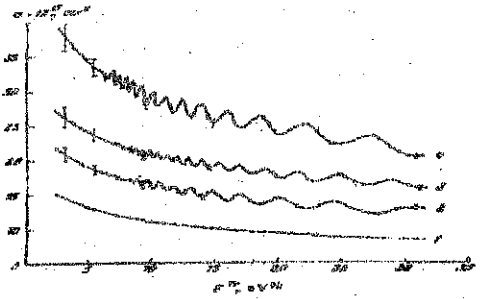


Fig.4.The charge exchange cross- secton of Mg^+ (cur. 1), Ca^+ (cur. 2), Sr^+ (cur. 3) and Ba^+ (cur. 4) ions on own atoms [4].

References:

1. Zapesochny I.P., Postoj E.N.,Aleksakhin I.S., Zh. Eksp.Teor.Fiz. v.68, 721 (1975).
2. Zapesochny I.P., Shpenik O.B., Sov.Phys.-JETP. v.23, 592 (1966).
3. Zapesochny A.I., Imre A.I., Aleksakhin I.S. et all. Sov.Phys.-JETP. v.63, 1156 (1986).
4. Panev G.S., Zavilopulo A.N., Zapesochny I.P., et all. Sov.Phys.-JETP. v.40, 23 (1974).

THE TWO-DIMENSIONAL THEORY OF REFLECTOMETRY DIAGNOSTICS OF PLASMA FLUCTUATIONS

E.Z.Gusakov, M.A.Tyntarev
Ioffe Institute, St.Petersburg, Russia

Reflectometry was widely used during the last decade in both large and small scale toroid plasma experiments, providing data not only on the plasma density profile but on th density fluctuation as well. However the information concerning the density turbulen was mostly qualitative since the spatial localization and wavenumber of fluctuations we estimated very roughly in the usual single access reflectometry experiment. This unce tainty had stimulated numerous theoretical papers [1–5] in which the microwave scatteri phenomena were studied both numerically in different approximations and models and a alytically in one-dimensional (1D) model based on WKB-approximation [5]. Till now t analytical treatment of the reflectometry scattering problem in realistic 2D model w performed.

An attempt to fill in this gap is undertaken in the present paper, where the 2D reflec tometry scattering problem is studied in Born approximation. Following [6] we write th backscattered power in the transmission line as $P_s = |A_s|^2$ using the receptivity theorem

$$A(\omega_s) = \frac{1}{4}\int \vec{j}_{\omega_s}(r)\cdot\vec{E}_a(r)d^3\vec{r}. \tag{1}$$

where

$$\vec{j}_{\omega_s} = i\frac{e^2}{m_e\omega}\sqrt{P_i}\hat{n}\vec{E}_a \tag{2}$$

is the nonlinear current in the case of O-mode reflectometry across the magnetic field. $\vec{E}_a(r)$ is the normalized receiving antenna beam, corresponding to the unit radiated power P_i is the incident wave power and a single antenna operation for emitting and receiving the signal is supposed. Further on we suppose that magnetic field is along z–axis, whereas the plasma is inhomogeneous along x–axis. The normalized antenna pattern is given by

$$\vec{E}_a(r) = \vec{e}_z E_a(x,y) = \vec{e}_z\int\frac{dk_y}{2\pi}W(x,k_y)f(k_y)e^{ik_y y} \tag{3}$$

where factor $f(k_y)$is determined by the beam distribution near antenna and the wave behaviour along the inhomogeneity direction is described by equation

$$\frac{d^2W}{dx^2} + \left[\frac{\omega^2}{c^2} - \frac{\omega_{p_e}^2(x)}{c^2} - k_y^2\right]W = 0 \tag{4}$$

Far from the cut off region the solution of Eq.(4) is expressed in WKB terms

$$W = \sqrt{\frac{8\pi\omega}{c^2k_i(x)}}\exp\left\{i\int_0^{x_r}k_i(x')dx' - i\frac{\pi}{4}\right\}2\cos\left\{\int_x^{x_r}k_i(x')dx' + \frac{\pi}{4}\right\}, \tag{5}$$

$k_i(x) = \sqrt{\dfrac{\omega^2 - \omega_{p_e}^2(x)}{c^2} - k_{yi}^2}$; $k_i(x_c) = 0$. In the vicinity of the reflection point the density profile is supposed to be linear

$$n_e(x) = n_0 \frac{x}{L} \tag{6}$$

the wave field is expressed in terms of Airy function.

Supposing that the reflectometry scattering takes place far from the cut off layer and using the harmonic density fluctuation $\delta n(\vec{r}) = \tilde{n}_0 \exp\{-i\kappa x - iqy\}$ one can substitute Eqs.(2), (3) and (5) into Eq.(1) and perform integrations using the stationary phase method. The final result is given by

$$A_s = \frac{e^2}{mc^2}\sqrt{P_i}\tilde{n}_0\sqrt{\frac{4\pi c^2}{\kappa}}\int_{-\infty}^{\infty} dk_y \sqrt{\frac{L_1}{\omega_{p_e}^2(x_1)}} f(k_y) f(q - k_y) \exp\left(i\Phi(x_*, k_y)\right); \tag{7}$$

where

$$\Phi = \int_0^{x_1} k(x', k_y)dx' + \int_0^{x_*} k(x', q - k_y)dx' + \mu_1 \int_{x_*}^{x} k(x', k_y)dx' + \mu_2 \int_{x_*}^{x} k(x', q - k_y)dx' - \kappa x.$$

Here x_1 the scattering point x, position is determined by the Bragg condition

$$\frac{d\Phi}{dx} = \mu_1\sqrt{\frac{\omega^2 - \omega_{p_e}^2(x_*)}{c^2} - k_y^2} + \mu_2\sqrt{\frac{\omega^2 - \omega_{p_e}^2(x_*)}{c^2} - (q - k_y)^2} - \kappa = 0; \tag{8}$$

L_n is the density scale in the scattering point.

Like the 1D resonant scattering signal [5], the 2D signal given by Eq.(7) increases with decreasing fluctuation wavenumber κ, but the physical reason for such a behavior is absolutely different. It is related not to the approaching of the cut off layer by the scattering point but rather to the increase of the coherence length

$$\delta x \cong [\Phi'']^{-1/2} = \sqrt{\frac{2c^2 L_*}{\omega_{p_e}^2}}\sqrt{\frac{k(x_*, k_y)k(x_*, q - k_y)}{\mu_1 k(x_*, k_y) + \mu_2 k(x_*, q - k_y)}}.$$

Simultaneously the scattering point is shifted to the plasma periphery as it is seen from Eq.(8). The resonant scattering for $\kappa \to 0$ is only possible, as it follows from Eq.(8), for $q \to 0$, and for mirror-like scattering $q \to 2k_y$. In these cases the coherence length $\delta x \to \infty$ and the stationary phase method certainly fails.

As it is clear from Eq.(8) the density inhomogeneity is eliminated in these two cases, so that the Bragg resonance exists all over the plasma including the cut off region. Such a non-localized resonance in the case $\kappa = 0$, $q = 2k_y$ is specific for the 2D model, where as the $\kappa = 0$, $q = 0$ resonance exists in the 1D model as well and corresponds to the forward scattering, mentioned in [2]. It was missed in [5], because the corresponding term in E_n^2 was omitted.

Strictly speaking the WKB approximation and Eq.(7) are nonadequate for descrip
of nonlocalized resonant scattering because the cut off region contributes to it strongly
rigorous study was performed with the emphasis on this case under the supposition
the density profile is linear (6) all over the plasma. Under this assumption the electric
(3) and nonlinear current can be expressed in terms of Airy function. The final expres
for scattered signal in this case takes a form:

$$A_s = \frac{2e^2}{mc^2}\sqrt{P_i}l^2\int\frac{dk_y d\kappa dq}{(2\pi)^3}f(k_y)f(q-k_y)\delta n(\kappa,q)C(\kappa,q)\exp\{i\Psi\},$$

where $\delta n(\kappa,q) = \int\int dxdy e^{iqy-i\kappa x}\tilde{n}(x,y)$; $\Psi = \int_0^{x_r} k(x',k_y)dx' + \int_0^{x_r} k(x',q-k_y)dx'$ and
scattering efficiency takes form:

$$C(\kappa,q) = \sqrt{\frac{\pi}{i\beta}}\int_{-\infty}^{+\infty}\frac{\exp\left\{i\frac{\beta^3}{12}\xi^3 - i\frac{\beta\sigma}{2}\xi - i\frac{\delta}{4\beta}\xi^{-1} - i(\xi-1)s\right\}}{(\xi-1+i\varepsilon)\sqrt{\xi+i\varepsilon}}d\xi,$$

where $l = \left(\frac{c^2}{\omega^2 L}\right)^{1/3}$; $\beta = \kappa l$, $s = \kappa L$; $\sigma = -l^2[k_y^2 + (q-k_y)^2]$; $\delta = l^4q^2(q-2k_y)^2$; $\varepsilon \to +0$.

In the case when the Bragg resonance condition (8) is satisfied in the plasma and
fluctuation wavelength is smaller then the plasma size ($s \gg 1$) the scattering efficien
takes a form

$$C(\kappa,q) \simeq -2\pi\sqrt{\frac{\pi i}{\beta}}\exp\left\{i\left[\frac{\beta^3}{12} - \frac{\beta\sigma}{2} - \frac{\delta}{4\beta}\right]\right\}.$$

which for $q \to 0$ and $k_y \to 0$ coincides with that obtained in 1D analysis [5]. However
divergence of $C(\kappa,q)$ at $\kappa \to 0$, unlike predictions of [5] is not saturated for $\kappa \sim l^{-1}$. T
saturation takes place at $\kappa \sim L^{-1}$ and for smaller $\kappa < L^{-1}$ the scattering efficiency is giv
by

$$C(\kappa,q) \simeq -\frac{4\pi i}{(2k_y-q)ql^2}\sin\left[(2k_y-q)ql^2\sqrt{\frac{L}{l}}\right].$$

To estimate the locality of reflectometry scattering diagnostics one can calculate t
signal, produced by the island-like density fluctuation

$$\tilde{n} = n_0\exp\left\{-\left(\frac{x-x_i}{w}\right)^2\right\}\cos q_0(y-y_0).$$

in the case of Gaussian antenna pattern

$$f(k_y) = 2\sqrt{\pi}\rho\exp\left\{-\frac{k_y^2\rho^2}{2}\right\}.$$

Supposing the island and the antenna beam to be wide enough, so that $L \gg w \gg l$,
$\rho > L^{1/4}\left(\frac{c}{\omega}\right)^{3/4}$ we obtain from Eq.(9)

$$A_s = 4\pi^{3/2}i\frac{e^2}{mc^2}\sqrt{P_i}n_0\frac{wl^{3/2}\cos q_0 y_0}{\sqrt{L-x_i}}\exp\left\{-\frac{q_0^2\rho^2}{4}\left[1+\frac{(L-x_i)l^4}{\rho^4}\right]+i\Phi\right\}.$$

$\Psi = \frac{4}{3}\left(\frac{L}{l}\right)^{3/2} - \frac{q_0^2 l^2}{2}\left(\frac{L}{l}\right)^{1/2}$. The signal increases but not steeply when the island approaching the cut off position. Its maximum is estimated by substituting $L - x_i = w$. The exponential signal dependence on the poloidal wavenumber $\sim \exp\left\{-\frac{q_0^2\rho^2}{4}\right\}$ proves that the signal is determined by nonlocalized resonance scattering at $k_y = q_0/2$.

When the probing wave cut off is in the wave zone of the antenna, so that $\sqrt{2L\frac{c}{\omega}} > \rho$, the scattering signal is given by

$$A_s = \frac{2\sqrt{2}i\pi^{3/2}e^2}{mc^2}\sqrt{P_i}n_0\frac{w\rho l^{3/4}\cos q_0 y_0}{(L-x_i)^{1/2}L^{1/4}}\exp\left\{-\frac{q_0^2\rho^2}{4}\left[2-\frac{x_i}{L}\right] - \frac{1}{8}w^2q_0^4\rho^2\left(\frac{l}{L}\right)^{3/2} + i\Psi\right\}. \quad (16)$$

where $\Psi = \frac{4}{3}\left(\frac{L}{l}\right)^{3/2} + q_0^2 l^{3/2}L^{1/2}(\frac{1}{2} + \frac{L-x_i}{L} - \frac{1}{8}\frac{w^2}{L^2}q_0^2\rho^2)$. For long scale fluctuations $q_0\rho <$ the signal decreases fluently when the perturbation moves towards plasma boundary $\sim (L-x_i)^{-1/2}$. On contrary for $q_0\rho \gg 1$, when the signal is received by the diagram recovery this dependence can be rather steep:

$$A_s \sim \exp\left\{-\frac{\rho^2 q_0^2}{4}\left(2-\frac{x_i}{L}\right)\right\}.$$

Such a behavior can be easily explained in the ray-tracing consideration after requiring poloidal projections of incident and scattered wave trajectories to be equal and applying the Bragg condition $k_{y_s} = k_{y_i} - q$.

To conclude, it should be mentioned that the analytical approach to the investigation of reflectometry diagnostics of plasma fluctuations in 2D geometry have proved to be an effective method for analysis of scattering efficiency. It provides exact expressions for the reflectometry scattering signals under realistic conditions. The signal is shown to be dominated by nonlocalized resonance scattering from large radial scale fluctuations. A fairly good radial localization of scattering near the incident wave cut off is possible for high poloidal wavenumber fluctuations.

This work was supported by INTAS grant 94-2236 and RFBS grant 96-02-17913.

References

[1] Zou X.L., Laurent L., Rax J.M. Plasma Phys. Control Fusion, **33** (1991), 903.
[2] Hutchinson I.H. Plasma Phys. Control. Fusion **34** (1992), 7.
[3] Irby J.H., Horne S., Hutchinson I.H., Stek P.C. Plasma Phys. Control. Fusion, **35** (1993), 601.
[4] Bruskin L.G., Mase A., Tamano T. Plasma Phys. Control. Fusion, **37** (1995), 255.
[5] Afeyan B.B., Chou A.E., Cohen B.I. Plasma Phys. Control. Fusion, **37** (1995), 315.
[6] Novik K.M., Piliya A.D. Plasma Phys. Control. Fusion, **35** (1993), 357.

f055

A temporal study of CV line ratio variations across the TJ-IU Torsatron

K. J. McCarthy, B. Zurro and C. Burgos
Asociación EURATOM/CIEMAT para Fusión, E-28040 Madrid, Spain

1. Introduction

We have previously reported the observation of variations in the intensity ratio of the helium-like carbon lines $1s2s^3S_1$-$1s2p^3P_2$ (2271.59 Å) and $1s2s^3S_1$-$1s2p^3P_{0,1}$ (2278.41 Å) in line of sight measurements across the TJ-I tokamak plasma [1]. We showed how these variations, which deviate from the 2^3P level statistical ratio $R = 1.67$, could be attributed to the selective populating of the 2^3P_2 by charge exchange involving hydrogen-like carbon and neutral hydrogen. We have also developed a model that reproduces these variations and we have postulated that the monitoring of such variations might provide a means of determining plasma neutral hydrogen concentration [2]. Recently, workers on Alcator-*C* [3] and Tore Supra [4] have reported similar variations in the line intensity ratios of several He-like ions that involve a line transition which originates in the same upper level, 2^3P. In each case charge exchange is believed to be the process involved.

The UV line intensity measurements on the TJ-I reported previously were centred about the peak of the discharge [2]. The use of a multipixel array detector together with the high spectral resolution achieved using a 1 m focal length monochromator allowed us to record the intensities of both lines simultaneously. However no temporal information was available to trace the development of the ratio variations along a discharge and it was necessary to vary the line of sight through the plasma on a shot to shot basis. In this paper we describe an experiment to simultaneously measure the temporal and spatial variation of these C V lines, at 2271.59 Å and 2278.41 Å, across plasma of the TJ-IU torsatron. This machine has a major radius of 60 cm, and an average minor radius of 10 cm, and for these experiments the plasma was created and heated by injecting 200 kW at 37.5 GHz at the second harmonic. The chamber was conditioned by glow discharge cleaning in He. The magnetic field coils were powered by capacitor banks and the discharge lasted around 30 ms. The typical maximum central electron temperature was about 180 eV and the maximum line averaged density was about 6×10^{12} cm^{-3}.

2. Experimental Approach

High resolution spectroscopic studies of lines at 2271.59 Å and 2278.41 Å have been performed on the TJ-I U using a 1 m focal length monochromator. The plasma radiation was observed through a quartz window on the machine. Line-integrated emission profiles of the C V lines were obtained using a fast rotating polygonal mirror which scanned the

...across-section in 0.4 ms and once every 2 ms. The resultant temporal resolution ...0.010 ms while the spatial resolution was slightly better than 1 cm. Two mirrors ...close to the rotating mirror directed the output towards the spectrometer. A quartz ...was used to focus the radiation onto the monochromator entrance slit. The resultant ...intensity was measured at the monochromator exit slit using a standard ...photomultiplier tube.

...drawback of the scheme used here is that only one line can be monitored during each ...discharge. However, by alternating the monochromator setting between each line during ...of discharges and by comparing the signals collected in other detectors, it was ...possible to compare the C V line ratios for similar discharges. These other signals include ...time evolution of the C V 2271.59 Å from a 1/4 m monochromator based system [5], ...multiple broadband light radiation monitor, an X-ray bolometer and microwave signals. ...signal from the first of these was also used to compensate the C V line signals for ...any time lag that may have existed between the C V line profiles being compared.

3. Results

...In Fig. 1a we show the space-time evolution of the 2271.59 Å line along a single TJ-IU ...discharge. In particular, the upper curve shows the temporal evolution of the global ...2271.59 Å line radiation collected using the 1/4 m monochromator. The lower curve ...shows repetitive scan profiles of the same line, using the 1 m monochromator. The ...evolution of the line radiation along the discharge and across the plasma radius are seen. ...In Fig. 1b, we show expanded smoothed profiles centred about the peak of the discharge ...for the latter.

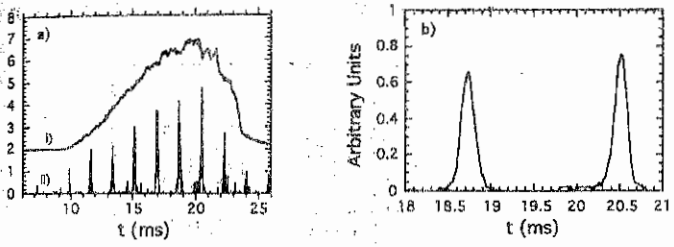


Figure 1a. i) Time evolution of the global 2271.59 Å line radiation. ii) Time-space evolution of the 2271.59 Å line. Fig. 1b. Expanded smoothed profile of curve ii).

...In Fig. 2, we show the time evolution of the line ratio R as a function of plasma radius. ...Here, the R values were determined using the smoothed profiles of the 2271.59 Å and ...2278.41 Å lines. For this we used two discharges which were similar and which

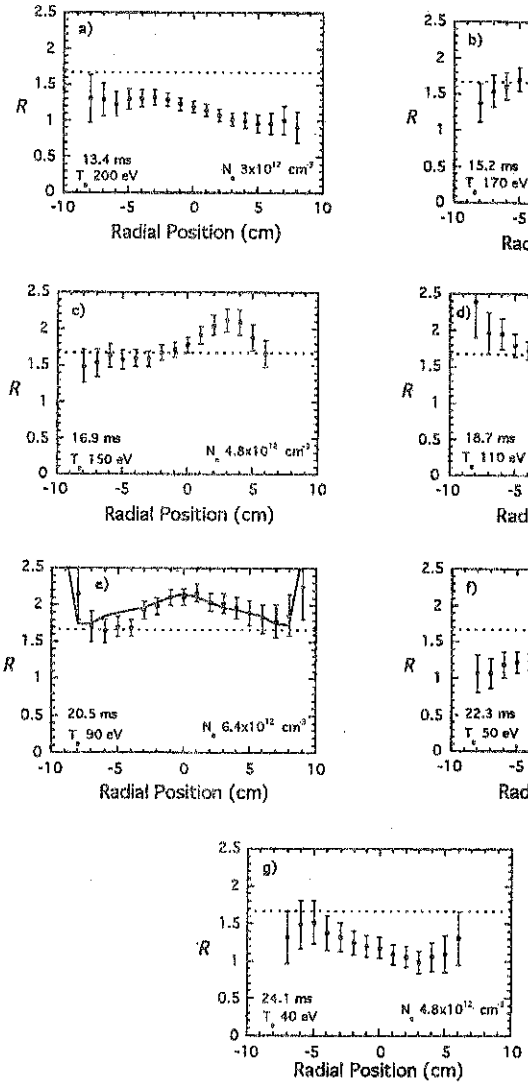


Figure 2: Time evolution of R for a TJ-IU discharge. The broken line represents the nominal R (1.67). Central electron temperatures and line-averaged electron densities are indicated.

measured in the same set of discharges, i.e. shots 4828 and 4833. Note: in each profile only signals which were above 5% of the peak were considered in order to avoid values with large errors.

Our measurements show that R varies both along the discharge and across the plasma radius. (See Fig. 2.) In Figs. 2a, 2f and 2g where $R < 1$, it is considered that a low electron density and/or low electron temperature gives rise to a non-statistical population distribution among the 2^3P levels.

4. Discussion

We have estimated the average He-like carbon concentration to be 2×10^{10} cm^{-3} along a chord through the plasma centre by using the 2271.59 Å line intensity for these discharges and a technique similar to that described in Ref. 5. In addition, we have been able to estimate the central neutral hydrogen density for a time near to the peak of the discharge, i.e. Fig 2e. To do this we have used the model described in Ref. 2, together with a line average electron density of 6.4×10^{12} cm^{-3}, as determined using a microwave interferometry technique, a central electron temperature of about 90 eV, and assuming a C V to C VI ratio of 0.35 (for a corona model). Thus, we estimate the central neutral hydrogen density to be close to 10^{11} cm^{-3}. In Fig. 2e we show how the result of the model is a reasonable fit to the data. There would appear to be some asymmetry in the plasma which makes a perfect fit difficult. Finally, the weak signals detected have resulted in large error bars but we still see considerable variations in R across the plasma.

In conclusion, we have observed variations in the R value across the plasma near the peak of the discharge. Several improvements can be made to our measurement technique. Firstly, the simultaneous measurement of both lines will remove any anomalies due to non-reproducibility of the plasma. Secondly, the monitoring of a C VI line will give a better fix to the ratio between C V and C VI and hence a better estimate of the neutral hydrogen density.

References

[1] K.J. McCarthy and B. Zurro, Proc. 22nd EPS Conference, Bournemouth, 1995, ECA Vol 19C, II-417

[2] K.J. McCarthy, B. Zurro, C. Burgos, J. Vega and A. Portas, Phys. Rev. E 52 (1995) 6671

[3] W.R. Hess, C. De Michelis, M. Mattioli, R. Guirlet, and M. Druetta, Nucl. Instrum. and Meths. B 98 (1995) 97

[4] E. Källne, J. Källne and A.K. Pradhan, Phys. Rev A 27 (1983) 1476

[5] B. Zurro, Rev. Sci. Instrum. 62 (1991) 118

APPLICATION OF CR-39 AND PM-355 NUCLEAR TRACK DETECTORS MEASUREMENTS OF FAST IONS FROM HIGH TEMPERATURE PLAS

M.Sadowski, A.Szydłowski, M.Jaskóła, T.Czyżewski
Soltan Institute for Nuclear Studies, 05-400 Otwock-Swierk n. Warsaw, Po

Introduction

Solid state nuclear track detector (SSNTD) materials are capable of deuteron, alpha particle, and other light ion track recording, and due to that they suited to corpuscular diagnostics in hot plasma experiments. Moreover, usefulness SSNTDs in thermonuclear experimental studies is justified by their high regist efficiency for ions, insensitivity to electrons and electromagnetic radiation, ab register high particle fluxes, and endurance to vacuum conditions. Furthermore, it that an appropriate SSNTD can provide the greatest resolution of any charged pa detection system developed so far [1].

In order to use such a detector for quantitative measurements and to advantage of its properties it is necessary to know its characteristics, i.e., a depend of track diameters on a particle type and energy for different etching conditions studies have been performed at Soltan Institute for Nuclear Studies for several yea 4]. This paper reports on calibration measurements of modern CR-39 and PM-355 NTDs, which make possible the accurate registration of fast ions emitted from plasmas.

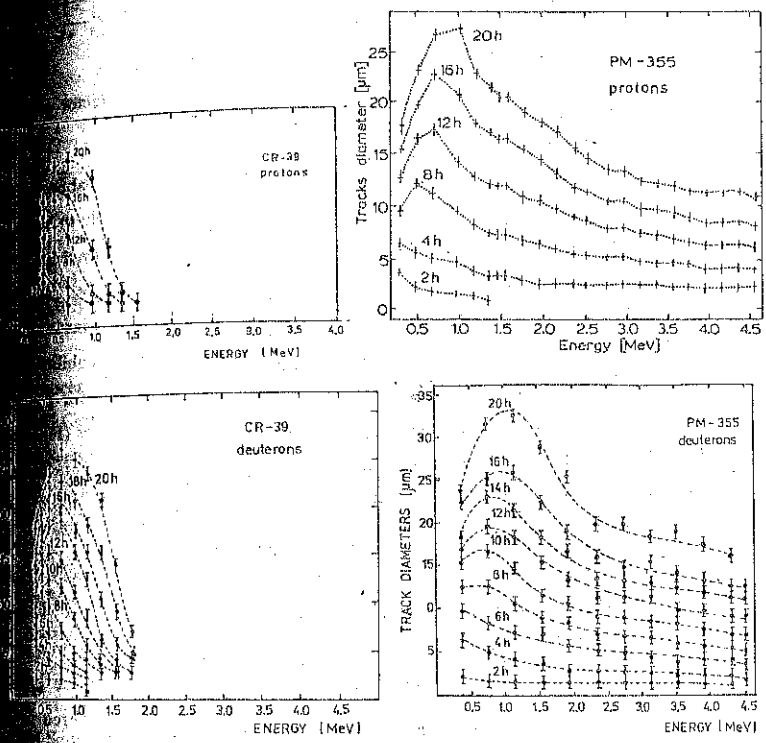
Experimental arrangement

In order to perform the calibration several samples of the CR-39 and PM plastics were exposed to fast proton, deuteron, and ^{4}He ion beams extracted from var accelerators. The investigated samples were bombarded with particles scattered by a Au-foil oriented perpendicularly to the accelerator beam [2]. The scattered particles monitored with a Si-detector, by means of which it was possible to control energy spe of the scattered particles, and to estimate the counting rate over the sample area. particles backscattered from the Au - foil hit the surface of the detector samples alm perpendicularly. Energy of the particles used to calibrate the samples was changed steps equal to 0.2 MeV within a range from 0.3 MeV to 4.5 MeV. After appropri irradiation the samples were etched under standard conditions (in the 6.25 N so solution of NaOH, at a temperature of 70^0 C) during periods lasting from 2 to 20

...wo hours the etching procedure was stopped, the samples were washed and dried, ...for that, track diameters were measured by means of an optical microscope.

...mental results

...general, the particle tracks were circular in shape (due to the vertical ...ation) and they could easily be distinguished from microdamages of the detector and ...ers of a considerably smaller diameter, which were probably caused by the ...round radiation. Results of detailed measurements of track diameters in the ...ted detectors, as obtained for protons, deuterons and ^{4}He ions (alphas) of ...energies and selected values of the etching time, are presented in Figs 1 and 2.



...Calibration characteristics of the CR-39 and PM-355 track detectors, as measured ...for protons and deuterons and for different etching times.

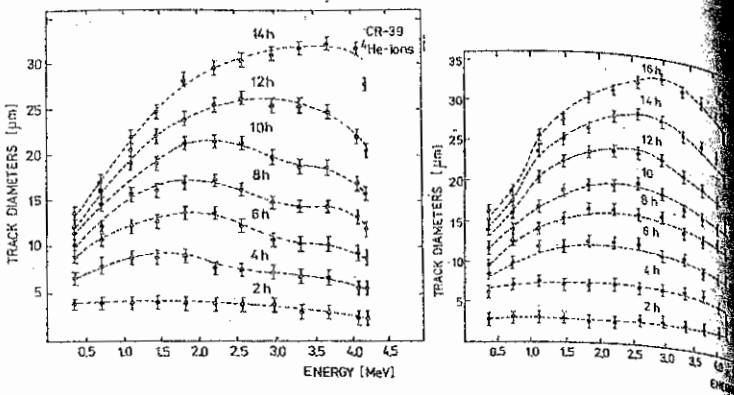


Fig.2. Calibration diagrams obtained for the CR-39 and PM-355 detector sam irradiated with ^{4}He ions of different energy.

All the experimental curves show distinct maxima at a given energy value, above w the track diameter decreases almost monotonically. Therefore, it is possible to estim a particle energy value from a track diameter within the considered energy range.

In general, the PM-355 detectors are more suitable for proton and deute measurements than CR-39 ones, because they demonstrate tracks of larger diameters they can be used within a wider range of proton and deuteron energies. Capability of proton and deuteron recording of the CR-39 plastic decreases strongly for p an energies higher than 1 MeV. Diameters of tracks induced by alpha particles (Fig.2.) not depend considerably on the particle energy value, and the calibration characteris of the investigated SSNTDs are very similar. It makes more difficult their application a quantitative energy analysis of alpha particles.

Samples of the PM-355 detector, which was calibrated as described above, w situated in the PF-360 plasma focus facility [6] at the same distances (about 340 m from the PF region, but at different angles to the z-axis. They were exposed to a se of successive PF discharges, and after that they were undergone the same etch procedure as the calibrated samples. A surface density of tracks as registered in t samples exposed at different angles, enabled angular distributions of fast deuterons a fusion produced protons emitted from PF discharges to be determined (Fig.3).

Several PM-355 detector samples were covered with Al-foils of different thickness exposed within the PF-360 facility to fusion produced protons. Measuring the track diameter distribution on the irradiated and etched samples, and using the calibration curves, it was possible to determine protons energy spectra, as shown in Fig.4.

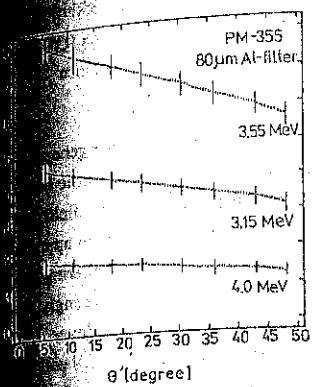


Fig.3. Surface density of the tracks registered with the PM-355 detector samples placed inside the PF-360 discharge chamber at different angles to the electrode axis.

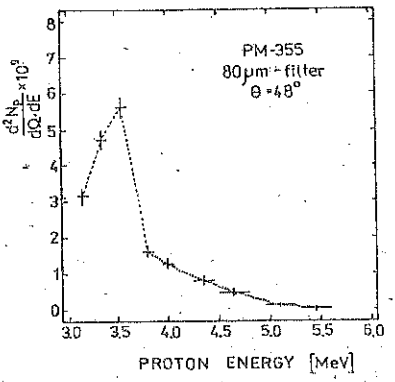


Fig.4. Energy spectrum of fusion-produced protons emitted from PF discharges performed in the PF-360 facility..

References

1. B.G.Cartwright, K.Shirk, P.B.Price: Nucl. Instr. Meth. **153** (1978) pp. 457-460.
2. M.Sadowski, E.M.Al-Mashhadani, A.Szydłowski, T.Czyżewski, L.Głowacka, M.Jaskóła, M.Wieluński: Nucl. Instr. and Meth. **B86** (1994) pp. 311-316.
3. M.Sadowski, E.M.Al-Mashhadani, A Szydłowski, T.Czyżewski, L.Głowacka, M.Jaskóła, C.Rolfs and M.Wieluński: Radiation Measurements **25** (1995) 175-176.
4. M.Sadowski, A.Szydłowski, M.Jaskóła, T.Czyżewski, and L.Głowacka: in Proc. 2nd National Symposium PLASMA '95 - "Research and application of plasmas", Warsaw, (June 1995) Vol.1, pp. 59-62.
5. E.M.Al-Mashhadani, M.Sadowski, A.Szydłowski: Rus.J.Plasma Phys **20** (1994) 196-198.
6. M.Sadowski, L.Jakubowski, J.Zebrowski, E.M.Al-Mashhadani: Proc. Int. Conf. on Plasma Physics (EPS, Innsbruck 1992) Pt.I, pp. 691-694.

One-dimensional fluctuation reflectometry: Enhanced cut-off response due to large amplitude localized fluctuations

I. Boucher, F. Clairet*, C. Fanack, S. Heuraux, G. Leclert, XL Zou*,

Laboratoire de Physique des Milieux Ionisés, URA CNRS 835,
Université Henri Poincaré, Nancy I, BP 239, 54506 Vandœuvre Cedex (France)
*DRFC, CEA Cadarache, 13108 St Paul-lez-Durance Cedex, France

1. Introduction

Theoretical and numerical studies of 1D fluctuation reflectometry are generally c
out under the assumption of the Born approximation, that is, the perturbed electric field
perturbed phase shift are proportional to the incident (unperturbed) electric field and
density perturbation amplitude [1]. Numerical calculations beyond the Born approxi
have been done only recently [2]. This study focused on the Bragg backscattering pro
the weakly nonlinear regime. The aim of the present work is to analyse strongly non
regimes both near the usual Bragg scattering region and near the cutoff layer. Indee
contradistinction with the small amplitude case [3, 4], for localized modulated Ga
perturbations, large phase shifts are produced near the cutoff.

2. Basic equations

We consider the O-mode propagation equation

$$\frac{d^2}{dx^2} E(x) + k_0^2 \left(1 - \frac{n(x)}{n_{cr}} - \frac{\delta n(x)}{n_{cr}} \right) E(x) = 0$$

where $n(x)$ is the unperturbed density, $\delta n(x)$ the density perturbation and n_{cr} the density a
cutoff for the frequency $\omega_0 = k_0 c$. The unperturbed density profile is assumed to be l
$n(x) = n_{cr}(x - x_0)/(x_c - x_0)$, where x_0 is the plasma boundary and x_c the cutoff. $L = x_c$
is the gradient length. The density perturbation is a modulated Gaussian pulse centered a
with a width w_f and a modulation wavenumber k_f

$$\delta n(x) = \delta n \exp[- (x-x_f)^2/w_f^2] \sin[k_f(x - x_f)]$$

In order to avoid that linear spectral effects [4] interfer with the nonlinear modifications
generally choose wide perturbations, $w_f > (k_f L/k_0^2)^{1/2}$. Eq. (1) has been solved by an u
finite difference scheme, for different normalized density gradient lengths L/λ_0, perturba
wavenumber k_f/k_0, perturbation width w_f/λ_0 and relative perturbation amplitude $\delta n/n_{cr}$. T
output of the code is the phase response, i.e. the phase shift $\Delta\phi$ versus the normalized posit
x_f/λ_0 of the perturbation.

Bragg backscattering at large amplitude

In the small amplitude (linear) regime, the maximum Bragg backscattering phase shift occurs at the position x_B where the Bragg resonance rule $k_f = 2k_0(x/L)^{1/2}$ is satisfied. The phase response in such a case is given for instance in [3, 4]. Figure 1 shows the phase response for a perturbation having $\delta n/n_{cr} = 0.2$, $k_f = 1.4k_0$ and $w_f = 10\,\lambda_0$, moving down the density gradient with $L = 100\lambda_0$. The Bragg position is at $x_B = 60\lambda_0$ and the cutoff at $110\lambda_0$.

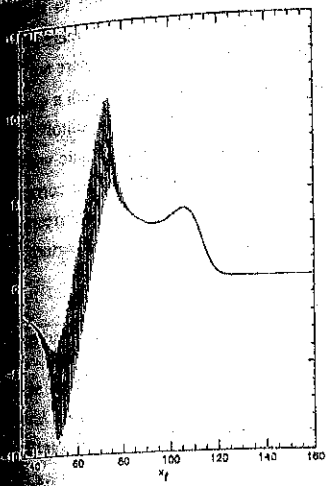


Fig. 1 - Phase shift $\Delta\phi$ (rad) versus x_f/λ_0, for $\delta n/n_{cr}=0.2$, $k_f=1.5k_0$, $w_f=20\lambda_0$

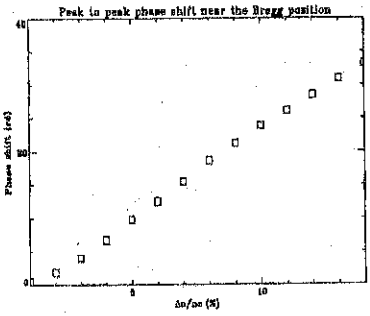


Fig. 2 - Maximum phase shift due to Bragg scattering versus $\delta n/n_{cr}$.

The maximum phase shift is no longer near x_B; on the contrary there are one maximum and one minimum whose separation increases with the perturbation amplitude. Superimposed to this large antisymmetrical behaviour, there is a modulation of wavenumber k_f, which is the remnant of the small amplitude response [4]. A close examination of the modulation shows that its right sides become very steep (as already visible on fig. 5 of Ref. 2) and that its peak-to-peak amplitude is 2π. Although only a nonlinear model could account for the detailed variation of the phase shift, one can give the following global picture. At large amplitude, the Bragg rule can be locally satisfied inside the density perturbation. The width of the region where Bragg backscattering occurs is of the order of $(x_B - (1/2)L\delta n/n_{cr}) < x_f < (x_B + (1/2)L\delta n/n_{cr})$. In a first approximation the phase variation over this region is directly related to the perturbation position in the density gradient. This accounts for the general behaviour of the phase response and allows a rough estimate of the total phase difference between the maximum and the minimum. Figure 2 gives the evolution of the total phase shift with the relative amplitude of the perturbation for a case where $w_f = 16\lambda_0$ and $k_f = k_0$.

4. Phase response in the cutoff region.

Figure 1 already shows that, contrarily to the small amplitude case [4] there is a large ph
variation as the perturbation crosses the cutoff layer. In order to separate the cutoff and Bi
regions, we choose a larger density gradient length, $L = 1000\lambda_0$. The cutoff is at $x \simeq 10$
The phase response versus the position x_f of the perturbation is shown on Fig. 3, for
$16\lambda_0$, $k_f = 1.5k_0$ and for values of the relative amplitude of the perturbation $\delta n/n_{cr} = 0.2$,
and 0.35. The maximum phase shift increases as $(\delta n/n_{cr})^2$. In addition to the sm
continuous variation of the phase shift as the perturbation reaches the cutoff, there are na
regions where the phase varies rapidly. Eventually, at very large amplitudes there are 2π p
jumps. Hence the phase shift increases by steps. Fig. 4 shows that, when such a quasi-p
jump occurs, the incident electric field is resonant in the cavity behind the cutoff where
refractive index is positive. The first resonance occurs when the characteristic width of
cavity is of the order of the Airy half-wavelength. Successive phase jumps correspond
successive harmonics of this resonance. For the purpose of illustration Fig. 4 corresponds to
simple well of the refractive index, but this remains true for modulated density perturbation

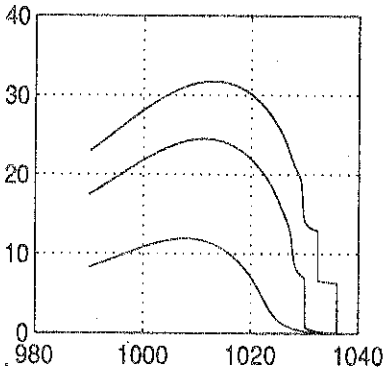


Fig. 3 - Phase shift (rad) versus x_f near the cutoff for $\delta n/n_{cr} = 0.2$, 0.3 and 0.35.

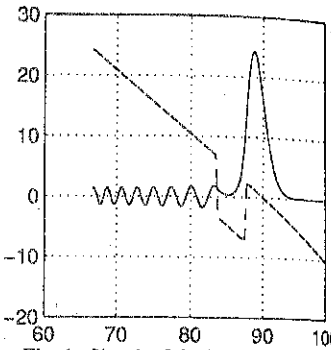


Fig. 4 - Sketch of the incident electric field (—) and the refractive index (---) at a phase jump.

5. Frequency sweep reflectometry.

In the previous analysis, the perturbation moves along the density gradient and the frequency kept constant. Conversely, one can keep the perturbation at a fixed position and sweep t frequency. This is the usual situation for profile reflectometry, where a group delay is deduc from the phase measurements. We choose a (non-normalized) gradient length $L = 1$ m and density perturbation with $w_f = 10$ cm and $k_f = 1$ cm^{-1}, located at $x = 30$ cm. Figure 5 shows evolution of the group delay obtained from the numerical determination of the phase, fo

amplitude $\delta n/n = 5\%$. Important perturbations of the group delay occur at the values frequency where the phase is rapidly varying.

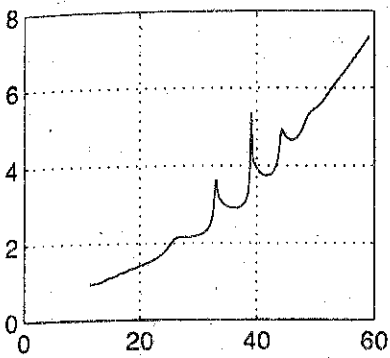


Fig. 5 - Group delay (ns) versus the incident wave frequency (GHz) for L=1m, $\delta n/n_{cr} = 0.05$, w_f=10cm, k_f=1cm^{-1}

Conclusions.

the phase shift of the reflected signal in the presence of large amplitude localized perturbations has several peculiarities:

- in the Bragg scattering region, the maximum phase shift moves out of the unperturbed Bragg position $x_B = (k_f/2k_0)^2 L$. Eventually there are two peaks of opposite sign, whose distance depends upon the perturbation amplitude and the density gradient length. The modulation of wavenumber k_f which is the essential characteristics in the small amplitude case steepens more and more, leading to quasi-phase jumps.
- in the cutoff region, the phase shift increases more rapidly, and becomes comparable to that due to Bragg scattering. There is no oscillation near the cutoff, and the quasi-phase jumps that occur lead to a steplike variation of the phase shift..
- in both regions, the occurrence of quasi-phase jumps corresponds to a local resonance of the electric field.

for frequency sweep reflectometry, the evolution of the group delay with the frequency shows spurious spikes due to large amplitude density perturbations ($\delta n/n > 5\%$).

References

[1] Zou XL, Laurent L and Rax JM, *Plasma Phys.Control. Fusion* **33**, 908 (1991).
[2] Chou AE, Afeyan BB and Cohen BI, *Rev. Sci. Instrum.* **66**, 1216 (1995).
[3] Afeyan BB, Chou AE and Cohen BI, *Plasma Phys. Control. Fusion* **37**, 315 (1995)
[4] C. Fanack et al, these proceedings.

Spectral effects in 1-D fluctuation reflectometry: Analytical and numerical investigation of the phase shift due to small amplitude localized fluctuations.

C. Fanack, I. Boucher, F. Clairet*, S. Heuraux, G. Leclert and X.L. Zou*
Laboratoire de Physique des Milieux Ionisés, URA CNRS 835,
Université Henri Poincaré, Nancy I, BP 239, F-54506 Vandœuvre Cedex, France
*Association Euratom-CEA, CE Cadarache, F-13108 St Paul-lez-Durance Cedex, France

1. Introduction

Reflectometry is used in all major tokamaks for density profile measurements. Density fluctuations can seriously perturb the phase shift determination, hence leading to an erroneous density profile. On the other hand, one can deduce some basic properties of the fluctuations from reflectometry measurements. One-dimensional models of fluctuation reflectometry have been studied by different authors [1]. In the phase shift due to density perturbations, the dominant process is Bragg resonant scattering, in which the incident wave is preferentially scattered at the particular location where its wavenumber is half the perturbation wavenumber. As a consequence, it is expected that the perturbed phase shift does not come from the cutoff layer. Afeyan et al [2] have studied some limit cases for Gaussian perturbations. However, it was found [3] that the shape of the density perturbation plays a role and that a significant response at the cutoff can be obtained. We explore in details in this paper these spectral effects due to the finite size and shape of the perturbations. Numerical results are compared with analytical formulae that allow to define the parametric dependence of the maximum phase shift either in the usual Bragg region or near the cutoff.

2. Basic equations and modelling.

The O-mode propagation equation for the electric field E(x) is written

$$\frac{d^2}{dx^2}E(x) + k_0^2\left(1 - \frac{n_0(x)}{n_{cr}} - \frac{\delta n(x)}{n_{cr}}\right)E(x) = 0 \qquad (1)$$

where $n_0(x)$ is the unperturbed density, $\delta n(x)$ the density perturbation and n_{cr} the density at the cutoff for the frequency $\omega_0 = k_0 c$. For the sake of simplicity, the unperturbed density profile is linear, $n_0(x) = n_{cr}(1 + x/L_n)$, and the density perturbation is either a modulated Gaussian pulse or a wavetrain centered at x_f, of width w_f, with a modulation wavenumber k_f

$$\delta n(x) = \delta n \exp[-(x-x_f)^2/w_f^2]\sin[k_f(x - x_f)] \qquad (2a)$$

$$\delta n(x) = \begin{cases} \delta n_0 \sin[k_f(x - x_f)] & |x - x_f| \le w_f \\ 0 & |x - x_f| > w_f \end{cases} \qquad (2b)$$

Eq. (1) has been solved by an usual finite difference scheme, for different normalized density gradient lengths L/λ_0, perturbation wavenumber k_f/k_0 and perturbation width w_f/λ_0. The relative perturbation amplitude is $\delta n/n_{cr}=10^{-3}$. The output of the code is the phae response, that is, the phase shift $\Delta\phi$ versus the normalized position x_f/λ_0 of the perturbation. $\Delta\phi$ can also be expressed in the Born approximation by the integral [2]

$$\Delta\phi = -2\pi(k_0L)^{2/3}\int d\xi\ \frac{\delta n(\xi)}{n_{cr}}\ Ai^2(\xi),\quad \xi = (k_0^2L^{-1})^{2/3} \qquad (3)$$

Spatial and spectral regimes of Bragg scattering.

Let us consider a Gaussian perturbation with the parameters $L/\lambda_0=1000$, $k_f/k_0=0.4$, so that Bragg scattering is dominant.

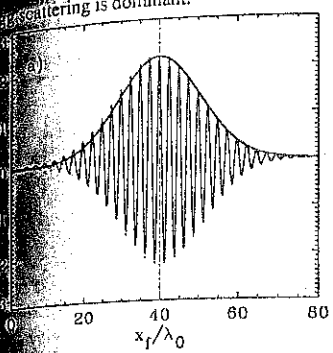


Figure 1- Gaussian perturbation, spatial case

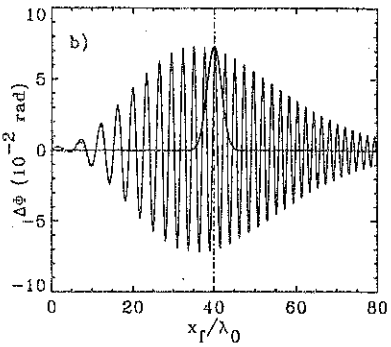


Figure 2- Gaussian perturbation, spectral case

Figures 1 and 2 give $\Delta\phi$ versus x_f/λ_0 for two different widths, $w_f/\lambda_0=15$ (Fig. 1) and $w_f/\lambda_0=2.5$ (Fig. 2). Obviously, there are two distinct behaviors. For wide perturbations, the phase response reproduces the spatial features of the perturbation: it has the same width w_f and the same modulation wavenumber k_f. Its maximum occurs at the usual Bragg position $x_B=k_f^2/4k_0^2$. Indeed the spectrum of large perturbations is sharply peaked at $k=k_f$, hence the Bragg rule scans the perturbation as it moves down the density gradient. Afeyan et al [3] have made an asymptotic analysis of this case and found

$$\Delta\phi \approx -\pi^{1/2}\frac{k_0L^{1/2}}{k_f^{1/2}}\frac{\delta n_0}{n_{cr}}\exp\left[-\frac{(x_f-x_B)^2}{w_f^2}\right]\sin(k_fx_f+\psi_G) \qquad (4)$$

$$\psi_G = \frac{4}{3}k_0L^{-1/2}x_B^{3/2} - k_fx_B + \pi/4$$

For the perturbation of Fig. 2, the phase response is now much broader than the perturbation itself. In addition, its modulation wavenumber varies continuouly. Indeed, the perturbation Fourier spectrum of the perturbation $\delta n(\chi)$ has a finite width, so that a given χ-component can resonantly scatter the incident wave at the location $x\neq x_B$ where the local Bragg rule $x=\chi^2L/4k_0^2$ is satisfied. As a result the phase response is an image of the Fourier spectrum. For this case, the expression of the phase response is

$$\Delta\phi \approx -\frac{\pi^{1/2}}{2}k_0w_f\frac{\delta n_0}{n_{cr}}\left(\frac{L}{x_f}\right)^{1/2}\exp\left[-\frac{k_0^2w_f^2}{L}(x_f^{1/2}-x_B^{1/2})^2\right]\sin\left(\frac{4\,k_0}{3L^{1/2}}x_f^{3/2}\right) \qquad (5)$$

It can be shown that the transition between these two cases (spatial and spectral) is given by a critical width

$$w_c = \left(\frac{k_f L}{k_0^2}\right)^{1/2}$$

It is interesting to study the case of perturbations with different spectral properties such wavetrain. In order to distinguish phenomena near the cutoff and near the usual Bragg po x_B, we choose a large gradient length $L = 1000\lambda_0$ and $k_f = 0.6k_0$.

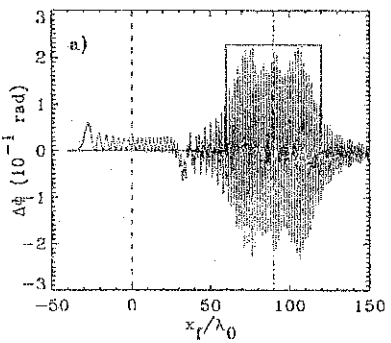


Fig. 3- Wavetrain, spatial case

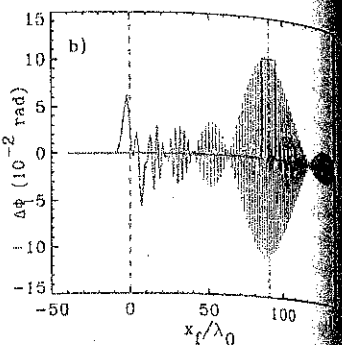


Fig. 4- Wavetrain, spectral case

The case of a wide pulse, $w_f = 30\lambda_0$ is shown on Figure 3. The phase response repro the spatial shape of the perturbation, that is, the amplitude stays roughly constant as long Bragg position x_B is in the pulse. However, because of the sharp boundaries perturbation envelope, there are always spectral effects whatever the width of the pulse is

For narrow pulses, $w_f = 5\lambda_0$, the spectrum shape $(\sin\chi/\chi)$ of a square funct clearly reproduced on Figure 4. An asymptotic analysis leads to the phase shift

$$\Delta\phi \approx -k_0 \frac{\delta n_0}{n_{cr}} \left(\frac{L}{x_f}\right)^{1/2} \frac{\sin[2k_0 w_f (x_f^{1/2} - x_B^{1/2})/L^{1/2}]}{2k_0 (x_f^{1/2} - x_B^{1/2})/L^{1/2}} \sin\left(\frac{4}{3} \frac{k_0}{L^{1/2}} x_f^{3/2}\right) \quad (7)$$

where the Fourier spectrum shape $\sin(\chi)/\chi$ appears.

4. Cutoff response due to sharp boundaries.

Another consequence of the sharp boundaries is shown on Figure 5. It displays case of a wavetrain with $k_f/k_0=2$ and $w_f/\lambda_0=10$, and a density gradient length $L/\lambda_0=100$ such a value of k_f there is no Bragg location x_B, but there is a now a significant response a cutoff. This is very different from the Gaussian case, where the cutoff response is negligi the Born approximation. An evaluation of the phase integral leads to the expression contribution of the leading edge

$$\Delta\phi \approx (4\pi^2)^{2/3} \frac{\delta n_0}{n_{cr}} \frac{k_0}{k_f} \left(\frac{L}{\lambda_0}\right)^{1/3} \mathrm{Ai}^2\left(\frac{x_f k_0^{2/3}}{L^{1/3}}\right)$$

similar contribution from the trailing edge ...rise to the interference pattern seen on ...of Figure 5. This Ai^2-like variation is ...reproduced on Figure 5. Contrarily to the ...of Bragg scattering, the cutoff response ...for large fluctuation wavenumbers k_f.

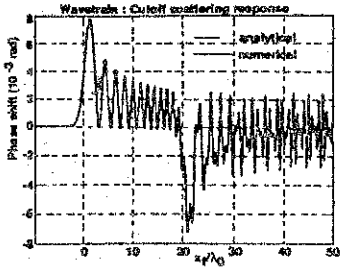


Fig. 5- Phase response of a wavetrain in the cutoff region

Conclusions

...phase response of an ordinary mode reflectometer to a modulated perturbation of finite size ...shown both numerically and analytically calculated. The agreement between the analytical ...pressions and the numerical computations is excellent. The scaling of the maximum phase ...$\Delta\phi_m$ versus the physical parameters L/λ_0, $k_{f/k0}$ and w_f/λ_0 depends upon the value of w_f ...respect to a critical length w_c. For $w_f > w_c$, the phase response is an image of the ...perturbation and the scaling of $\Delta\phi_m$ is $(L/k_f)^{1/2}$. For $w_f < w_c$, the phase response is an image ...the Fourier transform of the perturbation and $\Delta\phi_m$ does not depend on L and the scaling is ...Finally, a wavetrain produces a phase response in the cutoff region and $\Delta\phi_m$ scales as ...k_f. Therefore, the phase response of a wavetrain at large k_f (i.e. when there is no Bragg ...filtering, $k_f/k_0 > 2$) is much larger than that of a modulated Gaussian. The maximum phase ...for these regimes is summarized in Table 1.

Bragg (WKB region)		Bragg (cutoff)
Spatial regime	Spectral regime	Sharp edge effects (Square)
$w_f^2 > \frac{Lk_f}{k_0^2}$	$w_f^2 < \frac{Lk_f}{k_0^2}$	
$\sqrt{2\pi}\left(\frac{L/\lambda_0}{k_f/k_0}\right)^{1/2} \times \frac{\delta n_0}{n_{cr}}$ (Gaussian and Square)	$4\pi B \frac{k_0}{k_f}\frac{w_f}{\lambda_0} \times \frac{\delta n_0}{n_{cr}}$ $B = \pi^{1/2}/2$ (Gaussian) $B = 1$ (Square)	$0.29(4\pi^2)^{2/3}\frac{k_0}{k_f}\left(\frac{L}{\lambda_0}\right)^{1/3} \times \frac{\delta n_0}{n_{cr}}$

...ble I. Maximum phase shift $\Delta\phi_{max}$ (last row) for the different cases.

References

...] Zou XL *et al*, *Plasma Phys.Control. Fusion* **33**, 908 (1991) - Bretz N, *Phys Fluids* B4, ...(1992) - Mazzucato E and Nazikian R, Plasma Phys Control. Fusion 33, 261 (1991)
...] Moyer RB, Chou AE and Cohen BI, *Plasma Phys. Control. Fusion* **37**, 315 (1995).
...] C. Fanack *et al*, *22nd EPS Conf. Control. Fusion Plasma Phys.* **19C** , IV 409 (1995).

Current density profile evolution measured with the triple l... polarimeter at RTP

F.A. Karelse, J.H. Rommers, A.J.H. Donné, G.M.D. Hogeweij,
J. Howard*, Th. Oyevaar, F.C. Schüller and the RTP-Team
FOM-Instituut voor Plasmafysica "Rijnhuizen", Associatie Euratom-FOM, Postbus ...
3430 BE Nieuwegein, The Netherlands
**) Plasma Physics Laboratory, Australian National University, Canberra A.C.T. 02...*
Australia

Introduction

The Rijnhuizen Tokamak Project RTP (R_0= 0.72 m, a= 0.164 m, $B_T \leq$ 2.35 T, $I_p \leq$ 180... dedicated to the study of transport processes in tokamaks. As one research line, (simult... perturbations of the electron temperature (T_e), electron density (n_e), and current den... are used to probe the transport matrix.
In order to measure the j profile, the 19-channel heterodyne interferometer has been ex... with a polarimeter. In this paper, first measurements of evolving j profiles as determ... the polarimeter are presented. The j profile has been perturbed by means of pellet in... and ramps of the plasma current (I_p). The perturbation and subsequent relaxation h... measured, both in ohmic discharges and during Electron Cyclotron Heating (ECH).

Polarimeter

The interferometer/polarimeter consists of three Far Infrared (FIR) lasers pumped by a CO_2-laser. The system is described in detail in [1]. The main feature is that both the in... ometer signal (phase shift φ) and the Faraday rotation angle (α) are measured with a... detector per channel. This is accomplished by using two counter-rotating circularly po... probing beams, which represent the two characteristic propagation modes in the plasm... hence experience slightly different refractive indices (Faraday effect). The third laser gi... reference beam. A slight frequency difference between the three lasers leads to three fre... separated beat signals, thus enabling separate phase measurements on each of them. T... these signals are due to mixing of the local oscillator beam with either of the probing b... The averaged phase change of these beams corresponds to φ, whereas the difference yi... The phase change of the third beat signal, the mixing of the two probing beams, give... rectly.
The polarimeter data is filtered to a temporal resolution of 1 ms and a measurement e... 0.3 degrees, which in large part is due to as yet unsolved systematic errors. Figure 1... typical time traces of α and φ for one channel.

Data analysis

First the n_e profile is determined by Abel inversion of the interferometer data [2].
Since the central safety factor (q_0) is a parameter that immediately reflects a global cha... the j profile, we concentrated on the determination of q_0. As it is hard to get a reliable ... reconstruction of j, some parametrization of j is needed. For this purpose, the following ... has been used [3, 4]:

$$j(\rho) = j(0)\left(1 + (\frac{q_a}{q_0} - 1)\rho^2\right)^{-2},$$

where ρ is the normalized radius and q_a is the edge safety factor, determined by global p... parameters. q_0 is the free parameter to be fitted.

almost completely determined by the five inner channels, only these were used in the ... was evaluated by a reduced χ^2 test; fitted q_0 outside the 95% confidence interval ... error bars) were rejected.

... ramps

... high density, low q_a discharges have been analysed. In these discharges I_p was ... from 90 ($q_a = 4.4$) to 120 kA ($q_a = 3.3$) or vice versa in a time τ_{ramp} of 15-30 ms. In ... central ECH was applied during the ramp phase.

... current ramp, which is a perturbation from outside the plasma, q_a is changed ... while the q-profile relaxes to a new equilibrium in the magnetic diffusion time, for RTP ... 20 ms in Ohmic discharges and a factor of 2-5 longer in EC heated discharges.

... shows the result of the q_0-fit for a EC heated discharge (heating pulse from 100 to 275 ... which I_p was ramped down between 170 and 185 ms; χ^2 is plotted as well, showing that ... good quality fits in this case. Some increase of q_0 is observed, from an average level ... before the ramp, till ~ 1.0 after relaxation to the lower I_p. This small increase of q_0 is ... by the modest decrease of the inversion radius (r_{inv}), as observed by ECE. However, ... value of the inferred q_0 is slightly higher than expected; it should stay below 1.0 ... do not disappear at the lower I_p level. Due to the spatial resolution of the ECE ... (~1.5 cm), r_{inv} is not determined very precisely from the ECE data. Alternatively, ... use the assumption $q_a \cdot r_{inv} = a$ [4], which yields $q_0 = 0.76$ and 0.81 at the high and ... respectively; it predicts the change of q_0, but again the measured values are too ...

... disturbed plasmas

... pellets of two sizes can be injected into RTP. A small pellet contains $0.5 \cdot 10^{19}$ atoms, ... equals half the number of ions in a typical target plasma with $n_e(0) \simeq 6.5 \cdot 10^{19} m^{-3}$; ... pellet is 4 times larger. In total 16 discharges ($q_a = 3.3$) with pellet injection were anal- ... among which 11 with small pellets and five with large pellets. In half of the discharges ... switched on 8 ms after pellet injection, in order to reheat the plasma quickly and ... the relaxation of the perturbed j profile.

... expected effect of an injected pellet on j depends on its penetration depth. A pellet which ... reach r_{inv} causes T_e to drop only in the outer part of the plasma. On the other hand, ... penetrating beyond r_{inv}, flattens T_e to a uniform low value of typically 100-200 eV in ... [5]. Hence, the effect on j is expected to be peaking in the first case and flattening in the ... case.

... pellets the penetration depth varied between 5 and 7 cm. In these cases, no effect ... polarimeter data could be seen exceeding the error bars. Simulations indicate indeed a ... change of $j(0)$ of a few % only.

... pellets have a completely different effect: they do penetrate to the centre and cool the ... plasma dramatically. Fig. 3 shows the fitted q_0 together with χ^2 for a discharge with a ... tailoring at $t = 167$ ms and ECH starting at 175 ms. A marked increase of q_0 is observed, ... a maximum at ~ 20 ms after the pellet ablated.

... 15 ms no reliable fits could be obtained. In this time interval sharp density gradients ... increase the refraction of the laser beam, thus causing a drop of the signal level by $\simeq$ ... and hence a reduced S/N ratio. This partially explains the increased χ^2. The very large ... of χ^2 in the first few ms after pellet injection, however, indicate that Eq. 1 does not ... the strongly perturbed j profile well in this transient phase.

... has been compared with the evolution of q_0 predicted by a numerical simulation of the ... diffusion (full line in Fig. 3). In this simulation profiles of T_e measured with Thomson ... at various time slices after pellet ablation have been used as input, assuming Spitzer ... and $Z_{eff} = 2$. It can be concluded, that the measured rise of q_0 is well in agreement ... the prediction. However, the observed time scale of the perturbation is clearly slower than ... whilst the return to the standard ohmic j profile goes faster than predicted. No

explanation for this has been identified yet.

Conclusions

First measurements of evolving j profiles in RTP have been reported. The effect of ramp on q_0 is observed to be small, in agreement with the behaviour of r_{inv}. Large pell a strong flattening of j; an increase of q_0 by a factor of 2 has been observed. Generally, the inferred value of q_0 seems to be slightly higher than expected; the ca is under investigation. The used parametrization of j fails for heavily perturbed j pr are seen shortly after pellet ablation; a more suitable parametrization for such cases for.

A systematic study of the effect of ECH on the relaxation of j is subject of future st availability of measurements of the j profile opens the way to analysis of simultaneou bations of T_e, n_e and j.

Acknowledgements

This work was performed under the Euratom-FOM association agreement with fina port from NWO and Euratom.

References

[1] J.H. Rommers and J. Howard, Accepted for publication in Plasma Phys. Contr. Fusion
[2] N. Gottardi, J. Appl. Phys. 50(4) (1979), 2647-51.
[3] B.B. Kadomtsev, Phil. Trans. R. Soc. Lond. **A322** (1987), 125-31.
[4] F.C. Schüller *et al*, Proc. 18th Conf. Contr. Fusion Plasma Phys. 4 (1991), 185-88.
[5] Da Cruz *et al*, Phys Rev. Lett. **75** (1995), 3685.
[6] J. de Kloe, This Conference.

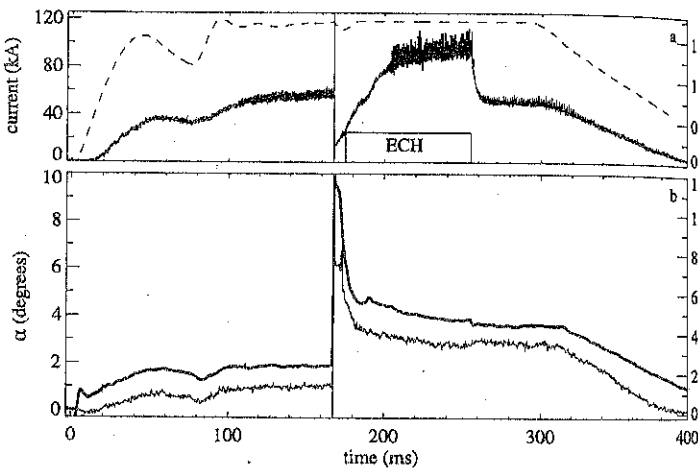


Figure 1: a) Time trace of the plasma current (dashed) and the central radiation temperatur from ECE measurements [6] (solid) with pellet injection at $t = 167$ ms. The block indicates the interval of ECH.
b) Typical polarimeter signal α (thin) and interferometer signal φ (thick) at $r/a = 0.61$.

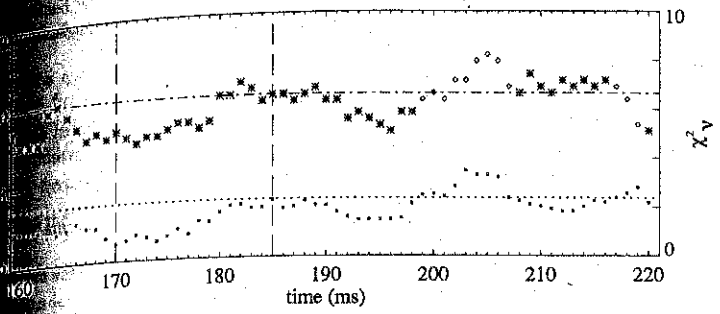


Figure 2: Time trace of q_0-fit of eq. (1) to the five inner channels of the polarimeter with a current ramp down between t = 170 and 185 ms (vertical lines) and ECH from 100 to 275 ms. Indicated is whether the fit point falls inside (stars) or outside (diamonds) 95% of the fit distribution. The small squares give the reduced χ^2 values corresponding to the fit points. The dashed line is the 95% confidence level.

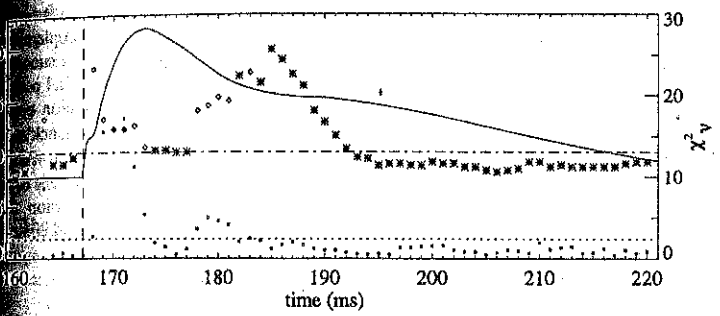


Figure 3: Time trace of q_0-fit of eq. (1) to the five inner channels of the polarimeter with pellet injection at t = 167 ms (points) and q_0-trace from magnetic diffusion simulation (solid line). Indicated is whether the fit point is within (stars) or outside (diamonds) 95% of the fit distribution. Just after the pellet, the fit is also outside 99.5%. The small squares give the reduced χ^2 values corresponding to the fit points. The dashed line is the 95% confidence level.

DETERMINATION OF THE TEMPERATURE OF NON-HOMOGENEOUS AND NON-STATIONARY PLASMA

B.Gross, *V.Zdrazil
Dept. of Electrical Machines & Apparatus, *Dept. of Physics; Faculty of Electrical Engineering and Computer Science, Technical University of Brno, Czech Republic

One of the methods for determing the plasma temperature is the method based on the reversal of certain spectral lines of radiation emanating from the plasma. The method has derived by Bartels [3], [4] and starts out from four very general assumptions:

1. One of the requirements is that the plasma is axially symetrical.
2. It is assumed that the intensity of the spontaneous radiation of the plasma decr monotonously from the axis of the plasma to its fringes.
3. It is assumed that in the frequency range of the considered spectral line the inten the spontaneous radiation of the plasma is constant.
4. Also in the frequency range of the considered spectral line the value of the absorp coefficient must drop monotonously from its maximum in the centre of the line minimum at the fringe of the line, i.e. in proportion with the growing differenc frequencies with regard to the centre of the line.

A plasma of a cylindrical shape satisfies the above conditions, as well as the spectral emitted by it. If the temperature of the internal parts of the plasma is not too high, it can assumed that the radiation emanating from the plasma is a predominantly spontan radiation. The electric arc plasma practically satisfies all the above stipulated assumptions accordance with Kirchhoff's radiation law under thermodynamic equilibrium conditions spectral density of the irradiation intensity depends only on the absolute temperature of emitter and the wavelength of the emitted radiation. By further deliberations, supplemented the requirement for the existence of a local thermodynamic equilibrium, Bartels succeeded finding a connection between spontaneous emission and temperature. This mutual connec is not in the first approximation unambiguous, since the intensity of the radiation emana from the peaks of the self-reversal can in one marginal case be governed by Planck's law radiation and in the other marginal case by Wien's law. The conditions in the electric plasma approach more the validity conditions of Wien's radiation law. On the basis of furt deliberations and mathematical rearrangements Bartels arrived at the conclusion that maximum temperature on the investigated beam which lies in a plane perpendicular to plasma axis, is equal to the expression

$$T_{\max} = T(r)_{r=v} = \frac{T_w(\nu)}{1 + \frac{kT_w(\nu)}{h\nu} \ln\left[M_\infty(\nu) Y_{\max}\left(P_\infty(\nu)\right)\right]} \qquad (1)$$

where r is the radial spacing from the plasma axis,
v is the spacing of the observed radiation beam from the plasma axis,
k, h are the Boltzmann's and Planck's constants, respectively,
ν is the frequency of the spectral line,

T_W is the temperature named according to Bartels the Wien temperature, since it is determined with the aid of Wien's radiation law by measuring the radiation intensity which emanates from the peaks surrounding the self - reversal.

The quantities M and p are parameters, the values of which depend on the frequency spacing from the centre of the investigated spectral line and on further quantities which characterize the physical properties of the plasma. But with a growing frequency spacing the values of these parameters approach the limiting values denoted M_∞, p_∞ which are no longer frequency dependent. The expressions for $M_\infty(\nu)$ and $p_\infty(\nu)$ are, however, extensive and are therefore not presented here. They can be found in the original Bartels papers.

The quantity $Y_{max}(p_\infty(\nu))$ has also been derived by Bartels and represents a solution of a transcendental equation. Its explicit expression is very complicated. For practical purposes it can, however, be replaced by the approximation

$$Y_{max}(p) = 0.736 + 0.264\,p^2$$

which has also been introduced by Bartels.

The equation (1) and the relationships for $M_\infty(\nu)$, $p_\infty(\nu)$ represent a system of equations for the determination of the maximum temperature on the observed radiation beam. An explicit solution of this system of equations is very complicated and therefore is being employed a computer aided iteration method.

At the beginning of the iteration, in the so called zero step, it is necessary to know the limiting values $M_\infty(\nu)$, $p_\infty(\nu)$. Bartels denoted these values as $M_{\infty G}$, $p_{\infty G}$ and specified them

$$M_{\infty G} = \sqrt{\frac{\vartheta_h}{\vartheta_i}} \qquad p_{\infty G} = \frac{6}{\pi} arctg \frac{\frac{\vartheta_h}{\vartheta_i}}{\sqrt{1+2\frac{\vartheta_h}{\vartheta_i}}}\,.$$

The parameters ϑ_h and ϑ_i, respectively are functions of the excitation and ionization voltage, respectively of the atoms of the element whose spectral line with self - reversal is being monitored. Upon the inclusion of collisions of plasma particles with electrons holds true

$$\vartheta_{h,i} = \frac{kT_W}{eV_{h,i} + \frac{1}{2}eV_j}$$

where V_h, V_i are the excitation voltages of the upper and lower term, respectively. V_j is the ionization voltage.

For a maximum temperature on the investigated beam in the zero step of the iteration holds true

$$ {}^{(0)}T(r)_{T=v} = \frac{T_w(v)}{1 - \frac{kT_w(v)}{h\nu} \cdot \frac{h\nu\left[M_{\infty G} Y_{\max}\left(p_{\infty G}\right)\right]}{1 - \frac{\vartheta_h}{\vartheta_l}}} $$

where the index on the top left for T(r) indicates the degree of iteration.

The thus computed temperature will be used for the determination of the quantities $M_{\infty}(v)$ and $p_{\infty}(v)$ which are then substituted into equation (1) and the whole procedure is repeated. If the difference of temperatures determined in the steps k and (k+1) of the iteration is smaller than the preselected arbitrarily small positive number, the iteration can be terminated, since the temperature has already been determined with the preselected degree of accuracy.

The presented method has hitherto been utilized for determining the temperature of a non-homogenous plasma in the stationary state. By the application of a suitable stroboscopic device the authors have succeeded in expanding the employment of this method also onto a non-homogenous plasma in a non - stationary state, i.e. onto a plasma of an electric arc fed by an AC current with an RMS value of 23.5 A and a frequency of 50 Hz. One copper and one carbon electrode was used. There have been observed the spectral lines of copper with the wavelengths 324.8 nm and 327.4 nm which exhibit a perceptible self - reversal. The stroboscopic device enabled the observance of the spectral lines for an arbitrarily long time with always the same preselected value of the AC current phase. Thus have been obtained radial temperature waveforms for various phase values (Fig. 1).

In Fig. 2 can be seen the dependence of temperature on time at points at a distance r from the axis of symmetry of the plasma. Along the horizontal axis are plotted values of the AC current phase. It can clearly be seen that in one half - period the temperature values are in the entire plasma volume lower than in the neighbouring half - period. This is apparently caused by the unequal thermal conductivity of the materials of the two electrodes. Copper apparently dissipates from the plasma more heat than carbon. During the half - period when copper is the anode, there occurs an overall temperature drop in the entire plasma volume.

In Fig. 3 is shown the temperature hysteresis of the plasma in the points on the axis of symmetry of the electric arc. The maximum (and minimum, respectively) of the plasma temperature and the maximum (and minimum, respectively) of the AC current are not attained at the same moment. The temperature values lag behind the current values.

In Fig. 4 there is then the spatial illustration of the radial temperature waveforms. Also here can readily be seen that the temperatures attained in mutually neighbouring half - periods are different.

Both computations and charts have been executed by the Excel 5 table processor.

References: [1] Bartels H.: Zeitsch. für Phys., 125 (1949), p. 597
[2] Bartels H.: Zeitsch. für Phys., 126 (1949), p. 108
[3] Bartels H.: Zeitsch. für Phys., 127 (1950), p. 243
[4] Bartels H.: Zeitsch. für Phys., 128 (1950), p. 546

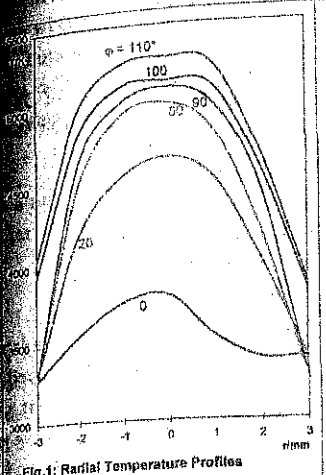


Fig.1: Radial Temperature Profiles

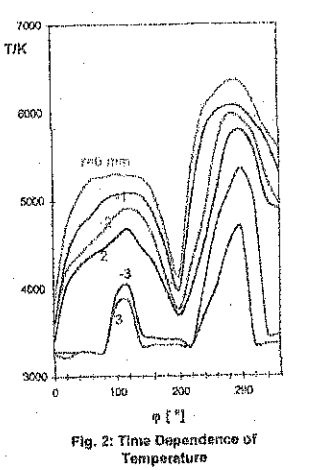


Fig. 2: Time Dependence of Temperature

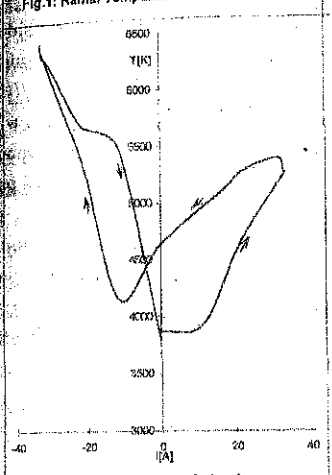


Fig. 3: Dynamical Characteristic of Temperature.

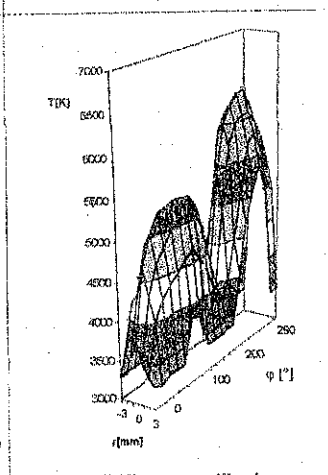


Fig. 4: Radial Temperature Waveforms.

Plasma Boundary Determination from Magnetic Measurements in Eddy Currents Presence for Tokamak

(Kiev, Ukraine, 24–28 June 1996)

V. F. Gubarev, N. N. Aksenov
Glushkov Institute of Cybernetics National Academy of Sciences of Ukraine
40, Acad. Glushkov Prsp. 252650 MSP, Kiev 22, Ukraine
Phone: (044) 266-2128 Fax: (044) 266-4124
E-mail:gvf@d310.icyb.kiev.ua
aks@d310.icyb.kiev.ua

1 Introduction

The approach of solving the plasma configuration reconstruction problem from external magnetic measurements in eddy currents presence is developed. It is proposed to substitute the eddy currents by the system of equivalent circular filaments located at the same area. Since the eddy currents are passive system with short in comparison with plasma discharge duration time dumping lumped electrical circuit model with uncertain coefficients is introduced for consideration of eddy currents evolution. Uncertain coefficients are determined by means of system identification based on magnetic measurements.

As for plasma the current filaments system are chosen in accordance with approach [1]. The filaments position and currents values in substitution model are determined from external magnetic measurements by the solving inverse problem using regularization.

The developed method permits the fast and accurate plasma position and shape determination in real time discharge. So it may be used for plasma and magnetic configuration control system in modern tokamak like ITER where it is necessary to take into consideration eddy currents because they cause magnetic field affecting plasma equilibrium.

2 The substitution models

The approach based on current filaments that substitute for the real plasma and eddy currents distribution is developed for this aim. Instead of real toroidal plasma current distribution $j_\phi(r, z, t)$ we introduce N_p circular current filaments located

$\{(r_i, z_i); i = \overline{1, N_p}\}$ of the plasma region. Number N_p of filaments, its ... and current values I_{0i} in each of it are evaluated so that external magnetic ... with appropriate accuracy is close to real one formed by plasma ... distribution j_ϕ.

... known values I_{0i} and positions r_i, z_i, N_p can be found from minimization of ... functional

$$\omega = \sum_{j=1}^{N_m} (y_j - y_{cj})^2 / \sigma_j^2. \tag{1}$$

... is a number of measured channels, y_j are the measured values of y_{cj}, σ_j ... standart error of the j-th measurement, y_{cj} are the field values defined by

$$\Psi(r, z, t) = \sum_{j=1}^{N_p} \Psi_0(r, z, r_i, z_i) I_{0i}(t), \tag{2}$$

... is Green function. It is obviously supposed that poloidal coils contribu- ... substracted from measured values y_j. The same way this procedure was ... ded on eddy currents. Real eddy currents in plasma surroundings are ... by N_e circular current filaments located where eddy currents may arise. ... additional N_e components are emerged in expression (2). It is convenient ... as a substitution vector of plasma currents, I_e as a substitution vector ... currents and $I^T = \{I_0^T, I_e^T\}$ as a total vector of the substitution currents. ... the minimization problem (1) is ill-posed one especially when dimention ... become large. In this case the solution of the problem (1) is sensitive ... errors in input data that is unstable. Regularization is used to provide ... stabilization of the solution. The smoothing functional $\omega + \alpha\Omega(I)$ may be ... instead of the residual one (1). Here $\Omega(I)$ is a stabilizer and α is a ... of regularization. The substitution eddy currents in contrast to plasma ... posses the significant peculiarity. During the stationary state and slow ... eddy currents are damping.

... the set of the desired solutions (1) may narrow down if the dynamic substi- ... model for induced currents is used in the capacity of constraint. The rough ... of acceptable model for induced currents in surroundings is described in ... which in many cases has the form

$$\mathcal{L}(I_e, L, R, M, J) = L\frac{dI_e}{dt} + RI_e + M\frac{dJ}{dt} = 0, \tag{3}$$

... J is a vector composed by plasma current and poloidal coils currents; L and ... matrices of a mutual induction, R is a diagonal matrix of resistances.

Matrices coefficients L,R,M are initially unknown. Therefore the system id
fication is used for its determination. Toward this end the developed in [3] m
is applied which permits to realize joint estimation of total substitution curr
and matrices L, R, M on the base of magnetic measurements. In accordance
[3] the observation interval $[t_0, T]$ is considered and minimization problem (
transformed to the minimization of the following smoothing functional

$$W = \int_{t_0}^{T} (w + \beta \mathcal{L})\, dt$$

Here β is a positive weighting coefficient that depends from i) noise ξ in mea
ment channels ii) sufficiency of the substitution currents and iii) mapping o
description (3) to the real dynamic processes. If level of noise in measuremen
negligible and substitution currents provide a good fitting similar to ideal
model (3) describes the processes inaccurately then $\beta \to 0$. Conversely it is
essary to choose value β as much as possible for equal to the real description
and for high level of noise. In all other cases as computational study shows
exists optimal value although it is not so indicative.

Practically without regularization it is impossible to find the element mini
ing the functional (4) and to realise joint substitution current I estimation
matrices L, R, M identification. The method based on introducing the stab
$\alpha\Omega$ in functional (4) is proposed. As a result the smoothing functional W
defined as follows

$$W_\Omega = W + \alpha\Omega(I, L, R, M)$$

As stabilizer Ω it is recommended to take the following combined expression

$$\Omega = \int_{t_0}^{T} I^2\, dt + \gamma \left(\sum_{i=1}^{N_e} \sum_{j=1}^{N_o} l_{ij}^2 + \sum_{i=1}^{N_e} r_i^2 + \sum_{i=1}^{N_e} \sum_{j=1}^{N_o} m_{ij}^2 \right)$$

where N_J is a dimension of vector J; γ is a weighting coefficient that provides a
uniform dimension for (6).

Regularization parameter α may be choosen in accordance with principle of t
residual which was developed in the theory of ill-posed problem. But in reality t
α value should be optimized with the noise and errors taken into account usi
numerical simulation.

Solution of the problem

of general minimizing problem based on (5) it is proposed to decompose a few more simple one. The quasistationary phase of the discharge with considered first. In this case the problem is turned into well known and determination of substitution currents for plasma only [1]. Acceptable for the coordinates of plasma current filaments and value of regularization may be found through the solving of simplified problem. Identification L, R, M may be also considered as independent problem. It is desirable statistics for best result. As numerical simulations shows the appropriate value of coefficient β is defined by equality $\beta = ||h||/||\xi||$ where $||\xi||$ is noise in measurement channels and $||h||$ is a norm of substitution model for given observation interval. The trial-and-error method is a possible way the suitable γ value in real tokamak condition.

system identification is a key problem for magnetic configuration reconin eddy currents presence. Numerical studies were held for choice of identificator and computational scheme of its realization. For simthe eddy currents are substituted one loop with two unknown parameters: time $\theta = l/r$ and looping coefficient $m/l = k$. First direct problem was for given θ_0 and k_0. Then measured values y_{cj} without noise and with noise evaluated. The solution of inverse problem in accordance with identification described in [3] gives a sharp estimation θ_0 and k_0 for case without noise. After that the intensity of noise are varied. The explicit dependence of $\theta \to \theta_0$ and $k \to k_0$ was obtained.

References

[1] Yu.K. Kuznetsov. The ITER Tokamak Plasma Magnetic Diagnostics. Plasma Physics Reports. Vol. 20, No 2 (1994) pp. 132-139

[2] Yu.I. Samoylenko, V.F. Gubarev and Yu.G. Krivonos. The Control of High Speed Processes in Thermonuclear Devices. Kiev, Naukova Dumka (1988) 384p. (Russian)

[3] V.F. Gubarev, N.N. Aksenov. The Solution of Estimation and Identification Problems by the Regularization Method. Problems of Control and Informatic. No. 5-6, 1994, pp. 21-29 (Russian)

G

BASIC COLLISIONLESS PLASMA PHYSICS

Percolation scaling law for turbulent diffusion.

J. H. Misguich, J.-D. Reuss.

Association Euratom-CEA sur la Fusion, DRFC,
Centre d'Etudes de Cadarache,
F-13108 Saint-Paul-lez-Durance Cedex (France).

Introduction:

...perties for transport laws in hot magnetized plasmas are presently of huge ...ecially in the perspective of building future large Tokamaks like the ITER ...the dependence of particle diffusion as function of the magnetic field strength, ...ading $D \simeq (1/B)^\gamma$ are considered in different cases: *gyro-Bohm* scaling ($\gamma = 2$), ...ling ($\gamma = 1$) or *Goldston* scaling ($\gamma = 0.5$), (see Petty, Luce *et al.*, 1995). Which ...oretical predictions for electrostatic turbulence ?

Problem:

...sider transport of particles in a strongly magnetized plasma (shearless slab), in ...ce of a k-spectrum of electrostatic turbulence with an average frequency of order ... particle drift motion is described by the non-linear (Langevin) equation

$$\frac{d}{dt}\mathbf{x}(t) = \frac{c}{B^2}\,[\mathbf{E}(\mathbf{x}(t),t)\times\mathbf{B}] \tag{1}$$

... B is parallel to the $z-$axis, and where the fluctuating electric field has components ... (x,y) plane, described by a k-spectrum between k_{min} and k_{max} around k_* and ...quency around ω_*.

Predictions for the diffusion scaling:

...aling properties of the diffusion coefficient can be represented for dimensional reasons

$$\boxed{D \simeq \frac{\omega_*}{k_*^2}\,A^\gamma} \tag{2}$$

...terms of the only dimensionless parameter A (Kubo number):

$$\boxed{A \equiv \frac{V_d\,k_*}{\omega_*}} \qquad \text{where} \qquad V_d \equiv c\frac{E}{B} \tag{3}$$

Different scaling are well-known in this simple problem. For $A \ll 1$, a general agreement considers that a quasi-linear scaling applies: $\gamma_{QL} = 2$ (*i.e.* transport in $1/B^2$). For $A \gg 1$, ...Bohm like scaling $\gamma_B = 1$ (*i.e.* transport in $1/B$) has often been considered: it comes from ...oretical predictions by Dupree (1967), Taylor-McNamara (1971), Montgomery (1975),

Misguich *et. al.* (1987), etc... It is also found *"in agreement"* with numerical simul
by Pettini *et. al.* (1988), De Leener *et. al.* (1987), Misguich *et. al.* (1989). But i
finally been rigorously proved to be *impossible*, by Grusinov, Isichenko and Kalda (1

So, for $A \gg 1$ a **percolation scaling** $\gamma_I = 7/10$ (*i.e.* transport in $1/B^{0.7}$) has
predicted by Isichenko (1990). The idea starts from the fact that for high values of
low values of the frequency, the potential "landscape" is almost the frozen, or critical
this statistical topography and the geometrical properties of the fractal potential c
are dominant for determining the motion of particles near the threshold of "percolat
The scaling exponent γ_I is deduced by using critical exponents from percolation th
We note that this result is <u>not</u> confirmed by the numerical simulations by Ottaviani (1
We present here a *first numerical confirmation* of this percolation scaling exponent (R
Misguich, 1996), at least for the model described below.

4. Model for the electrostatic potential

The model we consider is based on the following elements. The electrostatic pot
is composed of a set of plane waves with amplitudes distributed with a k^{-3} spect
This spectrum agrees reasonably well with Tokamak observations, along with theoret
predictions of $k^{-17/6}$(Terry and Diamond, 1985) or $k^{-10/3}$ (Zhang and Balescu, 19
Wavevectors are chosen in a circular annulus (k_x, k_y) between radii k_{min} and k_{max} m
suring the width of the spectrum. Spatial discretization is performed in a box $L_x L_y$
$L = N\lambda_{min} = N_0\lambda_{max}$, involving a few ($N_0 = 4$) large wavelengths λ_{max}, and
($N = 48$) small wavelengths λ_{min}. Wavevectors are discretized in the wavenumbers (n, m
expressed in units of the elementary wavevector $k_0 \equiv 2\pi/L$. Each plane wave has a separ
and random phase $\varphi_{n,m}$. The electrostatic potential considered takes the form

$$\Phi(x,y,t) = \frac{a}{2\pi} \sum_{n=-N}^{N} \sum_{m=-N}^{N} \frac{\Theta(n,m;N_0,N)}{(n^2+m^2)^{\frac{3}{2}}} \cos\left[\frac{2\pi}{L}(nx+my) + \varphi_{n,m} - \omega t\right] \quad (6)$$

where the Heaviside distribution $\Theta(n,m;N_0,N)$ is zero for values of (n,m) out of the
cular annulus. With the above parameters, the standing wave-ensemble involves 7
randomly phased waves with a periodically oscillating energy density. Since the ampli
of these oscillations depend on the realization choosen for the random phases, we ca
fully choose one among the representative realizations which have the "most probab
amplitude of fluctuations of the energy $\mathcal{E}(t)$.

5. Equation of motion

We simulate test particles which follow the electric drifts and satisfy the equations

$$\frac{d}{dt}\begin{pmatrix} x \\ y \end{pmatrix} = \frac{c}{B}\begin{pmatrix} -\nabla_y\Phi(x,y,t) \\ \nabla_x\Phi(x,y,t) \end{pmatrix} \quad (7)$$

which describe a non-autonomous Hamiltonian system with $H \equiv -\frac{c}{B}\Phi(x,y,t)$.

...erical simulation

...allel computer CRAY T3D, using 64 (among 128) elementary processors. ...ographies of the fields are kept in memory on a lattice of $M \times M$ pixels in ...o square L^2 ($M = 512$), with interpolations within the 16 nearest neighbouring ...e dependence of the electric field is calculated from a memorized table of values ...) and $\sin(\omega t)$ at each time step. The motion of an ensemble of $\mathcal{N} = 64$ test ...calculated in a given realization, by a 4th order Runge Kutta algorithm. The ...efficient is measured from the "asymptotic" slope of the root mean square ...(RMS). The RMS is averaged over the $\mathcal{N}$ trajectories and moreover over ...stroboscopic position taken as new "initial" conditions (time average).

...erical results

...nsionless diffusion coefficient

$$\mathbb{D} \equiv \frac{2\pi}{\omega\, \lambda_{max}^2} D \tag{6}$$

...only depends on

$$A \equiv \frac{2\pi}{\lambda_{max}} \frac{cE}{\omega B}, \tag{7}$$

...in a given scaling regime. Here $E = \sqrt{8\pi \langle \mathcal{E}(t) \rangle_\omega}$ is a measure of the electric ...plitude. The results obtained in the domain $A \gg 1$ are represented in **Fig.1** where ...represented, for each of the four values of the amplitude, the set of four results ...ting the diffusion coefficient obtained for a different set of $\mathcal{N} = 64$ particles. The ...ations of the results allow for an estimate of the error bar on the slope (Birge, 1947). ...find $\boxed{\gamma = 0.704 \pm 0.030}$ which is fully compatible with the Isichenko prediction.

...Conclusions

...low frequency electrostatic turbulence, we find that particle diffusion follows a *scal-*...*regime* as function of the Kubo parameter, which is compatible with the *Isichenko ...olution critical exponent*. The scaling law is found to be

$$\boxed{D \simeq \omega^{0.3} \left(\frac{E}{B}\right)^{0.7}} \tag{8}$$

...given domain of amplitudes, with the given discretisation parameters.

...References

...Dupree: Phys. Fluids 10, 1049-1055 (1967).

...Taylor, B. Mc. Namara: Phys. of Fluids 14, 1492-1499 (1971).

...Montgomery: "Plasma Physics", edited by C. De Witt and J. Peyraud, Les Houches 1972, p. 427 ...don and Breach, New York, 1975).

...Misguich, R. Balescu, H.L. Pécseli et al.: Plasma Phys. and Contr. Fusion 29, 825-856 (1987).

M. Pettini, A. Vulpiani, J.H. Misguich, R. Balescu, M. De Leener, J. Orban: EUR-CEA-FC R
(Centre d'Etudes de Cadarache, 1986).

M. De Leener, J.H. Misguich, R. Balescu: p. 4 in Proc. "II[d] European Fusion Theory Meeting"
Italy, Dec. 7-9, 1987).

J.H. Misguich, R. Balescu, R. Nakach: p.521 in "Plasma Physics and Controlled Nuclear Fusion
1988", Proc. 12th. Internat. Conf. on Plasma Physics and Controlled Thermonuclear Fusion,
12-19, 1988 (I.A.E.A., Vienna, 1989).

A.V. Gruzinov, M.B. Isichenko, Ya.L. Kalda: Sov. Phys. JETP 70, 263-269 (1990).

M.B. Isichenko, W. Horton: Comments on Plasma Phys. and Contr. Fusion 14, 249-262 (1991).

M.B. Isichenko: Rev. Mod. Phys. 64, 961-1043 (1992).

M.B. Isichenko: p.91 in "Statistical Description of Transport in Plasma, Astro- and Nuclear Phys
by J.H. Misguich, G. Pelletier and P. Schuck, Centre de Physique des Houches, (Nova Science P
York 1993).

J.-D. Reuss, J.H. Misguich, EUR-CEA-FC Report 1564 (Centre d'Etudes de Cadarache, Feb. 199
Rev. E (July 1996).

P.W. Terry, P.H. Diamond: Phys. Fluids 28, 1419-1439 (1985).

W.Y. Zhang, R. Balescu: Plasma Phys. Control. Fusion 29, 1019 (1987).

R.T. Birge, Revs. Mod. Phys. 19, 298 (1947).

C.C. Petty, T.C. Luce et. al.: Phys. Rev. Lett. 74, 1763 (1995).

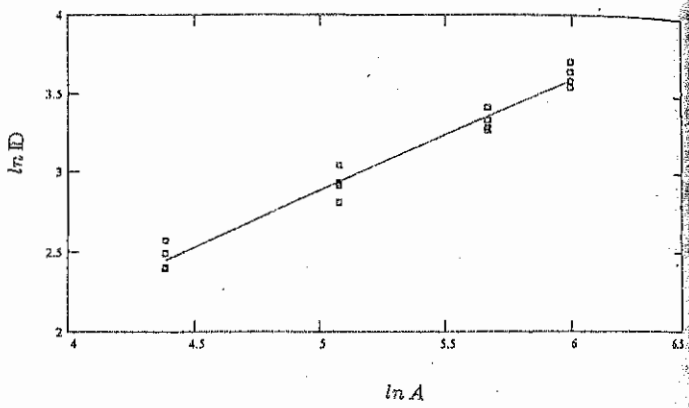


Fig. 1: Result of the linear regression calculation on the 16 numerical resul
$\mathbb{D}(A)$ in *log-log* scale, obtained from the simulation of 4 sets of 64 particles at 4 di
values of the amplitude. The resulting straight line has a slope $\gamma = 0.704$.

GEOMETRICAL APPROACH TO HAMILTONIAN FLUIDS

B. N. Kuvshinov*, T. J. Schep

Instituut voor Plasmafysica, "Rijnhuizen"; Association EURATOM-FOM
Postbus 1207, 3430 Nieuwegein, the Netherlands

*Russian Research Center "Kurchatov Institute", Moscow, Russia

geometry [1] is employed to investigate invariant properties of equations that the motion of continuous media [2]. The geometrical concept of invariance is in terms of Lie derivatives. Analogously to finite-dimensional systems, Hamil- are introduced as systems that annihilate an exact two-form. It is shown that ged fluids satisfy this local definition of a Hamiltonian structure. Symmetries and gauge transformations are briefly discussed.

fields

quantities can be adequately described in terms of scalars, vectors and, in general, tensors. A tensor field $\mathbf{T}$ is defined to be invariant with respect to a vector 's Lie derivative vanishes,

$$\mathcal{L}_{\vec{V}}\mathbf{T} = 0. \tag{1}$$

means that the tensor remains invariant when it is dragged along the integral curves field $\vec{V}$. The general expression in a coordinate basis for the Lie derivative of an tensor field $\mathbf{T}$ is

$$(\mathcal{L}_{\vec{V}}\mathbf{T})^{i\dots}_{k\dots} = V^j\frac{\partial}{\partial x^j}T^{i\dots}_{k\dots} - T^{j\dots}_{k\dots}\frac{\partial}{\partial x^j}V^i - \dots + T^{i\dots}_{j\dots}\frac{\partial}{\partial x^k}V^j + \dots. \tag{2}$$

follows that the Lie derivative of a scalar field f (a $\binom{0}{0}$ tensor) is the usual directional vative, $\mathcal{L}_{\vec{V}}\, f = df/dt = V^i\partial/\partial x^i f$, where V^i are the components of $\vec{V}$ and t is the ter along the flow lines. The Lie derivative of a vector field $\vec{W}$ (a $\binom{1}{0}$ tensor) with pect to the vector field $\vec{V}$ is the commutator of the vector fields $\mathcal{L}_{\vec{V}}\vec{W} = [\vec{V},\vec{W}] = W^j\partial V^i/\partial x^j - W^i\partial V^j/\partial x^j)\partial/\partial x^j$. The Lie derivative of an arbitrary p-form (a $\binom{0}{p}$ tensor) be expressed as $\mathcal{L}_{\vec{V}}\tilde{\omega} = \tilde{d}(\tilde{\omega}(\vec{V})) + (\tilde{d}\tilde{\omega})(\vec{V})$, where $\tilde{d}$ denotes the operation of external differentiation and $\tilde{\omega}(\vec{V})$ the contraction of the form $\tilde{\omega}$ and the vector $\vec{V}$. The Lie derivative and the external derivative commute, $\mathcal{L}_{\vec{V}}\tilde{d} = \tilde{d}\mathcal{L}_{\vec{V}}$.

The concept (1) of invariant fields is in agreement with the well-known hydrodynamical definitions of passively advected scalars and frozen-in vector fields. It extends this concept of invariance from scalars and vectors to arbitrary tensor fields. Geometrical invariants that are common to all fluid models are the velocity field $\vec{V}$, the initial positions of fluid elements x^i_0 (Lagrangian coordinates) and the one-form $\tilde{dt}$: $\mathcal{L}_{\vec{V}}\vec{V} = 0$, $\mathcal{L}_{\vec{V}}x^i_0 = 0$, $\mathcal{L}_{\vec{V}}\tilde{dt} = 0$. Other important invariants of ideal fluids are the specific entropy s for adiabatic flows and the density 4-form $\tilde{\Omega}_\varrho = \varrho\,\tilde{dt}\wedge\tilde{dx}^1\wedge\tilde{dx}^2\wedge\tilde{dx}^3$. The invariance of $\tilde{\Omega}_\varrho$ is equivalent to the mass conservation law: $d\rho/dt + \rho\nabla\cdot\mathbf{v} = 0$.

The equations of motion of invariant tensor fields (1) can be integrated. The flow field determines an one-parameter group g^t of transformation. The elements of g^t are the

transformations which transfer every point X_0 into a point X, that lies on th integral line of the field $\vec{V}$ and is labelled by the value of the parameter t along th Invariant fields behave under these transformations as under coordinate transform

$$T^{i\ldots}_{k\ldots}(x) = T^{i_0\ldots}_{k_0\ldots}(x_0)\Lambda^i_{i_0}\Lambda^{k_0}_k \ldots \quad .$$

Here, x^i_0 and x^i represent X_0 and X, respectively, $\Lambda^j_{j_0} = \partial x^j/\partial x^{j_0}_0$ is the transfor matrix and $\Lambda^{k_0}_k$ its inverse. Examples are the specific vorticity in Euler fluids $\vec{\omega}$ $\vec{\omega}/\rho|^{i_0}_{x_0}\partial x^i/\partial x^{i_0}_0$, frozen-in magnetic fields in ideal MHD $\vec{B}/\rho|^i_x = \vec{B}/\rho|^{i_0}_{x_0}\partial x^i/\partial x^{i_0}_0$ a density $\rho(x) = J\rho(x_0)$, J being the Jacobian of the transformation.

The geometrical point of view on invariance leads directly to the fundamental pro of invariant fields. According to a general theorem, the vector fields with respect to some tensor field $\mathbf{T}$ is invariant, compose a Lie algebra [1]. This means that if the field is invariant with respect to the vector fields $\vec{W}$ and $\vec{U}$, then the tensor is also in with respect to the commutator $[\vec{W},\vec{U}]$, i.e. $\pounds_{\vec{W}}\mathbf{T} = \pounds_{\vec{U}}\mathbf{T} = 0$ yields $\pounds_{[\vec{W},\vec{U}]}\mathbf{T} =$ The basic operations of differential geometry can be exploited to construct new in fields [2] from a set of given invariants. The operations of interest are the contr of a form with a vector, the tensor product, the exterior product of forms, ex differentiation, and taking commutators of vector fields. If the objects $\mathbf{T}_\alpha$, $\vec{W}_\beta$ $\alpha,\beta,\nu = 1,2,\ldots$) are invariant, then $\mathbf{T}_\alpha \otimes \mathbf{T}_\beta$, $\tilde{\omega}_\alpha \wedge \tilde{\omega}_\beta$, $\mathbf{T}_\alpha(\vec{W}_\beta,\tilde{\omega}_\nu,\ldots)$ and $\tilde{d\omega}_\alpha$ a invariant. Here, the symbol $\otimes$ denotes the tensor product and $\wedge$ denotes the ex (wedge) product of forms. An example is the invariant $f(s)\tilde{\Omega}_\varrho$.

Hamiltonian structure

Hamiltonian mechanics of finite-dimensional systems can be based upon the existe an exact 2-form that is annihilated by the flow

$$(\tilde{d\bar{p}})(\vec{V}) = 0,$$

where $\vec{V}$ is the vector tangent to the integral lines in extended phase space. Equati is illustrated in Fig. 1a, which shows that the cells of the 2-form $\tilde{d\bar{p}}$ are oriented the integral curves of the vector field $\vec{V}$. The most important consequence of Eq. (4) does not depend on the actual choice of the space and of $\bar{p}$, is the conservation o the flow $\vec{V}$,

$$\pounds_{\vec{V}}\tilde{d\bar{p}} = 0.$$

In extended phase space (t,q^i,p_i), the one-form is $\tilde{p} = -h(t,q^i,p_i)\tilde{dt} + p_i\tilde{dq^i}$, wh is the Hamiltonian function and (q^i,p_i) are canonical variables, and the velocity v along the flow is $\vec{V} = \partial/\partial t + \vec{v}$, $\vec{v} = \dot{q}^i\partial/\partial q^i + \dot{p}_i\partial/\partial p_i$. Substitution into (4) give canonical equations $\dot{q}^i = \partial h/\partial p_i$, $\dot{p}_i = -\partial h/\partial q^i$. Canonical systems can be equally described in terms of Poisson brackets.

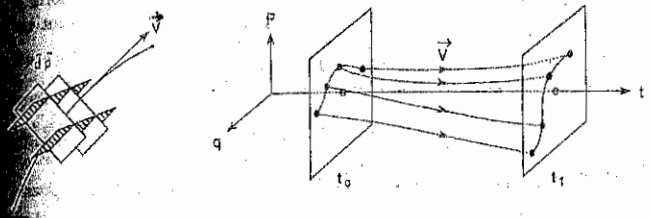
In the literature, the Hamiltonian formalism is generalised to continuous media by i ducing noncanonical Poisson bracket on a function space [3]. An alternative way has not been investigated, is to start directly from Eq. (4) and to consider different c of spaces and of one-forms $\tilde{p}$. All fluid models that satisfy Eq. (4) share the property the motion of separate fluid elements can be described by canonical equations [4].

Consider the motion of a continuous medium in $(n+1)$-dimensional extended coord space (t,x^i). In this space, the velocity vector is $\vec{V} = \partial/\partial t + \dot{x}^i\partial/\partial x^i$, $(i = 1,\ldots,n$

point of view that a Hamiltonian fluid is characterized by an invariant exact
is aligned with the velocity field, $\tilde{d}\tilde{p}(\vec{V}) = 0$. The one-form $\tilde{p}$ is given by

$$\tilde{p} = -h(x^i, t)\tilde{d}t + p_i(x^j, t)\tilde{d}x^i. \tag{6}$$

difference that the components p_i of the momentum are not independent variables
nctions of t and x^j. In other words, the curve $p(t_0, x_0^i)$ is transported to the curve
by canonical equations. This illustrated in Fig. 1b.



(a) A 2-form can be pictured as an egg crate. Equation (4) means that the flow does ... the planes of the 2-form. (b) A curve $p_i(x^j, t)$ in (x^i, p_i) space is advanced in ... according to canonical equations.

substitution of the velocity and of (6) into Eq. (4) gives the motion of an n-dimensional
fluid. In the case of 3(+1) dimensions one obtains

$$\partial\vec{p}/\partial t = -\nabla h + \vec{v} \times (\nabla \times \vec{p}), \tag{7}$$

where $\vec{v}$ and $\vec{p}$ are the 3D velocity and momentum, respectively. Under the choice

$$h = v^2/2 + \int \mathrm{d}P/\varrho + (e/m)\varphi, \quad \vec{p} = \vec{v} + (e/m)\vec{A}, \tag{8}$$

where $P(\varrho)$ is the pressure, Eq. (7) is the equation of motion of a charged, barotropic
fluid. With the more general choice

$$h = v^2/2 + I + (e/m)\varphi + \frac{\partial s}{\partial t}\int_0^t T\mathrm{d}t, \quad \vec{p} = \vec{v} + (e/m)\vec{A} - (\nabla s)\int_0^t T\mathrm{d}t, \tag{9}$$

Eq. (7) becomes the momentum balance of an adiabatic plasma fluid. Here, the tempera-
ture T, the specific entropy s, and the specific enthalpy I satisfy the general thermody-
namic relationship $\varrho^{-1}\nabla P = \nabla I - T\nabla s$. The integral invariant that corresponds to (9)
is the "three circulation theorem" derived by K. Elsässer [5].

symmetries and gauge transformations

Suppose that $\tilde{d}\tilde{p}$ is not only conserved by the flow $\vec{V}$, but also by the field $\vec{W}$,

$$\mathcal{L}_{\vec{W}}\tilde{d}\tilde{p} = 0. \tag{10}$$

The field $\vec{W}$ generates a symmetry of the system. According to the Poincaré lemma, it
follows that $\mathcal{L}_{\vec{W}}\tilde{p} = \tilde{d}\chi$. If we contract this expression with $\vec{V}$, we obtain

$$\mathcal{L}_{\vec{V}}(\tilde{p}(\vec{W}) - \chi) = 0. \tag{11}$$

Hence, the symmetry (10) generates the invariant scalar $\tilde{p}(\vec{W}) - \chi$. This is a ve
Noethers theorem. In the case of exact symmetry ($\chi = 0$), Noethers theorem ma
the projection of the 4-momentum along the direction of the vector field that det
the symmetry, is conserved. The invariant is identically equal to zero if $(\tilde{d}\tilde{p})(\vec{W})$
The Bernoulli law for stationary flows is an example of Noethers theorem. The sy
is generated by the vector field $\vec{W} = \partial/\partial t$ and is exact ($\chi = 0$).

The exterior derivative of an arbitrary function can be added to the one-form $\tilde{p}$ w
changing the structure of the equations of motion (4). This is equivalent to a
transformation $\tilde{p}^{(c)} = \tilde{p} + \tilde{d}\pi$. If the function π satisfies the relation

$$\mathcal{L}_{\vec{V}}\pi = -\tilde{p}(\vec{V}),$$

then $\tilde{p}^{(c)}(\vec{V})$ vanishes and $\tilde{p}^{(c)}$ is invariant, $\mathcal{L}_{\vec{V}}\tilde{p}^{(c)} = 0$. For adiabatic, charged fluid
determined by

$$\frac{\mathrm{d}\pi}{\mathrm{d}t} = -\frac{v^2}{2} + I + \varrho_e\varphi - (e/m)\mathbf{A}\cdot\mathbf{v}.$$

In the limit $e/m \to 0$, one obtains for barotropic fluids the Hollmann invariant [2].
In the zero-mass limit, $\tilde{p}$ is equal to $\tilde{A} = -\varphi\tilde{d}t + A_i\tilde{d}x^i$, so that the invariance of
identical to the invariance of the Faraday 2-form $\tilde{F} = \tilde{d}\tilde{A}$ and $\tilde{F}(\vec{V}) = 0$ gives ideal
law. The condition $p^{(c)}(\vec{V}) = 0$ gives

$$-\varphi^{(c)} + \tilde{A}^{(c)}\cdot\vec{v} = 0.$$

In particular, the contraction of the dual ${}^*\tilde{F}$ of $\tilde{F}$ with $\tilde{A}^{(c)}$ and $\tilde{d}t$ yields the inv
scalar $\mu = {}^*\tilde{F}(\tilde{A}^{(c)}, \tilde{d}t) = \vec{A}^{(c)}\cdot\vec{B}/\varrho$. It follows that the gauge (12) converts the conser
of the magnetic helicity integral into a local conservation law [6]. Another consequ
that the general 4-form $\tilde{\Omega}_\varrho^{(s,\mu)} = f(s,\mu)\tilde{\Omega}_\varrho$ is invariant, where f is an arbitrary fun
of the invariants s and μ.

Acknowledgements We are grateful to Dr. V. V. Yan'kov and Dr. F. Pe
for fruitful discussions. This work was performed as part of the research programm
the Association EURATOM-FOM with financial support from NWO and EURAT
The investigation described in this paper was made possible in part by Grant # 94-
from INTAS and by Grant # 95-02-03988-a from the Russian Fundamental Res
Foundation.

References

[1] V. I. Arnol'd, *Mathematical Methods of Classical Mechanics*, Springer-Verlag, N
York (1978); B. Schutz, *Geometrical Methods of Mathematical Physics*, Cambridge
versity Press (1980).
[2] A. V. Tur, V. V. Yanovsky, J. Fluid Mech., **248**, 67–106 (1993).
[3] P. J. Morrison, J. M. Greene, Phys. Rev. Lett., **45**, 790–794 (1980).
[4] V. V. Yan'kov, JETP Lett., **58**, 520–523 (1993); JETP, **107**, 414–430 (1995).
[5] K. Elsässer, Phys. Plasmas, **1**, 3161–3173 (1995).
[6] H. K. Moffat, in *Topological Fluid Mechanics*, ed. H. K. Moffat and A. Tsino
Cambridge University Press (1990), p.1–10; V. A. Gordin, V. I. Petviashvili, Sov.
Plasma Phys., **13**, 509–511 (1987); Sov. Phys. JETP, **68**, 988–994 (1989).

...ation of electron oscillations in bounded non-neutral plasmas with dust particles

...Yuri.Chutov, A.Yu.Kravchenko, P.P.J.M.Schram*, R.D.Smirnov
...Physical Electronics, Radio Physics faculty, Taras Shevchenko Kiev University,
Volodymyrska Str. 64, 252017 Kiev, Ukraine
...ment of Physics, Eindhoven University of Technology, P.O.Box 513, 5600 MB
Eindhoven, The Netherlands

...tron oscillations can appear in bounded non-neutral plasma clouds due to the initial ...of the electrons in the potential hole created by electrons and ions in these clouds [1-3]. ...oscillations are accompanied by a slow ion motion caused by an expansion of ...l plasma clouds due to the self-consistent electric field. Consequently, electron ...can take place in a non-stationary potential hole, and an interaction of fast electron ...with this slow ion motion takes place. This interaction causes an evolution of ...oscillations and a subsequent plasma turbulence [1-3]. It is of interest to investigate the ...of dust particles on these oscillations taking into account the results of recent ...of expanding plasmas with dust particles [4-6] and especially the influence of dust ...electron plasma waves [7].

...with a sharp boundary consisting initially of equilibrium electrons and ions with ...densities n_{eo}, n_{io} and temperatures T_{eo}, T_{io} as well as non-charged dust particles ...density n_d, expands into a vacuum due to the self-consistent electric field. The initial ...velocity of electrons and ions is equal to zero. The expanding plasma is considered to be ...collisionless due to the choice of the plasma parameters. Three-dimensional initial velocity ...distribution functions are assumed for electrons and ions in contrast to previous works [4,5]. ...self-consistent electron oscillations accompany this plasma expansion. The expanding ...interacts with dust particles, i.e. the collection of electrons and ions as well as Coulomb ...scattering by dust particles take place.

...computer modeling of the relaxation of these electron oscillations is carried out by ...means of the one-dimensional PIC method taking into account the dynamics of the three-...dimensional charging of dust particles due to the collection of electrons and ions. Electrons and ...ions are not assumed to be in equilibrium during a plasma expansion. Therefore the energy ...distribution functions of free electrons and ions can change due to the dependence of the ...process of their collection by dust particles on their energy. Coulomb collisions were taken into ...consideration in the framework of the method of stochastic differential equations [8].

Results

The evolution of electron oscillations in expanding plasma layers can be investigated ... analysis of various parameters of these plasma layers. In our case the total electron ... E_{ed} is used. Typical examples of simulated results are shown for a plasma layer with ... size $L = 32$ and $(n_{eo}/n_{io}) = 0.8$ in Fig. 1 where the time dependences of this ... divided by the initial total energy E_o are plotted. The results are given for this pla... expanding without dust particles (solid line) as well as for the plasma layer expanding ... particles of radius $R_d = 0.2$ and density $n_d = 1$ (dashed line). Note that L and ... divided by the initial Debye length L_D and time t is multiplied by the initial ion ... frequency ω_o.

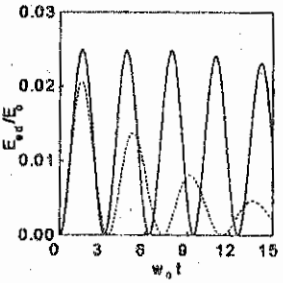


Fig. 1

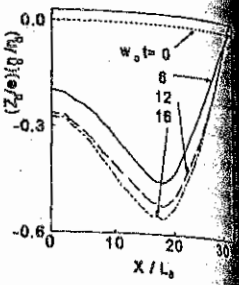


Fig. 2

The periodic change of the energy E_{ed} is the result of the electron motion with an ... velocity in electron oscillations. The maximum value of this energy corresponds to the ... of a large part of electrons through a plasma cloud center due to the positive initial charge ... plasma cloud. As was shown earlier [1-3], the initial frequency ω_o of the electron oscil... as well as the oscillation amplitude A_o depend on the initial plasma charge, on the ... geometry and on the initial electron temperature.

As can be seen from Fig. 1, the energy E_{ed} changes with the altering frequency ... cases (without and with dust particles) however the frequency ω and the amplitude ... electron oscillations change stronger in the case of a plasma layer expansion with dust par... In case of the plasma layer expansion without dust particles, the analysis shows that ... relaxation of electron oscillations is the result of the change in time of the non-par... potential well due to the slow expansion of the bounded plasma layer into a vacuum. ... reason is a particular case of the general cause of plasma turbulence, namely: the interac...

...motion in electron oscillations with the slow ion motion caused by the plasma

...of the plasma layer expansion with dust particles, the relaxation of electron ...companied by a relaxation of the spatial distribution of the dust particle charge ... well as the ion density n_i (Fig. 3). The non-monotonic distribution of the ... consequence of the various numbers of electrons and ions collected by dust ...various points of a plasma cloud in various phases of electron oscillations. These ...nd on the density of electrons and ions as well as on the collection time, but both ...change during the oscillation cycle due to the electron motion with an altering ...tron oscillations. As Fig. 3 shows, the ion density n_i changes not only closely to ...but in the central part of a plasma cloud also. This last circumstance is caused by a ...of electrons and ions by dust particles.

...laxation dependences of the frequency ω (crosses) divided by the initial ion plasma ... on the mean ion and dust charge $n_i + Zn_d$ as well as the amplitude A (circles) ...by the initial amplitude A_o on the mean electron density n_e, are shown in Fig. 4. ...pendences indicate on the scale given in Fig. 4, that an influence of dust particles on ...tion of electron oscillations cannot be caused by the decrease of the mean electron and ...ion only. Otherwise these functions would have to cross the point [0,0] in Fig. 4. The ...of this deviation is perhaps the non-uniform distributions of the dust particle charge (Fig.

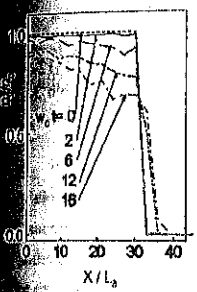


Fig. 3

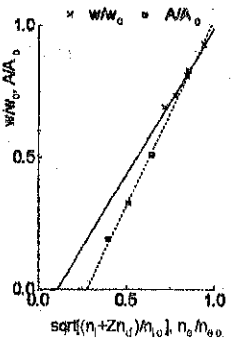


Fig. 4

...ze and the density of dust particles influence the relaxation of electron oscillations in ...unded plasma clouds. That is confirmed by the comparison of Fig. 5 and Fig. 6, where ...ulation results are plotted for $R_d = 0.1$ and $n_d = 1$, with Fig. 1 and Fig. 2, respectively.

As can be seen from this comparison, smaller dust particles cause a slower relaxati
electron oscillations.

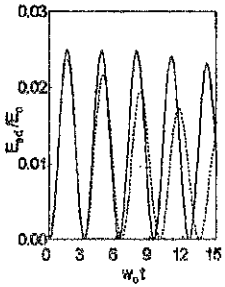


Fig. 5

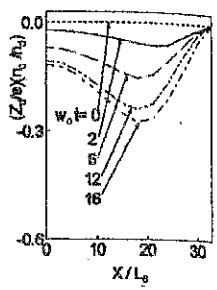


Fig. 6

This work was supported by INTAS in the framework of contract No 94-2959 and
grant from the Ukrainian Committee of Science and Technology.

References

[1] Yu.I.Chutov et al, Contr. papers XXI ICPIG, Bochum, Germany, Sept. 1993, V.2, p.
140.

[2] V.P.Kovalenko et al, Fisika Plasmy, - 1993 - v.19, - p. 279-287 (in Russian)

[3] V.P.Kovalenko et al, Ukrainian Phys. Journal, 1992, - v.37, - p. 851-853 (in Ukrainian)

[4] Yu.I.Chutov, A.Yu. Kravchenko, P. Schram. J. Plasma Phys. -1996- v.55.-p.87-94

[5] Yu.Chutov, A.Kravchenko, P.Schram, Proceedengs of the Workshop on Complex Pl
and Plasmas, 18-21 September 1995, Eindhoven University of Technology,
Netherlands

[6] Yu M.Y., Luo H., Phys. Plasmas, v.2 (1995), p 591-595

[7] Varma R.K., Shukla P.K., Krishan V. Phys.Rev. - 1993. - V. E47, N 5. - P.3612-3616

[8] Shvez M.F., Ivanov V.F. J. Comput. Math. and Math. Phys. -1988. - V.20, No 3. - P.
- 690 (in Russian)

Some properties of plasmas with dust particles

Yu.I.Chutov, A.Yu.Kravchenko, P.P.J.M.Schram*

...Physical Electronics, Radio Physics faculty, Taras Shevchenko Kiev University, Volodymyrska Str. 64, 252017 Kiev, Ukraine

...Dept. of Physics, Eindhoven University of Technology, P.O.Box 513, 5600MB, The Netherlands

...with dust particles can be realized in space, for example in rocket or meteorite traces in the ...sphere, as well as in many laboratory and technological devices, for example in controlled ...devices where dust particles are high Z-impurities [1].

...with dust particles are usually investigated under the assumption that the electrons and ... in equilibrium. However this assumption is not always correct for impulse expanding ...with one-dimensional velocity distribution functions because of the dynamics of the dust ...charging, namely: energy dependences of the electron and ion collection by dust particles and ...disequilibrium of electron and ion energy distribution functions caused by these dependences ... Therefore, it is of interest to investigate a relaxation of uniform plasmas without expansion ...and compare this relaxation with the case of expanding plasmas.

...In the present work the results of numerical simulations for various parameters of relaxing ...plasmas including the electron and ion energy distribution functions at various parameters ...of dust particles are reported. These results are compared with the case of relaxing bounded ...plasmas expanding into a vacuum.

...

...relaxation of a plasma with dust particles is investigated for two cases. The first one is the case ...of uniform infinite quasi-neutral plasma consisting initially of equilibrium electrons and ions with ...densities $n_{eo} = n_{io} \equiv n_o$ and temperatures $T_{eo} = T_{io} \equiv T_o$.. Dust particles with radius R_d and ...density n_{do} appear in this plasma at some initial time. A plasma relaxation starts due to a ...collection of electrons and ions by dust particles just after their appearance.

...In the second, more complex, case a uniform plasma layer is considered with a sharp ...boundary, initially also consisting of electrons and ions as well as uncharged dust particles, but this ...plasma layer expands into a vacuum due to the self-consistent electric field. In this second case, the ...plasma relaxation is caused not only by the collection of electrons and ions from the plasma on dust ...particles but also by the plasma expansion.

...In both cases, the plasma is considered to be collisionless because the plasma relaxation time is ...much less than the electron-ion collision time due to the choice of the plasma parameters. Three-

dimensional velocity distribution functions are assumed for electrons and ions in bo
contrast to previous works [2-4].

Various parameters of this relaxing plasma have been numerically simulated usin
method and taking into account the dynamics of the dust particle charge in the framew
orbit-limited-probe theory without the assumption about equilibrium of electrons
Coulomb collisions with dust particles are taken into account in the framework of the
stochastic differential equations. In same cases, both the electron and ion collection
particles and the Coulomb collisions have been simulated by the Monte Carlo method.

Results

Typical results of numerical simulations are shown in Fig. 1 - 3 for non-expanding pla
$n_d = 4$, $m_i / m_e = 256$, $R_d = 0.1$ and 0.32 (curves 1 and 2 in Fig. 2 - 3, respectivel
n_d is the number of dust particles in a Debye sphere, m_i / m_e is taken to be 256 in
obtain higher simulation precision, R_d is the radius of dust particles divided by the initi
length.

Simulated X-components of the electron and ion velocity distribution functions F_{ex}
plotted for $R_d = 0.32$ in Fig. 1. Other components of these distribution functions are
The functions F_{ex}, F_{ix} are divided by the initial electron and ion density, resp
Simulation results are plotted by various shapes (squares, circles, crosses etc.) for various
after the relaxation start. Solid curves in Fig. 1 are Gaussian with the corresponding widt
t are multiplied by the initial ion plasma frequency, X-components of electron and ion ve
v_{ex}, v_{ix} are divided by the ion sound velocity $(kT_e / m_i)^{1/2}$.

As can be seen from Fig. 1, the simulation results are very close to Gaussian. It means
electron and ion distribution functions are close to Maxwellian during a plasma relax
contrast to [2]. This is caused by the relatively faster influence of Coulomb collisions due
smaller radius of the dust particles and the three-dimensional velocity distribution fun
However plasma parameters relax due to the electron and ion collection.

The relaxation of the electron and ion densities n_e, n_i is shown in Fig. 2a, where the
density n_e is plotted with negative sign for convenience. The electron and ion densities
decrease continuously due to their collection by dust particles. The comparison of curves
shows that larger dust particles collect electrons and ions more effectively, of course. The
shows that the ion density n_i somewhat exceeds the electron density n_e because some
the electrons provides negative charge of dust particles Q_d just after the relaxation sta

of the charge Q_d is shown in Fig. 2b where $C = n_o / n_d$. Note that the dust Q_d depends on the ratio of electron and dust particle densities. The complex electron and ion collection, which is accompanied by a self-consistent change of plasma uses the non-monotonous change of this dust particle charge Q_d.

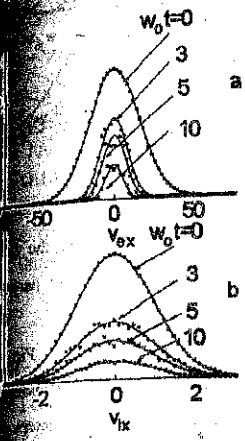


Fig. 1

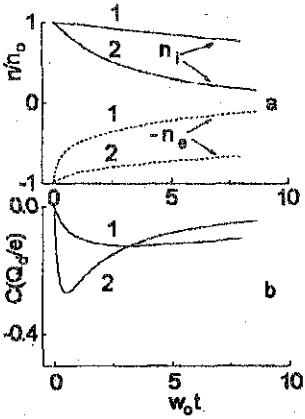


Fig. 2

results of the plasma relaxation are clearly seen from Fig. 3 in which the relaxation of the kinetic energy E_e of one electron (the electron temperature) as well as the corresponding energy E_i of one ion (the ion temperature) has been plotted. These energies are divided by the initial thermal electron energy E_o, ω_o is the initial ion plasma frequency. The initial abrupt decrease of the energy E_e is caused by the dominant collection of fast electrons by dust particles after the relaxation starts, because the fast electrons are always responding to any plasma disturbances more effectively than other plasma particles, of course. As can be seen from Fig. 2b, the negative charge Q_d of a dust particle is created simultaneously. The subsequent evolution of the energy E_e is connected with the evolution of the charge Q_d of a dust particle. In particular, the subsequent evolution of the mean electron energy E_e (Fig. 3) is caused by the subsequent collection of ions by dust particles with negative charge.

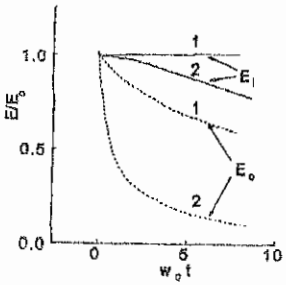


Fig. 3

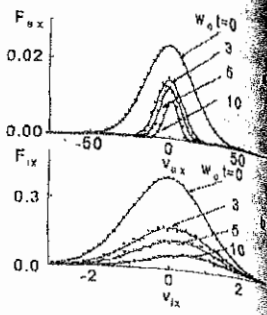


Fig. 4

Note that the obtained results can be related to various real plasmas using the corresp initial ion plasma frequency ω_o and the real relation of electron and dust particle co $C = n_o / n_d$.

The influence of a plasma expansion on a plasma relaxation is shown in Fig 4 in simulated X-components of the mean electron and ion velocity distribution functions $F_{e,i}$ have been plotted for the expanding plasma layer with the initial plasma parameters of F comparison of Fig. 4 with Fig. 1 shows that a plasma expansion leads to a slow shift of the ion distribution function only due to the ion acceleration in the self-consistent electric field.

The obtained results show that the assumption about equilibrium of electrons and ions constant temperature cannot always be used in investigations of non-stationary plasmas wit particles, in particular in investigations of strong waves in dusty plasmas, this assumpt unreliable.

This work was supported by INTAS in the framework of contract No 94-2959 and by a from the Ukrainian Committee of Science and Technology.

References

[1] de Angelis U. Physica Scripta. - 1992. - V.45. - P.465-474

[2] Yu.I.Chutov, A.Yu. Kravchenko, P. Schram. J. Plasma Phys. -1996- V.55. - P.87-94

[3] Yu.I.Chutov, A.Yu.Kravchenko, P..Schram, Contr. papers 22nd EPSC Contr. Fusion Plasma Phys., Bourenemouth, UK 3-7 July 1995, V.19C (1995) IV-453

[4] Yu.Chutov, A.Kravchenko, P.Schram, Proceedings of the Workshop on Complex Fluids Plasmas, 18-21 September 1995, Eindhoven University of Technology, The Netherlands

Shortwavelength Langmuir and Upper Hybrid Solitons

T.A.Davydova, A.I.Fishchuk
Institute for Nuclear Research, 252022,Kiev, Ukraine

As well known one-dimensional Langmuir and Upper Hybrid ... can be described by nonlinear Schrodinger equation with an ... nonlinear nonlocal term [1-3]

$$i\frac{\partial\phi}{\partial t} + A\frac{d^2\phi}{dx^2} + \phi\,(B + C\frac{d^2}{dx^2})|\phi|^2 + P\frac{d^4\phi}{dx^4} = 0 \qquad (1)$$

... is an electric field envelope. Higher order dispersion ... are of particular importance of solution of eq.(1) in the ... has singularities as in cusp-solitons [1] or collapses [4]. ... this report we try to find out conditions for which nonlocal ... and high order dispersion effects can lead to formation ... one- and two- dimensional solitons.

One-dimensional eq.(1) has three integrals: number of quanta

$$N = \int_{-\infty}^{\infty} |\phi|^2 dx\ , \qquad (2)$$

$$I = \frac{i}{2}\int_{-\infty}^{\infty}(\phi\frac{d\phi^*}{dx} - \phi^*\frac{d\phi}{dx})dx \qquad (3)$$

... Hamiltonian

$$H = \int_{-\infty}^{\infty}\left[A\left|\frac{d\phi}{dx}\right|^2 - P\left|\frac{d^2\phi}{dx^2}\right|^2 + \frac{C}{2}\left(\frac{d}{dx}|\phi|^2\right)^2 - \frac{B}{2}|\phi|^4\right]dx \qquad (4)$$

... restrict ourselves for simplicity with stationary solutions ... (with I=0) of the form

$$\phi = \phi\,(x + x_o)\ \exp\{i(\lambda t + \varphi_o)\} \qquad (5)$$

... give extremum to the Hamiltonian at fixed N [4].

... of the form (5) satisfy the equation

$$\phi'' + A\frac{d^2\phi}{dx^2} + \phi\,(B + C\frac{d^2}{dx^2})(\phi)^2 + P\frac{d^4\phi}{dx^4} = 0 \qquad (6)$$

... cusped solution of eq.(6) with B=P=0 is unstable even in one-dimensional space [5]. Fourth order dispersion corrections ($P\neq 0$) remove singularity from differential equation. The question is whether cusp-soliton transforms into more smooth and stable soliton or not? A particular smooth exact soliton solution of eq.(6) with ... 0, P>0, C<0, A>0 (or A<0, C>0, P>0) has the form [6]:

$$\phi = \left|\frac{2A}{C}\right|^{1/2}\mathrm{sech}\left(\left|\frac{A}{2P}\right|^{1/2}x\right)\exp\left(i\lambda t\right),\quad \lambda = \frac{A^2}{4P}. \qquad (7)$$

... we suppose for definity A>0. In the case P>0, C<0 an exact

eq.(6) has solution in the form of a kink-soliton

$$\psi = \left|\frac{A}{C}\right|^{1/2} \tanh\left\{ \frac{1}{2} \left|\frac{A}{P}\right|^{1/2} x \right\}$$

Soliton solutions of (6) for arbitrary values of λ can be ... numerically. Some restrictions on parameters where soliton solu... are possible can be found analytically.

For any localized solutions of eq.(6) with B=0 foll... integral equalities are fulfilled

$$\lambda = \frac{1}{3N} \int_{-\infty}^{\infty} \left\{ A\left(\frac{d\psi}{dx}\right)^2 - 5P\left(\frac{d^2\psi}{dx^2}\right)^2 \right\} dx$$

and

$$-2P \int_{-\infty}^{\infty} \left(\frac{d^2\psi}{dx^2}\right)^2 dx = \int_{-\infty}^{\infty} (3|C|\,\psi^2 - A)\left(\frac{d\psi}{dx}\right)^2 dx$$

We see that necessary conditions for soliton solutions are ... and $|\psi_{max}|^2 > A/3|C|$, if $P<0$. In the case $P>0$ one can easily ob... an upper possible value of λ: $\lambda \leqslant A^2/60\,P$.

More information about soliton parameters can be found ... variational method. As well known [4] stationary soliton "g... extremum to H (4) at fixed N. Using simple trial function

$$\psi(\xi) = (N\mu / 2)^{1/2} \operatorname{sech} \mu\xi$$

one obtains ajusting parameter μ from the condition $\partial H/\partial\mu = 0$. ... gives two solutions for μ if $P<0$ for $N > N_{cr} = (30\,|AP|)^{1/2}|C|^{-1}$. ... more shortwavelength soliton branch occurs stable according to ... Vakhitov-Kolokolov criterium ($\partial N/\partial\lambda > 0$), and the other is unstable. It is interesting that soliton (7) belongs to the stable branch, ... cusp soliton belongs to the unstable branch in the limit $P \to 0$. ... us note also that solitons in the case considered ($A>0$, $P<0$) can... resonantly interact with small amplitude linear waves $\psi \sim e^{-i\omega t}$, ... $\omega = Ak^2 - Pk^4 > 0$ because nonlinear frequency shift for soli... solution $\delta\omega = -\lambda$ was proved to be of opposite sign.

We have shown numerically that trial function of the form (... gives rather good approximation of the soliton solutions for value... of $\lambda < A^2/4P$. For $\lambda > A^2/4P$ any soliton solution has oscillating "tails". It is in agreement with an asymptotic behaviour of ... solution for $|x| \to \infty$ which can be easily found from linea... approximation (see Fig.1).

New types of solitons were found numerically in the case B=0, ... $P<0$, $C<0$. When $\lambda<0$ they are odd and oscillating functions of x wi... decaying envelope. For positive λ a smooth soliton solution exis... in the interval $0 < \lambda < \lambda_{cr} \sim 10^{-2}A^2/|P|$ (see Fig.2).

3. Two-dimensional structure of UH or Langmuir solitons can ... described approximately by scalar model

$$i\psi_t + A\Delta\phi + \phi(B+C\Delta)|\psi|^2 + PA^2\phi = 0 \qquad (9)$$

two-dimensional Laplace operator. Eq.(9) also conserves quanta N, momentum and Hamiltonian:

$$\int \left[A|\nabla\psi|^2 + \frac{C}{2}(\nabla|\psi|^2) - \frac{B|\phi|^4}{2} - P|\Delta\phi|^2\right] d\vec{r} \qquad (10)$$

known soliton solution of eq.(9) with A>0, B>0, C=0, P=0 is nonlocal defocusing nonlinearity [7] (term proportional to and forth-order dispersion term of such a sign that AP<0 stabilizing effect on soliton. Soliton solutions in were found numerically. In general case both effects may same order.

bility of the ground soliton which gives absolute maximum or H at fixed N may be proved using Laypunov method [4] for A>0, B>0, C>0 and P<0, and the inequality [4]

$$\int|\nabla\psi|^2 d\vec{r} > \int|\psi|^4 d\vec{r}\ (2N)^{-1} = y/2N \qquad (11)$$

denote $\int|\psi|^4 d\vec{r}$ by y.

(11) for function $|\psi|^2$ gives

$$\int(\nabla|\psi|^2)^2 d\vec{r} \geq \left(\int|\psi|^6 d\vec{r}\right)(2y)^{-1} \qquad (12)$$

using Holder's inequality we get

$$\int|\psi|^6 d\vec{r} \geq \left(\int|\psi|^5 d\vec{r}\right)^2 N^{-1} \geq y^4\left(\int|\psi|^3 d\vec{r}\right)^{-2} N^{-1} \geq y^4(Ny)^{-1}N^{-1} = y^3N^{-2}$$

expression (12) gives

$$\int(\nabla|\psi|^2)^2 d\vec{r} \geq y^2(2N^2)^{-1} \qquad (13)$$

estimation [10] $\int|\Delta\psi|^2 d\vec{r} \geq \left(\int|\nabla\psi|^2 d\vec{r}\right)^2 N^{-1}$ and (11) we get

$$\int|\Delta\psi|^2 d\vec{r} \geq y^2(4N^3)^{-1} \qquad (14)$$

estimation (11)-(14) we obtain

$$H \geq Ay/2N - By/2 + (C/4 + |P|/4N)\, y^2/N^2 = f(y)$$

function f(y) has minimum if and only if

$$N > N_{cr} = AB^{-1} \qquad (15)$$

this case H is bounded from below

$$H \geq -N(BN - A)^2/4(CN + |P|)$$

localized solutions of eq.(9) of the form $\phi(r)e^{i\lambda t}$ Hamiltonian may be written as

$$H = -\int\left[\frac{C(\nabla\phi^2)^2}{2} - P(\Delta\phi)^2\right]d\vec{r} < 0$$

see that for any possible integrable localized functions with $N > N_{cr}$, H is negative and bounded from below, which garantees existence and stability of two-dimensional soliton in the presence either defocusing nonlocal nonlinearity (C>0) or fourth-order dispersion (P<0).

REFERENCES

1. Porkolab M., Goldman M.V. Phys.Fluids, 19, (1976), 87
2. Sharma K.P., Shukla P.K. Phys.Fluids, 26, (1983), 84
3. Berzhiani V.I., Paverman V.S., Fiz. Plazmy, 9, (1983)
4. Petviashvili V.I., Jankov V.V.,Voprosy Teorii Plazmy
   Atomizdat, (1985), 3-55.
5. Litvak A.G., Sergeev A.M.,Pisma Zh. Eksp.Teor.Fiz.,27
6. Davydova T. A., Kargin A. Yu., Fiz.Plazmy, 19, (1993)
7. Davydova T. A., Fishchuk A.I., Ukr.Fiz.Zhur.,40, (199
8. Karpman V.I., Shagalov A. G. Phys. Lett. A160, (199
9. Kuznetsoiv E.A., Fiz.Plazmy, 2, (1976), 327.
10. Turitsyn S.K., Teor.Mat.Fiz., 64, (1985), 226.

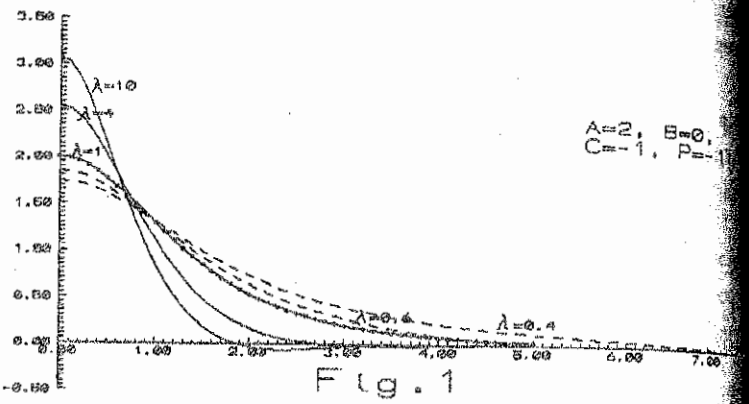
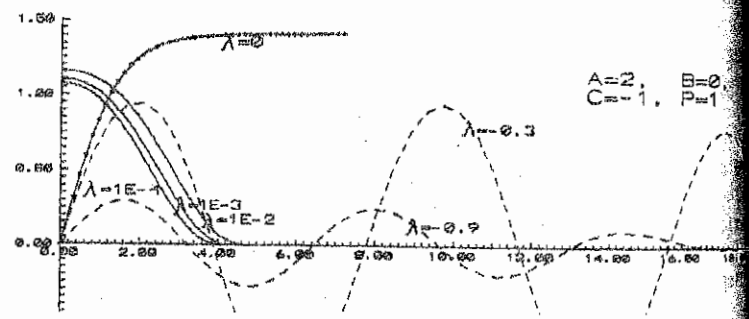


Fig. 1



INTERNAL KINK MODE STABILITY OF TOKAMAKS WITH FINITE EDGE CURRENT DENSITY IN PLASMA OUTSIDE SEPARATRIX

L.Degtyarev, A.Martynov, **S.Medvedev**
Keldysh Institute of Applied Mathematics, Russian Academy of Sciences, Moscow
F.Troyon, L.Villard
Centre de Recherches en Physique des Plasmas, Association Euratom – Confédération Suisse, Ecole Polytechnique Fédérale de Lausanne

Abstract

Large pressure gradients and current density at the plasma edge and accompanying edge-localized MHD instabilities are typical for H-mode discharges. Low-n external kink modes are a possible cause of the instabilities. The paper mostly deals with external kink modes driven by a finite current density at the plasma boundary (so called peeling modes). It was shown earlier that for a single axis plasma embedded into vacuum the peeling modes are stabilized when separatrix is approaching the plasma boundary [1]. For doublet configurations a finite current density at the internal separatrix does not necessarily lead to external kink instability when the current density vanishes at the boundary.

However, a finite current density at the plasma boundary outside the separatrix can drive outer peeling modes. The stability properties and structure of these modes depend on the plasma equilibrium outside the separatrix. The influence of plasma shear and pressure gradient at the boundary on the stability of the outer peeling modes in doublets is studied.

The stability of kink modes in divertor configurations with plasma outside the separatrix is very sensitive to the boundary conditions set at open field lines. The choice of the boundary conditions and kink mode stability calculations for the divertor configurations are discussed.

1 Equilibria Doublet equilibria with the same boundary as in [2] (aspect ratio and elongation $\kappa = 3.2$) was used in the computations.

The plasma profiles, with pressure gradient having a maximum at the separatrix and finite separatrix current density, were prescribed by

$$j' = \begin{cases} 1 - (1 - I_s)\bar{\psi}_{in}, \\ I_s(1 - \bar{\psi}_{out}), \end{cases} \quad , \quad p' = \begin{cases} p_0\bar{\psi}_{in}, & \text{inside separatrix} \\ p_0(1 - \bar{\psi}_{out}), & \text{outside separatrix} \end{cases} , \qquad (1)$$

where j is the surface averaged toroidal current density, $0 < \bar{\psi}_{in,out} < 1$ are the normalized poloidal fluxes inside and outside the separatrix, respectively, I_s controls the value of the current density at the separatrix, p_0 controls the maximal value of the pressure gradient at the separatrix.

A series of three doublet equilibria with $I_s = 0.1$ and different values of p_0 is used for stability calculations. The aspect ratio and the elongation of the single axis plasma inside the separatrix are $A = 4.6, \kappa = 1.7$ for all the equilibria. The normalized current and beta values are respectively $I_N = 1.31, 1.28, 1.24, \beta = 0\%, 1.68\%, 3.1\%$ for a safety factor on the magnetic axis $q_0 = 1.05$. The profiles inside and outside the separatrix are given in Fig.1.

2 Peeling mode stability Equilibria with a current density pedestal at the plasma boundary are characteristic for the H-mode regimes in divertor tokamak plasmas. A whole range of MHD phenomena accompany the discharges, in particular the roll-over effect in JET, is associated with low-n external kink peeling modes [3, 4].

On the other hand the kink mode stability computations of single axis plasma with separatrix at the boundary showed stability of the peeling modes [1]. However, if

the plasma outside the separatrix is still sufficiently conducting and a current
pedestal exists at the plasma edge outside the separatrix then a different sort
MHD instabilities — outer peeling modes can be driven unstable.

Peeling modes are unstable when a current density pedestal exists at the
boundary and a rational magnetic surface is located in vacuum close to the bo
(edge safety factor $q_s < m/n$). The following procedure is used to study the outer
mode stability dependence on shear and β. The external plasma layers are "scr
to produce the edge current density pedestal from the profiles (1). Then the va
q_0 is adjusted to get the value of $q_s < m/n$ and the unstable range in the q_s va
estimated. The conducting wall is chosen with the wall/plasma minor radius rati
than 2 and the effect of wall stabilization was weak enough.

The Fig.2 shows the $n = 1$ mode unstable ranges of $q_s < 3$ for the single axis pl
inside the separatrix embedded in vacuum with the boundaries defined by different
of $\psi_s \leq 1$ indicating the normalized poloidal flux left in plasma. The value of
corresponds to the separatrix at the boundary. Let us note that the current
pedestal for the single axis plasma is higher than $I_s = 0.1$ for $\psi_s < 1$. The un
range in the q_s values shrinks as ψ_s approaches 1 giving the stability for $\psi_s = 1$
pressure stabilization was observed in contrast to [4]. A possible explanation to
is different plasma geometry and profiles. The averaged curvature stabilization
can be derived from the localized peeling mode stability criterion [5] is absent fo
considered equilibria.

The Fig.3 shows the $n = 1$ mode unstable range of $q_s < 6$ for the doublet pla
The values of ψ_s indicate the normalized flux in the plasma outside the separatri
this case. The q-profile is nonmonotonic in the plasma outside the separatrix and
exists a region of negative shear (Fig.1). The peeling mode criterion indicates stabili
localized external modes in a region of negative shear. In general the global mode stab
should not follow the localized mode criterion. However, for $\beta = 0$ the marginally s
values of ψ_s for localized and global modes in the region of negative shear are quite c
to each other (see Fig.3a). The stability window at $\psi_s \to 1$ corresponds to the decre
current pedestal which vanishes for $\psi_s = 1$.

The finite beta effect on the outer peeling mode stability is shown in Fig.3b. T
stability window grows and the unstable q_s range is smaller. At the same time
stability window in ψ_s values given by the localized mode stability criterion is ge
narrower with higher beta.

The mode structure of the unstable displacements is that of typical peeling mode
$\psi_s \simeq 1$ and is less localized for the values of ψ_s near $q'(\psi) = 0$ (Fig.4).

3 Stability of divertor configurations

The divertor equilibria
plasma outside the separatrix were "cut" from the doublet equilibria computed with
CAXE code in the same way as in [2]. The stability code KINX-W has been modifie
include a Green's function technique vacuum treatment for the modes $n \neq 0$.

A characteristic feature of the divertor configuration is the presence of open magn
field lines penetrating the end plates. Boundary conditions there have a strong eff
on the plasma stability properties. Vanishing displacement condition at the end pla
was used in [2] for axisymmetric $n = 0$ mode stability calculations. However, in the c
of external kink modes these conditions lead to an unrealistic strong stabilizing eff
Our computations showed the stability of all external kink modes except the analog
$m = 1$, $n = 1$ external mode for very high values of normalized current corresponding
the Kruskal–Shafranov stability limit $q < 1$.

The ideal MHD energy principle is valid when the vanishing displacement condition
the end plates is assumed. The perturbed plasma normal magnetic field $\delta\mathbf{B} = \nabla \times (\xi \times$
also vanishes at the end plates in this case, where ξ is the plasma displacement, $\mathbf{B}$
the equilibrium magnetic field. This gives the boundary condition for the pertur
magnetic field in vacuum $\delta\mathbf{B}_v \cdot \mathbf{n} = 0$.

The formulation becomes more complicated with finite displacement at the end pla

one extra term enters the weak formulation of the stability problem $\int \delta B_n (n \cdot B) dS$ making the problem non selfadjoint. When both perturbed normal magnetic field and tangential plasma displacement at the end plates vanish this term drops out. However, the analysis shows that zero tangential displacement at the end plates is not sufficient to make the normal perturbed plasma magnetic field $\delta B_n = 0$. So the formulation with free normal displacement at the end plates is correct but not fully self consistent.

No divertor analogs of the outer peeling mode have been discovered up to now. Further investigation is needed to get a conclusive answer on the outer mode stability in divertor configurations.

Conclusions The outer peeling modes were studied in the doublet tokamak equilibria with H-mode like profiles. The computations show that the modes are stable when the mantle plasma outside the separatrix is thin enough despite the current density is neutral. As the mantle is getting thicker the outer peeling mode with distributed current appears. This mode can be stabilized at finite β.

The choice of the boundary conditions plays a major role in the stability of divertor plasma configurations. Realistic stability problem formulation for the equilibria with magnetic field lines should be worked out.

References

Boucher D. *et al.* ITER plasma modeling and MHD stability limits, 15th Int. Conf. on Plasma Phys. and Controlled Nuclear Fusion Research, Sevilla, Spain, September-October (1994), paper IAEA-CN-60/E-P-2

Degtyarev L.M., Martynov A., Medvedev S., Troyon F., Villard L. Influence of plasma near separatrix on ideal MHD stability in tokamaks 22th EPS Conf. on Controlled Fusion and Plasma Phys., Bournemouth, Proc. Contrib. Papers, Vol.19C(1995), Part I, p.217

Snijders P., Alper B., Bak P. *et al.* Influence of MHD instabilities on JET high performance, 22th EPS Conf. on Controlled Fusion and Plasma Phys., Bournemouth, Proc. Contrib. Papers, Vol.19C(1995), Part IV, p.61

Huysmans G.T.A., Chalis C.D., Erba M. *et al.* Influence of edge currents and pressure gradients on the MHD stability of low-n external kink modes, 22th EPS Conf. on Controlled Fusion and Plasma Phys., Bournemouth, Proc. Contrib. Papers, Vol.19C(1995), Part I, p.201

Wesson J.A. Hydromagnetic stability of tokamaks, Nucl. Fusion, Vol.18(1978), p.87

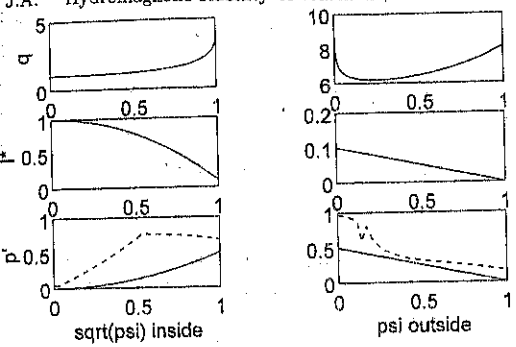


Fig.3. Plasma parameter profiles for the doublet equilibrium with $\beta = 1.68\%$. Pressure gradient profile locally optimized against ballooning mode stability is shown by a dashed line.

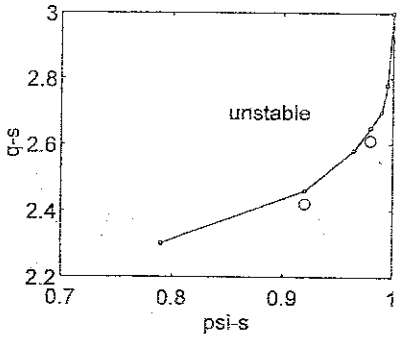


Fig.2. Peeling mode $n = 1$ instability region $q_s \leq 3$ for single axis plasma versus the value of normalized poloidal flux ψ_s left in the plasma. The points correspond to $\beta = 0$, the circles – to $\beta = 1.68\%$.

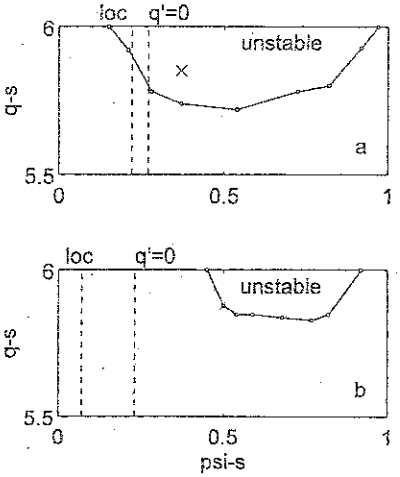


Fig.3. Outer peeling mode $n = 1$ instability region $q_s \leq 6$ for doublet plasmas versus the value of normalized poloidal flux ψ_s left in the mantle plasma. The locations of the safety factor minimum and marginally stable value of ψ_s for localized peeling mode criterion are marked.
a) $\beta = 0\%$ b) $\beta = 1.68\%$

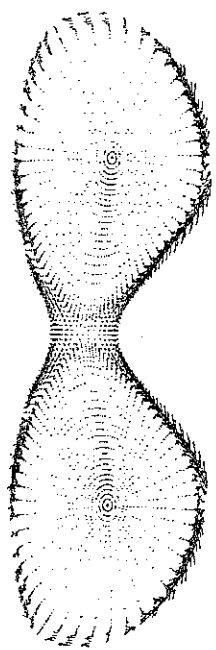


Fig.4. Outer peeling mode arrow plot for the doublet configuration

Mechanisms of self-intreraction of magnetoplasma surface waves at the plasma-metal interface.

N.A.Azarenkov , K.N.Ostrikov.
Kharkov State University, Svobody sq.4, Kharkov, 310077, UKRAINE.
Fax: (0572) 353977, e-mail: azarenkov@pem.kharkov.ua

Surface magnetoplasma waves (SW) propagating at the interface between a dielectric plasma and a metal nowadays are the subject of intensive studies [1]. The interest to this kind of wave perturbations is caused by both fundamental and applied aspects. The fundamental interest to the SW is mainly due to the fact that even the fact of their existance was doubtful for a long period of time [2]. The applied interest is caused by a possibility of using of the SW in a number of problems of plasma and semiconductor electronics, gas discharge physics. Here we consider the nonlinear self-interaction effects which are realized during the process of propagation of finite amplitude SW at the above-mentioned interface across an external magnetic field (the latter is parallel to the interface). We consider the situation when the SW phase velocities are supposed to significantly exceed the electron thermal velocities, and also the electronic free tracks are assumed to be less then the SW wavelengths and skin depths. In this case the equations of two fluid quasihydrodynamics can be used to adequately describe the nonlinear SW self interaction processes. In the present report we present the general expressions of the SW nonlinear frequency shift in the framework of the third order nonlinear susceptibilities formalism as well as discuss the following possible mechanisms of the nonlinearity leading to the SW self-interaction:

a) the nonlinearity caused by the nonlinearity of the basic set of quasihydrodynamical equations (hydrodynamical nonlinearity). Here there exists two possible self-interaction channels: the self-interaction through the second-harmonics generation and the self-interaction due to a ponderomotive force action.

b) the nonlinearity caused by the non-parabolic relation between electrons quasimomentum and energy. This kind of nonlinearity is typical for semiconductor plasmas and is analogous to the relativistic nonlinearity in gaseous plasmas.

c) the nonlinearity which is due to electrons heating in the wave field (heating nonlinearity).

d) Ionization nonlinearity.

Now let us briefly discuss the results associated with the use of the formalism of third order nonlinear susceptibilities as well as with the action of each mechanism mentioned above.

1. To describe the nonlinear properties of the studied SW, we start from the set of the Maxwellian equations. Using this basic set together with the necessary boundary condition $E_y=0$ at the interface we obtain the following nonlinear dispersion relation

$$D(\omega,k_2)=-\frac{\pi\omega}{c\varepsilon^{3/2}}\left[\varepsilon_2\left[1-\left(\frac{\varepsilon_1}{\varepsilon_2}\right)^2\frac{\varepsilon_2}{|\varepsilon_2|}\right]\left[\chi^{(3)}_{1111}+\varepsilon_1\Theta^{(3)}_{1331}+\sqrt{\varepsilon_1}\Theta^{(3)}_{1311}+\sqrt{\varepsilon_1}\Theta^{(3)}_{1113}\right]+\right.$$

$$\left.+\varepsilon_1(1-sign\,\varepsilon_2)\left[\chi^{(3)}_{2111}+\varepsilon_1\Theta^{(3)}_{2331}+\sqrt{\varepsilon_1}\Theta^{(3)}_{2131}+\sqrt{\varepsilon_1}\Theta^{(3)}_{2113}\right]-\right]|E|^2=\gamma|E|^2 \quad (1)$$

where $D(\omega,k_2)=k_2\varepsilon_2-\varepsilon_1\kappa_1$ is the SW linear dispersion relation, ω, k_2 are the eigenfrequency and wavenumber, respectively; ε_1, ε_2 are the components of magnetoplasma dielectric tensor, κ_1^{-1} is the SW skin depth, $\chi^{(3)}_{ijkl}$ is the third order nonlinear susceptibility tensor. The values describe the influence of so-called magnetic nonlinearities on the SW self-interaction. The general form of the SW nonlinear frequency shift is easily obtained from (1):

$$\delta\omega_{NL}=\gamma\left[\frac{\partial D(\omega,k_2)}{\partial\omega}\right]^{-1}_{\omega_0,k_{20}}|E|^2=\tilde{\gamma}|E|^2 \quad (2)$$

Here ω_0 and k_{20} are the solutions of the linear dispersion equation $D(\omega_0,k_{20})=0$. The general expression (2) for the SW nonlinear frequency shift is valuable under a problem of determination of the nonlinear susceptibilities of the medium. Namely, the comparison of the right-hand side of (2) with the value $\delta\omega_{NL}$ obtained experimentally, can provide the values of the components of the third-order susceptibilities tensor [3].

2. The hydrodynamic nonlinearities arise due to the presence of the nonlinear terms such as $\left(\vec{v}\nabla\right)\vec{v}$, $(e/mc)\left[\vec{v},\vec{H}\right]$ in the set of quasihydrodynamical equations [2]. The nonlinearities is assumed weak with the corresponding parameter $\mu=v_E/v_{ph}\ll 1$, v_E is the electrons oscillation velocity in the SW and the static surface-type perturbations are generated (the processes $\omega+\omega=2\omega$ and $\omega-\omega=0$ take place, the latter process is due to the ponderomotive force action). At the second stage the second harmonics and the static surface perturbations interact with the SW first harmonics (processes $2\omega-\omega=\omega$ and $0+\omega=\omega$, respectively) and such interactions lead to the arising of the nonlinear response at the frequency ω (its amplitude is proportional to $|E|^2E$).The nonlinear frequency shift and the nonlinear envelope waves arise as a result of this process. So, in the third approximation with respect to the SW field it is possible to obtain the following dispersion equation

$$\omega=\omega_0+Q|E|^2 \quad (3)$$

The exact expressions for ω_0 and Q of the magnetoplasma SW from different frequency ranges are given in [4]. With nonlinear dispersion equation (3) in mind, one can derive the nonlinear Shrodinger equation for the envelope amplitude

$$i\left(\frac{\partial E}{\partial t}+v_g\frac{\partial E}{\partial y}\right)+lvE+P_\parallel\frac{\partial^2E}{\partial y^2}+P_\perp\frac{\partial^2E}{\partial z^2}=Q|E|^2E \quad (4)$$

v_g is the SW group velocity, $P_{\parallel} = 0.5(\partial v_g / \partial k_z|_{k_{z0}})$, $P_{\perp} = v_g / 2k_{z0}$, ν is the nonlinear damping increment, E is the SW envelope amplitude. Dependent on the frequency and other parameters of the problem, various soliton-like solutions are possible [4].

In the semiconductor plasma the nonlinearity caused by a nonparabolic relation between electrons quasimomentum $\vec{p}$ and energy ε can also lead to the SW self-interaction. The relation is supposed to be described by the isotropic nonparabolic law according to Kane [5]. In this case the following correlation between $\vec{p}$ and ε is valid (a weak nonparabolicity is assumed) $\vec{v} = \left(\vec{p}/m_{eff}\right)\left(1-(p/\tilde{p})^2\right)$, where $\tilde{p}^2 = 2m_{eff}\varepsilon_g$, ε_g is the energy gap width, m_{eff} is the electrons effective mass. The latter relation is introduced into the basic system of quasihydrodynamic equations for high-frequency electrons motions. Following [5] one can conclude that the impact of this nonlinearity mechanism is the most significant in narrow-gap semiconductors and the results of the SW nonlinear evolution governed by (4) significantly depend on the kind of the sample band structure. Namely, in the materials with the inverse band structure the solutions of (4), which are impossible under the same conditions in gaseous plasma and in semiconductors with normal band structure, can be realized.

The plasma-like medium electrons getting additional energy from the SW field, can transfer it to ions, phonons, impurities and other scattering centers. This leads to the medium temperature variation, and, consequently to a variation of the effective frequency of electrons collisions

$$\nu(\Theta) = \nu(T) + \left.\frac{\partial \nu(\Theta)}{\partial \Theta}\right|_T \Theta(x, y, |E|^2),$$

where T is the equilibrium temperature (temperature variation is supposed small, i.e. a weak heating approximation is used). The results of studies of this nonlinearity impact [6] shows that the results of the SW self-interaction efficiency significantly depend on the dominant energy scattering mechanism as well as on the distance from the source of SW excitation ($y=0$). It is shown that near the point $y=0$ the impact of the heating nonlinearity is usually predominant over the other mechanisms considered above.

The expressions for the SW nonlinear frequency shift are also obtained under taking into account of the ionization nonlinearity in low-temperature gas-discharge plasmas. The presence of the SW field influences the basic processes in the discharge such as excitation, ionization, recombination, transport processes, etc. this fact leads to the disturbance of the equilibrium plasma density associated with the mechanism of ionization nonlinearity, which can be obtained from the equations of the energy and particle balance in a discharge and in the case of a local plasma heating under a volume recombination controlled regime can be written as follows:

$$\frac{\tilde{n}_e}{n_0} = \frac{|E_{x0}|^2}{E^2_{n(i)}},$$

where $E_{n(i)} = \left[\frac{3m_e(\omega^2-\omega_e^2)^2}{(\omega^2+\omega_e^2)u_{e,i}}\frac{\nu_{e0}}{\nu_{en}}\right]^{1/2}\frac{u_e}{e}$, ω_e is the electron cyclotron frequency, E_{st} is SW electric field x component; $u_{e,i}$ are the excitation and ionization potentials, ν_{e0} is excitation frequency, ν_{en} is the electron-neutral collisions frequency, indexes $n(i)$ correspond to different discharge regimes dependent on the electron temperature (n corresponds $T_E > \frac{2}{3}(u_i - u_e)$ and i to the opposite). The SW nonlinear frequency shift leading to the interaction effect is expressed as $\delta\omega_{NL} = \omega_0(\tilde{n}_e / 2n_0)$ under conditions discussed above.

The comparison of impacts of different mechanisms into the resulting SW nonlinear frequency shifts is performed for a number of definite cases.

[1] Azarenkov N.A., Kondratenko A.N., Ostrikov K.N. Sov.Radiophysics and Quantum Electronics, 1993, v.36, N5, p.335-390.

[2] Kondratenko A.N. Plasma waveguides, Atomizdat, Moscow, 1976.

[3] Azarenkov N.A., Kuzmenko A.V., Ostrikov K.N. Physica Scripta, 1995, v.52, N6, p.668-672

[4] Azarenkov N.A., Ostrikov K.N. Sov J. Comm.Techn.and Electronics. 1990, v.35, N2, p.325-330; 1991, v.36, N6, p.1161-1167.

[5] Azarenkov N.A., Kondratenko A.N. Ukr.Phys Journ, 1990,v.35, N11, p.1715-1719.

[6] Azarenkov N.A.,Ostrikov K.N Sov.J.Comm.Tech.and Electronics 1994, v.39, N4, p.688-693.

GLOBAL STRONGLY NONLINEAR STRUCTURES IN BOUNDED PLASMA-RELATIVISTIC BEAM SYSTEM

E.Fedutenko, A.Kozyrev, V.Lapshin

Kharkov State University, 310077 Kharkov, Ukraine.

...paper studies strongly nonlinear global structures formed due to an interaction of a relativistic electron beam with a bounded plasma immersed in external magnetic field. Anologous structures were often observed both experimentally (see for example [1] and references therein) and numerically as a result of self-organization processes in drift-wave turbulence in bounded magnetized plasmas. The possibility of the appearance of the localized structures in non-neutral inhomogeneous non-relativistic electron beams propagating in vacuum along the external magnetic field was shown in [3]. So, the study of global nonlinear structures in bounded plasma-beam systems as a possible final stage of nonlinear evolution of beam-driven instability might be of interest both from the point of view of general theory and possible applications in plasma electronics.

We consider a cylindrical wave-guide of radius R filled with the fully ionized electron plasma and immersed in strong external magnetic field $\vec{B}_0$ directed along the wave-guide axis which is chosen as $\vec{z}$ axis. The condition $\omega_{Pe}^2 \ll \omega_{Ce}^2$ is supposed to be satisfied, where ω_{Pe} and ω_{Ce} are electron Langmuir and cyclotron frequencies, respectively. We suppose an electron beam of small density ($n_{ob} \ll n_{op}$) to propagate along the external magnetic field with shear velocity $V_{oz} = V_o(r)$ which in general case may be of the order of the light velocity c. The beam density is supposed to be strongly nonuniform across the magnetic field ($n_{ob} = n_{ob}(r)$, $n_{ob}(R) \ll n_{ob}(0)$) that leads to the appearance of the finite axial beam velocity, namely $V_{o\varphi} = (\gamma v_{Te}^2/\omega_{ce})(dlnn_{ob}/dr)$, where v_{Te} and $\gamma = (1 - V_0^2/c^2)^{1/2}$ stand for thermal velocity of electrons and relativistic factor , respectively. Here and hereafter we suppose $V_{o\varphi}^2 \ll V_{oz}^2$. 3D wave perturbations are suppopsed to be excited in such a system. In the case when characteristic frequency ω, wavenumber k, and velocity v of perturbations satisfy the conditions $\omega \ll kV_o$, $v \ll V_o$ the oscillations may be considered as electrostatic ones and can be described by the following system of basic equations:

$$\frac{d\vec{v}_i}{dt} + (\vec{v}_i\nabla)\left(\vec{V}_{oi}/\gamma + \vec{v}_i\right) = \frac{e}{m_e}\nabla\Phi - \frac{e}{cm_e}(\vec{v}_i \times \vec{B}_o)$$
$$\frac{dn_i}{dt} + \nabla\left[(n_{oi} + n_i)\vec{v}_i\right] = 0$$
$$\nabla^2\Phi = 4\pi e(n_1 + n_2)$$

where $\frac{d}{dt} = \frac{\partial}{\partial t} + (\vec{V}_o/\gamma)\cdot\nabla$, Φ is the electrostatic potential of oscillation $i = 1, 2$, "1" stands for the beam part, "2" for the plasma one. Eqs.(1-3) considered along with following boundary conditions

$$v_r\,|_{r=R} = 0 \qquad n\,|_{r=R} = 0 \qquad \Phi\,|_{r=R} = const,$$

that correspond to the case of metalic chamber bounding the plasma $r = R$. We consider stationar perturbations, namely all perturbed values supposed to be functions of (r, Θ), where $\Theta = k_z z + m\varphi - \omega t$, k_z and m are the longitudinal and azimuthal wavenumbers, respectively. In this case ($\omega \ll \omega_{ce}$ Eqs.(1-3) can be reduced to the following model system of equations

$$\frac{\partial}{\partial\theta}\left\{\omega_d v_z + (mk_v + k_z)\frac{e\Phi}{m_e}\right\} = \frac{cm}{B_o}\{\Phi, v_z\} \quad (5)$$
$$\frac{\partial}{\partial\theta}\left\{\omega v_{2z} + k_z\frac{e\Phi}{m_e}\right\} = \frac{cm}{B_o}\{\Phi, v_{2z}\} \quad (6)$$
$$\frac{\partial}{\partial\theta}\left\{\omega_d n_1 - n_{ob}k_z v_z + k_n m\frac{e\Phi}{m_e}\right\} = \frac{cm}{B_o}\{\Phi, n\} \quad (7)$$
$$\frac{\partial}{\partial\theta}\{\omega n_2 - n_{op}k_z v_{2z}\} = \frac{cm}{B_o}\{\Phi, n_2\} \quad (8)$$
$$\nabla^2\Phi = 4\pi e(n_1 + n_2), \quad (9)$$

where $\omega_d = \omega - k_z V_{oz}/\gamma - mV_{o\varphi}/r$, $k_v = 1/(\gamma\omega_{ce}r)dV_{oz}/dr$, $k_n = 1/(\omega_{ce}r)dn_o/$

$$\{A, B\} = \frac{1}{r}\left(\frac{\partial A}{\partial r}\frac{\partial B}{\partial\theta} - \frac{\partial A}{\partial\theta}\frac{\partial B}{\partial r}\right) \quad (10)$$

...case the system (5-9) along with boundary conditions (4) de-
...well known beam instability in a bounded plasma with the growth
$(\ldots/\omega_{op})^{1/2}$. Below we show that at strongly nonlinear stage of this
...the global nonlinear structures can be created.

...dimensionless variables $\vec{r}/R$, $\vec{k}R$, $\vec{v}/V_{oz}(0)$, $n_{1,2}/n_{op_{1,2}} = N_{1,2}$,
... $\omega/\omega_{ce} = \Omega$, $\omega_d/\omega_{ce} = \Omega_d$, we can derive the following equation
...potential

$$\ldots\left(\frac{\beta_d}{\varepsilon_1} - \frac{\beta}{\varepsilon_2}\right) c_1\Psi + \frac{\beta}{\varepsilon_2}\frac{R^2}{r_{D1}^2}\nabla^2\Psi - \frac{\overline{k_z}}{\varepsilon_1}c_1\Psi - \frac{r_{D2}^2}{r_{D1}^2}\frac{\overline{k_z}c_2}{\varepsilon_2}\Psi + \frac{\kappa m}{\varepsilon_1}\Psi\right\} =$$

$$\ldots R^2\left\{\Psi, \nabla^2\Psi\right\}, \qquad (11)$$

$$\alpha = \frac{\omega_{be}\ R}{V_{oz}(0)}\ ; \qquad (\gamma, \gamma_d) = \alpha\frac{V_{oz}^2(0)}{v_{Te}^2}(\Omega, \Omega_d)\ ;$$
$$(\beta, \beta_d) = \alpha\left(\frac{n_{op}(0)}{n_{op}}\Omega\ ,\ \frac{n_{ob}(0)}{n_{ob}}\Omega_d\right)\ ; \qquad (12)$$
$$r_{D1} = v_{Tb}/\omega_{Pb}; \quad \varepsilon_{1,2} = \frac{v_{Te}^2}{\omega_{ce}RV_{oz}}\left(\frac{n_{o_{1,2}}(0)}{n_{o_{1,2}}}\right);$$

... are arbitrary constant. Using the symmetry property of the jacobian ... can construct the particular solution of Eq.(11) satisfying the boundary ...ons (4) in the following form

$$\Psi(r,\theta) = \Phi_1(r)cos\theta + \Phi_2(r), \qquad (13)$$

$$\Phi_1(r) = BJ_m(\overline{k_z}r), \qquad (14)$$
$$\Phi_2(r) = -\frac{\pi}{2}\left\{J_o(\sqrt{A}r)\int_0^r \xi F_m(\xi)N_o(\sqrt{A}\xi)d\xi -\right.$$

$$N_o(\sqrt{A}r)\int_0^r \xi F_m(\xi)J_o(\sqrt{A}\xi)d\xi\Bigg\} =$$

$$= -\frac{\pi}{2}\int_0^r \xi F_m(\xi)\left[N_o(\sqrt{A}\xi) - \frac{N_o(\sqrt{A}r)}{J_o(\sqrt{A}r)}J_o(\sqrt{A}\xi)\right]J_o(\sqrt{A}r),$$

$$F_m(r) = -\frac{1}{mR^2}\int_0^r d\xi\cdot\xi\cdot r_{Di}^2\left\{\left(\frac{\beta_d}{\varepsilon_1}-\frac{\beta}{\varepsilon_2}\right)c_1 + \frac{\beta}{\varepsilon_2}\frac{R^2}{r_{Di}^2}A - \right.$$

$$\left. - \left(\frac{c_1}{\varepsilon_1} - \frac{c_2}{\varepsilon_2}\frac{r_{02}^2}{r_{D1}^2}\right)\widetilde{k}_z + \frac{\kappa m}{\varepsilon_1}\right\},$$

where $J_m(x)$ and $N_m(x)$ are Bessel and Neumann functions of order m, respectively, the value $\widetilde{k}_z = (A - \overline{k}_z^2)^{1/2}$ satisfies the condition $\widetilde{k}_z R = x_{mi}$, x_{mi} is the ith zero of the $J_m(x)$, A and B are arbitrary constant. Obtained global solution may be considered as a final stage of the nonlinear evolution of the plasma-beam instability in bounded plasmas. Note that condition $\Phi_2(R) = 0$ defines the dispersion of strongly nonlinear global modes in the system considered.

References

[1] Sommeria J. et al, Nature, 1988, v. 331, p.689.

[2] Marcus P., Nature, 1988, v.331, p.693.

[3] Golub Ya.Ya. et al. In: Nonlinear World.-Singapore: World Scientific, 1990.-v.2.-p.857-866.

The research is supported by Ukranian State Committee on Science and Technologies, contract N 8303, and by International Atomic Energy Agency, grant N 8931/RO.

...ation and Control of a Steady-State, Non-Monotonic ...Double Layer in a Triple Plasma Machine

...Bak[1,2], JongGu Kwak[1,2], C.W. Park[3], J.M. Han[1], H.D. Choi[2], H.I. Bak[2], and S.K. Kim[1]

...Energy Research Institute(KAERI), POB 105, Yusong, Taejon 305-600, Korea
[2] Seoul National University, Seoul, Korea
...Research Institute of Standard and Science(KRISS), Taejon, Korea

...ductions

...double layer(DL) is a region of the non-neutral plasma consisting of ...two space-charge layers of opposite charge, and the phenomenon was first ...by Langmuir.[1] Since that time, the various DL structures have been ...in laboratory plasmas and have been found in numerical simulations.[2] ...the stationary non-monotonic double layers(NDLs) with a stable potential ...observed in the target chamber of an unmagnetized triple plasma device.[2] ...Klinger et al. reported only the observation of the NDL in the magnetized ...cross section of a long triple plasma device.[3]
...these structures, Hershkowitz et al. suggested that the existence of a ...potential dip in the axial direction was due to an ion pumping effect in ...direction.[2] Also Sekar et al. suggested that injected electron currents ...a deep potential dip on the low potential side of the strong DL due to the ...negative space charge.[4] Although there have been several published ...NDL experiments, they have not investigated the properties of them and ...observed these structures. Thus, the laboratory evidence for such ...NDLs in the triple plasma device deserves further experimental ...ation in order to study on the formation mechanism of the NDL and on the ...distinctions and similarities between NDLs and ordinary DLs.
...the present work, the stationary NDLs which have a stationary potential dip ...the low potential side are observed in the target chamber of the triple plasma ...The potential structures of the double layers are changed by varying the ...voltage of each control grid which located between target and source chambers. ...changes of the potential structures are qualitatively explained by the model of ...sheath which describes the relation of potential curvature and particle ...which are formed by controlling the incoming electron flux and ion flux ...target chamber.

...Experimental setup

...The triple plasma device used in this experiment consists of two identical source ...and a target chamber placed between them, as shown in Fig. 1. All three ...walls are held at ground potential. Two independent argon plasmas were ...in the two source chambers by ionizing electrons from filaments, and were

confined by surface multipole magnetic field. Each source plasma is separ
the target chamber by two grids such as grids A and B on the source ch
side, and
and D on
source cha
side. Each
grids is sp
about 1.5 c
Plasma in
chamber wa
controlled b
of four bou
grids. The
potential wa
measured b
emissive pro
made of a 0
mm φ - tung

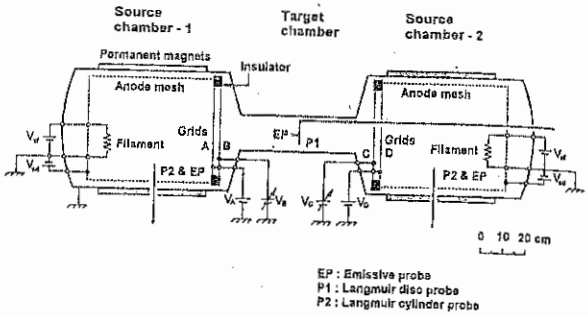


Fig. 1. Schematic diagram of the triple plasma device.

wire, using the floating potential method.[5] Stable double layers are achieve
appropriate values are chosen for source parameters, biases on all four grids,
respectively. For experimental conditions are followed; electron temperature a
plasma density in target chamber were 2 ~ 4 eV and 0.3 ~ 2.0 $\times 10^{6}$ cm^{-3}
respectively. Plasma potentials of sources are ϕ_{S1} = 45 V and ϕ_{S2} = 50 V, a
density is less than 10^{9} cm^{-3}. Working gas pressure was 1.0 ~ 3.6 $\times 10^{-4}$ mb
The base pressure in this experiment was less than 2.0 $\times$ 10^{-6} mbar.

III. Results and discussions

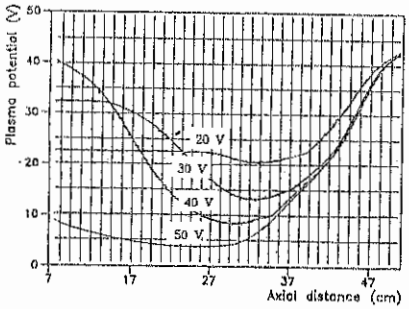


Fig. 2. Stationary potential profiles versus axial distance for four different bias voltages of the control grid B. Conditions of the rest grids ; V_A = 41 V, V_C = 45 V and V_D = 45 V.

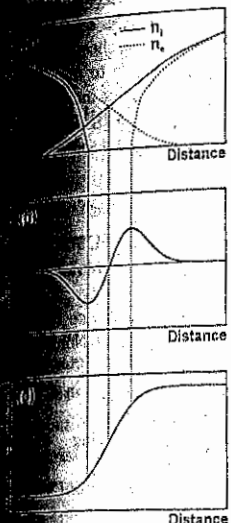
1. Dependence of NDL structure the biases of control grids

The NDL which has a stationa
potential dip was produced in the
target chamber of the triple plasma
device, by adjusting bias voltages o
four control grids, which located
between a target and source chambe
as seen in Fig. 1. The potentials w
measured along the axis of the targ
chamber, starting at position of 7 cm
from the position of the grid B, on
source chamber-1 side. These
experimental NDLs shows various
steady state potential structures, wh
the bias voltage on a control grid is

...ear an appropriate experimental condition, as shown in Fig. 2. The depth ... the potential dip of the NDL grow by increasing bias voltage of the ... in the range of V_B = 20 ~ 40 V. When V_B is more positive than the ...ential of the source-1, the potential dip abruptly decreases and the ...rofile shows the shape which is similar to that of a monotonic DL. In ...ments, it was thought that the potential profile was changed mainly by ...ion flux($n_i v_B$) from source-1 to target plasma, because the drift velocity ...ming ions was related by the difference of a bias voltage on the grid ...h a plasma potential of source-1(ϕ_{S1}) such as $v_B = \sqrt{2e(\phi_{S1} - V_B)/M}$, where ...ion mass. Thus, it is known that the potential structure of the NDL can ...led by changing v_B.

...itative interpretation for change of NDL structure

...change of the potential profiles of the NDL was interpreted qualitatively by ...ing incoming ion flux from plasma source. In this interpretation, the continuity of particle flux and description for sheath structure[6] were used. For a monotonic DL structure as seen Fig. 3, the high potential side is explained by the normal sheath structure with Bohm condition, because the structure shows a negative potential curvature which indicates the existence of positive space charge layer. And the low potential side is explained by positive potential curvature which indicates the existence of negative space charge layer, which is obtained in sheath structure when free electrons are added on the low potential side. Thus the high and low potential side of a monotonic DL can be interpreted by a charge density which is obtained by particle density profiles estimated by sheath structure. In order to interpret for change of NDL structure, an effect of drift velocity(v_B)of incoming ion is added. By decreasing the v_B of ions injected into a low potential side, it is estimated that potential curvature becomes more positive from a Poisson equation



...3. Particle density(a), ...ge density(b) and ...tential(c) profiles of a ...notonic DL.

$$\frac{d^2\chi}{d\xi^2} = e^{-\chi} - \left(1 + \frac{2\chi}{\Gamma^2}\right)^{-1/2} \qquad (1)$$

where $\chi = e(\phi - \phi_{cathode})/kTe$, $\xi = x(n_0 e^2/\varepsilon_0 kT_e)^{1/2}$and $\Gamma = v_B/C_S$. So the density profile shows that negative space charge layer is expanded on the low potential side as seen in Fig 4(a). Also the space charge near the low potential

side becomes more positive because n_i increases as v_{i0} decreases. This is by a particle continuity from source to such as

$$n_i = \frac{n_{iS} v_{iS} (= \Gamma(const.))}{v_{i0}}$$

Thus the NDL has a more negative po dip and the wide of the dip is broaden is decreased. Also the NDL becomes a monotonic DL when the incoming ions prevented($v_{i0} \sim 0$), as shown in Fig. 4.

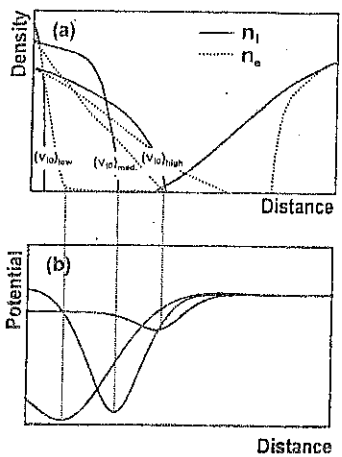


Fig. 4. Illustration of dependence of density(a) and potential(b) profiles on the velocity of incoming ion from plasma source for the NDLs.

VI. Summary

The various NDLs, which have the po dip in the stationary state, could be obse by independently varying bias voltage of control grid in triple plasma device. Als variation of NDL potential can be qualitati interpreted by using the simple sheath mo which relates potential curvature to partic density. Conclusively, the results indicate NDL structure can be controlled by incom particle flux from source to target.

V. References

[1] L.P. Block, "A double layer review", Astrophys. and Space Sci., 55(1978) 59.
[2] N. Hershkowitz, "Review of recent laboratory double layer experiments", Sp Sci. Rev., 41(1985) 351.
[3] T. Klinger and A. Piel, "Weak double layers in the triple plasma device KIW 1992 in Proceedings of the Fourth Symposium on Double Layers and Nonline Potential Structures in Plasmas, Innsbruck, Austria, p.226.
[4] A.N. Sekar and Y.C. Saxena, "Observations of strong double layers in a do plasma device", Plasma Phys. and Controlled Fusion, 27(1985) 673.
[5] N. Hershkowitz and M.H. Cho, "Measurement of plasma potential using collecting and emitting probes", J. Vac. Sci. Technol., **A6**(1988) 2054.
[6] F.F. Chen, "*Introduction to Plasma Physics and Controlled Fusion, Vol.1*", 29 Plenum Press, 1984.

Acknowledgement

The authors wish to thank Professor M.H. Cho and Dr. S.G. Lee for helpful discussions and Dr. J.W. Han for support during experiment in KRISS. This research was supported by the Ministry of Science and Technology (MOST).

Numerical Studies of Dipole Drift-Vortices

E. Westerhof, J. Rem

FOM-Instituut voor Plasmafysica 'Rijnhuizen'
Association EURATOM-FOM
Postbus 1207, 3430 BE Nieuwegein – Nederland

Introduction

The nonlinear evolution of electrostatic drift modes with potential ϕ in a shearless slab with a density gradient is given by the Hasegawa-Mima (HM) equation (or vorticity equation),

$$\partial_t(\nabla^2\phi + v_* x) + [\phi, \phi - \nabla^2\phi + v_* x] = 0, \qquad (1)$$

where v_* is the drift velocity associated with $n(x)$. Time is normalized to Ω_{ci}^{-1} and lengths to the ion gyroradius (at the electron temperature), and the Poisson bracket $[f, g] = (\partial f/\partial x)(\partial g/\partial y) - (\partial f/\partial y)(\partial g/\partial x)$ is used to write the convection with the $E \times B$ drift, as $[\phi, \cdot]$. Equation (1) reflects the conservation of generalized, potential vorticity $\bar{\omega} = \phi - \nabla^2\phi + v_* x$. Dipole solutions of HM have been obtained by Larichev and Reznik [1], and a large number of analytical and numerical studies of these dipoles, their stability and interaction, have been carried out (for a review see [2]). The dipole solutions are restricted to the range of propagation velocities $u_y < -v_*$, or $u_y > 0$, outside the range of phase velocities for linear waves.

We present a study of Larichev-Reznik dipoles by means of a Particle In Cell (PIC) code. As written in Eq. (1), HM is ideally suited for such an approach (cf. [3,4]). Not only is the conservation of vorticity trivial, also energy and generalized 'enstrophy' are found to be conserved well. Moreover, the particles conveniently provide fluid tracers, and contain a wealth of information for the interpretation of the dipole dynamics.

In the code, the particles represent finite fluid elements. Each particle is assigned an amount of generalized vorticity $\bar{\omega}$ consistent with given initial conditions. Each time step consists of the following procedures: a) assignment of generalized vorticity from particles to grid (Triangular Shaped Cloud algorithm [4]); b) solution of the potential, playing the role of streamfunction, on the grid according to $\phi - \nabla^2\phi = \bar{\omega} - v_* x$; c) the velocities then are calculated on the grid and interpolated (bilinear) to the particle positions; d) the particles are moved in time in accordance with this velocity. The equations are solved on a rectangular domain with periodic boundary conditions for ϕ. The initial conditions are taken from the analytical dipole solutions [1] or a superposition of these. Though these are not exact solutions on a periodic domain, consequent errors are found to be small, as the dipole fields decay exponentially at large distances. In our

first examples the dipole is perturbed by a finite tilt of its initial direction of prop
resulting in a stable or unstable oscillation of the dipole trajectory dependi
initial direction of propagation [5–7]. A second set of simulations has been p
for a dipole collision similar to Ref. [5]. Depending on the impact parame
differences in dipole dynamics are observed.

2. Tilt (In)stability

Two cases are presented of dipoles for which the initial direction of propagation
by 45° w.r.t. the y-axis. In both cases the background drift velocity is $v_* = 0.4$
dipole radius is $r_0 = 0.5$. The initial velocities are $u = .5$ and $u = -2.$ (in geo
terms these correspond to an eastward and a westward propagating dipole, respec
The calculated orbits of the 'centres of vorticity' of the dipole halves are pres
Figs. 1 and 2. The eastward moving dipole travels along a stable, oscillating tra
From the expressions in [6] the period and amplitude are expected to be $T = 2$
$\Delta x = 1.4$, respectively, in reasonable agreement with the period and ampli
presented in Fig. 1 (c.f. [7]). However, the oscillation is strongly damped.

The trajectory of the westward moving dipole instead is unstable (i.e. th
initially increases). Assuming no loss of vorticity from the dipole, it is expe
perform a cycloidal orbit with a net eastward motion or a figure eight. As is s
Fig. 2, this is indeed the case initially, but even before half a cycle is perform
dipole reverses its average motion eastward, moving along a stable, damped traj
Similar results are found for much smaller initial tilts as well. In summary, th
instability divides the dipoles into a stable $u > 0$ and a unstable branch $u < -$
net result of the instability being an approach towards the stable branch.

Further analysis of the particles initially inside one of the dipole halves, s
significant loss of particles (and hence generalized vorticity) from the dipole as
displaced in x. This loss of particles is a consequence of the breathing of the separa
of the co-moving streamfunction as the vorticity in each of the dipole halves ch
due to the displacement in x [8]. A difference in the loss from both dipole hal
responsible for the reversal of the motion in the tilt unstable case. Similarly the lo
responsible for the damping of the oscillation of the stable dipole.

3. Dipole Collisions

Next we analyze the dynamics of a dipole collision for the same parameters as in
drift velocity $v_* = 0.1$, dipole radii $r_0 = 0.5$, velocities $u_1 = .3$ and $u_2 = -.5$, in
positions $x_{1,2} = 0.$, $y_{1,2} = \mp 1.5$. The trajectories of the 'centres of vorticity' for
dipole half are given in Fig. 3. At the collision the original dipoles split. The halve
the different dipoles then form unbalanced dipoles, that travel along symmetric,
circular orbits. In the process, the weaker dipole halves are pulled around the stron
halves. After a half circle, a second collision occurs in which the original dipoles refo

Ref. [5] this collision is soliton-like: the original dipoles appear to survive But not entirely so. A detailed analysis of the present results obtained particles initially inside each of the dipole halves, reveals a significant from both dipoles: 25% from the weaker dipole 1 and still 14% from However, the lost particles accounted for only 4.2% and 1.2%, respectively, of vorticities in each dipole half. Apart from this detrainment and loss of centres of the weaker dipole have slightly separated. Both effects result in of the weaker dipole 1 by 13%. Dipole 2 has slowed down by just 2.2%. collision has been studied with a finite difference code. With the imple- the Arakawa scheme [9], 'enstrophy' and energy are well conserved and quite similar. A comparison is made of the behaviour of the conserved diffusion effects in the two numerical analyses.

soliton like behaviour is typical only of the special symmetric case of aligned impact parameter $b \equiv |\Delta x/r_0| = 0$, where Δx is the distance between the dipoles. Different values of the impact parameter result in widely different We find subsequently:

liton-like; $b = .2$: almost soliton like, but the asymmetric initial conditions are by the asymmetries in the reforming collision that leave the reformed dipole 2 the tilt instability; $b = .4$: due to increased asymmetry the impact parameter ond, reforming collision is increased even further, and only the stronger dipole but not without a large loss of vorticity from the colliding dipole half. Of the dipole, one half is almost completely torn apart; $b = .6$: reforming no longer the second collision, instead, while one dipole formed in the first collision one half of the stronger dipole survives as a monopole and one half of the dipole is destroyed; $b = .8$: the dipoles no longer split at the first collision, but slip along each other, such that one half of the weaker dipole is almost destroyed, tronger dipole is strongly perturbed to obtain a large tilt; $b = 1.$: the dipoles slip along each other, but both survive the collision now with a significant tilt.

knowledgement This work was performed under the Euratom–FOM Association ement with financial support from NWO and Euratom.

References

W.D. Larichev, G.M. Reznik, Oceanology **16**, 547 (1976). [2] W. Horton, A. wa, Chaos **4**, 227 (1994). [3] J.P. Christiansen, Journal Comp. Physics **13**, (1973). [4] R.W. Hockney, J.W. Eastwood, *Computer Simulation using Parti-* IOP Publishing Ltd (1988). [5] M. Makino, T. Kamimura, T. Taniuti, Journal Soc. Japan **50**, 980 (1981). [6] J. Nycander, M.B. Isichenko, Phys. Fluids B (1990). [7] J.S. Hesthaven, J.P. Lynov, J. Nycander, Phys. Fluids A **5**, 622 [8] O.U. Velasco Fuentes, G.J.F. van Heijst, J. Fluid Mech. **259** 79 (1994). A. Arakawa, J. Comp. Phys. **1**, 119 (1966).

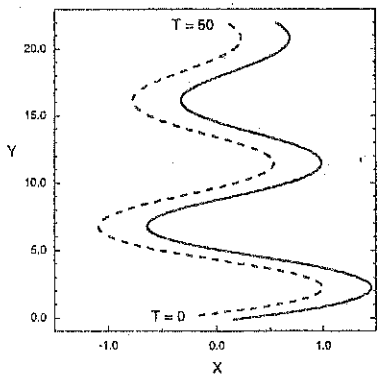


Figure 1. Trajectories of dipole halves (full line, $\bar{\omega}$ positive; dashed line, $\bar{\omega}$ negative) of a dipole tilted by 45° and with velocity $u = .5$ (eastward), radius $r_0 = 0.5$, and drift $v_* = 0.4$.

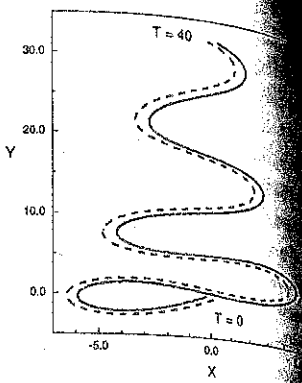


Figure 2. Trajectories of dipole ha (full line, $\bar{\omega}$ positive; dashed lin negative) of a dipole tilted by 45° with velocity $u = -2$ (westward), ra $r_0 = 0.5$, and drift $v_* = 0.4$.

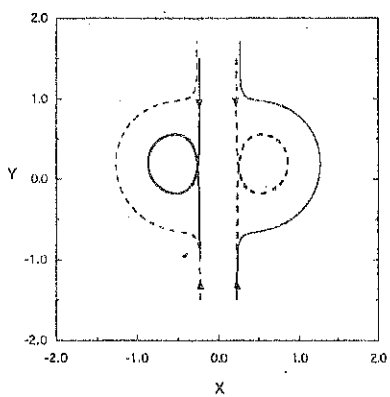


Figure 3. Trajectories of dipole halves (full line, $\bar{\omega}$ positive; dashed line, $\bar{\omega}$ negative) of two colliding dipoles with, resp., $u = -.5$ (fat curves), and $u = .3$, and with radius $r_0 = 0.5$, drift $v_* = 0.1$ and impact parameter $b = 0$.

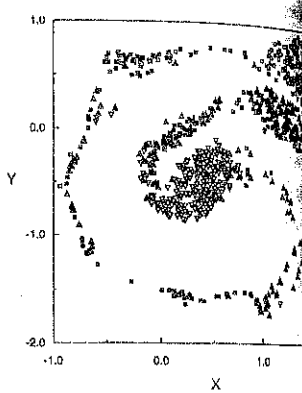


Figure 4. Result of a collision with im pact parameter $b = .6$ (other parameter as for Fig. 3). Every fifth particle from inside the dipoles is plotted: triangles for the stronger dipole with $u = -.5$ and squares for the weaker one with $u =$ filled symbols indicate dipole halves with $\bar{\omega}$ positive, open symbols $\bar{\omega}$ negative.

Drift Waves Destabilisation in a Toroidal Plasma

C.Riccardi, L.Gamberale, D.Caspani, L.Fattorini and M.Fontanesi

Dipartimento di Fisica, Università di Milano,

Via Celoria 16, 20133- Milano, Italy

lysis of density fluctuations spontaneously excited in a magnetized plasma is of terest in understanding of the anomalous transport in toroidal plasma devices and subject of several theoretical and experimental studies. Some experiments were ed to the measure of the turbulence and on the nonlinear coupling between ions, providing that turbulent fluctuations can be regarded as nonlinear wave-interactions of unstable modes of drift type[1-3].

r concerns the analysis of turbulence in a toroidal magnetoplasma Thorello. dy has been performed by evaluating wavenumber and frequency spectra and erence coefficients of density fluctuations, identifying the presence of drift and ion ic waves. We were able to analyse the way in which a quasi coherent drift wave ffuses in space and time. The experimental evidence of the destabilisation of the waves in high magnetic fields has been subject of several theoretical analyses[1] owed that a coherent drift mode can destabilise and generate a turbulent spectrum, ending on the ion gyro-radius, in particular when the ion gyroparameter $\beta=(k_{\perp}\rho$ where ρ_i is the ion gyro-radius calculated at the electron temperature.

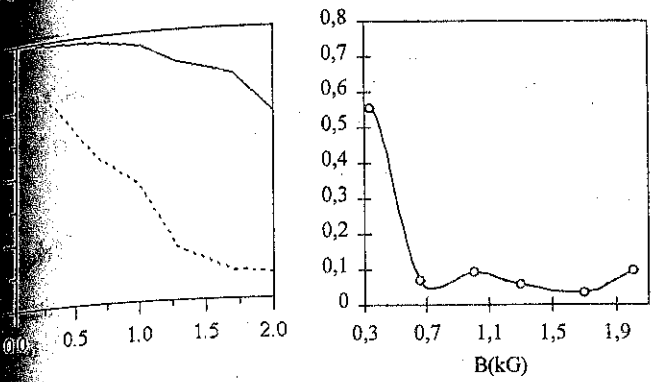
der to explore the presence of the nonlinear wave-wave interactions between the waves and the degree of the spatial coherence, we evaluate the poloidal and parallel erence and bicoherence, the ion gyroparameter β as a function of the toroidal netic field intensity. The wave coherence coefficient is defined by the following ula:

$$\gamma(\omega) = \frac{\left|\frac{1}{M}\sum_{i=1}^{M}\Phi_1^i(\omega)\Phi_2^{i*}(\omega)\right|}{\left[\frac{1}{M}\sum_{i=1}^{M}\left|\Phi_1^i(\omega)\right|^2 \frac{1}{M}\sum_{i=1}^{M}\left|\Phi_2^i(\omega)\right|^2\right]^{1/2}}.$$

where $\phi_1(\omega)$ and $\phi_2(\omega)$ are obtained by Fourier transforming the two signals f
esimo sample and M is the sample number. $\gamma(\omega)$ represents a measure of the
coherence of the ω-modes between the points x and $x+\Delta x$, x represents the
coordinates (parallel, poloidal or radial); so we can evaluate the total co
coefficient as integral over the frequencies, defined as $\gamma = \sum_f \gamma(f)$.

To investigate the occurrence of a non linear mechanism in the fluctuation spectr
have estimated the bicoherence coefficient following the procedure describ
reference[2,3] where the integrated bicoherence is obtained summating ove
frequencies which satisfy the selection rule $f = f_1+f_2$: $b^2(f) = \sum_{f1,f2} b^2(f_1,f_2)$. The
integrated bicoherence has been obtained in two ways: in the first way we di
integrate over the frequency : $b^2 = \sum_f b^2(f)$, where $b^2(f)$ is the integrated bicoherenc
the second way we integrate over the frequency weighting the bicoherence wi
frequency spectrum: $b^2 = \sum_f S(f) b^2(f)$, where $S(f) = |\Phi(\omega)^2|$, is the frequency spectr
Through previous analyses based on the estimation of the wave dispersion relatio
found that in our plasma are present two kind of waves: the electron drift waves dri
by density gradient (poloidal mode) and the ion acoustic waves (parallel mode).
In fig.1a the poloidal and parallel coherences have been evaluated as a function of
magnetic field. In correspondence of low magnetic field values the spatial polo
coherence is high so that the poloidal drift waves are quite stabilised. For these magn
field values the β parameter assumes values between 0.6 and 0.2,as shown in fig.1b.
With increasing the magnetic field value the waves destabilise as the iongyroradi
parameter β decreases below 0.1 (fig.1b), the spatial poloidal coherence coeffici
lowers (fig.1a). As concerns the ion acoustic waves we can see that the paral
coherence (fig.1a), obtained with two langmuir probes aligned along the paralle
coordinate, is high and weakly dependent on the magnetic field, so that the ion acous
waves are quasi coherent. From what has been said we can deduce that quasi-coher
modes are spontaneously excited for low magnetic fields and are characterised by
electron drift waves' dispersion relation. For higher magnetic fields the destabilisation

...and the development of turbulence occurs, in ... destabilised drift waves ... coherent ion acoustic waves are excited.



...patial poloidal (- - -) and parallel (—) coherence, and (b)β parameter as a function ...magnetic field intensity.

...the possible nonlinear interactions between waves, we observe that the total ...erence reaches high values in the plasma edge. The characteristics of drift waves ...different in the edge and in the plasma inner: we can see from fig.2a that the ...coefficient is high in the edge x=1 cm, where it reaches values higher than ... (b^2...), so that the nonlinear ineraction seems become between more than three ... From the shear layer x=3.5cm and toward the inner x>3.5 cm the bicoherence ... about b^2=0.2÷0.3. It has to be noticed that the bicoherence coefficients ...with probes in poloidal and parallel positions are similar and similar are the ...ficients evaluated analysing the ion saturation current and the floating potential ...tuations. This means that the nonlinear interactions becomes between waves and it is ... due to other nonlinear processes, for example produced by the probe sheaths. In ...the total weight integrated bicoherence and the total integrated bicoherence have ...shown: they have a similar behaviour. In fig.2b we can see the radial behaviour of ...normalized density fluctuations evaluated from the ion saturation current, I / I . The ...ty fluctuations reach the maximum value (15%) in the plasma edge and decrease ...towards the plasma center where they assume the value of 5%. We can say that

the nonlinear interactions between waves is strong in the plasma edge ($k<3$ cm
the density fluctuations are high and the poloidal modes are destabilised.

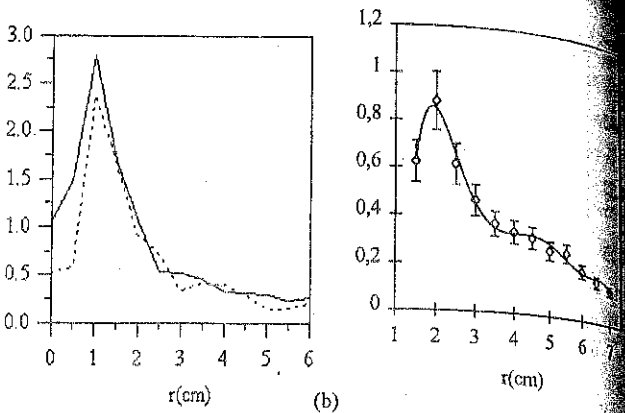


Fig.2 (a) bicoherence coefficient total (—) and total weight (- - -) as a function
magnetic field intensity; (b) normalised density fluctuations as a function of the radial po

In conclusion we see that the turbulent regime develops for the destabilisation of
modes. In presence of turbulence the density fluctuation spectra are characterised
spatial coherence coefficient ($\gamma\approx0.2$). In this regime the bicoherence analysis sh
large presence of three-wave coupling, so that the turbulence is due to the destabili
of drift modes, while ion acoustic modes are quite stabilised. We see also th
characteristics of the fluctuations are different going from the edge into the pl
inner: the nonlinear multiple wave interactions occurs in the edge where the pol
modes are not coherent and the amplitude of the relative density fluctuations is
while in vicinity of the shear layer and in the plasma inner the nonlinear interaction
weakly and neglegible and the level of the relative density fluctuations low.

References

1. Kauschke, G. Oelerich-Hill and A. Piel, Phys. Fluids B 2, (1990)

2. Kim, E. J. Powers, IEEE Transactions on Plasma Science, PS 7, 120 (1979)

3. K. Rypdal, F. Oynes, Physics Letters A 184, 114 (1993)

Experimental analysis of waves modifications in presence of ponderomotive effects

C.Riccardi, D.Xuantong*, L.Gamberale and M.Fontanesi

Dipartimento di Fisica, Università degli Studi di Milano

Via Celoria 16, 20133 Milano, Italy

Istituto di Fisica del Plasma C.N.R., Via Bassini 15, 20133 Milano, Italy

Ponderomotive effects produced by high power electrostatic waves in a magnetized plasma have been subject of several experimental studies and revealed different phenomena relevant to the plasma modification as density and temperature profiles[1]. They showed a density decrease in front of the launching system when the wave energy density is of same magnitude of the mean kinetic energy of the involved particle species, i.e., in case of electron plasma waves, when $\varepsilon_0 E^2 / (4 m_e \omega^2) \sim T_e$. Several theories were developed to the study of the wave and wave spectrum modification. It is known that the wave signal can experience filamentation along the magnetic field lines, and, as recently theoretically investigated can be modulated through the well known phenomenon of the modulation instability. The ponderomotive forces can so change the wave parameters, as the direction of wave propagation and the spectrum in frequency, and can produce heating phenomena and density deplection in the plasma.

This work is devoted to the experimental analysis of the ponderomotive effects with particular regard to the modifications of the wave parameters, as the wave envelope , the wave frequency spectrum and wavevector. In our experiment both density profiles and frequency-wavevector spectra of the signal injected in the plasma are experimentally investigated. The study of the wave spectrum in frequency and wavevector is performed with the digital correlation techniques apply to the ion saturation currents of several pairs of shielded Langmuir

probes. This method, well described in other previous works permit
the joint wavenumber frequency spectrum $S(k,\omega)$. In our case the local
$S(k,\omega)$ is obtained by pair probes located along the magnetic field (
toroidal locations) in order to estimate the wavevectors $k_{||}$. The
between two pins of the pair probes is 10 mm, so we can estimate
wavenumber between $|0 - 3.14|$ cm^{-1}. The probes can be move radially
can analyse also the wavenumber in several radial positions. In our exper
we varied the injected power up to reach 10 W and the wave frequency be
and 50 MHz, in order to excite an Electron Plasma Wave (EPW) with a slow
antenna. To have a simple estimation of the ponderomotive potential
plasma parameters we consider the following simple equation for
frequencies $\omega >> \Omega_i$:

$$V_{PM} = \sum_s \frac{1}{n_s} \frac{\omega_{ps}^2}{\omega^2} \frac{E^2}{8\pi} = \sum_s \frac{e^2 E^2}{2 m_s \omega^2} .$$

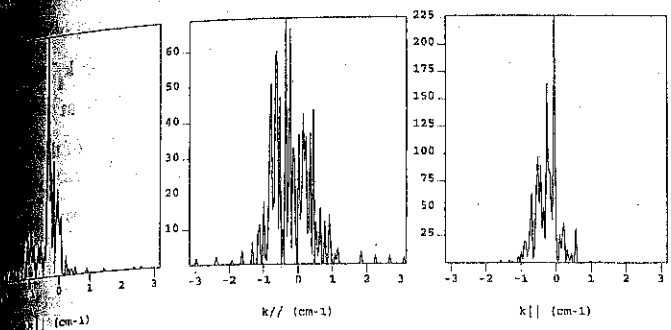
The Boltzmann balance equation permits then to establish the way in which
electron density n_e is affected by ponderomotive effects:

$$\frac{n_e}{n_{oe}} = e^{-V_{PM}/T_e}$$

where n_{oe} is the electron density in absence of RF and T_e the electron temper

The ponderomotive effect becomes relevant whenever its potential matches
thermodynamical energy of the electrons, i.e. when V_{PM}/T_e gets close to
may use the simplified expression of eq.1 to estimate the magnitude of
ponderomotive potential in our experiments for f = (6-50) MHz and so
threshold value: $P^{th} \cong 100$ mW. The wavevector spectra of the waves show
strong dependence on the power, as shown in fig.1 in which the $k_{||}$ spectra for
20 MHz and for three power values. At low power level (fig.1a) the spectrum
mainly peaked in $k_{||}$=0.2 cm^{-1}, as expected from the linear antenna-plasma
coupling theory. For P=150mW (fig.1b) the spectrum results broadened arou

$k_{\|}$=0.2 cm^{-1}, then at higher power (fig.1c) the spectrum is again



Experimental wave spectra as a function of the $k_{\|}$ wavevector obtained with an ... composed of two blades, f=20 MHz and a) P=10 mW, b) P=150mW, c) ... mW.

...broadening of the $k_{\|}$ spectrum has to be related to a strong modification of the ... envelope along the magnetic field lines. This modification depends on the ...ency signal and on the kind of the antenna system. We could explain this ...ening effect analysing the phenomenon on the modulation instability on the ...ostatic wave. The modulation instability is the phenomenon of waves ...ulation produced by low frequency waves (ion acoustic or magnetosonic ...es) generated by ponderomotive plasma density perturbation. In order to ...yse it we detect the wave spectrum in the low frequency range (f < 100 kHz) ...evaluate the phase velocity of the relevant waves.In fig.2 the low frequency ...spectra with and without rf has been plotted for a fixed $k_{//}$ value. In presence of rf ...wer the waves in the frequency range between 5 and 15 kHz are amplified with ...spect to the case in absence of rf. Considering the main peak at f=10kHz, the ...wavevector parallel to the magnetic field ranges between 0 and 0.5 cm^{-1}, so that ...phase velocity of these low frequency waves is of the order of the ion acoustic ...wave one: the measured phase velocity is $v_{ph} = 3\times10^5$ cm/sec and the ion acoustic ...locity is $v_s \sim 5\times10^5$ cm/sec, obtained considering an electron temperature of 0.3 ...V. From this analysis we can hypothese the presence of the modulation

instability due to ion acoustic waves. The effect of this phenome
modulation in space of the envelope of the wave along the magnetic fi
changing the parallel phase velocity. We see that the broadening of the sp
is sistematically between $0<|k_{\|}|<1$ cm^{-1}, in fact the waves with $k_{\|}$ higher
cm^{-1} are absorbed by Landau damping and can not be detected: at f=20M
$k_{\|}$=1cm^{-1} the phase velocity is about 3 times the thermal energy of the elec

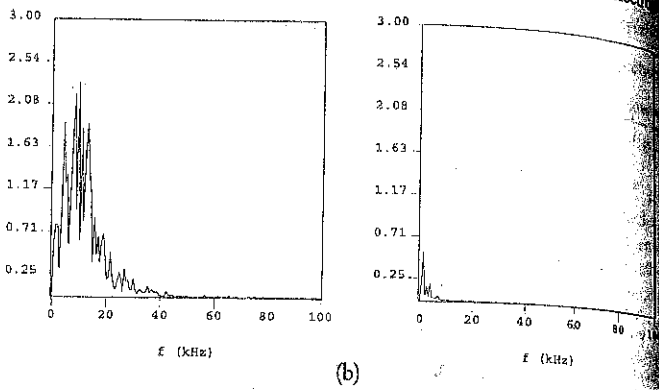


Fig.3 Experimental wave spectra as a function of the frequency and $k_{\|}$ wave
parallel to the magnetic field obtained with an antenna composed of two blades,
MHz , (a) with power (P=150mW) and (b) without.

The broadening of the spectra can be so responsible for the strong electron hea
via Landau damping. We have also find that above to a power level (300 m
the electron density and temperature reach the saturation values and
wavevector spectrum results again peaked (fig.1c). The interpretation of
saturation phenomenon lies in a strong plasma edge heating which was observ
in our measurements. As a consequence of this heating V_{PM}/T_e again becom
small and the thresold value for non-linear effects results increased.

References

G.J.Morales and Y.C.Lee, Phys.Rev.Lett.,35 p,930 (1975)

C.Riccardi, A.Penso, M.Fontanesi, E.Sindoni, Phys.Lett.A, 208,p.223(1995).

Interaction of Ultra-Short Electromagnetic Pulses with Plasmas

Kazuhiro Akimoto and Haruyuki Irie*

Research Development Corporation of Japan, Kawaguchi 332, Japan and School of Science and Engineering, Teikyo University, Utsunomiya 320, Japan

*Information Processing Center, Hiroshima University, Higashi-Hiroshima 739, Japan

This paper considers interaction of electromagnetic [em] wave packets with charged particles with emphasis on ultra-short pulses. Yet the results are valid for longer pulses also. Interaction of charged particles with sinusoidal waves has been extensively investigated. Meanwhile, there is rapidly increasing interest in ultra-short pulse technology[1,2] and its applications to plasma physics among others.[3-5] To properly treat such pulses wave packet effects must be incorporated as below. We here emphasize unipolar pulses (impulses) with "ultra-wide band"[3] frequency spectra. Should their pulse lengths be short enough they can penetrate through plasmas and other materials.[3]

Equation of motion of a particle in an em wave field is

$$m\frac{d\gamma v}{dt} = qE + \frac{q}{c}v \times B, \qquad (1)$$

where m, γ, q, v are the mass, the relativistic factor, the charge, and the velocity of the particle, c is the speed of light, and finally E, B are the electric field and the magnetic induction of the wave packet of our interest, respectively. We consider motion of a particle moving at velocity V in a

sinusoidal vacuum mode with $E=E_x$; both of them propagate
direction. Equation of motion then becomes in the non-relativis

$$m\frac{\partial v}{\partial t}+mV\frac{\partial v}{\partial z}=qE+\frac{q}{c}v\times B.$$

Solving this with the initial condition $v_x=v_y=0$ at $t=a$, one

$$v_x(t)=\mathrm{Re}\left[i\frac{q}{m}\frac{E}{\omega}e^{i(kz-\omega t)}\left\{1-e^{i\omega'(t-a)}\right\}\right],$$

where $\omega'=\omega-kV$. We then consider Gaussian em wave packets of
$E(t)=Eoe^{-[(z-ct)/l]^2+i(koz-\omega ot)}$ with $E(\omega)=\sqrt{\pi}\Delta t\,Eo\exp[-\{(\omega-\omega_o)\Delta t/2\}$
its Fourier spectrum, where $l=c\Delta t$ is the packet size ω_o is the
frequency and $k_o=\omega_o/c$. Consequently, the velocity of the particle

$$v_x(t)=\mathrm{Re}\left[i\frac{q}{m}\int_{-\infty}^{+\infty}\frac{E(\omega)}{\omega}e^{i(kz-\omega t)}\{1-e^{i\omega'(t-a)}\}d\omega\right]. \quad (2)$$

Interestingly, Eq.(2) can be evaluated using the plasma dispersion func

$$v_x=\mathrm{Re}[iqEo\Delta tX/(2m)], \quad (3)$$

where $X=Z1(\omega_o,t)Y(\omega_o,t)-Z1(\omega_o,a)Y(\omega_o,a)$,

$Z1(\omega,t)=Z(-\omega\Delta t/2-i\alpha t/\Delta t)$,

$Y(\omega,t)=\exp\left\{-i\omega\alpha t-(\alpha t/\Delta t)^2\right\}$,

and $\alpha=1-V/c$. In the derivation of Eq.(3) it was assumed that v_z
constant. However, the velocity v_z may be obtained through Hamil

$$Ho=mc^2\gamma-(\omega/k)Pz. \quad (4)$$

Here γ is the relativistic factor and $P_Z=\gamma mv_z$. Normalization of Eq.(4)

$$p_\perp^2+(1-v_p^2)p_z^2-2h_ov_p\,p_z=h_o^2-1, \quad (5)$$

where momenta are normalized by mc, and h_o, v_p (phase velocity) by
respectively. For particles that are initially at rest, i.e., $h_o=1$, Eq.(5) becom

$$p_z=p_\perp^2/2. \quad (6)$$

Thus we use (3) to calculate v_x, and then (6) to obtain v_z. Note that follo
Sheid and Hora,[5] a more rigorous solution of Eq.(1) can be found, whi
given simply by replacing A(u) in ref.(5) with Eq.(3) with properly cha
variables. Yet this method can easily be extended to more general cases

Let us now study the case of a unipolar impulse with the em fields $Ex = Eoe^{-(z-ct)^2/l^2}$ and $By = Boe^{-(z-ct)^2/l^2}$, where Eo and Bo are the maximum amplitudes of the pulse, respectively. If one sets $\omega_o = 0$ and a=-∞ in Eq.(3), it reduces to

$$v_x = \sqrt{\pi} qEo\Delta tX/(2m)\{1+erf(\alpha t/\Delta t)\}, \qquad (7)$$

where $erf(t)$ is the error function. After the interaction (t=∞) it settles to

$$v_x = \sqrt{\pi} qEo\Delta t/m. \qquad (8)$$

The particle is accelerated by E_x, while slowly rotating around B_y, gaining v_z. For ultra-short impulses such that $(qEo/mc)\Delta t<<1$, one obtains $v_x >> v_z$. It simply reflects the fact that the pulse electric fields are dc-like and transverse. Figures 1(a) and (b) compare for $l_n = l\omega/c = 5$ and 0.5 the values of v_x at $t=\infty$ obtained from Eq.(3) with numerical solutions of (1) for particles initially at rest ($t_n = \omega t$). Normalized maximum amplitudes of both pulses are $E_n \equiv eEo/mc\omega_o = 0.1$. Excellent agreement between the theory (solid curve) and test particle calculations (circles) is obtained. Fig. 1(a) shows that the maximum speed of the particle is given indeed by $E_n c=0.1c$, i.e., the quiver velocity, while Fig.1(b) depicts that the maximum speed due to the impulse is $0.0830c$; it is nearly equal to $0.0886c$ given by Eq.(8). Note that the final velocities for wave packets ($l_n>3$) are almost zero, while those

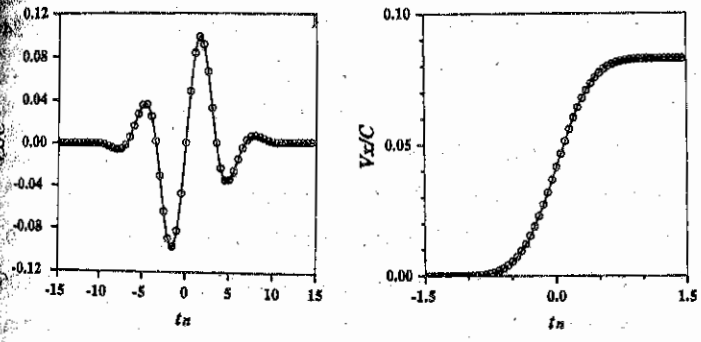


Fig. 1(a) v_x vs. t for $l_n = 5$ (b) $l_n = 0.5$

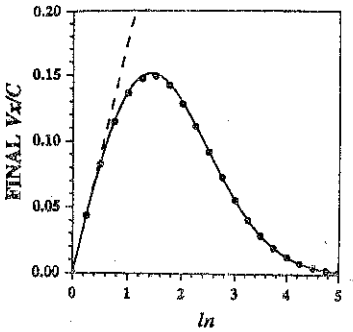


Figure 2 Final v_x vs. l_n

for impulses remain large due to the fact that as the l approaches zero the sum of electric field in a pulse becomes nonzero. This trend is clearly observable in Fig.2, which shows the dependence of final v_x on l_n. As the size is made shorter, final v_x increases until l_n is after that it decreases according to Eq.(8), which the dashed curve de (Filled circles denote numerical solutions of Eq.(1).) Thus Figure 2 sh that transition from ordinary packet to impulse occurs at $l_n \approx 1$, and final is given precisely through Eq.(3). Interestingly, at l_n=1.5 the maxim velocity surpasses the quiver velocity because total electric field of the pac is maximized there. Another important result is that as is infered from Eq with relatively small pulse amplitudes, initial velocity V hardly affects final However, with sufficiently large amplitudes and pulse moving slightly fa than the particle, strong acceleration is triggered through particle reflection

REFERENCES

1. D. H. Auston and M. C. Nuss, 1988 *IEEE J. Quantum Electron.* **24** 184.
2. D. You *et al.* 1993 *Opt. Lett.*, **18** 290.
3. K. Akimoto, *J. Phys. Soc. Jpn.* (in press) and references therein.
4. B. I. Cohen *et al.* 1995 *Rev. Sci. Instrum.* **66** 1241 and references therein.
5. W. Sheid and H. Hora, 1989 *Laser and Particle Beams* **7** 314.
6. K. Akimoto and H. Karimabadi, 1988 *Phys. Fluids* **31**, 1505; 1989 *Phys. Fluids B* **1**, 2530; H. Karimabadi *et al.* 1990 *Phys. Fluids B* **2**, 606.
7. K. Akimoto and H. Irie, *Proc. Int. Conf. on Plasma Phys.* (Nagoya, 1996, accepted).

STUDY OF THE TWO-PLASMON DECAY OF LOWER HYBRID WAVES BY ENHANCED SCATTERING TECHNIQUES

B.Brüsehaber*, E.Z.Gusakov, N.M.Kaganskaya, M.Krämer*, V.L.Selenin

Physico-Technical Institute of Russian Academy of Science
Polytekhnicheskaya 26,194021 St.Petersburg, Russia
* Institut für Experimentalphysik II, Ruhr-Universität Bochum,
D-44780 Bochum, Germany

The excitation of parametric instabilities (PI) is often observed in lower hybrid (LH) wave experiments in tokamaks. Recently, the parametric decay into two plasmons with comparable frequencies was observed in LH heating experiments on the FT-2 tokamak [1]. It was shown that the onset of the parametric decay is correlated with the density limit for current drive and with the start of fast ion generation. However, till now, the decay waves excited by the instability are not identified and there is no information on their wavenumber spectrum.

The present paper is devoted to the detailed study of such a two plasmon decay in laboratory experiments. The experiments were carried out on linear plasma devices in St.Petersburg [2] and Bochum [3] (denoted as P and B). In P the magnetized Ar plasma was produced in a glass tube of diameter $d = 5cm$ and length $l = 200cm$ by a hot cathode discharge. The magnetic field B was $0.1T$, the gas pressure $p \simeq 8 \cdot 10^{-4} Torr$, the electron density $n_e \simeq 10^{10} cm^{-3}$ and the electron temperature $T_e \simeq 2eV$, typically. In B, a plasma of different gases (H, He, Ar, Ne) was created in a metal vessel ($d = 13cm$, $l = 80cm$) by producing $200W$ RF power. The plasma parameters during the RF pulse were $B \simeq 0.1T$, $n_e \leq 2 \cdot 10^{10} cm^{-3}$, $T_e \simeq 4eV$, $p = 7 \cdot 10^{-3} Torr$, plasma radius $r_p = 5cm$. The measurements were performed in the afterglow of the discharge. In both experiments, a LH pump wave in the frequency range $4 - 30MHz$ was launched by a slow-wave antenna consisting of several (up to 4) concentric rings. The LH wave propagation and parametric decay was studied by the enhanced scattering (ES) diagnostics [4] and its modifications [5]. In this method, the plasma fluctuations are probed with an electromagnetic wave for which the upper hybrid resonance condition is satisfied inside the plasma volume and the radiation backscattered there is recorded. Near the resonance, the wavenumbers of the incident and scattered waves strongly increase thus enabling scattering from plasma waves with wavenumbers q much larger than the vacuum wavenumber of the probing wave. Hence, the scattering process is strongly localized in the upper hybrid resonance layer and its cross-section becomes very large. According to [5], the signal backscattered in the resonance is given by

$$A_s(t) = \frac{A_i}{16} \int \frac{d\Omega dq_\perp dq_\parallel}{(2\pi)^2} \frac{\delta n_{\Omega,q}}{n_e} \exp\left(iq_\perp x_{UH} + i\Omega t - iq_\parallel z_i\right) \kappa^2 I(q_\perp) \qquad (1)$$

where $|A_s|^2$ and $|A_i|^2$ are the scattered and incident powers at the antenna, $\delta n_{\Omega,q}$ is the spectral harmonic of the fluctuation, κ is the fraction of the incident microwave power absorbed in the resonance, $x_{UH} = x(\omega_i, B)$ is the position of the upper hybrid resonance

determined from the condition

$$\omega_i^2 = \omega_{pe}^2(x) + \omega_{ce}^2$$

and the factor $I(q)$ describes the dependence of the scattering efficiency on the fluctuation wavenumber [4]. In experiment P, the incident extraordinary wave frequency $f_i = 2.4GHz$ and power $P_i \simeq 0.1W$ was excited in the plasma by a waveguide. The scattered signal was picked up by the same or by a nearby waveguide. The typical ES spectrum observed at small LH pump power consists of two narrow lines. The first line $f = f_i$ corresponds to the incident wave while the second line, down-shifted by the pump frequency $f = f_i - f_0$, is associated with the wave backscattered from the inward propagating LH pump. At higher pump powers two additional broader satellites appear in the spectrum $f = f_i - f_1$ and $f = f_i + f_2$ (see Fig.1a). The satellite frequencies are about half the pump frequency $f_1 \cong f_2 \cong f_0/2$, but are not equal, as is seen from Fig.1b where the spectrum of the homodyne detected signal for the He discharge (B) is plotted. The frequencies satisfy the well-known parametric decay condition $f_0 = f_1 + f_2$. Curve 1 in Fig.2 shows the dependence of the parametric satellites on the pump power applied to the antenna. The threshold power for the onset of the PI (curve 2) is correlated with the saturation of the LH pump satellite in Fig.1. This correlation can be interpreted in terms of the strong influence of the PI on the LH wave propagation. Such an interpretation is similar to the conclusion of paper [1]. The PI takes place in the vicinity of the LH resonance point for the satellite frequencies. The shift of the maximum satellite position from the LH resonance point $d = (\omega_0/2 - \omega_{LH})/(\omega_0/2)$ is shown in Fig.3 for different gases (B). As is seen, the shift is positive for helium, neon and argon, but changes sign for hydrogen. The frequency range for which the PI is observed is also gas-dependent (Fig.4). The growth of the unstable wave frequency with the decrease of the ion mass is probably related to the fact that the LH pump, propagating in a finite axial system, is able to access the two plasmon decay layer where $\omega_0 = 2\omega_{LH}$. To measure the decay plasmon wavelength perpendicular and parallel to the magnetic field and to identify the modes, an interferometric ES technique was employed. This method is based on the fact that the phase of the scattered signal depends on the fluctuation phase $\exp(-iqx_{UH})$ in the upper hybrid resonance point given by eq.(1). The measurements were carried out in a two channel scheme. The reference signal was provided by the ES channel with fixed frequency and axial position or picked up from the LH ring antenna. The measuring signal $A_s(t)$ was filtered from the scattered signal (Fig.1), and, after homodyne conversion, mixed with the reference signal $A_r(t)$. For quasi-harmonic fluctuations, the integrated signal at the phase detector $A = < A_r(t)A_s(t) >$ - the interferometric ES signal (IES) - is proportional to the amplitude in the point $x = x_{UH}(t)$, given by eq.(2). The variation of the radial position of the scattering region was accomplished by changing the incident frequency or by minor local magnetic field variation near the antenna of the ES measuring channel. The radial structure of the IES signal for different axial measuring positions is shown in Fig.5(a,b) for the up- and down-shifted PI satellites of Fig.1, respectively. The PI localization, according to these figures, is independent of the axial position of the measuring channel, whereas the phase shift of the radial structure varies monotonously as the waveguide is shifted in $z-$direction by $\Delta z = 1cm$ for each curve. Using eq.(1), one can estimate a

...velength $\lambda_{2\perp} \cong 0.09cm$ and an axial wavelength $\lambda_{2\|} \cong 18cm$ for the up-shifted ... For the down-shifted plasmon, one obtains $\lambda_{1\perp} \cong 0.075cm$ and $\lambda_{1\|} \cong 14cm$. The ...ximate wave vectors of the plasmons are oppositely directed as it follows from the ...sign of the frequency shift in the spectrum of Fig.1. The parallel wave vectors are ...ll because the phase fronts of both satellites in the $r-z$–plane are similar ... The radial structure of the IES signal for the LH pump wave is also shown in ...figures (curve 1). The radial wavelength of the pump $\lambda_{0\perp} \cong 0.35cm$, estimated ...curve is in reasonable agreement with the decay condition for the wavenumbers ... As to the identification of the decay plasmons, we emphasize that their ...body parallel to the magnetic field is comparable to the electron thermal speed ... Such waves are strongly damped and exist only in the presence of a pump. ...are localized in the vicinity of the LH resonance for half the pump frequency ...the condition $\lambda_\perp \ll \lambda_\|$, they do not fulfill the linear LH dispersion relation. ...likely that the parametric instability observed is attributed to the decay into ...kinetic quasimodes [6].

...would like to acknowledge the financial support of this work by the INTAS 94-2236 ... RBSF grant 96-02-17913 and German-Russian Cooperation Contract 438113/146.

References

Budnikov V.N. 1991, Nuclear Fusion **31** 611

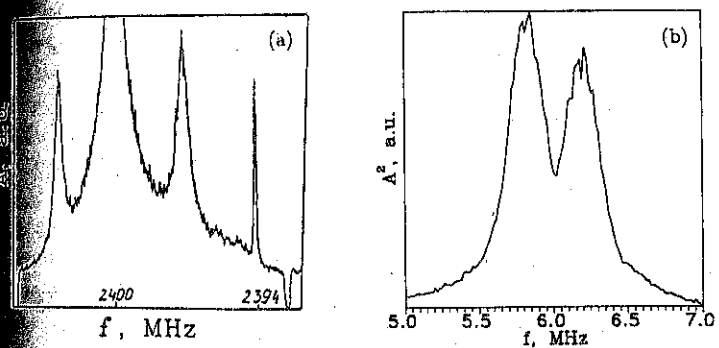
Budnikov V.N. et. al., Proc. Int. Conf. Plasma Phys. New Delhi 1989, Vol.3 1045

Brüsehaber B. and Krämer M. 1995, Plasma Phys. Control Fusion **37** 497

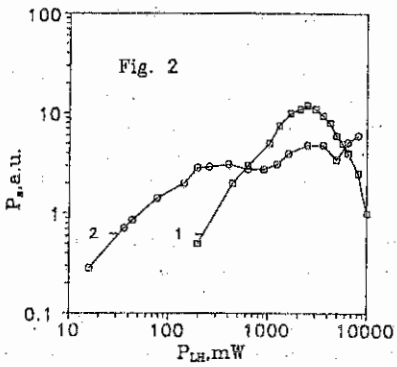
Novik K.M. and Pilya A.D. 1993, Plasma Phys. Control. Fusion **35** 357

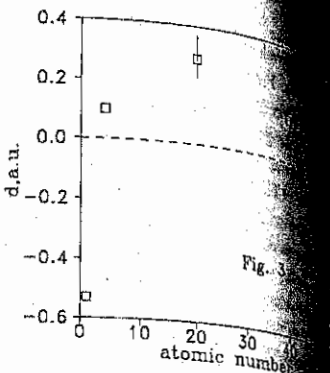
Arkhipenko V.I. et. al. 1993, Tech. Phys. Lett. **19** 333

Porkolab M. 1974, Phys. Fluids **17** 1432



...Parametric decay of the pump wave.- Total spectrum in P-experiment (a), ...ctrum (homodyne regime) in B-experiment (b).





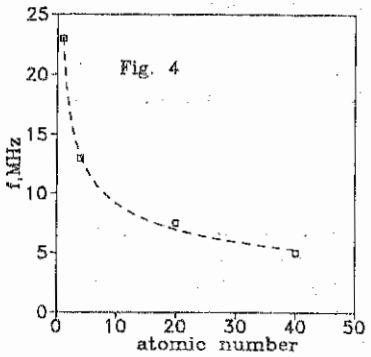


Fig.2 Dependence of the backsc... signal on the pump power for t... metric satellite (1) and the LH pum...

Fig.3 Localization of the maxim... the parametric decay signal for d... gases.

Fig.4 Dependence of the pump fre... at which the parametric decay sig... maximum on the ion mass.

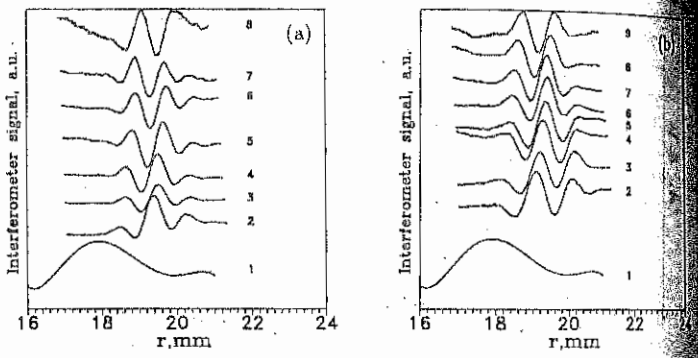


Fig.5 Interferometer traces for the pump (curve 1) and for the PI satellites (2-9) at different axial position of measuring antenna.- (a) Down-shifted satellite; (b) up-shifted satellite.

BALLOONING VORTICES IN A PLASMA WITH HOT PARTICLES

Zh.N.Andrushchenko, O.K.Cheremnykh
Scientific Center "Institute for Nuclear Research",
the National Ukrainian Academy of Sciences,
Kiev 252028, Ukraine

Abstract

Ballooning type perturbations in a plasma with hot particles are considered. The system of nonlinear equations which describes linear and nonlinear properties of these perturbations has obtained. In the linear approximation this system gives rise to the dispersion relation for ballooning perturbations in a plasma with hot particles. Steady-state solutions which describe localized vortex structures are found. It is shown that the presence of hot particles gives rise to a change in the region in velocity space within which vortex solutions exist.

Ballooning plasma oscillations play an important role in theoretical investigations, because the plasma pressure in magnetic traps has an upper limit imposed by ideal ballooning modes. As the amplitude grows these oscillations readily go over to the nonlinear regime, in which localized vortex structures form. Under the conditions found in thermonuclear devices the most important influence on these vortex structures comes from the high energy particles which arise due to thermonuclear fusion or as a result of auxiliary heating [1].

Consider a nonuniform plasma which contains positive charged particles (h) which temperature is considerably greater than that of the main plasma components. The magnetic field is directed parallel to the z axis and the plasma density varies in the x direction. The curvature of the magnetic field lines is modeled by an effective gravitational force $\vec{g} = (g,0,0)$. To describe the ballooning oscillations we use the hydrodynamic equations:

$$\frac{\partial N_j}{\partial t} + div\ (N_j \vec{V}_j) = 0,$$

$$\frac{\partial \vec{V}_j}{\partial t} + (\vec{V}_j \vec{\nabla}) \vec{V}_j = \frac{e_j}{m_j} \left(-\nabla\varphi + \frac{1}{c} \left[\vec{V}_j \times \vec{B} \right] \right) - \frac{\nabla P_j}{N_j m_j} - \frac{\nabla \pi_j}{N_j m_j} + \vec{g},$$

$$P_j = N_j T_j, \qquad j = i, e, h$$

Here φ is electrostatic potential, π_j is viscous str... tensor and the rest of the notations is standard.

We are interested in oscillations which characteris... frequency is small in comparison with the ion cyclotr... frequency and characteristic transverse scale is great... comparison with the ion Larmor radius. We assume that ... hot-particle density is small in comparison with the densi... of the main components of the plasma, $n_{0h} = \gamma n_0$, $\gamma \ll 1$, wha... n_0 is the equilibrium plasma density. So we neglect ... charge separation and instead of the Poisson equation use t... condition of plasma quasineutrality:

$$N_e = N_i + Z \cdot N_h, \qquad (3)$$

where Z is the charge state of the hot particles.

We neglect the perturbation of the longitudinal magnet... field under describing the electromagnetic fields. Transverse magnetic field we represent with help of vector potential Ψ...

$$\vec{B}_\perp = [\nabla\Psi \times \vec{z}]. \qquad (4)$$

The transverse electric field is potential $\vec{E}_\perp = -\nabla_\perp\varphi$, an... the longitudinal electric field has a form:

$$E_z = -\frac{\partial\varphi}{\partial z} - \frac{1}{c}\frac{\partial\Psi}{\partial t}. \qquad (5)$$

We consider the ion motion as two-dimensional and the electron motion as three-dimensional [2]. Then longitudinal current j_z created by electrons only:

$$j_z = -\frac{c}{4\pi}\Delta_\perp\Psi = -eN_e V_{ez}. \qquad (6)$$

The initial equations for the further analysis are the continuity equation for electrons:

$$\frac{\partial n}{\partial t} - V_i^* \frac{\partial\varphi}{\partial y} + \{\varphi, n\} + c_A^2 \frac{\partial}{\partial z}\Delta_\perp\Psi - c_A^2 \{\Psi, \Delta_\perp\Psi\} = 0, \qquad (7)$$

current closure equation:

$$\left(\frac{\partial}{\partial t} + V_i^*(1+h)\frac{\partial}{\partial y}\right)\Delta_\perp\varphi - V_0 \frac{\partial n}{\partial y} + \{\varphi, \Delta_\perp\varphi\} + (1+h)\, div\, \{n, \nabla_\perp\varphi\} +$$

$$+ c_A^2 \frac{\partial}{\partial z}\Delta_\perp\Psi - c_A^2 \{\Psi, \Delta_\perp\Psi\} = 0, \qquad (8)$$

equation which connects electrostatic and vector potentials:

$$\frac{\partial \Psi}{\partial t} = - \frac{\partial \varphi}{\partial z} , \qquad (9)$$

$$v_i^* = -\frac{\kappa c T_i}{e B_0 \nu_{ni}}, \quad n = \frac{\delta n}{n_0}, \quad h = \gamma Z \frac{T_h \omega_i}{T_i \omega_h}, \quad \kappa = -\frac{1}{n_0}\frac{dn_0}{dx}, \quad \kappa > 0.$$

spatial variables, time, potentials φ and Ψ are ized with respect to the ion Larmor radius, ion frequency, ion temperature and longitudinal magnetic respectively.

In the linear approximation for perturbations of the form $\exp(-i\omega t + i\vec{k}\vec{r})$ we obtain a dispersion relation for ballooning oscillations with hot particles:

$$\omega \left(\omega - \omega_i^* (1+h) \right) + \frac{k_y^2}{k_\perp^2} \kappa g - k_z^2 c_A^2 = 0. \qquad (10)$$

is easy to see that the presence of the hot particles gives to broadening of the plasma stability region.

The set of Eqs. (8)-(10) describes nonlinear structures ballooning type also. We are interested in time-independent olutions. The solution construction procedure is carried out by analogy to Larichev-Reznik work [3]. In the general case these solutions are expressed in terms of two arbitrary functions. When these functions are linear we obtain the (pole) vortices:

$$\Psi(r,\vartheta) = \begin{cases} \dfrac{v_0 v_i^*}{u \rho^2} \left(r_0 \dfrac{K_1(\rho r)}{K_1(\rho r_0)} - r \right) \cos\vartheta, & r > r_0, \\ -\dfrac{v_0 v_i^*}{u \lambda^2} \left(r_0 \dfrac{J_1(\lambda r)}{J_1(\lambda r_0)} - r \right) \cos\vartheta, & r \le r_0. \end{cases} \qquad (11)$$

Here J_1, J_2 are Bessel functions, K_1, K_2 are modified Bessel functions, the quality λ is defined from the condition:

$$\frac{K_2(\rho r_0)}{K_1(\rho r_0)} = -\frac{\rho}{\lambda}\frac{J_2(\lambda r_0)}{J_1(\lambda r_0)}, \qquad (12)$$

ρ^{-1} characterizes the spatial scale of the ballooning vortex:

$$\rho^2 = \frac{v_0 v_i^*}{u(u - v_i^*(1+h)) - \alpha^2 c_A^2} > 0,$$

u and α are some constants which characterize the velocity inclination angle of a vortex in surface (x,y).

The expressions (12) allow us to define the dimensionless potentials of the problem:

$$\Phi(r,\vartheta) = \frac{1}{1 - \frac{\alpha^2}{u^2} c_A^2 + b(1+h)} \left(F + \frac{\alpha^2}{u^2} c_A^2 v_0 r \cos\vartheta \right),$$

$$\varphi(r,\vartheta) = \Phi(r,\vartheta) + ur\cos\vartheta,$$

$$\Psi(r,\vartheta) = \frac{\alpha}{u} \left(\Phi(r,\vartheta) + ur\cos\vartheta \right),$$

$$n(r,\vartheta) = b\Phi - v_i^* r\cos\vartheta + \frac{\alpha^2}{u^2} c_A^2 \Delta_\perp \Phi.$$

The resulting solution has the form of a so-called dipole vortex. The condition for the existence of such a localized vortex structure is given by the inequality (14). In the region of unfavorable magnetic field line curvature ($g > 0$) the velocity of the vortex is determined by the inequality:

$$u > \alpha c_A \quad \text{and} \quad u < v_i^*(1+h). \tag{18}$$

In the opposite case ($g < 0$) the vortex can move only in the negative y direction:

$$v_i^*(1+h) < u < \alpha c_A. \tag{19}$$

4. Thus, the effect of the hot particles on dipole ballooning vortices reduces to a charge in the region in which they exist in velocity space: these occur in both linearly stable and unstable plasmas. For this reason even in a stable plasma ballooning perturbations can yield a contribution to the anomalous transport of heat and particles through vortex convection.

References

1. Kaladze, T.D., Fiz. Plazmy **13**, 1107 (1987) [Sov. J. Plasma Phys. **13**, 638 (1987)].
2. Petviashvili, V.I. and Pokhotelov, O.A., Fiz. Plazmy **12**, 1127 (1986) [Sov. J. Plasma Phys. **12**, 651 (1986)].
3. Larichev, V.D. and Reznik, G.M., Dokl. Akad. Nauk SSSR **231**, 1077 (1976).

Experimental Control of Chaos in a Glow Discharge using Spatial Autosynchronization

A. Atipo, Th. Pierre, G. Bonhomme

Laboratoire de Physique des Milieux Ionisés, U.R.A 835 du C.N.R.S.
Université Henri Poincaré, Nancy I
BP 239 F-54506 Vandoeuvre Cedex, France

Introduction

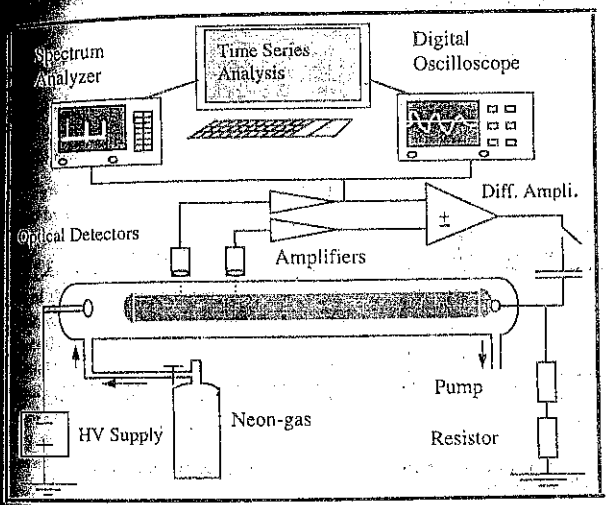
Despite the large number of experimental works carried out on the control of chaotic behavior of nonlinear dynamical systems [1], (i.e. the stabilization of unstable peridioc orbits embedded in a chaotic attrator) only very few results have been reported in field of plasma physics despite the occurrence of numerous chaotic situations and the crucial role of chaos in turbulence in plasmas [2].

We are reporting here on the stabilization of a spontaneously chaotic glow discharge in the positive column by strongly nonlinear ionization waves by means of a new autosynchronization method.

Experimental set up

The experiments are carried out in a cold cathode discharge tube, 4 cm in diameter and 60 cm long, filled with neon gas under pressures between 1 and 4 mbars.

An axially movable langmuir probe is measuring the floating potential fluctuations at the edge of the plasma and at a fixed axial position along the positive column. Axially movable and fixed optical detectors are used for the detection of the fluctuations in the ligth flux. The discharge current and its fluctuations are measured through a resistor in series with the discharge tube. The probe potential fluctuations and the optical signals are recorded by digital storage oscilloscopes and applied to a high resolution spectrum analyzer. The time series are transmitted to computer for further processing.



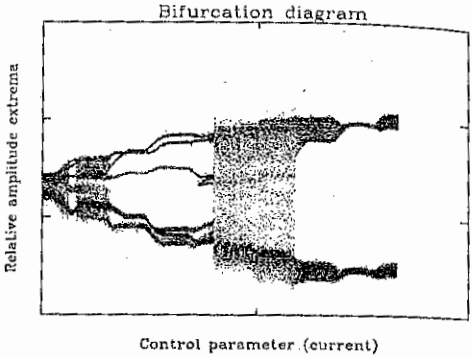
Discharge parameters

Current
0 - 60 mA

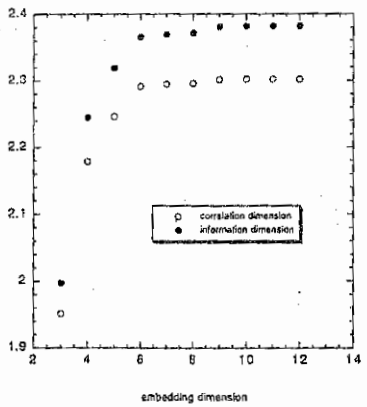
Voltage
300 - 1000 Volts

Neon gas
Pressure
1 - 4 mbars

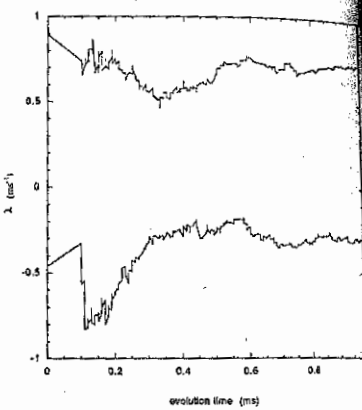
The neon discharge under pressures of a few mbars is unstable for ionization waves related to the modulation of the electron temperature and to the subsequent modul ionization rate. The existence of several eigenmodes with strong couplings lead excited chaotic dynamics.
The bifurcation diagram has been plotted (see below). When decreasing the discharg (*i.e.*, the control parameter), the discharge exhibits periodic regimes in some limited discharge current and chaotic regimes in other ones.



Several numerical tools are available to investigate chaotic states [3]. The phase s trajectory is reconstructed by means of the time delays method of Takens. The d coordinate vector is computed with the properly chosen delay obtained from the mu information. The results obtained show typical features of low dimensional chaos (see be for dimensionality and Lyapunov exponents).



Correlation and information dimension during the chaotic regime



Lyapunov exponents

...chaos
...space attractors have typically embedded within them an infinite number of ...odic orbits (UPOs). The main idea in controlling chaos is to use the high ...ity of the system to small perturbations to change the dynamical state.
...ntrolling chaotic systems, the basic ideas of the time-delay autosynchronization method ...ously proposed by K. Pyragas [4], is to realize an active continuous control of ...ntinuously by applying a signal continuously processed from a state variable of the ...system to a control parameter, achieving thus the stabilization of the targeted UPO with a ...ion of the feeback loop parameters.
...-dimensional dynamical systems, TDAS is described by the autonomous system

$$\dot{X} = P(X,Y)$$

$$\dot{Y} = Q(X,Y) + F_\tau(Y)$$

...$\{X(t), Y(t)\}$ is the state vector of the system, and the unperturbed phase space flow is ...given by Q.
...control signal $F_\tau(Y)$ is obtained by the linear control law:

$$F_\tau(Y) = K[Y(t-\tau) - Y(t)]$$

...τ denotes an appropriate time delay. It is chosen equal to the fundamental period ...of the orbit corresponds to a particular UPO to be stabilized. K is a constant. F_τ vanishes if ...the stabilization is achieved.
...previous paper [5] we have already reported on the efficiency of this method in ...controlling the chaotic regime of the ionization waves. But owing to the intrinsic propagating ...nature of these waves it is possible to use the modified following method.

...Spatial autosynchronization method

...Under some experimental conditions, ionization waves have a strong spatial ...correlation, and it is thus possible to replace the time delay τ by a spatial displacement δ, such ...that

$$Y(z,t-\tau) \rightarrow Y(z-\delta, t).$$

...This transformation is valid if the δ is chosen such that the condition: $\omega/k = V_\varphi = \delta/\tau$ ...is satisfied, while τ is fixed by the period duration of the periodic orbit to be stabilised.
...The control law:

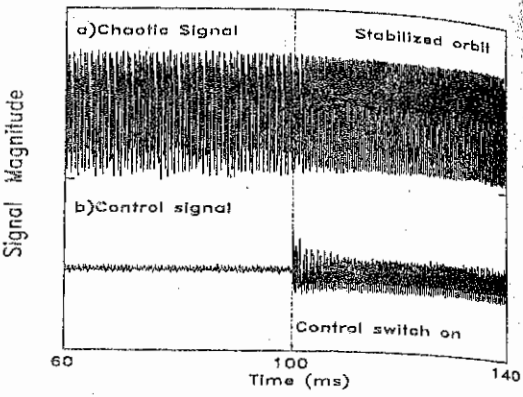
$$F_\tau = K[Y(z-\delta, t) - Y(z, t)]$$

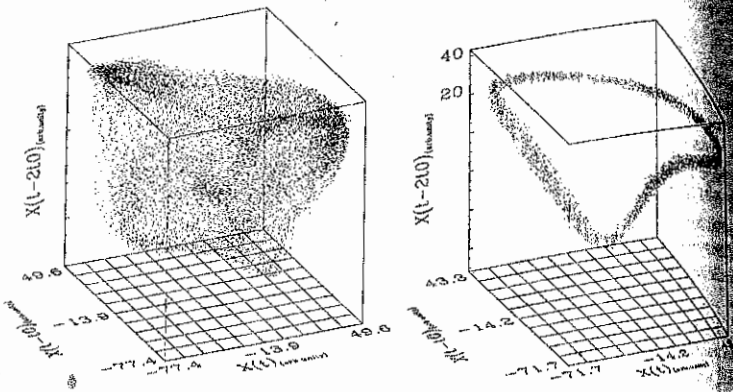
...is realized by using a conventional differential amplifier.
...The signals obtained from the two distant axially movable photodetectors are substracted, and ...the resulting signal is amplified up to a level of a few volts and applied to the anode.

...Interest of the method

...Chaos control methods need often either real-time processing or fast digitizers and memories. ...Consequently these methods are difficult to apply to relatively fast phenomena.
...The spatial autosynchronisation method which is a fully analog method is simpler in ...applications, and of a paticular interest for such phenomena, especially for fast, undriven ...dynamical systems.
...It only need, for the realization of the control signal, is to access to two distinct state ...variables exhibiting a phase relationship.

Results





a) before control switch on **b)** after control switch on

Phase space trajectory reconstruction (Takens method)

Conclusion

The chaotic regime of an unstable glow discharge is controlled using a continuous spatial autosynchronization method.The signals obtained from two distant axially movable detectors are substracted through a conventional differential amplifier, and the resulting signal applied to control parameter, leads to the stabilization of the discharge.

References

[1] T. Shinbrot, "*Progress in the control of chaos*", Advances in Physics 44_2, 73-111 (1995)
[2] T. Klinger *et al.*,Journal de Physique IV, Vol. 5, C6-131 (1995)
[3] H.D.I. Abarbanel, Rev. Mod. Phys. 65_3, 1331-1392 (1993)
[4] K. Pyragas and A.Tomasevicius, Phys. Lett. A **180**, 99 (1993)
[5] T. Pierre, G. Bonhomme, A. Atipo, Phys. Rev. Lett. 76_{13}, 2290 (1996)

Bernstein Modes in a Weakly Relativistic e^-e^+ Plasma

D.A. Keston, E.W. Laing, and D.A. Diver
Kelvin Building, Department of Physics & Astronomy,
University of Glasgow, Glasgow, G12 8QQ, Scotland, UK

Introduction

...our of an equal-mass (electron-positron), homogeneous and quasineutral plasma ...esence of a uniform magnetic field is examined. Two sets of comparisons are made: ...et and e^--ion plasmas, and between treatments of a progressively more relativistic ... equal-mass, opposite charge' plasma has useful symmetries.

...ical kinetic theory deals with the propagation of waves when the velocity distribution ...ibed by a nonrelativistic Maxwellian distribution function. In a fully relativistic kin... ...ment, the relativistic Maxwell-Boltzmann-Jüttner distribution replaces the classical ...wellian. Fully relativistic and nonrelativistic theories give markedly different results; a ...lativistic treatment is expected to illustrate the transition.

...ically the (electrostatic) Bernstein modes propagate perpendicular to the magnetic ...d resonate at electron cyclotron harmonics ($\omega \approx n\Omega_e$, with n an integer). In a classical ...plasma, there are gaps in the frequency spectrum away from $n\Omega_e$ where these modes ...not propagate, assuming static ions. The special symmetry of the e^-e^+ plasma allows ...retical treatment in which frequency gaps again occur, though in this case the result ...

...e^--ion plasmas, the introduction of a weakly (or fully) relativistic treatment sees ...broadening of the frequencies at which resonance occurs, and a downshift in those fre... ...encies as thermal velocities become more relativistic; these effects are mirrored in a e^-e^+ ...tment. However in e^--ion plasmas, waves at resonant frequencies are damped as a direct ...ult of modifying the classical static ion dispersion relation to accommodate relativistic ...ections[1]. In the e^-e^+ plasma treatment, no approximation dependent on the disparate ...sses of species is required, and the damping is consequently not present. Furthermore in ...the ultrarelativistic limit of the weakly relativistic dispersion relation for e^-e^+ plasmas, the ...Bernstein modes are not present and only the plasma oscillation remains perpendicular to ...the magnetic field, consistent with the predictions of the fully relativistic analysis of [4]. In ...the classical limit, the dispersion relation can be shown to relax to the nonrelativistic form.

Method

A plasma consisting entirely of electrons and positrons posseses significant th
Relativistic particle velocities are likely, and complicate any kinetic description
by investigating electron-positron (e^-e^+) plasmas, we expect to reveal simplific
the nature of the plasma.

There are strong indications that electron-positron plasmas may be found nat
atmospheres of pulsars and in extra-galactic jets (references in [2, 3]).

The propagation of waves in a *weakly* relativistic e^-e^+ plasma perpendicular to
equilibrium magnetic field is of particular interest. Kinetic theory seems the most
approach to plasmas in this domain.

Standard methods are adopted to model wave propagation [5]. The famili
Maxwell equations are assumed, and the distribution function describes momentum
space. In all that follows, the equilibrium distribution is *isotropic* (in fact, Maxwe
earising the Maxwell and Vlasov equations gives a set of equations for each spec
through self-consistent electric and magnetic fields. Maxwell's $\nabla \times \mathbf{B}$ equation
stated by expressing the perturbed $\mathbf{B}$ and distribution function in terms of $\mathbf{E}$,

$$\mathbf{k} \times (\mathbf{k} \times \mathbf{E}) + \frac{\omega^2}{c^2} \epsilon \cdot \mathbf{E} = \mathbf{0}$$

where ϵ is the *dielectric tensor*. This can then be abbreviated to $\mathsf{R} \cdot \mathbf{E} = 0$ where
resistivity tensor (with elements R_{xx}, R_{xy}, *etc.*).

For the special case of propagation perpendicular to the equilibrium magnetic
method shows that in a weakly relativistic e^-e^+ plasma, R is *diagonal*; electron-ion
have off-diagonal terms which are in most circumstances of much smaller magnitude
diagonal terms. These diagonal terms define three independent modes of propagati
the wave vector is chosen to be in the x-direction, thus a longitudinal mode has $E_x \neq 0$
then $\mathbf{k} \parallel \mathbf{E}$ and $\mathbf{E} \perp \mathbf{B}$. This corresponds to a purely electrostatic mode, with dis
relation given by $R_{xx} = 0$, the *Bernstein mode*. The classical Bernstein description (fo
e^-e^+ and e^--ion plasmas) is an infinite family of modes appearing at the cyclotron fre
and its harmonics (illustrated for e^-e^+ in figure 1). The other two modes are trans
respectively $R_{yy} = 0$ the *Extraordinary* and $R_{zz} = 0$ the *Ordinary Modes*.

The relativistic γ is introduced through the mass in $\mathbf{p} = m\mathbf{v} = m_0\gamma\mathbf{v}$, where
$\left(1 - \frac{v^2}{c^2}\right)^{-\frac{1}{2}} = \sqrt{1 + \hat{p}_\perp^2 + \hat{p}_\parallel^2}$, the 'hatted' notation indicates that quantities are dimens
thus $\hat{p}_{\perp,\parallel} = \frac{p_{\perp,\parallel}}{m_0 c}$.

The Bernstein Mode in e^-e^+ Plasma: [*x-axis* – $\hat{k}_\perp$ and *y-axis* – $\hat{\omega}$]

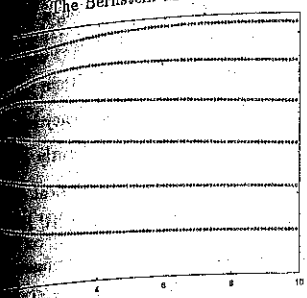


Figure 1: classical

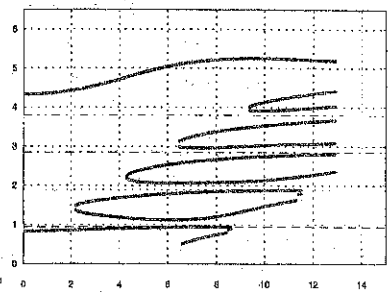


Figure 2: weakly relativistic ($a = 10$)

Weakly Relativistic Plasmas

Let the dimensionless ratio: $a = \frac{m_0 c^2}{kT}$. Take the weakly relativistic regime to be that for a in the range $10 - 100$.

By *weakly* relativistic we mean that a classical Maxwellian equilibrium distribution function is adopted in the numerator of the $p_\parallel$ integrals in R, but a *fully* relativistic γ appears in the denominator (compare (2) and (3)); this recovers the essential features. For *perpendicular* propagation, $\hat{k}_\perp = \frac{ck_\perp}{\Omega_{e0}}$, $\hat{k}_\parallel = 0$, in an e^-e^+ plasma, the relevant element of R is given by

$$R_{xx} = \hat{\omega}^2 - 2\hat{\omega}_{ep}^2 + \frac{4\hat{\omega}_{ep}^2}{\hat{k}_\perp^2}\left(\frac{a^{\frac{1}{2}}}{\sqrt{2\pi}}\right)\sum_{n=1}^{\infty}\frac{n^4}{\hat{\omega}^2}\int_0^\infty \hat{p}_\perp (J_n(a_e))^2 e^{-\frac{a\hat{p}_\perp^2}{2}} d\hat{p}_\perp \int_{-\infty}^{\infty} \frac{e^{-\frac{a\hat{p}_\parallel^2}{2}}}{\left(\gamma^2 - \frac{n^2}{\hat{\omega}^2}\right)} d\hat{p}_\parallel \quad (2)$$

where $J_n(a_e)$ is a Bessel function with $a_e = \hat{k}_\perp \hat{p}_\perp$ and $\hat{\omega}_{ep}$ is the dimensionless plasma frequency (in units of rest electron cyclotron frequency, Ω_{e0}, *i.e.* $\hat{\omega}_{ep}^2 = \frac{n_0 e^2}{\epsilon_0 m_0 \Omega_{e0}^2}$). To obtain the dispersion relation for Bernstein modes in weakly relativistic e^-e^+ plasmas a numerical solution to $R_{xx} = 0$ must be found (resulting in figure 2 for $a = 10$).

In a nonrelativistic limit, i.e. $\gamma = 1$, the R_{xx} element of the *nonrelativistic* resistivity tensor for perpendicular propagation is:

$$R_{xx} = \omega^2 + 4\pi\omega_{ep}{}^2\left(\frac{\Omega_0}{k_\perp}\right)^2 \lambda_e \sum_{n=-\infty}^{\infty} n^2 \int_0^\infty v_\perp (J_n(a_e))^2 e^{-\frac{mv_\perp{}^2}{2kT}} dv_\perp \int_{-\infty}^{\infty} \frac{e^{-\frac{mv_\parallel{}^2}{2kT}}}{\left(1 - \frac{n^2\Omega_0{}^2}{\omega^2}\right)} dv_\parallel \quad (3)$$

This equation may be solved *analytically* giving the dispersion relations for perpendicular propagation in an e^-e^+ plasma for the Bernstein mode (shown in figure 1).

$$\omega^2 = \omega_{ep}^2 \frac{2e^{-\Lambda}}{\Lambda} \sum_{n=-\infty}^{\infty} \frac{n^2 I_n(\Lambda)}{1 - \frac{n^2}{\omega^2}} \quad (4)$$

Compare figures 1 and 2 (both were calculated for $\omega_{ep} = 3$). Changes in the fo
dispersion relation occur as soon as any degree of relativity is considered: the
most superluminal modes (those where the phase velocity is greater than the speed
here $\hat{\omega} > \hat{k}_\perp$) and the disappearance of modes above the hybrid frequency mode are
obvious. Moreover, the shape of the figure $R_{xx} = 0$ curves is significantly different
cyclotron harmonics: instead of a single line corresponding to the classical disconti
relativistic broadening of the surface produces double intersection, with the curve
below the harmonic by the relativistic mass effect. This can be seen in figure 2.

The results of a previous fully relativistic theory [4] could only give an approximat
ment of this regime, since the fully relativistic code is only valid for $a < 10$. The
reported here therefore provides the link between exact treatments in the non-relativi
fully relativistic regimes. In this way, the transition between the extremes can be
revealing many intruiging aspects of the plasma behaviour. For example, although
disappear above the hybrid frequency, the double intersection of the R_{xx} in the pa
the large wavenumber behaviour suggest a richly structured medium; further investi
the phenomenological consequences with regard to plasma diagnostics is underway,
be reported soon.

References

[1] Robinson, P.A. 1987 *J. Plasma Physics* **37**, part 3, *435*

[2] Iwamoto, N. 1993 *Phys.Rev E* **47**, part I, *604*

[3] Zank, G.P. & Greaves, R.G. 1995 *Phys. Rev E* **51**, *6079*

[4] Rooney, C.E. 1995 *Wave Propagation in Relativistic Electron-Positron Plasmas.*

[5] Stix, T.H. 1992 *Waves in Plasmas.* American Institute of Physics, NY

DEVELOPMENT OF DYNAMICAL CHAOS UNDER NONLINEAR INTERACTION OF WAVES IN MAGNETIZED BEAM-PLASMA SYSTEMS

V. A. Buts, O. V. Manuilenko, A. P. Tolstoluzhskii

National Science Center
"Kharkov Institute of Physics and Technology"
Akademicheskaya st.1, Kharkov 310108 Ukraine

In this report we formulate conditions if being fulfilled the dynamics of the wave-to-wave coupling in the beam-plasma systems turns out to be chaotic. It is investigated the process of chaos arising at nonlinear interaction of waves in magnetized plasma with beam, compensated by charge electron beam and obtained necessary value of the wave amplitude for chaos arising.

As was demonstrated in [1] the dynamics of wave-to-wave coupling will be chaotic when $K = 2G/\delta$ becomes greater then unity ($K > 1$), where δ is the distance between frequences of different waves, G growth rate of three wave instability.

We consider the decay of HF ("t") electromagnetic wave with frequency ω_t, wave vector $\vec{k}_t$ and amplitude $\vec{E}_t$ which is propagated in magnetized ($\vec{H}_o = \{0, 0, H_o \to \infty\}$ - external magnetic field) compensated by charge electron beam, on the HF electromagnetic wave (ω_t, $\vec{k}_t$, $\vec{E}_t$) and LF beam wave ("p"). The basic system of equations consists of Maxwell equations for electromagnetic fields and hydrodynamic equations for plasma and beam. We neglect the movement of ions, assuming that background ions serves for neutralization of electron charge. The averaging over the time t_0 ($t_{sl} >> t_0 >> t_{fl}$, where t_{sl} and t_{fl} are periods of slow and fast variables, respectively) leads to following system of coupled equations (see, for example, [2]):

$$
\begin{aligned}
&\frac{\partial}{\partial t}\tilde{v}_{ex} + v_0\frac{\partial \tilde{v}_{ex}}{\partial z} = \frac{e}{m}\tilde{E}_z,\\
&\frac{\partial}{\partial t}\tilde{n}_e + v_0\frac{\partial \tilde{n}_e}{\partial z} = -\frac{\partial}{\partial z}(< n_e > \tilde{v}_{ex}),\\
&rotrot\tilde{\vec{E}} + \frac{1}{c^2}\frac{\partial}{\partial t^2}\tilde{\vec{E}} = \frac{4\pi e}{c^2}\frac{\partial}{\partial t}(\tilde{n}_e v_0 + < n_e > \tilde{v}_{ex}),\\
&\frac{\partial < v_{ex} >}{\partial t} + v_0\frac{\partial < v_{ex} >}{\partial z} = -\frac{e}{m}\frac{\partial \Phi}{\partial z} - \frac{1}{2}\frac{\partial < \tilde{v}_{ex}^2 >}{\partial z} - \frac{T_e}{m}\frac{\partial}{\partial z}ln < n_e >, \qquad (1)\\
&\frac{\partial < n_e >}{\partial t} + v_0\frac{\partial < n_e >}{\partial z} = -\frac{\partial}{\partial z}(< n_e >< v_{ex} > + < \tilde{n}_e\tilde{v}_{ex} >),\\
&\Delta\Phi = 4\pi e\delta n_e,\\
&< n_e >= n_{eo} + \delta n_e,
\end{aligned}
$$

where $\Delta = \frac{\partial^2}{\partial x^2} + \frac{\partial^2}{\partial y^2} + \frac{\partial^2}{\partial z^2}$, $\tilde{\vec{E}}$ - HF electromagnetic wave, $< n_e >$, $< v_e >$ - slow perturbations of plasma density and electrons velocity, n_{eo} - unperturbed plasma density, v_0 electron beam velocity, $\tilde{v}_{ex}$, $\tilde{n}_e$ - fast varying of electrons velocity and density, Φ - electrostatic potential of HF wave, $< ... >$ - the average over time t_o.

Assuming following form for HF electromagnetic field and LF density:

$$
\tilde{\vec{E}}(\vec{r}, t) = \frac{1}{2}\vec{E}_i(t)\exp(-i\omega_i t + i\vec{k}_i\vec{r}) + \frac{1}{2}\vec{E}_s(t)\exp(-i\omega_s t + i\vec{k}_s\vec{r}) + c.c.,
$$

$$\delta n_e(\vec{r},t) = \frac{1}{2}\delta n_p(t)\exp(i\vec{k}_p\vec{r}) + c.c.,$$

one can obtain from (1) the set of equation for slowly varying amplitudes of inter
waves:

$$i\frac{\partial \mathcal{E}_i}{\partial \tau} = \mathcal{E}_s\rho\exp(i\Delta\tau),$$
$$i\frac{\partial \mathcal{E}_s}{\partial \tau} = \mathcal{E}_i\rho^*\exp(-i\Delta\tau),$$
$$(\frac{\partial^2}{\partial\tau^2} + \Omega^2)\rho = -\mathcal{E}_i\mathcal{E}_s^*\exp(-i\Delta\tau),$$

where

$$\mathcal{E}_i = \frac{E_{iz}(\tau)}{E_{iz}(0)}, \quad \mathcal{E}_s = \frac{E_{sz}(\tau)}{E_{iz}(0)}\sqrt{\frac{\omega_i}{\omega_i}\frac{\omega_s}{\omega_s^*}\frac{\omega_i^*}{\omega_i}},$$

$$\rho = \frac{N(\tau)}{n_{eo}}[\frac{\omega_p^2}{k_{ps}^2}\frac{\pi m n_{eo}}{2E_{iz}^2(0)}\sqrt{\omega_i/\omega_i}(\frac{\omega_s}{\omega_s^*})^2(1+\frac{\delta^*}{k_{ps}}(\frac{k_{sz}}{\omega_s^*}+\frac{k_{iz}}{\omega_i^*}))^{-1}]^{1/3},$$

$$\tau = t[k_{ps}^2\omega_p^4\frac{E_{iz}^2(0)}{32\pi m n_{eo}}[1+\frac{\delta^*}{k_{ps}}(\frac{k_{sz}}{\omega_s^*}+\frac{k_{iz}}{\omega_i^*})](\frac{\omega_i}{\omega_i^*})^2\frac{1}{\omega_i\omega_s^*\omega_i^*}]^{1/3},$$

$$\Delta = \delta^*[k_{ps}^2\omega_p^4\frac{E_{iz}^2(0)}{32\pi m n_{eo}}[1+\frac{\delta^*}{k_{ps}}(\frac{k_{sz}}{\omega_s^*}+\frac{k_{iz}}{\omega_i^*})](\frac{\omega_i}{\omega_i^*})^2\frac{1}{\omega_i\omega_s^*\omega_i^*}]^{-1/3},$$

$$\Omega^2 = k_{ps}^2(\frac{\omega_p^2}{k_p^2}+V_{Te}^2)[k_{ps}^2\omega_p^4\frac{E_{iz}^2(0)}{32\pi m n_{eo}}[1+\frac{\delta^*}{k_{ps}}(\frac{k_{sz}}{\omega_s^*}+\frac{k_{iz}}{\omega_i^*})](\frac{\omega_i}{\omega_i^*})^2\frac{1}{\omega_i\omega_s^*\omega_i^*}]^{-2/3},$$

$$\delta^* = \delta - k_{ps}v_0, \quad \delta = \omega_i - \omega_s, \quad \omega_{i,s}^* = \omega_{i,s} - k_{ps}v_0,$$

$$N(t) = n_e(t)\exp(ik_{ps}v_0 t).$$

To obtain the set of equations (2) we assume that there is a space synchronism betw
coupling waves:

$$\vec{k}_i - \vec{k}_s = \vec{k}_p.$$

Term

$$\frac{\delta^*}{k_{ps}}(\frac{k_{sz}}{\omega_s^*}+\frac{k_{iz}}{\omega_i^*})$$

corresponds to $< \tilde{n}_e\tilde{v}_{ez} >$ in (1).

On the linear stage of the decay $\mid \mathcal{E}_i \mid = const$ we can obtain from (2) the desperso
relation (see [1]) and following expression for maximum values of the growth rates:

$$G = Im\omega = 1/\sqrt{2\Omega}, \quad \Omega^2 >> 1, \quad G = Im\omega = \sqrt{3}/2, \quad \Omega^2 << 1.$$

In the first case parameter $K << 1$ ($\delta \equiv \Omega$) and dynamics of the three wave coupling
regular. At large amplitudes of the incident wave $K >> 1$ and dynamics becomes chaotic

One may obtain following expression for value of amplitude of pumping wave at wh
the dynamics of the decay becomes chaotic:

$$E_{iz}^2 > \frac{8m^2}{e^2}\frac{1}{3\sqrt{3}}(\frac{\omega_i^*}{\omega_i})^2\frac{\omega_p\omega_i^*\omega_s\omega_s^*}{k_p^2}\frac{k_{pz}}{k_p}(1+\frac{\delta^*}{k_{ps}}(\frac{k_{sz}}{\omega_s^*}+\frac{k_{iz}}{\omega_i^*}))^{-1}. \quad (3)$$

...we obtain following expression for dynamical chaos arising under decay ...netic wave in magnetized plasma:

$$E_{is}^2 > \frac{8m^2}{e^2}\frac{1}{3\sqrt{3}}\frac{\omega_p\omega_i\omega_s^2}{k_p^2}\frac{k_{pz}}{k_p}(1+\frac{\delta}{k_{pz}}(\frac{k_{sz}}{\omega_s}+\frac{k_{iz}}{\omega_i}))^{-1}. \quad (4)$$

...to expressions (3) and (4) the value of amplitude of electromagnetic wave ...chaos outcome in case of the decay under magnetized electron beam is less ...the decay in magnetized plasma due to beam shift. Compare (4) with (5) ...see that in the case of decay in the unmagnetized plasma the value of ...tromagnetic wave necessary for the chaos outcome in

$$\frac{k_p}{k_{pz}}(1+\frac{\delta}{k_{pz}}(\frac{k_{sz}}{\omega_s}+\frac{k_{iz}}{\omega_i}))$$

...hen in the case of decay in the magnetized plasma.

...computer simulation confirm these results.

...was supported, in particular, by ISSEP, grant No PSU 052087.

...rences

...Bints, O.V. Mamilenko, A.P. Tolstolushsky. Development of Dynamical Chaos ...Nonlinear Interaction of Waves in Unbounded Unmagnetized Plasma. (This con-...ence).

...A.I., Akhiezer I.A., Polovin R.V., Sitenko A.G., Stepanov K.N. Plasma Elec-...dynamics. Pergamon, Oxford, 1975;

...Rudakov, V.N.Tsytovich. Phys. Rep., 40C1 (1978);

...M. Gorbunov. Sov. Phys. Usp., 109 (1973), No 4, p.631;

...C. Thornhill and D.ter Haar. Phys. Rep., 43 (1978), No. 2, p.45.

DEVELOPMENT OF DYNAMICAL CHAOS UNDER NONLIN... INTERACTION OF WAVES IN UNBOUNDED UNMAGNETIZED ...

V. A. Buts, O. V. Manuilenko, A. P. Tolstoluzhskii

National Science Center
"Kharkov Institute of Physics and Technology"
Akademicheskaya st.1, Kharkov 310108 Ukraine

The wave-to-particle and weak nonlinear wave-to-wave interactions determine fu... properties of plasma, electron beams, etc. The regular dynamics of these processes ... extensively studied. It is well established now that nearly all dynamical systems ... scribe plasmas phenomena and based on wave-to-particle and wave-to-wave type of ... in their extended phase space (a space of all canonical variables and parameters) ha... of chaotic behavior. The stringent analysis of dynamics in such regions is possibl... employing numerical methods. However, random character of trajectories in the... enables one to use methods of statistical physics for their description. Thus analytic... ria for defining of such regions are of paramount importance because they not only ... regions where the qualitative transition of the dynamics from regular to chaotic oc... also give an analytical description of a dynamical system in this region by means of ... of statistical physics. There exist a few criteria of transition to global stochastici... most simple and effective is a Chirikov's criterion [1]. Whereas this criterion is based ... definition of a nonlinear resonance, it is well adapted and widely used in the investig... processes comprising wave-to-particle interaction. In the present report formulate con... if being fulfilled the dynamics of the wave-to-wave type of coupling turns out to be ...

As known the energy transfer from one wave to others in nonlinear interaction h... character of an instability. Therefore one may assume that the dynamic of this coup... be chaotic when parameter $K \sim G/\delta$ becomes greater then unity, where G is the grow... of this instability which plays the role of width of a nonlinear resonance, δ is the d... between resonances of different waves. Observe that value of δ usually correspon... minimum frequency.

Such formulation is based on the qualitative picture of the process of weak no... interaction of waves. To find the criterion more rigorously we will consider the well... process of three wave decay. Let the wave of amplitude a_1 wave number k_1 and freque... decay into two waves (a_2, k_2, ω_2) and (a_3, k_3, ω_3). One more wave is assumed to exi... the following parameters (a_4, k_4, ω_4), $k_4 = k_3$, $\omega_3 - \omega_4 << \omega_1$. Suppose at first that ... wave do not influence on the decay. Then the amplitudes of three interacting waves ch... with time according to [2]:

$$\begin{aligned} \dot{a}_1 &= iV_1^* a_2 a_3, \\ \dot{a}_2 &= -iV_1 a_1 a_3^*, \\ \dot{a}_3 &= -iV_1 a_1 a_2^*. \end{aligned}$$

Where V_1 is the matrix element of interaction. On the linear stage ($|a_1| = const, \Phi_1 =$ ... of decay the amplitude $|a_2|$ and $|a_3|$ growth exponentially with increment $G = |a_1||V_1|$ ... phase $\Phi = 2\Phi_2 + 2\Phi_3$ changes obeys equation of mathematical pendulum:

$$\ddot{\Phi} + (2|a_1||V_1|)^2 \sin\Phi = 0.$$

from Eq.(2) that the half width of nonlinear resonance equals $4G$. If we replace by for i wave we obtain that on the linear stage phase $\Psi = 2\Phi_2 + 2\Phi_4 + 2\delta\tau$ [illegible] where $G_2 = |a_1||V_2|$, $\delta = \omega_1 - \omega_2 - \omega_s$. This means, that the distance [illegible] resonances is equal to 2δ. Assuming the width of nonlinear resonance for [illegible] small $G << G_2$ we obtain the condition of the nonlinear resonance overlapping [illegible] continuingly, the criterion of stochastic instability: $K = 2G/\delta > 1$.

[illegible] consider the decay of the HF electromagnetic wave ("i") with frequency ω_i, wave [illegible] amplitude $\vec{E}_i$ which propagated in the uniform, unbounded plasma on the HF [illegible] electromagnetic wave $(\omega_s, \vec{k}_s, \vec{E}_s)$ and LF Langmuir wave $(\omega_{pe}, \vec{k}_p, \phi)$ ([3], [4]). The [illegible] set of equations consists of the Maxwell's equations for electromagnetic fields and [illegible] motion equations for plasma electrons. We neglect the movement of ions, assuming [illegible] that conditions serves for compensation of electron charge. The averaging over the [illegible] $t_{fi} >> t_o >> t_{fl}$, where $t_{el} \sim \frac{1}{\omega_{pe}}$, $t_{fi} \sim \frac{1}{\omega_i}$ -periods of slow and fast variables, [illegible] leads to the following system of coupled equations:

$$\frac{\partial \vec{v}_e}{\partial t} = \frac{e}{m}\vec{E},$$
$$\nabla^2\vec{E} - \frac{1}{c^2}\frac{\partial^2\vec{E}}{\partial t^2} - \frac{\omega_{pe}^2}{c^2}\vec{E} = \frac{\omega_{pe}^2}{c^2}\frac{\delta n_e}{n_{eo}}\vec{E}, \qquad (3)$$
$$(\frac{\partial^2}{\partial t^2} + \omega_{pe}^2 - V_{Te}^2\nabla^2)\frac{\delta n_e}{n_{eo}} = \frac{1}{2}\nabla^2\langle\vec{v}_e^{\,2}\rangle,$$

[illegible] electron velocity (vary on the fast time-scale), $\vec{E}$ - electric field (vary on the fast [illegible] n_{eo} - equilibrium electron density, δn_e - electron density perturbation (vary on [illegible] time-scale), $< \ldots >$ - average over the time t_o. Assuming following form for HF [illegible] electric field and LF plasma density:

$$\vec{E}(\vec{r},t) = \frac{1}{2}\vec{E}_i(t)\exp(-i\omega_i t + i\vec{k}_i\vec{r}) + \frac{1}{2}\vec{E}_s(t)\exp(-i\omega_s t + i\vec{k}_s\vec{r}) + \text{c.c.},$$

$$\delta n_e(\vec{r},t) = \frac{1}{2}\delta n_p(t)\exp(i\vec{k}_p\vec{r}) + \text{c.c.},$$

[illegible] obtain from (3):

$$i\frac{\partial\mathcal{E}_i}{\partial\tau} = \mathcal{E}_s\rho\exp(i\Delta\tau),$$
$$i\frac{\partial\mathcal{E}_s}{\partial\tau} = \mathcal{E}_i\rho^*\exp(-i\Delta\tau), \qquad (4)$$
$$(\frac{\partial^2}{\partial\tau^2} + \Omega^2)\rho = -\mathcal{E}_i\mathcal{E}_s^*\exp(-i\Delta\tau),$$

[illegible] we neglected term $\sim V_{Te}^2$,

$$\frac{E_i}{E_{io}}\mathcal{E}_i = \frac{E_i}{E_{so}}\sqrt{\frac{\omega_s}{\omega_i}}, \rho = \frac{\delta n_p}{n_{eo}}[\frac{\omega_p^2\cos\alpha}{2k_p^2\sqrt{\omega_i/\omega_s}}\frac{\pi m n_{eo}}{E_{io}^2}]^{1/3}, \tau = t[E_{io}^2\cos^2\alpha\frac{e^2}{8m^2}\frac{k_p^2\omega_p^2}{\omega_i\omega_s^3}]^{1/3},$$

$$\Omega^2 = [\frac{8m^2}{e^2}\frac{1}{E_{io}^2\cos\alpha^2}\frac{\omega_p\omega_i\omega_s^2}{k_p^3}]^{2/3}, \Delta = (\omega_i - \omega_s)[\frac{8m^2}{e^2}\frac{1}{E_{io}^2\cos\alpha^2}\frac{\omega_i\omega_s^2}{k_p^2\omega_p^2}]^{2/3}.$$

To obtain the set of equations (4) we assume that there is space synchron... coupling waves. On the linear stage of the decay $\mid \mathcal{E}_i \mid = const$ we can obtain ... despersion relation:

$$(\omega^2 - \Omega^2)(\omega + \Delta) = 1$$

and following expression for maximum values of the growth rates:

$$G = \mathcal{I}m\omega = 1/\sqrt{2\Omega}, \quad \Omega^2 >> 1, \quad G = \mathcal{I}m\omega = \sqrt{3}/2, \quad \Omega^2 << 1.$$

In the first case parameter $K << 1$ ($\delta \equiv \Omega$) and dynamics of the decay must b... At large amplitudes of the incident wave $K >> 1$ thus decay must be chaotic. ... the region of parameters where $K >> 1$ is related to the so called modified decay ... obtain following conditions for arising of the chaotic dynamics of the decay:

$$E_{i0}^2 > \frac{8m^2}{e^2} \frac{1}{3\sqrt{3}} \frac{\omega_i \omega_p \omega_s^2}{k_p^2 \cos^2 \alpha}.$$

From (5) one may determine the value of amplitude of electromagnetic wave nece... chaos outcome. At $\omega_p = 6 \cdot 10^9 Hz$, $V_{pph} = 3 \cdot 10^9 cm/s$, $\omega_i/\omega_p = 3$ it is of $5.3 \cdot 10$...

The set of equations (4) has been solved numerically for the different values of the ... tude of incident wave. Time-dependent dynamics of amplitudes of coupling waves, ... of obtained realizations and auto correlations functions we show on fig. 1,2. W... condition (5) is not satisfied,the dynamic of the decay is regular (fig.1).

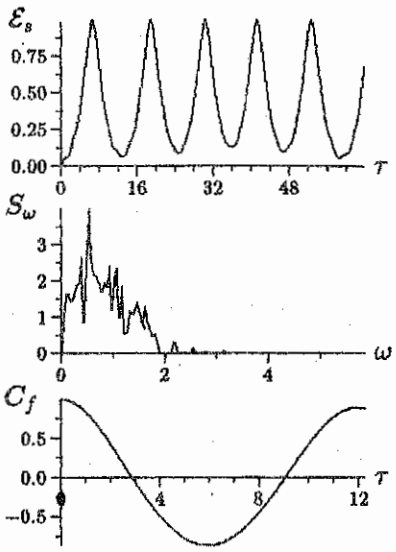


fig.1

case the behaviour of the decay is chaotic (fig.2).

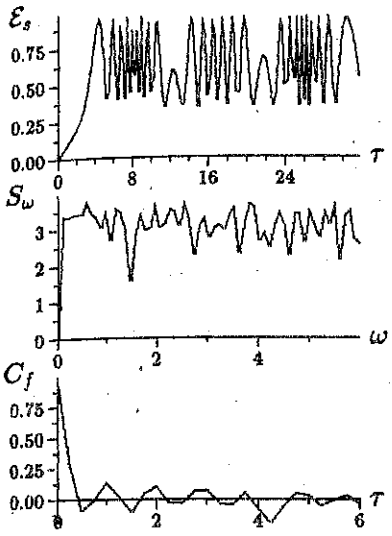


fig.2

criterion thus derived similar to other [2] allows one to find the parameters ... system dynamics becomes stochastic. As for the transition boundary to chaos, ... one needs more highly sensitive analytic and numerical analysis.

conclusion it is necessary to observe the following. Criterion really defines the range ... where the chaotic dynamics of nonintegrable systems reigns. But for the ... ones it does not work at all. So one should be cautious before using the criterion

work was supported, in particular, by ISSEP, grant No PSU 052087.

References

1. Chirikov B.V. Phys. Rep. 1979, v.52, p.265.
2. Zaslavskii G.M., Sagdeev R.Z. Introduction in Nonlinear Physics. (Russian) M., Nauka ... 1988.
3. ... A.S. Nuclear fusion. 1970, v.10, p.53.
4. Vedenitskii A.A., Repalov N.S. Zh. Tekh. Fis. 1970, v.40, p.32.

DEVELOPMENT OF DYNAMICAL CHAOS UNDER NONLIN... INTERACTION OF WAVES IN BOUNDED MAGNETIZED PL...

V. A. Buts, O. V. Manuilenko, A. P. Tolstoluzhskii

National Science Center
"Kharkov Institute of Physics and Technology"
Akademicheskaya st.1, Kharkov 310108 Ukraine

In the present report we formulate conditions if being fulfilled the dynamics of ... to-wave type of coupling in the bounded system turns out to be chaotic. It is ... the process of chaos arising at nonlinear interaction of waves in plasma wave ... strong magnetic field. It is obtained necessary value of the pumping wave amp... chaos arising.

As known, the energy transfer from one wave to another in their nonlinear ... has a nature of instability. It is turn out to be that the value of a twice growth ra... instability ($2G$) plays a role of the nonlinear resonance width in the wave-to-wa... coupling. Further, it is quite natural to assume that dynamics of this coupling will ... when parameter $K = 2G/\delta$ becomes greater then unity ($K > 1$), where δ is the ... between resonances of different waves. The proof of this statement is adduced in [1] ... that value of δ usually corresponds to a minimum frequency.

Let us consider the decay of high-frequency (HF) electromagnetic wave with f... ω_N, longitudinal wave number k_N and amplitude A_N which propagated in metal wa... completely filled by plasma and placed in a strong magnetic field, directed on axis ... guide ($\vec{H}_o = \{0, 0, H_o \to \infty\}$ - external magnetic field), on the HF electromagne... ($\omega_n,\ k_n,\ A_n$) and low-frequency (LF) plasma wave ($\omega_k,\ k_k,\ \Phi_k$) . In other words we c... the process $t \to t' + l$. The basic system of equations consists of the Maxwell's e... for electromagnetic fields and hydrodynamic equations for plasma electrons. We neg... movement of ions, assuming that background ions serves for compensation of cha... averaging over the time t_o ($t_{sl} >> t_o >> t_{ft}$ -periods of slow and fast variables, resp... leads to following system of coupled equations (see, for example, [2]):

$$\frac{\partial \tilde{v}_{ex}}{\partial t} = \frac{e}{m}\tilde{E}_x,$$

$$(\nabla^2 - \frac{1}{c^2}\frac{\partial^2}{\partial t^2})\tilde{E}_x = \frac{\omega_p^2}{c^2}\frac{\delta n_e}{n_{eo}}\tilde{E}_x,$$

$$\frac{\partial^2}{\partial t^2}\delta n_e - \frac{e n_{eo}}{m}\frac{\partial^2}{\partial z^2}\Phi = \frac{n_{eo}}{2}\frac{\partial^2}{\partial z^2}\langle \tilde{v}_{ex}^2 \rangle,$$

$$\nabla^2\Phi = 4\pi e\delta n_{e},$$

where $\nabla^2 \equiv \frac{\partial^2}{\partial x^2} + \frac{1}{r}\frac{\partial}{\partial r}(r\frac{\partial}{\partial r})$, $\tilde{E}_x$ - HF electromagnetic wave, δn_e - slow perturbati... plasma density, n_{eo} - unperturbed plasma density, $\tilde{v}_{ex}$ - the fast varying electrons spee... potential LF plasma wave, $< ... >$ - the average over time t_o. The general solution of ... may be represented as an expansion in eigenfunctions of the magnetized plasma wave ... (see, for example [3]). Assuming that the phase velocity of pumping wave is positive ... possible to receive the following system of equations:

$$\frac{d^2}{dt^2}n_k + \omega_p^2\frac{\kappa_k^2}{\kappa^2}n_k = -\frac{\omega_p^2}{8\pi m}\sum_n \alpha_k^{Nkn}\frac{\kappa_k^2}{\omega_n\omega_N}A_N A_n^* \exp(-i\Delta\tau)$$

$$i\frac{d}{dt}A_N = \frac{\omega_p^2}{4\omega_N}\sum_{n,k}\alpha_N^{Nkn}\frac{n_k}{n_0}A_n\exp(i\Delta\tau) \qquad (2)$$

$$i\frac{d}{dt}A_n = \frac{\omega_p^2}{4\omega_n}\sum_k \alpha_N^{Nkn}\frac{n_{k*}}{n_{eo}}A_N\exp(i\Delta\tau)$$

summation is conducted on indexes, satisfying conditions of space synchronism (for ...y are not adduced here terms, appropriate to waves with negative phase velocity), ... $\kappa_{\perp k}^2$ - transverse wave number, $\Delta = \omega_N - \omega_n$

$$\alpha_k^{Nkn} = \int_0^a \mathcal{J}_0(\kappa_{\perp n})\mathcal{J}_0(\kappa_{\perp k})\mathcal{J}_0(\kappa_{\perp N})rdr \Big/ \int_0^a \mathcal{J}_0^2(\kappa_{\perp k})rdr,$$

...radius of the wave guide. If the space synchronism is take place only for one set of ...ators, one may, obtain following system from (2):

$$i\frac{\partial\mathcal{E}_i}{\partial\tau} = \mathcal{E}_s\rho\exp(i\Delta\tau),$$
$$i\frac{\partial\mathcal{E}_s}{\partial\tau} = \mathcal{E}_i\rho^*\exp(-i\Delta\tau), \qquad (3)$$
$$(\frac{\partial^2}{\partial\tau^2} + \Omega^2)\rho = -\mathcal{E}_i\mathcal{E}_s^*\exp(-i\Delta\tau),$$

...dimensionless variables are expressed as follows:

$$\mathcal{E}_N = \frac{A_N(\tau)}{A_N(0)}, \mathcal{E}_s = \frac{A_n(\tau)}{A_N(0)}\sqrt{\frac{\omega_n}{\omega_N}\frac{\alpha_N^{Nkn}}{\alpha_n^{Nkn}}}, \rho = \frac{n_k}{n_{eo}}[\frac{\omega_p^2}{\kappa_k^2}\frac{\alpha_N^{Nkn}}{\alpha_k^{Nkn}}\frac{\pi m n_{eo}}{2A_N^2(0)}\sqrt{\omega_n/\omega_N\alpha_N^{Nkn}\alpha_n^{Nkn}}]^{1/3},$$

$$\tau = [\frac{A_N^2(0)}{32\pi m n_{eo}}\frac{1}{\omega_N\omega_n^2}\alpha_k^{Nkn}\alpha_n^{Nkn}]^{1/3}\Delta, \Delta = (\omega_N - \omega_n)[\kappa_k^2\omega_p^4\frac{A_N^2(0)}{32\pi m n_{eo}}\frac{1}{\omega_N\omega_n^2}\alpha_k^{Nkn}\alpha_n^{Nkn}]^{-1/3},$$

$$\Omega^2 = \omega_p^2\frac{\kappa_k^2}{\kappa^2}[\kappa_k^2\omega_p^4\frac{A_N^2(0)}{32\pi m n_{eo}}\frac{1}{\omega_N\omega_n^2}\alpha_k^{Nkn}\alpha_n^{Nkn}]^{-2/3},$$

In the case of wave guide the distance between two wave resonances is determined by ...tance on frequencies between two nearest radial harmonics. This distance can be enough ...all one. So, assuming, that the radius of wave guide considerably less than its length, on ...of obtained above criterion, we have the following expression for the value of amplitude ...pumping wave at which the dynamics of decay becomes chaotic:

$$A_N^2 > \frac{8}{3^{3/2}}\frac{m^2}{e^2}1/(\alpha_n^{Nkn}\alpha_k^{Nkn})\omega_p\omega_N\omega_n^2\kappa_k[1/\kappa_{\perp k} - 1/\kappa_{\perp k+1}]^3 \qquad (4)$$

As it following from (4), this quantity can be enough small for not very hi
of radial harmonics. At $a = 2.5cm$, wave guide length $L = 100cm$, $\omega_p =$
$V_{pph} = 3 \cdot 10^9 cm/sec$, $\omega_0/\omega_p = 10$, the chaos arising value of amplitude is $8 \cdot 10$
decay of third radial harmonics. At smaller field values the process of decay will
Computer simulation confirm these results.

This work was supported, in particular, by ISSEP, grant No PSU 052087.

References

[1] V.A. Buts, O.V. Manuilenko, A.P. Tolstoluzhskii. Development of Dynamica
under Nonlinear Interaction of Waves in Unbounded Unmagnetized Plasma. (P
ference).

[2] Akhiezer A.I., Akhiezer I.A., Polovin R.V., Sitenko A.G., Stepanov K.N. Plasm
trodynamics. Pergamon, Oxford, 1975;

L.I.Rudakov, V.N.Tsytovich. Phys. Rep., 40C1 (1978);

L.M. Gorbunov. Sov. Phys. Usp., 109 (1973), No 4, p.631;

S.G. Thornhill and D.ter Haar. Phys. Rep., 43 (1978), No. 2, p.45.

[3] A.N.Kondratenko. Zh. Tech. Fis., 33 (1963), p.1397.

K.S.Karplyuk, V.N.Oraevsky. Zh. Tech. Fiz., 38 (1968), p.1214.

...IATION SPECTRUM BROADENING IN BEAM-PLASMA ...INTERACTION, CAUSED BY INDUCED SCATTERING

V.A.Balakirev, I.N.Onishchenko, G.V.Sotnikov
"...Kharkov Institute of Physics & Technology" 310108 Kharkov, Ukraine
D.Yu.Sidorenko,
...Kharkov State University, 310077 Kharkov, Ukraine
M.Masuzaki, R.Ando, K.Kamada
...Physics, Faculty of Science, Kanazawa University, Kanazawa 920-11, Japan

...tion

...] it was found that in a single ...formation the efficiency of rela... ...on beam-plasma interaction is ...d by the factor $\lambda = (n_n/n_p)^{1/3}\gamma$ ...beam and plasma density, respec... ...ativistic factor). The maximum ...ciency is observed at $\lambda \simeq 1/2$. How... ...experimental investigations [2, 3] ...that at $\alpha = (n_b/n_p)^{1/3} \sim 1$, beam ...interaction demonstrated broadband ...some times higher than the plasma ...with the efficiency different from ...[1]. In the present work this in... ...studied for the arbitrary α ap... ...tion and for both beam and plasma ...motion. For the scattered REB the ...ng of the spectrum to more higher ...due to induced scattering of the ...plasma waves on REB particles is dis...

...o Electron Laser Mechanism of ...diation

...In [2] the effective generation mechanism ...lromagnetic radiation with broadband ...um at the REB-plasma interaction is ...ed. The base of this mechanism is ...ulated scattering of Langmuir oscillations ...EB particles (so called plasma FEL [4, 5]). The realization of such mechanism is possible if the REB has momenta dispersion. The interaction of the scattered REB with plasma leads to the excitation at plasma frequency with broadband spectrum in $\vec{k}$-space ($\vec{k}$ is wavenumber). Generated oscillations during the scattering on the particles of the same REB in its turn excite broadband radiation. So the stated mechanism allows to transform the oscillations with continious spectrum in $\vec{k}$-space into electromagnetic radiation with continious frequency spectrum.

Let us consider the process of induced scattering of Langmuir wave with frequency ω_p and wave number k_p on the portion of resonant REB particles with velocity $\vec{v}$. Oscillating in the field of Langmuir wave the REB particles radiate electromagnetic wave with frequency ω_t and wavenumber $\vec{k}_t$. This process is possible under resonant condition satisfying:

$$\omega_t - \omega_p = \left(\vec{k}_t - \vec{k}_p\right)\vec{v} \qquad (1)$$

The spatial growth rate at the plasma FEL process is determined by the following expression:

$$\varkappa = \frac{1}{2^{5/3}}\left(\beta_B \omega_t \overline{\omega} \sin\theta\right)^{1/3}. \qquad (2)$$

Here $\beta_B = eE_p/mc\overline{\omega}$, E_p is amplitude of the plasma wave pumping, $\overline{\omega} = \omega_p - k_p v\cos\theta_1$,

θ_1 is the angle of e.m. wave radiation, θ is the angle between directions of plasma wave and REB propagation. For the parameter of the experiment [3] the maximum frequency of e.m. radiation for $\theta_1^* = \pi/2$, $\theta = 0$ is $\omega = 2\gamma^2\omega_p = 32\omega_p$. Frequency spectrum is now under investigation.

2. Excitation dynamics of broadband oscillation at $\alpha \sim 1$.

Considered above the conversion mechanism of plasma oscillations into high frequency radiation is possible for the REB with significant momenta dispersion. For the hydrodynamic beam with a small dispersion and comparable beam and plasma densities ($\alpha \sim 1$) the excitation of broadband oscillations with frequencies essentially higher than plasma frequency takes place as a result of beam-plasma instability development. In this case the dynamics of the instability is chaotic and oscillations have a continuous frequency spectrum.

In the frame of one dimensional theory for the simulation of dynamics of the broadband oscillations we use the model of plasma slab of length L with periodic boundaries for fields and particles [6]. Electric field can be expanded in Fourier series over longitudinal coordinate. Selfconsistent equations set consists of equations for beam and plasma electrons motion in Lagrangiane variables

$$\frac{d\zeta_p}{d\tau} = \frac{\sigma_p}{\sqrt{1+\sigma_p^2}}; \quad \frac{d\sigma_p}{d\tau} = -\varepsilon_p, \qquad (3)$$

$$\frac{d\zeta_b}{d\tau} = \frac{\sigma_b}{\sqrt{1+\sigma_b^2}}; \quad \frac{d\sigma_b}{d\tau} = -\varepsilon_b,$$

$$\zeta_{p,b} = \zeta_{p,b}(\zeta_{0p,0b}, \tau), \quad \varepsilon_{p,b} = \varepsilon(\zeta = \zeta_{p,b}, \tau).$$

and the expression for the electric field:

$$e(\zeta,\tau) = \sum_{n>0}^{N} \frac{1}{\pi n} \int_0^{\Lambda} \sin\left[\frac{2\pi n}{\Lambda}(\zeta - \zeta_p)\right] d\zeta_{0p} \qquad (4)$$

$$-\alpha \sum_{n>0}^{N} \frac{1}{\pi n} \int_0^{\Lambda} \sin\left[\frac{2\pi n}{\Lambda}(\zeta -$$

Here $\varepsilon = eE/mc\omega_p$, $\zeta = \omega_p x/c$ – dimensionless intensity of the el… longitudinal coordinate and time, … $\zeta_{p,b} = \omega_p x_{p,b}/c$ – dimensionless … and coordinates of plasma and b… cles, $\Lambda = \omega_p L/c$. Integration in … filled over the initial positions of pl… and beam (b) electrons.

Numerical calculations are carri… $\Lambda = 10\pi$, initial value of relativis… $\gamma = 4$ and various value of param… n_b/n_p. Number of spatial harmonics … resonance harmonic with REB wa… $n = 5$.

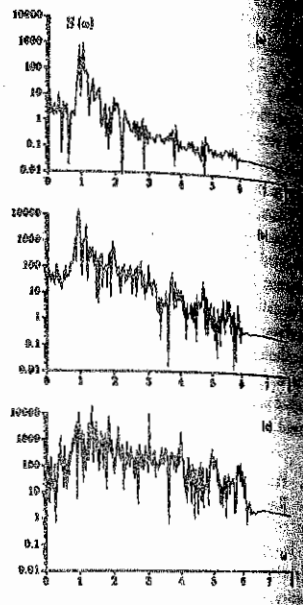


Fig. 1:

Results of simulation show that for … $\alpha(\alpha = 0.01)$ the exponential growth of th…

oscillations, conditioned
of the bunches, trapped by
frequency spectrum for this
in Fig.1a. In accordance
peaks in spectrum cor-
to plasma frequency and
the frequency displaced by
of the trapped bounces. As
monics the resonant harmonic
maximum value. The other
increasing at linear stage of
however they are still negligibly
atively to the main harmonic
energy loss of the beam is about
% of the beam is lost for the
HF-oscillations, the rest of en-
pended for beam and plasma

growth of α the dynamics of the
changing. As it follows from Fig.1b
correspondingly broadening.
oscillations have chaotic char-
trum is continuous and contains
up to $6\omega_p$ (for taking into ac-
This is especially seen in the
range of the spectrum. At
≥ 100) the resonant spatial har-
and divisible to it n=10,15,20
At $\tau = 150$ all of them grow
to the same values. However in
frequency range of the wavenum-
amplitudes correspond to the
that are divisible to the main one

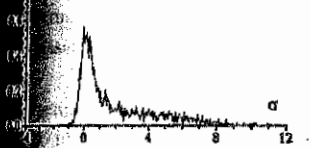


Fig. 2:

Analysis of the distribution function for
shows that at the nonlinear stage of the interaction the fast broadening of the distribution function of the beam and plasma electrons. The main part of the beam is decelerated, but the tail of accelerated particles appears. At $\tau = 250$ the distribution function is formed as a Maxwellian one with two temperatures $T_p = 150keV$, $T_b = 1.5MeV$(Fig.2). Total loss of the beam energy reached 45%. But for the wideband oscillations only 4% of the beam energy is expended, other part of the beam energy is lost for the beam and plasma heating.

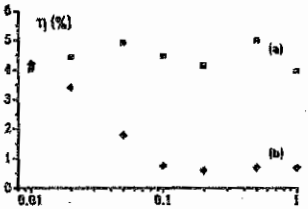


Fig. 3:

The dependence of HF-efficiency $\eta = \int_0^\Lambda \varepsilon^2(\zeta,\tau)d\zeta/\alpha(\gamma_0-1)\Lambda$ upon parameter α at the fixed $\gamma = 4$ is represented in Fig.3. Curve (a) is obtained taking the first maximum of the field amplitude. It is seen that this dependence curve (a) has not the single maximum contrary to the single mode model [1]. Moreover, averaged over late temporary range ($\tau = 200 - 300$) HF-efficiency (curve b) is sufficiently lower because of beam and plasma heating.

Conclusion.

For the case of large angle scattering beam the mechanism of plasma FEL brings to the spectrum broadening during beam-plasma interaction. This mechanism is mostly effective for the high current beam because of radiation intensity is proportional to the squared density of the beam particles. If REB is not

momenta scattered then at $\alpha \sim 1$ the beam-plasma instability itself leads to the excitation of broadband oscillations spectrum. For such values of α the nonlinear dynamics of the instability is chaotic. Excited oscillations are nonregular and has continuous spectrum.

It should be noted that at $\alpha \sim 1$ the fast thermalization of not only plasma particles but of the particles of the initially monoenergetic beam takes place. So the plasma FEL-mechanism mentioned above can make its contribution to the broadening of the radiation spectrum.

In part this work is supported by "JSPS Program on Japan-FSU Scientists collaboration".

References.

[1] N.G.Matsiborko, I.N.Onishchenko, V.D.Shapiro et.al. Plasma Phys. 14(1972)591;
T.E.Thode, R.N.Sudan. Phys.Rev.Lett. 30(1973)732

[2] K.G.Kato, G.Benford
Phys.Fluids 26(1983)36

[3] M.Masuzaki, R.Ando
et.al. Proc.8th Int.Con
Particle Beams, ed.B.N.B
B.A.Knyazev (World Sci
pore, 1991), V.2,p.683.

[4] V.A.Balakirev, V.A.Mi
Ya.B.Fainberg. Sov.J.P
12(1986)563.

[5] Yoshi H., Katsouleas
J.M. et.al. IEEE J.Quan
23(1987)1571.

[6] R.W.Hockey, J.W.Eastwood
puter simulation using par
McGrow-Hill Inc.

...nifestation of wave collapse in developed strong Langmuir turbulence in a magnetic field

...Burmasov, I. V. Kandaurov, E. P. Kruglyakov, O. I. Meshkov, A. L. Sanin, and L. N. Vyacheslavov

...Institute of Nuclear Physics, Novosibirsk, 630090, Russia

...effects of the collapse occurrence are observed experimentally: generation of tails of ...distribution function and high level of short-wavelength low-frequency density ... The later phenomenon is enhanced due to weak damping of ion-acoustic waves in ...(Te >>Ti) plasma used.

Introduction

...Zakharov's model [1] is the most widely used model to treat the strong ... regimes. The model describes Langmuir wave collapse , which has also been ... experiments. However, this model, in its original form, does not include the ... wave-particle interaction. Therefore, difficulties arise in determining the time- and ...averaged statistical characteristics of the steady state turbulence since, in this regime, ... plasma electrons can change the collapse dynamics . In addition, there are other ... factors that need to be taken into account to construct a realistic picture: the ... of a magnetic field in the plasma, plasma non-isothermality and electron-ion ... It is also difficult to take into account all these factors in numerical calculations ... of the fact that full-scale kinetic simulations are still far beyond the capabilities of ... computers. Experiments on the observation of spectra of Langmuir turbulence ... by a relativistic electron beam have been carried out under the conditions included ... above mentioned aspects. The obtained spectra are found strongly unstable relative ... low-frequency modulational instability [2] that shows the fulfillment of the strong ... regime. In the present paper, two experimental signatures of the collapse ... are found in this case. The short wavelength ion-acoustic turbulence and the ...thermal electrons are observed in the same region of the momentum space during the ... plasma interaction.

Experimental setup

...periments were carried out on the GOL-M device. The preliminary hydrogen plasma ...1.5·10^{13} cm^{-3}, T_{eo}=1 eV, D=6 cm, L=250 cm, magnetic field in homogeneous part is ...2.5 T, in the mirrors B_m=4.5 T) was created by a discharge. The beam with the energy ...ctions E=700 keV was injected into the plasma through one of the mirrors. The beam ...meters were: the maximum current I_b=2÷3 kA, the diameter d_b=2 cm, the duration of

the beam τ_b=200 ns. In the experiments, the Thomson scattering technique was studying a non-Maxwellian electron distribution function (Fig.1). Two simultaneously operating systems were employed for the observation of

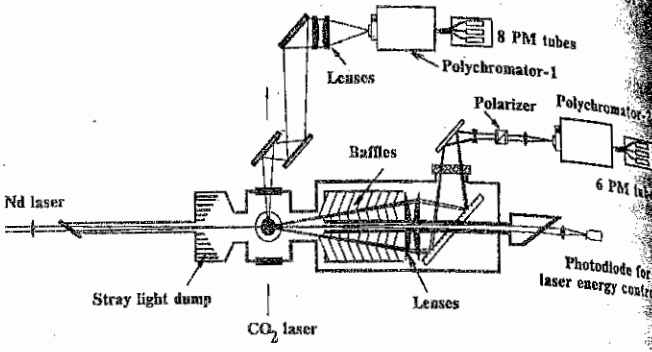


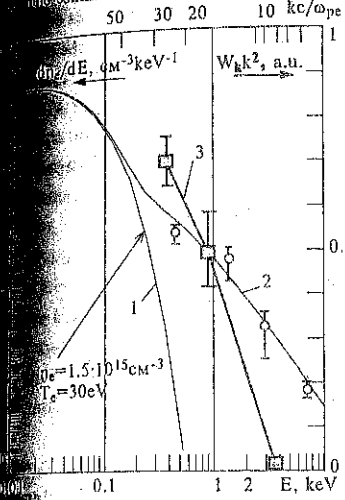
Figure 1. Collection system for light scattered at 90 and 8 degrees

scattered at the angles 90° and 8°, respectively. It is known, that the spectral density of scattered radiation is higher at the small scattering angles. Thus, the registration of light scattered at an angle of 8° was employed for studying the superthermal "tails" of the electron distribution function. The temperature and density of the bulk of plasma electrons were measured simultaneously by a 90° system. This system allows to measure an electron temperature with the range of 5—150 eV, where the upper value is limited by the plasma background light during the REB injection. The Nd-glass laser was used as a source of the probe beam with the following parameters: The pulse energy: up to 40 J / 15 J (wavelength 1060 nm / 530 nm); pulse duration: 8 — 10 ns, beam divergence: $2 \cdot 10^{-4}$ rad. The stray light occurred due to the scattering of the laser radiation on the elements of construction and, predominantly, on the low-temperature bulk of plasma electrons, was suppressed in a 8° system by the high-contrast interference filters (purchased from Barr Associates, Inc.) with the bandwidth adjusted to the positions of corresponding receiving channel of the polychromator-2.

The spectra of low frequency ion-acoustic fluctuations were studied with the same experiments by the collective laser scattering with a pulse CO_2 laser as a source of light (Q =10 J, $\tau = 10^{-6}$s). The detailed description of this technique can be found elsewhere [3, 4]. In the presented experiments, the scattered radiation was detected at the angles θ = 6°, 11° and 16° to the direction of the laser beam propagation

Experimental results

...llisional damping of Langmuir oscillations, the plasma electron temperature has ...om to 30÷50 eV during first 40 ns after start of the REB injection [2]. Thus, the ...nality condition ($T_e >> T_i$) was fulfilled practically during all the time of the REB ...with a plasma. The first measurements at 50 — 100 ns from the beginning of the ...ive clear signals in four receiving channels. When processing the signals, it was ...ted the distribution function has the power law: $f(E_e) \propto E_e^{-\alpha}$ for the energies ...eV (approximately 10 T_e). The scattered spectrum was calculated numerically for ...index of a power α, and its convolution with the instrumental functions of the ...was found. The value of α=2.5 provides the best fitting to the experimental data. ...of the distribution function is given in Figure 2. The spectrum of the ion-...illation is also shown in the figure. It is seen that both non-Maxwellian and ...ional ion-acoustic oscillations are positioned in the same region of the momentum ...The estimated total level of low-frequency turbulence is 2% $n_e T_e$.



...Distribution function of plasma electrons ...spectrum of ion-acoustic turbulence during the ...injection. 1) Maxwellian bulk, 2) high energy ...tail, 3) ion-acoustic waves

Discussion and conclusion

The intense short wavelength ion-acoustic oscillations that appear in strong Langmuir turbulence case and do not associated with the return current instability [3,4] is the main signature of the collapse occurrence. In an isothermal non-magnetized plasma, the collapse is a sole mechanism to shift the waves into the short wavelength region, where they could transfer their energy to small fraction of the plasma electrons. In case of $T_e >> T_i$ the short wavelength ion-acoustic oscillations produced by the collapse can switch on two other processes of the energy transfer through the turbulence. First, it is conversion on the ion acoustic oscillations [6, 7] — the nonlinear transfer of the Langmuir waves from the pumping region directly to the damping region. Second, in a magnetoactive plasma ...the magnetic addition to the dispersion of the Langmuir waves exceeds greatly the ...addition) it is the resonant scattering of the electron plasma waves, excited by REB,

along the lines of constant frequency in a momentum space. Both these processes
the collapse lead to a "tail" formation, i.e. to the heating of a small fraction
electrons. It is evident, that the heating of a non-Maxwellian part of the electron
function is connected with the Landau damping of slow Langmuir waves (real or
is in case of the conversion). The question is how to determine the main mech
transferring energy of turbulent oscillations towards the short wavelength side of the
It is unlikely that the fastest mechanism among those above mentioned, the resonant
of Langmuir waves on the ion-acoustic oscillations, provides the required energy flow
was proved earlier [2], the energy is pumped into the oscillations, propagating at
oblique angles according to the REB direction ($\theta < 30^{O}$). The dispersion permits inter
these waves only with the ion-acoustic waves with $k < 8\,\omega_{pe}/c$, which intensity is low
Besides the dispersion limits also the deceleration of Langmuir waves by rather hi
velocity, which corresponds to the energy of associated resonant electrons about 10 keV
value is much higher than that observed experimentally. The conversion rate can be
after the work [6], without regard to magnetic field, because for $k > 8\,\omega_{pe}/c$ the
addition in the dispersion exceeds the magnetic one. At the same time, the results of th
should be considered with care referring to our experimental conditions, where th
acoustic turbulence is not weak. The estimation of the conversion rate shows, that
provide the energy balance with the pumping. Features of the experimental spect
Langmuir turbulence [2] do not count, however, in favor of the conversion as th
mechanism of the energy transfer. The final examination of theoretical conclusions ab
dominant role of the conversion in the energy flow mechanism for $T_e >> T_i$, where the
acts only as the catalyst, is still requires some additional experiments.

References

1. V. E. Zakharov, Sov. Phys. JETP 35 (1972) 908.
2. L. N. Vyacheslavov, V. S. Burmasov, I. V. Kandaurov, E. P. Krurglyakov, O. I. M
and A. L. Sanin, Phys. Plasmas 2 (1995) 2224.
3. V. S. Burmasov, I. V. Kandaurov, E. P. Krurglyakov, O. I. Meshkov, A. L. Sanin
L.N.Vyacheslavov, in Proc XXII Europ. Conf. on Controlled Fusion and Plasma
(Bournemouth, England, June 1995) vol. 1 (1995) 445
4. V.S. Burmasov, I.V. Kandaurov, Eh.P. Kruglyakov, O.I. Meshkov, A.L. Sanin, and
Vyacheslavov, in Proc. XXII Int. Conf. on Phenomena in Ionized Gases (Hoboken,
August 1995), Vol.3, p.13 (1995).
5. P. K. Kaw, A. T. Lin, andJ. M. Dawson, The Phys. of Fluids 16 (1973) 1967
6. A. A. Galeev, R. Z. Sagdeev, V. D .Shapiro, V. I. Shevchenko, Sov. Phys. JETP 46 (
711.

NONLINEAR SURFACE WAVES IN ELECTRONIC PLASMA

V.Grimalsky, Yu.Rapoport

University, Physics Faculty, Astronomy Dept., 252022 Kiev, Ukraine
e-mail: rapoport@astron.univ.kiev.ua

sibility of propagation of Langmuir surface envelope solitons and modulation (MI) of surface wave propagating along the interface between plasma and dielectric) in frequency range $0<\omega<\omega_p/\sqrt{2}$ were investigated in Ref. [1,2] is electron Langmuir frequency). But in these works the boundary connected with the existence of surface current and charge were not Besides, it must be taken into account the possibility of resonance for harmonic of surface wave ($2\omega\approx\omega_p$). Pointed above factors may essentially the dynamics of nonlinear waves.

In this paper the propagation of nonlinear surface waves in semi-infonitive cold plasma is under investigation. Both volume nonlinearity mechanisms and nearity of movement of surface charge, and also the possibility of temporal for second harmonic of wave, are taken into account. The equations for varying amplitudes of first and second harmonics of surface wave are derived. the regions of propagation of envelope solitons, and also existence of modulation sibility, are presented taking into account pointed above factors.

Consider semi-infinite plasma ($z>0$), bounded by thin dielectric wall ($z=0$), this wall ($z<0$) there is medium with dielectric permittivity equal to *1*. Along the face in frequency interval $0<\omega<\omega_p/\sqrt{2}$, the surface Langmuir waves can propagate. dispersion equation has the form:

$$q + p\,\varepsilon(\omega) = 0,$$

where $\varepsilon(\omega)=1-\omega_p^2/\omega^2$, $q=(k^2-\omega^2\varepsilon(\omega)/c^2)^{1/2}$, $p=(k^2-\omega^2/c^2)^{1/2}$; k, q, p are longitudinal transverse wave numbers, respectively. Because these waves are mainly due to oscillations of surface charge [3], therefore, it is necessary to take into account the dynamics of surface charge under the investigation of nonlinear properties of these waves. Start from the Maxwell's equations and hydrodynamic equations for volume and surface charges in cold plasma

$$\frac{\partial n}{\partial t} + div\,(nv) = 0, \frac{\partial v}{\partial t} + (v\nabla v) = -\frac{e}{m}(E + \frac{1}{c}[v \times H]),$$
$$rotH = \frac{1}{c}\frac{\partial E}{\partial t} - \frac{4\pi}{c}env, rotE = -\frac{1}{c}\frac{\partial H}{\partial t}; \quad (1)$$
$$\frac{\partial \sigma}{\partial t} + nv_z(z = +0) + \frac{\partial}{\partial x}(\sigma v_x) = 0.$$

Here n is electron concentration, v is their velocity, σ is density of surface charge that surface current and charge are presented in appropriate boundary condition components of electromagnetic field. Consider surface waves propagating along x along y axis the system is homogeneous.

To derive the coupled equations for slowly varying amplitudes, the simplest is to use the bilinear relations like Lorentz lemma that gives possibility to take account as purely volume as surface mechanisms of nonlinearity. For this case relation is

$$\frac{\partial}{\partial t}\{\frac{1}{4\pi}(E_1E_2^* + H_1H_2^*) + mn_0v_1v_2^*)\} + \frac{c}{4\pi}div\{[E_1 \times H_2^*] + [E_2^* \times H_1]\} =$$
$$= mn_0v_2^*(v\nabla)v - \frac{en_0}{c}v_2^*[v \times H] + eE_2^*((n - n_0)v). \quad (2)$$

Here n_0 is unperturbed electron concentration, E_1, H_1, v_1 are positive-frequency components of nonlinear surface wave at fundamental carrier frequency ω; E_2^*, H_2^*, v_2^* are negative-frequency components of monochromatic surface wave with small amplitude at the same frequency (linear wave).

Take into account that in this system the resonance with second harmonic wave can take place [4] ($\omega \approx \omega_p/2$), therefore, it is necessary to describe the second harmonic by separate amplitude. Because in cold plasma the spatial dispersion is absent, only temporal resonance with second harmonic is possible where the second harmonic is not own mode of this system. The transverse profile of second harmonic is determined by second order of transverse profile of fundamental harmonic.

From relation (2) after integrating it on transverse coordinate z, the equation for slowly varying amplitude A_1 of first harmonic is derived. The equation for amplitude A_2 of second harmonic can be derived from following argument. From set of equations (1) the amplitude of second harmonic of surface wave can be expressed through fundamental one as $\varepsilon(2\omega)A_2 \sim A_1^2$. Near the resonance, it should be expanded $\varepsilon(2\omega) \approx \varepsilon(2\omega_0) + \varepsilon'(2\omega_0)\Delta\omega$ and then replaced $i\Delta\omega \to \partial/\partial t$.

sense, the equation for A_2 is derived under use of reductive perturbation

$$\frac{\partial A_1}{\partial t} + \frac{i\omega_{kk}}{2}\frac{\partial^2 A_1}{\partial x^2} + \alpha_{11}A_1^* A_2 + i\alpha_2 \mid A_1 \mid^2 A_1 + \Gamma_1 A_1 = 0;$$
$$i\omega_p \varepsilon(2\omega) A_2 - \alpha_{21}A_1^2 + \Gamma_2 A_2 = 0. \qquad (3)$$

$\partial\omega/\partial k$, $\omega_{kk}=\partial^2\omega/\partial k^2 < 0$, $\Gamma_{1,2}$ are dissipations for fundamental and second explicit expressions for positive coefficients α_{11}, α_{21}, α_2 are not presented because of complexity. Far from resonance ($\omega \neq \omega_p/2$), one can exclude A_2 from for the amplitude of fundamental harmonic A_1, the nonlinear Schroedinger tion (NSE) is obtained. Note that the nonlinearity coefficient is basically mined by input of surface nonlinearity. So, in the absence of retardation (at $\omega \approx \omega$ the input of surface nonlinearity is 3 times greater than one of volume nearity. Besides, the source of second harmonic that is due to nonlinearity of force and was omitted in [1] exists in the volume. In the vicinity of resonance, full set of equations (3) should be solved simultaneously. The possibility of gation of envelope solitons and existence of MI are of the greatest interest here. problems were treated numerically.

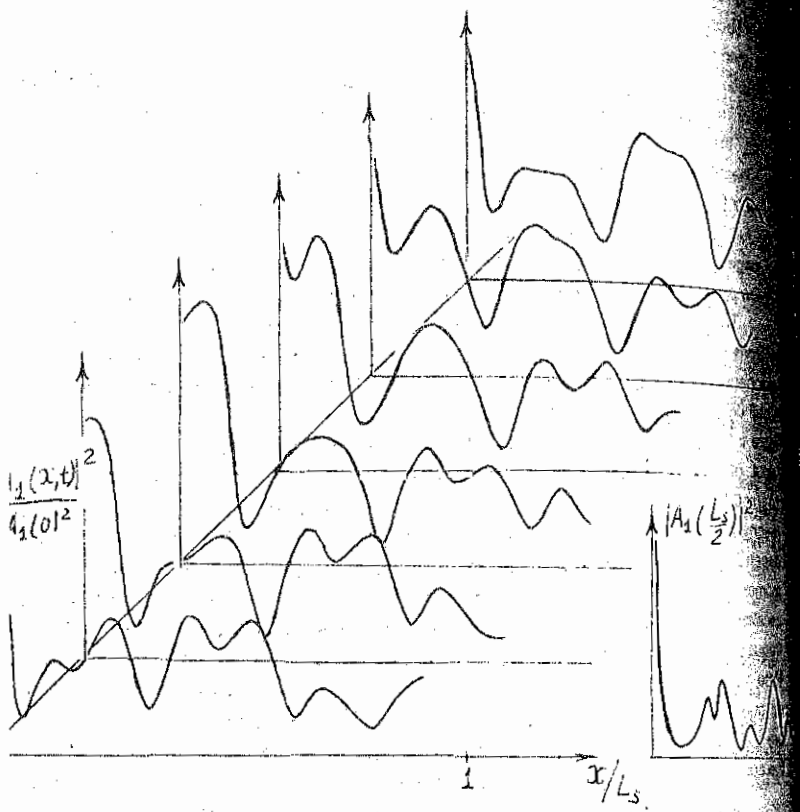
The results of numerical simulations of (3) show the next. The bright envelope ons of surface waves under pulse excitation can propagate in narrow vicinity of sonance $\omega \approx \omega_p/2$ under $\omega > \omega_p/2$, in the case of enough extensive wave packets and dissipation. These conditions are quite difficult for experimental realization. The interesting results are obtained for continuous regime of excitation when in the of system the constant amplitude of fundamental harmonic is maintained $A_1(x=0,t)=A_{10}$). MI of monochromatic surface wave is possible in the vicinity of sonance, namely, it is more expressed in the frequency region $\omega < \omega_p/2$. In Fig.1 the pendencies of amplitude of first harmonic on longitudinal coordinate for different time ments, and also its Fourier spectrum, are presented. One can see that here the self-illations of surface wave take place, they can be both regular and chaotic. In the quency region $\omega > \omega_p/2$, the dynamic regimes of wave propagation are not expressed. Note also that resonant pumping of second harmonic is also possible under taking into account purely volume nonlinearity (for example, when the surface properties of plasma quite different from volume one), then the structure of equations (3) is the same but coefficients under nonlinear terms have another values.

References.

1. Gradov O.M and Stenflo L.// Phys.Fluids. 1982. V.25 P.983.

2. Stenflo L., Yu M.Y., and Zhelyazkov I.. Beitr.Plasmaphys. 1983. V.23. P.62
3. Krall N. and Trivelpiece A. Principles of Plasma Physics. N.Y.: McCraw-H
1973.
4. Kondratenko A.N. Plasma Waveguides. Moscow: Atomizdat, 1976.
5. Taniuti T.// Progr. Theor. Phys. Suppl., 1974. No55. P.1.

Fig.1. The distribution of amplitude $|A_1(x)/A_1(x=0)|^2$ for sequential time mo
continuous regime of excitation at $\omega/\omega_p=0.48$. L_s is the length of interaction
the insertion the Fourier spectrum $|A_1(t)|^2$ at $x=L_s/2$ is presented.



Structures Near Marginal Stability Boundary in Tokamaks.

T.A. Davydova , A.Yu. Pankin

Institute for Nuclear Research, National Academy of Sciences of Ukraine,

pr. Nauki, 47, Kiev - 22, Ukraine

...tion of coherent long-lived large-scale structures of drift modes is often considered ... one of the main reason of transition to the regime of improved confinement in ... (L-H transition). Particularly the ion temperature gradient (ITG) driven modes were ...ently to dominate in some numerical simulations [2, 3]. The global linear structure of ...modes was investigated in toroidal magnetic field to obtain the characteristic correlation ...n of anomalous diffusion. A new type of extended toroidal ITG modes was recently ...ered [4, 5]. However as stressed in [5] "the precise connection between unstable linear ...and turbulence they produce is unclear". Significant difference between drift structures ...r and nonlinear simulations was noticed in [6]. Recent experiments also indicate that ...correlation length which determines the local transport is determined by nonlinear effects" ...A feature of drift turbulence is that density $n(r)$ and temperatures $T(r)$ profiles in a ...weak plasma often nearly satisfy conditions for marginal stability of strong reactive unstable ...ves [6]. Possibility of drift modes parametric exciting in shear and toroidal magnetic fields ...been found in [7, 8]. In [9] the nonlinear explosive instability was proposed as the driven ...anism for the subcritical turbulence. This instability near boundary of marginal stability is ...nearly modified [10]. Spatial-temporal evolution of this instability may be accomplished by ...formation of spatial nonuniform structures.

...this report we investigate the possibility of soliton formation in more detail. We show that ...resonantly interacting "zero energy" modes can form two kinds of envelope solitons ...ving with different velocities. We also show that nonlinear drift wave interaction in toroidal ...nuniform magnetic field can determine the characteristic scale of spatial wave structures.

...In this section we use a reactive slab fluid model [2] for description of nonlinear ITG modes ...olution. Near boundary of marginal stability the basic set of equations for amplitudes of three ...onantly interacting waves for which

$$\omega_{k_1} + \omega_{k_2} + \omega_{k_3} = 0, \quad \vec{k}_1 + \vec{k}_2 + \vec{k}_3 = 0 \tag{1}$$

...duces to the set of three equations [10]:

$$\hat{L}_i\Phi_i = V_{k_1k_jk_l}\Phi_j^*\Phi_l^*,\ i,l,j=1,2,3$$

where $\hat{L}_j = \left[\pm ik_{yj}\delta_j\left(\frac{\partial}{\partial t} - u_j\frac{\partial}{\partial y}\right) + \left(\frac{\partial}{\partial t} - u_j\frac{\partial}{\partial y}\right)^2 - \right.$

$$\left. 2ik_{yj}^2 a_j\left(k_{xj}\frac{\partial}{\partial x} + k_{yj}\frac{\partial}{\partial y}\right) - k_{yj}^2 a_k\left(\frac{\partial^2}{\partial x^2} + \frac{\partial^2}{\partial y^2}\right)\right]$$

Here normalization of all dimensionless quantities are the same as in [10]. Signs ± bef... first term in (3) correspond to two branches of linear η_i-modes:

$$\omega_j^{\pm} = \frac{1}{2}k_{yj}\left(1 - \frac{13}{3}\varepsilon_n\right) - \frac{3}{8}k_j^2(\varepsilon_n + \eta_i) \pm k_{yj}\delta_j$$

$$\varepsilon_n = \frac{d\ln B}{d\ln n},\ \eta_i = \frac{d\ln T}{d\ln n},\ u_j = \frac{\omega_j}{k_{yj}}$$

$$V_{k_1k_jk_l} = \left(\vec{k}_j \times \vec{k}_l\right)\cdot\vec{e}_i\left(k_j^2 - k_l^2\right)V,\ V = 2\varepsilon_n - \frac{2}{3} - \frac{\eta_i}{4},$$

$$\delta_j = 2\left[\varepsilon_n(\eta_{icr} - \eta_i)\right]^{1/2},$$

$$\eta_{icr} = \eta_{icr}^0 + k^2\left(2 - \frac{5}{18}\varepsilon_n - \frac{\eta_i}{2}\left(1 + \frac{1}{\varepsilon_n}\right)\right),\ \eta_{icr}^0 = \frac{1}{6} + \frac{49}{36}\varepsilon_n + ...$$

In (1) ω_j corresponds to one of two modes (4) which involves in resonant interaction ... boundary of marginal stability $\left(\eta_i \to \eta_{icr}^0\right)$, i.e. in the case

$$t_{nl}\left(\omega_j^+ - \omega_j^-\right) << 1$$

(where t_{nl} is the characteristic time of nonlinear interaction or "explosion" time) ... difference between two ITG branches is not essential. In the process of nonlinear interac... they are merging into "zero energy" modes. Temporal and spatial-temporal (for bound... condition imposed at fixed point)development of modified explosive instability of ITG mod... was described in [10] for equal and different signs of matrix elements $V_{k_1k_jk_l}$. It was sho... that after a time $t_{sat} = L/\min_{j=1,2,3} u_j$ in bounded region of length L steady state ... established if L is less than the explosive length for the corresponding "spatial" problem... was also shown that the system (2) in the case of equal signs of matrix elements adm... envelope soliton solution moving with constant velocity U in the direction of drift ... propagation of the form

$$\Phi_j = \Psi_j(\xi)\exp\left[i\left(s_jy + q_jx\right)\right],\ j=1,2,3$$

Ut; U, s_j, q_j are some constants and $\Psi_j(\xi)$ are localized functions of $(\xi - \xi_0)$. An expression for soliton velocity U was found approximately precise calculation of values of U shows that there exist two possible velocities of

$$\frac{\left(V_2 - V_3\right) + k_{y2}^3\left(V_1 - V_3\right) + k_{y3}^3\left(V_2 - V_1\right) \pm \sqrt{D}}{6k_{y1}k_{y2}k_{y3}},$$

$$u_j + a_j/u_j,$$

$$\left(V_2 - V_3\right) + k_{y2}^3\left(V_1 - V_3\right) + k_{y3}^3\left(V_2 - V_1\right)\Big]^2 +$$

$$k_{y2}^3\left(V_1 - V_2\right)\left(V_1 - V_3\right) > 0.$$

that the double nature of the "zero energy" mode which is formed from two linear manifests itself in the self-saturation process of spatial nonlinear structures

now we supposed that all background parameters of our model nonlinear system are In general case two-dimensional inhomogenity of magnetic tokamak field in particular importance for the formation of structure elements of turbulence. To show this we this section the standard model proposed in [4, 5] for description of toroidal ITG modes toroidal mode number in "strong ballooning representation" when spatial change of potential Φ in poloidal direction is more fast than in the radial one. In this case the equation was used for description of wave localization in poloidal direction in outer of the torus (see eq. (4) in [4] in the case θ_k=0):

$$\left[k\theta^2 + \lambda + V\Phi\right]\Phi = 0, \qquad (6)$$

$$\frac{\omega}{\omega_{t_i}^2\tau}\left[\frac{\omega^2 + \omega_{*i}\omega\tau}{\omega - \omega_{*i}\left(1 + \eta_i\right)} + k_\theta^2\rho_i^2\omega\tau - \omega_D\tau\right],$$

$$\frac{\omega\omega_D}{2\omega_{t_i}^2}\left(1 - 2s\right) + \frac{\omega^2}{\omega_{t_i}^2\tau}k_\theta^2\rho_i^2s^2,$$

$$\frac{2ck_\theta T_i}{eBR}, \ \omega_{t_i} = v_{t_i}/qR, \ \omega_{*i} = -\frac{ck_\theta T_i}{eBL_n},$$

$$\left(\frac{T_i}{m_i}\right)^{1/2}, \ \tau = \frac{T_e}{T_i}, \ \rho_i = \frac{V_{ti}}{\Omega_i}.$$

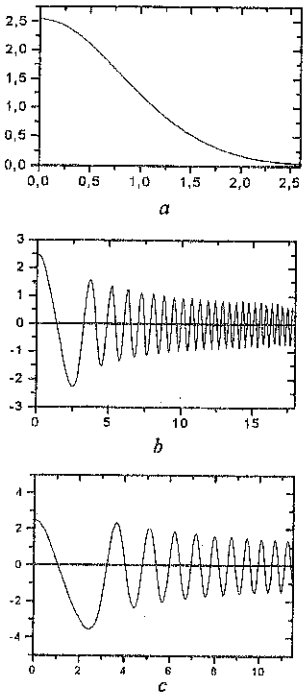


Fig. 1: Numerical solutions of Eq. (6): V=1; (a) κ=−1, λ=1; (b) κ=1, λ=1; (c) κ=1, λ=−1.

Here R is a large radius of the to... safety factor, s is a magnetic ... parameter. We have added to ... equation nonlinear term proportional to ... element V to describe qualitatively ... effects of mode coupling. Linear local ... relation $\lambda=0$ describes reactive instabili... condition

$$\omega_D\omega_{*i}(1+\eta_i) > \frac{\tau}{q}\left(\omega_{*i}-\omega_D\right)^2$$

Simple analysis [4, 5] show that well-lo... mode in θ-direction may exist only for n... κ and positive eigenvalues λ. In the ... positive κ eq. (5) was interpreted as de... extended modes escaping out of the poi... in both directions with imaginary eigenva... However nonlinear wave coupling ... essentially change this picture because co... admits stationary localized solutions both ... >0 and $\kappa<0$. Such solutions we have ... numerically (see Fig.1).

References

[1] Ottaviani M., Romanelly F., Benzi R., *Phys. Fl.* **B2** 67 (1990)

[2] Weiland J., *Current Topics in the Physics of Fluids* **1** 439 (1994)

[3] Connor I.W., *PPCF* **37** A119 (1995)

[4] Romanelly F., Zonca F., *Phys. Fl.* **B5** 4081 (1993)

[5] Taylor I.B., Wilson H.R., Connor I.W., *PPCF* **38** 243 (1996)

[6] Lee W.W et al. PCCNFR (IAEA, Vienna 1992), paper CN-56-D4-18.

[7] Davydova T.A., Jovanovic D., Vranjes I., Weiland J., *Phys. Scripta* **48** 603 (1993)

[8] Davydova T.A., Jovanovic D., Vranjec I., Weiland J., *Phys. Plasmas*, **1**, 809 (1994)

[9] Nordman H., Pavlenko V.P., Weiland J., *Phys. Fl.* **B5** 402 (1993)

[10] Davydova T.A., Pan'kin A.Yu., *Ukr. Fiz. Zhurn.* **40** 481 (1995)

...ce of small-scale fluctuations on coherent structures ...n ion-temperature-gradient-driven turbulence

V. M. Lashkin

Institute for Nuclear Research , 252022 , Kiev , Ukraine

...duction

...well known, the ion-temperature-gradient-driven drift wave turbulence (η_i - ...s an important mechanism for the anomalous cross-field ion thermal transport. ...linear theory of η_i modes ($\eta_i = d\ln T_i / d\ln n$) has been rather fully understood [1-6] ...for as well as toroidal geometries. At the same time, simulations [7] show that in ...stages of nonlinear evolution of the η_i modes large-scale coherent vortex structures ...emerge. Analytical localized solutions in the form of a travelling double vortex have ...been found in the shearless cases of absence of toroidal effects [8] and parallel ion motion ...(exact solutions) [9], in the case including the effects of shear and strictly two-dimensional ...($\partial/\partial z = 0$) (approximate solutions) [10], and, most fully (with the magnetic shear, ...finite ion Larmor radius effects and toroidicity) , in [11]. All such dipolelike ...structures are expected to be long-lived, and to develop as a result of a high level of ...fluctuations in the η_i turbulence.

...of this report is to give preliminary results about the interaction of the coherent ...structures with the surrounding small-scale η_i turbulence. An analogous problem was ...dealt in Ref. [12] considering the interaction of regular structures with weak drift-wave ...turbulence in the framework of the Hasegawa-Mima equation.

...Basic equations and results

...We start from the fluid model proposed in [5] governing electrostatic potential and ion ...temperature evolution. In this model electrons are assumed to be adiabatic and parallel ion ...motion are neglected. In this report we take for simplisity $T_e = T_i$. In the Fourier ...representation the basic set of equations ([5], (8a), (8b)) can be written in the form

$$L_{ij}(q)\Psi_j(q) = \int V_{ijl}\left(\vec{k}_1, \vec{k}_2\right)\Psi_j(q_1)\Psi_l(q_2)\delta(q - q_1 - q_2)\,dq_1\,dq_2 \quad , \qquad (1)$$

...where $q = \left(\vec{k}, \omega\right)$. $\Psi_1 = T(q)$, $\Psi_2 = \Phi(q)$ are Fourier components of ion temperature and ...electrostatic potential perturbations which are normalized as follows

$$T \to \frac{L_n}{\rho_i}\frac{\delta T_i}{T_i} \quad , \Phi \to \frac{L_n}{\rho_i}\frac{e\Phi}{T_e} \quad .$$

...Dimensionless time and space coordinate are ...introduced, $\vec{r} \to \vec{r} / \rho_i$, $\omega_* = c_s / L_n$, $\rho_i = c_s / \omega_{ci}$. Matrix elements $L_{ij}(q)$ are

$L_{11}(q) = -\omega + k_y A_k$, $L_{12} = k_y B_k$, $L_{21} = k_y C_k$, $L_{22} = -\omega + k_y D_k$, where we [illegible] notations

$$A_k = \frac{\varepsilon_n}{3}\left(7 - 2k^2\right), B_k = \frac{4}{3}\varepsilon_n\left(1 - k^2\right) - \eta_i + \frac{2}{3}\left(2 + \eta_i\right)k^2, C_k = \varepsilon_n\left(1 - k^2\right),$$

$D_k = 2C_k - \left[1 - \left(1 + \eta_i\right)k^2\right]/1 + k^2$, $\varepsilon_n = 2d\ln B / d\ln n$. Coupling coefficients V_{ijl} [illegible] are $V_{111} = V_{211} = 0$, $V_{112}\left(\vec{k}_1, \vec{k}_2\right) = \frac{i}{3}k_2^2\, \vec{z}\cdot\left(\vec{k}_1 \times \vec{k}_2\right)$, $V_{121}\left(\vec{k}_1, \vec{k}_2\right) = V_{[illegible]}$

$$V_{122} = 2\left(V_{112} + V_{121}\right) \quad , \quad V_{212}\left(\vec{k}_1, \vec{k}_2\right) = \frac{i}{2}k_2^2\frac{\vec{z}\cdot\left(\vec{k}_1 \times \vec{k}_2\right)}{\left[1 + \left(\vec{k}_1 + \vec{k}_2\right)^2\right]} \quad , \quad V_{221}\left(\vec{k}_1, \vec{k}_2\right) = V_{[illegible]}$$

$V_{222} = 2\left(V_{212} + V_{221}\right)$.

We separate $\Psi(q)$ into a regular $\Psi^R(q)$ and a turbulent $\Psi^T(q)$ component

$$\Psi_i(q) = \Psi_i^R(q) + \Psi_i^T(q) \,, \tag{2}$$

assuming $\left\langle \Psi_i^T(q) \right\rangle = 0$,where $\langle \ldots \rangle$ means ensemble averaging. Substituting (2) into [illegible] and averaging it in the usual manner one can obtain the following system of equations for Ψ_i^R and the turbulent field Ψ_i^T respectively

$$L_{ij}(q)\Psi_j^R(q) = \int V_{ijl}\left(\vec{k}_1, \vec{k}_2\right)\left[\Psi_j^R(q_1)\Psi_l^R(q_2) + \left\langle \Psi_j^T(q_1)\Psi_l^T(q_2)\right\rangle\right]\delta(q - q_1 - q_2)dq_1\, dq_2$$

$$L_{ij}(q)\Psi_j^T(q) = \int V_{ijl}\left(\vec{k}_1, \vec{k}_2\right)\left[\Psi_j^T(q_1)\Psi_l^T(q_2) - \left\langle \Psi_j^T(q_1)\Psi_l^T(q_2)\right\rangle\right]\delta(q - q_1 - q_2)dq_1\, dq_2$$

$$+2\int V_{ijl}\left(\vec{k}_1, \vec{k}_2\right)\Psi_j^R(q_1)\Psi_l^T(q_2)\,\delta(q - q_1 - q_2)dq_1\, dq_2 \,, \tag{4}$$

where we have used $V_{ijl}\left(\vec{k}_1, \vec{k}_2\right) = V_{ilj}\left(\vec{k}_2, \vec{k}_1\right)$. As one can see from (3) , the homogeneous turbulence (that is when the correlator in (3) is proportional to $\delta(q_1 + q_2)$) will not influence on the evolution of a regular structure. At the same time, as it follows from the last term on the right-hand side of (4), when the turbulence is initially homogeneous the regular structure will change it to become inhomogeneous. Then, in the presence of a regular structure the total turbulent field $\Psi_i^T(q)$ may be represented in the form

$$\Psi_i^T(q) = \Psi_i^{T(0)}(q) + \Psi_i^{T(R)}(q) \,, \tag{5}$$

where $\Psi^{T(0)}$ is the turbulent field in the absence of a regular structure and $\Psi^{T(R)}$ is the turbulence perturbation due to the structure existence. The latter is supposed to be small $\left\langle \left(\Psi_i^{T(R)}\right)^2 \right\rangle^{1/2} << \left\langle \left(\Psi_i^{T(0)}\right)^2 \right\rangle^{1/2}$ so that $\Psi_i^{T(R)}$ may be regarded as the linear responce of the turbulence to a regular structure. For the homogeneous turbulence we have

$$\left\langle \Psi_i^{T(0)}(q_1)\Psi_j^{T(0)}(q_2)\right\rangle = \left|\Psi\right|_{ij}^{2(0)}(q_1)\delta(q_1+q_2)\,, \qquad (6)$$

...inhomogeneous (total) one we introduce,following [12]

$$\left|\Psi\right|_{ij}^{2}(q,\vec{r},t) = \int \left\langle \Psi_i^{T}(q)\Psi_j^{T}(q_1)\right\rangle e^{-i(\omega+\omega_1)t+i(\vec{k}+\vec{k}_1)\vec{r}}\, d(\omega+\omega_1)\, d(\vec{k}+\vec{k}_1)\,. \qquad (7)$$

...(5) into (4) and restricting ourselves to terms linear in $\Psi_i^{T(R)}$ one can get

$$\ldots(q) = \int V_{ijl}(\vec{k}_1,\vec{k}_2)\left[\Psi_j^{T(0)}(q_1)\Psi_l^{T(0)}(q_2) - \left\langle \Psi_j^{T(0)}(q_1)\Psi_l^{T(0)}(q_2)\right\rangle\right]\delta(q-q_1-q_2)dq_1\,dq_2, \qquad (8)$$

$$\ldots(q) = 2\int V_{ijl}(\vec{k}_1,\vec{k}_2)\left[\Psi_j^{T(0)}(q_1)\Psi_l^{T(R)}(q_2) - \left\langle \Psi_j^{T(0)}(q_1)\Psi_l^{T(R)}(q_2)\right\rangle\right]\delta(q-q_1-q_2)dq_1\,dq_2 +$$

$$+2\int V_{ijl}(\vec{k}_1,\vec{k}_2)\Psi_j^{R}(q_1)\Psi_l^{T(0)}(q_2)\delta(q-q_1-q_2)dq_1\,dq_2\,. \qquad (9)$$

$$\tau^{R} << \tau^{T}\,, \qquad (10)$$

... is the characteristic time for local turbulent-spectra formation, τ^{R} is the ...ristic time for creation of inhomogeneity in turbulence due to presence of regular ..., the nonlinear terms for the turbulent fields in (9) can be neglected. Then, eq.(9) ...approximated by

$$L_{ij}(q)\Psi_j^{T(R)}(q) = 2\int V_{ijl}(\vec{k}_1,\vec{k}_2)\Psi_j^{R}(q_1)\Psi_l^{T(0)}(q_2)\delta(q-q_1-q_2)dq_1\,dq_2\,. \qquad (11)$$

...logy with (5) we write

$$\left|\Psi\right|_{ij}^{2}(q,\vec{r},t) = \left|\Psi\right|_{ij}^{2(0)}(q) + \left|\Psi\right|_{ij}^{2(R)}(q,\vec{r},t)\,, \qquad (12)$$

$$\ldots(q,\vec{r},t) = 2\int \left\langle \Psi_i^{T(0)}(q)\Psi_j^{T(R)}(q_1)\right\rangle e^{-i(\omega+\omega_1)t+i(\vec{k}+\vec{k}_1)\vec{r}}\, d(\omega+\omega_1)\, d(\vec{k}+\vec{k}_1)\,. \qquad (13)$$

...substituting (11) into (13),using (6) and carrying out the integrations one can obtain

$$\left|\Psi\right|_{ij}^{2(R)}(q,q_1) = G_{ijp}(q,q_1)\Psi_p^{R}(q_1)\,, \qquad (14)$$

$$\left|\Psi\right|_{ij}^{2(R)}(q,\vec{r},t) = \int \left|\Psi\right|_{ij}^{2(R)}(q,q_1)e^{-i\omega_1 t+i\vec{k}_1\vec{r}}\, dq_1\,, \qquad (15)$$

$$\ldots(q,q_1) = 2\left[\left|\Psi\right|_{il}^{2(0)}(q)L_{jm}^{-1}(q_1-q)V_{mpl}(\vec{k}_1,-\vec{k}) + \left|\Psi\right|_{lj}^{2(0)}(q_1-q)L_{im}^{-1}(q)V_{mpl}(\vec{k}_1,\vec{k}-\vec{k}_1)\right] \qquad (16)$$

...(16) the inverse matrix $L_{ij}^{-1}(q)$ has been introduced so that $L_{ij}^{-1}(q)L_{jm}(q) = \delta_{im}$. One ...show that $\left|\Psi\right|_{ij}^{2}(q,q_1) = \left\langle \Psi_i^{T}(q)\Psi_j^{T}(q_1-q)\right\rangle$ and we can use (14) to close the ...equation (3). One obtaines

$$\left[L_{ij}(q) - M_{ij}(q)\right]\Psi_j^{R}(q) = \int V_{ijp}(\vec{k}_1,\vec{k}_2)\Psi_j^{R}(q_1)\Psi_l^{R}(q_2)\delta(q-q_1-q_2)dq_1\,dq_2\,, \qquad (17)$$

$$M_{ij}(q) = \int V_{ijp}(\vec{k}_1,\vec{k}-\vec{k}_1)\delta_{jp}G_{jp}(q_1,q)dq_1\,. \qquad (18)$$

For the sake of simplicity we consider in this report the case when only $|\Psi|^{2(0)}_{22}$ ... $\langle \Phi^0 \Phi^0 \rangle \neq 0$). Then it turns out $M_{12} \neq 0$ and $M_{22} \neq 0$. Since the turbulence is ... be small-scale we put $q << q_1$ and under this assumption one can get

$$M_{22} \approx M_{12} = -\frac{16}{3}\int \left[\bar{z}\cdot\left(\bar{k}_1 \times \bar{k}\right)\right]^2 \left(\bar{k}_1 \cdot \bar{k}\right) k_1^2 |\Psi|^{2(0)}_{22}(q_1)\left[\frac{2}{3} L_{21}^{-1}(q_1) + \frac{k_1^2 L_{22}^{-1}(q_1)}{1+k_1^2}\right] dq_1 ...$$

Here we consider the case when linear η_i modes are stable so that $\eta < \eta^0_{ic}$, whe...

$\eta^0_{ic} = \frac{1}{6} + \frac{49}{36}\varepsilon_n + \frac{1}{4\varepsilon_n}$. Then, as one can see, $L^{-1}_{ij}(q)$ containes two poles con...

the two η_i modes $\omega^{\pm} = \frac{1}{2}k_y(A_k + D_k) \pm \frac{1}{2}k_y\sqrt{(A_k - D_k)^2 + 4B_kC_k}$. Taking int... the pole rule $\omega \to \omega + i0$ in (19) as a result we can conclude from (17) that for th... structure there is always the instability with the growth rate

$$\gamma = \frac{k_y}{2}\left|\mathrm{Im}\sqrt{(A_k - D_k)^2 + 4B_kC_k + M_{12}^2 + 2k_y(2C_k - A_k + D_k)M_{12}}\right| \quad (20)$$

3. Conclusion

In this report we have considered the stability of a large-scale coherent structure int... with small-scale η_i turbulence. We separated the total fields (ion temperatu... potential) into regular and turbulent parts and in the weak-turbulence limit clo... equation for the regular field. As a result it turns out that in the framewor... consideration there is always the so-called "self-organization" instability, i.e. the g... the regular structures due to η_i turbulent fluctuations.

References

1. Coppi B.,Rosenbluth M.N. and Sagdeev R.Z. , Phys. Fluids **10** , 582 (1967).
2. Horton W., Estes R.D. and Biskamp D. , Plasma Phys. **22** ,633 (1980).
3. Jarmen A.,Andersson P. and Weiland J. , Nucl. Fusion **27** ,941 (1987).
4. Andersson P. and Weiland J. ,Phys. Fluids **31** , 359 (1988).
5. Nordman H. and Weiland J. , Nucl. Fusion **29** , 251 (1989).
6. Hamaguchi S. and Horton W. , Plasma Phys. Contr. Fusion **34** , 203 (1992).
7. Hong B.G. and Horton W. , Phys. Fluids **B2** ,978 (1990).
8. Shukla P.K. , Phys. Scr. **36** , 500 (1987).
9. Shukla P.K. and Weiland J. , Phys. Lett. **A 136** ,59 (1989).
10. Hong B.G., Romanelli F. and Ottaviani M., Phys. Fluids **B3** , 615 (1991).
11. Horton W., Jovanovic D. and Rasmussen J. J. , Phys. Fluids **B4** , 3336 (1992).
12. Muhm A., Pukhov A., Spatschek K. and Tsytovich V. , Phys. Fluids **B4** , 336 (1992).

...nal Numerical Simulation of Propagation of the Finite ... Relativistic Electron Bunches (REB) in Tenuous and Dense Plasmas*

V.I. Karas', Ya.B. Fainberg,

...te of Physics and Technology, National Scientific Center, 310108 Ukraina,

V.D. Levchenko and Yu.S. Sigov,

...Keldysh Institute of Applied Mathematics, Moscow, 125047 Russia

Abstract

...simulation results on the wake-field excitation with the programmed finite ... REB in tenuous and dense plasmas are presented. The REB/background ... configuration is described by full set of 2D3V relativistic Vlasov equations for ...ma species and nonlinear Maxwell equations for self-consistent electromagnetic ... physical parameters in runs carried out are close to those used in laboratory ... at Kharkov IPT (Ya. Fainberg at all, 1994). The simulation points to the ... the reached value of electric field depends on charge distribution and choice of ... between bunches in programmed sequence.

...

...cle acceleration by means of charge density waves both in plasmas and in noncom... ...rge particle beams is the major trend in collective acceleration methods [1, 2]. The ... variable part can be made very high (up to n_e); consequently, the accelerating ... values on the order of $10^7 - 10^9 V/cm$. Chen et al. [4] suggested a modification of ...celeration method [1] consisting of the use of wave trains. Katsouleas [5] considered ...for different electron cluster profiles: a wedgelike one with a slow start growth and ...inal drop as well as a Gaussian-type distribution with different rise and fall rates. ...proof [5] that the use of such inhomogenious nonsymmetric clusters, instead of ...geneous-density ones, might ensure particle accelerating field E_{ac} values many times ...greater than the electric field stopping the cluster. The so-called transformation coef... $E_{ac} E_{st}^{-1} = \gamma_{ac}\gamma_b$ is equal to $T = 2\pi N - \pi N$, where N represents the number of ...ng along the cluster length. Excitation of nonlinear stationary waves in plasma by a ...periodically spaced electron bunches was studied in [6, 7], where the electric field of ...was shown to increase as γ rises in the case of plasma n_e and bunch n_b of comparable ... Nonlinear mode experiments on acceleration by means of wake fields emphasized the ...three-dimensional effects.

...are two distinct regimes where the plasma wake fields can provide large fields which ...of use in accelerator physics. If one utilizes an appropriate density plasma the short, ...beam can be used to drive large amplitude waves with high-gradient electric fields useful ...accelerating other particle bunches. On the other hand, the long, narrow beam can be ...focused by its self-magnetic field which are left unbalanced when the plasma response ...utilizes the beams space charge density.

...work is partly supported by the International Scientific Foundation, grant U27000 and Russian Foun... ...Fundamental Research, project no. 94-02-03688.

The wake field excitation was studied using 2D3V axially symmetric electro... COMPASS [10]. Previously, this code was used to simulate an induction accelera... ulated REB [12] and a single relativistic electron bunch or a sequence of such bun... [13]. Note that, as in experiments [7], the bunch initial transversal R_0 and lon... dimensions were smaller than c/ω_p at the REB density $n_b = \frac{1}{2}n_e$ (n_e is plasma d... computer simulation [13] showed the transversal dimension of a bunch, propagatin... to vary over a wide range.

This caused substantial changes in its density (more then order of magnitude) ... a change in the excited wake field. It is shown too that the amplitudes of long... transversal fields increase upon additional bunch injection. However these ampli... proportional to the number of injected bunches (as it should be in case of "rigid... For future experimental researches in the domain of intense microwave (wake) field... in plasmas and for use of these fields for charged particle acceleration it is expected ... a new electron accelerator being constructed at KhIPT. Its parameters are as follo... $W = 20MeV$; number of electrons per bunch $N \sim 10^{10}$; number of bunches from ... bunch repetition rate is $2797.16MHz$. The electron bunches will be injected into pl... following sizes: the length $L = 1m$ and the radius $R = 10cm$ (plasma density will b... within $n_e = 10^{10} - 10^{14}cm^{-3}$) with a minimum density longitudinal gradient. In our ... simulation we shall keep in mind these parameters.

Mathematical Model

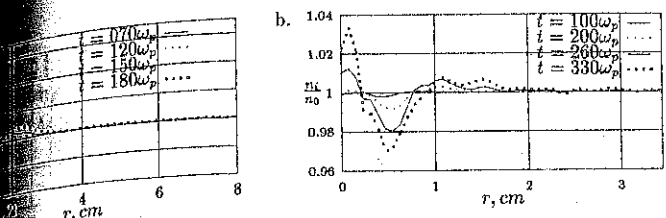
The REB dynamics is described by Vlasov relativistic equations (the Belyaev–Budker e... for the distribution function of each plasma specie and by the Maxwell equation s... consistent electric $\vec{E}$ and magnetic $\vec{B}$ fields. The two–component main plasma (m_i/m_e ... where m_i and m_e are the ion and electron mass respectively) is initially cold and fills co... the considered region $[0, L] \times [0, R]$. Usually, L and R are chosen to be $100cm$ a... respectively. A finite sequence of cold REB is injected in the plane $z = 0$ in accord... $n_b 0(R_0 - r)\theta(V_b t - z + (n-1)\lambda_p)\theta(z - V_b t + Z_0 + (n-1)\lambda_p)$.

Here n denotes the number of injected bunch. The beam velocity is $V_b = c\sqrt{1 - ...}$ the velocity of light; the initial bunch sizes $L_0 \times R_0$ were equal to $0.4cm \times 0.5cm$; λ_p ... ω_p is the Langmuir plasma frequency; and n_b is the REB average density. The quantity ... served as a scale for electric and magnetic fields. Bunches and plasma components can ... considered region through two boundary surfaces: $z = 0$ and $z = Z$. The plasma co... can also reenter the region. On the inner boundary the following conditions exist: ... surface at $r = R$ and open for electromagnetic wave radiation face and rear butt-end ... Explicit scheme were used in calculations.

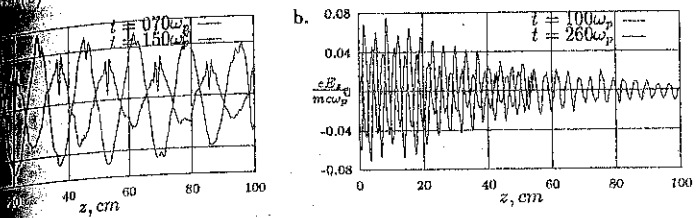
Four runs were considered to study the dependence of the exited fields: upon the ... N of bunches injected into plasma; on the density ratio of bunch and plasma; on the ... repetition rate; on the ratio of the bunch size R_0 and skin–depth c/ω_p. The parameters of ... runs are listed in the table:

run id		Var1	Var2	Var3	Var4
bunch density	n_b, cm^{-3}	$2 \cdot 10^{10}$	$2 \cdot 10^{10}$	$4.86 \cdot 10^{10}$	$4.86 \cdot 10^{10}$
plasma density	n_e, cm^{-3}	$4 \cdot 10^{10}$	$4 \cdot 10^{11}$	$9.72 \cdot 10^{10}$	$8.75 \cdot 10^{11}$
plasma frequency	ω_p, c^{-1}	$1.13 \cdot 10^{10}$	$3.57 \cdot 10^{10}$	$1.76 \cdot 10^{10}$	$5.27 \cdot 10^{10}$
skin–depth	$c/\omega_p, cm$	2.66	0.84	1.71	0.57
particles per bunch	N	$6.28 \cdot 10^9$	$6.28 \cdot 10^9$	$1.53 \cdot 10^{10}$	$1.53 \cdot 10^{10}$

The weight of model particles was assumed to be a function of their radial position...



dence of the ion density n_i upon the radial coordinate r ($z = 10.cm$) for Var1



Dependence of the longitudinal electric field E_z on z ($r = R_0 = 0.5cm$) for Var1(a)

assumed to have smaller numbers of particles in the less disturbed region distant The total number of macro particles was about 10^6. Note that all the calculations out using a PC/Pentium–66 computer and a high-speed particle–in–cell technique.

puter simulation showed the transversal dimension of the bunch, propagating in plasma, over a wide range at the conditions $R_0 < c/\omega_p$ and $L_0 < c/\omega_p$. Contrary to popular ation (with $L_0 \gg c/\omega_p > R_0$ or $R_0 \gg c/\omega_p > L_0$) we considered the conditions $L_0 \sim$ or $L_0 \sim R_0 \sim c/\omega_p$, which is corresponding to the experimental situation [14]. In significant nonlinearities in both plasma and beam behavior have been observed. As ll see subsequently in our simulation the ion motion plays significant role in the REB ation in the plasmas. The dependence of the ion density n_i upon the radial coordinate r ted in Fig.1 a,b. One can see that ions form the plasma channel due to their transversal on in self-consistent fields. The channel parameters are determined by density ratio of and plasma, and by size ratio of bunch radial size R_0 and skin–depth c/ω_p.

patial distribution of the longitudinal E_z and radial E_r electric field is presented on and 3 a,b. One can see that amplitudes of E_z and E_r increase with injection of each bunch. However, these amplitudes are not proportional to the number of injected this should be in the case of "rigid" bunches. This is due to transversal oscillations of particles in self-consistent fields caused by the lack of charge and current compensation. shape of bunches are presented in Fig. 4. One can see that the envelope shape in to Bennet equilibrium case. However the REB expansion is appreciably retarded by ation of the plasma channel with the ion radial motion. The conduct consideration of ee–dimensional nonlinear bunch–plasma behavior is useful for better understanding of

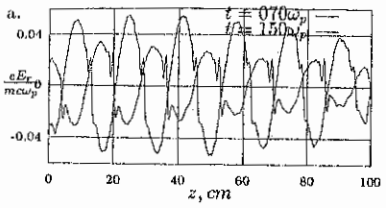


Figure 3: Dependence of the radial electric field E_r on z ($r = R_0 = 0.5$cm) fo
Var4(b)

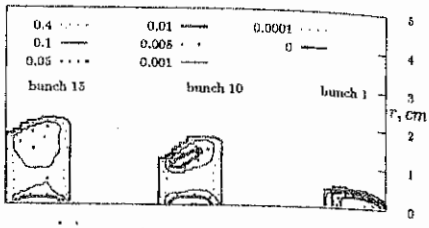


Figure 4: Var1: Density cross-section of bunches (number 1,10 and 15) at momen
over $z = 60$.

fundamental physics of the plasma wake–field acceleration and focusing.

References

[1] Y. B. Fainberg, *Proc. Symp. CERN* (1956), Vol. 1, p. 84.

[2] Y. B. Fainberg, Sov. J. Plasma Physics **13**, 350 (1987).

[3] Y. B. Fainberg, Plas. Phys. Rep. **20**, 549 (1994).

[4] P. Chen, J. M. Dawson, R. W. Huff, and T. Katsouleas, Phys. Rev. Lett. **54**, 69

[5] T. Katsouleas, Phys. Rev. A **33**, 2056 (1986).

[6] A. T. Amatuni *et al.*, Sov. J. Plasma Physics **11**, 417 (1985).

[7] J. B. Rosenzweig, *FERMILAB Conf. 90/40* (FNAL, Batavia, Illinois, 1990).

[8] J. B. Rosenzweig *et al.*, Phys. Rev. A **44**, 6189 (1991).

[9] N. Barov and J. B. Rosenzweig, Phys. Rev. E **44**, 4407 (1994).

[10] O. Batishchev, V. Karas', V. Levchenko, and Y. Sigov, Plas. Phys. Rep. **20**, 587 (19

[11] V. I. Karas' *et al.*, Journal of Particle Accelerators **37-38**, 281 (1992).

[12] O. V. Batishchev *et al.*, Sov. J. Plasma Physics **19**, 738 (1993).

[13] O. Batishchev, V. Karas', Y. Sigov, and Y. Fainberg, Plas. Phys. Rep. **20**, 583 (199

[14] N. Aizatskii *et al.*, Plas. Phys. Rep. **20**, 603 (1994).

...ations and Collective Wave Scattering in Collisional Plasma

A.G.SITENKO and S.M.ZINEVYCH
Bogolyubov Institute for Theoretical Physics
252143 Kiev, Ukraine

...ct. A kinetic theory treatment of plasma fluctuations is presented in which ...binary collisions are taken into account. A general expression for the correla... of random forces is found by applying the fluctuation–dissipation theorem. ...between fluctuations in a non–collisional plasma and fluctuations in hydro... studied. It is shown that binary collisions appreciably affect wave scattering

...**duction.** Electromagnetic wave scattering is successfully used as a method ...diagnostic both under laboratory conditions and in space plasmas. A pe... of electromagnetic wave scattering in plasmas is that coherent scattering by ...plasma excitations occurs along with Thomson incoherent scattering by indi... plasma particles. The coefficient of electromagnetic wave scattering in a plasma, ...to the transport coefficient, is determined by the spectral distributions of fluc... in density, macroscopic particle velocities, and magnetic field. In this paper ...sider the effect of pair collisions on plasma fluctuations.

...plasma fluctuations have been studied in detail in limiting cases of low and high ...of binary collision frequency. In the first case the plasma is usually described ...ems of a kinetic equation in which the binary collision integral is neglected. In ...cond case the plasma properties are described by the hydrodynamic equations. A ...difficulty in taking account of the effect of binary collisions on the electrodynamic ...erties of a plasma lies in the complexity of the solution of the kinetic equation ...the correct collision integral is used. Plasma fluctuations for arbitrary values of ...dimensionless binary collision frequency have been considered earlier in [1] by using the ...etic equation with a model collision integral. It was shown that particle collisions ...ticeably affect the collective fluctuations in plasmas.

...kinetic fluctuations in collisional plasma. We analyse plasma fluctuations ...regard for the Coulomb binary particle collisions. The Coulomb binary collisions ...described within the framework of the kinetic equation through the use of the ...ulon collision integral. Denoting the different kinds of charged particles by α and ... we can write the linearized collision integral in the form

$$\left[\frac{\partial f_\alpha}{\partial t}\right] = \frac{2\pi e_\alpha^2}{m_\alpha}\ln\Lambda \sum_\beta e_\beta^2 \frac{\partial}{\partial v_i}\int \mathrm{d}\mathbf{v}' \frac{u^2\delta_{ij} - u_i u_j}{u^3}$$

$$\times \left\{ \frac{1}{m_\alpha} f'_{\beta 0}\frac{\partial \delta f_\alpha}{\partial v_j} - \frac{1}{m_\beta} f_{\alpha 0}\frac{\partial \delta f'_\beta}{\partial v'_j} + v_j\left[\frac{1}{T_\beta} f'_{\beta 0}\delta f_\alpha - \frac{1}{T_\alpha} f_{\alpha 0}\delta f'_\beta\right]\right\}. \qquad (1)$$

...here $f_\alpha \equiv f_\alpha(\mathbf{v})$ and $f'_\beta \equiv f_\beta(\mathbf{v}')$ are the distribution functions of the particles α ...nd β, $\delta f_\alpha = f_\alpha - f_{\alpha 0}$, $|\delta f_\alpha| \ll f_{\alpha 0}$, $\mathbf{u} = \mathbf{v} - \mathbf{v}'$ is the relative velocity and $\ln\Lambda$ is

the Coulomb logarithm. Involving Fluctuation into consideration requires random Langevin sources to the collision term in the kinetic equation.

The fluctuations in the collisional plasma are studied by means of the fl dissipation theorem; on the right side of the kinetic equation which dete particle distribution function f_α we introduce a random force y_α:

$$\frac{\partial f_\alpha}{\partial t} + \mathbf{v}\frac{\partial f_\alpha}{\partial \mathbf{r}} + \frac{e_\alpha}{m_\alpha}\mathbf{E}\frac{\partial f_\alpha}{\partial \mathbf{v}} = \left[\frac{\partial f_\alpha}{\partial t}\right] + y_\alpha.$$

The kinetic equations are supplemented by the Maxwell equations for electr field.

Having taken as the generalized thermodynamic velocity $\dot{x}_\alpha$ the function

$$\dot{x}_\alpha = \left[\frac{\partial f_\alpha}{\partial t}\right] + y_\alpha,$$

we find the corresponding generalized thermodynamic force X_α from the rela

$$X_\alpha = -\frac{\partial \dot{S}}{\partial \dot{x}_\alpha},$$

where $\dot{S}$ is the time derivative of the entropy of the system

$$\dot{S} = -\sum_\alpha \int \mathrm{d}\mathbf{v}\mathrm{d}\mathbf{r}\left\{\left[\frac{\partial f_\alpha}{\partial t}\right] + y_\alpha\right\}\ln f_\alpha.$$

Due to the large difference in mass between the electrons and ions the exch energy between particles of the same kind occurs much faster than the exc energy between particles of different kinds. Therefore, the state of the plasm different electron and ion temperatures is quasi-equilibrium.

We limit ourselves to fluctuations close to thermodynamic equilibrium and that the deviations of quantities from their equilibrium values are small. Th derivative of the entropy is a bilinear expression in the thermodynamic veloci for the quasi-equilibrium state. Therefore the thermodynamic velocities $\dot{x}_\alpha$ a functions of the thermodynamic forces $X_\beta = \frac{\delta f_\beta}{f_{\beta 0}}$:

$$\dot{x}_\alpha = -\sum_\beta \int \mathrm{d}\mathbf{v}'\gamma_{\alpha\beta}(\mathbf{v},\mathbf{v}')X_\beta(\mathbf{v}') + y_\alpha.$$

Using (1) and (5) we find

$$\begin{aligned}\gamma_{\alpha\beta}(\mathbf{v},\mathbf{v}') = &-\frac{2\pi e_\alpha^2 \ln\Lambda}{m_\alpha^2}\delta_{\alpha\beta}\delta(\mathbf{v}-\mathbf{v}')\left[\frac{\partial}{\partial v_i}\left(f_{\alpha 0}B_{ij}\right)\frac{\partial}{\partial v_j'} + f_{\alpha 0}B_{ij}\frac{\partial^2}{\partial v_i'\partial v_j'}\right]\\ &+\frac{2\pi e_\alpha^2 e_\beta^2 \ln\Lambda}{m_\alpha m_\beta}f'_{\beta 0}\frac{\partial}{\partial v_i}\left[f_{\alpha 0}\frac{u^2\delta_{ij}-u_iu_j}{u^3}\right]\frac{\partial}{\partial v_j'}\\ &+\frac{2\pi e_\alpha^2 \ln\Lambda}{m_\alpha}\left(\frac{1}{T_\alpha}-\frac{1}{T_\beta}\right)\left\{\delta_{\alpha\beta}\delta(\mathbf{v}-\mathbf{v}')\left[\frac{\partial}{\partial v_i}\left(v_jf_{\alpha 0}B_{ij}\right) + v_jB_{ij}f_{\alpha 0}\frac{\partial}{\partial v_i'}\right]\right.\\ &\left.+e_\beta^2 f'_{\beta 0}\frac{\partial}{\partial v_i}\left[v_jf_{\alpha 0}\frac{u^2\delta_{ij}-u_iu_j}{u^3}\right]\right\},\end{aligned}$$

$$\ldots = \sum_{\gamma} e_{\gamma}^2 \int \mathrm{d}\mathbf{v}' \frac{u^2\delta_{ij} - u_i u_j}{u^3} f'_{\gamma 0}.$$

... kinetic coefficient $\gamma_{\alpha\beta}(\mathbf{v}, \mathbf{v}')$ in the relation (6) directly determines the ... function for the random forces

$$\ldots(t)\ldots_{\beta}(\mathbf{r}', \mathbf{v}', t') >= \delta(\mathbf{r} - \mathbf{r}')\delta(t - t') \left[\gamma_{\alpha\beta}(\mathbf{v}, \mathbf{v}') + \gamma_{\beta\alpha}(\mathbf{v}', \mathbf{v})\right]. \tag{8}$$

... distribution of the correlation function for the random forces is then given ... ression

$$\ldots_{\beta}(\mathbf{v}') >_{\mathrm{k},\omega} = \gamma_{\alpha\beta}(\mathbf{v}, \mathbf{v}') + \gamma_{\beta\alpha}(\mathbf{v}', \mathbf{v}). \tag{9}$$

... kinetic equation (2) and the Maxwell equations the fluctuations deviation of ... bution function and the consequent fluctuations in density and temperature ... can be expressed in terms of the random forces, we can then carry out ... over the random forces by means of (9).

... **fluctuations in fluid approach.** Now, let us consider the plasma ... the fluid approximation. The fluid approach to the description of plasma ... is applicable if the mean time interval between the binary collisions is much ... the characteristic times of macroscopic processes, and the mean free path ... ller than the characteristic distances for which the macroscopic quantities ... considerably. In order to derive hydrodynamic equations from the kinetic ... for each plasma component, we employ the Grad approach [2]. We assume ... on and ion distribution functions to be given by

$$\ldots_{\alpha} \left(\frac{m_{\alpha}}{2\pi T_{\alpha}}\right)^{3/2} \exp\left[-\frac{m_{\alpha}\left(\mathbf{v} - \mathbf{u}_{\alpha}\right)^2}{2T_{\alpha}}\right] \tag{10}$$

$$\left\{1 - \frac{\sigma_{ij}^{\alpha} m_{\alpha}}{2n_{\alpha}T_{\alpha}^2}(\mathbf{v} - \mathbf{u}_{\alpha})_i(\mathbf{v} - \mathbf{u}_{\alpha})_j - \frac{m_{\alpha}\mathbf{q}_{\alpha}\left(\mathbf{v} - \mathbf{u}_{\alpha}\right)}{n_{\alpha}T_{\alpha}^2}\left(1 - \frac{m_{\alpha}\left(\mathbf{v} - \mathbf{u}_{\alpha}\right)^2}{5T_{\alpha}}\right)\right\},$$

... $T_{\alpha}, \sigma_{ij}^{\alpha}$, and $\mathbf{q}_{\alpha}$ are, respectively, the particle number density, mean macro- ... velocity, temperature, viscous stress tensor, and electron or ion thermal flux. ... (10) in the kinetic equations with the Coulomb collision terms (2) and ... the relevant moments yields a set of hydrodynamic equations for the elec- ... ion plasma components, i.e.,

$$\ldots + \mathrm{div}(n_{\alpha}\mathbf{u}_{\alpha}) = 0, \tag{11}$$

$$\ldots \frac{\mathrm{d}_{\alpha}\mathbf{u}_{\alpha}}{\mathrm{d}t} + \frac{\partial p_{\alpha}}{\partial \mathbf{r}} - \frac{\partial \hat{\sigma}_{\alpha}}{\partial \mathbf{r}} \pm e n_{\alpha}\mathbf{E} = \mp \frac{m_e n_e}{\tau_{ei}}\left(\mathbf{u} - \frac{3}{5}\frac{\mathbf{q}_e}{n_e T_e}\right) + \mathbf{F}_{\alpha}, \tag{12}$$

$$\ldots + p_{\alpha}\mathrm{div}\mathbf{u}_{\alpha} + \mathrm{div}\mathbf{q}_{\alpha} - \sigma_{kl}^{\alpha}\frac{\partial u_k^{\alpha}}{\partial r_l} = \frac{1}{2}\mathcal{P}_{ii}^{\alpha}, \tag{13}$$

$$\sigma_{ij}^{\alpha} = \eta_{\alpha}\left(\frac{\partial u_i^{\alpha}}{\partial r_j} + \frac{\partial u_j^{\alpha}}{\partial r_i} - \frac{2}{3}\delta_{ij}\mathrm{div}\,\mathbf{u}_{\alpha}\right) + \frac{\eta_{\alpha}}{p_{\alpha}}\left(\frac{1}{3}\delta_{ij}\mathcal{P}_{kk}^{\alpha} - \mathcal{P}_{ij}^{\alpha}\right),\ \alpha = e, i,$$

$$\begin{cases} \mathbf{q}_e = -\kappa_e \nabla T_e + 0.804 n_e T_e \mathbf{u} + 0.536\tau_{ei}\left(\mathbf{Q}^e - \frac{5}{2}\frac{T_e}{m_e}\mathbf{F}^e\right) \\ \mathbf{q}_i = -\kappa_i \nabla T_i + 3.536\tau_{ei}\left(T_i/T_e\right)^{3/2}\sqrt{m_i/m_e}\left(\mathbf{Q}^i - \frac{5}{2}\frac{T_i}{m_i}\mathbf{F}^i\right), \end{cases}$$

In the latter, the following notation has been introduced:

$$\tau_{ei} = \frac{3}{4}\frac{\sqrt{m_e}T_e^{3/2}}{\sqrt{2\pi}e^4 n_i \ln\Lambda},\ p_{\alpha} = n_{\alpha}T_{\alpha},$$

$$\eta_e = 0.488 n_e T_e \tau_{ei},\ \eta_i = 1.179\left(\frac{T_i}{T_e}\right)^{3/2}\sqrt{\frac{m_i}{m_e}}n_i T_i \tau_{ei},$$

$$\kappa_e = 1.340\frac{n_e T_e \tau_{ei}}{m_e},\ \kappa_i = 8.839\left(\frac{T_i}{T_e}\right)^{3/2}\frac{n_i T_i \tau_{ei}}{\sqrt{m_i m_e}},$$

The equations obtained describe the plasma in the two-fluid approximation. Wh... riving (14) and (15), we employed the applicability conditions for the fluid appro... tion and disregarded the derivatives of the quantities $\hat{\sigma}, \mathbf{q}$, and of the relative ... $\mathbf{u} = \mathbf{u}_e - \mathbf{u}_i$. Moreover, we bore in mind that $m_i \gg m_e$. The Langevin sour... (11)—(15) are determined by

$$\mathbf{F}^{\alpha} = m_{\alpha}\int(\mathbf{v} - \mathbf{u}_{\alpha})y_{\alpha}(\mathbf{r}, \mathbf{v}, t)\mathrm{d}\mathbf{v},$$

$$\mathcal{P}_{ij}^{\alpha} = m_{\alpha}\int(\mathbf{v} - \mathbf{u}_{\alpha})_i(\mathbf{v} - \mathbf{u}_{\alpha})_j y_{\alpha}(\mathbf{r}, \mathbf{v}, t)\mathrm{d}\mathbf{v},$$

$$\mathbf{Q}^{\alpha} = \frac{1}{2}m_{\alpha}\int(\mathbf{v} - \mathbf{u}_{\alpha})(\mathbf{v} - \mathbf{u}_{\alpha})^2 y_{\alpha}(\mathbf{r}, \mathbf{v}, t)\mathrm{d}\mathbf{v}.$$

The correlation function for these sources are determined by the relevant integra... (9). It should be noted that

$$< (\mathbf{F}_e + \mathbf{F}_i)(\mathbf{F}_e + \mathbf{F}_i) >= 0,\ < (\mathcal{P}_{ii}^e + \mathcal{P}_{ii}^i)(\mathcal{P}_{jj}^e + \mathcal{P}_{jj}^i) >= 0.$$

The set of equations becomes much simpler in the one- fluid approximation. ... $T_e \approx T_i = T$, when the mass velocity is close to the ion velocity, $\mathbf{V} \approx \mathbf{u}_i$, the generali... Ohm law takes the form

$$\mathbf{j} = \sigma\mathbf{E} + \frac{\sigma}{2en}\nabla p - \frac{3}{5}\frac{e}{T}\mathbf{q} + \mathbf{f},\ \ \mathbf{f} = -e\tau_{ei}\int(\mathbf{v} - \mathbf{u}_e)y_e(\mathbf{r}, \mathbf{v}, t)\mathrm{d}\mathbf{v},\ \sigma = \frac{e^2\tau_{ei}}{m_e}. \quad (2)$$

Substituting the explicit expression for $\gamma_{\alpha\beta}(\mathbf{v}, \mathbf{v}')$, one obtains the correlation fu... tions for the Langevin sources to be given by (9). Contribution of binary collisions ... considerable when one considers the spectra of collective wave scattering.

References

[1] А.Г.Ситенко, А.А.Гурин, ЖЭТФ **49**, 1591 (1965);
[2] А.Ю.Кирий, В.П.Силин, ЖТФ **39**, 773 (1969);
[3] Л.Д.Ландау, Е.М.Лифшиц, ЖЭТФ **32**, 618 (1957).

Diffusion Influence on the Electron Density Fluctuations in Turbulent Magnetoactive Plasmas

I.F.Goutych, A.G.Sitenko, A.G.Zagorodny

Bogolyubov Institute for Theoretical Physics, 252143 Kiev, Ukraine

P.Schram

Eindhoven University of Technology, P.O. BOX 513, 560 MB Eindhoven, The Netherlands

Introduction

...ative new phenomenological approaches to the description of turbulent plasma ...tions have been intensively developed [1-4]. Within these approaches ...ation spectra are calculated in the same manner as in the case of stable stationary ...s with dielectric response functions and correlation functions of the Langevin ...ess averaged over the ensemble of large-scale turbulent motions. In this paper ...apply the phenomenological description to the study of turbulent diffusion influence ...ge fluctuations in magnetoactive plasmas.

Basic equations

...us consider a plasma with macroscopic random motion of volume elements. ...tistical properties of the ensemble of large-scale perturbations are assumed to be ...own.

...anging the equation for the microscopic phase density $\mathcal{F}(x,t)=\sum_{i=1}^{N}\delta(x-x_i(t))$ over the physically infinitesimal volume v_{ph}, which is much ...aller than the volume of large-scale perturbation v_T, one obtains

$$\left\{\frac{\partial}{\partial t}+\vec{v}\frac{\partial}{\partial \vec{r}}+\frac{1}{m}\left(\vec{F}^{ext}+\vec{\tilde{F}}\right)\frac{\partial}{\partial \vec{v}}\right\}\hat{\mathcal{F}}(x,t)=\left(\frac{\partial \tilde{\mathcal{F}}}{\partial t}\right)_B$$

...here $x\equiv(\vec{r},\vec{v})$, $\tilde{\mathcal{F}}(x,t)$ and $\vec{\tilde{F}}$ are the microscopic phase density and the intrinsic ...ronic force averaged over v_{ph}, $\left(\frac{\partial \tilde{\mathcal{F}}}{\partial t}\right)_T$ is the change of phase density per unit ...me under the action of the fluctuation force $\vec{\tilde{F}}=\vec{F}^{int}-\vec{F}$.

We assume that in the case under consideration, this random force gives rise to the relaxation of $\tilde{\mathcal{F}}(x,t)$ towards its value averaged over the large-scale perturbation ...olume [5]

$$\left(\frac{\partial \tilde{\mathcal{F}}}{\partial t}\right)_T=-\frac{1}{\tau_T}\left\{\tilde{\mathcal{F}}(x,t)-\frac{1}{v_T}\int_{v_T}d\vec{r}'P_{\tau_T}(\vec{r},\vec{r}')\,\tilde{\mathcal{F}}(\vec{r}',\vec{v},t)\right\},$$

...here τ_T is the relaxation time of turbulent perturbations, $P_{\tau_T}(\vec{r},\vec{r}')$ is the smoothening ...unction. For the Gausslan distribution

$$P_\tau(\vec{r}, \vec{r}') = \frac{1}{(2\pi)^{3/2} v_T} e - \frac{(\vec{r} - \vec{r}' - \vec{u}\tau)}{2v_T^{2/3}},$$

we have

$$\left(\frac{\partial \tilde{\mathcal{F}}}{\partial t}\right)_T = \frac{\partial}{\partial \vec{r}}\left[D \frac{\partial \tilde{\mathcal{F}}}{\partial \vec{r}} - \vec{u}\tilde{\mathcal{F}}(x, t)\right],$$

where

$$D = \frac{1}{2\tau_T} \int d\Delta\vec{r} (\Delta\vec{r})^2 P_{\tau_T}(\Delta\vec{r}) \quad \text{and} \quad \vec{u} = \frac{1}{\tau_T} \int d\Delta\vec{r} \Delta\vec{r} P_{\tau_T}(\Delta\vec{r})$$

are the turbulent diffusion coefficient and the drift velocity of the turbulent v... element. Obviously, in the case under consideration $\vec{u}$ should be treated as a ra... quantity.

Thus,

$$\left(\frac{\partial}{\partial t} + \vec{v}\frac{\partial}{\partial \vec{r}} + \vec{u}\frac{\partial}{\partial \vec{r}} - D\frac{\partial^2}{\partial \vec{r}^2} + \frac{1}{m}(\vec{F}^{ext} + \tilde{\vec{F}})\frac{\partial}{\partial \vec{v}}\right)\tilde{\mathcal{F}}(x, t) = 0.$$

In the polarization approximation, Eq.(4) generates an equation for fluctua...

$$\left\{\frac{\partial}{\partial t} + \vec{v}\frac{\partial}{\partial \vec{r}} + \vec{u}\frac{\partial}{\partial \vec{r}} - D\frac{\partial^2}{\partial \vec{r}^2} + \frac{1}{m}\vec{F}^{ext}\frac{\partial}{\partial \vec{v}}\right\}\delta f(x, t) = -\frac{e}{m}\delta\vec{E}(\vec{r}, t)\frac{\partial f(\vec{v})}{\partial \vec{v}},$$

where $f(\vec{v})$ is the distribution function.

The formal solution of Eq.(5) is given by

$$\delta f(x, t) = \delta f^{(0)}(x, t) - \frac{e_\tau}{m_\tau}\int_{-\infty}^{\infty} dt' \int dx' W(x, x', t - t')\,\delta\vec{E}(\vec{r}', t')\frac{\partial f}{\partial \vec{v}}(\vec{v}),$$

where $\delta f^{(0)}(x, t)$ is fluctuation in the system without self-consistent electric interac...
The correlation function of these fluctuations is described by

$$\langle \delta f^{(0)}(x, t)\,\delta f^{(0)}(x', t')\rangle = f(x', t')\,W(x, x', t - t') + f(x, t)\,W(x', x; t' - t),$$

$W(x, x', t - t')$ is the Green function satisfying the equation

$$\left\{\frac{\partial}{\partial t} + \vec{v}\frac{\partial}{\partial \vec{r}} + \vec{u}\frac{\partial}{\partial \vec{r}} - D\frac{\partial^2}{\partial \vec{r}^2} - \frac{1}{m}\vec{F}^{ext}\frac{\partial}{\partial \vec{v}}\right\} W(x, x', t - t') = \delta(t - t')\,\delta(x - x')$$

supplemented by the boundary condition $W(x, x', t - t') = |_{t<t'} = 0$.

3. Electron Density Fluctuations

Eqs. (7)-(8) make it possible to calculate fluctuation spectra for the given turbulent ensemble realization. Thus, turbulent plasma fluctuation spectra can be obtained by averaging the appropriate correlation functions over the random quantity $\vec{u}$.

Neglecting statistical dependence of the dielectric response functions on the Langevin sources, we obtain the electron structure factor in the magnetoactive plasma to be given by

$$\langle \delta n_e^2\rangle_{\vec{k}\omega} = \left|\frac{1 + \tilde{\chi}_i(k, \omega)}{\tilde{\varepsilon}(k, \omega)}\right|^2 \langle \delta n_e^2\rangle_{\vec{k}\omega}^{(0)} + Z_i^2 \left|\frac{\tilde{\chi}_e(\vec{k}, \omega)}{\tilde{\varepsilon}(\vec{k}, \omega)}\right|^2 \langle \delta n_i^2\rangle_{\vec{k}\omega}^{(0)},$$

where

$$\varepsilon(k, \omega) = 1 + \chi_i(k, \omega) + \chi_e(k, \omega)$$

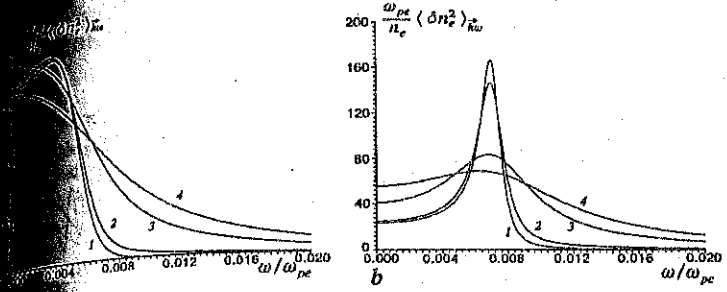


Fig.1

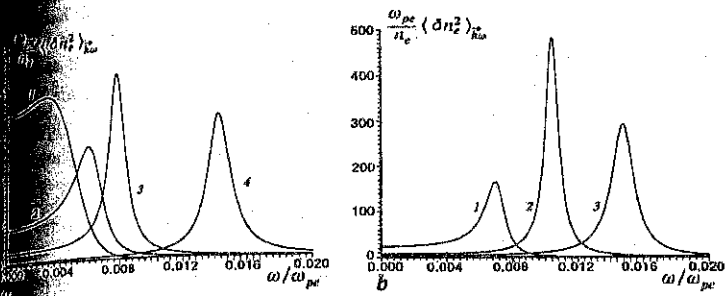


Fig.2

$$\langle \delta n_e^2 \rangle_{\vec{k}\omega} = \frac{4\pi e^2}{mk^2} \sum_{n=-\infty}^{\infty} \int d\vec{v} \int d\vec{u} \frac{J_n\left(\frac{k_\perp v_\perp}{\Omega}\right)\left(\frac{n\Omega}{v_\perp}\frac{\partial f(\vec{v})}{\partial v_\perp} + k_\parallel \frac{\partial f}{\partial v_\parallel}\right)}{\omega - n\Omega - k_\parallel v_\parallel - \vec{k}\vec{u} + ik^2 D} F(\vec{u}),$$

$$\langle \delta B^2 \rangle_{\vec{k}\omega} = 2 \sum_{n=-\infty}^{\infty} \int d\vec{v} \int d\vec{u} \frac{J_n\left(\frac{k_\perp v_\perp}{\Omega}\right) k^2 D f(\vec{v})\, F(\vec{u})}{\omega - n\Omega - k_\parallel v_\parallel - \vec{k}\vec{u})^2 + k^4 D^2},$$

$\omega = \omega B^{ext}/mc$, $F(\vec{u})$ is the distribution function of a turbulent volume element.

4. Numerical Analysis

Eqs. (9), (10) describe turbulent plasma fluctuations for an arbitrary relation between $\vec{k}\langle\vec{u}\rangle$ and k^2D. The limit of large turbulent correlation time ($\vec{k}\langle\vec{u}\rangle >> k^2D$) has been studied in detail in Ref. [2]. We consider the opposite limit $k^2D >> \vec{k}\langle\vec{u}\rangle$. In this limit Eqs. (10) reduce to the relevant relations for the stable plasma with the accuracy up to the replacement $\omega \to \omega + ik^2D$.

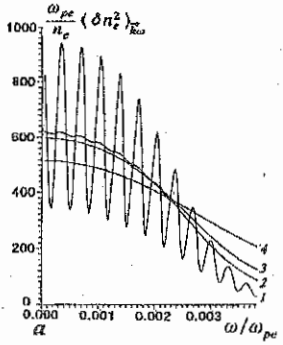


Fig.3

Numerical calculations reveal considerable dependence of fluctuation spe... the diffusion coefficients and their ratio D_i/D_e. Let us consider such spectra... low-frequency domain ($\omega \ll \omega_{pe}$). Fig.1 shows electron fluctuation spe... isothermal (a) and nonisothermal (b) plasmas for $D_i/D_e = 1$ and various va... $\Delta = k_e D_i/S_i$ ($1 - \Delta = 0$, $2 - \Delta = 1$, $3 - \Delta = 10$, $4 - \Delta = 20$). Fig.2 shows the... dependences for $D_i/D_e = 10^{-3}$ and other values of Δ ($1 - \Delta = 0$, $2 - \Delta$... $3 - \Delta = 1$, $4 - \Delta = 3$). The curves of the above figures were calcula... $k/k_e = 0.1$ ($k_e^2 = 4\pi e^2 n_e/T_e$), $\Omega_e/\omega_{pe} = 0.3$ and $\theta = 10°$, where θ is the ... between $\vec{k}$ and $\vec{B}_0$. Thus, for $D_i/D_e = 1$, diffusion leads to the line broadeni... formation of the Lorenzian line. For $D_i/D_e \ll 1$, diffusion produces the effect s... to the temperature difference. It can be explained by the changing of wave... velocity of due to intensive electron diffusion.

For $\theta = \pi/2$ and small Δ, the collective maxima related to the excitation of ... Bernstein modes can be observed (Fig.3). The curves of these figures are re... to the values $\theta = 89.9°$ ($1 - \Delta = 0$, $2 - \Delta = 0.5$, $3 - \Delta = 1$, $4 - \Delta$... $a - D_i/D_e = 1$, $b - D_i/D_e = 10^{-3}$). With increasing Δ, such maxima disappear ... diffusion gives rise to the effect similar to that for small θ.

The authors acknowledge the financial support of the Ukrainian State Commit... on Science, Technologies and Industrial Policy and INTAS Cooperation Progra...

References

[1] D.Gresillon, B.Cabrit, I.P.Villian. Plasma Phys. Contr. Fusion 34 (1992) 193...
[2] P.Sosenko, N.Muafa, D.Gresillon. Phys. Scr. 51 (1995) 647.
[3] A.G.Sitenko, A.G.Zagorodny. Ukr. Journ. Phys. 40 (1995) 389.
[4] A.G.Sitenko, A.G.Zagorodny, P.Schram. Europhys. Conf. Abstr. 19C (part IV) ... (1995) 231.
[5] Yu.L.Klimontovich. Theor. Mat. Fiz. 92 (1995) 312 (in Russian).

...ION TO ENSKOG-LANDAU KINETIC EQUATION USING ...Y CONDITIONS METHOD

...
...Omelyan, M.V.Tokarchuk
...Condensed Matter Physics
...tional Academy of Sciences
...290011 Lviv, Ukraine
tel. +380 322 427401
fax +380 322 761978
e-mail alex@icmp.lviv.ua

...lopment of methods to construct the theory for nonequilibrium processes in dense ...and plasmas is an important direction in the modern theoretical physics. More... ...duction of kinetic equations for such classical and quantum systems still remains ...problem in the kinetic theory. It is complicated additionally in the case of dense ...and plasmas where kinetics and hydrodynamics are closely related and should ...simultaneously [1,2].

...the Enskog-Landau kinetic equation for a system of charged hard spheres is ...To find the normal solution in a nonstationary case, so-called boundary conditions ..., which has been introduced in [3]. As a result, transport equations in the ... case are written. A limiting case of the stationary process is considered. A ...on of the obtained transport coefficients with those known previously from the ...kog method is given.

...consider the Enskog-Landau kinetic equation for a one-component system of charged ...[4]. It reads:

$$\left\{ \frac{\partial}{\partial t} + \boldsymbol{v}_1 \frac{\partial}{\partial \boldsymbol{r}_1} \right\} f_1(x_1;t) = I_E(x_1;t) + I_{MF}(x_1;t) + I_L(x_1;t), \tag{1}$$

... is the one-particle distribution function. The right-hand side of this equation is ...generalized Enskog-Landau collision integral, where each term can be considered ...collision integral. Their structure are as follows:

... the collision integral of the Enskog theory RET:

$$\ldots = \sigma^2 \int \mathrm{d}\hat{\boldsymbol{r}}_{12}\, \mathrm{d}\boldsymbol{v}_2\, \Theta(\hat{\boldsymbol{r}}_{12}\boldsymbol{g})(\hat{\boldsymbol{r}}_{12}\boldsymbol{g}) \times \tag{2}$$

$$\ldots (\boldsymbol{r}_1, \boldsymbol{r}_1 + \hat{\boldsymbol{r}}_{12}\sigma; t) f_1(\boldsymbol{r}_1, \boldsymbol{v}_1'; t) f_1(\boldsymbol{r}_1 + \hat{\boldsymbol{r}}_{12}\sigma, \boldsymbol{v}_2'; t) -$$

$$\ldots (\boldsymbol{r}_1, \boldsymbol{r}_1 - \hat{\boldsymbol{r}}_{12}\sigma; t) f_1(\boldsymbol{r}_1, \boldsymbol{v}_1; t) f_1(\boldsymbol{r}_1 - \hat{\boldsymbol{r}}_{12}\sigma, \boldsymbol{v}_2; t) \Big\},$$

... is the hard sphere diameter, $\boldsymbol{g}$ denotes vector of relative velocity for two particles, $\hat{\boldsymbol{r}}_{12}$ ... unit vector along the direction between centres of particles 1 and 2,

$$\ldots = \boldsymbol{v}_1 + \hat{\boldsymbol{r}}_{12}(\hat{\boldsymbol{r}}_{12} \cdot \boldsymbol{g}), \qquad \boldsymbol{g} = \boldsymbol{v}_2 - \boldsymbol{v}_1,$$
$$\ldots = \boldsymbol{v}_2 - \hat{\boldsymbol{r}}_{12}(\hat{\boldsymbol{r}}_{12} \cdot \boldsymbol{g}), \qquad \hat{\boldsymbol{r}}_{12} = |\boldsymbol{r}_{12}|^{-1}\boldsymbol{r}_{12};$$

... $(x_1;t)$ is the collision integral of the kinetic mean field theory KMFT:

$$\ldots(x_1;t) = \frac{1}{m} \int \mathrm{d}x_2\, \frac{\partial \Phi^l(|\boldsymbol{r}_{12}|)}{\partial \boldsymbol{r}_1} \frac{\partial}{\partial \boldsymbol{v}_1} g_2(\boldsymbol{r}_1, \boldsymbol{r}_2; t) f_1(x_1;t) f_1(x_2;t), \tag{3}$$

where $\Phi^i(|\boldsymbol{r}_{12}|)$ is a long-range part of an interparticle interaction potential; $I_L(x_1;t)$ is generalized Landau collision integral:

$$I_L(x_1;t) = \frac{1}{m^2}\frac{\partial}{\partial \boldsymbol{v}_1}\int \mathrm{d}x_2\, g_2(\boldsymbol{r}_1,\boldsymbol{r}_2;t)\left[\frac{\partial \Phi^i(|\boldsymbol{r}_{12}|)}{\partial \boldsymbol{r}_{12}}\right]\times$$
$$\left[\int\limits_{-\infty}^{0}\mathrm{d}t'\,\frac{\partial \Phi^i(|\boldsymbol{r}_{12}+\boldsymbol{g}t'|)}{\partial \boldsymbol{r}_{12}}\right]\left\{\frac{\partial}{\partial \boldsymbol{v}_1}-\frac{\partial}{\partial \boldsymbol{v}_2}\right\} f_1(x_1;t)\, f_1(x_2;t).$$

It is necessary to note that the quasiequilibrium binary correlation function $g_2(x_1,x_2;t)$ account complete interaction potential (hard core part plus long-range Coulomb tail).

One of a major problem at correct derivation and solution of kinetic equations consistency with local conservation laws of particle density (or mass), momentum, tot and substantiation of hydrodynamic equations and incomprehensible calculation of coefficients via molecular parameters. These conservation laws for classical systems have the structure as in [5].

To find a solution of the Enskog-Landau kinetic equation (1) using one or another there is necessary to take the advantage of local conservation laws in corresponding imations. So doing the expressions for kinetic coefficients will be defined through for momentum flow tensor $\overleftrightarrow{\Pi}(\boldsymbol{r};t)$ and energy flow vector $\boldsymbol{j}_\varepsilon(\boldsymbol{r};t)$ on the base of $f_1(x_1;t)$ and corresponding approximations for $g_2(\boldsymbol{r}_1,\boldsymbol{r}_2;t)$. So long as we find the that corresponds to linear hydrodynamical transport processes by gradients of thermodynamical parameters, densities of momentum flow tensor $\overleftrightarrow{\Pi}(\boldsymbol{r};t)$ and energy flow vector could be determined immediately with the help of the kinetic equation (1) without need formulas from [5].

Normal solution to this equation is found with use of boundary conditions method method differs from other ones for solving kinetic equations (Chapman-Enskog, Grad because it affords to obtain a nonstationary solution, and in a such way it may be description of nonstationary processes. To perform this local conservation laws are general form. It makes possible to take into account both kinetic and hydrodynamic The necessity of joint description of kinetics and hydrodynamics for dense systems highlighted in [1,2]. The solution reads:

$$f^{(1)}(x_1;t) = f^{(0)}(x_1;t)\left(1+\delta f^{(1)}(x_1;t)\right),$$

$$\delta f^{(1)}(x_1;t) = -\int\limits_{-\infty}^{t}\mathrm{d}t'\,\mathrm{e}^{-\varepsilon(t-t')}S(t,t')\left[f_1^{(0)}(x_1;t)\times\right.$$
$$\left\{\left(1+\frac{2}{5}\pi n\sigma^3 g_2(\sigma|n,\beta)\right)\left[\frac{mc_1^2}{2kT}-\frac{5}{2}\right]\boldsymbol{c}_1\frac{\partial}{\partial \boldsymbol{r}_1}\ln T(\boldsymbol{r}_1;t)+\right.$$
$$\left.\left.\left(1+\frac{4}{15}\pi n\sigma^3 g_2(\sigma|n,\beta)\right)\frac{m}{kT}\left[\boldsymbol{c}_1\boldsymbol{c}_1-\frac{1}{3}c_1^2\overleftrightarrow{I}\right]:\frac{\partial}{\partial \boldsymbol{r}_1}V(\boldsymbol{r}_1;t)\right\}\right]_{t'}.$$

Here $f^{(0)}(x_1;t)$ is locally equilibrium Maxwellian, $S(t,t')$ is determined similar to [3]. T evident influence into correction in this approximation to one-particle distribution functio $f_1(x_1;t)$ gives terms, which are connected with short-range interactions only. Particle

account here on the contrary to kinetic theory of dilute gases, where particles ...ed as point-like objects. Nevertheless, the influence of both the long-range and ...parts of interactions are also "hidden" in operator $S(t,t')$ (through operator ...lly, the expression (5) looks completely the same as the correction in [6]. But a ...the structure of the operator $S(t,t')$.

...and heat flow vector of the system has beeen calculated on the basis of ...ction for the trivial solution. The calculation of long-range part of interparticle ...ential, which is new in comparison with previous papers, could be pointed out.

$$\vec{\nabla} P(r_1;t) - \frac{4}{9} n^2 \sigma^4 g_2(\sigma|n,\beta) \sqrt{\pi m k T} \left[\frac{6}{5} \overrightarrow{S} + (\nabla \cdot V) \overleftrightarrow{I} \right] -$$

$$\left(1 + \frac{4}{15} \pi n \sigma^3 g_2(\sigma|n,\beta) \right) \int_{-\infty}^{t} \mathrm{d}t' \, \mathrm{e}^{-\varepsilon(t-t')} M^k(t,t') \left[\overrightarrow{S} \right]_{t'},$$

...the velocity shift tensor,

$$= \frac{m}{5} \int \mathrm{d}\boldsymbol{v}_1 \, \boldsymbol{c}_1 \boldsymbol{c}_1 S(t,t') \times \tag{6}$$

$$\left[f_1^{(0)}(x_1;t) \left(1 + \frac{4}{15} \pi n \sigma^3 g_2(\sigma|n,\beta) \right) \frac{m}{kT} \left(\boldsymbol{c}_1 \boldsymbol{c}_1 - \frac{1}{3} c_1^2 \overleftrightarrow{I} \right) \right]_{t'}$$

...kinetic part of transport equations;

$$= -\frac{2}{3} n^2 \sigma^4 g_2(\sigma|n,\beta) \sqrt{\frac{\pi k^3 T}{m}} \nabla T(\boldsymbol{r}_1;t) -$$

$$\left(1 + \frac{2}{5} \pi n \sigma^3 g_2(\sigma|n,\beta) \right) \int_{-\infty}^{t} \mathrm{d}t' \, \mathrm{e}^{-\varepsilon(t-t')} L^k(t,t') \left[\frac{1}{T} \nabla T \right]_{t'},$$

$$= \frac{1}{3} \int \mathrm{d}\boldsymbol{v}_1 \, \boldsymbol{c}_1 \frac{m c_1^2}{2} S(t,t') \times \tag{7}$$

$$\left[f_1^{(0)}(x_1;t) \left(1 + \frac{2}{5} \pi n \sigma^3 g_2(\sigma|n,\beta) \right) \left(\frac{m c_1^2}{2kT} - \frac{5}{2} \right) \boldsymbol{c}_1 \right]_{t'}$$

...other kernel of kinetic part of transport equations.

...us consider limiting case of the stationary process and determine kinetic coefficients: ...osities and heat conductivity. New transport coefficients reduce to already known ones ...[2] (obtained using of Chapman-Enskog method) if one neglects interparticle long-range ...relations ($g_2 \to 1$) and admits approximation of small angles of scattering. It should be ...ed that bulk viscosity has the same structure as in Chapman-Enskog method. But other ...nsport coefficients exhibit some distinctions. The structure for shear viscosity η and thermal ...nductivity λ is:

$$\eta = \frac{3}{5} \neq +2\, nkT \, \frac{\left\{ 1 + \frac{4}{15} \pi n \sigma^3 g_2(\sigma|n,\beta) \right\}^2}{\left\{ I_E^{(0)}(\delta f) + I_L(\delta f) \right\}}, \tag{8}$$

$$\lambda = \frac{3k}{2m} \neq + \frac{5k}{m} nkT \frac{\left\{1 + \frac{2}{5}\pi n\sigma^3 g_2(\sigma|n,\beta)\right\}^2}{\left\{I_E^{(0)}(\delta f) + I_L(\delta f)\right\}}.$$

Then the problem lies in calculating collision integrals $I_E^{(0)}(\delta f)$ and $I_L(\delta f)$, th... we should calculate collision integrals (2) (in the zeroth approximation on in... and (4) together in the first approximation on deviation δf, where δf is sub... (5). The matter of some difficulty is that correction (5) in its turn is expre... collision integrals $I_E^{(0)}(\delta f)$, $I_E(\delta f)$, which are available in the operator $S(t,t')$. Let u... that operator $S(t,t')$ in the stationary case reads $S(t,t') = \exp\left\{L_t(t-t')\right\}$, ... $I_E^{(0)}(\delta f) + I_{MF}(\delta f) + I_L(\delta f)$. So the first acceptable approximation should be tha... correction δf (5) is expressed via $I_E^{(0)}(\delta f)$, $I_L(\delta f)$ calculated with $\delta f'$, where f... $S(t,t') = 1$. For $I_E^{(0)}(\delta f)$ we obtain the results [1], for $I_L(\delta f)$ we can obtain the fo...

$$I_L(\delta f) = \frac{Z^4 e^4}{m^2} \frac{\partial}{\partial v_1} \int \mathrm{d}\boldsymbol{r}_{12}\, \mathrm{d}\boldsymbol{v}_2\, g_2\left(\boldsymbol{r}_1, \boldsymbol{r}_1 + \boldsymbol{r}_{12}; t\right) \frac{\boldsymbol{r}_{12}\boldsymbol{r}_{12}}{r_{12}^5} \frac{1}{g} \left\{\frac{\partial}{\partial v_1} - \frac{\partial}{\partial v_2}\right\}$$
$$\times \Big\{f_1\left(x_1; t\right) \delta f\left(\boldsymbol{r}_1 + \boldsymbol{r}_{12}, \boldsymbol{v}_2; t\right) + \delta f\left(x_1; t\right) f_1\left(\boldsymbol{r}_1 + \boldsymbol{r}_{12}, \boldsymbol{v}_2; t\right)\Big\},$$

where $\delta f(x;t)$ is evaluated from (5) with

$$S(t,t') = \exp\left\{L_t(t-t')\right\} = \exp\left\{\left[I_E^{(0)}(\delta f') + I_L(\delta f')\right](t-t')\right\}$$

at $\delta f'(x;t) = \delta f(x;t)\Big|_{S(t,t')=1}$. This stage of calculations needs explicit form fo... quasiequilibrium correlation function g_2 both on the contact and in r-space.

The reason for these differences were discussed in details in [3] and could be ... on results of this paper. At constructing of the normal solution for the Enskog-La... netic equation time derivatives $\frac{\partial}{\partial t}$ of hydrodynamical parameters of reduced descri... not vanish. Therefore, the normal solution to this equation could be used for hydro... description of fast processes.

[1] D.N.Zubarev, V.G.Morozov, I.P.Omelyan, M.V.Tokarchuk, Teor. Mat. Fiz. 96(1993)32...
[2] Yu.L.Klimontovich, Teor. Mat. Fiz. 92(1992)312.
[3] D.N.Zubarev, A.D.Khonkin, Teor. Mat. Fiz. 11(1972)403.
[4] D.N.Zubarev, V.G.Morozov, I.P.Omelyan, M.V.Tokarchuk, Teor. Mat. Fiz. 87(1991)11...
[5] D.N.Zubarev, *Nonequilibrium statistical thermodynamics*, Consultant Bureau, New York, 197...
[6] M.V.Tokarchuk, I.P.Omelyan, *Normal solution of Enskog-Vlasov kinetic equation using bou... dary conditions method*, in: Proceedings, Contributed papers of conference "Modern Probl... of Statistical Physics", vol. 1, (Lviv, February 3-5, 1987), p. 245-252 (in Russian).

HYDRODYNAMIC INTERACTIONS AND FLUCTUATIONS IN SUSPENSIONS IN COMPRESSIBLE FLUIDS

P.P.J.M.Schram and I.P.Yakimenko*

Eindhoven University of Technology, P.O.Box 513, 5600 MB, Eindhoven, The Netherlands

*Bogolyubov Institute for Theoretical Physics, 252 143, Kiev, Ukraine

Introduction

Recently [1] we have developed *the Green's function approach* to the theory of the hydrodynamic interaction in suspensions in incompressible fluids. In present paper we generalize and apply this approach to more general case of n spheres of radii a_i ($i = 1,...,n$) suspended in a viscous compressible fluid. Performing the technique of averaging over the volume of the sphere within the framework of the induced force density formalism [2] we derive the hierarchy of equations for the irreducible force multipoles which allow one to calculate the mobility and friction tensors and as a result to treat the dynamics of the system under consideration in regular and random velocity fields of compressible fluids.

Induced force formalism: basic set of equations

We start from the linearized equations of motion for an compressible fluid and for a rigid body which can be written in terms of the induced density formalism as [2, 3]

$$\frac{\partial}{\partial t}\rho v_i(r,t) = -\mathrm{div}P(r,t) + \sum_{j=1}^{n} F_j(r,t) + F_{ext}(r,t) \tag{2.1}$$

$$\frac{\partial}{\partial t}\rho(r,t) = -\rho_e \mathrm{div}v(r,t) \tag{2.2}$$

$$\frac{d}{dt}F_i(t) = -\int_{S_i} P(r,t)\cdot n\, dS + K_{i\,ext}(t) = K_i(t) + K_{i\,ext}(t) \tag{2.3}$$

$$\frac{d}{dt}T_i(t) = -\int_{S_i} (r - R_i(t))\times P(r,t)\cdot n\, dS + K_{i\,ext}(t) = T_i(t) + T_{i\,ext}(t) \tag{2.4}$$

$$P_{ij}(r,t) = p(r,t)\delta_{ij} - \eta\left(\frac{\partial v_i(r,t)}{\partial r_j} + \frac{\partial v_j(r,t)}{\partial r_i}\right) + \left(\frac{2}{3}\eta - \eta_V\right)\mathrm{div}v(r,t)\delta_{ij} + \sigma_{ij}(r,t) \tag{2.5}$$

$$p(r,t) = c_0^2 \rho(r,t) \tag{2.6}$$

Here $v(r, t)$, $\rho(r, t)$ and $p(r, t)$ are the velocity, density and pressure fields, σ the pressure tensor and σ a random stress tensor defined by its conventional stochastic properties [4]; $F_i(r, t)$ and $F_{ex}(r, t)$ the induced and external forces; η and η_v shear and bulk viscosity; ρ_e the uniform equilibrium density of fluid; $R_i(t)$, $u_i(t)$, $\Omega_i(t)$ the position, velocity and angular velocity of the i-th sphere with the mass m_i and the moment of inertia tensor I_i; $K_i(t)$ and $T_i(t)$ the force and torque exerted by the fluid on sphere i.

It is worthwhile to notice that Eq. (2.1) is valid *all over* the space if the induced force fields are chosen in such a way that [2, 3]

$$F_i(r,t) = \begin{cases} \rho \dfrac{\partial}{\partial t}\left[u_i(t) + \Omega_i(t) \times (r - R_i(t))\right], & |r - R_i(t)| < a_i \\ F_i^S(r,t), & |r - R_i(t)| = a_i \\ 0, & |r - R_i(t)| > a \end{cases}$$

$$v(r,t) = u_i(t) + \Omega_i(t) \times (r - R_i(t)), \quad |r - R_i(t)| \le a_i$$

$$\rho(r,t) = 0, \quad |r - R_i(t)| < a_i$$

These relations correspond to the case of widely known stick boundary conditions on the surfaces of each of n spheres. Moreover the variables involved are coupled via

$$K_i(t) = -\int_{|r - R_i(t)| \le a_i} dr F_i^S(r,t) \tag{2.10}$$

$$T_i(t) = -\int_{|r - R_i(t)| \le a_i} dr (r - R_i(t)) \times F_i^S(r,t) \tag{2.11}$$

3. Formal solution of the fluid equations of motion

Introducing the transverse and longitudinal Green's functions according to

$$G_T(r - r', \omega) = \frac{1}{4\pi\eta |r - r'|} e^{-\alpha_T |r - r'|}, \qquad (Re\, \alpha_T > 0) \tag{3.1}$$

$$G_L(r - r', \omega) = \frac{1}{4\pi c^2 |r - r'|} e^{-\alpha_L |r - r'|}, \qquad (Re\, \alpha_L > 0) \tag{3.2}$$

with

$$c^2 = c_0^2 - i\omega\rho_e^{-1}\left(\frac{4}{3}\eta + \eta_v\right), \quad \alpha_T^2 = -\frac{i\omega\rho_e}{\eta}, \quad \alpha_L^2 = -\frac{\omega^2}{c^2} \tag{3.3}$$

...ve the formal solution of the fluid equations of motion as

$$v_i(r+R_i,\omega) = v_0(r+R_i,\omega) + \sum_{j=1(r'\le a_j)}^{n} \int dr' \Big\{ F_j(r'+R_j,\omega) G_T(r-r'-R_{ij},\omega) + \frac{\partial}{\partial r'} F_j(r'+R_j,\omega) \cdot \frac{\partial}{\partial r'} \Big[c^2 \eta^{-1} G_L(r-r'-R_{ij},\omega) - G_T(r-r'-R_{ij},\omega) \Big] \Big\} \tag{3.4}$$

$$\rho_i(r+R_i,\omega) = \rho_0(r+R_i,\omega) + \sum_{j=1(r'\le a_j)}^{n} \int dr' F_j(r'+R_j,\omega) \cdot \frac{\partial}{\partial r'} G_L(r-r'-R_{ij},\omega) \tag{3.5}$$

...$R_{ij} \equiv R_j - R_i$.

...ducible force multipoles and average technique

...Naturally, the formal solutions given by Eqs. (3.4) and (3.5) cannot be used directly ...of the fact that the analytical structure of the induced fields $F_i(r, t)$ is unknown. ...these solutions can serve as the basis for deriving the set of equations for the ...called irreducible force multipoles which are defined by [5]

$$F_i^{(p)}(\omega) \equiv (p!)^{-1} \int_{(r\le a_i)} dr \overline{n_i^p} F_i^S(r+R_i,\omega) \tag{4.1}$$

...$\overline{n_i^p}$ is the irreducible tensor of rank p constructed with the vector $n_i = r / a_i$.

To realize this idea we introduce the operators of surface (S) and volume (V) ...ge according to

$$\Big(S_p^{(i)} A\Big)(r,\omega) \equiv (2p+1)!! a_i^{-p} (4\pi a_i^2)^{-1} \int_{|r-R_i|\le a_i} dr \overline{n_i^p} A(r,\omega) \delta\big(|r-R_i| - a_i\big) \tag{4.2}$$

$$\Big(V_p^{(i)} A\Big)(r,\omega) \equiv (2p+1)!! a_i^{-p} \Big(\frac{4}{3}\pi a_i^3\Big)^{-1} \int_{|r-R_i|\le a_i} dr \overline{n_i^p} A(r,\omega) \tag{4.3}$$

...Average technique in action : example

...Applying the operators (4.2) and (4.3) at $p = 0$ to Eq. (3.4) and the operator (4.3) at ...to Eq.(3.5) we come to the equation

$$K_i(\omega) = -12\pi\eta a_i (\alpha_T a_i)^2 \Big[(\alpha_L a_i)^2 A_T + 2(\alpha_T a_i)^2 A_L \Big]^{-1}$$

$$\times \Big\{ \Big[\Big(1 + \alpha_T a_i + \frac{1}{9}(\alpha_T a_i)^2 \Big) A_L - \frac{1}{9}(\alpha_L a_i)^2 A_T \Big] u_i(\omega)$$

$$-A_L\Big[\big(1+\alpha_T a_i\big)O_o^{S_i}v_o(r,\omega)+\tfrac{1}{3}(\alpha_T a_i)^2 O_o^{V_i}v_o(r,\omega)\Big]$$

$$-\tfrac{1}{27}i\omega\rho_e^{-1}a_i^2\big[(\alpha_L a_i)^2 A_T-(\alpha_T a_i)^2 A_L\big]O_1^{V_i}\rho_o(r,\omega)$$

$$-A_L\sum_{j\neq i(r\le a_j)}^{n}\int dr\,\Big\{e^{\alpha_T a_i}G_T(R,\omega)F_j(r+R_j,\omega)+F_j(r+R_j,\omega)\cdot\frac{\partial}{\partial r}\frac{\partial}{\partial r}$$

$$\Big[A_o G_L(R,\omega)-\alpha_T^{-2}e^{\alpha_T a_i}G_T(R,\omega)\Big]\Big\}-\tfrac{1}{27}i\omega\rho_e^{-1}a_i^2\big[(\alpha_L a_i)^2 A_T-(\alpha_T a_i)^2$$

$$\times B_o\sum_{j\neq i(r\le a_j)}^{n}\int dr F_j(r+R_j)\cdot\frac{\partial}{\partial r}\frac{R}{R}(\alpha_L R+1)G_L(R,\omega)$$

with $R=R_{ij}+r$; $A_{T,L}$, A_o and B_o constants expressed in terms of parameters ($\alpha_{T,L}$,

It is clearly seen from Eq.(5.1) that $r \ll R_{ij}$ in the domain of integration over volume of j-th sphere and this invites a power series expansion which immediately leads to the hierarchy of equations for the irreducible force multipoles defined by Eq.(4.1).

6.1. Generalized Langevin equations

By elimination of higher order multipoles in the above-mentioned hierarchy of equations the generalization of Faxén's theorem for the system under consideration can be established in terms of the friction tensors and the surface and volume averages of the unperturbed velocity $v_o(r,\omega)$ and density $\rho_o(r,\omega)$ fields. Substituting those results into the equations of motion (2.3) and (2.4) and using the statistical properties of the fluctuations the translational and rotational Langevin equations can be proved. For example,

$$-i\omega I_i\cdot\Omega_i(\omega)=-\sum_{j=1}^{n}\zeta_{ij}^{RR}(\omega)\cdot\Omega_j(\omega)+T_{i\,ext}(\omega)+T_{i\,R}(\omega) \qquad (6.1)$$

where $\zeta_{ij}(\omega)$ is the rotational friction tensor and $T_{i\,R}(\omega)$ the random source with the statistical properties defined by the conventional fluctuation-dissipation theorem, cf.[6].

References

[1] P.P.J.M.Schram and I.P.Yakimenko, Proc. Workshop on Complex Fluids and Plasmas, 18-21 September 1995, Eindhoven, The Netherlands.
[2] D.Bedeaux and P.Mazur, Physica **76** (1974) 235; **78** (1974) 505.
[3] P.Mazur and G. van der Zwan, Physica **92A** (1978) 483.
[4] L.D.Landau and E.M.Lifshitz, Fluid Mechanics (Pergamon Press, New York, 1959).
[5] P.Mazur and W. van Saarloos, Physica **115A** (1982) 21.
[6] B.P.Hills, Physica **80A** (1975) 360.

...ion Theory of Bremsstrahlung in a Plasma with Fluid-Like Random Motions

T.B.Chmyr, A.G.Zagorodny

Bogolyubov Institute for Theoretical Physics, Kiev 143, Ukraine

...duction

...e case of stable stationary plasma theoretical studies of bremsstrahlung may be performed ...s of various approaches (see, for instance refs.[1-5]), including the fluctuation approach ... within the fluctuation approach bremsstrahlung is treated as a fluctuation field scattering by ...fluctuations. Thit makes it possible to take into account individual-particle collisions, as well ...ective scattering processes.

...ently, much interested has been attracted to the phenomenological theory of electromagnetic ...ations in plasma with large-scale random motions [6-9]. Within these theories fluctuation spectra ...bulent plasmas can be calculated easily in the same manner as in the case of stable plasmas. ...field can be calculated in terms of dielectric response functions and correlation functions of the ...rent sources averaged over the ensemble of macroscopic chaotic motions [7,8].

...e purpose of the present paper is to generalize fluctuation theory of bremsstrahlung to the case ...bulent plasmas using the model of a plasma with fluid-like stochastic perturbations.

...Sources of Bremsstrahlung Radiation and Bremsstrahlung ...ntensity.

...e consider a plasma with developed turbulence assuming that there occur large-scale turbulent ...ations. As it was mentioned above, within the general theory of electromagnetic fluctuations, ...bremsstrahlung can be interpreted as the radiation generated in course of fluctuation field ...ering by electron density fluctuations. It is possible to show that in the high-frequency domain ...rrent which plays the role of bremsstrahlung source is given by [4,5]

$$J_{k,\omega} = \frac{e^2}{\omega m_e} \int \frac{dq}{(2\pi)^3} \int \frac{dx}{2\pi} \left[q + q \frac{(kK)}{K^2} \frac{\Omega}{\omega} + q \frac{(kq)}{K^2} \frac{\Omega}{\omega} \right] \delta n^e_{K,\Omega} \delta\phi_{q,x}, \qquad (1)$$

...here $K = k - q$, $\Omega = \omega - x$; $\delta n^e_{K,\Omega}$ and $\delta\phi_{q,x}$ are the Fourier components of the electron density ...d electron potential, calculated in the linear (with respect to fluctuation quantities) approximation. ...ainder of notations is conventional.

The current $J_{k,\omega}$ excites the bremsstrahlung field which satisfies the Maxwell equations. Calculat... the averaged energy characteristics of the exited field it is easy to find the bremsstrahlung intensity. ...troducing such an intensity as a power emitted by the system into the solid angle unit $d\Omega$ within ...e frequency range $d\omega$, one obtains

$$I_{k,\omega} = \frac{V\omega^2}{8\pi^2 c^3} \left(\delta_{ij} - \frac{k_i k_j}{k^2} \right) < J_i J_j >_{k,\omega}, \qquad (2)$$

...here $k = \Omega/c$, Ω is unit vector given the direction of the solid angle $d\Omega$ axis.

2 Fluctuation Spectra in a Plasma with Large-Scale Random Motion

In order to calculate the correlation functions of bremsstrahlung sources (1) it is necessary to find the fluctuation spectra of electron density and electric potential.

It has been shown in refs.[7-9] that the fluctuation spectra under consideration are given by relevant relations for microscopic quantities in terms of the response functions and the Langevin correlation functions averaged over turbulent pulsations. For example, spectral densities of correlation functions for electron density and electric potential fluctuations are given by [8,9]

$$< \delta n_e^2 >_{\mathbf{k},\omega} = 2\pi \left\{ \left| \frac{1+\tilde{\chi}_i(\mathbf{k},\omega)}{\tilde{\varepsilon}(\mathbf{k},\omega)} \right|^2 \tilde{S}_e(\mathbf{k},\omega) + \left| \frac{\tilde{\chi}_e(\mathbf{k},\omega)}{\tilde{\varepsilon}(\mathbf{k},\omega)} \right|^2 \tilde{S}_i(\mathbf{k},\omega) \right\},$$

$$< \delta\phi^2 >_{\mathbf{k},\omega} = \frac{32\pi^2 e^2}{k^4 \mid \tilde{\varepsilon}(\mathbf{k},\omega) \mid^2} \left\{ \tilde{S}_e(\mathbf{k},\omega) + Z_i^2 \tilde{S}_i(\mathbf{k},\omega) \right\},$$

$$< \delta\phi\delta n_e >_{\mathbf{k},\omega} = \frac{8\pi^2 e^2}{k^2 \mid \tilde{\varepsilon}(\mathbf{k},\omega) \mid^2} \left\{ [1+\tilde{\chi}_i(\mathbf{k},\omega)]\tilde{S}_e(\mathbf{k},\omega) - Z_i^2 \tilde{\chi}_e(\mathbf{k},\omega)\tilde{S}_i(\mathbf{k},\omega) \right\}.$$

Here

$$\tilde{\varepsilon}(\mathbf{k},\omega) = 1 + \tilde{\chi}_e(\mathbf{k},\omega) + \tilde{\chi}_i(\mathbf{k},\omega),$$

$$\tilde{\chi}_\sigma(\mathbf{k},\omega) = \frac{4\pi e_\sigma^2 n_\sigma}{m_\sigma k^2} \int d\mathbf{v} W_{\sigma\mathbf{k},\omega}(\mathbf{v}) \mathbf{k} \frac{\partial f_{0\sigma}(\mathbf{v})}{\partial \mathbf{v}},$$

$$\tilde{S}_\sigma(\mathbf{k},\omega) = \frac{n_\sigma}{2\pi} \int d\mathbf{v} W_{\sigma\mathbf{k},\omega}(\mathbf{v}) f_{0\sigma}(\mathbf{v}) + \text{c.c.},$$

$$W_{\sigma\mathbf{k},\omega}(\mathbf{v}) = \int \frac{d\omega'}{2\pi} \frac{i}{\omega' - \mathbf{kv} + i0} S_{T\sigma}(\mathbf{k}, \omega - \omega'),$$

$$S_{T\sigma}(\mathbf{k},\omega) = \int d\mathbf{v} \int d\mathbf{v}' \widetilde{W}_{\sigma\mathbf{k},\omega}(\mathbf{v},\mathbf{v}') F_\sigma(\mathbf{v}') + \text{c.c.},$$

$f_{0\sigma}(\mathbf{v})$ is the unperturbed distribution function for particles species σ, $F_\sigma(\mathbf{v})$ is the velocity distribution of large-scale volume elements involved into chaotic turbulent motion, $\widetilde{W}_{\sigma\mathbf{k},\omega}(\mathbf{v},\mathbf{v}')$ is the Fourier component of the transition probability of volume element transition in the phase space. Assuming that such transitions are governed by the Bhatnagar-Gross-Kroock kinetic equation it is easy to calculate $\widetilde{W}_{\sigma\mathbf{k},\omega}(\mathbf{v},\mathbf{v}')$ in the explicit form [8],that leads to

$$S_{T\sigma}(\mathbf{k},\omega) = \frac{i \int d\mathbf{v} F_\sigma(\mathbf{v})/(\omega - \mathbf{kv} + i\nu_\sigma)}{1 + i\nu_\sigma \int d\mathbf{v} F_\sigma(\mathbf{v})/(\omega - \mathbf{kv} + i\nu_\sigma)},$$

where $\nu_\sigma = 1/\tau_\sigma$, τ_σ is the mean free-path time for volume element motion.

In the limits of small and large τ_σ Eq.(8) is considerable simplified

$$S_{T\sigma}(\mathbf{k},\omega) = \frac{i}{\omega - \mathbf{kU}_d + ik^2 D_\sigma}, \quad \omega \ll \nu_\sigma, kS_\sigma \ll \nu_\sigma,$$

$$S_{T\sigma}(\mathbf{k},\omega) = i \int d\mathbf{v} \frac{F_\sigma(\mathbf{v})}{\omega - \mathbf{kv} + i0}, \quad \omega \gg \nu_\sigma, kS_\sigma \gg \nu_\sigma,$$

Here $\mathbf{U}_d = \int d\mathbf{v} \mathbf{v} F_\sigma(\mathbf{v})$, $D_\sigma = 1/(3\nu_\sigma) \int d\mathbf{v} v^2 F_\sigma(\mathbf{v})$.

...elation Functions of Bremsstrahlung Sources

...ain contribution into bremsstrahlung radiation to be determined by the wavenumber ... and $q \le \omega/S_e$ (S_e is the electron thermal velocity) it is possible to expand Eq.(1) ...(k/q). Then Eqs.(1)-(6) give the following correlation function of the bremsstrahlung

$$...>_{k,\omega} = < J_i J_j >_\omega^{(1)} + < J_i J_j >_{k,\omega}^{(2)}, \tag{10}$$

$$...>_\omega^{(1)} = \frac{4r_e^2c^4}{\omega^2}(Ze)^2 \int dx \int dq \frac{q_i q_j}{q^4} \frac{\tilde{S}_e(-\mathbf{q},\Omega)\tilde{S}_i(\mathbf{q},x)}{|\tilde{\varepsilon}(-\mathbf{q},\Omega)|^2} \left|\frac{1+\tilde{\chi}_e(\mathbf{q},x)}{\tilde{\varepsilon}(\mathbf{q},x)}\right|^2, \tag{11}$$

$$...>_{k,\omega}^{(2)} = \frac{2r_e^2c^4}{\omega^2}e^2 \int dx \int \frac{d\mathbf{q}}{q^4}\left(k_i - \frac{4(\mathbf{kq})}{q^2}q_i\right)\left(k_j - \frac{4(\mathbf{kq})}{q^2}q_j\right) \frac{\tilde{S}_i(-\mathbf{q},\Omega)\tilde{S}_e(\mathbf{q},x)}{|\tilde{\varepsilon}(\mathbf{q},x)\tilde{\varepsilon}(-\mathbf{q},\Omega)|^2}, \tag{12}$$

... Eqs.(11),(12) describe bremsstrahlung source correlation functions in the dipole and ... approximation respectively.

...consider the correlation functions (11) and (12) in more detail in the limits of large ($\omega \gg \nu_e$) ... ($\omega \ll \nu_e$) correlation times of turbulent perturbations. In the first limit the large-scale ...ucture factor is given by Eq.(9b). For the Gaussian volume element velocity distribution ...$(\alpha_e)^{3/2}\exp(-\alpha_e v^2)$ and the Maxwellian particle velocity distribution the presence of large-...ective motions can be shown to result in the renormalization of the particle temperatures,

$$T_e \to T_e\left(1+\frac{m_e}{2T_e\alpha_e}\right) \equiv T_e t_e \quad \text{and} \quad k_{De} \to \tilde{k}_{De} = \left(\frac{4\pi e_e^2 n_e/T_e}{1+m_e/(2T_e\alpha_e)}\right)^{1/2}. \tag{13}$$

...o account such a change it is possible to separate the contributions from individual particle ...ective processes. For the dipole part of correlation function one has

$$...J_j >_\omega^{(1)} = < J_i J_j >_\omega^{(1)i.p.} + < J_i J_j >_\omega^{(1)c}, \tag{14}$$

$$...J_j >_\omega^{(1)i.p.} = \frac{4r_e^2c^4}{\omega^2}(Ze)^2 n_i \int\limits_{q>\tilde{k}_e} dq \frac{q_i q_j}{q^4} \frac{\tilde{S}_e(-\mathbf{q},\omega)}{|\tilde{\varepsilon}(-\mathbf{q},\omega)|^2}, \tag{15}$$

$$...J_j >_\omega^{(1)c} = \frac{4r_e^2c^4}{\omega^2}\frac{(Ze)^2}{1+\tilde{Z}} n_i \int\limits_{q<\tilde{k}_e} dq \frac{q_i q_j}{q^4} \frac{\tilde{S}_e(-\mathbf{q},\omega)}{|\tilde{\varepsilon}(-\mathbf{q},\omega)|^2}; \qquad \tilde{Z} = Z\frac{\alpha_i(\alpha_e+m_e/2T_e)}{\alpha_e(\alpha_i+m_i/2T_a)}. \tag{16}$$

...ollective part (16) can be represented in terms of effective fluctuation temperature

$$...J_j >_\omega^{(1)c} = \frac{r_e^2c^4}{\pi\omega^2}\frac{Z^2}{1+\tilde{Z}} n_i \int\limits_{q<\tilde{k}_e} dq \frac{q_i q_j}{q^2} \tilde{T}(-\mathbf{q},\omega)\delta(Re\,\tilde{\varepsilon}(-\mathbf{q},\omega)); \tag{17}$$

$$\tilde{T}(\mathbf{q},\omega) = (2\pi)^2 \frac{e^2\omega}{k^2}\frac{\tilde{S}_e(\mathbf{q},\omega)}{Im\,\tilde{\varepsilon}(\mathbf{q},\omega)}.$$

...As regards the quadrupole part, it is possible to take into account only the collective part, which ...can be expressed in terms of effective temperature

$$...J_j >_{k,\omega}^{(2)c} = \frac{r_e^2c^4}{8\pi^2e^2\omega^2}\int\frac{dx}{x\Omega}\int dq\left(k_i - \frac{4(\mathbf{kq})}{q^2}q_i\right)\left(k_j - \frac{4(\mathbf{kq})}{q^2}q_j\right)\hat{T}(-\mathbf{q},\Omega)\bar{T}(\mathbf{q},x)\times$$
$$\times\delta(Re\,\tilde{\varepsilon}(\mathbf{q},x))\delta(Re\,\tilde{\varepsilon}(-\mathbf{q},\Omega)). \tag{18}$$

Now, let us specify the calculations for the Maxwellian particle distributions. In this

$$< J_i J_j >_\omega^{(1)} = \frac{16\pi}{3}\delta_{ij}\frac{r_e^2 c^4}{\omega^2 \bar{S}_e\sqrt{2\pi}}(Ze)^2 n_e n_i \left(\ln\frac{\sqrt{2}\bar{k}_m\bar{S}_e}{\omega} - \frac{C}{2}\right),$$

that differs from the relevant quantity for stable stationary plasma by the renormalized pa peratures. Here, $\bar{S}_e = S_e\sqrt{t_e}$, $\bar{k}_m = 3T_e t_e/e^2$.

If plasma contains small fraction of the high-energy electrons, i.e.

$$f_{0e}(\mathbf{v}) = \gamma\left(\frac{m_e}{2\pi T_e}\right)^{3/2}\exp(-\frac{mv^2}{2T_e}) + (1-\gamma)\left(\frac{m_e}{2\pi T_E}\right)^{3/2}\exp(-\frac{mv^2}{2T_E}), \qquad \gamma \sim 1, T_E \gg$$

the collision part can be approximated by Eq.(19), but in this case the collective contri significant

$$< J_i J_j >_\omega^{(1)e} = \frac{8\pi}{9}\frac{r_e^2 c^4}{\omega_{pe}\bar{S}_e}\frac{(Ze)^2}{(1+\bar{Z})}n_e n_i\left(\frac{q_0}{\bar{k}_e}\right)^3\left(\frac{T_E}{T_e}\right)\delta_{ij}\delta(\omega-\omega_{pe}),$$

$$\left(\frac{q_0}{\bar{k}_e}\right)^2 = [3\ln(T_E/T_e) - 2\ln(1-\gamma)]^{-1},$$

$$< J_i J_j >_{\mathbf{k},\omega}^{(2)e} = \frac{8\pi}{45}\frac{r_e^2 c^4}{\omega_{pe}\bar{S}_e}e^2 n_e^2\left(\frac{k}{\bar{k}_e}\right)^2\left(\frac{q_0}{\bar{k}_e}\right)^3\left(\frac{T_E}{T_e}\right)^2\delta(\omega-2\omega_{pe})\left[\left(\delta_{ij}-\frac{k_i k_j}{k^2}\right)+\frac{23}{16}\frac{k_i k_j}{k^2}\right]$$

In the limit related to the diffusion of volume elements ($\nu_\sigma \gg \omega$) Eq.(11) reduces to

$$< J_i J_j >_\omega^{(1)} = \frac{4r_e^2 c^4}{\omega^2}(Ze)^2 n_i \int\frac{d\mathbf{q}}{q^2}\frac{q_i q_j}{q^2}\frac{\bar{S}_e(-\mathbf{q},\omega)}{|\bar{\varepsilon}(-\mathbf{q},\omega)|^2}\frac{1+\bar{\chi}_e(\mathbf{q},0)}{\bar{\varepsilon}(\mathbf{q},0)}.$$

In this limit the collective contribution can be neglected.

In the case of small electron diffusion coefficient $D_e < S_e/k_m$ and $\omega > k_m^2 D_e$ volume diffusion leads to the additional contribution to the bremsstrahlung

$$< J_i J_j >_\omega^{(1)i.p.} = \frac{16}{3}\delta_{ij}\frac{r_e^2 c^4}{\omega^2}(Ze)^2 n_e n_i\left(\frac{1}{\sqrt{2\pi}S_e}\ln\frac{\sqrt{2}k_m S_e}{\omega} + \frac{2}{3}\frac{D_e k_m^3}{\pi\omega^2}\right).$$

In the case $\omega < k_m^2 D_e < k_m S_e$

$$< J_i J_j >_\omega^{(1)i.p.} \simeq \frac{32}{3}\delta_{ij}\frac{r_e^2 c^4}{2\pi\omega^2}(Ze)^2\frac{n_e n_i}{k_e D_e}.$$

Substituting the correlation functions (19)-(24) into Eq.(2) one obtains the bremsstrahlung emi sity of turbulent plasmas.

References

1.G.Bekefi. Radiation Processes in Plasma. J.Wiley & Sons, Inc. N.Y.-London-Sydney, 1965
2.S.Ichimaru. Basic Principles of Plasma Physics. N.Y. Interscience, 1975
3.A.G.Sitenco. Fluctuations and Nonlinear Wave Interactions in Plasmas. Pergamon, Oxford, 1982
4.D.Tidman, T.H.Dupree. Phys. Fluids, 8,(1965),1860
5.A.G.Zagorodny, A.S.Usenko,I.P.Yacimenko. Radiophysica (in Russian)
6.D.Gresillon, B.Cabrit, J.P.Villian. Plasma Phys. Contr. Fusion 34,(1992),1985
7.P.Sosenko, N.Maafa, D.Gresillon. Physica Scripta 51,(1995),647
8.A.G.Sitenko, A.G.Zagorodny. Ukr. Journ. Phys. 40,(1995),389
9.A.G.Sitenko, A.G.Zagorodny, P.Schram. Kinetic Description of Electromagnetic Fluctuations in a Plasma with Large Scale Random Motions. In: Europhys. Conf. Abstr. Volume 19C, part IV,p.273

...Alfven turbulence excitation by the external electric field $\mathbf{E}_0 \parallel \mathbf{B}_0$ in a low-β magnetoplasma

Yurii M. Voitenko
...tment of Space Plasma Physics, Main Astronomical Observatory,
Golosiiv, Kyiv-22, 252650, Ukraine

...oduction

...Alfvén wave (KAW) is the Alfvén wave with a large transversal wave vector ...onent, $k_\perp \gg k_z$ ($\mathbf{k}_\perp \perp \mathbf{B}_0$), so that the perpendicular wavelength become com... to the ion gyroradius, $\rho_i = V_{Ti}/\Omega_i$ (Hasegawa & Chen 1976). KAWs become ...mainly due to the extensive investigations by A. Hasegawa for the kinetic prop... of the Alfven waves, important in processes of plasma heating and current drive ...Hasegawa 1985 and references therein). It has been explicitly shown that finite ...yroradius and electron inertia effects produce E_z in Alfven waves, which brings ...collisionless wave-particle resonant interaction, resulting in the enhanced plasma ...ing and anomalous transport under the presence of kinetic Alfven waves. It was ...ecognized that due to the unique combination of their MHD scales along B_0 and ...ic properties, KAWs play an important, often major role in the dynamics of the ...laboratory and space plasmas, and excitation of KAWs by a resonant mode con... and by the drift wave instability has been widely discussed. At the same time, ...ite the central role of the macroscopic (usually accompanying by electric current) ...field in the plasma dynamics, there are only a few works on the current-driven ...instability in the earth's magnetosphere (Voitenko, 1989) and in the solar corona ...oitenko, 1995). It has been shown that in a wide range of the plasma parameters the ...rrent-driven KAW instability has lower threshold then ion-cyclotron and ion-acoustic ...tabilities, discussed before.

In the present work we study excitation of the KAW turbulence, produced by the ...o effects of the macroscopic electric field, discribed in the following section. The ...sideration is restricted to the plasma β lying in the range $10^{-3} < \beta < 1$, typical for ...many cases of laboratory and space plasmas.

2. Kinetic Alfven Instability in the Electromagnetoplasma

We take into account two processes, caused by $\mathbf{E}_0$ in the plasma: (i) (macroscopic) bulk electron motion with the velocity V_e, ($V_e = V_{Te}(E_0/E_{Dr})$ for sub-Dreicer electric fields, $E_0 < E_{Dr}$, and (time-dependent) $V_e = eE_0t/m$ for $E_0 > E_{Dr}$) and (ii) (microscopic) individual particle acceleration, $V_z = eE_0/m_{e,i}$, between collisions. The first one will be taken into account by introducing V_e to zeroth-order electron distribution function, while the second - by introducing $V_z = eE_0/m_{e,i}$ into the Boltzman equation for electrons and ions.

Considered wave dynamics the first one is well-known destabilising effect, caused by a free energy in moving electron component. We call the influence of E_0 on waves via (quasy-) steady electron motion as SME-effect ('steady motion E_0-effect'). SME-effect may lead to the various current-driven instabilities, the most favorable of which was regarded kinetic instabilities of ion-cyclotron and ion-acoustic waves. But, as was shown by Voitenko (1989, 1995), in many cases of magnetoactive plasma current-driven instability of kinetic Alfven waves dominates.

At the same time the influence of the second effect on the plasma wa... known, despite a series of works concerning electrostatic waves (see Kryshtal'... 1995 and references therein). Also there are only a few works about electro... whistler mode (see Das & Singh 1982 and references therein).

In the present work the influence of ambient electric field on the low-f... electromagnetic KAWs through the free particles acceleration between collisio... vestigated for a first time. We call this as 'accelerated (particle) motion ... (AME).

3. Dispersion relation and growth rate

Taking equilibrium distribution functions to be Maxwellian for ions and V_z-shi... V_0 Maxwellian for electrons, the calculations of the charge density and current ... as velocity space integrals by use of perturbed distribution function (Voitenk... are straitforward. For the magnetically non-compressible KAW we use quasine... equation and Ampere's law in the z direction:

$$\sum_\alpha e_\alpha n_\alpha = 0; \qquad \sum_\alpha j_\alpha = \frac{k^2 c}{4\pi} A_z.$$

For the low-frequency nontrivial solution of this system, $\tilde{\phi}$, $\tilde{A}_z \neq 0$, $\omega < \Omega$, we ob... well-known KAW dispersion

$$V_k = \omega/k_z = V_A K(\kappa) \geq V_A,$$

and quasilinear increment (decrement)

$$\gamma = \omega(\kappa/K)^2 (T_e/T_i) V_{Te}^2 \sum_\alpha (n_\alpha/n_0)(m_e/m_\alpha)[\pi(\partial \bar{f}_\alpha)/\partial V_z)_{V_z=V_k} + \delta_{B\alpha}].$$

Here $K = K(\kappa) = \kappa[1/(1-\Lambda_0) + T_e/T_i]^{1/2}$, $\Lambda_0 = I_0(\kappa^2)\exp(-\kappa^2)$, $\bar{f}_\alpha = 2\int dV_\perp V_\perp J_0^2(k_\perp V_\perp/\Omega_\alpha) f_\alpha(V_z, V_\perp)$, $\kappa = k_\perp \rho_i$ and $I_0(\kappa^2)$ is the modified Be... function. The terms

$$\delta_{E\alpha} = \sqrt{\pi/2}(E_0/E_{k\alpha}) V_{T\alpha}^2 \int dV_z (V_z - V_k)^{-1} \partial[(V_z - V_k)^{-1} \partial \bar{f}_\alpha/\partial V_z]/\partial V_z, \quad (4)$$

where $E_{k\alpha} = \sqrt{\pi/2} k_z T_\alpha/e_\alpha$, represent the influence of ambient electric field on the wave growth through the particles acceleration by E_0 between collisions (AME-effect). In above expressions we keep the possibility that in the resonant regions of the velocity space distribution functions deviate from equilibrium ones, which does not effect the waves dispersion but change their growth (or damping) rate due to SME-effect.

From (4) with Maxwellian $f_{e,i}$ it follows that for $T_e/T_i < 0.7 V_A/V_{Ti}$ dominating are electron terms, and electron AME-effect

1) supports current-driven instability of the KAW, caused by SME;

2) usually less important than SME for the KAW instability, but becomes significant near the instability threshold;

3) may lead to KAW growth if V_{0z} for the some reason is not developed.

The growth rate of the E_0-driven KAW instability is

$$\gamma = \sqrt{\pi/8}\omega(\kappa^2/K)(T_e/T_i)(V_A/V_{Te})(E_0/E_{cr} \quad 1), \quad (5)$$

...on condition for instability is roughly $E_0 > E_{cr}$, where threshold E_{cr} is

$$E_{cr} = \frac{V_k}{V_{Te}} \frac{E_{Dr} E_{ke}}{E_{Dr} + E_{ke}}. \tag{6}$$

$\omega/k_z \approx V_A(1+2\kappa^2)^{1/2}$ is the phase velocity of KAW along B_0, $\kappa = k_\perp \rho_i$, ... V_{Te} are Alfven and electron thermal velocities. The electric field scales of ...ility, determined by E_0-effects, are $E_{ke} = \sqrt{\pi/2} k_z T_e/e$ for AME and E_{Dr} for ...tting $k_z \to 0$ one obtains AME thresholdless instability, $E_{cr} \to 0$, i.e. any E_0 ...lead to wave growth. In fact k_z is restricted by minimal k_z^*, determined by finite ...L_z: $k_z^* \sim L_z^{-1}$ for $eE_0/m_e V_{Te}^2 < L_z^{-1}$, or by condition $k_z^* \sim eE_0/m_e V_{Te}^2$ for ...$> L_z^{-1}$.

...AME-dominated are long-λ_z KAWs, while SME-dominated are short-λ_z KAWs ...Ω/V_A, it is possible that both instability kinds are simultaneously developed, ...to different types of KAW turbulence.

...low-β plasma the threshold of SME KAW instability, $E_{0cr}/E_{Dr} \approx 0.1$, is well ...of the ion-acoustic, $E_{0cr}/E_{Dr} \approx 0.8$, and ion-cyclotron, $E_{0cr}/E_{Dr} \approx 0.3$, ...ities, discussed before.

Weak Kinetic Alfvén Turbulence

...to the MHD Alfven waves, KAW's undergo strong three-wave interaction, ...ining their amplitudes and spectra. To study KAW turbulence we have calcu... ...ticle number density and current density in fluctuating wave fields by use of ...econd-order distribution function (Voitenko 1996). Consequent substitution ...em (1) leads to the kinetic equations for Fourier amplitudes of of the KAWs ...etic potential:

$$(-\omega^2 + \omega_1^2) A_1 = \sum_{2,3} U_{1,2,3} A_2 A_3 \tag{7}$$

...atrix element of three-wave interaction

$$U_{123} = \frac{i\omega_1 V_A}{2B_0} \left(K_3 + \kappa_3^2 \frac{K_1}{\kappa_1^2} + \kappa_2^2 \left(\frac{K_1^2}{\kappa_1^2} - \frac{T_e}{T_i} + \frac{T_e}{T_i} K_3^2 \right) \frac{1}{K_1 K_2 K_3} \right)_s [\mathbf{k}_2 \times \mathbf{k}_3]_z. \tag{8}$$

...e subscripts 3, 2, 1 mean $\mathbf{k}_3$, $\mathbf{k}_2$, $\mathbf{k}_1(=\mathbf{k}_3 + \mathbf{k}_2,)$ correspondinly, and $(2,3)_s \equiv (3,2)$.

...ing asymptotics of $K(\kappa)$ in above expressions, we get increment for the resonant ...y instability

$$\gamma^{NL} \approx \Omega_i \beta_i^{-1} (B_k/B_0) \kappa^\nu, \tag{9}$$

...here $\nu = 3$ for $\kappa < 1$ and $\nu = 2$ for $\kappa > 1$. Hence, KAW will grow in accordance with ...(9) till amplitude riches nonlinear saturation value, B_k^s/B_0, determined by condition ...$\gamma = \gamma^{NL}$:

$$B_k^s/B_0 \approx (\gamma/\Omega_i) \beta_i \kappa^{-\nu}. \tag{10}$$

...oting that both matrix element of three-wave interaction (8), and dispersion (2) ...become uniform functions of the wavevector components in the limits of strong ($k_\perp \rho_i \gg 1$) and weak dispersion ($k_\perp \rho_i \ll 1$), we applied Zakharov's (1984) technique. to KAWs ...with dispersion (2) and matrix element of three-wave interaction (8), we found the ...weak turbulent spectra of the E_0-driven KAW turbulence. As a result, power-law Kolmogorov-type spectra of the weak KAW turbulence have been found: 1) $W_k \sim$

$(k_z)^{-1/2}(k_\perp)^{-4}$ and 2) $\sim (k_z)^{-1/2}(k_\perp)^{-5}$ in the long-wave limit ($k_\perp <$
$\sim (k_z)^{-1/2}(k_\perp)^{-3}$ and 4) $\sim (k_z)^{-1/2}(k_\perp)^{-3.5}$ in the short-wave limit ($k_\perp >$

It is interesting to note that spectra $\sim (k_\perp)^{-5}$ are often observed in
plasmas with intense field-aligned currents (see, e.g., Labelle and Treumann
supply a strong evidence of nonlinear spreading for long-wave KAW spectra
by the marginally unstable currents. This also indicate that current is limited
anomalous resistivity, produced with KAW-electron interaction (otherwise
KAW turbulence would be generated).

4. AME Kinetic Alfvén Instability

In the limit $k_z \to k_z^*$ AME instability is dominant. It has threshold E_{cr}
growth rate

$$\gamma = \sqrt{\pi/8}\kappa^2(T_e/T_i)(V_A/V_{Te})(\omega_E/K - \omega_A^*),$$

where $\omega_E = eE_0/m_eV_{Te}$ and $\omega_A^* = k_z^*V_A$ is Alfvén frequency. The maximal

$$\gamma_m = \sqrt{\pi/124}(1 + T_i/T_e)^{-1}(V_A/V_{Te})(\omega_E/\omega_A^*)\omega_E \approx 0.1\omega_E,$$

growth rate attains with

$$\kappa_m = \frac{V_{Te}/V_A}{2\pi(1 + T_e/T_i)}.$$

Since $\kappa_m \approx 2 - 5$ for typical plasma parameters, we can conclude that KAW
strong dispersion is excited by AME-effect. Nonlenear interaction spreads the
source located at $k_\perp \approx (2 - 5)\rho^{-1}$ and turbulence with spectrum $\sim k_\perp^{-3}$ should
excited in a weak electric field. Such spectra are often observed in Tokamaks and
lead to the $\gamma = 0.704$ scaling law for a diffusion coefficient (see Misguich & Reuss

As it follows from our consideration, the E_0-driven turbulence of KAW's should
the favorable turbulence in many cases of the space and laboratory electromagnetic
plasmas.

Acknowledgments

I wish to thank the company 'Drenaj' and personaly Director Badio M. F. for
financial support.

References

1. Hasegawa, A., & Chen, L.: 1976, *Phys. Fluids* **19**, 12, 1924.
2. Hasegawa, A.: 1985, *Advances in Physics* **34**, 1, 1.
3. Labelle, J. and Treumann, R. A.: 1988, *Space Sci. Rev.* **47**, 175.
4. Misguich, J. T., & Reuss, J.-D.: 1996, this Proceedings.
5. Voitenko, Yu.M.: 1989, *Super-Alfvén beams and kinetic Alfvén waves in space plasma*, Preprint 89-9P of Institute for Theoretical Physics, Ukraine, Kiev.
6. Voitenko Yu,M.: 1995, *Solar Phys.* **161**, 197.
7. Voitenko Yu,M.: 1996, this Proceedings.
8. Zakharov, V. E.: 1984, in: Handbook of Plasma Physics, Vol. 2, eds. A. A. Galeev and R. Sudan, Energoatomizdat, Moscow.

H

HIGH INTENSITY LASER PRODUCED PLASMAS AND INERTIAL CONFINEMENT

NEAR MODULATION OF STRONG ELECTROMAGNETIC WAVE IN WEAKLY INHOMOGENEOUS PLASMA

G.N.Burlak, V.V.Grimalsky, K.Ishkabulov,
National University named after T.Shevchenko 252022, Kiev, Ukraine
and N.Ya.Kotsarenko
Institute of Geophysics, UNAM, Coyocan 04510, Mexico DF, Mexico

ear interaction of strong electromagnetic (EM) radiation with real plasma, it is into account long-living, comparatively with duration of electromagnetic pump elties of density. The plasma region between peaks of density (local well) becomes with semi-transparent boundaries, where, as a result of parametric interaction with EM th of amplitude of Langmuir wave takes place with fast storage of nonlinear effects. me that in the vicinity of smooth bottom of well with the length L the EM waves with ω_2 resonantly interact with Langmuir one with difference frequency $\Omega = \omega_1 - \omega_2$, $\int dz<1$. Suppose that $\Omega>\omega_p$ where ω_p is the plasma frequency; in this case, out of the the parametric coupling conditions are not satisfied, and passed Langmuir waves are ted. In boundless system under overcritical conditions, the instability occurs here [1,2], se the velocities of waves are sharply different, this instability leads to amplification of slow and forming of three-wave solitons, like [3].

e that in such system except parametric nonlinearity, the own nonlinearity of Langmuir is essential. In fact, this nonlinearity appears after the growing of amplitudes and leads to tial instability and, later, to forming of NSE solitons (NSE - nonlinear Schroedinger). Mutual influence of both pointed above processes, additionally with dissipation and non-ection from boundaries, can be the reason of complex spatio-temporal soliton dynamics, the in giant modulation of passed radiation.

Because of finite value of inhomogeneity, the Langmuir wave is partially reflected at the edges 0, L. Reflection coefficients $R_{0,1} < 1$. In the simplest considered lower case, the backward (reflected) Langmuir wave does not interact with EM pump, because of absence of matching conditions, but it is subject to self-interaction and cross-modulation that is due to direct wave.

Neglecting on the parameter $(v/c)<<1$ (v and c are the velocities of Langmuir and EM wave, respectively) by temporal derivatives in equations for EM waves, one can write down the dimensionless equations for complex amplitudes as:

$$[\partial_\zeta + \partial_\tau + ig\,\partial^2_\zeta + i\alpha\,(|A_3|^2 + 2|A_4|^2) + \gamma\,]\,A_3 = A_1A_2^*;$$

$$[-\partial_\zeta + \partial_\tau + ig\,\partial^2_\zeta + i\alpha\,(2|A_3|^2 + |A_4|^2) + \gamma]\,A_4 = 0;$$

$$\partial_\zeta A_1 = -A_2A_3; \quad \partial_\zeta A_2 = A_1A_3^*;$$

(1)

with boundary and initial conditions $A_3(0,t)=f_3(t)+R_0A_4(0,t)$, $A_4(l,t)=R_lA_3(l,t)$, $A_3($ $A_1(0,t)= f_1(t)$, $A_2(0,t)= 0$. Here $\partial_\zeta =\partial/\partial\zeta$, $\partial_\tau =\partial/\partial\tau$; A_1 and A_2 are amplitudes of pump and EMW, A_3 and A_4 are amplitudes of direct and reflected Langmuir waves, $\zeta=z/l_n$ and $\tau=$ spatial and temporal variables, respectively, $l=L/l_n$, $f_{1,3}(t)$ are determined by input amplitu $\zeta=0$, $\gamma =\Gamma l_n$, Γ is the dissipation coefficient, l_n is nonlinear spatial scale, g is dispersion parame parameter of own Langmuir nonlinearity. Absorption of EM waves in the region of transpar assumed small. In this problem, the parameter γ has the sense of overcriticity parameter. In t of weak initial value of Langmuir wave (that is equivalent to α, g = 0 in (1)), the relative p waves is fastly established, and wave amplitudes may be considered as real. In this case, takin account relations $A_1^2+A_2^2=f_1^2(t)$, $A_1=f_1(t)\cos(\varphi)$, $A_2=f_1(t)\sin(\varphi)$, $A_3=\partial\varphi/\partial\zeta$, , one can redu order of set of equations (1). After the exclusion of backward wave, the closed equation for A_3 the following form:

$$\left(\frac{\partial}{\partial\zeta} + \frac{\partial}{\partial\tau} + \gamma\right) A_3 = 0.5\, f_1^2(\tau)\,\sin(2\varphi), \quad \varphi = \int_0^\zeta A_3(\zeta,\tau)d\zeta \qquad (2)$$

It is essential that the boundary modulation of pump is presented in (2) as variable coeffi near nonlinearity, this gives the possibility to control the regimes of nonlinear system.

Note that by means of substitution $u,v=b(\zeta-\tau)\pm(1/b)\int g^2(\tau)d\tau$, $\psi=2\varphi$, b=const, the equation can be rewritten as sine-Gordon-like equation:

$$\partial^2\psi/\partial u^2 - \partial^2\psi/\partial v^2 + [\gamma\, b/g^2(\tau)]\,(\partial\psi/\partial u - \partial\psi/\partial v) = \sin(\psi) \qquad (3)$$

this allows to interpret the stationary excitations in the system as solitons under $\gamma= 0$.

But in bounded medium this fact does not simplify the analysis because the boundary condi must be satisfied in moving boundaries. Additionally, the presence of dissipation and non-ideal reflection do not give the possibility to use the features connected with the full integrability of equation [4,5]. The complexity of dynamics is also due to the existence in this model non-stati solutions with self-similarity $\sim(u^2 - v^2)$ which is quite different from self-similarity of travelling wa $\sim(u \pm v)$ [4].

Let us determine from (2) the instability conditions assuming $|A_3|, |\varphi| \ll$ and $\sim \exp(i(\omega\tau-k\zeta))$. After simple calculations, the threshold condition can be presented as $\gamma <$ $-0.75\,\beta + 0.25\,\mathrm{Im}\,\Delta^{1/2}$, where $\beta=-\ln(R^2)/l > 0$, $\Delta=(2n\pi/l + i\beta)^2 - 8$, n=0,1,2...; $R^2 = R_0R_l$. U small $\beta<<1$ it must be $2^{1/2}l/\pi>n$. The mode with n=0 has minimal threshold (aperiodical instabilit $\beta<<1$ where $\gamma_{th}\approx0.707$. For the general case, under n=0, one can rewrite the threshold condition dimensional form:

$E^2_{s0} > E^2_{th} = (\alpha / Kk_2L^2)\ (2\Gamma L + \ln R^{-2})\ (\Gamma L + \ln R^{-2})$ (4)

...as a consequence from (4), that under the decreasing of reflection, the threshold ...singularity, this is due to the absence of own non-local excitations under $R^2 = 0$, ...portation of waves out of the region. At initial stage when the wave amplitudes are ...small noisy values, the parametric coupling with EM field is the most essential. But, ...ing of wave amplitudes, the modulational instability becomes more important (α, $g \neq 0$) ...the changing of wave phases and to local parametric mismatch. At this stage, it is ...into account both mechanisms of nonlinearity simultaneously.

...is in complicated way to derive the analytical solution of nonlinear set (1) with ...itions, in our work the computer simulations of equations (1) were made under ...meters. This gives the possibility within the unified approach to investigate all stages of ...rting from initial instability and then including the developed nonlinear regime.

...pulse had quite smooth fronts, this allowed to observe different dynamic regimes. In ...the following values were used: $f_1(\tau)=\exp(-a(\tau-1/a)^2)$, $a=0.0025$ was Gaussian pulse ...powerful EM wave, the noise $f_3(t)$ was simulated by random values uniformly distributed ...val $[0, f_{30}]$, $f_{30}=10^{-4}$, $A_{30}=0$, $l=5$ under different a, g, R^2 and values of overcriticity ...from 0.7 to 0.001. The simulations were made by numerical scheme of high order of ...error was controlled by means of the subdivision of step of grid.

...dynamical regimes were determined in our calculations, in dependence on values of ...parameters, namely the establishing of constant amplitude of Langmuir wave, and also ...powerful oscillations in the output of the system even under comparatively low ...threshold. The typical pictures of spatio-temporal dynamics are presented in Figs.1.

...the boundary values are quite small, in our calculations the Langmuir wave noises with ...plitudes are established in undercritical conditions ($\gamma > \gamma_{th}$) in the output of the system. In this ...shape of pump pulse is practically unchanged.

...ready under weak overcriticity, the output signal begins to be increased fastly, and wide ...pulse of Langmuir wave is formed in medium. This pulse moves slower during the passing ...output and it is stopped near the boundary. Such regime corresponds to establishing of ...generation of Langmuir wave. Note that already at this stage $\varphi(l) \sim \pi/2$ and, therefore, it is ...to neglect the nonlinearity of parametric interaction.

...further increase of overcriticity, the stationary regime becomes unstable, and the more ...dynamics is developed in the system. After the birth, with the increasing of amplitude, ...is decelerated, then it tends to the stationary shape and fastly leaves the region. Thus, ...begin to irradiate, but, as the result of partial reflections, they come into the input again. ...of dissipation, non-ideal reflection, and own nonlinearity, the stationary shape of Langmuir ...does not preserve, the process of forming of solitons starts from new phase and, for the first ...must lose coherency. But our calculations show another picture.

For not so long regions, the re-reflected pulses make the synchronous influence... temporal correlation occurs in the system and process of soliton generation demonstrates ... repetition. As a result, the regular oscillations of amplitudes appear in the output, and ... subjected by the giant periodic modulation (see Figs. 1a).

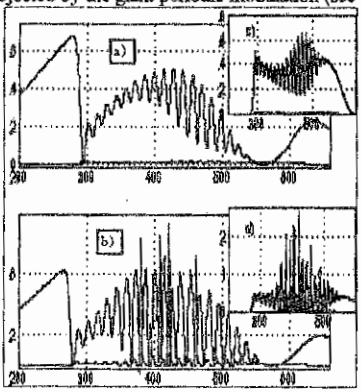


Fig.1 Modulation of EM pump wave $|A1(l,\tau)|^2$ in the output as temporal functions under a) R=0.5, g=0.1; b) R=0.55, g=0.2, and also α=0.4, γ=0.1. In the insertions c), d) the corresponding amplitudes of Langmuir wave $|A_3(l,\tau)|^2$ are presented.

For $R^2 \propto 0.5$, this dynamics is ... the moderate overcriticity. But, when ... Langmuir pulses was greater than critical ... narrowing and amplification of soliton ... Figs. 1b). Starting from this moment, the ... mechanism (NSE) dominates, and the ... parametric nonlinearity reduces to ... amplification with effective coefficient ... reason of strong changing of ... synchronism mismatch with pump. Be... soliton solution for NSE is $\exp(\gamma_e\zeta)/\mathrm{ch}(\ldots$ ...)] in the system with weak amplification ... corresponds qualitatively to dynamics ob...

Under greater overcriticity, the both ... of nonlinearity begin to play an equal ro... process of forming of solitons becomes ... tangled. In that case, the modulation of ... pump wave demonstrates the chaotic fea...

References.

1. Krall, N., Trivelpiece, A., Principles of plasma physics, McGraw-Hill Book Co (1973), 470...
2. Cross, M.C. and Hogenberg, P.C., Rev. Mod. Phys., 65 (Pt.2), 851 (1993).
3. Burlak, G.N., Grimalsky, V.V., and Kotsarenko, N.Ya., Sov. Phys. - JETP, 63, 872 (1986)...
4. Lamb, G.L., Jr., Elements of Soliton Theory, Univ. of Arizona (1980), 360pp.
5. Zakharov, V.E., Manakov, S.V., Novikov, S.P., and Pitaevskii, L.P., The Theory of Soliton... Inverse Scattering Method, N.Y., Consultants Bureau (1984), 320pp.
6. Giacomelli, G., Meucci, R., Politi, A., and Arecchi, F.T., Phys.Rev.Lett., 73, 1099 (1994)...
7. Molchanov, O.A., Low Frequency Waves in Near-Earth Plasmas, Moscow, (1985), 270pp. ... Russian)
8. Gdalevich, G.L., Gubskii, V.F., Izhovkina, N.I., and Ozerov, V.D., Kosmicheskie Issledovan... 32, 98 (1994).

ERMINATION OF APPEARANCE AND DEVELOPMENT CONDITIONS FOR PLASMAS PLUME-SOURCE PRODUCED BY HIGH INTENSITY LASER: THEORY AND NUMERICAL EXPERIMENT

M.A.Razumova and **A.D.Suprun**

Department of Physics, Kyiv T.Shevchenko University,
prospekt Glushkov 6, 252022, Kyiv, Ukraine

ppearance and development of plasmas corrosive plume may be called a cen- in variety of all problems accompanying the material laser treatment both ve and destructive.

his paper we discuss the problems of providing of conditions for sublimative plume in connection with the dynamics of plume-source and formation of crater.

quite evidently there is a time period between a beginning of pulse influence on a beginning of surface destruction. This time period usually does not take into ation. However, it is necessary in order to reach the boiling temperature T_b (or sublimation temperature) and is of principle for strict formulation the criterion ive destruction process (i.e. when liquid phase have no time for formation). The perature dynamics from some initial value T_0 to the boiling (sublimation) tem- being considered, a basis for the problem is the corresponding edge-boundary problem which in fact reduces to the third edge boundary problem. On infinity the is set and equal to the initial temperature T_0. At the boundary $z = 0$ which one sets an energy flux having form of a Π-like pulse of duration τ_0. In general parameters of material are not allowed to assume constants or linear functions on ture and this considerably complicates the problem which at first sight seems a ly standard problem of mathematical physics. Having investigated this question [1] and liquid [2] phase, we have succeeded in showing that the material heat ivity dependence on temperature in the range from normal temperature to the temperature evidently (the investigation is carried on) with good accuracy (the does not exceed 10%) can be approximated the following equation:

$$\lambda = \lambda_0 + \lambda_1 (T_m/T)^2,$$

T_m is the melting temperature, λ_0 and λ_1 are the known parameters which depend rial parameters (density, specific heat, sound velocity etc.). For $T_0 \ll T_m$ the

second term can change nearly on two orders. For $T_0 \leq T_m$ and the correspondi... between λ_0 and λ_1 the dependence of λ on T can be sufficiently weak and negl... we just restrict ourselves to such case $\lambda = const$ to be concentrated on a... of obtaining the plume-source formation threshold and the criterion of the su... surface destruction process.

The second, in our opinion seemingly the less principal peculiarity of thi... is taking into account an interaction between radiation and volume (the real ab... but not only the surface interaction (the case of ideal absorption). And what's m... radiation intensity used can lead to that the interaction between radiation and... turn out to be essentially nonlinear [3] considerably affecting the plume- source for... threshold and the criterion of sublimative process.

We first restrict ourselves to the simplest case namely an approximation... surface absorption which is illustrative enough and besides appropriate enough... als, strongly absorbing semiconductors and insulators with width no less 1 μm... irradiation by the laser pulse of optical and near ranges.

The simplest dependence of surface temperature on the time obtained with the... approximations is the following:

$$T_s(t) = T_0 + \frac{2q_s}{\sqrt{\pi\lambda\rho C}}\left[\sqrt{t} - \Theta(t-\tau_0)\sqrt{t-\tau_0}\right], \qquad (1)$$

where q_s is the irradiated energy flux, ρ is the material density, C and λ -the... heat and the heat conductivity, respectively, $\Theta(x)$ - the step function which equal... $x > 0$ and 0 for $x \leq 0$.

An analysis of this dependence (or analogous one for more general case) allows... find all the characteristics and criteria of interest. At first one can find the energy thr... for the plume-source appearance. This threshold is defined by the condition $T_s(\tau_0) \geq ...$ (the point $t = \tau_0$ always corresponds the maximum for both this and analogous... general dependence), whence it follows:

$$q_s \geq q_s^b, \quad \text{where} \quad q_s^b \equiv \frac{\sqrt{\pi\lambda\rho C}(T_b - T_0)}{2\sqrt{\tau_0}} \qquad (2)$$

Then one can obtain the criterion for the sublimative destruction process (... when liquid phase have no time for formation). It is determined by the general condition... $t_\phi \geq t_1 - t_2$ where t_ϕ - the time of liquid phase origination and the times t_1 and t_2 ... the roots of equation $T_s(t) = T_m$. This equation is evidently to have the roots only when... a maximum value $T_s(\tau_0)$ exceeds T_m or when the flux q_s satisfies the inequality $q_s > q_s^m$... where the q_s^m has the expression analogous to the q_s^b (2) in which T_b is replaced by T_m... Solving the equation $T_s(t) = T_m$ in respect to t, we obtain the criterion searched in the...

$$t_\phi \geq \tau_0\left(\xi + \frac{1}{2} - \frac{3}{16\xi}\right), \qquad \text{where} \qquad \xi \equiv \frac{q_s^2\tau_0}{\pi\lambda\rho C(T_m - T_0)^2} \tag{3}$$

Our investigation is directed to find out the physical structure of liquid time t_ϕ in order to use this criterion of sublimative process to prog- material treatment regime. However, this relation has another interesting espect. For the case when the destruction is absent but the surface get heat erature exceeding the melting point ($q_s^m < q_s < q_s^b$), the latest inequality can criterion for the experimental determination of the time t_ϕ . An idea of this is simple enough. It consists in the following. Varying the q_s, τ_0 and T_0 under of material one can get that during and after pulse influence the liquid originating (melting stops) or *vice versa* starts originating (melting starts). itting in the latest inequality the parameters q_s, τ_0 and T_0 corresponding to of the beginning (or stopping) of melting, one can evaluate the value of liquid ation time t_ϕ.

ase of nondestructive surface treatment by laser irradiation ($q_s^m < q_s < q_s^b$) has some more interesting aspect potentially useful for controlled fusion. sidered as strict inequality it means that the correspondent regime provides of material (the solid state) in overheat state during the time period when Using the corresponding periodicity of pulses one can reach that the material the overheat state in periodic regime so long as it needs existing on the whole temperature exceeding the melting temperature T_m without transforming in This regime can be used to prepare a target to effective transformation in uid with the given parameters (pressure, density, convective velocity, ionization temperature etc.)

Now we fix our attention on the determination of two characteristics especially for modeling the plume dynamics. One of them is the effective pulse duration respect to the destruction process. It is determined by equality $\tau_e = \tau_0 - t_3$, where the less root of equation $T_s(t) = T_b$. Solving this equation one can obtain:

$$\tau_e = \tau_0(1 - \frac{q_s^b}{q_s}),$$

is the threshold value of flux (see (2)), and t_3 is the initial time of destruction Since the destruction process are not stopped at the same time with the pulse ($t = \tau_0$) and carries on actually up to decreasing of temperature to the melting the second characteristic being of interest is aftereffect time. This time was defined it includes the pulse duration. Holding on this definition, we find $t_4 = t_1 - t_3$,

where the time t_1 is the greater root of the equation $T_s(t) = T_m$ aforesaid
(see (3)) the t_1 is determined by equality

$$t_1 = \tau_0(\xi + \frac{1}{2} + \frac{1}{16\xi}).$$

We also have obtained the barodynamical system of equations which
corrosive crater and plasmas plume dynamics. In particular for the plume
corrosive crater the system consists of the two connected equations, one of
conditionally call the plume-source dynamics equation and another - the corr
development equation. Because of the cumbersome expressions they are not
ever, it should be noted that the equation for plume-source is directly depend
of the four parameters aforesaid, namely, the destruction threshold q_s^b, the effe
duration τ_e and the aftereffect time t_4. Also this system indirectly depends on
rion of sublimative process, since it does not include the mechanisms of melt
simplest case ($1D$-approximation) of the equation system solution has been co
[4].

In conclusion, we cite the solution for the surface temperature dynamics
of finite absorption coefficient $k < \infty$ (the solution (1) corresponds to the appro
$k = \infty$):

$$T_s(t) = T_s^{(0)}(t) + \frac{q_s}{\lambda k}\left[J(ak^2t) - \Theta(t-\tau_0)J(ak^2\{t-\tau_0\})\right]$$

where $a \equiv \lambda/\rho C$ is the thermal conductivity, the term $T_s^{(0)}(t)$ coincides with
term of Eq.(1) and the function $J(r)$ is defined by the equality

$$J(r) \equiv \exp(r)\mathrm{Erfc}(\sqrt{r}) - 1, \qquad \text{where} \qquad \mathrm{Erfc}(x) = \int_x^\infty \exp(-t^2)dt.$$

Analytically one can only find the threshold. The value (2) is found to be the
boundary of this threshold and to be always increased when the absorption coeffic
is decreased.

References

[1] G.Leibfried. Gittertheorie der Mechanischen und Thermischen Eigenschaften
Kristalle. Berlin, 1955.

[2] E.I.Khar'kov, V.I.Lysov, V.E.Fedorov. Thermodynamics of metals. Kiev. 1982.

[3] M.A.Razumova, A.D.Suprun, L.V.Shmelyova. Functional Materials /to be publish

[4] A.D.Suprun, S.Ya.Shevchenko. Functional Materials. 1995.V.2,N2. P. 191-193

...stigation of the expansion of an aluminum micro–pellet cloud in a hot plasma

...J.S. Bakos[1], B. Kardon[1], S. Kálvin[1], G. Kocsis[1], G. Mank[2], G. Petravich[1], A. Pospieszczyk[2], G. Veres[1]

...Institute for Particle and Nuclear Physics,
...-1525 Budapest, Hungary
...Plasmaphysik, Forschungszentrum Jülich, Ass. Euratom–KFA,
...D-52425 Jülich, Germany

...micro-pellets (10^{14}–10^{15} atoms), serving as temporally and spatially well ... of impurities, were injected into tokamak plasmas and the expansion of ... observed using a two dimensional framing CCD camera and other optical ... The aim of the investigations was to get knowledge on the local radial ($B_\perp$) ... transport of impurities. As these pellets contain not more than 10^{15} ... not represent a global perturbation to the target plasma, and this way both ... and transport processes can be analyzed in more clear circumstances than ... mm sized pellets.

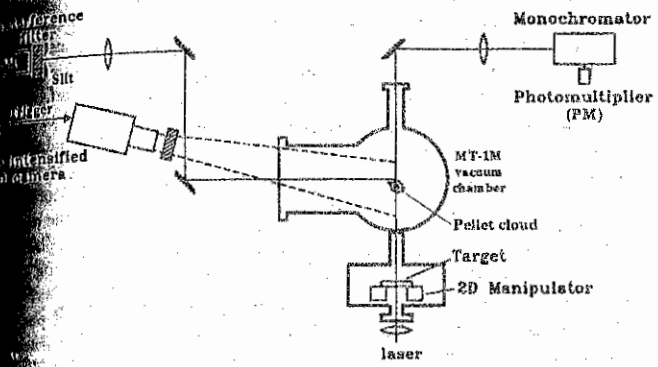


Fig. 1. Experimental arrangement at the MT-1M tokamak.

...experiments presented here were performed on the MT-1M tokamak, the arrange... shown in *Fig. 1.* The micro-pellets were accelerated up to 1 km/s velocity by an ... pulse[1], and were injected radially into the plasma, where they were com... ablated after covering a distance of 5-7 centimeters. The time evolution of the ... emitted by Al atoms, Al^+ or Al^{++} ions during the whole ablation process was ... along the pellet path by a photomultiplier. An image intensified CCD camera ... with different interference filters made two-dimensional pictures of the ablation ... Another photomultiplier collected light only along a small portion (a few mm) of ... path which triggered the exposure of the CCD camera when the pellet passed ... the radial position viewed by this photomultiplier.

$B_\parallel$ expansion of the pellet cloud. Time integrated pictures of the pellet ... taken by the CCD camera armed with different interference filters. The da... lengths were 3944, 6243 and 5697 Å for Al atoms, Al^+ and Al^{++} ions, respecti... a filter centered at 5460 Å it was verified that the radiation is not continu... radiation.

The toroidal width of the pellet traces at different line radiations was det... the CCD camera pictures. For $40 \times 40 \times 10 \mu m^3$ size pellets the Al atom trace w... 1 mm wide. The FWHM of the radiation trace was about 3 mm and 10 mm ... and Al^{++} ions, respectively. For $11 \times 18 \times 5 \mu m^3$ size pellets the atomic trace ha... width as in the case of the larger pellets, while the ion FWHMs were approxima... 60 mm, respectively.

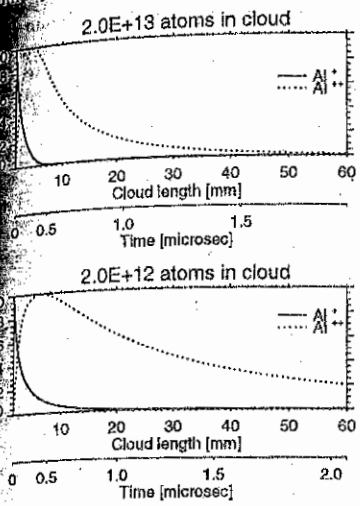
The ablation of the micro-pellets was calculated by a code based on the N... Shielding (NGS) [2] model. It was found, that the shielding of the incident ele... flux does not exceed 30-40 %. Calculated penetration depths are in good agre... experimental observations. The calculated diameter of the atomic cloud (ioniza... was found to be determined by the material of the pellet and the ionization b... atoms in the background plasma. This way the atomic cloud size is indepen... pellet diameter, in agreement with the experimental findings.

To understand the extension of the ionic radiation along the magnetic field ... one-dimensional Lagrangian model was constructed for the cloud expansion. T... treats the pellet cloud as a cylindrical cell, and all parameters (densities, tem... ... etc) are assumed to be constant inside the cell, as it is done in Ref. [3]. A... the cell contains only singly ionized Al ions, their number is set equal to the n... atoms ablated while the pellet covers a distance of the atomic cloud diameter. ... $B_\perp$ diameter and $B \parallel$ length of the cylinder are set equal to 1 mm. Due to the lo... of material deposited in the cell, the pressure of the cloud cannot distort the ... field. The expansion is assumed to be only along the field lines, thus the diame... cylinder is fixed. The cloud electrons become heated by the background plasma ... and the increasing pressure of the cloud electron gas expands the cell along the ... Temperature dependent ionization both by background plasma and cloud elect... taken into account. The model calculates the cloud $B_\parallel$ size, and different parame... n_e, T_e) in it as a function of time. *Fig. 2.* plots the product of the ion fraction ... the total electron density (cloud+background plasma) as a function of cloud lengt... pellet sizes. The time scale is also plotted for reference. The non equidistant ... indicates the accelerating expansion of the cloud. The cloud length where the cu... below 50 % is compared to the experimentally determined radiation FWHMs, ...

Although the exact toroidal radiation distribution of different ionization s... cannot be calculated with this simple model, the range where different ions can b... should be comparable to the width of their radiation distribution. Indeed the resu... sented in *Fig. 2.* show agreement with measured radiation distribution half width ... a factor of 2, and correctly reproduce the trend that smaller pellets cause wider ... distributions.

Analysis of striation. As it was shown previously[4] the time integrated picture ... emitted by the ionized cloud exhibits striations, very similar in appearance to ... observed during the ablation of mm sized hydrogen and impurity pellets[5]. The ...

radiation emitted by the Al^{++} ions in the cloud exhibits pronounced ...rly as the H_α signal during hydrogen pellet ablation.



...2. Result of single cell calculations for the larger and smaller pellet ...se. Background plasma parameters are $n_e = 1 \times 10^{13} cm^{-3}, T_e =$ *...200eV*

...the Al atoms emitted from the surface of the ablating pellet are step by step ionized ...vels, detecting the radiation distribution of different ionization states one gets ...tion on different stages of the cloud evolution. To analyze the size and shape of ...the cloud at a given time instance single 1 μs exposure pictures were made with ...CD camera. For this purpose pellets with approximately 300 m/s velocity were ...d for which the pellets travel only 0.3 mm during the exposure. The pellet size was ...$0 \times 10 \mu m^3$ (10^{15} atoms).

...The typical size of the atomic cloud was less than a millimeter both in toroidal and ...direction, the maximum of this distribution was considered as the position of the ...As the exposure was triggered by the atomic line radiation of the pellet cloud (see ...), the atomic cloud appeared in all pictures at the same radial position within 1 mm. ...Mostly the clouds of the different ions were elongated along the magnetic field lines, ...radial ($B_\perp$) size was only slightly larger ($\approx$ 1.5 mm FWHM) than the atomic cloud ...their radial position coincided with the atomic cloud position. The toroidal extent of ...elongated clouds is equal to the width of the pellet trace as seen in the time integrated ...ures, and thus these pictures can be interpreted as one-dimensionally expanding clouds ...g the magnetic field lines.

...In some pictures the Al^{++} cloud deviated from the usual size and shape and it was ...larger as 5–10mm in the radial direction. Surprisingly, there were cases when the center

of mass of the Al^{++} cloud radiation was ahead of the pellet. To reveal whether extension of the Al^{++} cloud is connected to the fluctuations observed in the vertical ing photomultiplier's signal, averages of several pictures and their ($B_\perp$) light distr are shown in *Fig. 3.* when the photomultiplier signal is at maximum (a) and at minimum *(b).* It is clearly shown, that at maxima of the photomultiplier radial light distributions are symmetrical, whereas at minima they are asymmetr asymmetry is most obvious when the radial distribution is plotted some mm the toroidal position of the pellet.

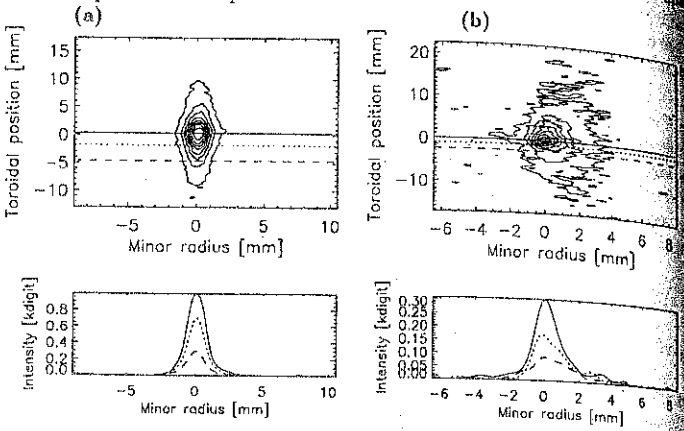


Fig. 3. Contour plot of an average of several 1μs exposure pictures and radi ($B_\perp$) light distributions along indicated lines. Pictures were taken when tota light emission measured by photomultiplier is at maximum (a) and when i at minimum (b).

The results in *Fig. 3.* show, that there is a direct connection between the of the ionized pellet cloud and the temporal fluctuations of the total emitted ligh the cloud is wide across the magnetic field, its radiation is less intense as seen photomultiplier. This behavior can be understood if one considers that the cloud density decays faster if the cloud is wider, and as a consequence the excitation becomes less effective. The radiation of the atomic and the Al^+ cloud never exte such widths as the Al^{++} ion radiation, this way the wide clouds are formed at a late of the cloud evolution, when atoms and singly ionized ions are no more present in in turn indicates, that in the case of our Al micro-pellets the formation of striation barely a consequence of changes in the ablation rate, but also changes in the ionized expansion.

Acknowledgments. This work was sponsored by the Hungarian Science Foundat (OTKA) under contract numbers 17489 and 14068, and by joint DFG–MTA support contract number 78.

References

[1] S. Zoletnik, G. Kocsis, G. Bürger, et al. *Rev. Sci. Instrum.* 66 2904 (1995)
[2] P.B. Parks, G.A. Gerdin, L.L. Vahala, *Nucl. Fus.* 34 417 (1994)
[3] L.L. Lengyel, *Phys. of Fluids* 31 1577 (1988)
[4] J.S. Bakos, B. Kardon, S. Kálvin, et al., *IEEE Trans. Plasma Sci.* 24 29 (1996)
[5] C.T. Chang, *Phys. Rep.* 206 143 (1991)

HIGH-CURRENT ION BEAM ACCELERATION AND STABILITY IN TWO ACCELERATING CUSPS OF INDUCTION LINAC

Vyacheslav I. Karas' [1], Nadya G. Belova[2]

[1] National Scientific Center "Kharkov Inst. of Physics and Technology"
310108 Akademicheskaya Str. 1, Kharkov-108, Ukraine

[2] Inst. of Physics and Technology of RAS, 117218 Krasikov Str. 25a, Moscow, Russia

The 2.5-dimensional numerical simulation of the hollow high-current ion beam (HHCIB) dynamics in two magnet-isolated accelerating gaps separated by the drift gap are presented. The previous results show that the good charge and current compensations of the ion beam by the specially injected background electron beam and the thermal electron injection into drift gap of the induction linac are possible. With the aim of increasing the ion beam acceleration rate in the two cusps linac we have studied the self-correlation between an accelerating electric field and an electron beam energy. It is shown that the proposed method of the ion beam compensation ensures the beam stability relative to both the diocotron filamentation instability and transit-time instability.

Introduction

Several approach to producing high-current ion beams by means of induction accelerators are now studied for controlled thermonuclear fusion research [1].

One of these methods involves the transport of several beams with sourse currents of $\sim$ 1A in a linac with subsequent current enhancement by raising the energy through combining the beams and applying an accelerating pulse [2]. Another way of obtaining a large beam current at low kinetic energy makes use of the collective focusing techniques in which the space-charge forces are balanced by neutralizing the beam ions with electrons, while the electron current is suppressed by the magnet-isolated accelerating gaps. At present kiloampere ion beams are obtained from this type of linear high-current induction accelerator (linac) (see e.g. [3] and Refs. in that). A number of important physical problems discussed in [3] must be studied since the power and brightness requirements for ion beams in inertial controlled thermonuclear research are very stringent.

During the last six years, we carried out systematic investigations of the dynamics of relativistic electron and nonrelativistic ion beam propagation in both an electric field and an axisymmetric nonuniform magnetic field. In [4]–[6], the investigation results of the acceleration, and the charge and current compensation of HHCIBs in one and two linac cusps are reported. These results have shown that both in the presence and in the absence of an accelerating electric field, the following effects take place: (1) charge and current compensation of HHCIB in the accelerating gaps; (2) stability of the ion beam during times that substantially exceed the inverse ion Langmuir and Larmor frequencies.

The performed numerical simulations have also shown that a required charge neutralization of the ion beam is only achieved within accelerating gaps of linac. In the drift space between two accelerating gaps the current and charge compensation of the ion beam proved to be insufficient because of a substantial difference in the electron and ion velocities acquired up to the time of the transit of the beams through the drift gap. As a result, the positive potential of the self-consistent field in the drift space leads to the spread and deceleration of the ion beam and, consequently, to the degradation of the beam brightness. The positive space charge in the drift gap can be compensated by injecting thermal electrons into it. In [7] several ways of the cold electron injections for the space charge suppression of HHCIBs in the drift gap of a linac were investigated. It was shown that a preliminary injection of cold electrons permits to

eliminate broadening and decelerating an ion beam in the drift gap and to provide its additio

Decreased to minimum of the negative influence of the self-consistent fields we will try t the process of the ion beam acceleration.

In this work, the investigation was directed to reaching of the optimal relation between th electric field parameters and the compensating electron beam parameters at which the ion effectively accelerated and at a time is remaining compensated and not losing a stability.

Results of computer simulation

Geometry of the investigated system is shown in fig.1. The mathematical and discrete m described in [4, 7]. The discrete model is developed for the study of both relativistic and non axisymmetric plasma configuration, is realized dimensional axisymmetric numerical code. culations were carried out using IBM PC AT computers.

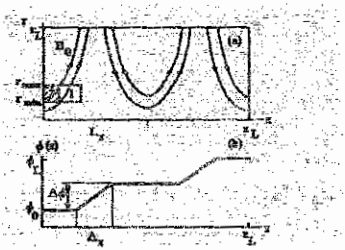
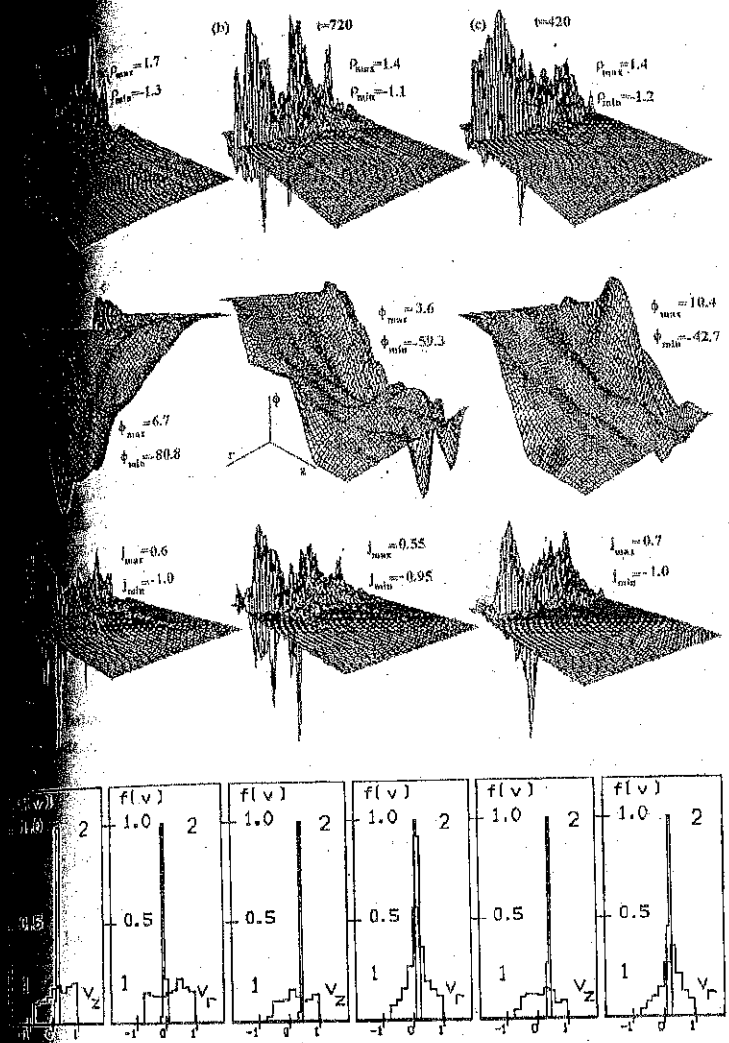


Figure 1: Configuration of external magnetic field lines and localization of the injection of hollow electron (1) and ion (2) beams in the simulated region (a); and the distribution of the scalar potential $\phi(x)$ at the outer boundary $r = r_L$ (b).

For searching the optimal relation bet parameters of the accelerating electric field compensating electron beam energy the poten ference across the accelerating gap and the of the relativistic electron beam were varied low magnetized relativistic electron beam (Lar dius r_{Le} is substantially smaller than the size cusp L_z and the chamber radius r_l) and high unmagnetized ion beam (Larmor radius r_{Li} greater L_z and r_L) were injected along z-axis cases the beam current densities were equal to $q_e n_{0e} V_e = q_i n_{0i} V_i$. The ion beam velocity was V_i The minimum and maximum beams radii were $r_{min} = 30$ and $r_{max} = 32.5$.The size of one cusp radius of the chamber were $L_z = 78.5$ and $r_L = 157.5$ respectively. The amplitude of the external was $\mathcal{B}_0 = 1.76$. The mass ratio was $m_i/m_e = 100$, $m_e = 20m_0$. The number of particles in was $N_e = 64$, $N_i = 180$. The number of the nodes was equal to $(J_z \times J_r) = (64 \times 64)$. The time st varied within the range $0.025 - 0.05\omega_{pe}^{-1}$ for solving the equations of motion and $0.0125 - 0.025\omega_{pe}^{-1}$ solving the wave equations. The parameters of the electron and ion beams have satisfied the condition of the electron beam transport together the ion beam through the magnetoinsulated accelerating ga ($V_e = 0.8 \div 0.85$). The preliminary injection of the thermal electrons with the Maxwellian distribution function with the temperature $T_{ee} = 0.002$ into drift gap was used. The calculations were continued during about ten reciprocal Langmuir ion frequency.

The preliminary injection of the thermal electrons into the drift gap upgrades the characteristics of HHCIB as shown in fig.3 in which the time dependencies of the mean ion beam velocities for the case without the thermal injection ($\diamond$), and with one for three cases of the potential difference ($\times$) - (a), ($+$) - (b), and ($\dashv$) - (c).

Further (below) the results of three cases distinguished by the potential difference across one cusp ($\Delta\phi = 0.8$ - (a), $\Delta\phi = 15.0$ - (b) and $\Delta\phi = 30.0$ - (c)) are shown. Fig.2 illustrates the distribution of the total charge densities $\rho(r, z)$, the scalar potential $\phi(r, z)$, the total axial current densities $j_z(r, z)$, and the distribution functions $f(\vec{V})$ of electrons (1) and ions (2) versus the longitudinal (V_z) and transverse (V_r) velocities at the stationary state. The distributions presented in fig.2 show that the applied external electric field, which accelerates ions and retards electrons, does not prevent the electron beam drift



Distributions of the total charge density $\rho(r, z)$, scalar potential $\phi(r, z)$, axial current density and distributions functions $f(V)$ of electron (1) and ion (2) beams versus the longitudinal (V_z) transverse (V_r) velocities at the stationary state for the cases $\Delta\phi = 0.8$ – (a), $\Delta\phi = 15.0$ – (b), and = 80.0 – (c). In the case (a), one cusp is simulated.

through the accelerating gaps. From the functions $j_z(r,z)$ it is clearly seen that not only the ... also the current compensation of the ion beam occur. The distribution functions $f(V)$ of ... and ion beams illustrate that the ion beam generally retains monoenergetic shape, because ... V_z and V_r does not exceed 10%. The electron beam spread in the velocities is nearly 100% ... does not prevent the charge compensation of the ion beam by electrons.

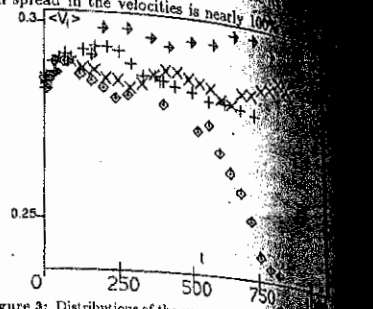


Figure 3: Distributions of the averaged ion velocity ... versus the time ohne the thermal electron injection ... one × (case a), ÷ (case b), and + (case c).

As a result of increasing the difference potential across the accelerating gap up to $\Delta\phi = 30.0$ (the electron beam velocity $V_e = 0.8, \gamma \approx 1.7$) in variant (c) the kinetic electron beam energy $\mathcal{E}_{eb} = (\gamma - 1)m_e c^2 < e\Delta\phi/2$. This case has demonstrated that the electrons localize mainly in the first part of the cusp. The ion beam is accelerated at first and then one is decelerated as seen in fig.3 (+). The thermal electrons can not neutralized the space charge and current of the ion beam (see fig.2c).

More optimal relation between the potential difference $\Delta\phi = 15.0$ and the kinetic ele... energy $\mathcal{E}_{eb} \approx 18.0$ at the parameters $V_e = 0.85, \gamma \approx 1.9$, was sufficient to overcome the potential d... As a results the ion beam is accelerated and then its velocity is a constant $< V_i > \approx 0.30$ in ... simulation (fig.3.÷). Fig.2(b) illustrates that the self-consistent field of the positive charge is ... and an additional focusing of ion beam by the negative space charge of the thermal electrons ... As a result the better characteristics of the ion beam can be produced in linac.

Conclusions

The performed investigations of the beams propagation through the magnet-isolated acce... gap of the induction linac has permitted to choose the optimal regime of the acceleration, the cha... current compensations of HHCIBs in two accelerating gaps of linac.

The authors are grateful to Prof. Ya.B.Fainberg for useful discussions.

References

[1] A.I. Faltens, and D. Keeffe, *Proc. Lin. Accel. Conf.*, Santa Fe, **LA-9234c**, 205 (1981).

[2] R.O. Bangerter, Part. Accel. **37–38**, 3 (1992).

[3] V.I. Karas', V.A. Kiyashko, E.A. Kornilov, Ya.B. Fainberg, Nuclear Instruments and Methods in Physics Research **A278**, 245 (1989).

[4] N.G. Belova, V.I. Karas', Yu.S. Sigov, Fiz. Plazmy **16**, 209 (1990)

[5] N.G. Belova, V.I. Karas', Part. Accel. **37–38**, 225 (1992).

[6] N.G. Belova, V.I. Karas', *Proc. IEEE Part. Accel. Conf.* (Washington DC, V.1, 1993)

[7] N.G. Belova, V.I. Karas', Plasma Physics Reports **21**, 1005 (1995).

1

ASTROPHYSICAL AND GEOPHYSICAL PLASMAS

THE THEORY OF DECAMETER JOVIAN RADIOEMISSION S–BURSTS WITH POSITIVE DRIFT

T.E.Shcherbinina, A.G.Boev

Institute of Radio Astronomy of Ukrainian National Academy of Science

Kharkov 310002, Ukraine

It is known [1] that short-periodic Jovian S-bursts have negative frequency drift in the frequency range (to the 39,5 MHz). The law of emissive frequency is:

$$\frac{df}{dt} = -\gamma f^2, \qquad (1)$$

where $\gamma = 1/s^{-1}$.

The explanation of this fact is given in the papers [2,3], where the mechanism of the decameter S-radioemission generation was proposed. The explanation is made on the basis of Cherencov's emission mechanism of plasma waves with an anomalous dispersion and linear transformation of these waves into electromagnetic ones on condition that Io-Jupiter flux tube is disturbed. The frequency of emission is

$$f(s) = [\omega_p^2(s) + \omega_b^2(s)]^{1/2}, \qquad (2)$$

where $\omega_p(s)$ and $\omega_b(s)$ - local plasma and cyclotron frequencies of flux tube Io-Jupiter respectively, s - the length along the axis of the tube.

In this case negative frequency drift is the result of the motion of emission origin (radiation beam) along flux tube from Jupiter to Io with the velocity $v \approx 0{,}08c$. It was shown that electron concentration must satisfy following distribution:

$$n(s) = \frac{m}{4\pi e^2} f'^2(s_0) \exp[-\frac{2\gamma}{v}(s - s_0)] - \omega_b^2(s)], \qquad (3)$$

where s_0 is s at the starting-point.

The electron concentration dependence along the axis of the tube for magnetic field model of Jupiter O_4 [4] is shown in Figure 1(solid line).

However, besides S-bursts with the negative drift the bursts with positive frequency drift ($\frac{df}{dt} > 0$) are observed [5] (for example, see Figure 2). The amount of those bursts is not very large, and they have the linear frequency drift, but respective the negative γ in (1).

The existence of S-bursts with positive drift is not understood.

We propose the generation mechanism of decameter Jovian radioemission [illegible] with positive drift, based on properties of flux tube Io-Jupiter and Cherencov's [illegible] mechanism.

The variation of emissive frequency (2) with the time, connected with motion [illegible] beam from Jupiter to Io is:

$$\frac{df(s)}{dt} = v\frac{df(s)}{ds} = \frac{v}{f(s)}\left(\frac{2\pi e^2}{m}\cdot\frac{dn(s)}{ds} + \frac{e^2}{2m^2c^2}\cdot\frac{dB^2(s)}{ds}\right).$$

Spatial structure of magnetic field is known [5] (value of the field decreases [illegible] the Jovian surface), and derivative $\frac{dB^2(s)}{ds}$ in (4) is always negative.

Nevertheless, frequency drift $\frac{df}{dt}$ may be positive, if derivative $\frac{dn(s)}{ds}$ is positive. For profile of electron concentration (3) $\frac{dn(s)}{ds}$ is always negative, and that permits to explain the experimentally observed S-bursts with negative frequency drift.

To explain the existence of S-bursts with positive drift we will suppose that flux tube Io-Jupiter has more complex spatial structure of electron concentration that in [illegible] from papers [2,3]. There are electron density oscillations of certain type (Figure [illegible] dashed line) in flux tube, which can lead to appearance of the regions on concentration profile, where derivative $\frac{dn}{ds}$ is positive. On the basis of this fact analysis of experimental data is made. For S-bursts in the frequency range from 14 to 16,56 MHz (Figure 2) [illegible] γ consists -0,98 s^{-1}. The next results were obtained:

a) frequency drift is positive if the following condition between local variations of concentration Δn and ΔB take place:

$$\Delta n > 9{,}716|\Delta B^2|;$$

b) for experimentally observed S-bursts (Figure 2) relative variation of electron concentration is $\frac{\Delta n}{n} \approx 0{,}09$ on the value of plasma inhomogeneity spatial scale $l_n \approx 620$ km. The estimation of height of the origin of such bursts lead to the $h \approx 0{,}5R_J$ from Jovian surface.

3. To explain the appearance of S-bursts with positive drift let's consider the formation mechanism of dynamic spectra of Jovian S-radioemission [3]. It is based on the supposition that low-frequency waves, which propagate along the flux tube, influence on the parameters of flux tube Io-Jupiter. There are systems of periodic regions ("windows")

...ney (S,S' in Figure 3), from which plasma emits in the direction to the Earth. It ...in paper [6] that the range of observed emissive frequency is limited by the ...diregion ab, which is seen in the window of transparency:

$$f(a) - f(b) = f(s)\Delta L / l_n ,$$

...the variation scale of emission frequency $f(s)$ along the axis s. If the slope ...distance are small (5-10°) value $\Delta L = \frac{\lambda}{2}$.

...on interval ab with $\Delta L = \frac{\lambda}{2}$ electron concentration increases, local emissive ...$f(s)$ also increases in comparison with the frequency, relative the middle ...ration $\bar{n}$, and lead to appearance of S-bursts with positive drift. The estimations ...found scales of inhomogeneity ($l_n \approx 620$ km) correlate with the scales of low-...hydrodynamic waves (magnetosound), providing the observed periodicities of ...spectra of Jovian S-radioemission [6].

...S-bursts with positive frequency drift, which were discussed early, are generated ...heights $0,3 \div 0,4 R_J$ from Jovian surface. However, it seems possible that such bursts can ...in the low Jovian ionosphere.

...ually, electron concentration has maximum on the height near 1700 km, and ...monotonically decreases to the Jovian surface [7]. When in this region the formation ...electron beams, which generate decameter radioemission, is possible, the frequency ...may be positive.

...The experimental analysis of existence of such S-bursts is very interesting in point ...of study the properties of the low Jovian ionospere.

References

...T.D., Desch M.D. Jupiter. - M.: Mir, 1979. V.3. - P. 91-144 (in Russian).

...A.G., Luk'yanov M.Yu. Astron. journ. - 1991. - 68, № 4. - P. 853-862 (in Russian).

...A.G., Luk'yanov M.Yu., Tsvyk N.A. Kinematics and physics of celestial bodies. 1993. ...6. P. 27 36 (in Russian).

...Acuna M.X., Ness N.F. Jupiter. - M.: Mir, 1979. - V.3. - P. 248 266 (in Russian).

...Dulk G.R.A. An atlas of selected spectra of the Jupiter's S-bursts. Physics department ...University of Tasmania. - November, 1979. - 198 p.

...A.G., Luk'yanov M.Yu., Tsvyk N.A. Kinematics and physics of celestial bodies. 1993. ...6. P. 37 46 (in Russian).

...Slobel D.F., Altreya S.K. Physics of the Jovian Magnetosphere. Cambr. Univ. Press, 1983. ...67.

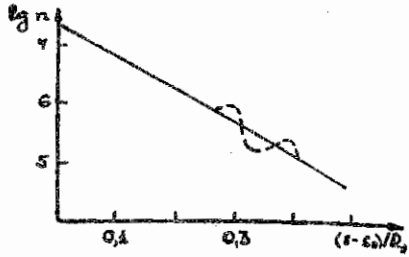


Fig 1.

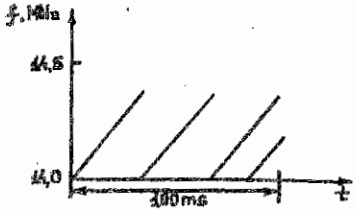


Fig 2.

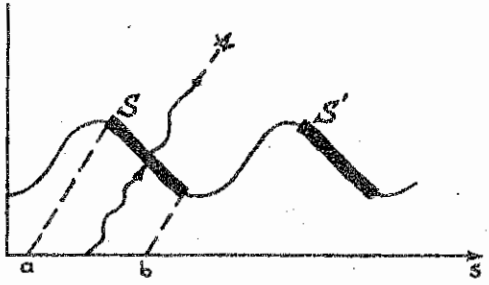


Fig 3.

PROPAGATION OF ELECTRON BEAMS IN SOLAR MAGNETIC LOOPS

V. N. Mel'nik

Institute of Radioastronomy of Ukrainian Academy of Sciences, 310002 Kharkov, Ukraine

E. P. Kontar

Kharkov State University, 310077, Kharkov, Ukraine

Microwave radiation has complex time structure i. e. consists of many bursts (spikes).It is supposed that the emission is caused by the fast electron beams having been accelerated in the low atmosphere [1]. The conditions in the corona give us that quasilinear time is much smaller than the time of beam off in space. This fact allows us to use gas-dynamic description [2]. In case the level of plasma turbulence is low one uses quasilinear equations:

$$\frac{\partial f}{\partial t} + v\frac{\partial f}{\partial x} = \frac{4\pi^2 e^2}{m^2}\frac{\partial}{\partial v}\left(\frac{W}{v}\frac{\partial f}{\partial v}\right) \tag{1}$$

$$\frac{\partial W}{\partial t} = \frac{\pi\omega_p}{n}v^2 W\frac{\partial f}{\partial v}, \omega_p = kv \tag{2}$$

where $W(v,x,t)$ - spectral energy density of Langmuir waves, $f(v,x,t)$ - electron distribution function. The electron distribution function of electron source is two monoenergetic beams $f_1 = n_1\delta(v-u_1)$ and $f_2 = n_2\delta(v-u_2)$ when $n_1, n_2 << n$ - plasma number density and beam velocities $u_2 > u_1 >>$ v_T - thermal electron velocity. There are two steady states in the uniform problem of relaxation of two monoenergetic beams. When the slow beam is dense there are two steps on the steady electron distribution function. Thus, in zerous approximation the electron distribution function contains two plateaux:

$$f(v,x,t) = \begin{cases} p_1(x,t), & v < u_1(x,t) \\ p_2(x,t), & u_1(x,t) < v < u_2(x,t) \\ 0, & v > u_2(x,t) \end{cases}$$

where $p_1(x,t)$, $p_2(x,t)$ - plateau heights and $u_1(x,t)$, $u_2(x,t)$ - their maximal velocities. In case the slow beam is not dense only one plateau is formed

$$f(v,x,t) = \begin{cases} p(x,t), & v < u_2(x,t) \\ 0, & v > u_2(x,t) \end{cases}$$

Integrating the kinetic equations (1,2) the main equations are obtained for plateau heights and their velocities as well as for spectral energy density of plasma waves. The solution of the system of equations obtained presents two or one beam-plasma structures moving with constant velocities. These velocities are determined by the source. The solution when a source of the particles is time dependent contains three possible cases.

1) The beam of slow electrons is dense $n_1/u_1 > n_2/(u_2 - u_1)$. There are two beam-plasma structures moving near the point of injection with constant velocities: $u_1/2$ - slow structure, $(u_2+u_1)/2$ - fast one. A part of electrons of slow structure is accelerated into fast one that changes their shapes. As a result they turn to have been pulled in each other direction. At the distances far from the source the velocity of the fast structure becomes $u_2/2$. Decreasing of the fast beam-plasma structure velocity takes place because after the plateau $p_2(x,t)$ overtakes plateau $p_1(x,t)$ both plateaus start to evolve as one. An average velocity of electrons decreases, so and the velocity of this structure becomes less.

2) The slow is moderate dense $n_1/u_1 < n_2/(u_2-u_1)$ and $n_1/u_1^2 > n_2/(u_2^2-u_1^2)$. There are also two beam-plasma structures, but their velocities are $u_2/2$ and $u_1/2$. The slow structure is formed later than the fast one. Again a part of slow structure electrons is accelerated into fast one and their shapes are not symmetrical because of their "interaction".

3) In case the slow beam is not dense $n_1/u_1^2 < n_2/(u_2^2 - u_1^2)$, the slow beam-plasma structure is not formed. The slow beam-plasma is "absorbed" by the fast structure which velocity is $u_2/2$. Its shape remains symmetrical.

Beams of high energy electrons move in the solar magnetic loops in rather strong electric fields [3], so a problem of influence of an external electric field on formation of beam-plasma structures arises. Let us consider the

relaxation time τ_q is much smaller than both the flying-off time t acceleration time τ_E. (Earlier this problem was considered by Rytov the condition $\tau_q \approx \tau_E$). At the conditions there is possible going kinetic equations

$$\frac{\partial f}{\partial t} + v\frac{\partial f}{\partial x} + \gamma E = \frac{4\pi^2 e^2}{m^2}\frac{\partial}{\partial v}\left(\frac{W}{v}\frac{\partial f}{\partial v}\right), \gamma = \frac{eE}{m} \tag{3}$$

$$\frac{\partial W}{\partial t} = \frac{\pi\omega_p}{n} v^2 W \frac{\partial f}{\partial v}, \omega_p = kv \tag{4}$$

"gasdynamic" ones

$$\frac{\partial p}{\partial t} + u/2\frac{\partial p}{\partial x} = 0, \tag{5}$$

$$\frac{\partial u}{\partial t} + u\frac{\partial u}{\partial x} = \gamma, \tag{6}$$

$$\frac{\partial}{\partial v}\frac{W}{v^3}\frac{\partial W_o}{\partial v} = \frac{m}{\omega_p}\left(\frac{\partial p}{\partial t} + v\frac{\partial p}{\partial x}\right), \tag{7}$$

$$\frac{\partial W_o}{\partial t} = 0, W_o\frac{\partial u}{\partial t} = 0, v = u \tag{8}$$

where $p(x,t)$ and $u(x,t)$ - plateau height and its maximal velocity, and $W(v,x,t)$ - the spectral energy density of Langmuir waves. We shall find a solution of equations (5)-(8) in the case there is a monoenergetic source at $x=0$

$$f_b = f_o\psi(t)\delta(v - u_o) \tag{9}$$

It appears that electrons propagate in plasma in the form of beam-plasma structure as in the case of electric field absence [5]. But in the electric field beam-plasma structure moves with an acceleration according to the law

$$x_{max} = \frac{\gamma t^2}{8} + \frac{u_o t}{2} \tag{10}$$

The form of the beam-plasma structure is asymmetric the front edge is as

$$p(x,t) = p(T) = \frac{f_o u_o \psi(-T)}{(u_o - \gamma T)^2 (u_0 - 2\gamma T)}, T = t - \frac{2}{\gamma}(\sqrt{u_o^2 + 2\gamma x} - u_0)$$

and the rear edge

$$p(x,t) = p(T) = \frac{f_o(u_o + 1\gamma T)\psi(T)}{u_o^2(u_o + 2\gamma T)}, T > 0$$

We have also for the maximal velocity $u(x,t)$

$$u(x,t) = \sqrt{u_o^2 + 2\gamma x}$$

Besides a fast electron number, their energy and plasmon energy increase when electric field is accelerating ($\gamma > 0$) and decrease in the opposite case. This is explained by "pulling out" of electrons from bulk plasma and their acceleration in the first case and by slowing down of fast electrons and their absorbing by plasma in the second one. In the latter the beam-plasma structure disappears at $x_{st} = 3u_o^2/8\gamma$ because all electrons are absorbed. Our consideration allows to understand observed [3] asymmetry of hard X-ray emission from loop footpoints, namely: brighter X-ray emission comes out from the footpoints, where electric current moves upwards and high energy electrons are accelerated by the electric current moves downwards and correspondingly electrons are slowed down.

References:

1. Benz,A.,Magun,A.,Stelling,W.and H.S.U., Solar Physics. vol. 141, No 2,1992, pp. 335-346.

2. Rutov,D.D. and Sagdeev, R.Z., Zh.Eksp.Teor.Fiz.,vol.58,No 2, 1970, pp. 739-745.

3. Abramenko, V.I.,Goposyuk,S.I.,Ogir,M.B.,M.B.Bulletin Crimean Astrophys. Observatory,1993,vol.87,p.3.

4. Rutov,D.D.Zh.Eksp.Teor.Fiz.,vol.52,No 2, 1967,p.1378.

5. Mel'nik,V.N.,Plasma Physics Reports,1995,vol.21,No 1,p.89.

NEAR MECHANISM OF ELECTROMAGNETIC DIATION GENERATION IN SPACE PLASMAS

OKHIMUK A.K., YUKHIMUK V.A., FALKO O.G.
Astronomical Observatory, National Academy of Sciences, Ukraine;
Shevchenko University, Kyiv, Ukraine.

The wave field measurements by the satellites have discovered the wide of the different oscillations and waves in the near-Earth and planetary plasmas. It was shown that the electrostatic waves with the quency like upper hybrid frequency exist near the electromagnetic radiation The significant results on the description of the wave phenomena in the sphere plasma were received during the heating experiments [1,2]. The most esting of them are the secondary electromagnetic radiation of the ionosphere sma due to its irradiation by the powerful electromagnetic wave.

The satellite observations show that the most stable electrostatic mode in the magnetosphere is the upper hybrid wave (UHW) [3]. UHW could be the ource of the electromagnetic radiation in the magnetosphere plasma. At the heating experiments in the latter the cascade decay processes can exist. Under the ction of the powerful electromagnetic wave created by the Earth transmitter the UHW will be excited and will cause the secondary electromagnetic emission.

During the powerful solar flashes the charged particles are accelerated to the great energies. The energetic particles flows are throwed to the crown and to the interplanetary space. These flows can excite the UHW which will generate the electromagnetic emission.

The UHW transformation into the electromagnetic radiation is the widespread processus in the space plasma. This problem was studied in [4,5]. The UHW can decay into the lower-hybrid and electromagnetic waves or diffuse on the kinetic Alfven waves. Parametric three-wave interaction with the UHW is studied in [6] where the ordinary electromagnetic wave was chosen as the pump wave.

In the present work the decay of the upper-hybrid pump into the electromagnetic waves and the kinetic Alfven waves (KAW) is examined.

Energy and momentum conservation demand that

$$\omega_0 = \omega + \omega_j, \quad k_0 = k + k_j, \tag{1}$$

where ω_0 and k_0 are frequency and wave vector of the upper-hybrid pump, ω and k - of the KAW; indexes j=1, 2 designate the values corresponding to the ordinary electromagnetic wave and to the left polarized electromagnetic wave.

For the description of the three-wave parametric interaction we use the two-fluid magnetohydrodynamic equations. The nonlinear current appeared as a result of the upper-hybrid pump resonant interaction with the low frequency KAW causes the generation of ordinary or left-mode electromagnetic wave radiation. The electromagnetic wave field added to the upper-hybrid pump field generates the low-frequency force which amplifies the KAW.

The nonlinear dispersion equation describing the decay of the upper-hybrid pump into KAW and the ordinary electromagnetic wave (index 1) or left-mode electromagnetic wave (index 2) is

$$E_A \times E^*_{1,2} = |\mu_{1,2}|\Phi_0|^2 \tag{2}$$

where $\Phi_0 = e\varphi_0/T_e$, is the pump wave potential, $E_A = 0$ and $E_{1,2} = 0$ are the

...tion equations for KAW and the ordinary (index 1) or left-mode (index 2) ...magnetic wave, $\mu_{1,2}$ are the coupling coefficients.

...posing in (2) that

$$\omega_2 = \omega_r + i\gamma_1, \quad \omega_1 = \omega_{1r} + i\gamma_1, \quad (|\gamma_1| \langle\langle \omega_r, \omega_{1r})$$

...anding the corresponding expressions into series we get the ordinary ...magnetic wave growth rate as

$$\gamma_1 \cong \sqrt{W}\, v_{Te}\, \omega_{pe} k \omega_A / (2 v_A \omega_0), \qquad (3)$$

...re

$$W = |E_{0x}|^2/(4\pi n_0 T_e), v_{Te} = \sqrt{T_e/m_e},$$

... and ω_A are Alfven velocity and frequency, E_{0x} is pump wave amplitude, ... is electron Langmuir frequency.

The left-mode electromagnetic wave growth rate is

$$\gamma_2 \cong \sqrt{W}\, v_{Te}\, \omega_{pe} c (\omega_A/\omega_0)^{3/2} / \left(2 v_A^2\right). \qquad (4)$$

Results discussion.

For the evaluation of growth rate and time values we use the data given in [7]. ...the typical values of the magnetosphere plasma in the satellite GEOS-1 area are: ... $\sim 10 cm^{-3}$; $T_e, T_i \sim 1eV$; $E_{0x} \sim 1 mV/m$; $\omega_{pe}/\omega_{He} \sim 10$; $W \sim 10^{-5}$; $v_{Te}/v_A \sim 10$.

For the ordinary electromagnetic wave we get that

$$\gamma_1 \sim 2s^{-1}, \tau \sim 0.5s.$$

and for the left-mode electromagnetic wave

$$\gamma_2 \sim 20s^{-1}, \tau \sim 0.05s.$$

These results show that the left-mode electromagnetic wave generati
more quickly then for the ordinary electromagnetic wave.

It should be noted that our results agree with the conclusions of [4], wh
decay of the UHW into the left-mode (ordinary) electromagnetic wave
lower-hybrid wave were examined. The threshold conditions are realized su
collision frequency in this magnetosphere region is comparatively
($\gamma_0 \sim 10^{-4} s^{-1}$) and Landau damping is negligible.

The nonlinear three-wave parametric interaction may be observed also
Earth`s ionosphere during the heating experiments, in the magnetosphere
Jupiter, during solar flashes etc.

Therefore the upper-hybrid wave transformation into the electromagnet
radiation is the widespreaded phenomenon for the space.

References.

1. Stubbe P. et al. - J.Geophys.Res. - 1984, 89A, p.p. 7523-7536.
2. Stubbe P. et al. - J.Geophys.Res. -1994, 99A, p.p. 6233-6246.
3. Oya H. et al. - J.Geomag.Geoelectr. - 1990, 42, p.p. 441-442.
4. Murtaza G., Shukla P.K. - J.Plasma Phys. - 1984, 31, p.p. 423-436.
5. Yukhimuk A.K. et al. - Kinematics and Physics of Celestial Objects - 1995, 11, p.p. 71-77.
6. Yukhimuk A.K., Yukhimuk V.A. - Kinematics and Physics of Celestial Objects - 1994, 10, p.p. 67-73.
7. Decreau P.M. et al. - J.Geophys.Res. - 1982, 87A, p.p. 655-712.

...tion of the Inherent Atmosphere of the Spacecraft Moving in the Vicinity of the Sun with Solar Wind

I.K.Konkashbaev, A.I.Konkashbaev, L.B.Nikandrov,
...kh Institute for Innovation and Thermonuclear Research, 142092, Troitsk, Russia

V.D.Kusnetsov, V.N.Oraevsky , V.V. Fomichov
...eo of Terrestrial Magnetism, Ionosphere and Radio Wave Propagation of the Russian Academy of Sciences, 142092, Troitsk, Moscow Reg., Russia

1. INRODUCTION

The problem of the inherent atmosphere of the spacecraft moving in the vicinity of the ...with their probable influence on ***in-situ*** measurements of the solar corona plasma is a ...of the report including theoretical and numerical study of the problems of the vapor ...formation and its interaction with the ambient natural plasma. Spacecraft measurements ...solar corona plasma parameters allow better understanding of the processes that occur ...Sun and in the wind. Now it is shown that there is discrepancy between the measured ...theoretically predicted solar wind velocities especially for the polar region where the ...wind velocities reaches (700-800) km/s according the ***ULISSES*** measurements. This ...that the solar wind gains additional acceleration whose mechanism is still unknown.

Two projects are under discussion. In 2001-2003 years the jointed USA-Russia ...Fire and Ice" is planned [1,2]. The Solar Probe mission of the Sun with the polar ...sent via the Jupiter at different heliocentric distances comprise two space vehicles with ...lion $R \approx 4 \cdot R_\odot$ (USA Probe) and $R \approx 10 \cdot R_\odot$ (Russian Probe) traversing the intermediate ...ity of the Sun and combining in observations of the Sun. In the second project ***"Interhelios"*** the spacecraft sent via the Venus makes some turns between the Sun and the ...Mercury at heliocentric distance $R \approx 20 \cdot R_\odot$. These observations in the polar region and ...torial plane will allow to investigate the corona heating and solar wind acceleration ...mechanisms.

Realization of the Solar Probe missions depends on two problems. The first one is the ...protection of on-board scientific complex against the powerful solar radiation for the ***"Ice and Fire"*** project. The second one is the spacecraft inherent atmosphere formed as a result of ...vaporization and sputtering of the spacecraft surface. Interaction of this atmosphere (neutral

and ionized) with the ambient plasma can affected on-board measurements and [illegible] must be taken into account at the stage of designing the spacecraft and its scientific [illegible]

The present paper deals with the problem of inherent atmosphere of [illegible] moving in the vicinity of the Sun, and their probable influence on *in-situ* measurements [illegible] plasma parameters.

2. INHERENT ATMOSPHERE FORMATION

The solution of problem of heat protection of the on-board equipment [illegible] using a special shield (radiator) that would absorb solar radiation and re-emit it [illegible] from the probe in the form of Planck radiation at shield surface temperature from $T_S(2 \cdot R_\odot)$ = 1000 K to $T_S(4 \cdot R_\odot)$ = 2500 K, therefore materials tolerable to high temperatures must be used. As it follows from estimates the inherent atmosphere of the spacecraft moving at distance from the SUN less $10 \cdot R_\odot$ forms due to vaporization by the Sun radiation. For the USA Probe the radiation power S = 400 W/cm^2 at the perihelion $R = 4 \cdot R_\odot$ the vapor cloud density $n_a = 10^{10}$ cm^{-3} exceeds the natural plasma density $n_o = 10^5$ cm^{-3}.

The second reason of the inherent atmosphere formation is the interaction with the ambient natural plasma. High velocity of the Probes V > 100 km/s corresponding to the relative energy of interacting ions (H,He) E of hundreds eV at perihelion results to the strong sputtering, Fig.1. The sputtering yield $Y > 10^{-2}$ atom/ion is enough for formation of the cloud with the density $n_a = 10^5$ cm^{-3} in ten times exceeding $n_o = 10^4$ cm^{-3} at perihelion $R = 10 \cdot R_\odot$. So, the sputtering can be a main reason of the inherent atmosphere formation for the Russian Probe.

The third reason of the inherent atmosphere formation is the outgassing because most of high-temperature materials are porous and can contain a large amount of absorbed gases. Now there are no reliable data on the gas release rate from real used materials. From rather rough estimates it follows that n_a can exceed n_o even for the ***"Interhelios"*** Probe at $R = 20 \cdot R_\odot$ with the T_S = 1000 K.

3. INTERACTION OF INHERENT ATMOSPHERE WITH AMBIENT PLASMA

The vapor cloud will became ionized by the photoionization, solar corona electrons and due to the turbulent ionization due to the effect of "the critical ionization" similar to that of the plasma torus of the *Io*, the Jupiter's satellite. For the electron ionization the ratio η =

$\frac{R_o n_o(\sigma v)}{4V_n}$ with R_o the characteristic size of the probe does not depend on n_o

the maximum density of the neutrals nearby the Probe surface or the critical flux
e surface $S_{crit} = 10^{15}$ cm^{-2}. This S_{crit} is achieved for the USA Probe due to the
tion only but for the Russian Probe and the ***"Interhelios"*** Probe - due to the gas
the ion concentration n_i can increase due that certain sputtered particles (up to some
escape in the form of ions. This problem needs in more detail investigations as well
sibility of the turbulent ionization.

some part of neutrals is ionized the inherent atmosphere interaction with the
plasma frozen into magnetic field B has from of the two-beam interaction with the
velocity U close to the spacecraft velocity of hundred km/s, Fig.1. For case $n_i = n_a$
pressure is comparable with $B^2/8\pi$ and an interaction can be a strong. The two-beam
bilities resulting in electromagnetic/electrostatic waves excitation affects on accuracy
interpretation of ***in-situ*** measurements. According present-day knowledge interaction of
ssionless coronal plasma and natural plasma with comparable densities results to the
ck wave in the perpendicular magnetic field $B \perp U$, Fig.2. From the energy and mass
servation laws

$$\frac{2\gamma}{\gamma-1}\left(\frac{B_0^2}{8\pi}+\frac{1}{2}\rho_0 V_0^2\right)\frac{V_0}{\rho V}-\frac{2\gamma}{\gamma-1}\frac{B_0^2}{8\pi}\frac{V_a}{\rho V}+\frac{\gamma+1}{\gamma-1}\left(\frac{B_0^2}{8\pi}+\frac{1}{2}\rho_0 V_a^2\right)\frac{V_a}{\rho V}=0\ ,$$

$$d(\rho V)=-\frac{mN}{\tau};\ N_*=n_* V_*;\ N=N_*\exp\left(-\frac{r}{V_*\tau}\right)(r_*/r)^2$$

follows that the shock wave arises on the distance $R_C/R_O \approx 30(N_*/10^{15})$ with N_*,
density and velocity of vapor nearby the Probe surface. These conclusions have been
refined because of large uncertainties of the used data. Therefore the concept of Solar Probe
mission needs additional detailed substantiation based on experimental and theoretical study
of the inherent atmosphere formation and its interaction with the ambient magnetized natural
plasma.

REFERENCES

1. USA/Russia Joint meeting. Program: Mars Together and Fire and Ice. Solar Probe, 1994, JPL, Pasadena, CA, USA.

2. Alekseev V.A., Konkashbaev I.K., Kuznetsov V.D. et all. Problems of Spacecraft Measurements in the Solar Corona. - Astronomical Journal (Russian), 1996, Vol.2.

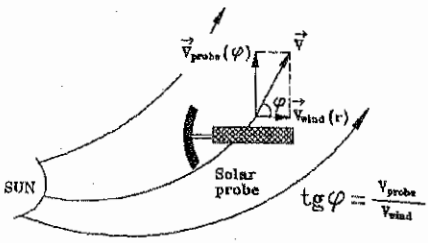


Fig. 1 Solar wind flow in the probe coordinate system.
$\varphi_A = 70^0$, $\varphi_B = 50^0$.

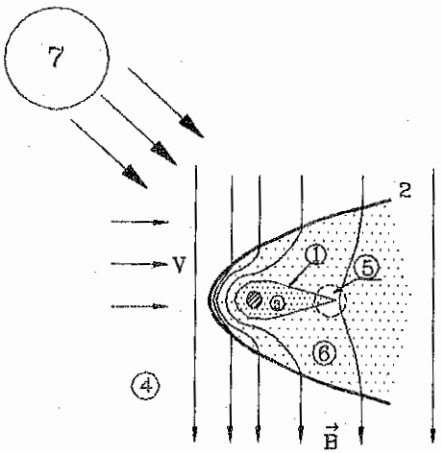


Fig. 2 Presumble solar corona plasma interaction with the probe atmosphere.
1. Intersurface boundary.
2. Region of the turbulent interaction of the probe atmosphere with the natural plasma.
3. Probe atmosphere.
4. Undisturbed corona plasma flow.
5. Magnetic field lines reconnection zone.
6. Cometopause.
7. Sun.

...ation of Large-Scale Structures in Gradient-Drift and Rossby Wave Turbulence

A.V.Chechkin [a),(b)], A.V.Tur[c)], V.V.Yanovsky [a),(b)]

(a) Theoretical Division Institute for Single Crystals National Acad.Sci.Ukraine, Lenin ave.60, Kharkov 310001, Ukraine

...stitute for Theoretical Physics National Science Center Kharkov Institute of Physics and Technology, Akademicheskaya 1, Kharkov 310108 Ukraine

(c) Observatoire Midi - Pyrenees, 14, avenue Edouard-Belin, F31400 Toulouse, France

...ffects of generation of large-scale structures are studied, those appear in gradient-...wave turbulence in plasmas and Rossby wave turbulence in atmosphere and ocean. The ...l reason for them to appear is associated with change of the sign of effective ...ortex) viscosity in large-scale motions of the medium ("**negative viscosity**"). Therefore, ...mping of large-scale motions is replaced by their amplification which is limited due to ...near effects. The small-scale wave field is stationary and maintained by an external ...rce. Such a formulation is fruitful for studying the effects (characterized by the turbulent ...sity) of smaller scale motions upon larger scale motion. In Ref.[1] the negative viscosity ...e due to excitation of a single gradient-drift wave (with wavelength greater than the ion ...mor radius at electron temperature) in a magnetized inhomogeneous plasma has been ...wn, and special solutions of a weakly nonlinear equation for large-scale perturbations have ...n studied. Contrast to the papers on fluid hydrodynamics (see, e.g., [2,3]) in this report ...e deal with generation of large-scale structures in gradient-drift and Rossby wave ...mbulence, where the wave dispersion plays an essential role.

...We start with the well-known model two-dimensional equation which describes space-time ...olution of the potential field in a magnetized inhomogeneous plasmas [4], or the stream ...nction in fluid hydrodynamics [5]. In dimensionless units

$$\frac{\partial \psi}{\partial t} - \frac{\partial}{\partial t}\Delta\psi - \frac{\partial \psi}{\partial x} + \nu\Delta^2\psi - \left[\nabla\psi, \nabla\Delta\psi\right]_z = F \quad , \tag{1}$$

...here $\Delta = \partial^2/\partial x^2 + \partial^2/\partial y^2$, ν is the (dimensionless) ion viscosity in plasmas or the ...kinematic viscosity in fluids. In linear approximation Eq.(1) describes gradient-drift or Rossby ...wave propagation with the frequency

$$\omega_d = -\frac{k_x}{1+k^2} \quad , \tag{2}$$

...and the damping rate

$$\nu_d = \frac{\nu k^4}{1+k^2} \quad . \tag{3}$$

Following a known method, used in turbulence theory, we introduce a sou
right hand side (r.h.s.) of Eq.(1). The role of this source is to maintain a station
the wave turbulence.

We divide the field ψ into average and fluctuating components, $\psi = \overline{\psi} + \psi^T$, h
get closed equation for $\overline{\psi}$ the following assumptions are used:

(i) average quantities vary on space and time scales which are larger than the cha
scales of fluctuation fields;

(ii) the Reynolds number for small scale motions $Re_l \approx V^T l / \nu << 1$ (V^T is a cha
velocity, l is a characteristic size of small-scale field).

Furthermore, according to multiscale expansion schemes, we introduce "slow" v
and "fast" variable $\vec{x}$. The average quantities depend on slow variable only, wh
fluctuating components depend on both fast and slow variables. The equation for $\overline{\psi}$
form [6] (nonlinear on $\overline{\psi}$ terms are omitted)

$$\left(\frac{\partial}{\partial t} - \frac{\partial}{\partial t}\Delta_s - \frac{\partial}{\partial X} + \nu\Delta_s^2\right)\overline{\psi} = \varepsilon_{mn}\varepsilon_{jk}\Big[\eta_{mpk}\frac{\partial^3\overline{\psi}}{\partial X_p\partial X_n\partial X_j} -$$

$$-\nu_{mk}^{(1)}\frac{\partial^2\Delta_s\overline{\psi}}{\partial X_n\partial X_j} + \nu_{mpk}^{(2)}\frac{\partial}{\partial X}\left(\frac{\partial^3\overline{\psi}}{\partial X_p\partial X_n\partial X_j}\right) + \nu_{mlpk}^{(3)}\frac{\partial^4\overline{\psi}}{\partial X_l\partial X_n\partial X_p\partial X_j}\Big],$$

where $\Delta_s = \partial^2/\partial X^2 + \partial^2/\partial Y^2$, ε_{mn} is a unit antisymmetric tensor of the second r

$$\eta_{mpk} = \int\int d\vec{k}d\omega\Pi_1(\vec{k},\omega)2k_mk_pk_kk^2(\omega-\omega_d)\ ,$$

$$\nu_{mk}^{(1)} = \int\int d\vec{k}d\omega\Pi_1(\vec{k},\omega)\nu_dk_mk_kk^2\ ,$$

$$\nu_{mpk}^{(2)} = \int\int d\vec{k}d\omega\Pi_2(\vec{k},\omega)4k_mk_pk_kk^2\nu_d(\omega-\omega_d)\ ,$$

$$\nu_{mlpk}^{(3)} = \int\int d\vec{k}d\omega\Pi_2(\vec{k},\omega)8k_mk_lk_pk_kk^2\left[\nu k^2(\nu_d^2-(\omega-\omega_d)^2+\omega\nu_d(\omega-\omega_d)\right]$$

$$\Pi_1(\vec{k},\omega) = \frac{\Phi(\vec{k},\omega)}{(1+k^2)\left[(\omega-\omega_d)^2+\nu_d^2\right]}\ ,$$

$$\Pi_2(\vec{k},\omega) = \frac{\Phi(\vec{k},\omega)}{(1+k^2)^2\left[(\omega-\omega_d)^2+\nu_d^2\right]^2},$$

$\Phi(\vec{k},\omega)$ is a space-time spectral function of the small-scale field.

The first term on the r.h.s. of Eq.(4) gives correction to the frequency in dispe
equation for the large-scale motions. The next three terms are the viscous-type ones
lead either to damping (positive effective viscosity) or to growth (negative effec
viscosity) of large-scale motions. If we set $1+k^2 \to k^2$ (no dispersion) and $\omega_d = 0$ (
eigenfrequency) then one can recover the corresponding results of Refs.[2,3] concer
two-dimensional fluid hydrodynamics. In particular, we emphasize that neglecting
character of isotropic small-scale fluctuations leads to the positive effective viscosity.

Let us consider the particular forms of the wave spectrum $\Phi(\vec{k},\omega)$.

1. Coherent wave spectrum.

We take the spectrum of the Rossby waves as follows:

$$= \frac{\langle \psi^2 \rangle}{2} [\delta(\omega - \omega_0)\delta(\vec{k} - \vec{k}_0) + \delta(\omega + \omega_0)\delta(\vec{k} + \vec{k}_0)], \quad (5)$$

is the variance of fluctuations,

$$\omega_0(\vec{k}_0) = -\frac{k_{0x}}{1 + k_0^2} .$$

sent the results for the particular case $\vec{k}_0 = k_0\vec{e}_x$. Taking $\overline{\psi}$ in the form

$$\overline{\psi} = exp\left(-i\Omega t + i\vec{K}\vec{X}\right) , \quad (6)$$

linear dispersion equation for the large-scale perturbations:

$$= \frac{K_x}{K^2} - \frac{i}{1+K^2}\left[\nu K_x^4 + \left(\frac{7\langle \psi^2 \rangle}{\nu} + 2\nu\right)K_x^2 K_y^2 - \left(\frac{\langle \psi^2 \rangle}{\nu} - \nu\right)K_y^4\right] . \quad (7)$$

while to note that this equation describes not only the large-scale component of but also the large-scale structures. Indeed, it follows from Eq.(7) that the most (that is, rapidly growing) are those large-scale perturbations which are to the direction of small-scale wave propagation, that is, K_x=0 and ReΩ=0. It the negative viscosity effect leads not only to nonlocal energy transfer from waves to large-scale waves, but also to the generation of stationary structures ed along one of the coordinates ("zonal dissipative structures" [1]) The growth perturbations is

$$\gamma = \left(\frac{\langle \psi^2 \rangle}{\nu} - \nu\right)\frac{K_y^4}{1 + K_y^2} . \quad (8)$$

ν^2.

wave spectrum.

the spectrum of the waves as follows:

$$\Phi(\vec{k}, \omega) = \frac{1}{\pi}\frac{\Delta_k}{(\omega - \omega_d)^2 + \Delta_k^2}\Phi(k) , \quad (9)$$

and $\Phi(k)$ are the functions of modulus $\vec{k}$. Taking $\overline{\psi}$ in the form (6) we get a linear equation

$$\Omega = -\frac{K_x}{1+K^2} - i\frac{\nu_{eff} K^4}{1+K^2} , \quad (9)$$

$$\nu_{eff} = \nu + \pi\int dk\ \Phi(k)\frac{k^5}{(1+k^2)^2}\frac{\nu k^4 - \Delta_k}{(\nu_d + \Delta_k)^2} . \quad (10)$$

("narrow spectrum approximation") we get

$$\nu_{eff} = \nu + \frac{\langle \psi^2 \rangle}{2\nu} , \quad (11)$$

points to the absence of nonlocal energy transfer towards the large-scale region.

ν_d ("broad spectrum approximation") we get

$$\nu_{eff} = \nu - \pi \int_0^\infty dk\ \Phi(k) \frac{k^5}{(1+k^2)^2 \Delta_k} \quad ,$$

and ν_{eff} can be negative. We may estimate the criterium for the negative viscosity

$$\langle \psi^2 \rangle > \nu\Delta \quad ,$$

where Δ is some effective spectral line broadening. It resembles an analogous cri... the coherent waves, if we substitute ν by Δ.

If $\nu_{eff} < 0$, then two possibilities exist for the energy flow from the small-scale ... first one is nonlocal energy transfer from small-scale waves to large-scale ones. ... scale waves grow, and it may occurs, that soon the spectral gap between two wave ... disappears, two-scale approximation is violated, and the turbulence becomes nonst... We note, however, that this circumstance does not violate the validity of our conc... because we consider an initial stage of instability only. Another possibility is associ... the energy flow from small-scale waves to large-scale stationary structures highly ... along one of the coordinates. Such a new mechanism of the energy transfer allow... maintain the stationary level of the turbulence.

In summary, the results of the report are as follows:

1. With the use of two-scale expansion the equation is obtained which descri... evolution of the average field in the presence of a small-scale wave field. The ... expressions are obtained for the terms describing the influence of small-scale ... namely, the viscous-type terms and the dispersion term. These expressions allow ... study the evolution of large-scale motions under the assumption that the spectr... stationary small-scale wave field is known.

2. The results obtained admit a transition to the hydrodynamics of a viscous incompr... fluid. The previously known results on the eddy viscosity of large-scale motio... recovered.

3. It is shown that the coherent wave motions lead to the negative effective viscosity ... criterion of large-scale instability due to the negative viscosity effect is derived.

4. Opposite to the case of small-scale isotropic motions of a viscous incompressible ... small-scale isotropic gradient-drift and Rossby wave motions can lead to the negat... effective viscosity. This difference is due to the dispersion of the waves. It is demonstr... that the effective viscosity can be negative if the spectral line broadening is greater than ... linear damping rate associated with the ion (molecular) viscosity.

1. A.V.Tur, A.V.Chechkin, V.V.Yanovsky, Phys.Fluids **B4**, 3513 (1992).
2. D.Montgomery and T.Hatori, Plasma Phys.Contr.Fus. **26**, 717 (1984).
3. B.Dubrulle and U.Frisch, Phys.Rev.A **43**, 5355 (1991).
4. J. Pedlosky, Geophysical Fluid Dynamics. New York:Springer-Verlag, 1979.
5. A.Hasegawa and K.Mima, Phys. Fluids **21**, 87 (1978).
6.A.V.Chechkin, M.I.Kopp, A.V.Tur, V.V.Yanovsky, Preprint KFTI 94-6 (1994).

A NONSTEADY MAGNETIC LATERAL SHOCK WAVE IN COSMIC PLASMA

A.A. Boeva

Kharkov University, 310077 Kharkov, Ukraine

...theory of radiational shock waves is an important branch of both high-...ro and magnetic hydrodynamics. The processes taking place in MHD-...ables [1], a number of cosmic events such as shocks propagation in star at-...sp, gas motion in solar wind, Supernova bursts create the necessity for ...ecount of different extra factors (magnetic field, radiation, ionization, me-...homogeneity, complex gas composition etc.) [2].

...diating waves without radiation magnetic field (both steady and non-...) have been studied quite in detail [2]. The properties of a transverse shock ...plasma with magnetic field but without radiation are considered in the pa-...[3].

The goal of the presented paper is investigating the properties of steady and ...teady MHD-shocks with radiation and finding out the joint influence of mag-...field and electromagnetic radiation generated by the shock.

The investigation is carried out in the assumption that plasma radiates as a ...kbody. Besides, the density ρ_0 and magnetic field H_0 of the disturbed medium ...dicated as

$$\frac{H_0}{\rho_0} = b = const$$

In the paper it was found the domains of the plasma parameters wh... influence of the both factors - magnetic field and radiation is considerable... also constructed the dependences of the gas parameters behind the wave... (velocity, pressure, density) against the magnetic parameter b and the coor... along the track of the shock propagation.

1. In the fig.1 it is shown the domains of the magnetic field and temper... variation (H,T) which correspond to some cosmic and laboratory conditions... the domains close to the straight line the influence of magnetic field and radia... are equally important.

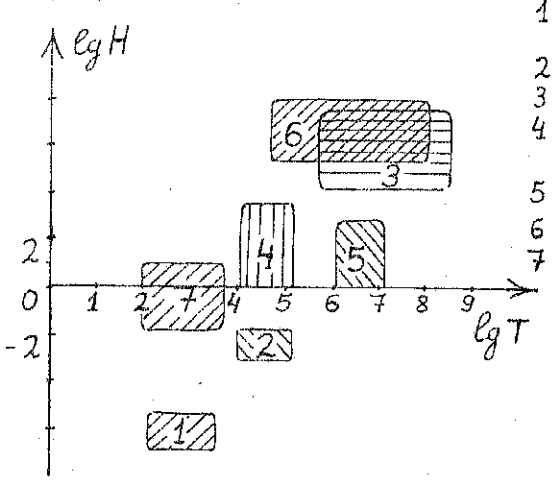
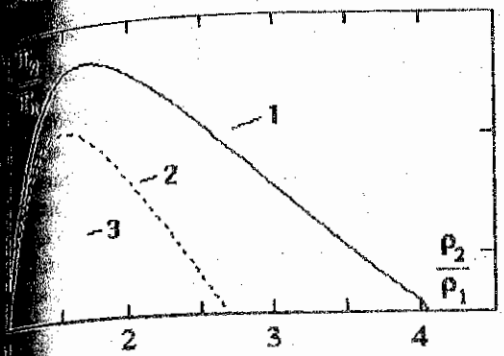


fig.1

2. Let's first consider a steady shock wave because, it mentioned above, its motion hasn't been studied completely so far. The most interesting thing in such waves is the adiabatic curve which is the analogue of Hugoniot adiabat. The influence of electromagnetic emission on break conditions is taken into account as in

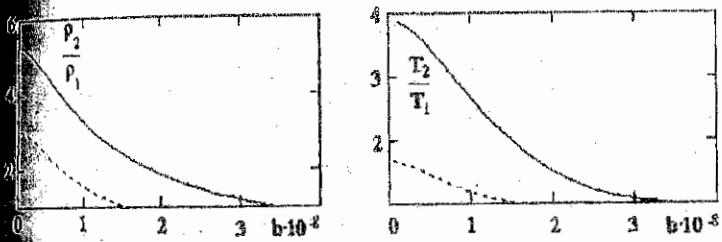
radiational pressure. The terms expressing the radiational energy flux important role if the nonhomogeniety scale $L \approx 10$cm.



The plots of the adiabatic curve of different values of b are shown in the fig.2.

$10^8 \frac{Gr cm^3}{g}$, 2 — $b = 1 \cdot 10^8 \frac{Gr cm^3}{g}$, 3 — $b = 1 \cdot 10^8 \frac{Gr cm^3}{g}$.

The variations of the gas parameters behind the wave front against the mag- parameter b are shown in the fig.3. The values ρ_2, T_2 concern the flow be- the shock front, ρ_1, T_1 the undisturbed flow. The dependences correspond to ferent magnitudes of the mass flux J



—— $J = 5 \cdot 10^4 \frac{g}{cm^2 s}$, —— $J = 10 \cdot 10^4 \frac{g}{cm^2 s}$.

fig.3

3. Let's consider a nonsteady shock wave. For its investigation the ... mate Whitham's method was used [4]. Following the method for obtaining ... rameters behind the wave front the characteristics equations were used. ... the dependences of the parameters behind the front along the path of ... propagation are constructed (U is the front wave velocity, u is the velocity ... gas behind the front wave).

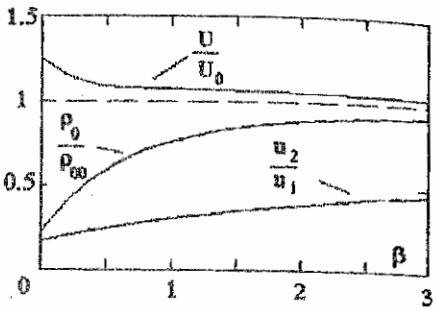


fig.4

BIBLIOGRAPHY

1. Великович А.Л., Либерман М.А. Физика ударных волн в газах и пла... ме., М., : "Наука", 1987, 295 с.

2. Климишин И.А. Ударные волны в оболочках звезд. Ф.М., 1984., 216 с.

3. Боева А.А., Карвицкий Г.Э. Распространение поперечной магнитоги... родинамической ударной волны в неоднородной плазменной среде. Ки... нематика и физика небесных тел., 1996. (в печати).

4. Уизем Дж., Линейные и нелинейные волны., М., Мир, 1977., 578 с.

Large-scale Structure Formation in the Cometary Ionosphere due to Plasma Streams

O.P. Verkhoglyadova *(Space Physics Lab., Dept. of Astronomy and Space Physics, Kiev University, Ukraine)*

Paraboloidal envelopes and rays are typical plasma structures in cometary ionospheres. It follows from numerous observations that envelopes are often connected with rays [1]. Thus, one can trace formation of rays with propagation of dense envelopes from the cometary head to the tail.

The electromagnetic formation mechanism for plasma envelopes and ray structures in the cometary ionosphere is considered. It is likely that the above plasma structures are caused by interaction between the cometary plasma and the solar wind [2,3]. Given plasma stream along the cometary tail in the extended outer regions of the cometary ionosphere, an aperiodic filamentation instability can result in formation of separate envelopes in cometary head and a straight ray system in the plasma tail [4]. The stream filamentation instability results in global plasma stratification and is physically concerned with attracting (pinching) of micro-currents streaming in the same direction against a background plasma [5].

The study is carried out within framework of paraboloidal geometry, namely the plasma streamlines and magnetic fieldlines are directed along the surfaces of two sets of orthogonal paraboloids of revolution in the region of interaction [6].

The linear 3D problem is studied in the curvilinear geometry in terms of hydrodynamic equations for 4 components with taking into account electron scattering on plasma waves. We consider stratification in the orthogonal direction to the surfaces of undisturbed magnetic fieldlines and plasma streamlines.

When consider small disturbances of the physical values, one obtains that plasma density is represented in Coulomb wave functions of the zero order and depends on k that is a parameter defined from the dispersion equation and acts as a wave number. Near the cometary head the instability development gives rise to formation of a set of paraboloidal envelopes. Moving along the cometary tail one can obtain the system of quasiparallel rays directed

along the tail axis. The wave number k_0 approximately evaluates the inverse size or thickness of cometary envelopes and rays as in the previous papers [2,3]:

$$\lambda_0^{stream} \sim k_0^{-1} \simeq 24 - 240\ km.$$

It should be noted that plasma filaments are larger than those of stream approximately by the ratio of ion masses $\sqrt{m_{i2}/m_{i1}}$, i.e.

$$\lambda_0^{plasma} \simeq 100 - 1000\ km.$$

Formation time for these structures on the linear stage of instability is

$$\tau_0 \sim (\gamma(k_0))^{-1} \simeq 4^s - 8^{min}.$$

The numerical simulation by CIC method is undertaken to study the linear filamentation processes. The main set of equations for components of vector potential A_1, electrical field E_2, magnetic field H_3 and components of velocities $V_{1\alpha}, V_{2\alpha}, V_{3\alpha}$ for particles are obtained in terms of the "short-wave" approximation from the starting set of the MHD-equations. Using this simulation method it is convenient to derive plasma densities from known distribution of particles and fields on the grid by the CIC method [7].

Typical data depict a physical process which can take place in a thin paraboloidal layer of $x_1 \simeq const$ crossing the cometary ionosphere. On the linear stage of the filamentation instability the density structures, which will be called filaments, are formed from an initial noise. On the nonlinear stage plasma and stream particles group together and form more large and more dense structures via coalescing of initial filaments. The plasma structures are larger than those of the stream, i.e. their thickness could reach the value of $10^3 - 10^4\ km$.

Formation of more large plasma structures composed of parallel current systems via coalescence process is typical for the filamentation instability [8]. The coalescence stops when a defined thickness is reached which value is determined by skin properties of the background cometary plasma. In [2] it was shown that instability development gives rise to formation of dense plasma structures with thickness about maximum possible one on the linear stage of the instability development. The thickness of filaments along a layer depends on the following plasma parameters:

$$l \sim \frac{V_{01} m_{i1}}{H_0 \sqrt{1 + \frac{n_{i2} m_{i1}}{n_{i1} m_{i2}}}} \qquad (3)$$

magnetic field (H_0) and stream velocity (V_0) exert primary control over scale of structures. Strong magnetic field suppresses the instability. heating is sufficient for the stability of small-scale structures and also suppress the filamentation process. In [2] these situations were and respective linear criteria for the plasma parameters were obtained dispersion equation.

proposed mechanism is an attempt to explain formation of both envelopes and ray system in the cometary ionosphere as a result of stream instability development. The influences of an asymmetry of the ionosphere and of initial inhomogeneity of the cometary plasma are lines of further investigations of the proposed mechanism.

ferences:

Bonev T., and K. Jockers, H_2O^+ ions in the inner plasma tail of comet 1990 V, *MPAE-W-12-93-23*, 41 pp., Max-Planck-Institut fur Aeronomie, 1993.

Verkhoglyadova O.P., Kotsarenko N.Ya., Pasko V.P., Churyumov K.I. (1993) *Sov. Astron. Lett.*, 19(9), 823-867.

Kotsarenko N.Ya., Verkhoglyadova O.P., Churyumov K.I., (1994) *Planet. Space Sci.*, 42(9), 733-736.

Verkhoglyadova O.P. (1996) *Planet. Space Sci.*, 44(4), 407-416.

Miller, R.B., *An Introduction to the Physics of Intense Charged Particle Beams*, Plenum Press, New York, 1982.

Schmidt H.U., and Wegmann R., An MHD model of cometary plasma and comparison with observations, in *Cometary plasma processes*, edited by A.D. Johnstone, pp. 49-63, Geophysical Monograph 61, AGU, 1991.

Hockney, R.W., and J.W. Eastwood, *Computer simulation using particles*, 540 pp., McGraw-Hill International Book Company, 1981.

Pasko, V.P., Nonlinear dynamics of dissipative filamentation instability of electron stream in magnetized plasma, *Pisma v ZhTF*, 17, N20, 13-17, 1991.

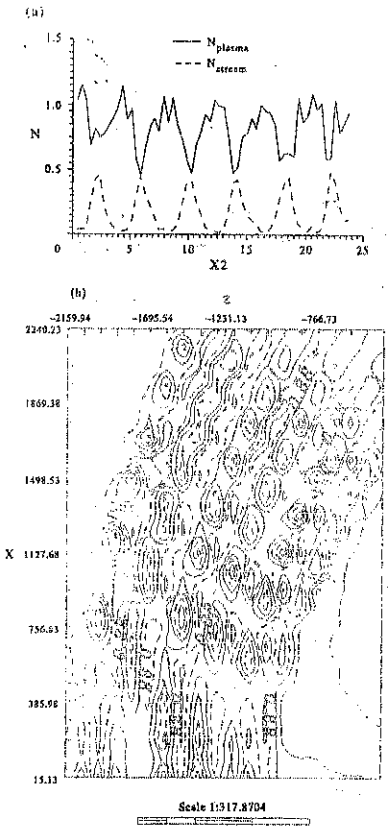


Fig. 1. Result of filamentation process development for the case of strong magnetic field. (a) Dependency of cometary plasma density (solid lines) and stream density (dashed lines) on the coordinate x_2 along the simulation layer. (b) Isodensities for the cometary plasma

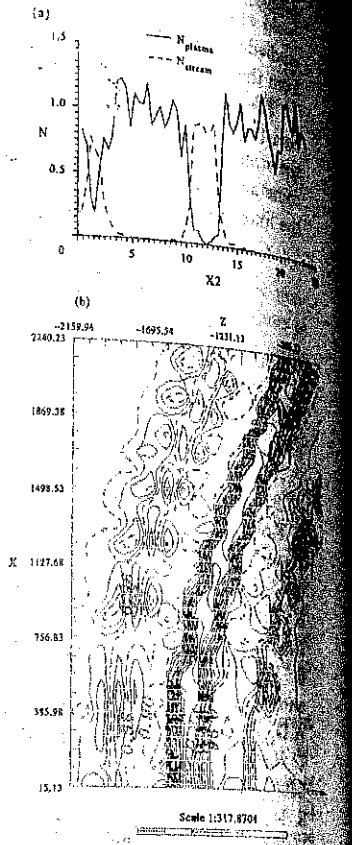


Fig. 2. Result of filamentation process development for the case of weak magnetic field. (a) Dependency of cometary plasma density (solid lines) and stream density (dashed lines) on coordinate x_2 along the simulation layer. (b) Isodensities for cometary plasma

ON THE POSSIBLE GENERATION OF GAMMA-BURSTS IN THE PLASMA PINCHES

Farshi E. H.*, Trubnikov B. A., Vlasov V. P., Zhdanov S. K.**

* Atomic Energy Organization of Iran, Tehran, IRAN
R. R. Center "Kurchatov institute", Moscow, RUSSIA
** Moscow Engeneering Physics Institute, Moscow, RUSSIA

The hypothesis is considered that the cosmic gamma-bursts are generated by bremsstrahlung of the electrons accelerated in discharges of "lightning" type arising in "peripheral plasma shells" of stars. Such shells could be formed between stars as a result of the long-duration accumulation of the plasma "wind" (similar to "solar wind") in those places, where it meets with the wind from neighbouring stars. The possibility of it, that in the same discharges the ions are generated and accelerated as cosmic rays, is also considered .

Introduction

Approximately once in 24 hours the devices on satellits register the short-time powerful flash of the cosmic gamma-radiation, however, the distances to their sources and their nature remain to be unknown. By a number of features in their energy spectra it was previously considered that they arose on the old neutron stars which were not directly observed. However, present the supervisions on satellites ("Granat"-Russia and "GRO"-USA) do not confirm the existence of such features [1-3], and so some authors consider other possibilities of gamma-burst generation (GB), not connected with neutron stars.

So in our papers [4,5] it is assumed that GB arise in the discharges of "cosmic lightning" type within interstar plasma clouds. This hypothesis is criticized in [6], where it is supposed that the discharges occur in the Sun-system limits at distances of the order 100 a.u. Note also there the possibility of GB birth is considered as a result of comet collisions.

Previously in a number of papers (see, for example, [8-10]) we considered the possibility of acceleration for galactic cosmic rays (GCR) in electrical discharges of hypothetical "cosmic lightnings" with currents. On their cylindrical channel, due to an instability, the narrow necks should emerge from which the plasmoids of quasi-neutral plasma should be extruded along the axis. In this situation the velocities of electrons and ions should be equal, so the energy of protons should be $m_p/m_e \sim 2000$ times greater, than the energy of electrons.

In a given study the question under discussion — is whether the observable GB are the direct manifestation of such "cosmic lightnings", and whether GCR (as a proton component) and GB (as an electron component giving the bremsstrahlung) emerge in them simultaneously.

The power of galactic cosmic rays and gamma-bursts

As known, the GCR energy density is equal $1\ eV \cdot cm^{-3}$, and at the volume of Galaxy $10^{67} cm^3$, their total energy is equal $\sim 10^{56}\ erg$. However, approximately during 100 mln. years they diffusionally leave the Galaxy, so for their sustainment the capacity $W_{GCR} = 2 \cdot 10^{40}\ erg/s$ is necessary. At the "pinch-mechanism" the power 2000-times smaller would belong to electrons, $W_e \sim 10^{37}\ erg/s$, from all the GCR-sources, number of which in Galaxy we tried to compare with the number of gamma-burst sources.

Approximately one GB, $\sim 1 \div 10\ s$ long, is registered with the flows of energy from the minimum 10^{-6} to the maximal $10^{-3}\ erg \cdot cm^{-2} s^{-1}$ during 24 hours. However, the distances, R,

to them are unknown. It is natural to assume that the weak GB-s correspond to large dist... R_{max}, and the powerful, to short distances R_{min}, and then we have the ratio $R_{max}/R_{...}$ $\sqrt{1000} = 31.6$. At the average GB duration equal 3 s we have an evaluation of the total e... of one GB:

$$E_1[erg] = 4 \cdot 10^{-2} R^2_{min,cm} = 4 \cdot 10^{-5} R^2_{max,cm}. \qquad (1)$$

Then we assume, that GB are related not with the neutron stars but with usual stars. S... 1 GB is observed for 24 hours, the relationship (1) corresponds, on average, to the "stationa... capacity $W = 5 \cdot 10^{-10} R^2_{max,cm}$ erg/s in the sphere with the radius R_{max} and with the vol... $V = (4/3)\pi R^3_{max}$. In the neighbouhood of the Sun the density of the star matter is equ... $\rho = 0.05\ M_\odot\ ps^{-3}$ ($1\ ps = 3 \cdot 10^{18}\ cm$), so the number of stars in the mentioned sphere is equ... $N = \rho V/M_\odot = 7.4 \cdot 10^{-57} R^3_{max,cm}$.

Hence, we have the "stationar" capacity of GB per star $W_{1star} \approx 0.7 \cdot 10^{47} R^{-1}_{max,cm}$ erg/s. And since the Galaxy has 10^{11} stars, we must to ascribe to them the total capacity of GB $W_\gamma = 0.7 \cdot 10^{58} R^{-1}_{max,cm}$ erg/s. And if we assume that $W_\gamma = W_e$, then we shall find $R_{max} \approx 220$ ... and this length appears to be shorter than the width of the galactic disk. Then the energy of one typical GB would be equal $E_1 \approx 2 \cdot 10^{37}$ erg.

It is remarkable that the same evaluation of energy per one GB was taken previously f... the hypothesis about neutron stars, as GB-sources too. In our representation, for close GB-s... find $R_{min} \approx 7$ ps that approximately corresponds to the average distance between stars. T... number of stars in a sphere with the radius R_{max} is equal to $N \approx 2$ mln. that provides t... observable isotropy in the distribution of GB-sources in their directions.

The received evaluations look like rather reasonable and permit to assume that GCR a... GB are being generated simultaneously in the "cosmic lightnings" which occur from time t... time in the clouds of magnetized cosmic plasma, the properties of which are discussed below.

3. The assumed characteristics of plasma clouds

In an interstellar space there are large molecular clouds, where new stars can often emer... However, we are interested in the smaller plasma clouds which are not directly observed. It... possible to assume that they arise in those places, where the plasma "star winds" emitted ... adjacent stars collide. In the neibourhood of the Sun we have:

star number density $n = L^{-3} = 0.05\ ps^{-3}$,

the average distance between them $L = 2.7\ ps = 8 \cdot 10^{18}$ см,

and their relative velocities $v = 20\ km/s$.

If L is assumed to be the radius of a plasma shell, the cross-section of shell collisions will b... equal $\sigma = \pi L^2$, the number of collisions of one shell with another during a unit of time is equal... $\nu = n\sigma v = \pi v/L \approx 8 \cdot 10^{-13}\ s^{-1} \approx 7 \cdot 10^{-8}$ for 24 hours. Multiplying this value by $N = 2 \cdot 10^6$ ... number of stars in a sphere of the radius R_{max}, we receive 0.14 $[GB/(24h)]$, that is rather close to the observable frequency "one GB per day". This proximity, which we can improve by a small change of multipliers, by our opinion, is a rather remarkable fact also.

The duration of GB ($\sim 3\ s$) indicates that the length of breaking the neck of a pinch should be of the order of $\lambda \sim 10^{11}$ см. It corresponds to the diameter of the Sun, and, as noted in [6], for the hypothesis under consideration the most important question is: how the energy, by giving one GB, can be concentrated in the area with such dimensions?

4. Can "star wind" generate gamma-bursts ?

...ullet is assumed that GB occur at the distances of the order of $R_{min} \sim 100$ a.u. = ... and then $E_1 \sim 10^{29}\ erg$. But when $R_{min} = 7\ ps = 2 \cdot 10^{19}$ см, then $E_1 = 1.6 \cdot 10^{37}\ erg$. ...ently, for explanation of the latter value we must assume that the total pinch length, l, ...ots of lightning" feeding it, can considerably exceed the length of the most narrow part, ...dually pinched by forces of magnetic pressure. Most probably, the currents are closed, ...plasma clouds often have toroidal configurations. It would be of interest to note that ...structures (but with huge dimensions $\sim 50\ ps$!) are observed close to the center of our ...However, we are interested in smaller structures of "solar wind".

...the neibourhood of Earth the solar wind has the velocity $v = 400\ km/s$, density of particles ...ly protons - "p") $n = 50\ cm^{-3}$, and bears inself the "frozen" magnetic field. If these ...istics are the same on whole sphere surrounding the Sun, the total expense of the mass ...ity the wind will be $dM/dt = 4\pi R^2 m_p n v = 10^{13}\ g/s = 10\ mln.tons/s$. At the average ...s between the stars $L = 2.7\ ps$ and at their relative velocity $v = 20\ km/s$ the "time of ...two neibouring stars is equal $T = L/v = 4 \cdot 10^{12}\ s = 130000\ years$. During this period ...lar wind carries away the total mass $\delta M = 3.6 \cdot 10^{25}\ g$ (for comparison the mass of the ...is equal $6 \cdot 10^{27}\ g$). In contrast to it, at the velocity of the wind $v = 400\ km/s$ the time of ...age to the distance $L/2 = 1.3\ ps = 4 \cdot 10^{18}\ cm$ would be equal $t_{L/2} = 10^{11}\ s \approx 3000\ years$. ...we surround mentally the Sun by the cube with 6 borders, on one border we shall have ...ass $\delta M/6 = 6 \cdot 10^{24}\ g$, moving with the velocity $400\ km/s$, and, hence, having the total ...etic energy $K \approx 5 \cdot 10^{39}\ erg$. This energy, in principle, is sufficient for generation of 300 GB ...the energy $1.6 \cdot 10^{37}\ erg$ each.

...these very approximate evaluations increase 20 times only, the energy $E \sim 10^{41}\ erg$ in ...discharge could supply not only the electron component of GB, but the sustainment of the ...ton component of GCR too. Below we discuss the possible ways of discharge formation.

The preliminary contraction of a pinch and its rapid break

It is possible to assume that at the collision of plasma winds from adjacent stars the kinetic energy of the winds is converted, at their stoppage, into the potential energy of a magnetic field. As known, the average magnetic field of the Galaxy (it is in a dynamic balance with GCR) is equal $< B >= 10^{-5} \div 10^{-4}\ Gs$, and we assume, as the first way, that the magnetic field induced by the stopped (and accumulated for a long time) plasma star wind, has approximately such a value, and it is not chaotic, but forms, at the beginning, separate closed toroids with the minimal radius r_{min} and with the maximal radius r_{max}. At the maximal radius the internal field $B_\varphi \sim r^{-1}$ is assumed to be equal to the external field $< B >$, so the condition of equality between the pressure outside and inside the toroid is fulfilled here.

Therefore the toroid is not expanded itself here, but it can expand towards the z-axis due to the ploughing and extension of a plasma from the centre up and down along the z-axis, as it is conditionally represented in Fig. 1. At the initial average internal field $B_\varphi \sim 10^{-4}\ Gs$, and at the accepted by us energy of one GB ($E = 1.6 \cdot 10^{37}\ erg$), the volume of a toroid should be equal $V = 4 \cdot 10^{40}\ cm^3$. Then, its initial dimensions should be of the order of $r_{max} \sim 10^{15} - 10^{16}\ cm \sim 10^{-2} - 10^{-3}\ ps$. Approxymately such a length, $l \sim 10^{15}\ cm$, should also be for the central pinch under formation. However, for explanation of the GB duration ($\sim 3\ s$), we must assume that the length of its most narrow part — neck (see Fig. 1) — is smaller.

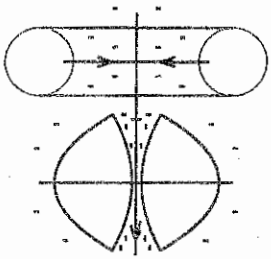


Fig 1, Evolution of magnetic torus and formation of a pinch with neck.

Before the final break the length of the neck [illegible] 10^{12} cm at its diameter of the order of $D \sim 10^{11}$ [illegible] the initial radius of the central pinch decreases [illegible] of magnitude, and, respectively, the magnetic [illegible] its boundary increases similarly, reaching before [illegible] the value of the order of $B_{max} \sim 1$ Gs at the [illegible] $J \sim 5 \cdot 10^{11}$ A. During the process of plough[illegible] density of plasma increases 8 orders of magnitude in [illegible] central pinch. If, for instance, at the beginning it [illegible] equal $n \sim 10$ cm^{-3}, then to the instant of the [illegible] break we have $n \sim 10^9 - 10^{10}$ cm^{-3} in the area with the volume of the order of $V = (\pi/4)\lambda D^2 \sim 10^{34}$ cm^3.

We note that the possibility of such GB generation, at the annihilation of a closed magnetic field loop, was mentioned previously qualitatively in the review [11], applicably to the magnetosphere of a neutron star. The similar way of pinch formation was proposed also in [12] applicably to the solar flares.

The situation, caused by collision of two plasma winds carryng the oppositely-directed "frozen" magnetic fields, could be the second possible approach. In this situation the so called "neutral current layer" (flat pinch) arises in the plane of collision.

For a rather long time it can be in equilibrium, but exceeding some critical parameter it loses the stability and, due to reconnection of magnetic force lines, breaks into some cylindryal pinches. Such a picture was observed in the experiments [13] with flat pinches. However applicably to cosmic GB for such configurations of currents, it is difficult to evaluate the possible length of pinches, in contrast to the above-discussed approach with the magnetic toroid.

In conclusion the authors express their gratitude to Dr. I. L. Rosenthal for his useful critical remarks on this work.

References

[1] Terechov O.V., Denisenko D.V., Lobachev V.A., at all, Lett. Astr. J. (rus.), 1994, v. 20, N 5, p. 423.
[2] Meegan C.A., Fishman G.J., Wilson R.B. et al., Nature, 1992, v. 355, p. 14.
[3] Kurt V.G., The Earth and Universe (rus.), 1993, N 2, p. 3.
[4] Trubnikov B.A., Zhdanov S.K., Vlasov V.P., Preprint of Kurchatov Institute IAE-5580/6, 1992.
[5] Trubnikov B.A., Zhdanov S.K., Vlasov V.P., Contributed papers of 21st EPS Conf. on Contr. Fusion and Plasma Physics, Montpellier, France, 1994, Part III, p. 1486.
[6] Rosenthal I.L., Astronomical Journal (rus.), 1994, v. 71, N 4, p. 542.
[7] Luchkov B.I., Lett. Astr. J. (rus.), 1994, v. 20, N 4, pp. 308-310.
[8] Vlasov V.P., Zhdanov S.K., Trubnikov B.A., Pis'ma JETP (rus.), 1989, v. 49, N 11, p. 581.
[9] Trubnikov B.A., Uspehi Fisicheskich Nauk (rus.), 1990, v. 160, p. 167.
[10] Trubnikov B.A., IEEE Transactions on Plasma Science, 1992, v. 20, N 6, pp. 898-904
[11] Schaefer B.E., Scientific American, 1985, v. 252, No. 2, p. 40-46.
[12] Airapet'yan V.S., Vichrev V.V., Ivanov V.V., Rosanova G.A., Astrophysics (rus.), 1990, v. 32, N 3, p. 405
[13] Fadeev V.M., Kvarzhava I.F., Komarov N.N., Nuclear Fusion, 1965, v. 5, N 3, p. 202.

"SEMI-RELATIVISTIC" MODEL OF THE COSMIC RAY GENERATION IN A PLASMA PINCH

Farshi E. H.*, Trubnikov B. A., Vlasov V. P., Zhdanov S. K.**

* Atomic Energy Organization of Iran, Tehran, IRAN
R. R. Center "Kurchatov institute", Moscow, RUSSIA
** Moscow Engineering Physics Institute, Moscow, RUSSIA

The "semi-relativistic" model is proposed for the plasma state equation in a fully skinned pinch. This model is ultrarelativistic in thin parts, necks, and, respectively, nonrelativistic in thickened parts, bulges of the plasma pinch. Such a model allows one to solve analytically the equations of plasma motion that gives the energy spectrum of accelerated particles of the type $dN/dE \sim \gamma^{-2}(\ln\gamma)^{-3/2}$, where $\gamma = E/Mc^2$. This theoretical spectrum is close rather to the spectrum of galactic cosmic rays, $dN/dE \sim E^{-\nu}$, with the "observed" index $\nu = 2.74$.

Introduction and basic equations

In [1-4] the hypothesis is considered that the cosmic rays (and, possibly, gamma-bursts also) are generated in the discharges of "cosmic lightning" type. The cylindrical channels of such discharges must be unstable with respect to formation of the necks. From these necks the ejection of plasma takes place with the formation of accelerated particles beams. In this model the energy spectrum of accelerated particles has a power-law dependence $dN/dE \sim E^{-\nu}$ with the theoretical index $\nu_{th} = 1+\sqrt{3}$ which is very close to the observed index $\nu_{ob} = 2.74$. However, the value ν_{th} was obtained under assumption that inside the pinch the plasma state equation is nonrelativistic in its own coordinate system.

In the present paper the "semi-relativistic" approximate model is proposed for the plasma state equation; with allows one to obtain the analytical solutions for all the functions.

So, we have the 4 coordinates $x^0 = \tau = ct, x^1 = x, x^2 = y, x^3 = z$ with the metrics $(ds)^2 = (cdt)^2 - (dr)^2 = g_{ik}dx^i dx^k = \gamma^{-2}(d\tau)^2$ and 4-velocity $u^i = dx^i/ds = (\gamma, \mathbf{u})$, $\mathbf{u} = \gamma\boldsymbol{\beta}, \beta = v/c = (1-\beta^2)^{-1/2}$. The equations of relativistic hydrodynamics have the form

$$\nabla_i n u^i = 0,\ \nabla_i T^i_k = 0, T^i_k = (e+p)u^i u_k - p\delta^i_k \qquad (1)$$

where 3 scalar values stand for, respectively, the energy, e; pressure, p, and for the density, n, of particles in the plasma own coordinate system.

We shall solve these equations for the plasma pinch with the radius $a(\tau, z)$ in the so called "narrow channel approximation", when the values e, p, n and $v = v_z$ are assumed to be the constants over the cros-section πa^2 of a pinch. In this approximation it is useful to introduce $\rho_* = na^2/n_0 a_0^2$, $u = \sinh y$ and two operators $\hat{P} = \gamma\frac{\partial}{\partial\tau} + u\frac{\partial}{\partial z}$, $\hat{Q} = u\frac{\partial}{\partial\tau} + \gamma\frac{\partial}{\partial z}$.

Then, from Eq. (1) we derive the basic equations (see, also [3]):

$$(e+p)\hat{P}y = -\hat{Q}p, \quad \hat{Q}y = -\hat{P}\ln\rho_*, \qquad (2)$$

to which we must add the state equation of a plasma in its own coordinate system.

"Semi-relativistic" model of a pinch

The function $\rho_*(\tau, z)$ is equal "1" at $\tau \to -\infty$, when the cylindrical pinch is nonperturbed. In the process of perturbation development we arrive at the limit $\rho_* \to 0$ in thin necks and at $\tau \to +\infty$ in thick bulges.

In these bulges the pressure decreases, and here we can use the nonrelativistic approximation $e \approx n_i M_i c^2$ and the adiabatic law with the nonrelativistic index "5/3":

$p = p_e + p_i = 2p_i = p_0(n_i/n_{i0})^{5/3} = p_0(a_0/a)^2$.

The last relation follows from the equality of gaseous and magnetic pressures, $p = B^2/8\pi$, on

the surface of the pinch, if the field $B = B_\varphi = 2I/cn$ is created by the constant current I, as we assume here. Finally, the system of two equation (1) can be rewritten for the bulges in the form:

$$\hat{P}y = -\hat{Q}x, \quad \hat{Q}y = \hat{P}\ln x, \quad x = \frac{x_0}{\rho_s}, \quad x_0 = \frac{5\theta_{i0}}{M_i c^2} \ll 1, \theta_{i0} = \frac{p_{i0}}{n_{i0}}. \tag{3}$$

The opposite situation we have in the necks, where the pressure increases and here we can use the ultrarelativistic expressions for energies and the adiabatic law for the state equation with the index "4/3" ($\alpha = e, i$):

$$e = e_e + e_i, \; e_\alpha = 3p_\alpha, \; p = p_e + p_i, \; p_\alpha \sim n_\alpha^{4/3}, \; e + p = 8p_i, \; p = p_0(a_0/a)^2. \tag{4}$$

So, for the necks the system (1) can be rewritten in the form:

$$\hat{P}y = -\hat{Q}\ln x, \quad \hat{Q}y = \hat{P}\ln x, \tag{5}$$

and, coupling both equations (3, 5), we can introduce the approximate "semi-relativistic" pinch model described by the equations:

$$\hat{P}y = -\hat{Q}\ln(1+x), \quad \hat{Q}y = \hat{P}\ln x, \tag{6}$$

where $-\infty \le y = y(r,z) \le +\infty$, $0 \le x = x(r,z) \le \infty$.

3. Solutions for the nonrelativistic plasma state equation (3)

Previously the model (3) with the nonrelativistic plasma state equation in its own coordinate system was considered in papers [1-3], and it is useful to remind the solution for this model. For the solution of the nonlinear equations (3) we introduce — as the first step — two inverse functions $r(x,y)$, $z(x,y)$, and — as the second step — two "main" functions
$T(x,y) = \gamma r - uz$, $Z(x,y) = \gamma z - ur$.
Then, for them one has the linear equations:

$$T'_y = -Z - Z'_x, \quad Z'_y = xT'_x - T, \quad \hat{L}T - T + T''_{yy} = 0, \quad \hat{L} = x\frac{\partial^2}{\partial x^2} + x\frac{\partial}{\partial x} \tag{7}$$

with the "initial conditions" $T = -\infty$ at the point $x = x_0$, $y = 0$. This condition means that at $t \to -\infty$ the pinch is not perturbed and this guarantees the selection of the so called "spontaneous solutions". As shown in [1-3], it is more correct to rewrite the last equation in the form with the "effective Laplacian",
$\Delta^{eff}T = "0" = -4\pi\rho^{eff}$,
where the "effective charge density" is equal $\rho^{eff} = const \cdot \delta(x - x_0)\delta(y)$.

The equation $\hat{L}T = -k^2T$ at $k^2 = 1 + n = 1, 2, 3, \ldots$ has the solutions $T \sim xe^{-x}L_n^1(x)$ with the Laguerr's polynomials L_n^1. Therefore the last equation (7) has the following general solution

$$T(x,y) = w\sum_{n=0}^{\infty} C_n\lambda_n Y^{\sqrt{n+1}}, \quad \text{where} \quad w = xe^{-x}, \quad Y = \exp(-|y|) = \gamma - \sqrt{\gamma^2 - 1}. \tag{8}$$

Here C_n are arbitrary coefficients, and $\lambda_n \sim L_n^{(1)}(x)$ are the normalized Laguerr's polynomials:

$$\lambda_0 = 1, \; \lambda_n = (wn\sqrt{n+1})^{-1}\left(\frac{d}{dx}\right)^n(wx^n), \quad \int_0^\infty \lambda_m\lambda_n w\,dx = \delta_{m,n}. \tag{9}$$

An arbitrary function can be presented as the series of these polynomials, in particular, the delta-function and its derivative have the form

$$\delta(x - x_0) = \sum_{n=0}^{\infty} c_n\lambda_n(x), \quad \frac{d}{dx}\delta(x - x_0) = \sum_{n=1}^{\infty} c_n\frac{d}{dx}\lambda_n(x), \quad c_n = w(x_0)\lambda_n(x_0). \tag{10}$$

We assume that at the "initial instant", $t = -\infty$, the pinch is not perturbed, and this condition means that $T(x, y) = -\infty$ at the "point" $x = x_0$, $y = 0$. The full break of neck corresponds to $x = \infty$, when $T = 0$, and at this "critical" instant all the accelerated particles will be collected in the bulge, where $x = 0$. Therefore the distribution function for the momenta of these particles at this instant is equal

$$dN = n\gamma\pi a^2 dx = N_0\rho_*\gamma dx = F du, \quad F = \frac{dN}{du} = N_0 x_0 (\frac{dx}{x dy})_{T=const} = \frac{N_0 x_0}{\gamma}(T'_x)_{x\to 0}, \qquad (11)$$

where $N_0 = \pi a_0^2 n_0$. As shown in [1-3], the series (9) for T must begin from the number $n = 0$, if perturbation is periodical along the pinch. However, the typical perturbation is focal, and for it the series (9) must begin from $n = 1$. Then, in the ultra-relativistic limit (at $Y \approx 1/2\gamma$) we obtain the energy spectrum of the power type
$dN/dE \sim E^{-\nu}$ with the index $\nu = 1 + \sqrt{3}$,
which is close to the value $\nu_0 \approx 2.74$ "observed" for the galactic cosmic rays.

4. Solutions and spectrum for the "semi-relativistic" model (6)

By the analogous way, from the system (6) one can take the equations:

$$Z'_y = xT''_x - T, \quad T'_y = -Z - (1 + x)Z'_x, \quad \hat{H}T = T + T''_{yy} = "0" = -4\pi\rho_{eff}. \qquad (12)$$

Here $\hat{H}T = x(1 + x)T''_{xx} + xT'_x$ is the hypergeometric operator, and the equation $\hat{H}T = -k^2T$ has the real solution in the form of a sum with two hypergeometrical functions $F(a, b; c; x)$:

$$T = C_k x S_k(x), \quad S_k(z) = (1 - z)^{ik}F(1 + ik, 1 + ik; 2; z) + (1 - z)^{-ik}F(1 - ik, 1 - ik; 2; z) \quad (13)$$

where $z = x/(1 + x)$ — the new argument, and $C_k = const$. Namely the sum (but not diversity!) provides the correct limit $S = 2 + (1 - k^2)x + ...$, $T \sim x$ at $x \to 0$ in the bulges of a pinch.

On the other side (at $x \to +\infty$, $z \to 1$ in the necks), we have the asymptotics $S_k(z \to 1) = -k^{-1}\sin[k\ln(1 - z)]$, and then we use these assimptotics and the definition of delta-function $\delta(k) = (\pi k)^{-1}\lim_{a\to\infty}\sin(ka)$. Then, from two equations:

$$\frac{d}{dz}[(1 - z)\frac{d}{dz}T_1] = -\frac{k_1^2 T_1}{z(1 - z)}, \quad \frac{d}{dz}[(1 - z)\frac{d}{dz}T_2] = -\frac{k_2^2 T_2}{z(1 - z)}, \qquad (14)$$

we can obtain the orthogonality condition for the $S_k(z)$-functions:

$$\int_0^1 S_1 S_2 \frac{z}{1 - z} dz = \frac{\pi}{2k_1 k_2}\delta(k_1 - k_2). \qquad (15)$$

Using this condition, we can find, in particular, the representation for the delta-function and its derivative

$$\delta(z - z_0) = \int_{-\infty}^{\infty} c_k S_k(z)\, dk, \quad \frac{d}{dz_0}\delta(z - z_0) = \int_{-\infty}^{\infty} c_k^1 S_k(z)\, dk, \qquad (16)$$

where
$c_k = 2\pi k^2 x_0 S_k(z_0)/(1 - z_0)$, $c_k^{(1)} = dc_k/dz_0$.

Now, omitting the constant, let us consider the "main" equation which we shall write in the "operator form":

$$\hat{P}T = \hat{H}T - T + T''_{yy} = \delta(y)\frac{d}{dz_0}\delta(z - z_0), \quad T = \int_{-\infty}^{\infty} A_k z S_k(z) Y^q\, dk. \qquad (17)$$

Then, taking account of the relations
$d|y|/dy = sign(y)$, $d[sign(y)]/dy = 2\delta(y)$, $d^2Y^q/dy^2 = [q^2 - 2q\delta(y)]Y^q$,
we find for the left part:

$$\hat{P}T = \int_{-\infty}^{\infty} A_k z S_k Y^q[q^2 - k^2 - 1 - 2q\delta(y)]\, dk.$$

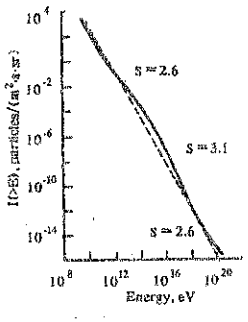
From this we have $q = \sqrt{1+k^2}$ and, taking account of $S_k(z_0 \ll 1) = 2$, we also have

$$\int_{-\infty}^{\infty} A_k z S_k q \, dk = -\frac{d}{2dz_0}\delta(z-z_0), \quad A_k = -\frac{k^2}{\pi q}\frac{d}{z_0 dz_0}\left[\frac{z_0}{1-z_0}S_k(z_0)\right] = -\frac{2k^2}{\pi z_0 q}. \tag{19}$$

Then, the "time" is equal

$$T = -\frac{2}{\pi z_0} z J(z,y), \text{ where } J(z,y) = \int_{-\infty}^{\infty} S_k(z)\frac{k^2}{\sqrt{1+k^2}}\exp(-|y|\sqrt{1+k^2})\,dk, \tag{20}$$

and at $z = 0$ we have $J(z=0,y) = (4/|y|)K_1(|y|)$, where K_1 is the Bessel function of the imaginary argument which has the asymptotics $K_1 \approx \sqrt{\pi/2|y|}\exp(-|y|)$ at $|y| \gg 1$.



Finally, we show that the expression (12) for the spectrum of accelerated particles is valid (since $x \to 0$) in both cases, (3) and (6). Therefore the final momentum distribution for the "semi-relativistic" model (5) takes the form

$$dN/dp \sim K_1(|y|)/\gamma|y| \sim \gamma^{-2}(\ln\gamma)^{-3/2}. \tag{21}$$

at $\gamma \gg 1$. In the ultrarelativistic limit this "semi-relativistic" spectrum is close to the "non-relativistic" spectrum $dN/dE \sim \gamma^{-s}$, with the index $s = 1+\sqrt{3}$. As shown at Fig. 1, both these spectra (broken line) are close to the observed spectrum (solid line) of the galactic cosmic rays.

References

[1] Vlasov V. P., Zhdanov S. K., Trubnikov B. A., Pis'ma v JETP (rus), 1989, v. 49, N 11, p. 581.
[2] Trubnikov B.A., Uspehi Fisicheskich Nauk (rus.), 1990, v. 160, p. 167. See also Trubnikov B.A., IEEE Transections on Plasma Science, 1992, v. 20, N 6, pp. 898-904
[3] Trubnikov B. A., Vlasov V. P., Zhdanov S. K., item p. 905.
[4] Trubnikov B. A., Vlasov V. P., Zhdanov S. K., *About possible generation of cosmic rays and Gamma-bursts in the plasma pinches*, Pis'ma v ZhETF, v.62, N 2, p.86.

RADIOEMISSION OF THE MODULATED ELECTRON BEAM IN THE ACCIDENTALLY INHOMOGENEOUS PLASMA

I.O. Anisimov

Taras Shevchenko University, Radiophysics Dpt., 64Volodimirska st., 252017, Kyiv, Ukraine

The discussed mechanisms of the radioemission of non-modulated electron beams in the ionospherical plasmas are: the beam-plasma discharge burning [1], the development of the radioemission instabilities in the beam-plasma systems [2], the excitation of injector potential oscillations by the fronts of the injection current pulses [3]. In all these cases the radioemission parameters are caused by the beam-plasma system, and the frequency spectrum is rather wide.

For modulated beams the radiation frequency (or spectrum) is caused by the character of the modulation. The mechanisms of the radioemission in this case are the Cherenkov excitation of the eigenmodes of the background plasmas that are in the synchronism with a beam [4] and the transitional radiation on the regular plasma inhomogeneities [5]. The ionospherical plasma is accidentally inhomogeneous, so the transitional radiation may be caused by this accidental inhomogeneity.

The radioemission of the half-infinite thin modulated electron beam in the accidentally inhomogeneous planarly-stratified cold isotropic plasma is calculated. The alternative component of the beam current is written as

$$\vec{j}(\vec{r},t) = \vec{e}_z j_m \alpha(\rho)\beta(z)\exp(i\omega t - i\kappa z - z/L), \qquad (1)$$

$$\alpha(\rho) = \begin{cases} 1, \rho \le a; \\ 0, \rho > a; \end{cases} \qquad \beta(z) = \begin{cases} 1, z \ge 0; \\ 0, z < 0, \end{cases}$$

where ρ, φ, z are cylindrical co-ordinates, $\kappa = \omega/v$, v is the beam velocity, L is the relaxation length. The modulation frequency ω is assumed to be high comparatively to the Langmuir frequency of the background plasma. The plasma concentration is assumed to depend only on z. It means that the beam radius is small comparatively to the transversal dimension of the plasma inhomogeneities.

H_φ component of the electromagnetic field that is exited in plasma with the permittivity $\varepsilon(z)$ by the given current (1) can be found from the equation

$$\frac{\partial}{\partial\rho}\left[\frac{1}{\rho}\frac{\partial}{\partial\rho}\left(\rho H_\varphi\right)\right]+\frac{\partial^2 H_\varphi}{\partial z^2}-\frac{1}{\varepsilon(z)}\frac{\partial\varepsilon(z)}{\partial z}\frac{\partial H_\varphi}{\partial z}+k_o^2\varepsilon(z)H_\varphi=\frac{4\pi}{c}\frac{\partial j_z}{\partial\rho}, \quad (2)$$

where $k_o=\omega/c$. It is difficult to find the solution of the stochastic equation (2) with the accidental coefficient $\varepsilon(z)$. So let us assume additionally that

$$\varepsilon(z)=\varepsilon_o+\varepsilon_1(z), \qquad |\varepsilon_1(z)|<<\varepsilon_o \quad (3)$$

(this assumption is usually valid for the ionosphere). Consequently the solution of (2) can be find as a row of the consistent approximations after ε_1:

$$H_\varphi=H_o+H_1+\ldots$$

The equations for the zero approximation and for the first approximation are:

$$\frac{\partial}{\partial\rho}\left[\frac{1}{\rho}\frac{\partial}{\partial\rho}\left(\rho H_o\right)\right]+\frac{\partial^2 H_o}{\partial z^2}+k_o^2\varepsilon_o H_o=\frac{4\pi}{c}\frac{\partial j_z}{\partial\rho}, \quad (4)$$

$$\frac{\partial}{\partial\rho}\left[\frac{1}{\rho}\frac{\partial}{\partial\rho}\left(\rho H_1\right)\right]+\frac{\partial^2 H_1}{\partial z^2}+k_o^2\varepsilon_o H_1=\frac{1}{\varepsilon_o}\frac{\partial\varepsilon_1}{\partial z}\frac{\partial H_o}{\partial z}-\varepsilon_1 k_o^2 H_o. \quad (5)$$

The solution of (4) consists of two parts. One part is the electromagnetic radioemission caused by the longitudinal restriction of the beam (the beam current increases abruptly in the plane $z=0$). It can be written in the far radiation zone as

$$H_o^{rad}=\frac{2\pi a j_m}{Rc}\frac{J_1(ka\sin\theta)}{\kappa-k\cos\theta-i/L}\exp\left(-ikR-i\frac{3\pi}{4}\right), \quad (6)$$

where $k=k_o\sqrt{\varepsilon_o}$, and R,θ,φ are the spherical co-ordinates. The total radiated power for the case of the long ($kL>>1$) thin ($ka<<1$) non-relativistic ($v<<c$, consequently $\kappa>>k$) beam is

$$P^{resir}=\frac{2I_m^2\sqrt{\varepsilon_o}}{3c}\left(\frac{v}{c}\right)^2, \quad (7)$$

where $I_m=\pi a^2 j_m$ is the magnitude of the beam alternative current.

Another part is the Eugene electromagnetic field of the beam in the homogeneous plasma. If $kL>>1$, it can be given in the form

$$H_o^{beam} = \begin{cases} -\dfrac{4\pi a j_m}{c} F\left(k_z = -\kappa + i/L, \rho\right) \exp\left(-i\kappa z - z/L\right), z > 0; \\ 0, z < 0, \end{cases} \quad (8)$$

where

$$F\left(k_z, \rho\right) = \begin{cases} -K_1\left(\sqrt{k_z^2 - k^2}\, a\right) I_1\left(\sqrt{k_z^2 - k^2}\, \rho\right), \rho \le a; \\ -K_1\left(\sqrt{k_z^2 - k^2}\, \rho\right) I_1\left(\sqrt{k_z^2 - k^2}\, a\right), \rho > a, \end{cases}$$

$K_\nu\left(x\right)$ and $I_\nu\left(x\right)$ are modified Beset functions.

The scattering of the field (7) on the plasma inhomogeneities gives rise to the transitional radiation that can be found from (5):

$$H_1^{rad} = \frac{i\pi^2 a j_m}{c} \int_0^\pi \frac{\varepsilon_1\left(\kappa + k\cos\vartheta\right)}{\varepsilon_o} \frac{\kappa\left(\kappa + k\cos\vartheta\right) - k^2}{\kappa^2 - k^2\cos^2\vartheta} J_1\left(ka\sin\vartheta\right) \times$$

$$\times H_1^{(2)}\left(k\rho\sin\vartheta\right) \exp\left(ikz\cos\vartheta - z/L\right) k\sin\vartheta d\vartheta, \quad (9)$$

where

$$\varepsilon_1\left(K\right) = \frac{1}{2\pi} \int_{-\infty}^{\infty} \varepsilon_1\left(z\right) \exp\left(-iKz\right) dz$$

is the spatial Furrier spectrum of the accidental plasma inhomogeneities.

During the ensemble averaging of the energy flow density the stationarity of the random function $\varepsilon_1\left(z\right)$ must be taken into account :

$$\left\langle \varepsilon_1\left(\kappa + k\cos\vartheta\right) \varepsilon_1^*\left(\kappa + k\cos\vartheta'\right) \right\rangle = G_\varepsilon\left(\kappa + k\cos\vartheta\right) \delta\left(k\cos\vartheta - k\cos\vartheta'\right),$$

where $\delta\left(x\right)$ is the Dirac function, $G_\varepsilon\left(K\right)$ is the spectrum intensity of the random function $\varepsilon_1\left(z\right)$. Consequently the radial component of the energy flow density for the non-relativistic thin beam ($\kappa >> k, ka << 1$) can be given in the form:

$$\Pi_\rho = \frac{2\pi^2 j_m^2 k^3 a^2 G_\varepsilon\left(\kappa\right)}{\varepsilon_o^3 \omega c \rho} \exp\left(-2z/L\right).$$

The radiated power from the unit beam length can be written as

$$P_L = \frac{4\pi\omega^2 I_m^2}{3\varepsilon_o^{3/2} c^3} G_\varepsilon\left(\kappa\right) \exp\left(-2z/L\right),$$

and the total radiated power is

$$P^{trans} = \frac{2\pi L\omega^2 I_m^2}{3\varepsilon_0^{3/2} c^3} G_\varepsilon(\kappa). \qquad (10)$$

This radiation is caused by the narrow ($\Delta K/K \sim v/c$) band of the spectrum intensity $G_\varepsilon(K)$. Its magnitude can be significant only if the level of the background plasma fluctuations is not very small - in the aurora ionosphere, for example.

The spectrum intensity is assumed to have a Gaussian distribution with the maximum at $K = \kappa$ and with the width $\Delta K \sim \kappa$. Then $G_\varepsilon(\kappa) = \sigma_\varepsilon^2 v/\omega\sqrt{2\pi}$, where σ_ε is the variance of the random function $\varepsilon_1(z)$. For the auroral region the spectrum intensity along the magnetic field has a maximum at the wavelength 10 m [6], the Langmuir frequency of the background plasma $\omega_p = 6\times 10^7 s^{-1}$, the cyclotron frequency is $\omega_H = 1.1\times 10^7 s^{-1}$. Let us assume the beam modulation frequency to make $\varepsilon_0 = 0.1$, then the influence of magnetic field can be neglected in the first approximation for the case of the beam injection along the field lines. For the auroral region the relative density fluctuations level is about 10^{-3}, then $\sigma_\varepsilon/\varepsilon_0 = 10^{-2}$. To satisfy the condition $K = \kappa$ for the modulation frequency let us take $v/c = 0.3$. Then for $L = 150m, I_m = 1A$ from (10) $P^{trans} = 2.5W$. This power is enough to be detected in the active beam-plasma experiments in the ionosphere. For the same data from (7) $P^{restr} = 0.6W$.

References

1. Е.В.Мишин, Ю.Я.Ружин, В.А.Телегин. Взаимодействие электронных потоков с ионосферной плазмой. М., Гидрометеоиздат, 1989. 264с.

2. А.С.Волокитин, Г.В.Лизунов. // Физика плазмы. 1993, **19**, 6, 723-731.

3. В.А.Федоров. // Геомагнетизм и аэрономия. 1984, **24**, 2, 205-210.

4. Н.Я.Коцаренко, Г.В.Лизунов, А.А.Силивра. // Космич.исслед. 1988,**26**,6,874-879.

5. И.А.Анисимов, С.М.Левитский. // Физика плазмы. 1994, **20**, 9 ,824-827.

6. Н.Д.Филипп. Рассеяние радиоволн изотропной ионосферой. Кишинев, Штиница, 1974. 188с.

ON THE POSSIBILITY TO OBSERVE THE WHISTLER MODES TRANSITIONAL RADIATION IN THE BEAM-PLASMA EXPERIMENTS IN THE IONOSPHERE

I.O.Anisimov, *O.I.Kelnyk*

Taras Shevchenko University, Radiophysics Dpt., 64 Volodimirska St., 252017, Kyiv, Ukraine

The detection of electromagnetic waves radioemission of electron beams that where injected from the spacecraft board was one of the well-known results of the active beam-plasma experiments in the ionosphere. Waves in the band between the high hybrid and electron cyclotron frequencies were registered in ARAKS, STS-3, "Electron echo" and some other experiments [1]. This waves may be identified as the whistler modes. The discussed mechanisms of the whistler excitation were the beam-plasma instability [2] for non-modulated beams and Cherenkov radiation [3] for modulated beams. The transitional radiation of the modulated electron beams on the concentration jump of the background plasma is treated in this report as a possible mechanism of the whistler modes radiation. The plasma concentration jump can appear at the boundary of the plasma cloud that is injected from the spacecraft for its neutralisation (see, for example, [4]). The situation can take place when the electron beam injected from the spacecraft board can move through the border to the dense plasma region. Than the transitional radiation of the beam directed backwards relatively to the beam velocity can be registered on the spacecraft board. The directivity diagram and total radiated power for such radioemission are calculated in this report.

The cold collisionless plasma with the electron concentration

$$n_p(z) = \begin{cases} n_1, z < 0; \\ n_2, z \geq 0 \end{cases} \qquad (1)$$

is treated. The constant magnetic field H_0 is parallel to z-axis. The alternative current density caused by the modulated electron beam that is assumed to be given can be written as

$$\vec{j}(\vec{r}, t) = \vec{e}_{z\,m} I \frac{\delta(r)}{\pi r} \exp(i\omega t - i\kappa r), \qquad (2)$$

where r, φ, z are cylindrical co-ordinates, $\kappa = \omega / v$, v is the beam velocity, and the modulation frequency ω satisfies the whistler approximation conditions:

$$\omega_{pe} >> \omega_{He} >> \omega >> \omega_{pi}. \tag{3}$$

Here $\omega_{pe,i} = \sqrt{\frac{4\pi n e^2}{m_{e,i}}}$ are the electron and ion Langmuir frequencies, $\omega_{He} = \frac{eH_0}{m_e c}$ is the electron cyclotron frequency.

The beam current (2) can be written as Furrier-Bessel integral:

$$\vec{j} = \vec{e}_z \int dj(k_\perp) = \frac{\vec{e}_z I}{2\pi} \int_0^\infty J_0(k_\perp r) \exp(i\omega t - i\kappa z) k_\perp dk_\perp. \tag{4}$$

The current wave $dj(k_\perp)$ excites the electromagnetic wave with the same ω and $k_\perp$ on the concentration jump due to the transitional radiation mechanism. The magnitude longitudinal electric field of the excited wave is

$$dE_z(k_\perp) = T(k_\perp) \frac{i4\pi}{\omega \varepsilon_{//}} dj(k_\perp), \tag{5}$$

where $\varepsilon_{//} \approx -\omega_{pe}^2 / \omega^2$ is the longitudinal component of the permittivity tensor, and the transformation coefficient $T(k_\perp)$ is calculated in [5]. For the case $n_2 >> n_1$ it has a form

$$T\left(\sqrt{\frac{\omega}{\omega_{He}\cos\theta}} \frac{\omega_{pe}}{c} \sin\theta\right) = \frac{\beta \frac{\omega_{pe1}}{\omega_{He}} \sqrt{\frac{\omega}{\omega_{He}}} tg\theta}{1 - \frac{\cos\theta}{\sqrt{1-\sin^2\theta}} \frac{1-\cos\theta}{1-\frac{1+\sin^2\theta}{\cos\theta}}}, \tag{6}$$

where $\beta = v/c$, θ is an angle between the wave vector of the radiation in the region "1" and z-axis. The magnitudes ratio for the radiation backwards and forward is directly proportional to n_2 / n_1, so in this approximation almost the whole radiated

power will go backwards.

The radiation field in the far zone can be received by integrating (5) using the stationary phase method:

$$E_z = A\sum_{\alpha=1}^{2} G\left(\theta_\alpha,\psi\right);$$

$$E_r = \left(\frac{\omega_{He}}{\omega}\right)^2 A\sum_{\alpha=1}^{2} G\left(\theta_\alpha,\psi\right)ctg\theta_\alpha;$$

$$H_\varphi = \frac{\omega\varepsilon_{III}}{ck_{wh}} A\sum_{\alpha=1}^{2} G\left(\theta_\alpha,\psi\right)\frac{ctg\theta_\alpha}{\sqrt{\cos\theta_\alpha}}, \qquad (7)$$

where

$$A = \frac{ik_{wh}I_m}{\omega\varepsilon_{III}R}\exp(i\omega t);$$

$$G\left(\theta_\alpha,\psi\right) = (i)^{2-\alpha}T\left(\theta_\alpha\right)\frac{\sin^{1/2}\theta_\alpha\left(1+\cos^2\theta_\alpha\right)}{\cos^{7/4}\theta_\alpha\sin^{1/2}\psi}\left|\frac{\partial^2 S}{\partial\theta^2}\right|^{-1/2}_{\theta=\theta_\alpha} \times$$

$$\times\exp\left[-ik_{wh}RS\left(\theta_\alpha,\psi\right)\right];$$

$$S(\theta,\psi) = \frac{\cos(\theta-\psi)}{\sqrt{\cos\theta}}; \qquad (8)$$

$k_{wh} = \frac{\omega_{pe}}{c}\sqrt{\frac{\omega}{\omega_{He}}}$ is the whistler wave number, $\theta_{1,2} = arctg\left(\frac{1\pm\sqrt{1-8tg^2\psi}}{2tg\psi}\right)$ are the stationary phase points, ψ,ϕ,R are the spherical co-ordinates ($r = R\sin\psi, z = R\cos\psi$). Two stationary phase points appear because the dependence of the energy flow direction on the angle between the wave vector and the magnetic field is not monotonic, i.e. two waves with different $k_\perp$ can give a contribution to the energy flow P_R of the given direction.

The directivity diagram and total radiated power were calculated numerically

from (7-8). The radiation takes part at the angles $\psi < \psi_{max} = arctg\, 1/2\sqrt{2} \approx 20°$. For the usual conditions of the active beam-plasma experiments ($I_m = 1A$, $\beta = 0.1$, $H = 300 - 700km$) the total radiated power $P = 1 - 10W$, the corresponding efficiency is about 10^{-3}. The directivity diagram has a form of the narrow cone with a maximum at $\psi \approx 7 - 9°$ (fig.1).

This estimation shows that the whistler modes transitional radiation on the considerable plasma inhomogeneities that can be formed in the vicinity of the spacecraft has a magnitude enough to be registered experimentally. The comparison of these results with the calculations of the whistler modes Cherenkov excitation [3] shows that for the assumed conditions the efficiency of the transitional radiation is greater by about an order of magnitude.

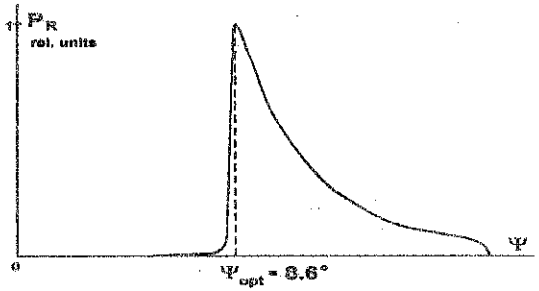


Fig. 1
Directivity diagram of the whistler modes radioemission.

References

1. Н.И.Ижовкина, С.А.Пулинец, Е.П.Трушкина. // Космич. исслед. 1986, 24, 1, 139-142.

2. Е.В.Мишин, Ю.Я.Ружин, В.А.Телегин. Взаимодействие электронных потоков с ионосферной плазмой. М., Гидрометеоиздат, 1989. 264с.

3. Н.Я.Коцаренко, Г.В.Лизунов, А.А.Силивра. // Космич. исслед. 1988, 26, 6, 874-879.

4. В.Н.Ораевский, Ю.Я.Ружин, В.С.Докукин. // Проект АПЭКС: научные задачи, моделирование, методика и техника проведения эксперимента. М., Наука, 1992. С.29-40.

5. И.А.Анисимов, Д.Г.Стефановский. // Радиотехн.и электроника, 1991, 36, 1, 108-117.

TO THE PROBLEM OF GENERATION MECHANISM OF SOLAR TYPE III BURSTS

A.N.KRYSHTAL

Department of Cosmic Plasma Physics, Main Astronomical Observatory of the National Academy of Sciences of Ukraine, 252650, Golosecvo, Kiev, Ukraine.

Modelling of physical conditions in solar atmosphere in case of partial violating of local thermodynamical equilibrium (LTE), carried out on the base of Fraunhofer line profile's analysis, has detected an essential contribution of photosphere processes to the energy balance of a flare [1]. An existence of temperature heterogeneities, which move deep into the atmosphere during a flare, permits in the framework of this model to make an assumption about wave character of photosphere's excitation. Different types of plasma waves can be generated in the lower atmosphere of flare loop structure due to a rise and development of plasma instabilities. One of the main sources of these instabilities may be a large-scale electric field E_0 [5,6]. Specific temporal and spatial behaviour of this field [7] admits the "direct initiation" of instability by field E_0 and provides the stationary scenario of instability development [5]. A principal possibility of generation in solar atmosphere the second harmonic of weakly-oblique Bernstein modes has been shown in paper [6]. In present paper the complete numerical analysis for chromosphere plasmas has been carried out together with exact taking into account an influence of Landau damping. This damping can essentially change the process of instability development [5].

To obtain the value of a growth rate the method described in [5,6] has been used. The final expression for this growth rate (in Ω_e units) has the form :

$$\Gamma_\omega = \gamma/\Omega_e = z\{[2G_1\varepsilon_r(zp\tau)^{-1} - G_2]\nu^* - G_3\} \times$$
$$\times[G_4 - \varepsilon_r(\nu^*)^2(p\omega_r^2)^{-1}(2/\tau)^4 G_5 + G_6]^{-1}, \quad (1)$$

where

$$G_1 = (1+\tau)^{-1/2}[1+7\tau/4+48(2+7\tau)(zp^2\tau\omega_r^2)^{-1}], \quad (2)$$
$$G_2 = 1 - z\tau/2\omega_r^2 - 2(zp^2\tau\omega_r^2)^{-1}(1+9\tau/4)(1+\omega_r^2/z+\omega_r^2\exp(-z)/3), \quad (3)$$
$$G_3 = 2\Phi[1+(\nu^*)^2p^4\exp(z)\varepsilon_r(p\tau - 2(2\pi)^{1/2})/4], \quad (4)$$
$$G_4 = 1+\tau(1+\omega_r^2\exp(-z)/3) + 3(1+17\tau/6)/(p\tau)^2, \quad (5)$$
$$G_5 = (1+\tau)^{-3/2}[1+15\tau(1 - 2z/5\omega_r^2)/4 + 16\tau\omega_r^2/z^2], \quad (6)$$
$$G_6 = zp^4\nu^*\Phi[(1+p\nu^*(2\pi)^{1/2})\omega_r^2\exp(-z)z^{-1} + 4Sc_rp^3(1+\tau)^{1/2}(4p\nu^*(2\pi)^{1/2} - 1)]/4, \quad (7)$$
$$S = z^2\exp[-(p\tau)^2/2]/2; \quad (8)$$
$$\Phi = [\pi(1+\tau)/2]^{1/2}(1 - k_r^2)\,pS\omega_r^2\exp(-z)/z, \quad (9)$$
$$p = z^{-1/2}k_r^{-1}; \quad \tau = \nu\omega_r^2\exp(-z)/4; \quad c_r = E_0/E_d = eE_0/(m_ev_{ei}V_T). \quad (10)$$

In equation (1)-(10) the following notations were used:

$$k_r = k_z/k_L\ ;\ z = k_L^2V_T^2/\Omega_e^2\ ;\ \omega_r = \omega p/\Omega_e\ ;\ \nu^* = \nu_{ei}/\Omega_e\ ; \quad (11)$$
$$V_T^2 = k_bT_e/m_e\ ;\ \omega p^2 = 4\pi ne^2/m_e\ ;\ \Omega_e = eB_0/m_ec. \quad (12)$$

where V_T, ω_p and Ω_e are electron thermal speed, electron plasma frequency and electron gyrofrequency respectively, E_0 and B_0 are the amplitudes of external electric and magnetic fields, k_z and $k_\perp$ are longitudinal and perpendicular components (with respect to $B_0 \parallel E_0$) of perturbation wave vector respectively. The value ν_{ei} denotes the ion-electron collision frequency.

With taking into account the results of well known models of solar chromosphere [1,5,7] the electron temperature T_e, particle number density n_e and magnetic field amplitude B_0 were assumed to lie in intervals

$$9{,}7\times10^{15} \le n_e \le 1{,}3\times10^{19}\ (m^{-3}), \tag{13}$$

$$4000 \le T_e \le 35000\ K, \tag{14}$$

$$0{,}01 \le |B_0| \le 0{,}15\ (Tl). \tag{15}$$

These suppositions automatically lead to the following intervals of reduced values :

$$0{,}1 \le \omega_r^2 \le 0{,}5625, \tag{16}$$

$$0{,}01 \le x \le 0{,}25, \tag{17}$$

$$0 \le \alpha_r \le 0{,}20, \tag{18}$$

$$0 < k_r \le k_r^{max}. \tag{19}$$

The value of maximum tilt angle $k_r^{max} = tg(k_r^{max})$ was determined from the condition :

$$|(\omega - k_z\alpha_r V_T - 2\Omega_e)/k_z V_T| \gg 1. \tag{20}$$

The existence of clearly expressed maximum at the point with coordinates $x = 0{,}25$; $k_r = 0{,}012$ and $\omega_r = 0{,}75$ at $\alpha_r = 0{,}20$ (and $\alpha_r^{min} = 0{,}043$), where $\Gamma_\omega = 2{,}13\times10^{-5}$, for "connected pair" (i.e. for given equation of state of solar atmosphere) $n_e = 1{,}0\times10^{11}\ cm^{-3}$ and $T_e = 6500$ K [5] certainly proves the existence of instability. It is evidently from general physical considerations that ω_r has not to be a variable. But the absence of such kind of solar atmosphere's equation of state, where together with "connected pair" $n_e(H)$ and $T_e(H)$ as functions of height H above the photosphere, the value $B_0(H)$ (corresponding to them) could be presented, is the main reason to consider ω_r as a variable in the context of given problem. For the mechanism of "direct initiation" of instability [5] only the value $\alpha_{\Gamma} = (\alpha_r)_{\Gamma=0}$ at which a growth rate $\Gamma_\omega = 0$ has certain physical significance. And the value α_r^{min} at which Γ_ω becomes positive ("comes out" to the area $\Gamma_\omega > 0$) is determined with the accuracy which depends on the value of relative density fluctuation $(\delta n/n) = \delta_n$. In present work this value was supposed to be $\delta_n \le 0{,}01$.

The instability considered above can have an interesting physical consequences. The proved possibility of "quasi-Bernsteinian" second harmonic's generation in lower atmosphere of solar flare at small values of $\alpha_r \ll 1$ can mean the principal possibility of correlation of microwave radiation from a region near the footpoint of the loop and radiation of type III burst in coronal region. "Runaway" electrons from dense plasma of lower layers can therewith be the main source of this burst. At $n_e = 1{,}0\times10^{11}\ cm^{-3}$ and $\alpha_r = 0{,}12$ the needed "initial" value of electron beam density $N_b \sim 5\times10^5\ cm^{-3}$ [3] can be provided. This beam accelerated in field E_0 can elevate along the loop and reach in rarefied coronal plasma the

velocity value $V_b \sim 0{,}2c$ (where $c = 3 \times 10^{10}$ cm/sec) [8], which is enough to generate the solar type III burst in frequency range 300-500 MHz. Just before this time the second harmonic of weakly-oblique "quasi-Bernsteinian" modes can be emitted from a region near the footpoint in the form of microwave radiation in the range 10-50 GHz. Such situation corresponds to the case, when the burst's source is located in the loop above the microwave source [3].

The most recent observational program carried out for active region NOAA 7128 with the help of stereoscopic method [2] at OVRO (13-15 April 1992) has allowed to detect the correlation between soft X-ray emission (SXRE) and microwave radiation in frequency range 10-14 GHz. At the same time investigation, which gives the positive result for mutual correlation of type III bursts and metric spikes [3], hasn't obtained any correlation between type III bursts and microwave radiation (and bursts of hard X-ray emission (HXRE) too). But it does not mean that this result has to be considered as final one, because it is well known fact, that physical conditions in different flares can differ greatly [4]. Anyway, the principal possibility of such effect, based on the results of present work, permits to expect an essential progress in realization of the role of large-scale electric fields in flare processes.

Author thanks the Administration of the First Kiev branch "Ukrneftegasbank" for their friendly help and financial support.

REFERENCES

[1] Alikaeva,K.V. et al.,1995, Kinematics and Physics of Celestial Bodies, 11, No.2, 11-24.

[2] Aschwanden,M.J. et al.,1995, ApJ., 454, 512-521.

[3] Benz,A.O. et al.,1996, A&A, 309, No.1, 291-300.

[4] De Jager,C.,1959, Structure and Dynamics of the Solar Atmosphere, Springer.

[5] Kryshtal,A.N. &Kucherenko,V.P.,1995, J.Plasma Physics, 53, part 2, 169-184.

[6] Kryshtal,A.N.,1992, Proceedings of the 26th ESLAB Symposium (Killarney,Ireland,16-19 June,1992), ESA SP-346, 301-306.

[7] Poletto,G.and Kopp,R.A.,1986,The Lower Atmosphere of Solar Flares (ed.D.F.Neidig), Sacramento Peak, 453-460.

[8] Zheleznyakov,V.V.,1964, Radioemission of the Sun and Planets, Nauka (in Russian).

NONLINEAR LOW-FREQUENCY WAVES IN MAGNETIZED SPACE PLASMA

N. Ya. Kotsarenko, Yu. G. Rapoport, A. A. Shvidkij, **Yu. V. Khotyaintsev**
Kiev Shevchenko University, Astronomy and Space Physics Department

First publications on the nonlinear theory of magnetohydrodynamic waves in plasma has been made in 50-60^s (look [1]-[3]). In recent times variety of structures in plasma are investigated [4] theoretically and experimentally, specially in connection with large scale space experiments such as international project INTERBALL. Automodel solutions for the structures of an arbitrary amplitude are of special interest to investigate the possibility of observation of these structures. Despite the number of publications on this problem until current moment, nonlinear structures are purely investigated. We obtained automodel integral, useful for performing the estimates, made the comparison of exact solution of automodel equations with small parameter method. The regions of existence of structures and spectral peculiarities, useful for the intendification of given structures with the results of satellite observations, were studied.

We consider cold magnetized collisionless plasma. Such plasma is governed by two-liquid magnetohydrodynamics and Maxwell equations.

$$\frac{\partial \vec{v}_\alpha}{\partial t}+\left(\vec{v}_\alpha \vec{\nabla}\right)\vec{v}_\alpha=-\frac{q_\alpha}{m_\alpha}\left(\vec{E}+\frac{\vec{v}_\alpha}{c}\times\vec{H}\right) \quad (1a), \quad \frac{\partial n_\alpha}{\partial t}+\mathrm{div}\left(n_\alpha \vec{v}_\alpha\right)=0 \quad (1b),$$

$$\mathrm{rot}\,\vec{H}=\frac{4\pi e}{c}\left(n_i\vec{v}_i-n_e\vec{v}_e\right) \quad (2a), \quad \mathrm{rot}\,\vec{E}=-\frac{1}{c}\frac{\partial \vec{H}}{\partial t} \quad (2b), \quad \mathrm{div}\,\vec{H}=0 \quad (2c)$$

Here m_α, $\vec{v}_\alpha$, n_α, q_α — mass, velocity, density and charge of electrons (α=e) and ions (α=i) respectively. We consider the waves propagating along Z axis. The external magnetic field will be $\vec{H}_0=\left\{\vec{H}_0\sin\theta,0,\vec{H}_0\cos\theta\right\}$. Let all variables be the functions of one automodel variable $\xi=z-v_0t$, where v_0 is a wave velocity. Full magnetic field is presented in the form $\vec{H}=\vec{H}_0+\vec{h}(\xi)$. Neglecting the electron inertia from the initial system of equations we obtain

$$v_{ex}=v_{ix}=v_i, \qquad \left(1-\frac{v_i}{v_0}\right)\cos\theta\frac{d\tilde{h}_x}{dx}=\left(1-\frac{v_i}{v_0}-\beta\cos^2\theta\right)\tilde{h}_y \quad (3),$$

$$\left(1-\frac{v_i}{v_0}\right)\cos\theta\frac{d\tilde{h}_y}{dx}=-\left(1-\frac{v_i}{v_0}-\beta\cos^2\theta\right)\tilde{h}_x+\frac{v_i}{v_0}\sin\theta, \quad \frac{v_i}{v_0}=\beta\frac{\tilde{h}_x^{\,2}+\tilde{h}_y^{\,2}}{2}+\beta\sin\theta\tilde{h}_x,$$

where $\tilde{h}_{x,y} = h_{x,y}/H_0$, $x = \frac{\omega_{Bi} v_0}{C_A^2}\xi$, $C_A = \frac{H_0}{\sqrt{4\pi n_0 (M+m)}}$ — Alfven velocity, $\beta = \frac{C_A^2}{v_0^2}$. We can integrate this system and obtain the integral

$$\left(\tilde{h}_y^2 + \tilde{h}_x^2 + 2\tilde{h}_x \sin\theta + \alpha\right)^2 = 4\alpha\,\tilde{h}_x \sin\theta + c \quad (4) \qquad \text{where } \alpha = 2\left(\cos^2\theta - 1/\beta\right).$$

The results of numerical soluton for the case of soliton $c=\alpha^2$ are presented on fig. 1, namely, the automodel variable dependence of density for compression soliton (a) and for raritive soliton (b). Curve 1 presents the solution of exact equations (3), curve 2 presents approximate solution obtained rfom the small parameter mathod). Comparison of exact solution (fig.2, curve 1 for dependence of rarity soliton half-width on amplitude $\varepsilon = v_1/v_0$) with small parameter method (fig.2, curve 2) has been made. We can mention that results of exact and approximate solutions are in a good agreement even for not small (ε>0.3). So small parameter

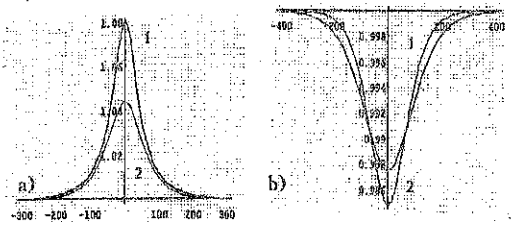


Fig. 1 Dependence of density for compression soliton (a) and for raritive soliton (b).

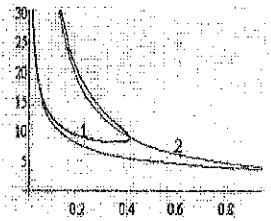


Fig. 2 dependence of rarity soliton half-width on amplitude

mathod can work out of the formal borders of application region. Such calculations has been made for dependence of soliton velocity on amplitude. The characteristic size of given soliton in magnetosphere on the 3-4 R altitude for the anglele $\theta \approx 10$ is 10^3 km.

Let us consider periodical structures ($\alpha \neq c^2$, $\alpha = c^2$ is the case of the solitary wave) . Depending on the parameters $i = c - \alpha^2$ and $\beta = 1/v^2$ we can distinguish regions of existence of different types of structures (fig. 3). In the region II two types of structures exist: first type (a), periodical sequence of significantly nonlinear pulses, second type (c), quasi harmonical waves. When we shift from the region II to the region I the second type

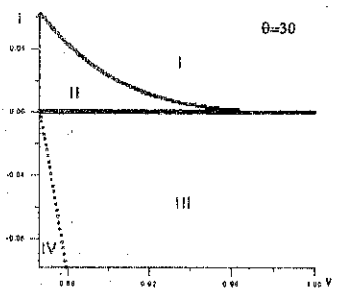


Fig. 3. Bifurcation curves.

disappears. In the region III we have structure (b) which is a hybrid of structures of the two above mentioned types. Bold line at i=0 corresponds to the case of solitary wave. There are no periodical waves in the region IV.

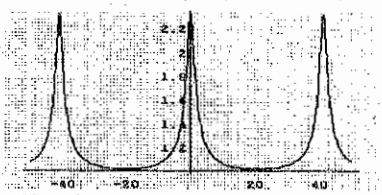


Fig. 4. Automodel coordinate dependence of dencity for the case (a).

Let us consider the above mentioned types of structures.

Case (a). This type of structure presents periodical sequence of significantly nonlinear compressive pulses (fig. 4). The automodel variable dependense of the magnetic field components and the corresponding curve in the phase plane h_x, h_y are presented on fig. 5. This



Fig. 5. Case (a)
(a) automodel coordinate dependence of field components,
(b) phase plane h_x, h_y.

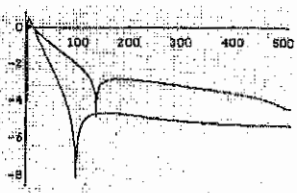


Fig. 6. Spectrum for the case (a) (logariphmic scale).

type of structures has some interesting spectral peculiarities. The Fourier transform of the magnetic fied components is presented on fig. 6. Spectrum is comparatively wide and has a peculiarity in the form of a sharp minimum. This spectral peculiarity may be used for the identification of given structures with the results of satellite observations.

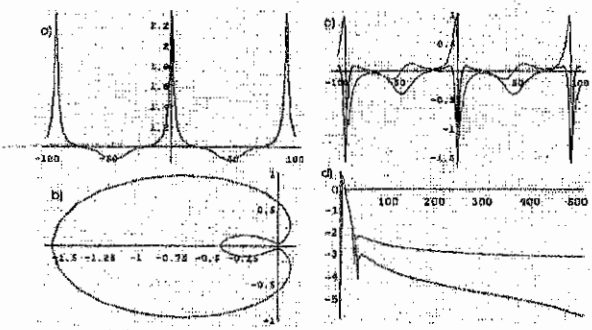


Fig. 7. Case (b)
(a) automodel variable dependense of density,
(b) phase plane h_x, h_y,
(c) automodel variable dependense of field components,
(d) spectrum (logariphmic scale).

Case (b). This type of structures presents periodical sequence of compressive and raritive pulses (fig. 7a)

. The automodel variable dependense of the magnetic field components and the corresponding curve in the phase plane h_x, h_y are presented on fig.7 b and c . For this structure spectrumis not so wide as in the previous case but the peculiarity remains (fig. 7d).

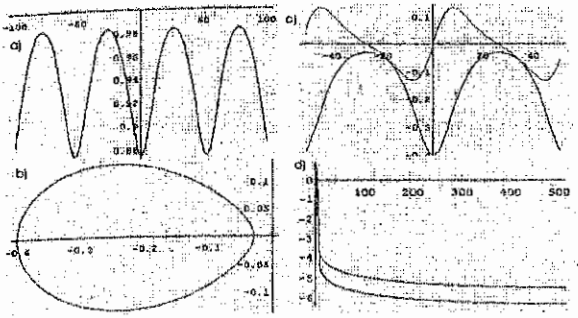


Fig. 8. Case (c)
(a) automodel variable dependense of density ,
(b) phase plane h_x, h_y ,
(c) automodel variable dependense of field components ;
(d) spectrum (logariphmic scale).

Case (c). Structures of this type are quasiharmonical rarilive waves (fig. 8a). The automodel variable dependense of the magnetic field components and the corresponding curve in the phase plane h_x, h_y are presented on fig.8 c and b. Spectrum is practically monohromatic and substantially differs from the spectrums of the two above mentioned types of structures (fig.8d).

Estimates of the characteristic size of structures investigated in the Earth magnetosphere are presented in tab. 1.

H	θ=30	θ=30	θ=30
KM	$\nu = \cos\theta$ I=0.0005	$\nu = \cos\theta$ I=0.0005	$\nu = \cos\theta$ I=-0.0005
500	160	210	400
1000	360	470	900
3-4 R	960	1250	2400

Tab. 1 Characteristic structure size.

1. Sagdeev R. Z. Voprosi teoriji plasmi / Pod red. M. A. Leontovicha, v.4, p.20. M.: Gosatomisdat, 1964.
2. Kellog P.J. Solitary Waves in Cold Collisionless Plasma, Physics of Fluids p. 1555-1571, vol. 7, n 10, 1964.
3. B. A. Tverskoj. Ob odnomernih avtomodelnih, raspostranjajushihsa v plasme vdol magnitnogo. JETP, 1962, v. 42, 3, p. 833-838.
4. Danilov A. V. Bistrie magnitozvukovie volni konechnoj amplitudi v razrejennoj plasme JETP, v. 101, 1 p. 89-97, 1992.

PLASMA-CURRENT-PRODUCED CHARGING OF A DUST PARTICLE

V.P.Kubaichuk, A.G.Zagorodny

Bogolyubov Institute for Theoretical Physics
14b Metrolohichna str., 252143 Kiev, Ukraine

The study of dusty plasma relaxation requires the understanding of the dust particle charging dynamics. One may expect that the dust particle polarization produced by an approaching electron or ion should influence both the charge accumulation rate and the stationary charge value since the image charge considerably modifies the interaction between dust and plasma particles [1]. In this paper we consider the polarization influence on the evolution of dust particle charge accumulation and calculate charging cross-sections in an equilibrium plasma consisting of electrons and singly charged ions.

The metal dust particle is simulated by a conducting ball of radius a. The energy of interaction between the charged ball and a plasma particle is given by [1]

$$V(r) = \frac{Qq}{r} + \frac{q^2}{2r^2(r^2-1)}, \qquad (1)$$

where $r = \rho/a$; ρ is the distance between the plasma particle and the ball center; $Q=Ze$ and q are the ball charge and the plasma particle charge, respectively.

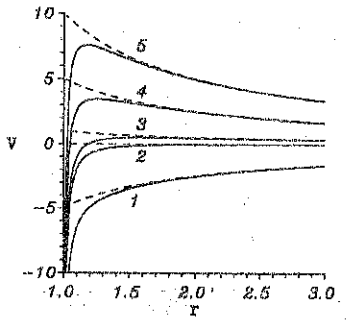


Fig 1. Interaction energy V versus distance r for various Qq. 1: $-5e$; 2: 0; 3: e; 4: $5e$; 5: $10e$. e is the electron charge.
Dashed lines show the Coulomb intraction energy.

As follows from (1), the energy is a monotonic function of r only for attraction ($Qq<0$). In the case of repulsion ($Qq>0$), the interaction energy steeply increases in the vicinity of the ball surface as long as the first term dominates, and then decreases due to the second term and tends to $-\infty$ as $r \to 1$ (see Fig.1).

In order to calculate the cross-section of plasma-particle capture by the ball, we regard the particle as being captured as soon as it touches the ball surface, i.e., when the distance between the plasma particle and the ball center is smaller than or equal to the ball radius. This corresponds to $r_{cap} \le 1$. The latter quantity is determined by the condition

$$1-\frac{V(r)}{E}-\frac{b^2}{r^2}=0, \qquad (2)$$

where b is the impact parameter, $E=mv^2/2$ is the plasma particle kinetic energy.

Having found the approximate solution of Eq.(2) with the potential energy (1), we derive an expression for the capture cross-section, i.e.,

$$\sigma=\pi(1+(2-\frac{V_{max}}{E})\sqrt{\frac{q^2}{2E(1-\frac{V_{max}}{E})}}-\frac{Qq}{E}\sqrt{1-\sqrt{\frac{q^2}{2E(1-\frac{V_{max}}{E})}}}), \qquad (3)$$

where V_{max} is the maximum interaction energy determind by the condition $dV(r)/dr=0$.

The accuracy of this formula is verified by comparing the values obtained making use of the analytic expression (3) to the numerical solutions of the exact problem. The error does not exceed 1%.

The dust particle charging is produced by the current

$$I(Q)=\frac{dQ}{dt}=\sum_{\alpha}\int e_{\alpha}f_{\alpha}\sigma_{\alpha}(v_{\alpha},q)dv_{\alpha}, \qquad (4)$$

where $\alpha=i,e$ correspond to particle species (electrons and ions), f_{α} is the relevant Maxwell distribution, the quantities σ_{α} are given by (3).

The numerical results obtained from Eq.(4) for the case of singly charged potassium ions are shown in Figs 2, 3.

We see that polarization effects are greater for smaller dust particles, weakly depend on the plasma density, are nearly insensitive to the electron temperature T_i, and weaken as the electron temperature T_e increases. Moreover, polarization considerably influences the charging dynamics (especially for small dust particles) though does not change the time needed for the accumulated charge to attain its stationary value.

REFERENCES

1. J.A.Stratton. Electromagnetic Theory. McGraw Hill, N.Y., 1941
2. R.G.Newton. Scattering Theory of Waves and Particles. McGraw Hill, N.Y., 1967

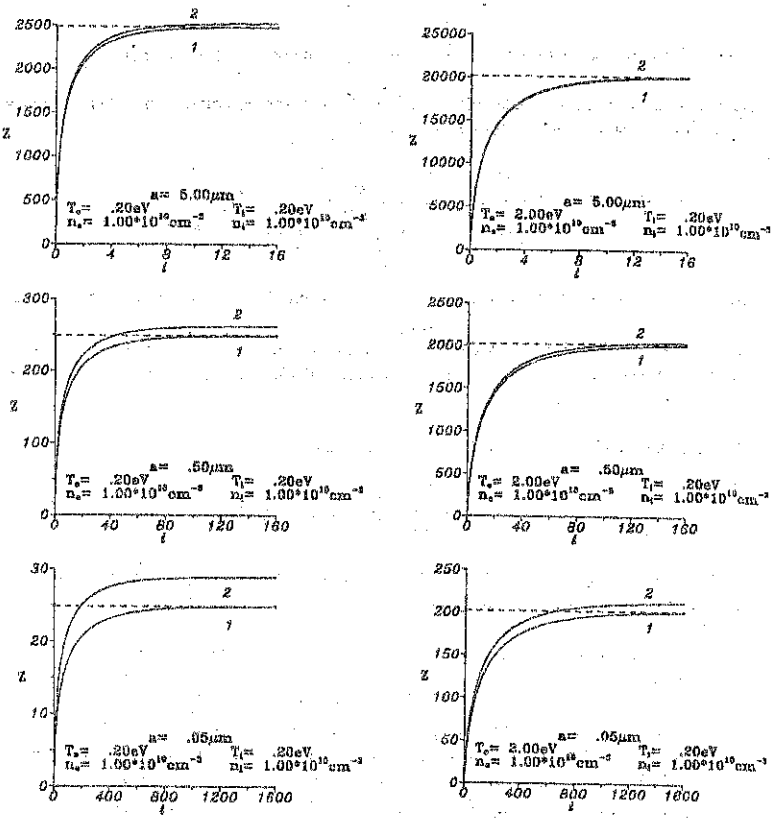


Fig. 2. Charging dynamics for various dust particle radii and component temperatures. Z is the ball charge, t is time in electron plasma frequency units. 1 - Coulomb potential, 2 - potential with regard for polarization. Dashed lines show the equilibrium charge determind by the condition $I(Q) = 0$ for the Coulomb potential.

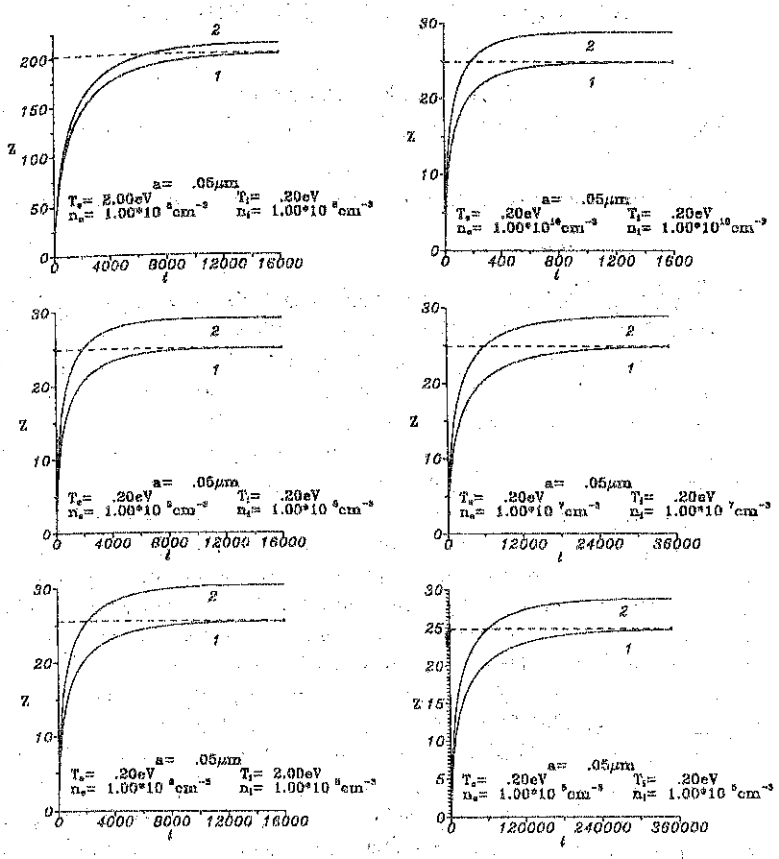


Fig. 3. Charging dynamics for various component temperatures and plasma densities.
Z is the ball charge, t is time in electron plasma frequency units.
1 - Coulomb potential, 2 - potential with regard for polarization.
Dashed lines show the equilibrium charge determind by the condition
$I(Q) = 0$ for the Coulomb potential.

EFFECTIVE FORCES IN DUSTY PLASMAS AND COLLOIDAL SUSPENSIONS

O.Bystrenko, A.Zagorodny
Bogolyubov Institute for Theoretical Physics, 252143, Kiev, Ukraine

K.Heinzinger
Max Planck Institute for Chemical Physics, 55020 Mainz, Germany

INTRODUCTION. One of the basic problems of dusty plasma (DP) physics is that of the mechanism and nature of effective forces between grains. Of special interest is the question of a possibility of attraction between like-charged dust grains. It is particularly important for understanding phase transtion phenomena recently observed in DP [1,2]. However, up to date this problem remains in many respects unclear. It is commonly accepted, that along with usual screening, the processes of charge exchange are significant and may even result in grain attraction [3]. At the same time, attraction of colloidal particles is theoretically obtained for charged colloidal suspensions [4], which strongly resemble DP, except that the grain charges are constant. Obvious similarity of ordering phenomena in both cases suggests a common mechanism of effective interaction. One more elusive point here is to what extent the attraction derived for a system of great number of colloidal particles has a collective nature. Putting in other way, it is unclear, wether it remains in the system consisting of small number of grains.

The present work is an attempt to answer the above questions by means of Monte Carlo (MC) computer simulations. The idea is to study the average energies for various fixed configurations of dust grains immersed into plasma background in order to make inferences about effective interactions. In this work we investigate the interaction between two grains. The model can be described as follows:

-dust grains are represented by hard spheres of constant charge fixed near the centre of a closed MC box;

-neutralizing plasma background is simulated by a single component consisting of sufficiently large number of point charges;

-the system is considered to be in thermal equlibrium.

The last-mentioned assumption is based on a high assymetry in charge

and mass of DP, which makes it possible to apply the adiabatic approach and regard plasma component as a gas being in thermal equilibrium.

Direct simulations for the system in question with real assymmetry ($1{:}10^4$) run into computational problems arising from a very large number N of plasma particles. To reduce that number a scaling procedure was used. Essentially, its point is as follows. At sufficiently large N quantities

$$g = \frac{2Qq}{k_B T \sigma}, \tag{1}$$

- potential energy of a plasma particle (in the units of $k_B T$) on the surface of a grain, and

$$v = \frac{\pi \sigma^3}{3V_{box}}, \tag{2}$$

- specific volume occupied by grains, - can be regarded with a good accuracy as dimensionless parameters of the problem. (Here Q and q are the grain and the plasma particle charges, respectively; k_B is the Boltzmann's constant; σ is the diameter of the grain). It means, that any transformation of quantities entering (1) and (2) and keeping g and v invariant, should retain approximately basic thermodynamical properties of the system such as average energy, unary distribution functions, etc. (except for fluctuations), and, therefore, can be used for scaling.

NUMERICAL RESULTS. In numerical simulations we investigated dependence of the total average energy of the system on the distance between grains and radial dust-plasma distributions. The number N of particles simulating plasma background was chosen 48; MC simulations were carried out using the conventional Metropolis algorithm. The total length M of a chain in each computer run was 72,000 configurations; the first 24,000 configurations were discarded to pass the relaxation. Selected runs were done for N=98, 192 and M=192,000; 384,000. The obtained data for the same v and g correlate well; discrepancy does not exceed 20% indicating that the number N=48 is sufficient for our rather qualitative study.

We investigated in detail the region of parameters $v=10^{-3}$, g=2.0-16.0. The results are represented in the figures. As the obtained data evidence, with increasing g effective repulsion changes near the point g =8.0 to attraction. Experimentally, the range of parameters characteristic of ordering phenomena can be estimated as $v=10^{-4} - 10^{-6}$; g=5.0-50.0 for both DP and charged colloidal suspensions. However, MC simulations in this region are rather

difficult as the time needed for relaxation increases considerably. Selected runs performed with $v=10^{-6}$ indicate that qualitatively the same behavior of the system should be expected.

An unusual point in our results is the absence of repulsion at short distances needed to prevent a collapse of grains. It is especially evident, when a high intensity of effective interaction is considered; the latter is on the order of 10^7 eV. However, the problem of that sort is present and still remains unsolved in analytical approaches as well. By and large a good agreement of our results with those of Ref.[4] should be noted.

CONCLUSIONS. By means of Monte Carlo simulations it was shown, that the effective repulsion between two like-charged grains immersed in one-component plasma background changes to attraction with increasing the plasma concentration and lowering the temperature. The point of transition corresponds to the region of parameters, where ordering phenomena in dusty plasma were experimentally observed.

In conclusion the authors would like to thank Prof. P.Schram for interest in the work and fruitful discussions.

REFERENCES

[1] J.H.Chu and Lin I. Coulomb lattice in a weakly ionized colloidal plasma. Physica A 205, 1994, p. 183-190.

[2] R.L.Merlino et al. Laboratory experiments on Dusty Plasma. International Conference on Plasma Physics, Foz Iguacu, 1994, p. 295-302.

[3] Tsytovich V., Khodataev Ya., Bingham R. Formation of Dust Molecule in Plasma as First Step to Super-Chemistry. Comments in Plasma Physics and Controlled Fusion, 1996 (to be published).

[4] E.A.Allayarov, L.I.Podloubny, P.P.J.M.Schram, S.A.Trigger. Effective macroion interaction in colloidal systems: possibility of attraction. Workshop on Complex Fluids and Plasmas, Eindhoven, 1995.

FIGURE CAPTIONS

Fig. 1. Change in average energy vs. distance; the diameter of the grain is σ=0.099; standard deviations at selected points are shown.

Fig. 2. Radial dust-plasma distribution functions for the same σ.

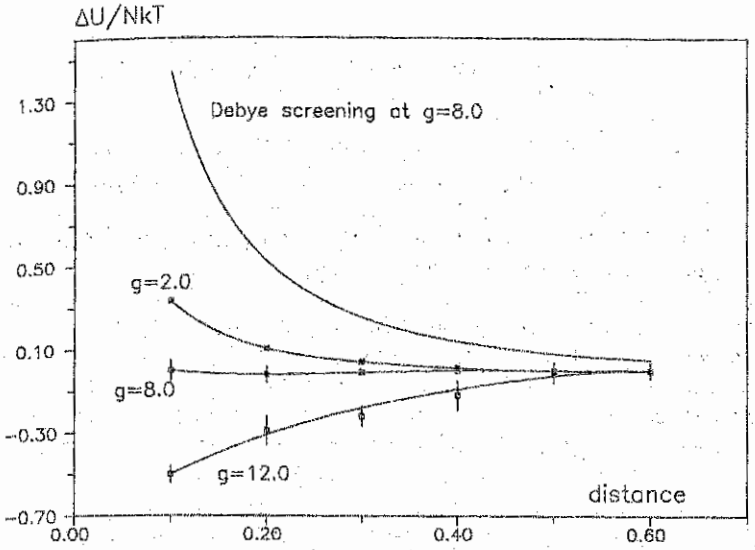

ΔU/NkT
Debye screening at g=8.0
g=2.0
g=8.0
g=12.0
distance
1.30
0.90
0.50
0.10
-0.30
-0.70
0.00
0.20
0.40
0.60

Fig.1

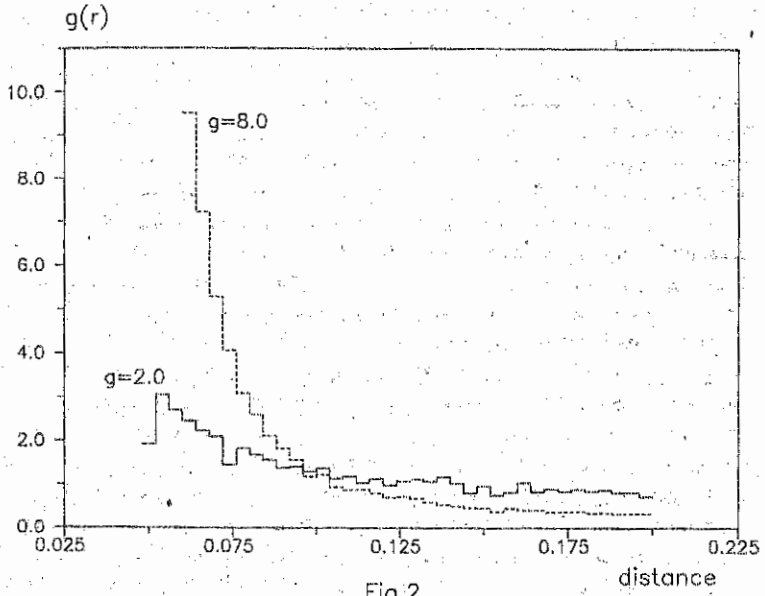

g(r)
g=8.0
g=2.0
distance
10.0
8.0
6.0
4.0
2.0
0.0
0.025
0.075
0.125
0.175
0.225

Fig.2

Cyclical Variations of the F2 Region Parameters from the Incoherent Scatter Radar Data

D.A.Dziubanov, Ye.I.Grigorenko, V.A.Pulayev, V.N.Lysenko

Institute of the Ionosphere, 310002, Kharkov, Ukraine

The incoherent scatter (IS) radar of the Institute of Ionosphere is currently the unique facility located at midlatitudes of the European region. Since the ionosphere of the Earth does not exhibit the spherical symmetry because of the discrepancy between the geographical and geomagnetical poles the data obtained from the Kharkov radar cannot be the close replica of the data collected from the similar fasilities in other areas. It goes without saying that these data can be primary employed in the creation and elaboration of global ionospheric models.

Experimental and theoretical investigations are carried out at the Institute of the Ionosphere by utilizing the Kharkov incoferent seatter radar data for studying global ionosheric processes. On April 28, 1993 the measurements with the Millstone Hill radar to investigate longitudinal variations of ionospheric parameters was made according to the joint program . The solar activity at this period was close to the middle level (W~100). The results obtained in the European and North-American regions in general showed satisfactory agreement. However, there was a certain difference: for example, the maximum value of electron density at Kharkov was observed near midday, but at Millstone Hill the daily maximum was shifted towards evening hours. It also had an influence on electron temperature variations. At Kharkov when daytime value of the critical frequency was 9 MHz a decrease in the electron temperature was observed at the F2 layer peak, and the electron temperature height gradient was -3K/km. At Millstone Hill a decrease of the height gradient was observed during the evening electron density maximum period and seen to be weaker. In addition, in a joint efforts with the Institute for Applied Geophysics (Russia) the data obtained in the European and North-American regions were analysed. In these investigations we have succeeded in explaining the summer difference in the electron density in these regions by longitudinal variations of neutral oxigen concentration in the thermoesphere. These variation are caused by the discrepancy between the

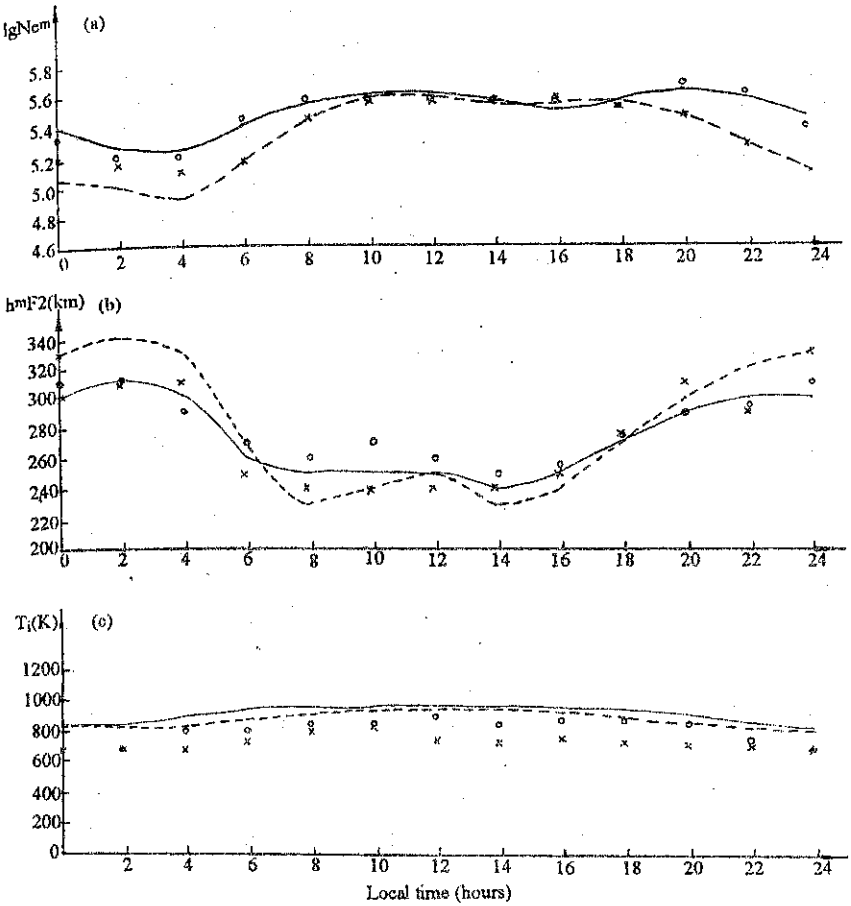


Fig.1 - Comparison of IRI-90 values and experimental data for June (solid line, circles) and September (dashed line, crosses) at low solar activity (W=10). There are: a - electron density at the F2 layer peak, b - height of the F2 layer peak, c - ion temperature at 300 km.

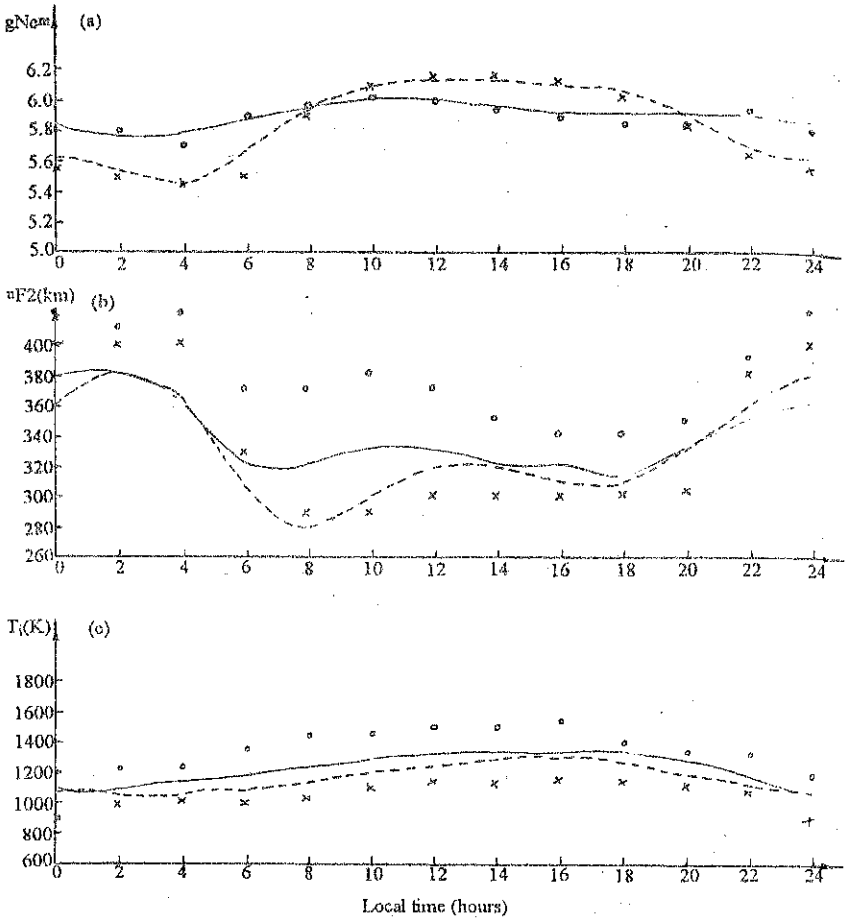


Fig.2 - Comparison of the IRI-90 values and experimental data for June (solid line,circles) and September (dashed line,crosses) at high solar activity (W=150).There are: a - electron density at the F2 layer peak, b - height of the F2 layer peak,c - ion temperature at 300 km.

geographical and geomagnetic poles and the dislocation of the north geomagnetic pole towards the Northern hemisphere. In these conditions the circulation pattern in the thermosphere of the European and North-American regions is found to be different and leads to atomic oxigen longitudional variations.

A comparison was made between the experimental data and the International Reference Ionosphere (IRI-90) model. The experimental data corresponding to high (W=150) and low (W=10) solar activity were utilised. The diurnal electron density variations in the F2 layer peak and the electron and ion temperatures at 300 km were compared. In general there is an agreement between the results of the model computations and the observational data. It is extended to the electron density in the F2 region peak since this value occurs in the world-wide network of ionosonds. It is reasonable to consider those cases where an appreciable difference between the model and experiment is observed, since the experimental data can be employed for the model development. An example of such differences at low and high solar activity is given on Fig.1, Fig.2 and in the Table 1, where Δ = IS value - IRI-90 value.

W = 10

Table 1.

month	Δlg Ne	ΔhmF2, km	ΔTe, K	ΔTi, K
March	0.3, night	-(20-30) night	- 400	- 100
June	insignif.	insignif.	-200, night	- 100
September	insignif.	insignif.	- 400, night	- 100
December	0.2, night	-(30-40) night	- 500, night	insignif.

W = 150

month	Δlg Ne	ΔhmF2, km	ΔTe, K	ΔTi, K
June	insignif.	- 50	insignif.	-200, day
September	insignif.	insignif.	- 600, day	-100, day
December	insignif.	20 - 40	-(200-400)	insignif.

The results of the comparison indicate that in specific cases the IS data derived in Kharkov can be used for the development of the IRI-90 model.

The Phase Relationships of Electron Density and Ionospheric Plasma Temperature Variations in the Gravitational Wave Propagation

Yu. I. Podyachy
Institute of the Ionosphere, 310002, Kharkov, Ukraine

In the recent years the researchers who are involved in the study of the upper atmosphere and ionosphere are particularly interested in the waves capable of propagating through the atmosphere stratified by the gravitational field. These waves were somewhat irrelevantly designated as internal gravity waves (IGW). There exists a vart number of phenomena giving rise to these waves. From among them the best known are sudden commencement of magnetic storms, earthquakes, passage of the solar terminator, powerful explosions on construction sites, etc. A widely applicable technique for the IGW observations consists in recording with the aid of onground radio-physical methods that can be used to bring about the ionospheric plasma disturbances. In this case the ionised medium serves as an indication of the waves propagating in a neutral gas.

In terms of linear approximation, i.e. once the photochemical processors and additional IGW-induced ionisation is neglected the characteristics of the ionospheric disturbances being observed coincide with the corresponding wave characteristics [1].

The Institute of the ionosphere of the National Academy of sciences and the Ministry of Education of Ukraine had set up a research VHF incoherent scatter radar complex intended to diagnose the ionosphere over an altitude range of 100 to several thousand kilometers. These radar facilities make it possible to make measurements of electron density, electron and ion temperatures and other ionospheric plasma parameters.

With the IGW propagation the magnitude of ionospheric electron density (N_e) variations is determined by the ion-neutral frequency collision and the mutual orientation of the wave vector and geomagnetic field. If the collision

frequency is far greater than that of the wave, the relative change in N_e is expressed as [2]

$$\frac{N_e}{N_{eo}} = \frac{v_n l_B}{\omega} \{(k l_B) + i(l_B l_z)[\frac{1}{2H} + \frac{d}{dz}(\ln N_{eo})]\}$$

(v_n is the neutrals velocity l_B, l_z are the unit vectors of the magnetic field and the vertical axis).

The wave-induced change in T_e also depends on the magnitude of the heat input and cooling rates which, in their turn, are attended with the variations in the photoionisation and photoelectron heat efficiency, the latter being electron density-dependent. This chain of the interdependent processes accounts for the considerable difficulties associated with the elaboration of the temperature variation theory.

The data obtained from ionospheric parameter measurements using the incoherent scatter radars represent the height-time dependencies of Ne and the charge particle temperature.

An example of the diagrams of the dependencies is shown in fig.1 which gives a clear picture of the wave ionospheric structure. The N_e and T_e variation amplitudes in the above example were equal to 20% respectively.

The time series composed of N_e and T_e that were measured at a single height undergo a spectral analysis which provides on estimate of their mutual spectral characteristics including the coherence spectrum $K_{12}(f)$ and the phase spectrum $F_{12}(f)$:

$$K^2_{12}(f) = \frac{L^2_{12}(f)+Q^2_{12}(f)}{C_{11}(f)\,C_{22}(f)}; \quad F(f) = \operatorname{arctg}\left(\frac{Q_{12}(f)}{L_{12}(f)}\right).$$

Here $L_{12}(f)$, $Q_{12}(f)$ are the sine and cosine component of the mutual power spectrum of the process being analyzed.

Fig. 2 shows an example of the results obtained. As evident from the coherence spectrum, the basic process which is responsible for the electron density and electron temperature fluctuations being observed accounts for the wave

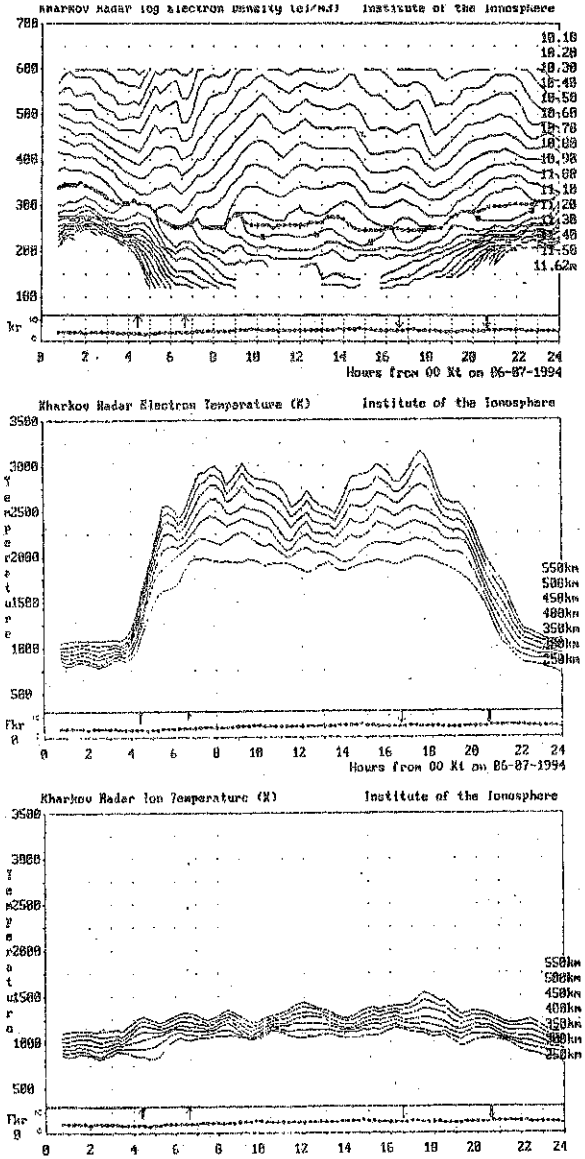


Fig. 1. An example of the diagrams of the height-time dependence of N_e, T_e, T_i.

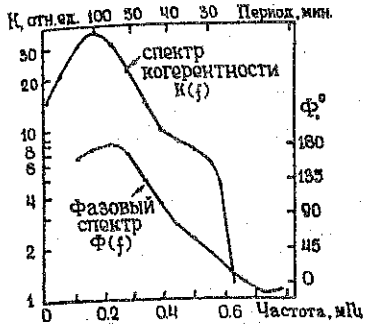


Fig. 2.
The coherence and phase spectra of the variations electron concentration and electron temperature in the internal gravity waves

with a period of 100 min. (The coherence spectrum value is maximum for this period). It gives rise to the opposite phase N_e and T_e variations (the phase spectrum at a corresponding frequency is 180°). As the frequency increases the phase opposition of their variations is reduced to zero. This is due to the fact that a neutrals density increase caused by the positive wave half-period there is an increase in the heat input Q and the ion-formation rate q. If the electron density does not increase with a rise in Q or its relative increase is small, then Te tends to increase. In case the relative increase of N_e is greater than that of Q, T_e is seen to decrease. Thus, the waves whose period of up to 30 min results in small disturbances give rise to inphase N_e and T_e variations whereas the 1 - 1.5 hour period waves bring about opposite phase variations.

References

1. Prasad S.S., Furman D.P. Atmospheric gravity waves: their effect on ionospheric temperature and composition. - Journ. Atmosph. and Terr. Phys., v. 37, 1975, p. 17-30.
2. Hooke W.H. The ionospheric response to internal gravity waves. - Journ. Geoph. Res., v. 75, N 28, 1970, p. 5535-5544.

The Role of Excite Molecular Ions in the Variation of the E-Layer Peak Height with Changeable Solar Activity

T.G.Zhivolup
Institute of the Ionosphere, 310002, Kharkov, Ukraine

One of the basic problems in the E layer theory is the behaviour of its peak height h_mE depending on the level of solar activity.

Now consider the influence of the oscillation-excited ions NO^+ on the h_mE variations depending on the level of solar activity.

According to the theory allowing for the excited ions [1], the E layer peak height is formed between the two levels: one which is associated with the maximum of on the ion-forming rate funotion h_q and the other related to the maximum concentration of excited ions NO^+ at h_a.

Consider the h_a behavior as the solar activity increases. For this purpose let us make theoretical calculations of $h_a(F_{10.7})$ dependence using the expression [1]

$$\frac{d}{dh}\lg(T)=\frac{d}{dh}\lg\frac{n_a}{(A+n\gamma)}, \qquad (1)$$

where T is the atmospheric temperature, n is the natural particle concentrations, γ is the rate of collision deactivation reaction A-is the probability of radioactive transition from the excited state to the basic one. We believe that T(h) and n(h) correspond to the Jacchia-71 model [2],and h_mE is located close to h_a.

Then

$$\frac{d}{dh}\lg(n_a)=0.$$

Using the diffusion equation for each atmospheric component n_i of the Jacchia-71 model we transform equation (1) in the followry way:

$$\frac{dT}{dh}\frac{\gamma}{A}\frac{g}{k}\rho, \qquad (2)$$

where g is the free fall accelaration, k is the Bolzman constant, ρ is the atmopheric density. This expression relates the atmopheric temperature gradient to its density and is the equation for determining h_a-the peak height of the excited ions NO^+.

Define the magnitude of the h_mE change in the transition from the solar activity minimum to its maximum. For this purpose using the relation (2) we obtain the $h_a(F_{10.7})$ dependencies and determine the amount of the sudden change in h_q associated with a more rapid increase in the intensity of the line 102.6 nm as compared to the line 97.7 of solar radiation with increasing solar activity for each season.

The $h_a(F_{10.7})$ dependencies were obtained from three values of h_a estimated for each season to account for three definite values of the exosphere temperature T_z and the rate of collision deactivation reaction $\gamma=2*10^{-15}cm^3s^{-1}$.

In order to calculate the profiles $\rho(h)$ the modified Jacchia-71 models were utilized for summer, winter and equinox seasons. The estimated profiles $\rho(h)$ were corrected for the values of the Groves model [3] at 110 km in the 500 latitude for March, June, September and December.

The amount of the jump h_q for all seasons was taken to be equal to 0.4H and assigned to the solor activity level $F_{10.7}$=207 for March, $F_{10.7}$=200 for June, $F_{10.7}$=215 for September and $F_{10.7}$=202 for December.

According to the calculation that were made in the transition from the low to high solar activity the magnitude of h_mE decrease for March was 4.98km, for June-5.47 km, for September-4.95km and for December-3.25km. In this case h_a shows a smooth linear decrease in the transition from low to high SA and the magnitude of its decrease is 1.44 km for March, 1.44-for June, 1.35-for September and 1.53km for December.

The contribution of the sudden change h_q to the magnitude of decreasing h_mE is more significant as compared to the magnitude of the h_a drop.

Fig. shows the comparison between the theoretical dependencies $h_a(F_{10.7})$ and the emphirical ones obtained from the incoherent scatter data for March, June, September and December.

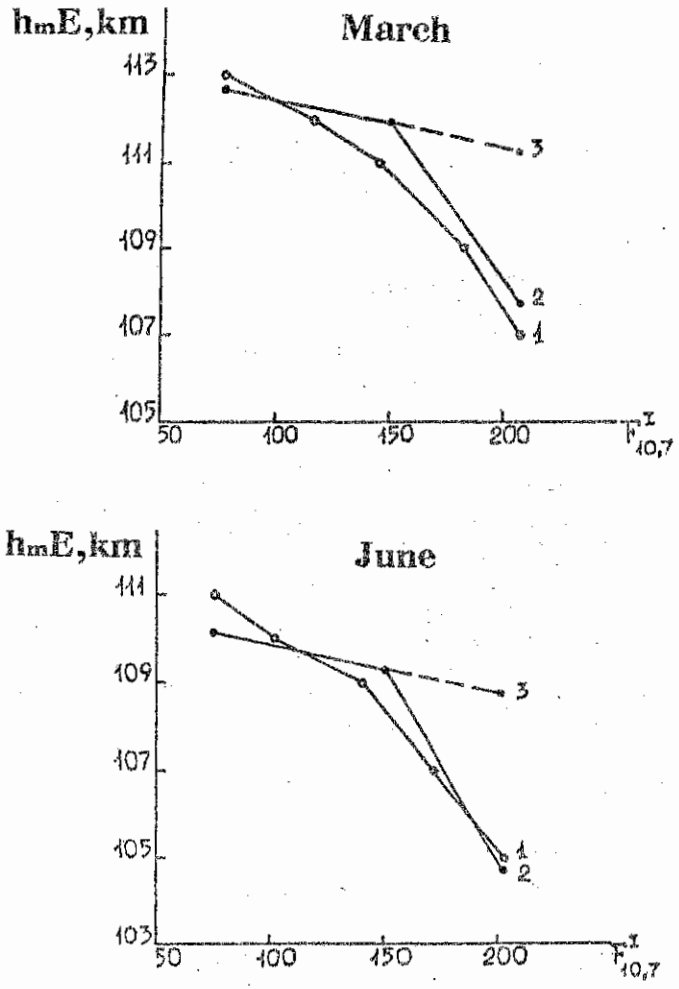


Fig. Comparison between the empirical afternoon dependencies h_{mE} ($F_{10.7}$) (1) for March and June and the theoretical dependencies (2) allowing for the sudden change in h_q in the transition from low to high solar activity; 3 - theoretical dependence h_a ($F_{10.7}$)

It is seen that the theoretical dependencies $h_a(F_{10.7})$ are in good agreement with the experimental data: the predicted and experimental relations $h_a(F_{10.7})$ show the identical behaviour (a slow, monotonous h_mE decrease with increasing $F_{10.7}$=73-150 and more abrupt drop in h_mE with $F_{10.7}$>150) and basically they differ from one another by less than 1 km. Thus, by considering the oscillation-excited ions it became possible to provide an insight into the monotonous linear decrease of the E layer peak height in the transition from low to medium solar activity.

REFERENCES

1. Antonova L.A., Ivanov-Kholodny G.S. Solar activity and ionosphere (at heights of 100-200 km)/M.:Nauka,1989,169p.

2. Jacchia L.G. Revised static models of the thermosphere and exo- sphere with empirical temperature profiles/ Spec. Rep. N 332. Smith- son. Astrophys. Observ., Cambridge, Mass. 1971.

3. Groves G.V. Seasonal and latitudinal models of atmospheric temperatures, pressure and density, 25 to 110/ Air Force Cam- bridge Labs., L.G. Harnison Field, Mass. 1970.

J

LOW-TEMPERATURE PLASMAS

Experimental Study and Modeling of a Pulsed Helicon Discharge

M. Krämer and Th. Enk
Institut für Experimentalphysik II, Ruhr Universität Bochum,
D-44780 Bochum, Germany

1. Introduction

Helicon waves are widely used to produce high density magnetized plasmas /1,2/. A reliable self-consistent description of the helicon discharge must consider both the energy and particle conservation as well as the helicon wave physics. As a first step, we employ here a simple model taking into account the most important processes in the discharge. The particle and energy balance equations are treated such that the spatial partial derivatives (associated with the different loss term) are expressed by the scale lengths in the corresponding directions. The scalings thus obtained are compared with the experimental findings.

2. Experiment

The experimental data are obtained from measurements carried out on a pulsed helicon wave discharge both during the plasma-producing rf pulse as well as in the afterglow of the discharge. The plasma is generated by rf power pulses ($P_{rf} = 1.5kW$, $f_{rf} = 25MHz$, $T_{pulse} = 2ms$, $f_{pulse} = 25Hz$) through a modified Shoji-type antenna (4 helical current paths) /3/. The plasma and experiment parameters are $n_e \leq 7 \times 10^{19} m^{-3}$, $T_e \approx 4eV$, $B_0 \leq 0.16T$, $p = 1Pa$ argon, tube radius and length = $2.8cm$ and $140cm$, respectively. Electric probes (n_e (in rel. units) and T_e), $4mm$-interferometry (line-integrated density) and diamagnetic loop (power losses and thermal energy $n_e T_e$ integrated over cross section) are used to determine the plasma parameters, while, by means of magnetic probes inside and outside the plasma, we measured the spatial distribution of the rf magnetic fields from which the wavenumber spectra can be inferred.

3. Model

It is well-known from experiments that in the high density mode of the helicon discharge the rf power is transported out of the antenna volume by $m = +1$ and $m = -1$ helicon waves in parallel and antiparallel direction with respect to B_0, respectively. Owing to axial damping, the wave power is absorbed along the plasma column. It is therefore appropriate to employ the model of a plasma waveguide /4/. The absorbed power per unit length is then related to the axial rf power flux and the wave damping via

$$\frac{dP}{dz} = 2k_i P, \quad k_i = \frac{\nu_c}{\omega_{ce}} k_\perp, \tag{1}$$

where $\nu_e = \nu_{ei} + \nu_{en}$ consists of the collisional frequencies of the electron with the ions and neutrals, respectively, and $k_\perp = \chi / r_p$ (r_p: plasma radius) is determined by the boundary conditions for the fields at the plasma edge.

The power absorbed by the electrons (eq(1)) is balanced by the various losses in the helicon discharge. The predominat losses are collisional losses due to inelastic collisions (ionization (ν_I, U_I) and excitation (ν_*, U_*)) and electron heat conduction along and across the magnetic field. The energy balance equation can then be written as

$$\frac{3}{2}\frac{\partial (n_e k_B T_e)}{\partial t} = Q_{abs,e} - Q_{coll,e} - \nabla \cdot (\kappa_{e\perp} \nabla_\perp + \kappa_{e\parallel} \nabla_\parallel) T_e(r,z,t) \tag{2}$$

where $\kappa_{e\perp} = 4.66\,\nu_e\,n_e\,k_B T_e/(m_e\omega_{ce}^2)$ and $\kappa_{e\parallel} = 3.4 \quad n_e\,k_B T_e/(m_e\nu_e)$ The particle balance is given by the diffusion equation

$$\frac{\partial n_e}{\partial t} = \nu_I\, n_e - \nabla\cdot(D_\perp\,\nabla_\perp + D_\parallel\,\nabla_\parallel)\,n_e(r,z,t), \tag{3}$$

where $D_\perp = k_B T_e\nu_e/(m_e\omega_{ce}^2)$ and $D_\parallel = k_B T_e/(m_i\nu_{in})$. In principle, the system of the above partial differential equations is to be solved simultaneously which is a complex and difficult task. However, to obtain only scaling laws for the main experimental parameters characterizing the helicon discharge we simply replace the derivative with respect to r and z by inverse scale lengths, in particular, $\nabla_\perp \to \alpha/r_p, (\alpha = 2.4)$ and $\nabla_\parallel \to \pi/L_p$ where the lowest diffusion modes are assumed. In the stationary case ($\frac{\partial}{\partial t} = 0$), the two balance equations can then approximately be expressed as

$$\nu_I - (\frac{\alpha}{r_p})^2 D_\perp - (\frac{\pi}{L_p})^2 D_\parallel \;=\; 0, \tag{4}$$

$$\frac{2\nu_e\chi P}{\omega_{ce} r_p} - \pi r_p^2[n_e(\nu_I U_I + \nu_e U_e) + (\frac{\alpha}{r_p})^2\kappa_{e\perp}T_e + (\frac{\pi}{L_p})^2\kappa_{e\perp}T_e] = 0, \quad \chi = 3.83 \tag{5}$$

and solved by a root-finding algorithm.

4. Results and Discussion

In the highly ionized helicon discharge, electron neutral collisions can be neglected, $\nu_{en} \ll \nu_{ei}$, so that the diffusion equation in the afterglow ($\nu_I \approx 0$)becomes

$$\frac{\partial n_e}{\partial t} = \frac{A(t)}{2}\left(\frac{\partial^2}{\partial r^2} + \frac{1}{r}\frac{\partial}{\partial r}\right) n_e^2(r,t), \quad A(t)/(m^5/s) \;=\; 2.9\times 10^{12}\frac{(T_e/eV)^{1/2}\ln\Lambda}{(B_0/T)^2} \tag{6}$$

We solved this equation numerically starting with the measured density profile at $t = 0$ and taking into account the temporal decrease of T_e. Reasonable agreement between the computed and measured density profiles is achieved (Fig.1) thus confirming that electron-ion collisions are dominant.

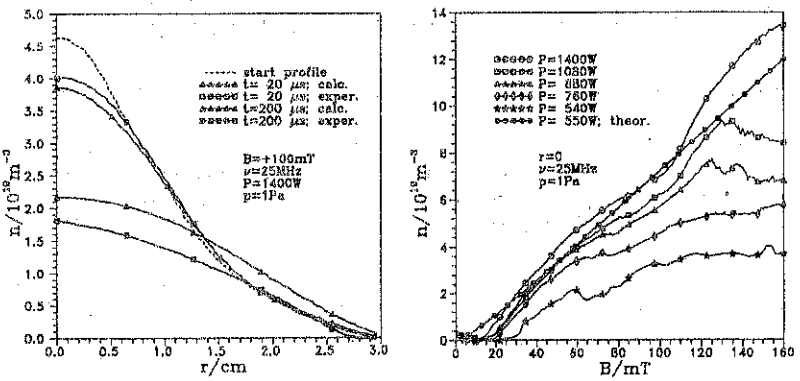


FIG. 1. Radial density profiles in the afterglow; Fig.2. Peakdensity vs.magnetic field strength

Fig.2 shows the dependence of the measured plasma density on the magnetic field strength and the rf power. The diagram contains also a curve computed from the self-consistent model. Apart from the fact that the computed powers are 2 - 3 times smaller than those launched to the plasma, reasonable agreement is achieved. These values are also in accordance with the diamagnetic loop measurements (see below). Furthermore, the temperature obtained from the model are between 3 and $4eV$ in accordance with the measured values. Information on the axial wavenumbers and the azimuthal modenumbers were obtained from magnetic probe measurements. The probe signals were taken by means of a network analyzer (measuring amplitude and phase) and Fourier-analyzed. From the azimuthal spectra thus obtained (Fig.3a), it can be seen that, on the different sides of the antenna, $m = +1$ and $m = -1$ modes are mainly excited depending on the direction of wave propagation with respect to $\mathbf{B_0}$, respectively. The axial wavenumber spectra (Fig.3b) exhibit one maximum as well whereby the mean wavenumber and the spectral width are approximately equal. It is apparent that the waves propagate preferably in one direction (i.e. there is no standing wave field). From the decrease of the spectral power along the z-axis, we can calculate the axial damping decrement. Both wavelength ($13 - 20cm$) and damping length ($18 - 36cm$) fit with the values obtained from the model.

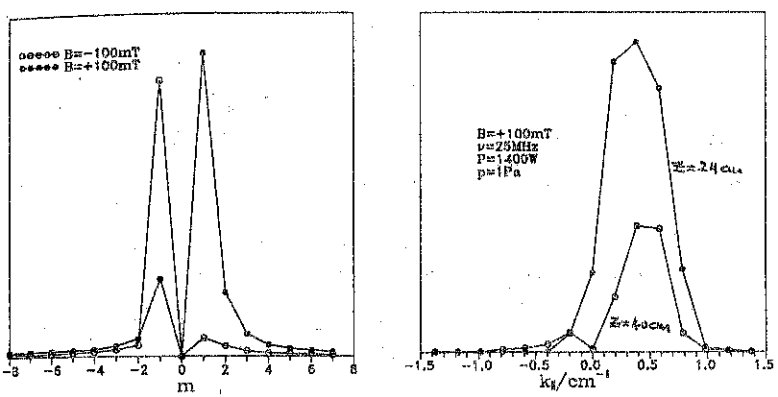


FIG. 3: Azimuthal modenumber (a) and axial wavenumber spectra (b)

The induced voltage measured by means of a diamagnetic loop is a direct measure of the power losses and, thus, the power absorbed by the electrons. By moving the loop along the plasma column, the rf power deposition can be obtained. Fig. 4 (top) shows the time-integrated induced voltage of the diamagnetic loop, $I(t) = \int_t^\infty U_{ind}(z,t')dt'$ which is proportional to the energy density W(z,t) (integrated over the cross section). Just after the rf pulse ($t = 2\mu s$), W is a flat curve with a maximum inside or near the antenna so that the energy density changes only slowly along the plasma column. However, W decreases strongly between 15 and $25cm$ apart from the centre of the antenna. From probe measurements we know that the electron temperature decreases much faster than the density. Hence, T_e must peak in this region ($z \approx 20$) while n_e is maximum between 40 and $50cm$ (see Chen /5/). The temporal decrease of the energy, i.e. the lost power, plotted in Fig.4 (bottom) shows the pronounced asymmetry of the discharge. The power maximum is on that side of the antenna where the

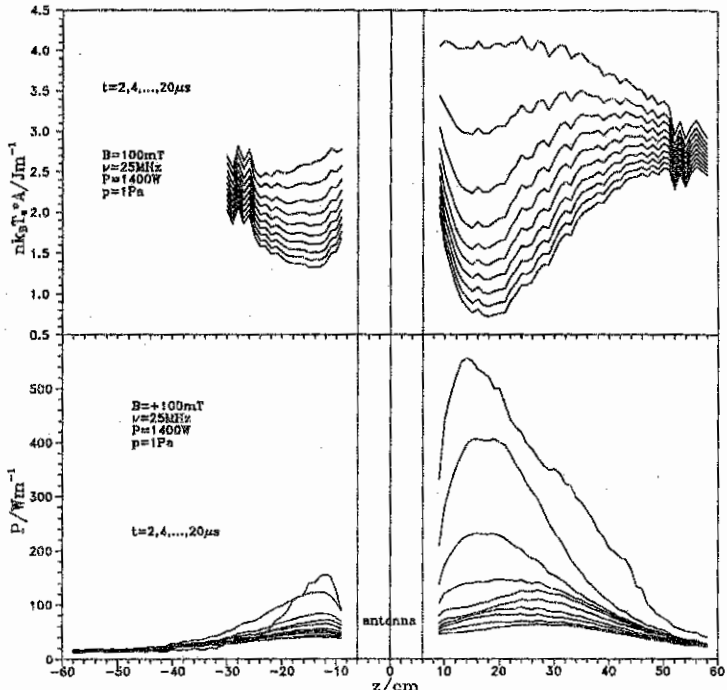


FIG. 4. Energy density and lost power per length vs. z

$m = +1$ mode propagates parallel to $\mathbf{B}_0$. It is not clear what causes the power decrease near the antenna. Most likely, the curves on both sides of the antenna are to be connected such that the power decreases monotonically in the antenna region. Making this assumption and taking into account a factor 3/2 (corresponding to the 3 degrees of freedom) one obtains about 600 W total power. We believe that a significant part of the power is lost at the tube walls inside the antenna.

The above results are in agreement with the observations of other groups. The comparison of our findings with the model calculations shows that the helicon wave discharge is mainly governed by the helicon wave absorption ($\propto k_i$) which determines the plasma parameters through the balance equations rather than through the wave dispersion. This is also supported by the fact that the measured wavenumber spectral widths are much smaller than expected from the antenna current spectrum /6/.

/1/ Boswell R W 1984 Plasma Physics 26 1147
/2/ Chen F F 1991 Plasma Phys. Contr. Fusion 33 339
/3/ Krämer M, Fischer B and Enk Th 1994 Int. Conf. Plasma Phys., Brasil 3 37
/4/ Allis W P, Buchsbaum S J and Bers A Waves in Anisotropic Plasmas MIT Press (1963)
/5/ Chen F F 1996 et al. Plasma Sources Sci.Technol. 5 173
/6/ Fischer B, Krämer M, and Enk Th 1994 Plasma Phys. Control. Fusion 36 2003

Electron emission from materials processed by pulsing gas-discharge plasmas

Yu.I.Chutov, T.E.Lisitchenko, V.L.Melnichenko, N.S.Baranchuk, P.L.Dan'ko
Department of Physical Electronics, Radio Physics faculty, Taras Shevchenko Kiev University, Volodymyrska Str. 64, 252017 Kiev, Ukraine

Introduction

Electrical breakdowns are the main reason of a destruction of protection coverings in thermonuclear reactors. These breakdowns are mainly caused by both the electron emission from the protection coverings and the induced electric voltage. Investigations of this emission allow to compare the breakdown stability of various protection coverings including materials processed previously by plasmas as well as to choose the most suitable protection. That is especially important for the dielectric materials which emission properties essentially depend on the plasma processing degree, in particular on a number of electrons collected from plasma on their surface [1,2]. Surface electric charges which are created on dielectric surfaces due to plasma interactions with these surfaces, can strongly influence on these interactions also. The aim of this work is experimental investigation of this emission from various materials, including dielectric surfaces, processed by plasmas of pulsing discharges.

The pulsing discharge [3] is a special type of altering current discharges which basic parameters essentially change in a time, unlike high frequency discharges. However these changes differ essentially from the applied voltage change, unlike low frequency discharges,. Such pulsing discharge can be realized under the condition that the external voltage is essentially modified in a gas-filled gap by a charging of the internal dielectric surfaces (barrier discharges) or external capacitors in cases of metal electrodes.

Experiment

Investigations of emission properties of dielectric materials require to use impulse measurement methods because of a influence of their surface charge created during the electron emission. Controlled charging of these materials by a pulsing discharge is one of the possible research methods.

Pulsing discharges are generated between two dielectric surfaces in various gases, namely: argon, neon, helium or deuterium. Two types of experimental devices are used. The first type of these devices is shown in Fig. 1. A gas fills the gap with the size 0.5 cm between plane butt-ends of two cylinders in this device.

The thickness of each butt-end is equal 0.5 cm also. One butt-end was made from a glass, other butt-end was made from quartz and was covered by a thin film from the investigated dielectric matter. Metal electrodes E with the diameter 4 cm were closely put to other sides of these butt-ends. The second type of the devices consist of metal electrodes which can be covered by a dielectric film. Separated capacities can be used in the external circuit in this case.

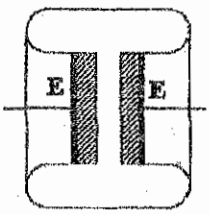


Fig. 1

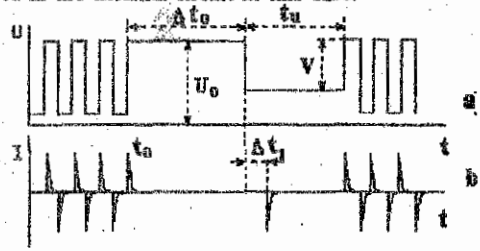


Fig. 2

The package of "meander" impulses with the frequency 100 kHz and the amplitude 0.8 - 1.2 kV is applied to the metal electrodes E (Fig. 2a) and generated the pulsing discharge with altering current impulses (Fig. 2b). The electric charge on inner dielectric surfaces changes due to these current impulses.

The package of "meander" impulses is turned off in some moment t_o = 0.1 s so that some voltage U_0 is applied during some time Δt_o = 0.03 - 3 s and inner dielectric surfaces were relaxed after interacting with a relaxation plasma. The voltage between electrodes sharp change in time moment $t_o + \Delta t_o$ so that the voltage V appear between dielectric surfaces. This voltage creates the single gas breakdown after some time delay Δt_1 (Fig. 2b). The package of "meander" impulses is turned on again according to Fig. 2a and all measurement cycle is made repeatedly. The statistical mean delay time τ_o is established from results of these repeat measurement. The statistical mean number N_e of electrons which start the single gas breakdown can be established from this delay time τ_o. As a rule, these electrons are emitted from cathode surfaces.

Results

The obtained results show that the electron emission depends on parameters of plasmas which interact with a surface, and a surface material as well as charges

which were previously condensed from a plasma of the pulsing discharge on a dielectric surface.

Typical experimental results are shown in Fig. 3 where dependencies are plotted of the statistical mean number N_e of electrons, which are emitted from the cathode surface, on the time Δt_o (Fig. 2) for various experimental conditions including metal electrodes. These results are obtained in deuterium at the pressure 3.5 Torr and $V = 1.15$ kV for electrodes prepared from glass (1), BN (2), Fe (3), TiN (4) and C (5). As can be seen from Fig. 3, the number N_e of emitted electrons decreases with some characteristic time which is a relaxation time for investigation surfaces.

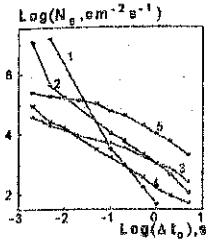


Fig. 3

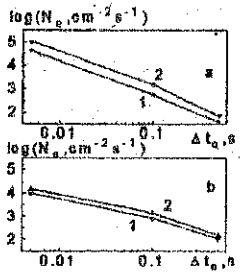


Fig. 4

The number N_e depends also on a surface material but these dependences correspond various conditions because they were obtained at the same voltage V but the breakdown voltage V_b depends on a material. Therefore dependences are shown of the number N_e on the time Δt_o in Fig. 4 for the same over voltage $V - V_b$ where curves 1 and 2 were obtained in deuterium at the pressure 3.5 Torr for $V - V_b = 100$ and 200 V, respectively

As can be seen from Fig. 4, some difference is between the electron emission of various materials at the same over voltage. It means that there is a principal possibility to compare applied properties of various matters contacting with plasmas in particular protection properties of these materials in plasma reactors.

The relative stability of materials relating to breakdowns can be established from measurement results of electron emission taking into account the dependence of this emission on a gas, the ion and light flux intensity on materials as well as on the over voltage depended from the breakdown potential at the given experimental conditions.

This work was supported by a grant from the Ukrainian State Committee of Science and Technology.

In this work, the electron emission from various materials is determined from the statistic experimental measurements of the delay time of a gas single breakdown between electrodes covered by TiN or BN film. This single breakdown was generated by the single impulse voltage applied in some time after the finish of the pulsing discharge used for the plasma processing of materials. The pulsing discharge was generated by the "meander" voltage applied to the external metal electrodes.

This work was supported by a grant from the Ukrainian State Committee of Science and Technology.

References

[1] Yu.I.Chutov, N.S.Baranchuk, Pis'ma J.Tech.Phys., v.1 (1975) 238 (in Russian)
[2] N.S.Baranchuk et al., Ukr.Phys.Journal, v.37 (1992) 1042 (in Russian)
[3] Yu.I.Chutov et al., J.Tech.Phys., v.44 (1974) 355 (in Russian)

COMPUTER MODELING OF A PLASMA JET EXPANDING INTO VACUUM VESSEL

Yu.I.Chutov, A.Yu.Kravchenko, V.S.Yakovetsky
Department of Physical Electronics, Radio Physics faculty, Taras Shevchenko Kiev University, Volodymyrska Str. 64, 252017 Kiev, Ukraine

Introduction

Plasma jets are applied to many laboratory and technological devices, for example to MHD - generators and plasma dynamic lasers, to the plasma processing of various materials and the plasma etching, etc. A good control of the plasma parameters is very necessary for these applications. However in all these cases, plasma jet interactions with solid state surfaces take place so that essential changes of plasma jet parameters can take place, especially at ionization -recombination processes in plasma jets. Experimental difficulties cause the necessity of theoretical simulations of these parameter changes, especially closely to solid state surfaces.

The aim of this work is numerical calculations of parameters of the supersonic quasineutral argon plasma jet expanding into the cylindrical vacuum vessel and interacting with inner surfaces of this vessel.

Model

The quasineutral low ionized argon plasma jet enters with the axis supersonic velocity v_0 into the cylindrical vacuum vessel with radius R_c and length L_c through the round hole with radius R_n (Fig. 1) at some initial time. All plasma parameters are constant in this cross-section during a simulation time. The plasma consists of heavy particles (neutral atoms and single ionized ions) as well as electrons.

The plasma jet moves in this vessel with some expansion, interacts with its walls and departs trough the side hole with the length L_h. Some elementary processes take place in the plasma jet, namely: three particle electron-ion recombination, the ionization by the electron impact, the electron-ion energy exchange due to Coulomb collisions, the surface recombination as well as the electron heat conduction and the viscosity of electrons and heavy particles. It is assumed that the electron density n_e is equal the ion density n_i ($n_e=n_i$) and the ion temperature T_i is equal the atom temperature T_n ($T_i = T_n = T_h$). Some difference between the electron temperature and the temperature of heavy particles is assumed in this plasma due to the large difference between the electron mass and the ion one.

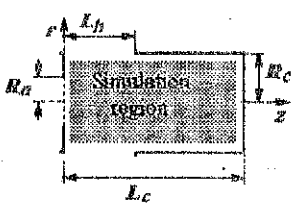


Fig. 1

In some cases, an interaction is investigated of this plasma jet with a plane wall for comparing.

The following set of hydrodynamic equations are used for electrons as well as for heavy particles (ions and atoms) with taking into account elementary processes indicated above:

$$\rho\left(\frac{\partial w_\alpha}{\partial t} + (\vec{w} grad) w_\alpha\right) + \frac{\partial P}{\partial x_\alpha} + \frac{\partial \pi_{\alpha\beta}}{\partial x_\beta} = 0, \quad \{\alpha,\beta\} = \{z,r\} \tag{1}$$

$$\frac{\partial n_n}{\partial t} + div(\vec{w} n_n) = n_e^2 n_i \Gamma_r - n_e n_h \Gamma_i \tag{2}$$

$$\frac{\partial n_e}{\partial t} + div(\vec{w} n_e) = n_e n_h \Gamma_i - n_e^2 n_i \Gamma_r \tag{3}$$

$$\frac{\partial (n_h E_h)}{\partial t} + div(n_h E_h \vec{w}) + div(P_h \vec{w}) = Q_{eh} + Q_h visc \tag{4}$$

$$\frac{\partial (n_e J_e)}{\partial t} + div(n_e J_e \vec{w}) + \vec{w} grad P_e + div(\chi\, grad J_e) = -Q_{eh} + Q_{ion.-rec.} + Q_e visc \tag{5}$$

where ρ is the total plasma density, $P = P_h + P_e$, is the total plasma pressure, $\vec{w}$ is the plasma velocity vector, $P_h = P_i + P_n$, and P_e is the partial pressure of heavy particles and electrons, n_e, n_n, n_h is the density of electrons, atoms and heavy particles, J_ε, E_h is the density of the heat electron energy and the total energy of heavy particles, respectively.

The rate of the energy exchange between electrons and heavy particles due to elastic collisions is given by [1]

$$Q_{eh} = 3 n_e (m_e / m_h) \nu_{eh} k (T_e - T_h), \tag{6}$$

where ν_{eh} is the mean rate of electron collisions with heavy particles, m_e and m_h is the electron mass and the heavy particle one, respectively.

The rate of both the three body recombination Γ_r and the ionization Γ_i is given according to [2]. One electron received at one act of three body recombination the energy given by

$$Q_{ion.-rec.} = -H_i \left(n_e n_h \Gamma_i - n_e^2 n_i \Gamma_r\right) \tag{7}$$

The flux of electrons and ions to vessel walls is given by

$$\vec{\Gamma} = \left(1 + C_s i / |\vec{w}|\right) n_e \vec{w} / 4 \tag{8}$$

where $C_s i = \sqrt{kT_e / m_h}$ is the ion sound velocity. It is assumed that all electrons and ions which reach vessel walls, recombine there and return back as neutral atoms.

The member $div(\chi(J_e) grad J_e)$ describes in (5) the electron heat conduction where

$\chi(Je) = -\dfrac{0.97}{m_e^{1/2} Ze^4 \Lambda} Je^{5/2}$ is the coefficient of this heat conduction.

The viscosity heat extraction is given by $Q_{visc} = -\pi_{\alpha\beta}\frac{\partial W_\alpha}{\partial x_\beta}$, where $\pi_{\alpha\beta} = -\eta_0 W_{\alpha\beta} = -(\eta_{0_e} + \eta_{0_h})\, W_{\alpha\beta} = \pi_{e\alpha\beta} + \pi_{h\alpha\beta}$ is tensor of the viscosity strength without a magnetic field. Following viscosity coefficients are taken for electrons and heavy particles:

$$\eta_{0_e} = 0.73 \cdot n_e \cdot T_e \cdot \tau_e, \qquad \eta_{0_h} = 0.96 \cdot n_h \cdot T_h \cdot \tau_h,$$

where $\tau_e = \frac{3\sqrt{m_e}T_e^{3/2}}{4\sqrt{2}\pi\Lambda e^4 Z^2 n_e}$, $\tau_h = \frac{3\sqrt{m_h}T_h^{3/2}}{4\sqrt{2}\pi\Lambda e^4 Z^4 n_h}$, Λ is Coulomb logarithm, m_e, m_h is the electron mass and the mass of a heavy particle respectively.

The modified method of big particles [3] is used for the computer modeling of this problem. In this method, the complex set of equations is separated on simpler components which describes separated physical processes. The general solution consists of additive members of time influences of each process on spatial parameter distributions. Each process is simulated with the corresponded minimum characteristic time what allows to obtain higher simulation precision. The dynamic separation boundaries are marked by some special symbols what allows to follow up a motion of these boundaries.

Results

Spatial distributions were simulated of main parameters of argon plasma jet for different times after the enter of this jet into the vacuum vessel, namely: the jet velocity field, the full plasma pressure, the electron temperature, the temperature of heavy particles as well as the ionization degree. Simulation parameters are shown in Table 1.

Table 1

Variant	n_n m^{-3}	n_e m^{-3}	T_e eV	T_h K	$u=\lvert\dot{w}_0\rvert$ m/sec	L_c m	R_c m	L_h/L_c	R_n m
1	10^{22}	10^{21}	1	300	3×10^3	5×10^{-2}	5×10^{-3}	1/4	10^{-3}
2	10^{22}	10^{21}	1	300	5×10^2	5×10^{-2}	5×10^{-3}	1/4	10^{-3}
3	10^{22}	10^{21}	1	300	3×10^3	5×10^{-2}	5×10^{-3}	1	10^{-3}
4	10^{22}	10^{21}	1	300	5×10^2	5×10^{-2}	5×10^{-3}	1	10^{-3}

In these simulations, the pressure, the temperature, the velocity, the coordinate and the time are divided by the characteristic parameters, namely: the neutral atom pressure $P_0 = n_0 kT_0$, the characteristic temperature $T_0 = m_h W_0^2 / k$, the initial jet velocity w_0, the characteristic size R_n and the characteristic time $t_0 = R_n / W_0$, respectively. Values of these parameters are shown in Table 2.

Table 2

Variant	P_0, Pa	T_0, K	R_n, m	W_0, m/sec	t_0, sec
1	6.01×10^4	4.36×10^4	10^{-3}	3×10^3	3.33×10^{-7}
2	1.67×10^3	1.21×10^3	10^{-3}	5×10^2	2.00×10^{-6}

Simulation results show that jet velocity fields differ essentially from these fields for the case of a plasma jet reflection from a plane wall and depend from the relation of the plasma jet velocity and the characteristic molecule velocity. In case of relative large jet velocities (Variant 1 in Tab. 1), a opposite plasma flow is formed along walls in the direction to the exit hole of the vessel due to the interaction plasma jet with the vessel wall. In case of relative small jet velocities (Variant 2 in Tab. 1), the plasma flow is only in the region between the enter hole and exit one but the larger part of the vessel is filled by a non-moving plasma.

Spatial distributions of the total static pressure are shown in Fig. 2 and Fig. 3 for variants 1 and 2 in Tab. 1, respectively. These distributions show a complex phenomena in the vessel. As can be seen from Fig. 2 in the case of relative small jet velocities (variant 2 in Tab. 1), the region is formed of high pressures with some waves which have nearly a plane front and propagate under some corner to the vessel axis. These waves propagate in the region of non-moving plasma where a flow velocities are very small. In the case of relative large jet velocities (variant 2 in Tab. 1), the region is formed of nearly uniform and relative low pressures which is separated by a steady shock wave from the region of a moving plasma.

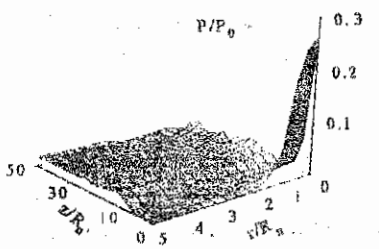


Fig. 2

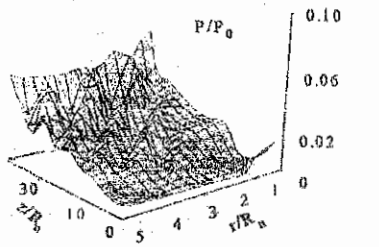


Fig. 3

Spatial distributions of main plasma jet parameters were obtained at different times, namely: the jet spread, the full plasma pressure, the electron temperature, the temperature of heavy particles as well as the ionization degree. These results show the essential influence of the plasma jet interaction on plasma parameters. First of all, shock waves can be appeared due to the plasma jet interaction with vessel walls. Besides, the rotate motion of plasma is appeared near the inner vessel angles.

References

1. S.I.Bragynsky. In: Problems of plasma theory. 1963, v.1, p.183-272 (in Russian)
2. L.I.Gudzenko, S.I.Yakovlenko. Plasma Lasers. - M.: Atomizdat. - 1988. - 254 p. (in Russian)
3. O.M.Belozerkovsky, Yu.M.Lavydov. Method of big particles in the gas dynamics. - M.: Nauka, 1982. - 392 p. (in Russian)

ELASTIC CHARGED PARTICLE SCATTERING BY CENTERS WITH COULOMB AND SHORT-RANGE POTENTIALS

A.G.Sitenko, O.I.Gerasimov*, N.N.Khudyntsev*
Bogolubov Institute for Theor. Physics, 252130, Kiev, Ukraine
* Odessa Hydrometeorological Institute, 270016, Odessa, Ukraine

1. The aim of the present paper is to calculate the amplitude and the cross-section of elastic charged particle, for example electron, scattering from the system in which one Coulomb potential and any number of short-range potentials are included. Within this calculation the zero-radius potentials (ZRP) model [1-4] will be used as multicentred pseudopotential. Our interest in this system was stimulated by the problem of the interpretation of the electron-scattering experiments for complex molecular ions, ionized gases and low-ionized plasma [5,6], on the one hand; and on the other hand, by the problem of generalization and developing of theories of scattering from a single Coulomb center combined with a short-range potential well [3,7,8] and from a superposition of ZRPs [9] in numerical calculations of electron scattering from a hydrogen molecle [10] and, also, because of the possibility of an exact solution of the problem in this case.

2. Consider elastic scattering of a monochromatic charged particle beam with energy E from a multicentred target which includes a single Coulomb and N short-range potentials where the latter describe a superposition of ZPRs. Let us assume that the target particles are structureless and also can be considered as being at rest during the elementary act of scattering. Putting the origin O of the coordinate system in the center of the Coulomb potential and following the general theory of ZPRs [1-4] we write the stationary Schrodinger equation for the whole system: electron plus target, in the following dimensionless form,

$$\left[-\frac{1}{2}\Delta_r + \frac{\alpha}{r} - E + 2\pi \sum_{j=1}^{N} a_j \delta\left(\mathbf{r} - \mathbf{R}_j\right) \frac{\partial}{\partial \rho_j} \rho_j \right] \Psi\left(\mathbf{r}; \{\mathbf{R}\}\right) = 0 , \qquad (1)$$

where $\Delta_r = \partial^2/\partial r^2$, $\rho_j = \left| \mathbf{r} - \mathbf{R}_j \right|$, a_j is the scattering length for the j-th ZPR, $\alpha = -1$ for attractive and $+1$ for repulsive Coulomb potentials, respectively, $\Psi(\mathbf{r},\{\mathbf{R}\})$ is the wave function of the whole system, which includes the dependence on all coordinates of the target particles, $\{\mathbf{R}\} = \mathbf{R}_1, \ldots, \mathbf{R}_N$, as parameters. In (1) and below will be used a

Coulomb system of units in which $a_c = \frac{h^2}{mZe^2}$ and $E_c = \frac{mZ^2e^4}{h^2}$ are the length and energy scales respectively, $\delta(z)$ is the Dirac delta function.

Equation (1) is not a closed due to the inclusion, along with $\Psi(\mathbf{r},\{\mathbf{R}\})$ of N unknown function $\Psi(\mathbf{r},\{\mathbf{R}\})$. Taking into account the physical properties of the wave functions, eq. (1) will be considered with a typical boundary condition in the following form,

$$\frac{1}{\rho_j\Psi_\eta}\frac{\partial}{\partial\rho_j}\rho_j\Psi_\eta\Big|_{\rho_j\to 0} = -\frac{1}{a_j} \equiv \kappa_j, \quad j=1,2,...,N \qquad (2)$$

3. Introducing the Green function for the Shrodinger equation with the Coulomb potential unperturbed by short-range potentials in closed form, which was first obtained by Hostler and Pratt [10-12],

$$G(\mathbf{r},\mathbf{r}') = \frac{\Gamma(1-\eta)}{2\pi|\mathbf{r}-\mathbf{r}'|}\left(\frac{\partial}{\partial ikx} - \frac{\partial}{\partial iky}\right) W_{\eta,\frac{1}{2}}(-ikx)\, M_{\eta,\frac{1}{2}}(-iky), \quad k = \sqrt{2E}, \qquad (3)$$

we can write down an exact solution of (1), namely

$$\Psi(\mathbf{r},\{\mathbf{R}\}) = \Psi^{+}(\mathbf{r}) + \sum_{j=1}^{N}\Psi(\mathbf{R}_j,\{\mathbf{R}\})\, G(\mathbf{r},\mathbf{R}_j), \qquad (4)$$

where $\Psi^{+}(\mathbf{r}) = e^{\pi\alpha/2k}\Gamma(1-\eta)e^{ikr}M(\eta,1;i(kr-\mathbf{kr}))$ is the Coulomb wave function for the continuous spectrum, $x = r + r' + |\mathbf{r}-\mathbf{r}'|$, $y = r + r' - |\mathbf{r}-\mathbf{r}'|$, $\Gamma(z)$ is the gamma-function, $W_{\mu,\nu}(z)$, $M_{\mu,\nu}(z)$ are Whittaker functions, $M(a,b;z)$ is the confluent hypergeometric function, $\eta = i\alpha/k$.

The set of coefficients $\Psi(\mathbf{R}_j,\{\mathbf{R}\})$ can be determined as a result of solving a system of algebraic equations which follows from (2) and (4). We just represent here the final result of this calculation, namely

$$\Psi(\mathbf{R}_j,\{\mathbf{R}\}) = \frac{\Delta_j}{\Delta}, \qquad j = 1,2,...,N, \qquad (5)$$

where Δ_η and Δ_j are the main and j-th auxiliary definitors of the system of boundary conditions (2), respectively, and

$$\xi(R) = 2\pi\frac{\partial}{\partial\rho_j}\rho_j G(\mathbf{r},\mathbf{R}_j)\Big|_{\rho_j\to 0}. \qquad (6)$$

We emphasise that expressions (4) and (5) are obtained without any additional approximation and thus represent an exact solution.

4. Using the known asymptotic properties of $\Psi^{+}(r)$, $W_{\mu,\nu}(z)$ and $M_{\mu,\nu}(z)$ [13,14] with the help of (4)-(6) we obtain an expression for the wave function of the scattered electron Ψ_{sc} in the following form,

$$\Psi_{sc}\left(\mathbf{r},\{\mathbf{R}\}\right)=\left[f_c(\vartheta)+f_c\left(\{\mathbf{R}\}\right)\right]\frac{e^{ikr-\eta\ln 2kr}}{r}, \qquad (7)$$

where $f_c(\vartheta)=-\dfrac{1}{2k^2\sin^2\dfrac{\vartheta}{2}}\dfrac{\Gamma(1-\eta)}{\Gamma(1+\eta)}e^{2i\eta\ln\sin\frac{\vartheta}{2}}$ is the Coulomb amplitude and ϑ is the angle of scattering.

Thus, from (7) it follows that the expression

$$f_c\left(\{\mathbf{R}\}\right)=\frac{1}{2\pi}e^{i\pi\eta/2k}\,\Gamma(1-\eta)\sum_{j=1}^{N}\Psi\left(\mathbf{R}_j,\{\mathbf{R}\}\right)\Xi\left(R_j,\omega_j\right) \qquad (8)$$

can be considered as the amplitude of scattering from the multicentred short-range pseudopotential in the Coulomb field. Note that in (8)

$$\Xi\left(R_j,\omega_j\right)=M'_{\eta,\frac{1}{2}}\left(-ikR_j\left(1+\cos\omega_j\right)\right)+\frac{1}{2}M_{\eta,\frac{1}{2}}\left(-ikR_j\left(1+\cos\omega_j\right)\right) \qquad (9)$$

and ω_j is the angle between the vectors $\mathbf{r}$ and $\mathbf{R}_j$. Also note, that for the definition, we put here that the Coulomb potential is repulsive and $M'_{\eta,\frac{1}{2}}(z)=\dfrac{d}{dz}M_{\eta,\frac{1}{2}}(z)$.

As follows from (7)-(11) the amplitude $f_c\left(\{\mathbf{R}\}\right)$ is not the same as the known Coulomb or ZRP amplitudes, separately. At the same time, because the the $\Psi\left(\mathbf{R}_j,\{\mathbf{R}\}\right)$ are determined for the whole set $\{\mathbf{R}\}$, $f_c\left(\{\mathbf{R}\}\right)$ cannot be considered as a pair-additive function which includes the contributions from pair-wise complexes of the type: Coulomb centre plus ZRP, only. We emphasise the factorization of the amplitude $f_c\left(\{\mathbf{R}\}\right)$ as a function of all angular arguments.

5. The using the asymptotic properties of Whittaker functions [13,14] for the case of complexes of the type: Coulomb plus ZRP, which are shifted one from another by a vector $\mathbf{R}$ as follows from (4)-(10) in the limit when $kR\ll 1$ ($R\gg L$, where L is a typical scale of the system) under the condition $1/ka_c=0$ we have the known result

$$f_{c,1}=-\frac{1}{k-\eta^{-1}}=f_1 \qquad (10)$$

For the complexes of the type: Coulomb and two ZRP which are centred at the points $\mathbf{R}_1$ and $\mathbf{R}_2$ on the same way in the limit $R_{1,2}\gg L$, $kR_{1,2}\ll 1$ and $|\mathbf{R}_1-\mathbf{R}_2|=R$ kept fixed we obtain the known result which is usually called the Brueckner formula,

$$f_{c.l.2} = \frac{2}{k - \eta^{-1} + (2\pi R)^{-1} \exp(ikR)} \qquad (11)$$

Note that in the case of scattering from complexes of the common type of complex set of (R) which can be considered as a generalization of the Brueckner and Landau and Smorodinsky results.

The analysis of respective limiting transitions see in details in [16].

REFERENCES

[1]. Schwinger J. Phys. Rev. 89, 834 (1953)

[2] Bethe H. Phys. Rev. 76, 38 (1949)

[3] Blatt I., Weisskopf V. Theoretical Nuclear Physics (Wiley, N.Y., 1952)

[4]. Sitenko A.G., Tartakovsky V.K. Lectures on the Theory Of the Nucleus (Pergamon Oxford, 1975)

[5]. Massey H. Negative Ions (Cambrige Univ.Press, Cambrige, 1976)

[6]. Khrapak A.G., Yakubov I.G. Electrons in dense Gases and Plasma (Nauka, M., 1981)

[7]. Landau L.D., Smorodinsky Ya.A. JETP 14, 289 (1944)

[8]. Drukarev G.F. Electron Collisions with Atoms and Molecules (Nauka, M., 1978)

[9]. Dalidchik F.I. JETCh 10, 303, 579 (1974)

[10]. Hostler L., Pratt R. Phys. Rev. Let. 10, 469 (1964)

[11]. Mapleton M. JMP 2, 478 (1964)

[10]. Hostler L., Pratt R. Phys. Rev. Let. 10, 469 (1964)

[11]. Mapleton M. JMP 2, 478 (1964)

[12]. Hostler L. JMP 5, 591 (1964)

[13]. Bateman J., Erdelyi A. Higher Functions 1 (Nauka, M., 1973)

[14]. Abramovitz M., Stigun I. Handbook of Math. Functions (W., 1964)

[15]. Brueckner K. Phys. Rev. 89, 834 (1953)

[16]. Gerasimov O.I., Sitenko A.G. TMP 99, 81 (1994)

SURFACE HELICONS IN PLASMA–LIKE MEDIA AND THEIR COLLISIONLESS DAMPING

V.M.Yakovenko[a)], I.V.Yakovenko[b)]

[a)]Institute of Radiophysics and Electronics of National Academy of Sciences,
12 Acad.Proskura st. Kharkov 310085, Ukraine
[b)] Research and Design Institute "Molnia" of the Kharkov Polytechnical University
47 Shevchenko st., Kharkov 310013, Ukraine

Using the Maxwell equations with a magnetic dipole, material equations for plasma and boundary conditions, the authors have discovered the losses of the dipole energy on the excitation of the surface helicons.

On the basis of the expression for the losses the kinetic equation has been set up for surface helicons as a result of the processes of their emission and absorption by the conduction electrons. The collisionless damping of the surface helicons has been found and its dependence on the wave vector has been analyzed.

The investigations of the processes of the electromagnetic wave interaction with the charge carriers in conductive media arouse the increasing interest. It occurs in connection with new technological possibilities of obtaining pure semiconductive materials, for example, structures with the ballistic carriers of charges. These processes which are based on the elementary effects of the Cherenkov transmission and the braking radiation of charged particles in limited media lead to the collisionless damping (or in the inequilibrium media to an increase of plasma oscillations). These oscillations have a variable electric field component in the direction of moving particle [1],[2]. In this case the particle is braked by the wave electric field. The study of the surface helicons interactions with the charged carriers has been made under the conditions when a projection of the oscillation electric field to the direction of the motion of the particle is equal to zero but the magnetic field component is not equal to zero. In such a case, the interaction between the surface helicon and the magnetic dipole of the charge which moves along the external d–c magnetic field becomes possible. The similar mechanism of damping of volume helicons in the infinite medium has been investigated in [3].

It is known [1] that the surface helicons exist on the boundary of plasma–like media (for example, semiconductor—vacuum) in the magnetic field $\mathbf{H} = (0, 0, H)$ which is parallel to the boundary (axis $0x$ and $0y$) and have the following spectrum

of oscillations

$$\omega_q = \frac{cH_0 q_x^2 q_z}{2\pi e n_0 q} \tag{1}$$

where ω_q is the frequency, $\mathbf{q} = (q_z, q_x)$ is the wave vector, n_0 is the electron concentration, c is the velocity of light. The depth of the field penetration in a semiconductor or vacuum is determined by the quantaties $q_{y1}^{-1} = (q_z^2 - q_x^2)^{-1} q$ and $q_{y0}^{-1} = q^{-1}$ respectively.

To obtain the spectrum of oscillations (1) and the components of the electromagnetic fields it is necessary to use the system of the Maxwell equations and the material equations in the form:

$$\operatorname{rot} \mathbf{E} = -\frac{1}{c}\frac{\partial \mathbf{H}}{\partial t}; \quad \operatorname{div} \mathbf{H} = 0 \tag{2}$$

$$\operatorname{rot} \mathbf{H} = 0; \quad y \geq 0 \tag{3}$$

$$\operatorname{rot} \mathbf{H} = \frac{4\pi e n_0}{c}\mathbf{v}, \; \mathbf{E} + \frac{1}{c}[\mathbf{v}\mathbf{H}_0] = 0, \; y < 0. \tag{4}$$

The continuity conditions on normal components of the magnetic field H_y and tangential ones H_x are met on the boudary of the media $y = 0$; the component H_z are not continuous which is connected with the presence of the surface current along H_0. The analysis of the more precise Maxwell equations and material equations of plasma shows that the conditions of the surface helicons existence may be written as follows [1]

$$|\varepsilon_{xx}| \gg |\varepsilon_{zz}|, \; |\varepsilon_{xy}| \gg |\varepsilon_{zz}|, \; 1 \leq \frac{q_z^2}{q_x^2} \leq \left|\frac{\varepsilon_{xx}\varepsilon_{zz}}{\varepsilon_{xy}^2}\right| \tag{5}$$

where ε_{ij} are the components of the dielectric permeability tensor of the magnetic active electron—hole plasma of the semiconductor [4].

From the equations (1)–(4) it follows that the full energy of the surface helicon $\mathcal{E}$ is equal to $\int \left(H^2/8\pi\right) dV$, where the integration is made over the whole domain of the field localization $\left(q_{y1}^{-1} \leq y \leq q_{y0}^{-1}\right)$.

Now consider the interaction of the surface helicons with the magnetic dipole that moves along H_0 with the velocity v_0 at the distance a from the medium interface $\mathbf{M}(r,t) = \mathbf{M}_0\delta(x)\delta(y+a)\delta(z - v_0 t)$, $\mathbf{M}_0 = (0, 0, M_0)$.

In this case in order to obtain the field components in the semiconductor plasma it is necessary to use the following equation instead of equation (2)

$$\operatorname{rot} \mathbf{E} = -\frac{1}{c}\frac{\partial \mathbf{B}}{\partial t}; \; \operatorname{div} \mathbf{B} = 0; \; \mathbf{B} = \mathbf{H} + 4\pi\mathbf{M}. \tag{6}$$

The change of the surface helicon energy resulting from its interaction with the magnetic moment M may be given as

$$\frac{\partial \mathcal{E}}{\partial t} = -\int H_z \frac{\partial M_z}{\partial t} dV. \tag{7}$$

The solutions of the homogeneous and heterogeneous equations (2)–(4) can be expressed as a sum of time and space harmonics, for instance

$$\mathrm{H}(r,t) = \sum_{q_x q_z} \mathrm{H}(y) e^{i(q_x x + q_z z - \omega t)}.$$

The $H_z(r,t)$ component of the surface helicon can be obtained in terms of M_0 by using the boundary conditions at $y = 0$; $y = \pm\infty$. Then the expression (7) at $q_{y1}a \ll 1$ takes the form:

$$\frac{\partial \mathcal{E}}{\partial t} \equiv \sum_q \hbar\omega_q \frac{\partial N_q}{\partial t} = \frac{4\pi^2 M_0^2}{S} \sum_q \omega_q^2 \frac{q_z^2}{q q_x^2} (q_x^2 - q_z^2)\, \delta(\omega_q - q_z v_0) \tag{8}$$

where S is the area of the surface of the semiconductor, N_q is the number of the surface helicons with the energy $\hbar\omega_q$.

It can be easily shown that the particle of any sign charge with mass m which rotates round the Larmor circle with a velocity v posses the magnetic moment $\mathrm{M}_0 = -(1/2)(mv_\perp^2 \mathrm{H}_0/H_0^2)$.

So formula (8) describes the Cherenkov radiation of the surface helicons by the charged particle which performs the spiral motion whose axis is parallel to H_0. We suggest further that n_k particles are in some state "k" which possess the magnetic moment $M_k = -(mv_{k\perp}^2)/(2H_0)$ and move with a velocity v along H_0. Then it is easy from formula (8) to obtain the expression for the change in the number of the field quantums N_q in the state "q" (spontaneous radiation of the surface helicons)

$$\frac{\partial N_q}{\partial t} = \frac{4\pi^2 \omega_q q_z^2 q_{y1}}{\hbar S q q_x^2} \sum_k M_k^2 n_k \delta(\omega_q - q_z v_{kz}). \tag{9}$$

On the other hand, the kinetic equation which describes the change in the bozon number as a result of their emission and absorption by electrons (fermions) can be written as follows:

$$\frac{\partial N_q}{\partial t} = \frac{2\pi}{\hbar^3} \sum_k |W_{kq k'}|^2 \delta(\omega_q - q v_k)[(N_q + 1)n_k - N_k n_{k'}] \tag{10}$$

where $\mathrm{n}_k \ll 1$, $W_{kqk'}$ is the matrix element of the hamiltonian interaction between the electrons and electromagnetic field oscillation, $\mathbf{k} = \mathbf{k}' + \mathbf{q}$, $\mathcal{E}_k = \mathcal{E}_{k'} + \hbar\omega_q$, $\mathcal{E}_k =$

$(\hbar^2k^2/2m)$ is the electron energy. Since with $N_q \ll 1$ both equations (9) and (10) are identical, the expression for the matrix element can be obtained in the following way:

$$|W_{kq k'}|^2 = \frac{2\pi h\omega_q q_x^2 q_{y1}}{V q q_w^2} M_k^2 \tag{11}$$

where $V = Sq^{-1}$ is the volume of the interaction space of the surface helicons and the electrons. Then the decrement of the collisionless damping of the surface helicons ($N_q \gg 1$) can be provided from the equation (10) going from the integration to summation in the space $\mathbf{p} = \hbar\mathbf{k}$

$$\gamma = \frac{1}{N_q}\frac{\partial N_q}{\partial t} = 2\pi\frac{V\omega_q}{\hbar}\int |W_{kq k'}|^2 \frac{\partial f_0(\mathcal{E})}{\partial \mathcal{E}}\delta(\omega_q - q_x v_x)\mathrm{d}\mathbf{p}. \tag{12}$$

Here $f_0(\mathcal{E}_k) = (2\pi\hbar)^{-3}n_k$, $\mathcal{E}_k \gg h\omega_q$. Taking into account the equation (11) for a non-degenerate electron gas we obtain the following value for the decrement

$$\gamma = -\frac{8\sqrt{\pi}c^2 q_x^6\sqrt{q_w^2 - q_x^2}v_T}{\sqrt{2}q^3\omega_0^2}. \tag{13}$$

Here $\omega_0 = \sqrt{4\pi e^2 n_0/m}$ is the plasma frequency of the electrons, $v_T = \sqrt{T/m}$ is the mean electron thermal velocity. Note that the absence of the typical multiplier of the Landau damping $\exp(-m\omega_q^2/2Tq_x^2)$ is due to the fulfilment of the inequality $q_x^2 v_T^2 \gg \omega_q^2$.

In this case, of course, $\omega_H^2 \gg q_z^2 v_i^2 \gg \nu^2$, where ν is the typical frequency of collisions of the electrons with a change of the momentum. From equation (13) it follows that $\gamma = 0$ at $q_w = q_x$. As q_w increases the decrement grows up, when $q_w = 2q_x^2$ has a maximum equal to $\gamma_{\max} \approx \sqrt{\pi}(c^2 v_T q_x^3)/\omega_0^2$, decreases in proportion to q_w^{-2}. As the collisional damping of the surface helicons is the magnitude of the order $(c^2 q_x^2 \nu)/\omega_0^2$ then it is smaller than the collisionsless damping when $q_x v_0 > \nu$.

References

[1] N.N.Beletsky, V.M.Svetlichny, D.D.Khalameida, V.M.Yakovenko, *Electromagnetic phenomena of SHF-range in inhomogeneous semiconductor structures*, (Naukova Dumka, Kiev, 1991, 216), [in Russian].

[2] V.M.Yakovenko, I.V.Yakovenko, Phis. Lett.,A196 (1994) 290.

[3] E.A.Kaner, V.G. Skobov, JETF 45, N° 3,(1963),610.

[4] V.V.Vladimirov, A.F.Volkov, E.Z.Meilikhov, *Plasma of semiconductors* (Atomizdat, Moscow, 1979, 252) [in Russian]

EXCITATION AND ABSORPTION OF WAVES IN A HELICON PLASMA SOURCE

K P Shamrai, V P Pavlenko and V B Taranov

Institute for Nuclear Research, 47 prospekt Nauki, Kiev 252022, Ukraine
Department of Technology, Uppsala University, Box 534, S-751 21, Uppsala, Sweden

Abstract. The processes of excitation and absorption of waves are considered in a helicon plasma source driven by various antennas. The anomalous absorption of helicons originating in their conversion into electrostatic waves at a plasma edge is described by an effective collision frequency which is shown to be of the same order of magnitude independently of the antenna design. The calculated value of effective frequency conforms satisfactorily to that needed for the explanation of experimental results. The volume power input realized by helicon waves is shown to be more enhanced in the anti-resonance regimes, and more peaked near the plasma axis in the case of axially symmetric antenna.

Helicon plasma source is a conventional name for an inductively coupled radio-frequency source with resonance excitation of helicon waves [1]. Among a variety of inductively coupled low-pressure sources of dense plasma the helicon one generates highest plasma densities, up to 10^{13} cm^{-3}, at relatively low specific power inputs ranging 50 to 100 mW/cm^3, and in a wide area of gas pressures from a few tenths to a few tens of mTorr. Devices of this type were suggested for various applications including plasma materials processing, gas laser pumping, plasma generation in magnetic traps, and plasma particles accelerators (see, e.g. [2]).

The waves excited in helicon plasmas by external antennas were treated in numerous papers with a usual assumption that they are pure helicons. An encouragement for this viewpoin is found in a set of experiments where the radially long-scale wave fields which are typical for helicon waves were indeed measured with magnetic probes in a bulk plasma [1,3]. Moreover, the field pattern which was observed with a precise technique was shown to be in an excellent agreement with that calculated using the real non-uniform density profiles [3].

Nevertheless, some unexpected difficulties were met in trying to correlate the power dissipated in a plasma by helicon waves with a total power supply [1,4]. The traditional mechanisms of the wave dissipation, e.g. binary collisions, or collisionless Landau damping, typically turn out to be rather weak. They do not allow to explain for a variety of helicon sources the total absorbed power as that contributed via helicons. The collisional damping is inefficient because of low gas pressures (normally, about a few mTorrs). The Landau damping is negligible in those experiments where the phase velocities of excited waves are rather high, so that the number of particles coupled to the waves is extremely small.

The problem with a scanty power dissipated by helicons via collisions was solved in Ref.[1] by introducing the effective collision frequency $\nu_{eff} \approx 10^3\nu$, where ν is the frequency of electron binary collisions. So anomalous electron collisions were supposed in Ref.[1] to originate in the oscillating two-stream instability, which was estimated at the utmost growth

rate. Apparently, such a strong instability should be followed by a strong plasma turbulence. However, the further experiments have shown that the behaviour of helicon plasmas does not demonstrate the signs which normally accompany strongly turbulent regimes.

One more possible mechanism for helicon wave damping, which may occur at rather high rf power inputs and is nonlinear in nature, implies that the wave transfers the energy to a group of electrons trapped in a longitudinal electric field [4]. Rather deep modulation of the optical emission mooving away from the antenna with the phase velocity of the helicon wave was observed in experiments [4] with a precise time-resolved technique. It was attributed to the presence in plasma of a considerable population of electrons accelerated due to trapping in a helicon wave. Nonetheless, the measured phase velocity of helicon wave in that experiment was rather high as compared to the thermal electron velocity, so that the number of particles trapped by helicon wave seems to be too low to explain its strong damping.

The confusion with the power balance made with the traditional mechanisms of wave damping indicates the presence of some *latent* channel for helicon damping which was apparently slipped away of measuring instruments. This additional channel was found out in Refs.[5,6] to be realized via electrostatic waves which are generated in helicon plasmas under certain conditions. The generation mechanism was identified in Ref.[6] as substantially collective, it originates in the linear conversion of helicon waves near the plasma edge. A general physical picture for the wave excitation and power absorption in a helicon source looks like follows [6-8].

The plasma waves of two kinds can exist in a frequency range typical for helicon sources. A driving antenna excites only helicon waves which are strongly coupled to the antenna rf current while the waves of the second kind which are well electrostatic cannot be excited directly owing to weak coupling. The further destiny of helicon waves depends on conditions at a lateral surface of a plasma column.

If a plasma either makes a good contact with a conductive sidewall, or is separated from that wall by rather small vacuum gap of width d below the critical value

$$d_{cr} = a\frac{k^2a^2}{4\left(1+k^2a^2\right)}$$

where k is the longitudinal number of the excited wave, and a is the radius of a plasma column, the helicon and electrostatic waves turn out to be coupled weakly. Then, the excitation of helicon waves is not followed by the generation of electrostatic waves. In this case, the helicon waves utterly govern the source operation, and one can realize the resonance wave discharge supported solely by helicon waves [7].

Provided the vacuum gap is rather wide, $d > d_{cr}$, the helicon wave is no more capable of independently existing in a plasma with non-conducting boundary. Its radial electron rf current cannot neither be closed through a vacuum gap, nor vanish at a plasma edge. The contradiction is resolved with the generation of the electrostatic wave which pushes electrons near the plasma edge in a counterphase with the helicon wave thus letting the radial electron current be zero. Arising due to such specific mechanism of surface mode conversion electrostatic wave

takes almost all energy away of helicon one, and thus realize a principal contribution of an rf power to plasma. The group velocity of the electrostatic wave across the magnetic field is small as compared to that of helicon wave. As a result, the amplitude of electrostatic wave highly exceeds that of helicon wave.

The generation of the electrostatic wave may be suppressed in radially bounded plasma provided the azimuthal electric field of the helicon wave has a node at a lateral plasma surface, that is the number of radial half-wavelengths over a plasma radius is an integer. Then, the radial electron rf current of the helicon wave vanishes, since it is primarily a $\mathbf{E}\times\mathbf{B}_0$ electron drift in crossed wave electric field $\mathbf{E}$ and external magnetic field $\mathbf{B}_0$, and the electrostatic wave is not excited. Such a specific structure of the wave field may be realized in the special anti-resonance regime of the source excitation.

The fields excited by antenna are combined of spatial harmonics with various longitudinal, k, and azimuthal, m, wavenumbers. Each of modes consists of a helicon component which is excited directly by the antenna current, and of an electrostatic one arising due to the surface mode conversion. The latter is found to be a principal partner since its amplitude highly exceeds that of helicon wave. This is so in a general case, but the situation inverts for some harmonic if the correlation of parameters is such that the anti-resonance condition holds, that is the azimuthal field of helicon wave vanishes at the plasma edge. Both for azimuthally symmetric and for anti-symmetric antennas this condition takes the following form [6,8]

$$n = p\,\frac{c}{4\pi e}\,\frac{kB_0}{\omega a} \qquad (1)$$

where n is the plasma density, ω the wave frequency, e the electron charge, c the speed of light, and p is some numerical factor depending on antenna design and ranging 2 to 4.

Far from anti-resonances, a spatial structure of the electrostatic wave, and thus a spatial distribution of the rf power release were found to depend on that how the strength of external magnetic field B_0 correlates with the critical value

$$B_{cr} = \frac{m_e c}{e}\,\frac{\omega^2}{\nu}\,\frac{1}{ka} \qquad (2)$$

where m_e is the electron mass.

In high-B_0 region, $B_0 > B_{cr}$, the electrostatic waves do not penetrate into a bulk plasma and release their energy in a narrow layer of width $a(B_0/B_{cr})$ near the plasma boundary. They are extremely short-scale accross the magnetic field, and so could not be resolved by magnetic probes in cited experiments. Thus, the excitation of electrostatic waves due to the surface mode conversion may stand for that latent channel for the effective helicon damping which was needed to conform the power balance to helicon plasmas.

At $B_0 > B_{cr}$, helicon waves realize a volume power input while electrostatic waves result in a surface one. Although the latter turns out to provide a principal fraction of the total power input, the volume helicon channel seems to be rather important for effective plasma production in helicon discharges. The radial distribution of heliconic power release turns out to be rather peacked at a plasma centre for the case of $m = 0$ antenna, while it is substantially uniform for

an axially anti-symmetric antenna. The volume fraction of the power input is enhanced in the anti-resonance regimes of a helicon source operation. In the low aspect-ratio devices, the power is really supplied to the plasma via a few lowest harmonics. As a result, the satisfaction of condition (1) for one of them can give a considerable increase of the volume power input via helicon channel provided a total input is fixed.

Apparently, the less number of different harmonics antenna excites the more effective redistribution of the power input in favour of the volume helicon channel may occur in the anti-resonance regime. The analysis show that a few-fold gain in favour of the volume power input may be attained in a helicon source which is driven by the azimuthally symmetric $m = 0$ antenna and operates in the anti-resonance regime [8].

Thus, the only mechanism for a substantial damping of helicon waves arises from their conversion into electrostatic waves at the non-conducting edge of a plasma column. To make a power balance in a helicon source proceeding from the helicon waves only one should put in consideration an effective collision frequency

$$\nu_{eff} = \mu \omega_B k a \tag{3}$$

where ω_B is the electron gyro-frequency, and μ is a numerical factor which depends on antenna design, but in any case does not deviate strongly from the unity. The effective frequency (3) is much higher than the binary one, and the value of just this order was needed to conform the experimental data to calculations in Refs.[1,4]. The effective frequency (3) turns out to be independent of the collision frequency because it is defined by the efficiency of the conversion of helicon wave into electrostatic one at the edge of a plasma column.

References

[1] Boswell R W 1984 *Plasma Phys. Control. Fusion* **26** 1147

[2] Chen F F 1996 in *High Density Plasma Sources*, edited by O. A. Popov (Noyes, Park Ridge, NJ, in press); UCLA Report PPG-1520

[3] Light M and Chen F F 1995 *Phys. Plasmas* **2** 1084

[4] Ellingboe A R, Boswell R W, Booth J P and Sadeghi N 1995 *Phys. Plasmas* **2** 1807

[5] Vorob'ev N F and Rukhadze A A 1994 *Fizika Plazmy* **20** 1065

[6] Shamrai K P and Taranov V B 1995 *Phys. Lett.* A **204** 139

[7] Shamrai K P and Taranov V B 1994 *Plasma Phys. Control. Fusion* **36** 1719

[8] Shamrai K P and Pavlenko V P 1996 *Preprint UPTEC* 96 037R

WAVE SPECTRA AND IMPEDANCE OF ANTENNAS DRIVING HELICON PLASMA SOURCES

K P Shamrai, V P Pavlenko and V B Taranov

Institute for Nuclear Research, 47 prospekt Nauki, Kiev 252022, Ukraine
Department of Technology, Uppsala University, Box 534, S-751 21, Uppsala, Sweden

Abstract. The impedance is calculated of different antennas driving helicon plasma sources. At given power input, different antennas are shown to generate in plasma the fields comparable in magnitudes, but the azimuthally symmetric antenna needs a few-fold enhanced operation voltage. The resistance of antenna loaded by the wave excitation is found to minimize near the anti-resonance states, and this provides a necessary condition for the stability of a helicon discharge.

Helicon sources permit the generation of dense plasmas in relatively low magnetic fields. They have good prospects for various applications, especially for plasma materials processing. The helicon source operation is governed by an rf current antenna which is coupled inductively to a plasma. Various antennas of different but rather simple design which were suggested to drive sources may be classified into two essentially different groups.

The first includes so called straight antennas which are made up of the rf current-carrying parts directed either along or across the external magnetic field. Three types of straight antennas are used in experiments, that is double-loop (Boswell's) [1], Nagoya [2,3], and single-loop (Kiev) [4] ones. All these antennas are azimuthally anti-symmetric, and so they excite in plasma the odd azimuthal harmonics, primarily the $m = \pm 1$ ones. Azimuthally symmetric straight antennas driving $m = 0$ harmonics are also used in some experiments [5] (see figure 1).

The second group puts together so called helical antennas. They include current-carrying parts which are twisted along the magnetic field either clockwise (R-antennas) or counter-clockwise (L-antennas). Antennas of this type are azimuthally anti-symmetric, and were designed originally in the hope to refine the coupling to right or left circularly polarized waves, the R-antennas having been supposed to effectively excite helicon waves.

All straight azimuthally anti-symmetric antennas turn out to be topologically equivalent, and are reducible to the simplest (Kiev) one by either longitudinal or azimuthal doubling. At equal dimensions, the impedance of Nagoya antenna is shown to make doubled that of Kiev, and one half of Boswell's ones.

The straight antennas are found to be "pure" driving systems with reference to wave spectra. The symmetry of these antennas is compatible with that of plasma cavity, and so the wave spectra are excited in mode-to-mode coupling with antenna spectra which turn out to be rather simple. In this case, each of plasma cavity modes can satisfy the boundary conditions separately, and so may be excited by antenna independently.

Of two kinds of plasma waves which can exist in the range of generator frequencies and

plasma parameters typical for helicon sources only helicon waves are excited directly by an rf current antenna [6,7]. These waves are strongly coupled to the azimuthal parts of antenna while their coupling to longitudinal parts is extremely small. The waves of the second type which are well electrostatic turn out to be weakly coupled to antenna and cannot be excited directly. But the origin for weak coupling of electrostatic waves is rather different for azimuthally symmetric and anti-symmetric antennas. For the m=0 antenna, the weak coupling is obliged to a negligibly small value of the azimuthal electric field of electrostatic wave, while in the anti-symmetric case the reason for this originates in a compensation of contributions arising from different antenna parts. Nevertheless, the electrostatic waves are effectively excited near the plasma edge due to the specific mechanism of surface wave conversion of helicon waves.

The impedance of a straight antenna turns out to be a sum of partials introduced by the antenna load due to excitation of various harmonics with different longitudinal, $k = l\pi/L$, where L is a device length, and l is an integer, and azimuthal, m, wavenumbers. The peculiarities of impedance behaviour are defined by the anti-resonance properties of a plasma cavity excited by antenna. The anti-resonance implies the satisfaction of the following condition

$$n = n_H \equiv p\,\frac{c}{4\pi e}\,\frac{kB_0}{\omega a} \qquad (1)$$

where n is the plasma density, B_0 the external magnetic field, ω the wave frequency, a the radius of a plasma column, e the electron charge, c the speed of light, and p is some numerical factor depending on antenna design and ranging 2 to 4. Under condition (1), the appropriate harmonic does not excite the electrostatic wave, and this is followed by a substantial reduction of its impedance partial. As a result, the total resistance minimizes near the anti-resonance (1) where it may be represented in the following form

$$R = R_0 + \text{const}\left[\left(\frac{n - n_H}{n_H}\right)^2 + \frac{\nu}{\omega_B}\,\frac{\pi}{k^2 aL}\right] \qquad (2)$$

Here ν and ω_B are collision and gyro-frequencies of electrons, and R_0 is the resistance introduced by the rest of harmonics excluding the anti-resonating one. The value of R_0 weakly depends on the plasma density within the interval of substantial variation of the second addend in Eq.(2), but the contribution of this second addend decreases rapidly with growing longitudinal wavenumber k, and so the resistance minima may be displayed for the lower anti-resonances only.

As is clear from Eq.(2), the half-width of the resistance minimun takes the form

$$(\delta n)_{A\text{-}R} = n_H\left(\frac{\nu}{\omega_B}\,\frac{\pi}{k^2 aL}\right)^{1/2}$$

The isolines of the total antenna resistance and reactance calculated numerically are shown

in the plane plasma density - magnetic field in figures 2 and 3 for azimuthally symmetric and anti-symmetric antennas, respectively. As is clear, the resistance minimizes near the ground anti-resonance while the minima at higher anti-resonances are "blurred".

The impedance of $m = 0$ antenna turns out to be higher than that of the anti-symmetric antenna. As is clear from the Joule law, this implies that to provide the same power feed the current in $m = 0$ antenna may be reduced as compared with the case of anti-symmetric antenna. The strengths of fields excited by both antennas are comparable at equal power inputs, while the amplitude of antenna voltage should be enhanced for the $m = 0$ antenna.

If the plasma density is slightly below n_H, one can see from Eq.(2) that

$$\partial R/\partial n < 0 \quad \text{at} \quad B_0 = \text{const} \tag{3}$$

This condition was pointed out in Ref.[8] as the necessary one for a stability of the discharge. Indeed, under condition (3) some fluctuational increase (decrease) in plasma density results in decrease (increase) of the resistance, and hence, according to the Joule law, of the power absorption followed by a discharge return to the initial density. Thus, a nearly anti-resonance regime of a helicon discharge, $n_H - n < (\delta n)_{A\text{-}R}$, which is accompanied both by the enhanced volume power absorption and by the discharge stability seems to be preferential as a dense-plasma mode of the helicon source operation.

The analysis of traditional helical antennas show that both R- and L-antennas are not able to isolate the generation of the waves polarized either clockwise or counter-clockwise. First, in bounded plasmas of helicon sources the polarization of helicon waves vary across the plasma column. Second, the purely azimuthal current-carrying parts which are inevitably included into the antenna design are equally coupled to the oscillations of both polarizarions. Thus, helical antennas seem to excite effectively the odd azimuthal modes of both polarizations. Some difference between R- and L-antennas arises in long aspect-ratio devices concerning the preferential direction of wave radiation.

The helical antennas turn out to be "non-pure" or "mixing" ones. Their wave spectra are rather complicated owing to twisted geometry which is incompatible with the symmetry of a plasma cavity. The multi-mode regime of the source excitation is intrinsic for helical antennas, and in this respect they present some advantages for the homogenization of the rf power input.

References

[1] Boswell R W 1984 *Plasma Phys. Control. Fusion* **26** 1147

[2] Shoji T, Sakawa Y, Nakazawa S, Kadota K and Sato T 1993 *Plasma Sources Sci. Technol.* **2** 5

[3] Light M and Chen F F 1995 *Phys. Plasmas* **2** 1084

[4] Katyukha V P, Kirichenko G S, Rusavskii A V, Taranov V B and Shamrai K P 1994 *Rev. Sci. Instrum.* **65** 1368

[5] Jiwari N, Iwasawa H, Narai A, Sakaue H, Shindo H, Shoji T and Horiike Y 1993 *Jpn. J. Appl. Phys.* **32** 3019

[6] Shamrai K P and Taranov V B 1995 *Phys. Lett.* A **204** 139

[7] Shamrai K P and Pavlenko V P 1996 *Preprint UPTEC* 96 037R

[8] Shamrai K P and Taranov V B 1994 *Plasma Phys. Control. Fusion* **36** 1719



Figure 1. Schematic views of (a) azimuthally anti-symmetric and (b) symmetric straight single-loop antennas, and of (c) helical R-antenna in a plasma cavity.

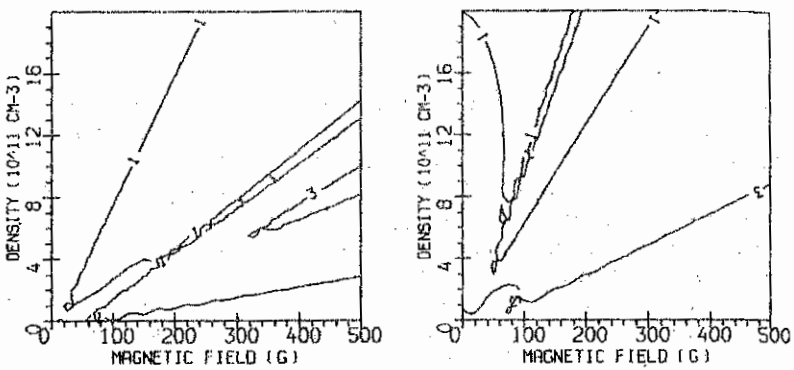


Figure 2. The isolines of total resistance (left) and reactance (right), in Ohms, calculated for the azimuthally symmetric antenna with parameters $L = 40$ cm, $\omega/2\pi = 13.56$ MHz, $R = 9.5$ cm, $a/R = 0.66$, and $\nu/\omega = 0.1$. R is the radius of conducting wall.

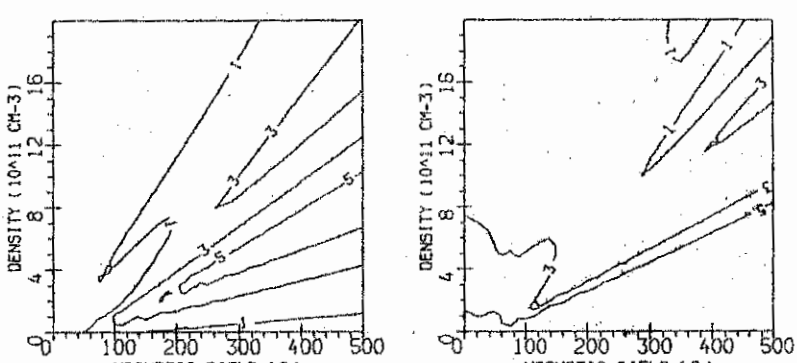


Figure 3. The same as in figure 2 but for the azimuthally anti-symmetric antenna.

On Fractal Dimension of Plasma Leader Channel under Electrical Breakdown

Kononov A.V., **Poritsky P.V.**, Starchyk P.D., and Voitenko L.M.
Scientific Centre "Institute for Nuclear Research", 252022 Kyiv, Ukraine

Electrical breakdown of gases, liquids and insulators frequently occurs by means of the narrow plasma streamer channel that inhibits a strong tendency to branching into complicated stochastic pattern [1,2]. In order to describe these structures it is usefull to take into consideration the fractal formalism. In that way a number of interesting results have been obtained with the using of computational simulation on the basis of the equation of potential [3,4]. However, an analytical approach allows us to obtain more detailed information about the space properties of branching structures and a physical processes under their forming.

A characteristic process of development of electrical breakdown by means of the forming of the high conductive plasma streamer has some stages. This process initiates with the motion of weak-luminous pilot-streamer, which moves forward continuously from cathode to anode. The weak-ionised channel produced by pilot-streamer becomes unstable. A secondary ionisation takes place in the channel for a some time, and as a consequence of that more bright radiation and more high conduction are appeared. That process represents motion of the branching leader which spreads fast and stagly inside the channel produced by pilot-streamer. The velocity of single stage can be reached 10^9 cm/s. Motion of a leader is due to an additional ionisation which is produced by the increasing of electric intensity or by the amplification of photoinisation as a consequence of irradiation of channel plasma. The problem is to determine types of elementary processes which cause the high conduction.

Thus, a leader type of streamer is characterised by bright radiation and non-regular motion. In this paper we propose an analytical approach to the description of the branching properties of the leader type of streamer channel on base of the theory for the reaction-diffusion growth on fractal clasters [5,6]. Consider a radial discharge in continuum. In that case the spreading of a leader is described by the equation of a reaction-diffusion growth in fractal geometry where the diffusion coefficient is used in the form of the diffusion coefficient of the channel plasma and the reaction order parameter γ corresponds to the order of ionisation reaction:

$$\frac{\partial p}{\partial t} = \frac{1}{x^{D-1}} \cdot \frac{\partial}{\partial x}\left[K x^{-\sigma} x^{D-1} \frac{\partial p}{\partial x} \right] + R p^{\gamma} \qquad (1)$$

where $p = p(x, t)$ is the density of probability, which represents the belonging of the space point to the channel; x and t are radial and time dimensionless coordinates; D is fractal dimension, σ is the anomalous diffusion parameter ($\sigma = D - d_E$, d_E – is the dimension of Euclidean resting space); R is parameter which represents the part of ionisation in the process of structure growth and which has a different value for the different types of discharge; γ is parameter corresponded to the order of ionisation reaction, and is determined via spectral fractal dimension d_s: $\gamma = 1 + d_s/2$, where $d_s = 2D/(\sigma + 2)$.

It is considered the two ionisation processes: both the ionisation by means of electron strike and photoionisation. Spectral fractal dimension corresponds to an effective number of degrees of freedom in physical system. It should be have in mind that for the case of electron strike ionisation it is essential the influence of external electric field because of that the derived direction is appeared . According to that an effective spectral dimension is introduced in the following form $d_{sf} = d_s - 1$, where (-1) points the derived direction. Thus, for the case of prevail ionisation by electron strike we have $\gamma_e = 1 + (d_s - 1)/2$, and for the photoinisation $\gamma_f = 1 + d_s/2$.

The eq. (1) has the solution at the form $p(x, t) \propto t^{\alpha} x^{\beta}$, where α, β are parameters depended on D, d_E, γ. It should be pointed that the evolution of channel have a dynamical character due to the density of probability depends obvious on time. For the fractal cluster should be valid the dependence $p(x, t) \propto x^{D-d_E}$ (according to such rule the density of particles numbers on fractal is distributed in a space [4]), wherefrom we obtain that the fractal dimension D is the certain function of γ , d_E. The value of D may be obtained from algebraic equation:

$$\frac{2D^2 - 3D(d_E - 1) - 1 + d_E(d_E - 2)}{2(D - d_E + 2)} + \frac{1}{\gamma - 1} = 0, \qquad (2)$$

Substituting into eq. (2) the values of γ for different cases of ionisation, it may be obtained the corresponding values of D. In that way, in three-dimensional space for the case of prevail ionisation by electron strike we obtain $D = D_e = 2.15$, and for the case of prevail photoinisation $D = D_f = 2.25$. It should be pointed that the global space properties of fractal structure are characterised by the fractal dimension D. The sense of this result in that the process of electrical breakdown is more intensive in a

case of photoinisation mechanism. Also, it is shown that the growth of a leader channel should be non-regular and the velocity of its spreading is variable in time.

Thus, the character of evolution and the parameters of the fractal structure of leader channel are determined by the prevail type of ionisation. The parameters of fractal structure (fractal dimension and spectral fractal dimension) have the different values in dependence on the mechanisms of channel growth by means of the ionisation by electron strike or photoinisation. The process of electrical breakdown is more intensive under the prevail photoionitation growth and channel have a more strong tendency to branching by comparison with the case of ionisation by electron strike. Also, it is shown that the growth of a leader channel should be non-regular and the velocity of its spreading is variable in time.

It should be pointed that the considered theoretical model of electrical breakdown in continuum may be modified and improved with the involving of the others elementary processes: ion diffusion, recombination processes, secondary order ionisation *etc.* Also, the considered theory may be applied to describe an initial stage of arc ignition in the controlled fusion reactors.

References

[1] Meek J.M., Craggs J.D. *Electrical Breakdown of Gases* (Wiley,New York,1978).

[2] Feder J. *Fractals* (Plenum,New York,1992).

[3] Niemeyer L. , Pietronero L., Wiesmann H.J. *Phys.Rev. Lett.* (1984) -82.-p.1033.

[4] Kuperštokh A.L. *Pisma v Zhurn. Tekhn. Fiz.* (1992) -18.-p.91.

[5] Clement E., Sander L.M., Kopelman R. *Phys.Rev.* (1984) -A39.-p.2305.

[6] Milovanov A.V., Zelenyi L.M. *Phys.Fluids* (1993) -B5.-p.2609.

Frequency-Resonant Behaviours of Plasma Density in the Helicon RF Plasma

J. G. Kwak[1,2], J. G. Bak[1,2], Y. S. Yoo[3], C. W. Park[3],
S. W. Cho[4], S. K. Kim[2], H. D. Choi[1], H. I. Bak[1]

[1]*Department of Nuclear Engineering, Seoul National University, Seoul, Korea*
[2]*Nuclear Fusion Lab., Korea Atomic Energy Research Institute, Taejon, Korea*
[3]*Quantum metrology division, Korea Research Institute of Standard and Sciences*
[4]*Department of Physics, Kyonggi University, Suwon, Korea*

1. Introduction

Plasmas generated by helicon waves have drawn considerable interest because of its properties to produce high density plasmas with a modest rf input power compared to other rf discharges. Chen *et. al.* suggested that the dense plasma production is related to the efficient Landau damping of helicon waves by electrons[1].

Several authors reported that they verified Chen's hypothesis through measurements of the damping rate of helicon waves[2] and of the non-thermal electron tails in the electron energy distribution[3]. Recent measurement results by Blackwell and Chen using rf compensated Langmuir probes, however, could not secure any evidence of high energy electrons[4]. Therefore, it is not conclusive yet that Landau damping is the most dominant damping mechanism in the helicon plasma source. Subsequently, Shamrai and Taranov[5] explained high plasma density in helicon plasmas in terms of collisional damping of electron with electron/neutral particles and verified their resonance discharge concept by the experimental result that the plasma density followed calculated stable discharge line which is proportional to magnetic field as the dispersion relation of helicon waves. However, the linear dependence of the plasma density on the magnetic field can result from the confinement effect, even if the helicon wave does not play an important role in plasma productions via Landau or collisional damping. Hence, it is necessary to confirm the dispersion relation by varying other parameters such as the antenna length, the tube size, and the rf frequency. While it is difficult or impossible to vary the antenna length and the tube size in a continuous manner, it is simple for the frequency of the rf input source. This led us to the investigation of the frequency dependence of the plasma density in helicon plasmas.

In this work, frequency dependences of helicon plasmas on the plasma density are investigated by varying the argon gas pressure, the input rf power and the magnetic field. The resultant variations of the plasma density with the wave frequency are discussed in terms of antenna coupling and the dispersion relation.

2. Experimental apparatus and diagnostics

The experimental setup is shown schematically in Fig. 1. The source chamber is a 15 cm diameter Pyrex tube with a length of 65 cm. The reaction chamber is made of stainless steel, with the diameter and length of 35 cm and 45 cm, respectively. The vacuum chamber is evacuated with a turbomolecular pump and the base pressure is 2×10^{-7} Torr. The argon gas pressure is monitored by a

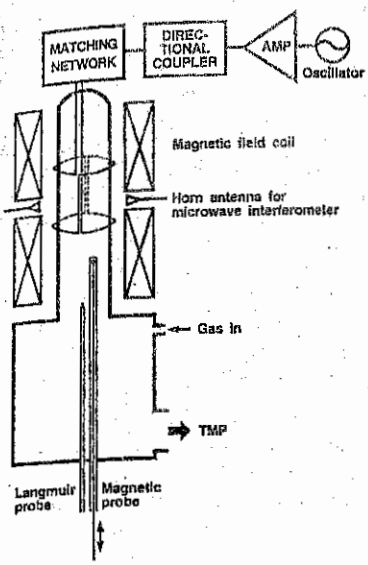


Fig. 1. Schematic diagram of the helicon plasma apparatus.

capacitance manometer. A magnetic field B_o is applied with two solenoid magnets, up to 1300 G maximum at the center of antenna. The antenna is configured as the Nagoya type III, i.e. a half wavelength, m = 1 antenna, 18 cm in length.

The rf signal is generated with a synthesizer and the frequency is increased in steps of 25 kHz through the preset frequency range selected by a personal computer. The rf signal is fed into an amplifier which has a flat bandwidth of 10 kHz to 220 MHz. The rf power is monitored with a directional coupler. The impedances of the amplifier output and the antenna are matched with two vacuum variable capacitors. The amplifier is run in the pulse mode with a pulse width of 25 msec and the duty cycle of 10 %. The line-averaged electron density at the center of antenna is measured with a 70 GHz heterodyne interferometer. The wavelength of the local rf magnetic field is measured by a probe interferometry technique.

3. Results and discussion

The frequency dependence of $<n_e>$ measured at the center of the antenna is shown in Fig. 2 for various gas pressures. As the argon gas pressure is increased, the electron density increases. In addition, the frequency of step-like density increase shifts to lower region. Note the abrupt density increases at 7, 9, 10 MHz with P_{Ar} = 4, 3, 2 mTorr, respectively. At lower frequency than the transition, the discharges are unstable and density oscillations are observed in the frequency range of 5 kHz ~ 20 kHz. Relative amplitude of the density oscillations, $\delta n/n$ is about 6 %. Stable and calm discharges are obtained after the density jump. The transition and density oscillations are also observed in the downstream region as well as the antenna region. The dashed line in Fig. 2 are calculated line-averaged electron densities from the well-known dispersion relation of helicon waves

$$\frac{n}{B_o} = \frac{\sqrt{k_{\parallel}^2 + k_{\perp}^2}}{e\mu_o}\left(\frac{k_{\parallel}}{\omega}\right) \qquad (1)$$

of free space, ω is the wave frequency, $k_{\parallel}$ is the component of the total wave number parallel to the B_0 and $k_{\perp}$ is given by the boundary condition. The density transitions and their behaviors shown in this work are explained in terms of the coupling resonance of the rf power to plasmas[6]. When the frequency and axial wavelength of antenna are made to coincide with those of a natural plasma mode,

there will take place a resonant buildup of the amplitude of oscillations in the plasma. This leads to the increase in the plasma density. The resonance frequency and wavelength in helicon plasmas are determined from the dispersion relation, eq. (1) for the given plasma density and magnetic field. So, the resonance frequency is proportional to B_0 and inversely proportional to the plasma density. $<n_e>$ is measured as a function of rf frequency with input rf power increasing from 1000 W to 1500 W. The argon gas pressure is 3 mTorr, and the magnetic field is 800 G at the center of the antenna. The results are shown in Fig. 3. As rf power is increased, $<n_e>$ increases and the transition point shifts to lower frequency as expected. At lower frequency than the jump, large density oscillations are also occurred. $<n_e>$ is measured as a function of rf frequency for B_0 = 725 G, 800 G, 982 G, 1086 G. The result is shown in Fig. 4. The input rf power is 1500 W, and argon gas pressure is 3 mTorr. Density jumps are occurred around 5.8, 7.5, 9, 11.2 MHz for B_0 = 725 G, 800 G, 982 G, 1086 G respectively. Jump frequency is proportional to the B_0 as expected from the dispersion relation of helicon waves. To confirm the fact that jump point is the resonance frequency which satisfies the dispersion relation, the axial wavelength is measured for 725 G and 982 G, and the result is shown in Fig. 5. The wavelength has the minimum value around the frequency where the plasma density increases abruptly, and becomes longer as the frequency is far away from the resonance point.

4. Conclusions

The variations of $<n_e>$ at the center of antenna are investigated for various argon gas pressure and rf power in the frequency range of 5 MHz ~ 14 MHz. The abrupt change in the plasma density is found. The transition frequency shifts to lower one, as P_{Ar} or P_{RF} is increased. The transition frequency shifts to higher one as the magnetic field is increased. The wavelength measurements show that wavelength is changed passing the transition point and has the minimum value around the transition point. The observed transition in the plasma density is explained qualitatively in terms of dispersion relation of helicon waves.

References

[1] F. F. Chen, Plasma Phys. Controlled Fusion **33**, 339 (1991).
[2] A. Komori, T. Shoji, K. Miyamoto, J. Kawai and Y. Kawai, Phys. Fluid. B3 893 (1991).
[3] P. K. Loewenhardt, B. D. Blackwell and S. M. Hamberger, Phys. Plasmas 1(4). 875 (1994).
[4] D. D. Blackwell and F. F. Chen, Bull. Am. Phys. Soc. **39**, 1727 (1994).
[5] K. P. Shamrai and V. B. Taranov, Plasma Phys. Control. Fusion **36**, 1719 (1994).
[6] M. A. Lieberman and A. J. Lichtenberg, *Principles of plasma discharges and material processing*, John Wiley & Sons, New York, 1994.

Acknowledgement

One of authors(J.G.K.) is grateful to Dr. T. Shoji at Nagoya University for his kindly comments on the helicon device and interpretation of experimental results and this research is supported by the Ministry of Science and Technology(MOST).

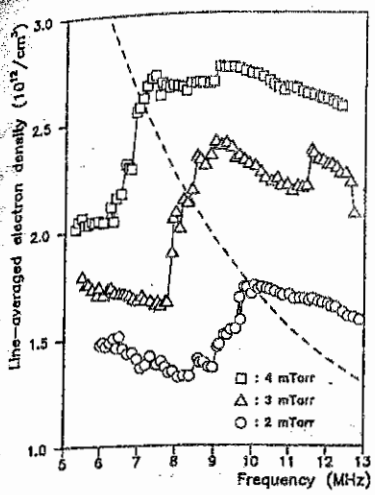


Fig. 2. Line-averaged electron density vs. frequency for various gas pressures with P_{RF} = 1200 W, and B_o = 800 G.

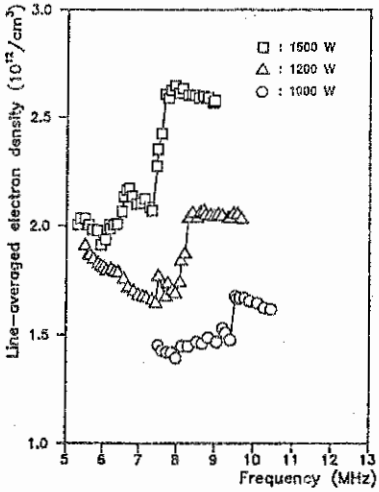


Fig. 3. Line-averaged electron density vs. frequency for various rf powers with P_{Ar} = 3 mTorr, and B_o = 800 G.

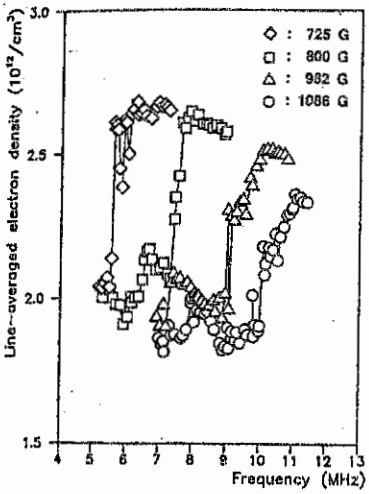


Fig. 4. Line-averaged electron density vs. frequency for various magnetic field with P_{Ar} = 3 mTorr, and P_{RF} = 1500 W.

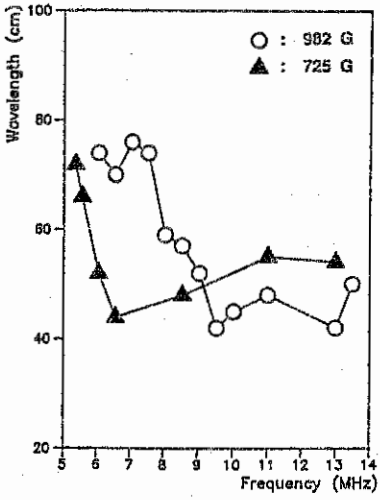


Fig. 5. Measured wavelengths of $\tilde{b}_z$ vs. frequency for B_o = 725 G and 982 G with P_{Ar} = 3 mTorr, and P_{RF} = 1500 W.

ANALYTICAL MODEL OF ELECTRIC FIELD PATTERN IN A COLLISIONAL LOW PRESSURE RF DISCHARGE

Lisovskiy V.A., Yegorenkov V.D.

Kharkov University, Department of Physics and Technology,

31 Kurchatov street, Kharkov, 310108, Ukraine

Radio frequency (RF) low pressure discharge is widely applied in various technological processes: etching semiconductor materials, depositing dielectric (oxide, diamond-like) thin films etc. To optimise plasma technologies one should study physical processes taking place in the interelectrode gap and supporting the discharge burning. One can clarify the mechanisms of many phenomena occurring in an RF discharge if one knows the electric field patterns in electrode sheaths E_{sh} and in the quasineutral plasma E_{pl}. This report presents an analytical model permitting to calculate these quantities E_{pl} and E_{sh} in a low pressure RF discharge. We also give the results of measuring E_{pl} and other plasma parameters (plasma density n_i, electron temperature T_e and electrode sheath thickness d) in the RF discharge in argon.

The measurements have been performed at the frequency $f = 13.56$ MHz of the RF field within the RF voltage range $V \leq 10^3$ V, the spacing between plane parallel stainless steel electrodes of 100 mm in diameter has been kept within the limits $L = 6 - 54$ mm. The pressure range under study was $p = 10^{-2} - 2$ Torr. The quantities E_{pl}, n_i and T_e have been measured with single and double probes.

Consider the collisional RF discharge ($\omega \ll \nu$, $\omega = 2\pi f$, ν is the electron-atom collision frequency) burning between infinite electrodes spaced L apart. The uniform plasma layer $L - S$ thick is located symmetrically between the electrodes. The RF voltage $V_\sim = V \exp(-i\omega t)$ with the constant voltage amplitude is applied across the interelectrode gap. For the normal projection of the electric induction to be continuous $\vec{D}$ at the boundary the following relation

should hold

$$\varepsilon_0 E_{sh} = \varepsilon_0 \varepsilon E_{pl}, \quad \varepsilon = 1 - \frac{\omega_p^2}{\omega(\omega + i\nu)} \approx 1 - \frac{\omega_p^2}{\nu^2} + i\frac{\omega_p^2}{\omega\nu}, \qquad (1)$$

where ε_0 is the vacuum dielectric permeability, ε is the plasma dielectric permeability, ω_p is the electron plasma frequency. In the quasistatic approximation $V = \int \vec{E} d\vec{r}$ therefore $V = SE_{sh} + (L - S)E_{pl}$. Then we find

$$E_{pl} = \frac{V}{L}\left(1 - \frac{\omega_p^2}{\nu^2}\frac{S}{L} + i\frac{S}{L}\frac{\omega_p^2}{\omega\nu}\right)^{-1}, \qquad (2)$$

$$E_{sh} = \frac{V}{L}\left(1 - \frac{\omega_p^2}{\nu^2} + i\frac{\omega_p^2}{\omega\nu}\right)\left(1 - \frac{\omega_p^2}{\nu^2}\frac{S}{L} + i\frac{S}{L}\frac{\omega_p^2}{\omega\nu}\right)^{-1}. \qquad (3)$$

For a collisionless RF discharge such a problem has been solved (G. Bekefi *Radiation processes in plasmas*, 1966, Wiley). From equations (2,3) one can obtain not only the amplitude values of the fields in plasma $|E_{pl}|$ and in sheaths $|E_{sh}|$. Expressions (2,3) contain the real and imaginary parts and therefore one can conclude on the phase shift between the RF voltage and the fields in plasma and sheaths. Figs. 1 and 2 show $|E_{pl}|$ and $|E_{sh}|$ calculated with the application of plasma density n_i, electron temperature T_e at the plasma centre and the sheath thickness d measured by us. One sees that $|E_{pl}|$ at low pressures drops uniformly with RF voltage increasing. With pressure growing a maximum appears at low V (near the discharge extinguishing potential) in the dependence of $|E_{pl}|$ on RF voltage. Probably, it is due to the increase of the plasma layer resistance occurring with pressure increasing. At low RF voltages the plasma density is small ($n_i \sim 10^7 - 10^8\ cm^{-3}$) and the noticeable part of the RF voltage drop occurs in the quasineutral plasma. Therefore at sufficiently large pressures and low RF voltages with V increasing $|E_{pl}|$ approaches a maximum and then it diminishes quickly due to the increase of the plasma density. The second maximum in the $|E_{pl}|$ pattern is observed under $\alpha - \gamma$ transition of the RF discharge. At this sufficiently large pressure ($p \sim 1$ Torr) with RF voltage increasing the plasma density at the central part of the discharge behaves nonmonotonously (it decreases, passes through a minimum and then grows) (Lisovskiy V.A. et al

- Pis'ma v Zhurn.Tekhn.Fiz., 1993,V.19,N.21,p.90). Therefore the quasineutral plasma layer cannot be regarded as uniform during $\alpha - \gamma$ transition and in the γ - regime of burning and here our model is already inapplicable. Figs.3 and 4 show phase shift angles between the RF voltage and fields in plasma and sheaths, respectively. At low pressures the field in the sheath actually coincides in phase with the RF voltage and the field in plasma lags behind the RF voltage in phase somewhat more than by $3\pi/4$. At higher pressures the phase shift associated with the field in the sheath increases and at low V the field in the sheath can lead the RF voltage by $\pi/6$; however with V increasing the phase shift decreases quickly to a very small value. On increasing the pressure the phase shift between the RF voltage and the field in plasma decreases and at low V and $p = 1.5$ Torr the field in plasma may lag behind the RF voltage only by $\pi/8$. With RF voltage growing this phase shift increases. If the condition $(\omega_p^2/\nu^2)(S/L) = 1$ holds the field in plasma lags behind V by $\pi/2$ and with RF voltage growing further the phase shift also increases a little (Fig.3). We have also calculated the field in plasma according to formulas from (Popov O.A., Godyak V.A. - J.Appl.Phys., 1986,V.59,p.1759)

$$|E_{pl}| = \frac{m}{e} v_0 \mu, \quad v_0 = \sqrt{2} I_a / (e\pi R^2 K_r\, n_e(0)) \tag{4}$$

where I_a is the amplitude of the active RF current in plasma, e and m are the electron charge and mass, respectively, R is the chamber radius, $n_e(0)$ is the plasma density at the discharge centre, K_r is the form-factor. In these calculations we have used for the quantities I_a, n_i and K_r, the values we have measured ($K_r \approx 0.9$ under our conditions). The values calculated in this way agree satisfactorily with $|E_{pl}|$, calculated from (2) and with we have measured by the double-probe technique. The results we have obtained also agree with the results of numerical simulation by other authors (Makabe T., Nakano N., Yamaguchi Y. - Phys.Rev.A, 1992,V.45,p.2520). Thus this report presents the analytical model describing the electric field patterns in the quasineutral plasma and in the electrode sheaths of a collisional RF low pressure discharge.

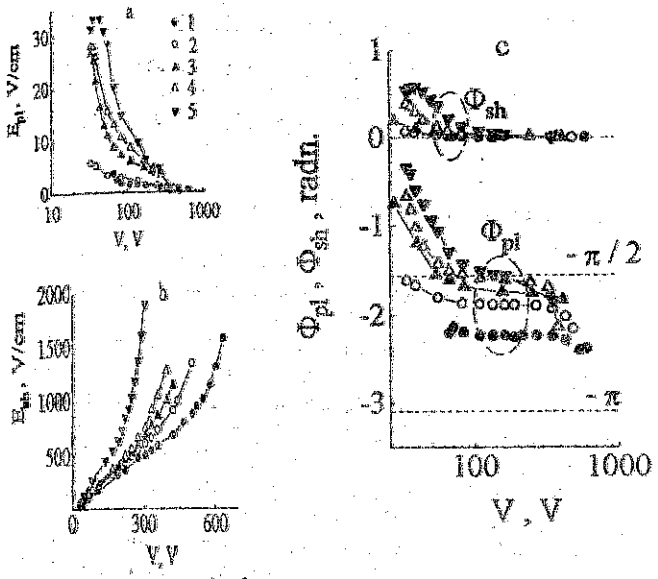


Fig. 1. Field in plasma $|E_{pl}|$
(a), field in the sheath $|E_{sh}|$ (b) and phase shifts between RF voltage and field in plasma Φ_{pl} and field in the sheath Φ_{sh} (c) against RF voltage. Argon pressure: 1 - p=0.1 Torr, 2 - 0.35, 3 - 0.5, 4 - 1, 5 - 1.5 Torr. L=10 mm.

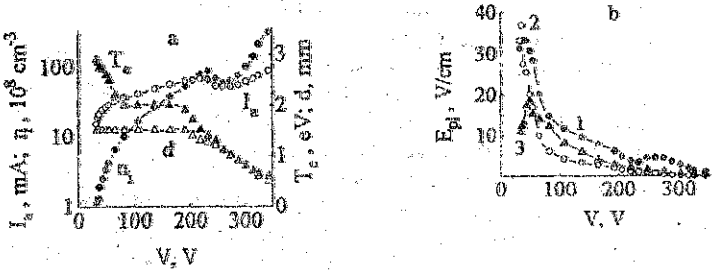


Fig. 2.(a) Conductance current I_a, plasma density n_i, electron temperature at the discharge centre T_e and electrode sheath thicknesses d against RF voltage.
(b) Field in plasma $|E_{pl}|$ against RF voltage: 1 - calculations according to formula (2), 2 - calculations according to formula (4), 3 - double probe measurements. L=10 mm. p=1.5 Torr.

DETERMINATION OF ELECTRON TRANSPORT COEFFICIENTS FROM BREAKDOWN CURVES OF RF AND COMBINED DISCHARGES

Lisovskiy V.A., Yegorenkov V.D.
Kharkov University, Department of Physics and Technology
31 Kurchatov street, Kharkov, 310108, Ukraine

The electron drift velocity V_d and the ratio of the electron diffusion coefficient to the electron mobility D_e/μ_e are two of the fundamental quantities describing the electron motion in a gas under the influence of the electric field. The drift velocity V_d characterizes the electroconductance of a weakly ionized gas whereas the measured values of the ratio D_e/μ_e are directly related to the average energy of the chaotic motion of electrons in a steady regime determined by the ratio of the electric field strength to the gas pressure E/p .

Up to date a number of techniques has been developed to measure these parameters (the time-of-flight method, the method recording the photon pulses etc.). The detailed description of these techniques together with the results obtained may be found elsewhere [1,2]. These techniques permit to determine the values of V_d and D_e/μ_e in the range $E/p \leq 200 - 300$ V/(cm Torr). At higher values E/p an electric discharge breaks down between the electrodes of a device and in a number of cases the measurements are impeded.

This report applies the breakdown curve data of a purely RF and combined (RF + DC electric field) low pressure discharges to determine the electron drift velocity values V_d in the range $E/p \approx 50 - 2000$ V/(cmTorr) and the ratio of the longitudinal diffusion coefficient to the electron mobility D_L/μ_e in the range $E/p \approx 1 - 500$ V/(cmTorr). Whereas for the above mentioned techniques the discharge breakdown is undesirable, the method for the determination of electron transport coefficients suggested in this report is based on studying the electric breakdown of gases.

The necessary data on breakdown of the RF and longitudinal combined discharges have been measured in this report in argon in the pressure range $p = 10^{-3} - 20$ Torr with the RF field frequency $f = 13.56$ MHz, RF voltage $U_{rf} \leq 10^3$ V and DC voltage $U_{dc} \leq 600$ V (the DC and RF voltages have been applied across the same electrodes). The stainless steel electrodes of 100 mm in diameter have had a changeable spacing in the range $L = 6 - 20$ mm. The RF voltage has been fed to one electrode whereas another one has been grounded. To eliminate the DC self-bias a choke of several mH's has been switched across the electrodes. Earlier papers [3,4] have given the details of measuring the breakdown curves of RF and combined discharges.

The electron drift velocity V_d has been determined from the inflection point location of the RF discharge breakdown curve (Fig. 1a). Consider the electron motion in an uniform RF electric field. The electron drift velocity in an RF

field is equal to

$$v_{dr} = \frac{eE_{rf}}{m\nu_{en}}\cos(\omega t), \tag{1}$$

where e and m are the electron charge and mass, E_{rf} is the RF field amplitude, ν_{en} is the electron-atom collision frequency, $\omega = 2\pi f$. The drift velocity amplitude value $V_{dr} = eE_{rf}/(m\nu_{en})$ is the maximum instantaneous electron velocity related to the maximum value (amplitude) of the RF field. The electron displacement amplitude in the RF field is equal to $A = eE_{rf}/(m\nu_{en}\omega) = V_{dr}/\omega$. On decreasing the pressure the electron displacement amplitude increases and, as has been shown in [3], at the turning point $A = L/2$. Thus we have for the electron drift velocity $V_{dr} = L\pi f$; for fixed RF frequency f and the interelectrode spacing L at the turning point the electron drift velocity is constant and it does not depend on the nature of the gas. The coordinates of the turning point (pressure p_t and RF voltage U_t) permit to calculate the ratio E/p corresponding to the electron drift velocity value obtained. The data on the electron drift velocity determined in this way (fig. 2a) agree satisfactorily with measured [5-9] as well as calculated [7,10,11] results of other authors.

Now consider the method determining the ratio of the longitudinal diffusion coefficient to the electron mobility D_L/μ_e. Let us take the RF breakdown equation [12]

$$exp\left(\frac{B_0 p}{2E_0}\right) = A_1 pL\left(1 - \frac{E_0/B_0 p}{C_2 L/\Lambda}\right) \tag{2}$$

and the equation of the gas breakdown in RF and weak DC electric fields [4]

$$exp\left(\frac{B_0 p}{2E_1}\right) = A_1 pL\left(1 - \frac{E_1/B_0 p}{C_2 L/\Lambda}\right)\left\{1 + \left(\frac{E_{dc} L_{rf1}}{2\pi D_e/\mu_e}\right)^2\right\}^{-\frac{1}{2}}. \tag{3}$$

Divide (3) by (2) and obtain the expression for D_e/μ_e:

$$\frac{D_e}{\mu_e} = \frac{E_{dc} L_{rf1}}{2\pi}\left\{\left(\frac{L_{rf1}}{L_{rf0}}\right)^2 exp\left(B_0 p\frac{E_1 - E_0}{E_0 E_1}\right) - 1\right\}^{-\frac{1}{2}}, \tag{4}$$

where

$$L_{rf0,1} = L\left\{1 - \frac{E_{0,1}/B_0 p}{C_2 L/\Lambda}\right\}, \tag{5}$$

E_0 and E_1 are the effective breakdown fields without and in the presence of the external DC electric field E_{dc}, A_1, B_0 and C_2 are the molecular constants [4], Λ is the vacuum wavelength of the RF field. To derive (2) and (3), the discharge has been assumed to occur between infinitely large plane electrodes and the radial electron diffusion can be neglected, the electrons diffusing only to the electrodes (along the electric field direction). Therefore we actually get from (4) D_L/μ_e and not D_e/μ_e where D_L is the longitudinal diffusion coefficient. As is known [6], the electron diffusion coefficients along and across the electric field

are not the same. Therefore to calculate D_L/μ_e we have applied the breakdow curves of the combined discharge with $L \leq 23$ mm, i.e. with the interelectro spacing being considerably less than the electrode diameter. Besides, equatio (3) has been derived for a weak DC electric field not contributing to the g ionisation. That is why we have treated only the rising section of the dependen $U_{rf1} = \psi(U_{dc})$. Fig. 2b shows the values of D_L/μ_e obtained according to o method to agree satisfactorily with the results of other authors [6,7,9,10].

Thus we suggest in this report a method of determining the electron dri velocity V_d, and the ratio of the longitudinal diffusion coefficient D_L/μ_e to th electron mobility from the measured breakdown curves of RF and longitudin combined low pressure discharges. The data we have obtained according to th method suggested agree satisfactorily with measured and calculated results o other authors.

References

[1] Huxley L.G.H., Crompton R.W. *The diffusion and drift of electrons i gases*, 1974, Wiley, New York.

[2] Raether H. *Electron avalanches and breakdown in gases*, 1964, Butter worths, London.

[3] Levitskii S.M. - Zhurn. Tekhn. Fiz., 1957, V.27, p.970.

[4] Lisovsky V.A., Yegorenkov V.D. - J.Phys. D: Appl. Phys., 1994, V.27 p.2340.

[5] Jager G., Otto W. - Z. Phys., 1962, V.169, p.517.

[6] Wagner E.B., Davis F.J., Hurst G.S. - J. Chem. Phys., 1967, V.47, p.313

[7] Kucukarpaci H.N., Lucas J. - J. Phys. D: Appl. Phys., 1981, V.14, p.200

[8] Al-Amin S.A.J., Lucas J. - J. Phys. D: Appl. Phys., 1987, V.20, p.1590.

[9] Nakamura Y., Kurachi M. - J. Phys. D: Appl. Phys., 1988, V.21, p.718.

[10] Sakai Y., Tagashira H., Sakamoto S. - J. Phys. D: Appl. Phy 1977,V.10,p.1035.

[11] Tagashira H. - Proc. XV Int. Conf. on Phenomena in Ionized Gases, Invit Papers, 1981, Minsk, p.377.

[12] Kihara T. - Rev. Modern Phys., 1952, V.24, p.45.

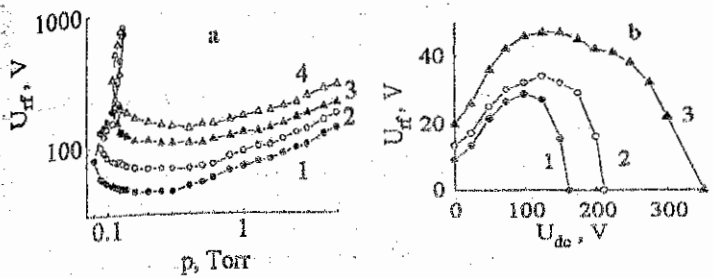


Fig.1. (a)- Breakdown curves of RF and combined discharge in argon: 1 - U_{DC}=0, 2 - 25 V, 3 - 50 V, 4 - 100 V.
(b)- RF breakdown voltage U_{RF} against the constant voltage applied U_{DC} under argon pressures: 1 - p=0.2 Torr, 2 - 1 Torr, 3 - 3 Torr. L=23 mm.

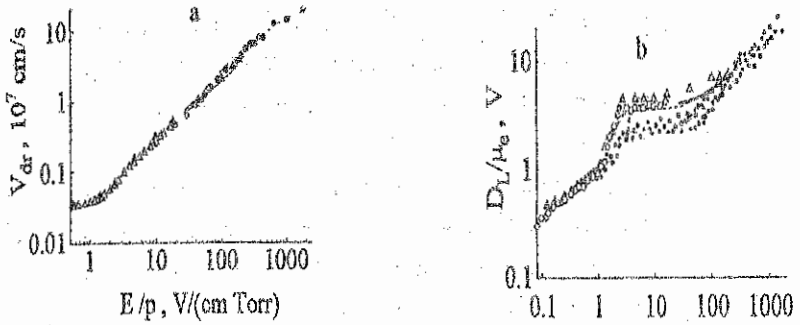


Fig.2. (a) Drift velocity V_{dr} dependence against E/p: * - our results, ° - measured data [5], solid triangles - measured data [7], blank triangles - measured data [9], solid line - calculations [10], dash line - calculations [11], broken line - calculations [7].
(b) Ratio D_L/μ_e against E/p: * - our results, ° - measured data [9], solid triangles - measured data [6], blank triangles - measured data [7], solid line - calculations [11], dashed line - calculations [7].

THE EFFECT OF SLIGHTLY EXCITED ELECTRON PLASMAS ON PHASE TRANSITIONS IN SOLIDS

G.E.Chaika*, V.G.Levandovskii*, V.P.Siomyk**

*Ukrainian State Academy of Communications, Solomenskaya str. 7, 252022, Kiev,Ukraine

**Bogolubov Institute for Theoretical Physics, 252130, Kiev,Ukraine

An investigation of an external action influence on segnetoelectric electron subsystem (light radiation primarily) caused the discovery of the anomalous photogalvanic phenomenon [1-2]. It was noted that radiation processing of segnetoelectric in polar phase leads to initiation of the uniform stationary current that is proportional to absorbtion coefficient and field intensity, and the current direction is defined by spontaneous polarization. Such anomalous photocurrent been associated in [3-4] with specific asymmetry of interband nondiagonal elements of the matrix density as a result of phase transition and the electron density reconstruction.

The purpose of our report is to demonstrate that the electron subsystem excitation may result not only to the anomalous effects in the electron subsystem of segnetoelectric-semiconductors (SGSC), but initiates the crystal structure reconstruction under definite conditions.

By now the role of electron excitations in formation of crystal lattices is far from being clarified. According to traditional concepts of solid structure, free charge carriers (electrons and holes) and electrically active defects (impurity atoms and crystal imperfections) are independent of one another. Thus electron (hole) statistics is reduced to redistribution of charge carriers over specified energy levels of crystal defects at a given temperature. Some doubt has been cast on such an approach in [5], where it was shown that the electron subsystem in turn affects the generation of

defects. The process is essentially nonlinear because it is accompanied by self-consistent electron (or hole) capture at local energy level of created electrically active defect. For an electron in the conduction band there exist some probability of giving rise to a defect generation associated with electron transition from conduction band to a lower energy level of that defect, so that free energy of the system "crystal having a defect plus an electron" would reach its minimum value. More recently the above conclusion was derived by quantum mechanical calculations [6-9].

Such situation may be realized in SGSC with orientational polarization when a crystal lattice ion may occupy one of two sites with potential wells A or B so that segnetoelectric phase corresponds to A-state and paraelectric - to B.

In present report we consider SMSC n-type (p-type may be considered identically) with N_d impurity atoms per unit volume having local donor-type energy level ε_d . Let ions or atoms been involved in phase transition may be either in the state A with activation energy W_A and local acceptor-type level ε_A (paraelectric phase) or in the state B with corresponding energies W_B and ε_B. We can use the Gibbs distribution for such system and obtain the following relation for the probability of the state

$$P = \frac{Q_n^n}{n!}\cdot\frac{Q_p^p}{p!}\cdot\frac{N!}{(N-N_A)!N_A!}\cdot\frac{N!}{(N-N_B)!N_B!}\cdot\frac{N_A!}{(N_A-n_A)!n_A!}\cdot \frac{N_B!}{(N_B-n_B)!n_B!}\cdot\frac{N_d!}{(N_d-n_d)!n_d!}\exp\left(-\frac{\Delta\varepsilon}{\theta}\right), \qquad (1)$$

Here N, N_A, N_B are concentrations of states and $N=N_A+N_B$ so as the atom may be only either in the state A or in B; Q_n (Q_p) is the state density and n (p) is an electron (hole) concentration in the conduction (valency) band; θ is the temperature in energetically units (θ=kT); $\Delta\varepsilon$ is the energy difference for two states. With the help of energy concervation law and the equation of quasineutrality

$$N_d+p=n+n_d+n_A+n_B \qquad (2)$$

one can obtain the expression for $\Delta\varepsilon$

$$\Delta\varepsilon = N_A W_A + N_B W_B - n_d\varepsilon_d - n_A\varepsilon_A - n_B\varepsilon_B + p\varepsilon_g - \varepsilon_i, \qquad (3)$$

where ε_i is the energy of ion interaction with self-consistent field of other ions; ε_g is a width of forbidden band and energies of local levels ε_d, ε_A, ε_B are counted from the bottom of the conduction band. In Eq.(3) we take into account the effect of electron capturing from conduction band at local acceptor level selfconsisted with defect creation.

After minimization of probability P upon N_A, N_B, n_A, n_B, n, p with the help of the well known relation $d(\ln x!)/dx \approx \ln x \quad (x >> 1)$ one can obtain the following system of equations (including Eq.(2)) for stationary concentrations:

$$p \cdot n = Q_g^2; \tag{4}$$

$$N_A = \Im_A \sqrt{1 + n/Q_A}; \tag{5}$$

$$N_B = N - N_A; \tag{6}$$

$$n\left(n + Q_p\right)\left(\Im_A + \sqrt{1 + n/Q_A}\right) = Q_A\left(Q_g^2/n + N_d\right)\sqrt{1 + n/Q_A}; \tag{7}$$

$$n\left(n + Q_p\right)\left(\Im_B + \sqrt{1 + n/Q_B}\right) = Q_B\left(Q_g^2/n + N_d\right)\sqrt{1 + n/Q_B}; \tag{8}$$

Here:

$$\Im_{A,B} = N \exp\left(-\frac{\left(W_{A,B} - \varepsilon_i\right)}{\theta}\right);\ Q_g^2 = Q_n Q_p \exp\left(-\frac{\varepsilon_g}{\theta}\right);\ Q_{A,B} = Q_n \exp\left(-\frac{\varepsilon_{A,B}}{\theta}\right).$$

Phase transition temperature may be obtained from the condition for equality of free energies $F = -\theta \ln P$ in two stable states. This condition leads to the system of nonlinear algebraically equations that can be solved numerically.

Thus the phase transition in SGSC are found to be in closely relations with an electron subsystem behavior. We can see from expressions (2-9) and espessialy from Eqs.(5,6) that concentrations N_A, N_B and order parameter $\eta = \left(N_A - N_B\right)/\left(N_A + N_B\right)$ are defined by not only the lattice temperature but by electron subsystem state also. If the last is excited by external actions (electrical field, irradiation and so on) the value of η depends upon the type of the action. For example in subcontact layers of SGSC where electron concentration depends on the

electric field significantly, segnetoelectric film with a width of about Debye length may be created under the definite polarity of electrical intensity. At the same time the whole crystal would be in paraelectric state. So the applied electric field may change the width of segnetoelectric film. Thus the detail investigation of the phenomenon opens some prospects for changing properties of SMSC by controlled external actions.

1. Fridkin V.M., Grekov A.A., Johov P.V., Savchenko E.A., Rodin A.I., Verhovskaya K.A. Ferroel. **8**, 433-437 (1974) (Russian)
2. Glass A.M., von der Linde, Negren T.I. Appl. Phys. Lett. **25**, 233-238 (1974)
3. Krystophel N.N., Gulbis A.V. Izvestiya AS ESSR, ser. phys.-math **28**, 268-271 (1979) (Russian)
4. Bursian E.V., Girshberg Ya.G.,Truna N.N. J. Phys. Soc. Jap. **49**, 1073-1079 (1980)
5. Vinetskii V.L. Fizika Tverdogo Tela **10**, 867-875 (1968) (Russian)
6. Chaika G.E., Vinetskii V.L. Phys.St.Sol.(b). **98**, 727-734 (1980)
7. Chaika G.E., Grechko L.G., Levandovskii V.G. Proceedings of the IV Intern. Workshop on Nonlinear and Turbulent Process in Physics, Kiev, **1**, 66-69 (1989)
8. Chaika G.E., Levandovskii V.G. Ukr. Fiz. Journ. **37**, 904-908 (1992) (Ukrainian)
9. Chaika G.E., Grechko L.G., Levandovskii V.G. Functional Materials **2**, 169-172 (1995).

EVOLUTION OF THE SPACE CHARGE WAVES OF THE ELECTRON BEAM IN THE OVERCRITICAL PLASMA BARRIER

I.O.Anisimov*, *S.V.Dovbakh**, *I.Yu.Kotlyarov**, *S.M.Levitsky**, *G.V.Lizunov**, *O.V.Opanasenko***, *D.B.Palets***, *L.I.Romanyuk*****

**Taras Shevchenko University, Radiophysics Dpt., 64 Volodimirska St., 252017, Kyiv, Ukraine*

***Scientific Centre "Institute for Nuclear Researches of the National Academy of Sciences", 47 Nauki Ave., 252650, Kyiv, Ukraine*

The mechanism of electromagnetic waves transport through the barriers of overcritical plasmas by means of electron beams was proposed in [1]. The incident wave being reflected from the barrier border modulates the electron beam that is moving into the barrier and excites fast and slow space charge waves (SCW) in it. In the overcritical plasma the slow SCW is amplified due to the polarisation instability. When leaving the barrier, slow SCW is transformed (due to the transitional radiation) into the electromagnetic wave with the same frequency and polarisation as the incident wave. The experimental observation of this effect is described in [2].

The significant element of this mechanism is the amplification of the slow space charge wave (SCW) of the electron beam inside the barrier. Only the barrier with the rectangular plasma density profile was treated in [1], i.e. the plasma inside the barrier was assumed to be homogeneous. But this assumption is not true for the experimental situations [2]. This report is devoted to the theoretical and experimental study of the SCW evolution in the electron beam that moves across the overcritical plasma layer with an inhomogeneous density profile. The influence of the non-linear effects that limit the amplification of SCW in overcritical plasmas and consequently limit the width of a barriers that can be transilluminated by means of electron beams is also studied theoretically for the model of the rectangular plasma density profile.

The evolution of the longitudinal SCW in the electron stream moving along the density gradient of the planarly stratified cold isotropic plasma is treated theoretically in the linear approximation.

The slow and fast SCW are independent in the homogeneous plasma. The coupling between these waves appears due to the plasma inhomogeneity. It can cause the amplification of both SCW's in the undercritical plasmas due to the energy transfer

from the slow wave (with the negative energy) to the fast wave (with the positive energy). It can also cause the growth of the fast SCW in the overcritical plasmas, while in the overcritical homogeneous plasma this wave decreases. The most effective coupling between the beam modes is attained in the local plasma resonance regions (LPRR). Maximum of the electric strength and minimum of the electric induction are reached there. The computer simulation results for a parabolic density profile agree with the analytic calculations (see fig.1).

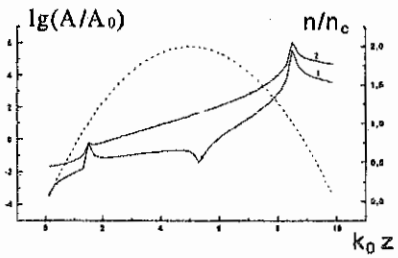


Fig.1
Spatial dependence of the fast (1) and slow (2) SCW magnitudes for the parabolic density profile (dotted line).

The estimations were done for the range of the SCW magnitudes where the linear theory is valid. For our experiments the minimal signal level is limited by the plasma noise in the region before the barrier, the maximal level is limited by the electron stream nonlinearity. The SCW magnitude in the linear regime can vary by a factor of $10^3 - 10^4$.

The experimental setup is described in details in [2] (see fig.2). The plasma barrier

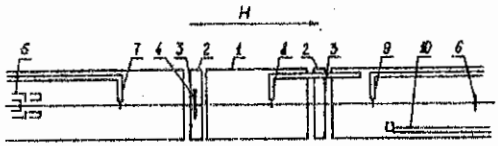


Fig. 2

Experimental setup: 1 - cylindrical anode; 2 - cathode blocks; 3 - reflectors; 4 - cathode ring; 5 - electron gun; 6 - collector; 7 - modulator; 8-10 - HF probs.

was formed by the Penning discharge with the heater cathode in argon with the pressure $(1-10)\times 10^{-4}$ mm Hg. The barrier width was about 20 sm. The axial

distribution of the plasma density in the barrier was approximately parabolic. The electron beam had an energy $0.5-2.0$ eV and a current $0-10$ mA. It could be modulated by the voltage of the frequency $2.6-3.8$ GHz. The HF probe could be moved along the discharge camera.

The typical axial distribution of the signal in the barrier is given on fig.3. The maximum is registered in the barrier origin. Its position is independent from the initial beam modulation level. When the barrier density is increased or the signal frequency is decreased, this maximum moves to the barrier boundary. Its position coincides with the position of the LPRR. Consequently it is the maximum of the SCW electric strength that is predicted by the linear theory (see fig.1).

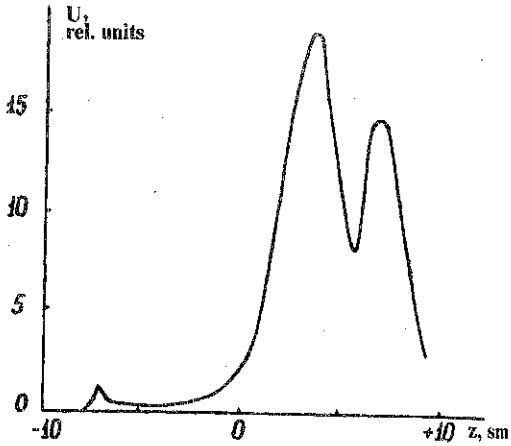


Fig.3
Spatial dependence of the HF probe signal

The dependence of the SCW amplification on the parameters of the beam-plasma system near the barrier origin qualitatively matches to the theoretical predictions. But the monotonic growth of the SCW intensity in the overcritical plasma that is predicted by the linear theory often does not take place. In this cases the additional maximum is formed between two LPRR's. Its position is independent from the initial level of the beam modulation, and its magnitude is directly proportional to this level. When the beam current is increased or its velocity is decreased, this maximum moves to the barrier origin. The plasma supercriticality decrease gives the same effect. This maximum probably appears due to the non-linear effect of the intrinsic oscillations of the beam-plasma system on the SCW.

In the second LPRR near the barrier end the third maximum of the signal is detected. It corresponds qualitatively to the linear theory (see fig.1).

The non-linear effect that limits the amplification of SCW in overcritical plasmas wave seems to be the concurrence between the slow SCW and the beam exited Langmuir wave - at least for the barriers with rectangular concentration profile and monoenergetic electron beam. The Langmuir wave is the eigenmode of a beam-plasma system. It is amplified resonantly, and its increment excesses over the increment of SCW that is amplified due to the non-resonant polarisation mechanism. So if the initial magnitude of SCW is not very large, the Langmuir wave firstly reaches the magnitude enough for the trapping of the beam particles, and it interrupts the SCW amplification. Consequently the maximum width of the overcritical plasma barriers that can be transilluminated for electromagnetic waves by means of electron beams is limited by the length of the Langmuir instability development in the beam-plasma system until the moment of the beam electrons trapping. SCW grows linearly until the beam trapping by the Langmuir wave, consequently the maximum SCW magnitude is directly proportional to its initial level.

The analytic estimates and computer simulation (using the program ES-1 [3]) confirm this ideas.

Effects of the mode concurrence in a beam-plasma systems are already described (see, for example, [4]), but attention was usually paid to the regime of the resonant instability suppression by means of the deep initial modulation of the electron beam. This work has treated the opposite situation.

The work was supported, in part, by the Ukrainian Fund for Fundamental Researches and the International Soros Science Education Program (ISSEP) through grant No APU 052007.

References

1. И.А.Анисимов, С.М.Левитский. // Журн. техн. физ., 1989, **59**, 7, 50-54.

2. И.А.Анисимов, С.М.Левитский, А.В.Опанасенко, Л.И.Романюк. // Журн. техн. физ., 1991, **61**, 3, 59-63.

3. Ch.K.Burdsall, A.B.Langdon. Plasma Physics, via Computer Simulation. McGraw-Hill Book Company, 1985.

4. А.Н.Кондратенко, В.М.Куклин. Основы плазменной электроники. М., Энергоатомиздат, 1988.

ACCELERATION OF QUASI-NEUTRAL PLASMA BUNCHES IN CROSSED EH-UNDULATED FIELDS

Victor V.Kulish, *Peter B.Kosel, Oleg B.Krutko

Sumy State University, Sumy, 244007, Ukraine

*University of Cincinnati, Cincinnati, Ohio, 45221-0030, USA

The new conception of charged particles and plasma beams acceleration was stated. It is based on the use of the crossed transversal periodic reversed vortex electric and magnetic field as an acceleration system. The general nonlinear self-consistent theory of such devices was developed. The number of new physical effects which occur in such devices were investigated.

Introduction

The aim of this paper is presentation and further development of new conception of plasma and charged particles acceleration [1]. To the authors opinion the systems that designed on the base of this conception can be very promising for such technological purposes as surface modification, doping and etching of materials and other ones. They possess number of peculiar properties which make them be unique. First of these properties is the possibility of unidirectional simultaneous acceleration of positive and negative charged particles [1]. It may take place on the way of plasma electron-ion dipole or two-stream acceleration. Second one is simplisity of design of such devices (the basic elements of them are usually electromagnets). Third peculiarity is the possibility of simultaneous acceleration, cooling and compression of plasma or charged particles beams.

1. The principle of operation

The discussed accelerator should be defined as the transversal induction EH-undulated accelerators (TIEHA). The scheme of accelerating fields that affect to the charged particles in such devices is shown on the Fig.1. This drawing illustrates the general principle of operation of presented accelerators. The key point of idea is undulated character of vortex electric (E) and magnetic (H) fields. These vectors are directed at a right angle and are displaced in undulation phase by quarter of period relative to each other. Such fields are called as EH-undulated. We can see that the trajectories of negative (electrons) and positive (ions) charged particles have the like-sin shapes [1]. Beside that the oscillation phases of particles that have different charge sign are displaced by half of period. It is obviously that the particle motion is featured by the opposite directions in the transversal plan. However the both sorts of particles

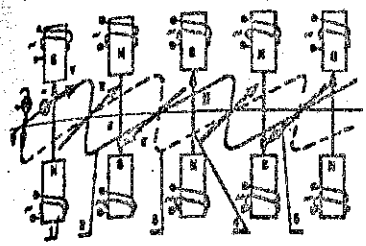


Fig.1 The scheme of fields and trajectories of negative (-e) and positive (+e) charged particles in the transverse induction EH-ubitron accelerator. Here: 1 is electromagnets, 2 is trajectories of negative particle, 3 is trajectories of positive particle, 4 is vector of magnetic induction B, 5 is vector of electric field intensity,V are vectors of particles velocities.

(electrons and ions) can be accelerated simultaneously along the same longitudinal direction of EH-ubitron system.

2. Model and setting up a problem

We consider the linear polarized EH-undulated field. Its vector-potential:

$$\vec{A} = \frac{1}{2}\vec{e}_x\left[A(z,t)\exp(ip) + A^*(z,t)\exp(-ip)\right], \qquad (1)$$

where A(z,t) is the slowly varying complex amplitude of vector-potential, $p = kz$ is phase, $k = 2\pi/\lambda$ is a wave number, z is the longitudinal coordinate, λ is a period of undulation, $\vec{e}_x$ is an unit vectors of OX axis.

The simplest transverasally-unstricted model of the quasi-neutral (in the whole) plasma bunch that drifts along positive direction of OZ axis is considered. The profile of bunch is taken in form of predetermined function $\varphi(z - v_0 t)$ (v_0 is initial velocity). Beside the field (1) we take into consideration the intrinsic electric [2] and magnetic [3]

$$\vec{E}_i = -\vec{\nabla}\varphi_i = \vec{e}_z E^{(a)}; \qquad \vec{B}_i = \frac{1}{2}\vec{e}_y\left[B^{(a)}(z,t)\exp(ip) + B^{(a)*}(z,t)\exp(-ip)\right], \qquad (2)$$

fields in the interaction volume. Here, φ_i is the scalar potential of intrinsic electric field, $B^{(a)}(z,t)$ is slowly-varying amplitude of additional generated magnetic field, $\vec{e}_y$ and $\vec{e}_z$ an unit vectors of OY and OZ axis's respectively.

We set the problem of investigation of acceleration process of plasma bunch in the external (1) and intrinsic (2) electromagnetic fields as well as investigation of influence of intrinsic electromagnetic fields (2) to the acceleration process. The self-consistent dynamic of system is described by the system of Boltzman's and Maxwell's equations. The solutions of these equations can be obtained on the way of the method of averaging kinetic equation and theory of hierarchic nonlinear oscillations [4] use.

3.Analysis and results

The "cold" plasma bunch that consists of electrons and protons are taken. The focusing longitudinal magnetic field is taken as superweak. Using the algorithm [4] we can obtain following self-consistent equation for the intensity of intrinsic electric field:

$$\frac{\partial^2 E}{\partial \xi \partial \xi} + \left(P_2 \varphi + P_3 \frac{\partial \varphi}{\partial \xi} t \right) E = P_1 \frac{\partial \varphi}{\partial \xi} |A|^2 \qquad (3)$$

where P_j are the nonlinear coefficients whose explicit forms are not written because of their complexity, $\xi = z - v_0 t$. The intrinsic magnetic field should be taken into account through the appropriate renormalizing of external magnetic field amplitude. The intrinsic electric field (2) is concerned with plasma space redistribution in the EH-undulated system which is caused by plasma acceleration process. In the general case there are two mechanisms of intrinsic electric field generation. First of them occurs when the acceleration process forces the sort α particles to be out of quasi-neutral state locally. It may be realized by acceleration not only of quasi-neutral plasma but also of plasma that charged in whole. Second one refers to polarization of plasma bunch. The cause of it is the difference between masses of electrons and ions. In this connection the electrons have more velocities than ions have. In this case we have two possible regimes of acceleration. Namely they are collective regime and two-stream regime. The collective regime will occur if plasma bunch length lesser than total EH- ubitron system length. Here, the electrons which lighter than ions leave ions behind. So the intrinsic electric field appears between noncompensated regions of electron-ion plasma bunch. Two-stream regime will take place if plasma bunch length far more than total EH-ubitron system length. Therefore the overwhelming majority of electrons places at the end of acceleration section. In this case the intrinsic longitudinal electric field appears as well.

The effect of inrinsic electric field generation can play the important role. It illustrates on the Fig. 2 and Fig. 3. The parameters of system are following. The average induction of magnetic component of EH-undulated field is 5 kGs, the average intensity of electric one is 25 Gs, the period of undulation is 2 cm. Profile of plasma bunch is taken in form of soliton $1/ch^2(\xi)$. On the Fig.2 the comparative features of acceleration of the electrons by the two-stream and collective (dipole-like) regimes of interaction electrons and ions. In first case (curve 1) the acceleration temp of electrons is rather high (~10 MeV/m). But in second case the energy of electron has the complicated

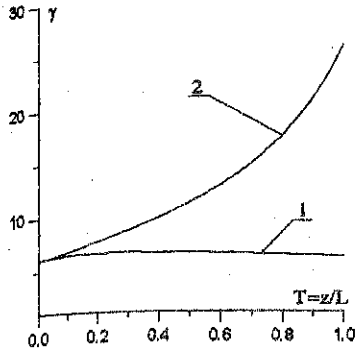


Fig.2

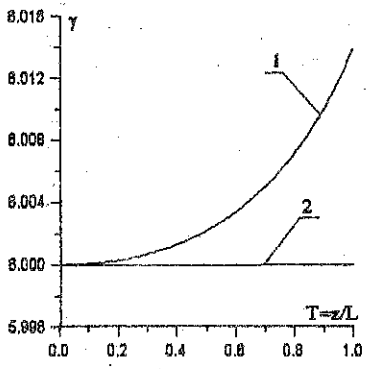


Fig. 3

Fig.2 Comparative features of electron acceleration process by the dipole-like and two-stream mechanisms regimes. Curve 1 illustrates the dependence of relativistic electron factor by dipole-like regime Curve 2 illustrates the kindred dependence by two-stream regime. Parameters are stated in the text of paper.

Fig.3 Comparative features of ion acceleration process by the dipole-like and two-stream mechanisms regimes. Curve 1 illustrates the dependence of relativistic ion factor by dipole-like regime Curve 2 illustrates the kindred dependence by two-stream regime. Parameters are stated in the text of paper.

dynamic. What is the cause of it? It is the transferring of electrons' energy into energy of ions' motion at the sacrifice of capture of electrons by electric field of ions. The thing is that the curve 2 was calculated in the case of plasma bunch length had been taken as 1m (i.e. equal to total length of EH-undulated system), but curve 1 was calculated if bunch length had been taken as 0.4 cm. So curve 2 illustrates the two-stream regime of acceleration, when both plasma component are being accelerated almost independently. Curve 2 shows the dipole-like regime, when intrinsic electric field affects to the acceleration process strong. The analogous dependences for ions' acceleration process are presented on the Fig.2. It is easy to see that the appearing on intrinsic electric fied leads to additional acceleration of ions and leveling of electrons and ions energies.

References

1. Kulish V.V., Krutko O.B. // Pisma v Journ. Techn. Fiziki, 1995, **21**, 9, 52-55. (Russ).

2. Zakharov V.P.,Kisletsov A.V.,Kulish V.V.//Fizika Plazmy, 1986, **12**, 1, 77-80. (Russ).

3. Kulish V.V., Kuleshov S.A., Lysenko A.V.//Int. J. of Infr. and Mill. W., 1993, **14**, 3.

4. Kulish V.V., Lysenko A.V. // Fizika Plazmy, 1993, **19**, N2, 216-227.(Russ).

Investigations of High-Pressure Glow Discharge with High-Speed Pumping

V.A.Antonov, A.A.Bruev, V.I.Golota, V.V.Mukhin, I.A.Pashchenko, G.V.Taran and S.N.Shilo

National Science Center "Kharkov Institute of Physics and Technology",

310108, Kharkov, Ukraine

Plasma-chemical processes in air are important in a number of problems in physics and engineering, such as: the description of processes in the top of atmosphere, ozonizers, high-voltage switches, etc. Recently the experimental and theoretical investigations of gas discharges in atmospheric air [1] are in many respects stimulated by prospects of development of plasma-chemical clearing equipment.

We investigated the DC discharge at atmospheric pressure with high velocity of gas flow. The experiment was carried out on stand consists of: a system of air preparation, plasma-chemical reactor, high-voltage supply unit, measuring devices. The gas mixture was pumped at atmospheric pressure with productivity from 0.01 m^3/hour up to 50 m^3/hour. The discharge was produced in a cylindrical system of electrodes with a gap of 5-30 mm and volume of discharge zone up to 0.025 m^3. The cathode consisted of metal cylinder and anode was an array of uniformly spaced needles. The air input and output in plasma-chemical reactor was executed tangentially that supplied the most favorable proceeding of plasma-chemical reactions.

The design peculiarities of plasma-chemical reactor and high-speed pumping of air and certain choice of electrode materials allowed to achieve steady burning of discharge. The high-voltage supply unit is intended for maintenance of a dc working voltage up to 20 kV on plasma-chemical reactor.

As a result the electrodynamical parameters of plasma-chemical reactor were determined. The discharge voltage was 8-15 kV and power was up to 3 kW. The volt-ampere characteristics (vac) of plasma-chemical reactor were received for different distances among the needles of anode and for different gaps between the electrodes. Vac were subjected to the exponential low at distances between needles more than 10 mm (fig.1, curve 1) and less than 10 mm (fig.1, curve 2) - square low. For stable stationary work of plasma-chemical reactor at small velocities of air flow it is necessary to choose distance between a needles of anode (d) so that $d \geq h$, where h- interelectrode gap. So the VAC of plasma-

chemical reactor is described by following dependence $I = AU\,(U-U_0)$, where A is the constant coefficient and U_0 - the potential of discharge beginning.

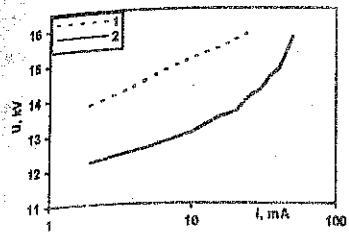


fig.1. VAC. 1 - d=5mm, 2 - d=15mm

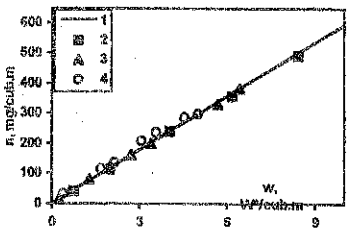


fig.2. Concentration of ozone. 1- theory, 2 - 31m^3/h (pumping), 3 - 100 m^3/h, 4 - 160 m^3/h.

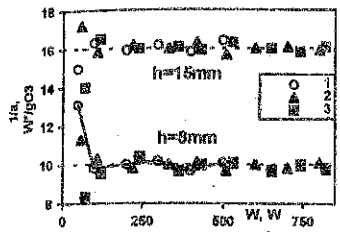


fig.3. Required power for 1g O_3 production. 1 - 31m^3/h (pumping), 2 - 100 m^3/h, 3 - 160 m^3/h.

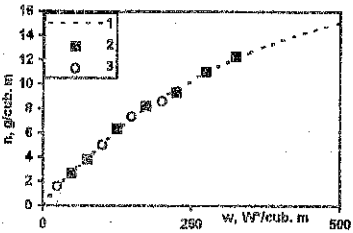


fig.4. Concentration of ozone. 1- theory, 2 - 1 l/min (pumping), 2 - 5 l/min.

The ozone concentration was registered optically on a wave length 253.7 nm and varied up to 13 g/m^3. Experimental dependences of concentration of ozone from applied power, speed of air pumping, interelectrode gap were received (fig. 2-4). For velocities of gas flow larger then 5 m/sec we receive linear dependence of concentration from specific power at a given gap: $n=\alpha w$, where n is ozone concentration, $1/\alpha$ is required power for 1g O_3 production, w is specific power. The values of $1/\alpha$ obtained in experiment are indicated on fig.3. (Large error at low powers is explained by non-uniformity of discharge). It was established that at reduction of interelectrode gap the value of required power for 1g O_3 production reduces, so at $h=15mm$ $1/\alpha=16W^*/gO_3$ and at $h=8mm$ $1/\alpha=10W^*/gO_3$.

Also the dependence of ozone concentration on specific power was obtained at small velocities of gas pumping (<0,5 m/sec). There the specific power dependence of ozone concentration is given by form $n=n_0\,(1-exp(-\alpha/n_0\ w))$, where n_0 is the concentration of saturation. The results are represented on fig.4.

For optimization of plasma-chemical reactor's parameters more detailed study of synthesis's products making mechanism, energy distribution channels and plasma-chemical processes are required.

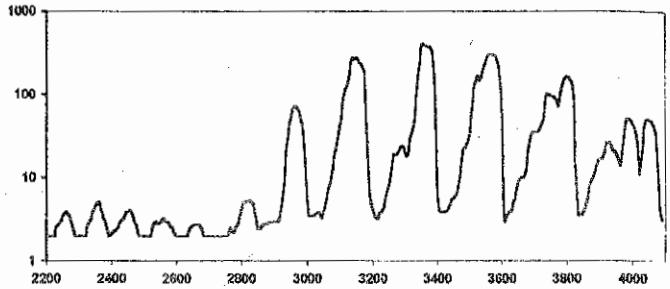


Fig.5. Part of the discharge spectrum (II positive series of N_2)

The ozone making mechanism was repeatedly discussed in the literature. The mathematical model of ozone synthesis in conditions of barrier discharge is submitted in [2], kinetics of processes, excited by space discharge in a oxygen in [3], investigation of ozone building-up processes in high-pressure glow discharge in a flow of air in [4]. Assumed there main channels of molecular oxygen dissociation (the energy of dissociation is 5,12eV) by direct electronic impact through excitation of Hertzberg ($A^3\Sigma_u^-$) and Shuman-Runger ($B^3\Sigma_u^-$) bands and in processes of electronic attachment with further dissociation requires high energies (>4,5eV). However, in our conditions energy of electrons (3-4 eV) is not enough for going on of these processes. In given work we carried out spectrometric research of glow discharge at atmospheric pressure with high-speed pumping of air. Along with step excitation by electronic impact and subsequent dissociation of molecular oxygen it is proposed a possible ozone making mechanism in which the nitrogen represents itself as a "buffer" for transfer of a significant share of the discharge energy to a oxygen.

The obtained discharge spectrum was identified by us as the II positive series of N_2 ($N_2\left(C^3\Pi_u\right) \rightarrow N_2\left(B^3\Pi_g\right)$), Vegard-Kaplan ($N_2\left(A^3\Sigma_u^+\right) \leftrightarrow N_2\left(X^1\Sigma_g^+\right)$) and Shuman-Runger ($O_2\left(B^3\Sigma_u^-\right) \leftrightarrow O_2\left(X^3\Sigma_g^-\right)$) bands [5-7]. On this base we can speak about step excitation of electronic levels by electronic impact and about presence of metastable electronic state $N_2\left(A^3\Sigma_u^+\right)$.

Electronic circuit of molecules N_2 and O_2 we can represent by formula:

$$\nu_{e'e''} = \nu_e + \omega_e'\left(\upsilon' + 1/2\right) - x_e'\omega_e'\left(\upsilon' + 1/2\right)^2 + \ldots \quad -\left[\omega_e''\left(\upsilon'' + 1/2\right) - x_e''\omega_e''\left(\upsilon'' + 1/2\right)^2 + \ldots\right]$$

where $\nu_{e'e''}$ is the energy of vibrational transition, υ' u υ'' are oscillation quantum numbers, ω_e is energy of vibrational quantum, $x_e\omega_e$ is the constant of anharmonicity, ν_e is energy of electronic transition. As a result availability of molecular nitrogen state $\left(N_2\left(A^3\Sigma_u^+\right)\right)$ and molecular oxygen state $\left(O_2\left(B^3\Sigma_u^-\right)\right)$ with similar energies was established.

Now it is possible to assume energetically allowed channel of almost resonant transfer of energy from molecular nitrogen $\left(N_2\left(A^3\Sigma_u^+\right)\right)$ to molecular oxygen $\left(O_2\left(B^3\Sigma_u^-\right)\right)$: $N_2\left(A^3\Sigma_u^+, \upsilon = 0; 6.1116eV\right) \rightarrow O_2\left(B^3\Sigma_u^-, \upsilon = 0; 6.1183eV\right)$, $N_2\left(A^3\Sigma_u^+, \upsilon = 1; 6.2893eV\right) \rightarrow O_2\left(B^3\Sigma_u^-, \upsilon = 2; 6.2864eV\right)$, $N_2\left(A^3\Sigma_u^+, \upsilon = 2; 6.4638eV\right) \rightarrow O_2\left(B^3\Sigma_u^-, \upsilon = 5; 6.4436eV\right)$, $N_2\left(A^3\Sigma_u^+, \upsilon = 3; 6.6344eV\right) \rightarrow O_2\left(B^3\Sigma_u^-, \upsilon = 7; 6.66eV\right)$, $N_2\left(A^3\Sigma_u^+, \upsilon = 4; 6.8018eV\right) \rightarrow O_2\left(B^3\Sigma_u^-, \upsilon = 9; 6.7914eV\right)$, $N_2\left(A^3\Sigma_u^+, \upsilon = 5; 6.9654eV\right) \rightarrow O_2\left(B^3\Sigma_u^-, \upsilon = 12; 6.9681eV\right)$.

It is known that the dissociation of molecular oxygen occurs basically at excitation of $O_2\left(B^3\Sigma_u^-\right)$ state. As a result two atoms of oxygen $O\left(^3P\right)$ and $O\left(^1D\right)$ will be formed. Thus the offered parallel ozone making mechanism can be presented by the following circuit:

$$N_2 \rightarrow N_2\left(A^3\Sigma_u^+, \upsilon\right) \rightarrow O_2\left(B^3\Sigma_v^-\right) \rightarrow O^* \rightarrow O_3$$

Literature:

1. Ю.С.Акишев и др., Экспериментальное исследование и численное моделирование тлеющего разряда постоянного тока атмосферного давления, Физика плазмы, 1994, т.20, №6, сс. 571-584.
2. А. И. Демьянников, А. А. Дементьев. Журнал физической химии, 1994, т. 68, № 7, с. 1214.
3. Захаров А.И., Клоповский К. С., Осипов А. П. и др. Физика плазмы, 1988, т. 14, в. 3, с. 327.
4. Беспалошников А. А., Блохин В. И., Воронин В. Б., Мыслин В. А. и др. ХВЭ, 1982, т. 16, № 4, с. 344.
5. Немец В. М., Петров А. А., Соловьёв А. А. Спектральный анализ неорганических газов. - Л.: Химия, 1988.
6. Радциг А. А., Смирнов Б. М. Справочник по атомной и молекулярной физике. - М.: Атомиздат, 1980.
7. Р.Пирс, А.Гейдон Отождествление молекулярных спектров. - М: Иностранная литература, 1949.

INVESTIGATION OF THE QUASISTATIONARY PLASMA FLOW IN THE AXIAL MAGNETIC FIELD AND MODELING EXPERIMENTS ON THE CURRENT DISRUPTION

V.V.Chebotarev, I.E.Garkusha, V.V.Garkusha, N.V.Kulik, V.A.Makhlay, N.I.Mitina, D.G.Solyakov, V.I.Tereshin, S.A.Trubchaninov, A.V.Tsarenko, H.Wuerz*

Institute of Plasma Physics of the National Science Center "Kharkov Institute of Physics & Technology", 310108 Kharkov, Ukraine
**) Forschung Centrum Karlsruhe, INR, Postfach 3640, D-76021, Karlsruhe, Germany*

1. Introduction

The plasma streams generated by powerful quasistationary plasma accelerator QSPA Kh-50 can be used for filling the magnetic confinement system (of special type [1]) as well as for carrying out the modeling experiments on power loading the divertor plates of tokamak-reactor [2]. The evidence of prospect of such modelling experiments have been done in earlier research (for instance [3, 4, 5]) carried out with high power plasma streams but with smaller plasma pulses duration.

The main goal of recent experiments is analysis of characteristics of the plasma penetration and flow in the external axial magnetic field as one of the element of the magnetic trap. In addition, some preliminary experiments on powerful plasma interaction with graphite target placed in magnetic field were fulfilled.

2. Experimental device

Experiments were carried out on full block quasistationary plasma accelerator QSPA Kh-50 device, described in [3, 4]. This device was upgraded by replacing of 2nd and 3d parts of vacuum chamber (1.5 m in diameter and 1.2 m in length each) with magnetic system and smaller in diameter vacuum chamber. Axially-symmetric magnetic field was produced by four large in size magnetic coils. The first magnetic coil was located on the distance of 120 cm from accelerator output. Each coil is 32.5 cm in thickness and 120 cm in outer diameter. The inner diameter of coil, determining the radial size of vacuum chamber, is 42 cm. The distance between each couple of coils is 15 cm. The inner diameter of small vacuum chamber inserted into coils was 38 cm. The magnetic coils were supplied by condenser bank. The value of

electric current was increased from the first coil to 3d and 4th to produce magnetic field slowly increased with length, on the distance more than 100 cm, and more or less homogeneous magnetic field at the vicinity of 3d and 4th coils with magnetic field strength up to 2 T. Such geometry of magnetic field was chosen for best agreement of injected high power plasma with magnetic field. The half period of magnetic field achieved 16 ms. The diagnostic chamber for test experiments with material target was placed between 3d and 4th magnetic coils.

Experiments were carried out in different modes of accelerator operation. The ultimate plasma parameters were as follows: maximum plasma power - up to 400 MW/cm^2, plasma energy density - up to 5 kJ/cm^2, maximum energy of protons - 0.9 keV, plasma density ~≥ 10^{16} cm^3, pulse duration - 0.1-0.15 ms.

3. Plasma injection into magnetic field

The value of a magnetic field B_z displaced by a plasma propagating along the magnetic system (oscillogram in fig. 1) was measured by the local magnetic probes for different axial and radial probe positions. Some radial profiles of magnetic field values in plasma B_z^{plasma} derived as (B_{z0} - B_z) and normalized on the value of vacuum magnetic field B_{z0} are shown in fig.1 (curve 1 - for B_{z0} = 0.28 T, distance z from accelerator output z = 155 cm; curve 2 - for B_{z0} = 0.5 T, z = 195 cm). It follows from this picture that plasma radius is reduced and magnetic field penetrates more strongly into plasma with plasma propagation along the magnetic system. At the vicinity of 3d and 4th magnetic coils (the region with homogeneous magnetic field) the magnetic field value in plasma is of an order 70% of the vacuum magnetic field. The dependence of the magnetic field in a plasma, normalized by the value of vacuum magnetic field for the same cross-section, is shown in fig.2 for measurements carried out between 2d and 3d coils. One can see from this figure that the magnetic field penetration into plasma is increasing with increasing

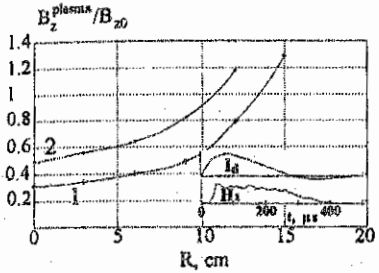


Fig. 1. Radial profiles of the normalized magnetic field in plasma: 1 - cross-section between 1st and 2d magnetic coils; 2 - between 2d and 3d coils; oscillograms of discharge current I_d and magnetic field B_z.

value of the vacuum magnetic field. So for plasma parameters mentioned above and B_{z0} of an order 2T one can expect that value $\beta = 8\pi nkT/B_{z0}^2$ will be within 0.1 and 0.2.

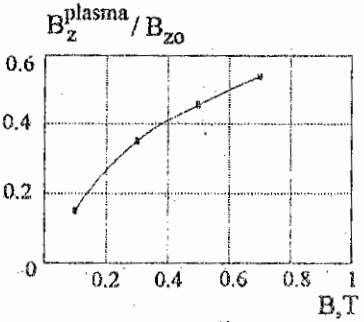


Fig. 2. Normalized value of the magnetic field in a plasma as a function of vacuum magnetic field (z = 195 cm).

The plasma parameters behaviour in dependence on vacuum magnetic field was as follows. The plasma density has been increased with increasing the magnetic field value. In particular, it was varied from (2-3)x10^{15} cm^{-3} for zero magnetic field up to (2-3)x10^{16} cm^{-3} for B ≈ 1 T. The total energy of a plasma stream measured behind the magnetic system was about 120-150 kJ. Therefore plasma with the energy content of an order 30-40% of total energy of the plasma stream (350-400 kJ) generated by accelerator passes through the magnetic system. Plasma energy density evaluated for the near axis region of plasma stream in magnetic field achieved 4-5 kJ/cm^2.

4. Disruption modelling experiments

High power plasma streams with plasma energy density up to 5 kJ/cm^2 were utilized for disruption modelling experiments. Targets of MPG-7 graphite with diameter 8 cm were positioned at an axis of homogeneous magnetic field (between 3d and 4th magnetic coils) and irradiated by plasma streams propagating along the magnetic field normally to target surface. It was shown that the transient plasma layer was formed close to the graphite target surface with plasma density more than one order of value exceeding the density of incident plasma. This layer behaviour was similar to what we obtained in our previous experiments with no magnetic field [2]. Due to the formation of such transient layer, only small part (within

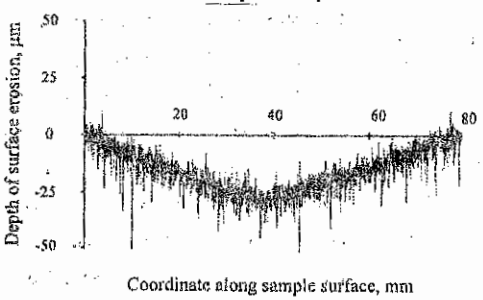


Fig. 3. Erosion profile of graphite surface.

5 to 10 %) of incident plasma energy, reached the target surface. This was the reason for reduced erosion of target surface.

Fig. 3 shows the erosion profile of graphite surface irradiated by 20 pulses of plasma with parameters mentioned above in the magnetic field of 1 T. The erosion coefficient for near axis region of target is of an order 2 μm per pulse or (0.4-0.5) μm/kJ. Comparing with previous results obtained with similar plasma parameters, but energy density ≤ 3 kJ/cm^2, in large vacuum chamber with no magnetic field, obtained erosion coefficient is at least two times smaller. This may be due to more strong screening effect of transient layer in magnetic field presence. The other difference between recent and previous results is that irradiation of target surface in magnetic field provides more homogeneous surface erosion.

5. Conclusions

Despite a large cross-section of plasma stream generated by QSPA, part of plasma stream with an energy (30-40) % of the energy of incident plasma stream passes through the magnetic system with magnetic field strength ≤ 1 T. The vacuum magnetic field effectively penetrates into plasma on the length of an order 1.2 m. It's penetration is the more effective the higher vacuum magnetic field value. This means that the disruption simulation experiments may be more or less adequately carried out in this installation. The erosion coefficient of MPG-7 graphite surface is of an order (0.4-0.5) μm per 1 kJ of incident plasma energy density. The transient plasma layer formed close to the target surface is strictly decreasing the value of energy deposited directly on the surface.

References

[1] Tereshin V I 1995 *Plasma Physics and Controlled Fusion*, 37 A177-A190

[2] Chebotarev V V, Garkusha I E, Garkusha V V et al 1996 *J. Nucl. Mater.* 11296 C

[3] Arkhipov N I et al 1994 *Proc. 18th SOFT, Karlsruhe, Germany*

[4] Wuerz H et al 1995 *J. Nucl. Mater* 220-222 1066-70

[5] Arkhipov N I et al *J. Nucl. Mater.* 11296 C

[6] Tereshin V I et al 1992 *Plasma Devices and Operations* 2 155-65

[7] Volkov Ya F et al 1992 *Sov. J. Plasma Phys.* 18(11) 718-23
Morozov A I et al 1994 *Plasma Phys. Rep.* 20 801-4

PD

POSTDEADLINE PAPERS

Post deadline paper for Kiev EPS Conference

Record central beta produced by NBI in the START Spherical Tokamak

M J Walsh, R Akers, R Buttery, D Codling, N Conway, M Gryaznevich, T Gunston, T C Hender, I Jenkins, O.J.Kwon*, R Martin, M Mironov†, M P S Nightingale, S Petrov†, C Ribeiro, D C Robinson, R T C Smith, A Sykes, S E V Warder

UKAEA Fusion, Culham, Abingdon, Oxon, OX14 3DB, UK
UKAEA/Euratom Fusion Association
*Dept. Physics, Taegu University, Seoul, Korea
†Ioffe Institute,St Petersburg, Russia

Abstract

The Neutral Beam Injector loaned by the Oak Ridge National Laboratory is producing effective plasma heating in the START spherical tokamak at UKAEA Fusion, Culham Laboratory. High values of volume averaged beta $\beta_T = 8\%$ and values of central beta $\beta_o = 48\%$ have been obtained; this value of central beta is considered to be the highest yet achieved in a tokamak plasma.

Introduction

The Troyon beta limit [1] implies that high values of beta should be achievable at low aspect ratio - indeed this is one of the perceived attractions of the Spherical Tokamak (ST). To see this, we use the original form of the Troyon limit $\beta_T = \beta_N \dfrac{I_p}{aB_T}$ which can be re-written, using $q_{cyl} = \dfrac{2.5a^2(1+k^2)B_T}{RI_p}$, in the form

$$\beta_T = \beta_N \frac{2.5(1+k^2)}{Aq_{cyl}} \qquad (1)$$

where β_T is the volume averaged beta $\beta_T = \dfrac{2\mu_o}{VB_T^2}\int pdV$, I_p(MA) is the plasma current, a(m) and R(m) are the plasma minor and major radii, $A = R/a$ is the aspect ratio, k the elongation, and B_T(T) the vacuum toroidal magnetic field at the geometric centre of the discharge. Use of the value $\beta_N = 4$ in (1) recovers the expression derived by considerations of ballooning mode stability in Sykes et al [2].

The ST combines high natural elongation k with low aspect ratio A. Moreover it can obtain low q_{cyl} whilst edge q, q_s is significantly higher, since $q_s \sim \dfrac{A}{A-1} q_{cyl}$ [3]. Typical plasmas in START for example have aspect ratio A = 1.3 with elongation k from 1.5 to 2, and stability (at low beta) has been demonstrated experimentally at safety factors down to $q_{cyl} \sim 1$, $q_s \sim 4$. Expression (1) therefore implies very high values of β_T may be attainable, if β_N remains high.

The beta limit diagram for START is therefore at least as large as shown in Fig 1. This figure is adapted from the DIII-D plot shown in Stambaugh [5], with the inclusion of the more recent record value of $\beta_T = 12.5\%$ achieved in DIII-D [6]. Note that the DIII-D data is limited to $I/(aB) < 3.5$; above this value the safety factor q_s becomes less than 2. We shall show that $I/(aB) > 8$ should be accessible in START.

Theoretical predictions

It is known that the requirement $q_s > 2$ on the edge safety factor is not a sufficient condition for kink stability (with remote wall) as aspect ratio decreases [3]. Scoping calculations on the stability of the n = 1 external kink in a force-free $\beta = 0$ model are shown in Fig 2a for a range of low aspect ratios with elongation $k = 1.6$, triangularity $\delta = 0.25$, and $q_o = 1.15$. For a remote wall ($r_w/a = 10$) which is relevant to START, it is found that $q_s > 3$ is sufficient for stability at $A = 1.3$, but that for $A = 1.2$, $q_s > 4$ is required. The dependence on elongation for the same conditions is shown in Fig 2b, for aspect ratio A = 1.3. It is found that the q_s sufficient for kink stability rises to 3.8 as elongation increases to 2.0. The q-limit is relatively insensitive to the current profile.

When finite plasma pressure is included, calculations using ERATO have shown that for $A = 1.3$, $k = 1.6$, $\delta = 0.3$, $q_o = 1.05$ and $q_s = 5$, $\beta_T = 28\%$ (that is, $\beta_N = 4.5$) should be stable to both low n kinks (with a remote wall) and $n = \infty$ ballooning modes [4]. This (computational) point is shown in Fig 1.

To summarise therefore, operation with $q_s \geq 5$ should be sufficient for n = 1 kink stability and as indicated in Fig 1 this potentially gives access to very high β_T, especially for highly elongated plasmas.

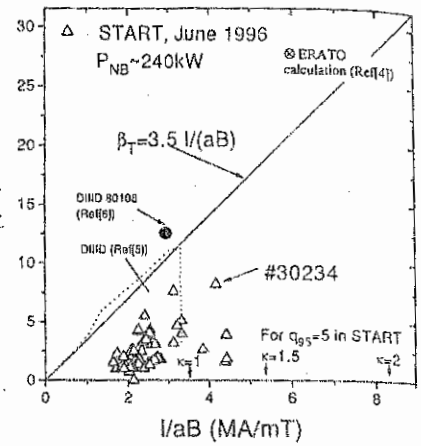


Fig 1 β_T diagram for START at aspect ratio A = 1.3. Values of I/aB corresponding to $q_s = 5$ in START are shown for elongations 1, 1.5 and 2.

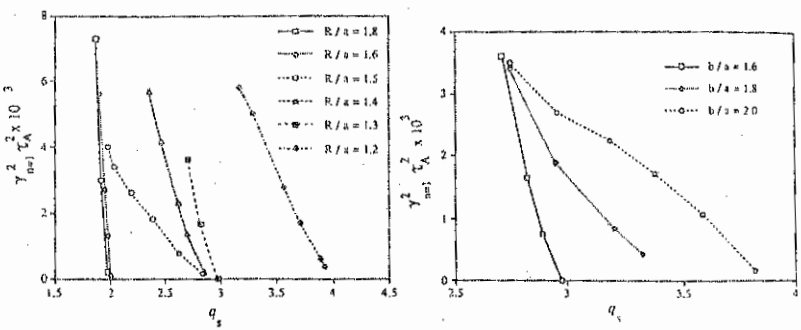


Fig 2 n = 1 external kink growth rate (β=0 model) for triangularity $\delta = 0.25$, current profile $\langle J_\phi \rangle \sim (1-\psi^4)$, $q(0) = 1.15$, with remote wall ($r_w/a = 10$), for (a) different R/a with elongation $\kappa = 1.6$, (b) different κ at aspect ratio R/a = 1.3

Results from START

Previously values of $\beta_T \leq 3.9\%$, $\beta_o < 20\%$ and $\beta_N \leq 1.8$ have been achieved Ohmically in START [7]. First beam injection experiments began in January 1996, using the 40keV, 0.5MW injector loaned from ORNL. Beam performance is being increased in stages, and present operation is at 25keV, with some 240kW of Hydrogen beam power injected into the START vessel. For this campaign, the working gas is H_2.

It is found that application of beam injection in START provides a combination of improved stability, higher density, and effective heating of both ions and electrons [8] which can considerably raise the beta values

The highest total β value (i.e. including the estimated fast ion component) achieved to date in START is in shot 30234. The parameters of this discharge are R = 0.314m, a = 0.249m, k = 1.8, R(axis) = 0.377m (measured from a multichord SXR camera and the 30-point Thomson scattering), I_p = 214 kA, I_{rod} = 324kA (reduced from 450kA over 10ms). The high beta continued to increase in this shot for a further 4ms (about 2 confinement times) before an 'Internal Reconnection Event' reduced the plasma energy content. From code calculations the predicted NBI absorption is about 70% after shine-through and orbit losses have been allowed for, and so it is estimated that 170kW of power is absorbed in this example. This is substantially less than the Ohmic power of ~ 430kW.

The 30-point Thomson scattering diagnostic measures the electron thermal pressure (Fig 4a). The thermal ion pressure is estimated by measuring the central (thermal) ion temperature by a Neutral Particle Analyser and by charge exchange spectroscopy and assuming the same radial profile as the electrons, with dilution factor of 0.8. The total thermal pressure is shown in Fig 4b (dot-dashed curve).

The total plasma pressure - i.e. including the fast ion component - can be estimated by equilibrium reconstruction. Fig 3 shows the output from a free-boundary Grad-Shafranov code, where the plasma shape and current profile is adjusted to fit Thomson, CCD, and magnetic data from an array of B_z coils in the centre limiter and from outer flux loops (Fig 3). The total pressure is adjusted to match the Shafranov shift of the magnetic axis, which is determined by SXR camera. The combination of high elongation (k ~ 1.8 in this shot) and large Shafranov shift (25% in this shot) make this a relatively well determined process. The resulting total pressure is shown in Fig 4b (full curve).

A second method is to calculate the fast ion population from a Fokker-Planck code, using an accurate equilibrium model and assuming 240kW of injected power.

This is then added to the thermal component to give the total pressure shown by the dashed curve in Fig 4b.The equilibrium code modelling gives β_T = 8.5%, β_o = 48%; the kinetic pressure model gives β_T ~ 8.2%, β_o ~ 42%.

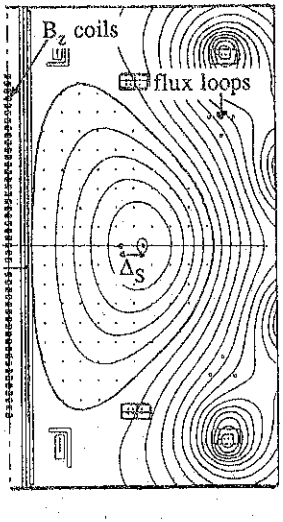


Fig 3 Equilibrium reconstruction of shot 30234, matching plasma shape parameters, magnetic data and Shafranov shift

No results have yet been obtained from diamagnetic loop analysis as this is more difficult to interpret in the low aspect ratio configuration.

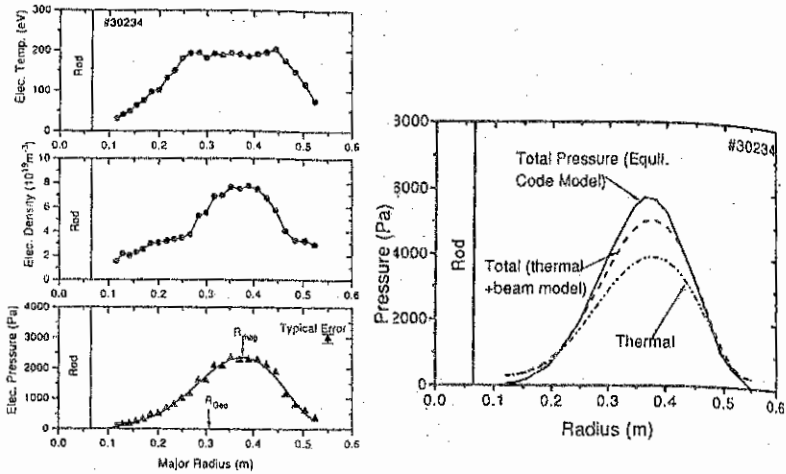


Fig4 *(a) Profiles of electron temperature, density and pressure (obtained by Thomson scattering)* *(b) Components of plasma pressure*

As suggested by the scales of the axes in Fig 1 there is considerable potential for the attainment of even higher beta and the injector is being upgraded to equal (and eventually to exceed) its nominal rating of 40keV, 0.5MW.

These early results give a convincing demonstration of the effectiveness of beam heating in Spherical Tokamak plasmas which will be further exploited in START and its successor machine, MAST, which is now under construction at Culham.

Acknowledgement
We wish to acknowledge the enthusiasm and practical assistance of ORNL personnel, in particular Martin Peng and Jim Tsai.
This work is supported by the UK Department of Trade and Industry, Euratom and the US DoE.

References

[1] F Troyon et al, Plasma Physics and Controlled Fusion 26 (1a) p209 (1984)
[2] A Sykes, M F Turner & S Patel, Proc. 11th EPS, Aachen II p363 (1983)
[3] S.G. Bespoludennov et al, Sov.J.Plasma Physics 12 (7) (1986)
[4] T C Hender et al, Proc. 22nd EPS conf, Bournemouth III p233(1995)
[5] DIIID team, Proc. 13th IAEA Conf, Washington I p69 (1991)
[6] E J Strait et al, Proc. 21st EPS, Montpellier I p242 (1994)
[7] M J Walsh et al, Proc. 22nd EPS, Bournemouth III p33 (1995)
[8] M J Walsh, this conference

RESONANCES IN STRONG EXTERNAL FIELDS IN ATOMIC SPECTRA
AUTOIONIZATION RESONANCES IN Tm

A.Glushkov#*,S.Borik#,N.Gavrilov#,V.Polischuk#

#Dept.Appl.Math.&Lab.At.-Nucl.Spectr.,OHMI,Perekopskoy diviz. str.12"6"-29, Odessa, SU-270009, Ukraine (for contact)
*Institute of Spectroscopy of Russian Academy of Sciences, Troitzk, Moscow reg.,SU-142092, Russia.

Abstract: It has been examined some new effects connecting with behavior of the Tm autoionization resonances in external electric field ,in particular, effect of a drastic nonlinear broadening of the reorientational autoionization resonances.

The effects of electric fields on the autoionization states (AS) are interesting from several points of view [1-6]. The study of the decay processes for Rydberg states is important for laser spectroscopy,in particular, a multistage ionization method [3] and its applications. One should note the great role of AS at the processes in plasma and gases, f.e. in the determination of the excitation & deexcitation rates of ions, in the examination of dielectron recombination in plasma (cf. [1-2]). Especially interesting effects occur in the complex atoms when its broad autoionization resonances mix with much narrower resonances of the opposite parity by means external electric field.Such the effects are of a great importance for laser spectroscopy.The theoretical study of the Tm represents an undoubted interest for experimental spectroscopy, f.e. in controlling the population & decay kinetics of excited states or a selective ionization using laser radiation [7-9].

In this paper we examine some new effects connecting with behavior of the Tm AS in an electric field, in particular, an

effect of drastic nonlinear broadening of the reorientational type autoionization resonances in field, predicted in [8-10]. The main autoionization channels for here examined Tm states are illustrated in fig. The availability of two pairs of near -lying ionization limits (with vacancy states $4f7/2$ & $4f5/2$) provides two main types of the autoionization decay (AD):

$$4f^{-1}_{5/2}6s1/2(J12)nl \text{--} 4f^{-1}_{7/2}6s1/2(J12')Tm^{+} + e \text{ leje}, \quad \text{(BFD)}$$
$$n>7, \qquad J12=2;3, \quad J12'=3;4$$
$$4f^{1}_{J}6s1/2(J12)nl \text{--} 4f^{1}_{J}6s1/2(J12')Tm^{+} + e \text{ leje}, \quad \text{(ROD)}$$
$$n\geq 25 \qquad J12=3, \quad J12'=2;4 \qquad J=5/2,7/2.$$

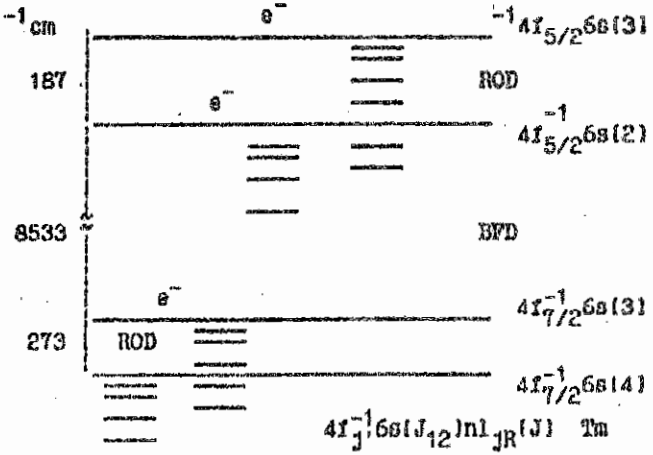


Fig. Position of the near lying first ionization limits $4f^{-1}_{J}6snl$ Tm and scheme of the autoionization decay of $4f^{13}6snl$ Tm autoionizing Rydberg states (from ref.[7]).

These AD channels are discussed in detail in [8]. ROD means reorientation AD and BFD means Beutler -Fano AD. The states $4f^{-1}_{5/2}6s_{1/2}$ (J12=3)nl undergo simultaneously both BFD and ROD. Contrary to the BFD, the ROD -a low energy process preserving all the single electron quantum numbers of atomic residue:

$4f^{13}$ and 6s1/2. The ROD can be of monopole or quadrupole type. We mean here the multipolarity of the interaction causing the AD. The states with J12=2,4 do not undergo ROD. Nevertheless, their admixing with states undergoing the ROD significantly amplify the monopole ROD of the latters. In table one can see the values of the energy E, the autoionization widths G for $4f^{13}6s(3)ns,np$ states (n=25) [7-9]. For these Rydberg series, the only possible AD is the ROD. Any "2" states of the different parity can be mixed by an electric field. The mixing leads to redistribution of the autoionization widths. In a case of the degenerate or near-degenerate resonances this effect becomes observable even at a moderately weak field. In a case of Tm we

deal with reorientationally decaying ns& np series converging to the same ionization limit, i.e. these are nearly degenerate states of different parity. Among them one can find some pairs of ns and np states with widths G differing by several orders. We examine $f^{-1}_{7/2}6s(3)25s(5/2)$ state decaying due to quadrupole interaction and $f^{-1}_{7/2}6s(3)25p_{1/2}(5/2)$ state undergoing the monopole ROD. Calculation procedure of atomic characteristics of multielectron systems in the presence of electric field is presented in ref. [9-11]. Here we only note the diagonalization of the complex energy matrix leads to the complex energy correction: RedE-iG/2 , where RedE is the level shift, G is the level width including both radiation & autoionization widths. If the effect of AD is only included in matrix M , G presents only the autoionization width of the state. Only Re M is diagonalized. The imaginary part is converted by means the matrix of eigenvectors C_{mk} obtained by diagonalization of Re M:

$$\mathrm{Im}\, M_{ik} = \sum_{ij} C^{*}_{mi} M_{ij} C_{jk} \quad .$$

This procedure is correct to terms of the order of ImM/ReM. The field matrix element : $V_{12} = e \langle ns_{1/2} | r | np_{1/2} \rangle$.

The calculation results for the examined states widths are presented in tabl. for different values of the field strengths. One can see that even at a weak electric field it takes place

a strong change of the width of the autoionization resonance. Detailed spectroscopic information about RS levels is needed to optimize the excitation &ionization of the atom.An optimal scheme presumes a compromise between high excitation probability and high decay rate that determines the lower and upper boundaries for the AD rate.An use of ROD channel,investigated here essentially increases a possibility of such a compromise. New possibilities of the optimization of the laser resonance ionization scheme with accounting for these effects are of a great importance.

Authors are grateful to Prof.L.N.Ivanov for support of this work and help.

Table. Autoionization widths G and energies E (in cm^{-1}) for different values of the field strengths e ($V.cm^{-1}$).

State	$4f^{13}_{7/2}6s1/2(3)25s[\frac{5}{2}]$	$4f^{13}_{7/2}6s1/2(3)25p_{1/2}[\frac{5}{2}]$
E, e=0	49854,7	49865,3
G, e=0	1,177D-05	1,207D-01
G, e=50	1,164D-04	1,206D-01
G, e=100	4,269D-04	1,203D-01
G, e=150	9,340D-04	1,198D-01

References

1. Atomic excitation and recombination in external fields. Proc. of the Workshop on Atomic Spectra and Collisions in external fields.Gaithersburg,1984.Ed.Nayfeh M.H.,Clark C.W.
2.Rydberg states of atoms and molecules (New-York.:Cambridge Univ.),1983.Ed.:Stebbings R.F.,Dunning F.B.
3.Letochov V.S.,Mishin V.I.,Puretzky 1977 Prog.Quant.Electr.

5 139.
4.Ivanov L.N.,Letochov V.S. 1975 Quant.Electr.(Sob.) 2 585.
5.Bekov G.I.,Ivanov L.N.,Letochov V.S.,Vidolova-Angelova E. 1980 Opt.Comm. 35 194-98
6.Vidolova-Angelova E.,Ivanov L.N.,Ivanova E.P.,Angelov D.A. 1986 J.Phys.B: At.Mol.Phys. 19 2053.
7.Vidolova-Angelova E.,Ivanov L.N.,Angelov D.A. 1988 J.Phys. B:At.Mol.Phys. 21 3877 .
8.Vidolova-Angelova E.,Ivanov L.N. 1991 J.Phys.B:At.Mol.Phys. 24 4147.
9.Glushkov A.V., Ivanov L.N. 1992 Abstr.111 Symp.on atomic spectroscopy (Chernogolovka, Moscow reg.)
10.Glushkov A.V.,Ivanov L.N. Preprint ISAN N2-AS,1992.
11.Glushkov A.V.,Ivanov L.N. 1993 J.Phys.B:At.Mol.Phys. 26 L379.

SPECTROSCOPY OF THE ATOM IN LASER FIELD: DEFORMATION OF RADIATION ATOMIC LINES. MULTI-PHOTON PROCESSES. ABSORPTION SPECTRA OF DENSE NONIDEAL PLASMA: QED APPROACH

A.V.Glushkov#*,T.Buyadgi#,A.Kivganov#,G.Prepelitsa#
#Dept.Appl.Math.&Lab.At.-Nucl.Spectr.,OHMI,Perekopskoy diviz. str.12"6"-29, Odessa, SU-270009, Ukraine (for contact)
*Institute of Spectroscopy, Russian Academy of Sciences (ISAN), SU-142092, Troitzk, Moscow region, RUSSIA

Abstract. Within quantum electrodynamics it has been considered the interaction of atomic system and laser pulse with Gaussian shape.As example, it has been carried out estimate of the 3-photon resonant,4-photon ionization profile of H.

1. The interaction of the atomic systems with the external alternating fields,in particular, laser emission fields has been the subject of intensive experimental and theoretical investigation (see ref.[1-14]). The appearance of the powerful laser sources allowing to obtain the radiation field amplitude of the order of atomic field in the wide range of the wavelengths results to the systematic study of the nonlinear interaction of radiation with atoms.Calculation of the deformation and shifts of the atomic lines in strong laser field, definition of the k-photon emission and absorption probabilities and atomic levels shifts, study of laser emission quality effect on characteristics of atomic line are the most actual problems to be solved. It's of the great interest the multiphoton ionization.At present time,a progress is achieved in the description of the processes of interaction atoms with the harmonic emission field [2]. But in the realistic laser field the according processes differ in significant degree from ones in the harmonic field. In ref.[3] it has been proposed a new consistent QED approach

to investigate the interaction of atom with the laser field (see also [4-6]).It has been considered the case of a laser pulse with Lorentzian shape. In this paper we consider the interaction of atomic system and laser pulse with Gaussian shape. Interaction "atom-laser field" is described by means a set of characteristics which are directly observed in the experiment: the radiation emission & absorption lines. There position &shape fully determine spectroscopy in the field.

2. Let us describe the interaction of atom with laser field by means the following potential:

$$V(r,t) = V(r) \int dw\, f(w-w_0) \sum_{n=-\infty}^{+\infty} \cos[w_0 t + w_0 n\tau], \quad (1)$$

where n is the whole number. The potential V represents the infinite duration of laser pulses with known frequency τ. Here we consider the effect of interaction of the atom with the single pulse.An interference of pulses gives additional order of the littleness $1/\tau$.The representation V(rt) as the infinite sequence of pulses is a formal moment connected with the use of the stationary perturbaion theory (PT) formalism.The function f(w) is Fourier component of the laser pulse. Let us consider the pulse with the Gaussian shape:

$$f(w) = I \exp\{-\ln 2\, (w/D)^2\} \quad (2)$$

We will calculate for any "a" level the imaginary part of the energy shift $\mathrm{Im}E_a(w_0)$as the function of the laser pulse central frequency. An according function has a shape of the resonant curve. Each resonance is connected with the transition a-p,in which a definite number of photons is absorpted or radiated.Let us consider the following situation: the a-p transition with the absorption of k photons (a, p -discrete levels). For resonance which corresponds to this transition, we calculate the following values:

$$dw(pa|k) = \int dw\ \mathrm{Im}E_a(w)(w-w_{pa}/k) / N \ , \qquad (3)$$

$$m_m = \int dw\ \mathrm{Im}E_a(w)(w-w_{pa}/k)^m / N \ ,$$

where $N=\int dw\ \mathrm{Im}E_a$ is the normalizing multiplier; w_{pa}-position of the nonshifted line for atomic transition a-p; $dw(pa|k)$-the line shift due k-photon absorption; $w_{pa}=w_{pa}+k\,dw(pa|k)$. We take into account only the contribution of the single resonance. The first moments m_1, m_2 and m_3 determine the atomic line center shift, dispersion & coefficient of the asymmetry. To calculate m_m we need to get the expansion of E_a into the PT series and use the Gell-Mann and Low adiabatic formalism for calculation of dE_a. The moments are calculated in the PT lowest second order (the littleness PT parameter is V/E; V is the field vibration amplitude; E is the typical energy of the electron transitions). The nonadiabatic parameter is V/kE, where k is the quantum process parameter. Thus one can see that the adiabatic approach is correct at least in the same degree as the PT is. After corresponding calculations, we get:

$$dw(pa|k) = \frac{\pi D}{(k+1)k}\,[\ E(p,w_{pa}/k) - E(a,w_{pa}/k)\ ] \ ,$$

$$m_2 = D^2/k \ , \qquad (4)$$

$$m_3 = \frac{4\pi D^3}{k(k+1)}\,[\ E(p,w_{pa}/k) - E(a,w_{pa}/k)\ ] \ ,$$

$$E(j,w_{pa}/k) = \frac{1}{2}\sum_{p_i} V_{jp_i} V_{p_i j} \left(\frac{1}{w_{jp_i} + w_{pa}/k} + \frac{1}{w_{jp_i} - w_{pa}/k}\right)$$

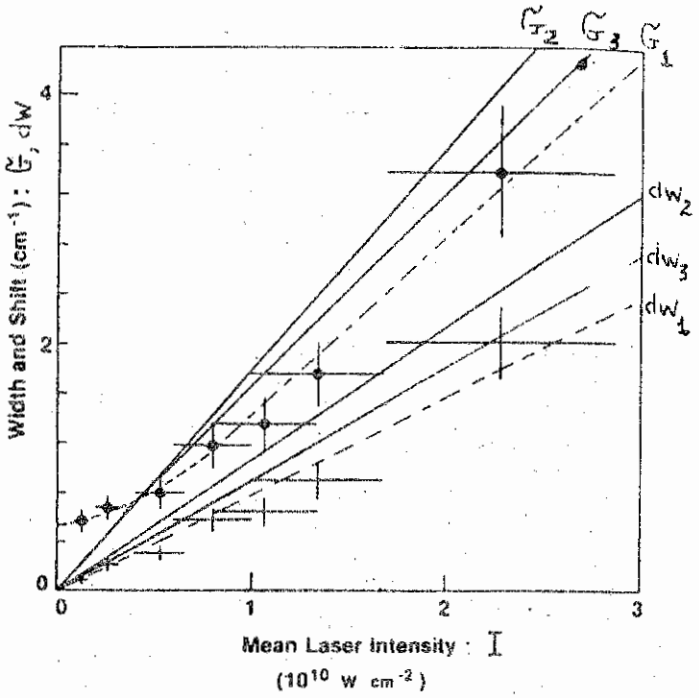
The summation in (4) is fulfilled on all states of atomic system. The obtained expressions for dw and m_n describe the main characteristics of the absorption line near resonant frequency w_{pa}/k. One can see that these characteristics are determined not only by the radiation frequency, but also by the quantumness of the process. The lines asymmetry arises as the central (resonant) part of the line is shifted more strongly than wings; the line wings are deformated weaker.

3. As example, we carried out estimates of the three-photon

resonant, four-photon ionization profile of atomic hydrogen (1s-2p : 365 nm). In fig. there is presented the shift of the resonance profile as the function of the mean laser intensity at the temporal & spatial center of the uv pulse: theoretical prediction of Zoller [9]- 1, our result -2, the experimental data [11] of Kelleher, Ligare and Brewer - 3 (multimode Gaussian bandwidth of 0,25 cm^{-1}; the full width at half maximum).One can see an excellent agreement between the theoretical predictions&experimental data.In conclusion we should want to note that the analogous quantum-electrodynamical approach may be proposed for description of optical properties of dense plasma by means the set of moments m.To define m_1 , the Gell-Mann & Low adiabatic formalism is used (T=0,T=0). Some calculations:4-photon ionization Cs profile, shift for the Ar-plasmas [n=10^{17} cm^{-3}; T=15000 K] and the H-plasmas are in progress. Authors are grateful to Prof.Dr. L.N.Ivanov for useful comments.

References

1. Kleppner D. In.:Les Houches Summer School.Ed.Adam J.C.& Ballian R. NY.:Gordon & Breach Sci.Pub.1981.
2. Delone N.B., Kraynov V.P. Atom in the strong light field. Moscow, Atomizdat,1984.
3. Ivanov L.N. Izv.AN of USSR. 48 1273 (1984) .
4. Glushkov A.V.,Ivanov L.N. Preprint ISAN N2-AS,1992.
5. Glushkov A.V., Ivanov L.N. Phys.Lett. 170 33 (1992).
6. Glushkov A.V. Abstr.IY Europ.Conf.At.Mol.Phys. Riga,1992.
7. Janjusevic M.,Mittleman M. J.Phys.B. 21 2279 (1988).
8. Georges A.T., Lambropoulos P. Adv.Electr.& Electr.Phys. 54 191 (1980).
9. Zoller P. J.Phys.B. 15 2911 (1982).
10. Lompre L.A.,Mainfray G.,Manus C.,Marinier J.P. J.Phys.B. 14 4307 (1981).
11. Kelleher D.E., Ligare M.,Brewer L.R. Phys.Rev.Lett. 31 2747 (1985).
12. Casati G. Nuovo Cim.110B 671 (1995).
13. Ullrich C.A.,Erhard S., GrossE.K.U. In: Super Intense Laser Atoms Physics IV. Kluwer,1996. Ed.Muller H.G.
14. Glushkov A.V. et al in press (1996).


Γ2
Γ3
Γ1
dw2
dw3
dw1
Width and Shift (cm⁻¹) : Γ, dw
0
2
4
0
1
2
3
Mean Laser Intensity : I
(10¹⁰ W cm⁻²)

SPECTROSCOPY OF Ne-LIKE MULTICHARGED IONS AND Ne-LIKE PLASMA AS AN ACTIVE MEDIUM FOR X-RAY LASING:ATOMIC DATA

A.Glushkov#*, S.Ambrosov#, S.Dan'kov#, A.Efimov#
#Dept.Appl.Math.&Lab.At.-Nucl.Spectr.,OHMI,Perekopskoy diviz. str.12"6"-29, Odessa, SU-270009, Ukraine (for contact)
*Institute of Spectroscopy, Russian Academy of Sciences (ISAN), SU-142092, Troitzk, Moscow region, RUSSIA

Laboratory X-ray investigations supplemented recently with new ideas concerning resonant photoionization as a pumping mechanism (c.f.[1]).It is known that the spectral intensity of a pump line would be more than 10^{10} w/cm^{2}mA.In this case a presence of strong electric microfields complicates the prediction of the spectroscopic characteristics for ions.As result a comprehensive theoretical model to describe laser enhancement in plasma is't elaborated yet. Ne - like scheme for lasing represented to be one of the promising schemes. In this light precise calculations of energies & transition probabilities,excitation crossections-of a great importance

In paper there are presented results of the calculations and compilation of data [3] for wavelengths of some 3-3,3-4 electron& 2-2 vacancy transitions for Ne-like isoelectronic sequence (Z=19-84) on base of the perturbation theory with model zeroth approximation [4-6] (see table: Z=20-26).

Authors are grateful to Prof.Dr. E.P.Ivanova for useful comments.

References

1. Gulov A.V. & Ivanova E.P.,Int.Conf. "Short wave laser ampliphication" ,Samarkand, (1990).
2. Ivanov L.N.,Ivanova E.P.,Glushkov A.V. and Kramida A.E. 1985 Phys.Scripta. 24, 512.
3. Glushkov A.V.& Ivanova E.P., 1986 JQSRT. 36, 127.
4. Ivanov L.N.,Letochov V.S. Com.Mod.Phys.D 16, 95 (1992).
5. Ivanova E.P. Habil.Doctor thesis, Moscow, (1992).
6. Glushkov A.V.,Ivanov L.N. Phys.Lett.A.170, 33 (1992).
7. Glushkov A.V.,Ambrosov S.V. et al, Int.J.Quant.Chem., to be submitted.

Table. Theoretical energy levels of Ne-like ions (in 100 cm^{-1})

Conf.	Term	J/Z	20	21	22	23	24	25	26
	^3P	2	28021	32355	36987	41915	47142	52668	58491
		1	28110	32456	37099	42040	47278	52815	58648
$2p^5 3s$		0	28314	32728	37453	42492	47846	53518	59510
	^1P	1	28399	32815	37543	42585	47943	53618	59613
	^3S	1	29543	34025	38809	43892	49276	54961	60944
	^3D	2	29777	34271	39063	44154	49543	55230	61215
$2p^5 3p$		3	29779	34283	39090	44199	49611	55326	61345
		1	29860	34369	39179	44290	49702	55416	61433
	^3P	2	29928	34446	39266	44389	49874	55543	61591
		1	30159	34743	39643	44861	50399	56260	62446
		0	30083	34638	39500	44669	50147	55933	62029
	^1P	1	30065	34631	39511	44705	50215	56043	62191
	^1D	2	30159	34748	39654	44878	50423	56290	62484
	^1S	0	30983	35636	40596	45946	51528	57416	63633
	^3P	0	31961	36655	41650	46946	52544	58445	64649
		1	31993	36694	41696	47000	52607	58517	64730
$2p^5 3d$		2	32056	36769	41785	47103	52737	58649	64878
	^3F	4	32090	36800	41812	47126	52742	58663	64888
		3	32136	36851	41868	47185	52805	58727	64953
		2	32205	36931	41947	47825	52915	58847	65084
	^1F	3	32260	36990	42021	47354	52990	58930	65174
	^3D	1	32407	37168	42232	47602	53278	59261	65550
		2	32488	37282	42390	47818	53566	59631	66027
		3	32500	37296	42411	47844	53597	59674	66077
	^1D	2	32453	37243	42348	47770	53512	59576	65965
	^1P	1	32869	37706	42856	48322	54104	60205	66627
	^3S	1	35318	40108	45313	50830	56674	62832	69311
$2s2p^6 3s$	^1S	0	35555	40477	45714	51262	57139	63328	69840
	^3P	0	36930	41975	47334	53007	59007	65321	71958
		1	36945	41993	47356	53033	59038	65357	71999
$2s2p^6 3p$		2	36987	42050	47431	53128	59159	65508	72185
	^1P	1	37104	42176	47565	53271	59310	65667	72352
	^3D	1	39239	44500	50078	55972	62199	68743	75615
$2s2p^6 3d$		2	39241	44503	50083	55979	62207	68753	75628
		3	39244	44508	50090	55989	62220	68770	75650
	^1D	2	39476	44768	50379	56305	62564	69143	76049

ELLIPSOMETRICAL INVESTIGATIONS OF STAINLESS STEEL MIRRORS IRRADIATED BY CHROMIUM IONS

A. F. Bardamid, L. V. Poperenko, M. V. Vinnichenko, V. S. Voitsenya*, K. I. Yakimov

National Kyiv Taras Shevchenko University, Kyiv, Ukraine

*Kharkiv Institute of Physics and Technology, Kharkiv, Ukraine

The aim of the present investigation is to further clarify the nature of optical properties' changes for the metallic mirrors after their preliminary irradiation by highly energetic metallic ions and further sputtering by other ions.

The samples were prepared by mechanical polishing from stainless steel 00X16N15M3B. The specimens of the stainless steel mirrors were implanted by Cr^+ ions with E_i=3 MeV and dose 11 dpa [1, 2].We have studied non implanted mirrors as well as implanted.

As a method of investigation of mirror's microstructure we have applied transmittion electron microscopy (TEM). On the base of TEM data, model of the reflective surface for further optical studies was constructed. The measurements of optical properties were carried out by means of both angular and spectral ellipsometrical techniques because of their unique sensitivity to structural modifications of surface. The angular dependencies measurements of the phase shift Δ between p- and s- components of linearly polarized light and azimuth of restored linear polarization ψ were carried out on laser ellipsometer ЛЭФ-3М-1 with working wave length λ=632.8 nm. Then, we have determined principal angle of incidence φ_0 ($\Delta=\pi/2$) and value of the angle of incidence under the minimum of $tg\psi(\varphi)$ dependence. Calculations of refraction n and absorption k indices were performed using certain values of the φ_0 and corresponding azimuth of restored linear polarization ψ_0 with further calculations of reflection coefficient (RC) [3]. The spectral measurements of the optical conductivity and RC were fulfilled on the ellipsometer within probing photons' energy range 1-5 eV by Beattie method.

TEM has not revealed significant changes in mirrors' microstructure after the irradiation by Cr^+ (irradiated sample in comparison with non irradiated one) under the rough resolution.

It was very interesting to study changes of microrelief of subsurface's layers of stainless steel mirrors by means of ellipsometrical measurements under implantation and irradiation by different ions. Results of optical measurements are presented on Fig. 1, 2. As a result of angular ellipsometrical studies it was observed the decrease of principal angle from 77^0 (non irradiated sample) to 75.5^0 (sample after irradiation by Cr^+ ions) and RC's decrease on ~10% at the wavelength 632.8 nm. Dependencies of $\cos\Delta(\varphi)$ before and after irradiation are shown on the Fig. 1.

Besides, spectral dependencies of optical conductivity (OC) and reflection coefficient were measured for stainless steel mirrors. Optical conductivity spectra of irradiated by Cr^+ ions and non irradiated mirrors are shown on Fig. 2. OC spectra have Drude-like dependency within 1-2 eV before implantation as well as after implantation by chromium ions. The non implanted sample has peculiarities of OC within 2-3 eV and 4-5 eV. Implantation led to smearing of the peculiarities and to decreasing of OC values in whole spectral range. RC slightly decreases within 1-2 eV and increases within 2-5 eV. Additionally, we have studied dependence of optical parameters from positioning of probing laser beam spec on the implanted steel specimen by angular ellipsometry. It was obtained that optical parameters have high homogeneity through the surface.

According to [4], consideration of such surfaces is possible using effective medium approximation. We ought to study continuous inhomogeneous effective layer instead of real layer. It is possible to apply Lorents-Lorents approximation. Using such model we shell infer that the higher the thickness of the dielectric layer on the metallic surface the smaller the corresponding principal angle and reflection coefficient. That is why, on the basis of TEM measurements we may conclude that bombardment by Cr^+ does not cause significant changes of microrelief of stainless steel mirrors. Significant changes of the optical properties of stainless steel mirror after the Cr^+ ion bombardment would be associated with carbon layer arose on the mirror's surface after the implantation without modification of surface's microstructure. Thus, the increasing of RC within the ultraviolet region of spectrum could be associated with decreasing of surface's roughness under the growth of carbon layer that is in accordance with tunneling microscopy data. The Auger spectrometer measurements have shown an increased carbon content in the subsurface layer after ion treatment [2]. One of the reasons for of a fairly great

amount of carbon on the irradiated sample is in the presence of organic oil vapors coming to the irradiation chamber from operating turbomolecular pumps.

It is interesting that for copper mirrors irradiated by Cu^+ ions grows of the carbon layer has not observed. It would be explained in following way. Ion beam of copper ions is consisted from Cu^+ and Cu^{++} ions. In case of Cu^{++} ions appeared O^{++} ions that could not be separated from Cu^{++} ions. As a result, C and O^{++} forms CO_2 molecule on the surface of the copper mirror that leave the surface. Besides, implantation by Cu^+ (E=3 MeV) ions of copper mirrors with further sputtering by He^+ (E=4 keV) leads to more significant modification of the surface's microstructure than simple sputtering by He^+ of non implanted areas of copper mirrors [6]. The latter is in good agreement with TEM data for such samples. The roughness of the mirror on the implanted by copper ions area is caused by blisters of 2.5 μm and on the half of the area the holes appears instead of blisters, that is shown on the TEM microphotograph. Blistering phenomenon [4] is typical for the metal's surface sputtering by light ions. Appearing of the holes could be caused by breaking up of blisters' covers; the greater the thickness of removed layer the bigger dimensions of blisters and the area occupied by them becomes large. On the non implanted area of copper mirrors changes of microrelief after the He^+ treatment were not so noticeable.

This work was supported in part by the International Soros Science Education Program (ISSEP) through grant N PSU062017.

1. V. S Voitsenia, V. V. Gann, et al. Fizika Plasmy, **20** (1994) 237 (in Russian)

2. Yu. N. Borisenko, V. V. Bryk, et al. Plasma Devices and Operations, **3** (1994) 157

3. A. M. Borbat et al. "Optical Measurements," Kiev, Tehnika, 1967, P. 331 (in Russian)

4. D. E. Aspnes, J. B. Theeten. Phys. Rev. B., **20** (1979) 3292

5. "Sputtering of solids by ion bombardment," Ed. by R. M. Berish , Moscow, Mir, 1986, P. 360 (in Russian)

6. L. V. Poperenko, A. F. Bardamid, et al. Proceedings of XII Interen. Conf. VIP'95, Zvenigorod, 2 (1995) 329

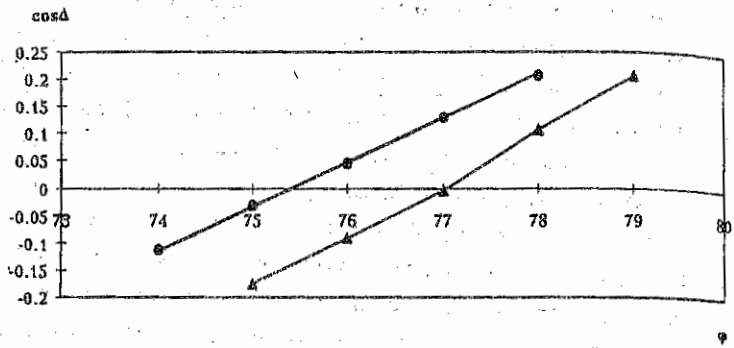


Fig. 1 Angular depsndencies of the ellipsometric parameter cosΔ for stainless steel mirrors irradiated by Cr^+ (3 MeV, 11 dpa) ions (⊕) and non irradiated by Cr^+ (▲)

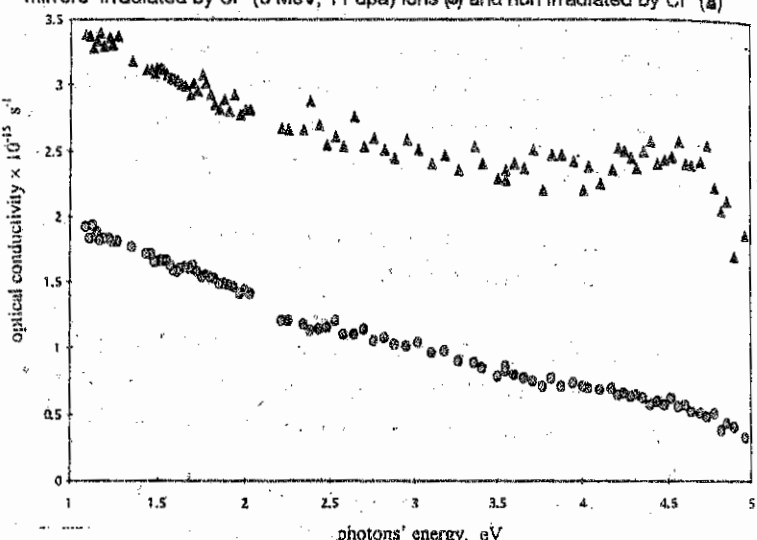


Fig. 2 Optical conductivity spectra of the irradiated (⊕) and non irradiated (▲) samples of the stainless steel mirrors

Spectroscopic investigation of Carbon IV

M Tunklev, L Engström, C Jupén, I Kink, I Martinson
and A Meigs*

Department of Physics, University of Lund, Sweden.
*JET Joint Undertaking, Abingdon, Oxfordshire, OX14 3EA, UK.

INTRODUCTION

One of the most common impurity ions in plasma physics is carbon. In view of the importance of this element a detailed spectral analysis of C IV has been carried through. Using 1.5 - 3MeV ion beams from the Pelletron accelerator at Lund we have recorded high-resolution beam foil spectra at 500 - 5000 Å. The analysis is based on data from previous investigations by B. Edlén using a spark source [1], and on new observations based on beam foil technique and from plasma spectroscopy at JET. Some of the most reliable transitions from the stark effected term system of K. Bockasten [2] has also been used for building up the new term system. The advantage of using several different methods in the analysis is clearly to have all their different merits and to avoid the drawbacks. A number of 105 transitions between 200-7750 Å are now building up the new term system from which accurate extended semi empirical calculations can be performed if necessary. Energy levels up to n=12 is given, table 1, from which VUV resonance transitions can be calculated with higher precision than previous experiments, and may thus be preferred as wavelength standard for calibration of spectra. The ionization energy has been determined to 520176.1 ± 1.5 cm^{-1} , which implies an accuracy comparable to 1/5 of the QED effect. The paper was recently published as a JET preprint, Maj. -96 [3], and is to be submitted to Physica Scripta.

EXPERIMENT

Intense beams of C ions were obtained from the 3 MV Pelletron tandem accelerator at Lund. The ions were accelerated to 1.5, 2.5 or 3 MeV energy and directed through a thin carbon foil. The optimum energy for the production of C^{3+} is around 1.5 MeV. But the additional energies allowed us to make charge-state classifications of the

observed lines by studying their relative intensities as a function of energy. Furthermore, at the higher energies all C II and all but the most intense C III lines have disappeared, leaving a cleaner spectrum of only C IV and C V lines. The light emitted by the foil-excited ions was analyzed with a Minuteman 310 NIV 1 m normal incidence vacuum monochromator, which can be equipped with a number of interchangeable concave gratings. The present work is based on spectra recorded in the 500 - 5000 Å range, using a number of different grating/detector combinations to optimize the experimental conditions. The different detectors used were a CsI coated channeltron, an EMR 541 photomultiplier equipped with a LiF window and a Hamamatsu R 585 photomultiplier. Both a 600 l/mm and a 1200 l/mm grating were used. Several transitions could thus be detected in 3rd or even 4th order giving an accuracy of 0.05 Å for well resolved transitions below 2400 Å. For transitions in the visible range an uncertainty around 0.1 - 0.15 is obtained. Parts of the spectra has been used for previous analysis on C V [4] and core excited levels in C IV [5].

To determine the wavelengths of the observed lines we followed a two step procedure. First the peak positions were found using both an automatic peak-finding routine and an interactive program (CARATE [6]) that fits a sum of Gaussians to the observed spectrum. These peak positions were then converted to absolute wavelengths using polynomial calibration functions derived from accurately known in-beam reference lines. By weighting different observations of the same transition and calculate their weighted mean value the most accurate wavelength is achieved. Combining the transitions identified in this work with the previously known material a well connected term system is established. The best estimates of the energy levels are derived from the observed transitions in a least-squares procedure where each line is weighted by its estimated wavenumber uncertainty.

The JET charge exchange spectra used in this work are obtained along a vertical line of sight intersecting the neutral beam perpendicularly, where no Doppler shifts should affect the measurements. The spectra were recorded by means of the new KT3D spectrometer, equipped with a 300 l/mm grating and imaging around 12 cm of the divertor region. The spectrometer with its CCD detector covers an interval of about 500 Å at each setting between 4000 and 8000 Å, with an observed line width ranging from 1.5 to 4 Å. The uncertainty in the peak positions is estimated to 0.1 - 0.2 Å.

Table 1: Energy levels in C IV.

Level	Energy [a] /cm^{-1}	ΔE^{b} /cm^{-1}	N[c]	o-c[d] /cm^{-1}
$2s\,^2S$	0.0	0.0	12	0.0
$3s\,^2S$	302847.8	0.2	8	0.0
$4s\,^2S$	401346.5	0.6	9	0.8
$5s\,^2S$	445365.7	0.5	9	-0.6
$6s\,^2S$	468782.5	0.2	6	0.1
$7s\,^2S$	482704.0	1.2	1	-0.6
$8s\,^2S$	491649.1	0.7	1	-0.4
$9s\,^2S$	497735.6[e]			
$10s\,^2S$	502062.0	1.3	1	-0.9
$11s\,^2S$	505249.4[e]			
$12s\,^2S$	507663.4[e]			
$2p\,^2P_{1/2}$	64483.8	0.5	10	0.0
$2p\,^2P_{3/2}$	64591.0	0.5	10	
$3p\,^2P_{1/2}$	320048.9	0.2	7	0.0
$3p\,^2P_{3/2}$	320080.4	0.2	7	
$4p\,^2P_{1/2}$	408308.6	0.6	9	-0.4
$4p\,^2P_{3/2}$	408321.8	0.5	9	
$5p\,^2P_{1/2}$	448854.2	0.2	6	0.3
$5p\,^2P_{3/2}$	448861.2	0.2	6	
$6p\,^2P_{1/2}$	470772.8	0.5	6	-1.0
$6p\,^2P_{3/2}$	470776.6	0.5	6	
$7p\,^2P$	483946.9	1.3	4	-1.8
$8p\,^2P$	492478.2	0.5	3	0.7
$9p\,^2P$	498314.2[e]			
$10p\,^2P$	502481.8	1.2	1	-1.3
$11p\,^2P$	505564.1[e]			
$12p\,^2P$	507905.1[e]			
$3d\,^2D_{3/2}$	324878.5	0.8	6	-0.7
$3d\,^2D_{5/2}$	324887.7	0.8	6	
$4d\,^2D_{3/2}$	410334.4	0.4	8	1.0
$4d\,^2D_{5/2}$	410338.3	0.4	8	
$5d\,^2D_{3/2}$	449885.5	0.5	11	-1.0
$5d\,^2D_{5/2}$	449887.5	0.5	11	
$6d\,^2D_{3/2}$	471369.6	0.3	6	0.0
$6d\,^2D_{5/2}$	471370.8	0.3	6	
$7d\,^2D$	484320.0	0.5	6	-2.0
$8d\,^2D$	492726.1	0.6	4	-1.2
$9d\,^2D$	498489.5[e]			
$10d\,^2D$	502608.7	1.3	1	-2.1
$11d\,^2D$	505659.9[e]			
$12d\,^2D$	507978.9[e]			

Level	Energy [a] /cm^{-1}	ΔE^{b} /cm^{-1}	N[c]	o-c[d] /cm^{-1}
$4f\,^2F$	410431.5	1.1	5	-0.2
$5f\,^2F$	449941.3	0.7	5	1.2
$6f\,^2F$	471402.4	1.2	3	0.8
$7f\,^2F$	484341.9	0.4	4	-0.2
$8f\,^2F$	492740.8	0.5	3	-0.1
$9f\,^2F$	498499.1[e]			
$10f\,^2F$	502617.8[e]			
$11f\,^2F$	505665.2[e]			
$12f\,^2F$	507983.0[e]			
$5g\,^2G$	449945.2	1.9	1	-0.2
$6g\,^2G$	471405.8	0.9	2	1.1
$7g\,^2G$	484345.6	1.3	2	1.4
$8g\,^2G$	492743.8	1.9	2	1.4
$9g\,^2G$	498500.1[e]			
$10g\,^2G$	502618.6[e]			
$11g\,^2G$	505665.8[e]			
$12g\,^2G$	507983.4[e]			

a: Fine structure splittings in the *np* series are given as $\Delta_{np}=\Delta_{2p}(n^*_{2p}/n^*_{np})^3$, whereas in the *nd* series the hydrogenic values are used.
b: Relative uncertainty. An absolute error estimate is obtained by adding 1 cm^{-1}, corresponding to the uncertainty in the ground level.
c: Number of combinations.
d: Difference between the observed energy value and that calculated from the semi-empirical series formulae. For the *ns* and the center-of-gravity of the *np* and *nd* series the Ritz formalism is used whereas for the *nf* and *ng* series we have applied the polarization formula.
e: Extrapolated value from the series formulae (as defined in footnote d).

REFERENCES

[1] B. Edlén, Nova Acta Reg. Soc. Sci. Ups 9 No. 6 (1934).
[2] K. Bockasten, Arkiv Fysik 10, 567 (1956).
[3] M. Tunklev et al, JET preprint JET-P(96)15 (1996).
[4] L. Engström, P.Bengtsson,C. Jupén and M. Westerlind, J.Phys. B25, 2459 (1992).
[5] L. Engström, R. Hutton, N. Reistad, I. Martinsson, S. Huldt, S. Mannervik and E. Träbert, Physica Scripta 36, 250 (1987).
[6] L. Carlén, Internal Report LUNFD 6 (NFFK-7014) University of Lund (1982).

Influence of the Earth electrostatic field on sodium atoms emission from the D-ionosphere

V.M.Ivchenko, V.M.Malnev and Eu.V. Martysh
Taras Shevchenko Kyiv University,
252017 Kyiv, Ukraine

In this communication we consider the increasing mechanism of sodium atom emission from the *D*-ionosphere under the action of the perturbation of atmospheric electric field before the strong earthquake. This emission can be observed in the night time and may be a forerunner of the coming earthquake.

It is well known that the *D*-ionosphere contains a considerable amount of nitrogen and sodium. It happens to be that the eighth vibration level of a nitrogen molecule practically coincides with the first excited state of a sodium atom with an energy $E_{Na} = 2{,}1\ eV$. Thus, the resonant transfer of the energy of vibration excited nitrogen to the sodium electron excitation regularly occurs in the following elementary process

$$N_2(v >> 1) + Na \rightarrow N_2(v') + Na^*, \qquad (1)$$

where N_2 denotes a nitrogen molecule, v and v' are vibration quantum numbers of a nitrogen molecule before and after reaction, Na and Na^* denotes sodium atoms in the ground and excited states, relatively.

The cross-section of process (1) is quite large and according to the experimental measurements is $5 \times 10^{-15} cm^2$ [1]. Obviously that the resonant sodium radiation can be observed in the spectrum of night ionosphere. We have to note that this mechanism is supplementary to the conventional chemical excitation of sodium atoms, which gives a contribution of the sodium doublet about 200 Rayleigh in the radiation of the night ionosphere [2].

The vibration excited nitrogen molecules can appear in the process of the inelastic electron-nitrogen collisions. At the night time at normal conditions, the electron concentration in the ionosphere *D*-layer is of the order of $10^4 cm^{-3}$ and the corresponding electron temperature does not exceed 500K. At these conditions, a number of vibration excited nitrogen molecules is exponentially small.

The situation may change, if an additional source of hot electrons appears. It was reported that before and at the time of the strong earthquakes in its epicenter do-

main, the perturbations of the atmospheres electrostatic field with amplitude of $10-10^3 V/m$ have been registered on the Earth surface [3]. These localized perturbations can also manifest themselves in the ionosphere as well. The calculation of the electric field distribution with an altitude shows that the perturbation efficiency of the electric field in the ionosphere is much higher at the night time than at the day time. It strongly depends on a localization domain of the perturbation and happens to be $30-70\ mV/m$ (for large seismic sources ~100 km and when the electric field in the epicenter on the Earth surface is of the order of $10^3 V/m$) [4].

The influence of the seismic electric field on the background distribution of the ionosphere plasma in the night D–domain is considered in [4] as well. The maximum effect takes place in the upper part of the D–domain where the Pedersen ion drift is the most strong. The character of the ionosphere perturbation depends on a direction of the electrostatic field induced by a seismic source in the epicenter of coming earthquake. This electric field may cause a considerable increase of metal ions in the D–domain at altitudes ~120 km for account of the electrophoresis separation of heavy ions. There is a maximum of the electron concentration, as well, which is by one order higher than the initial electron concentration in the same domain. The typical dimensions of this layer are ~100 km in a length and ~10 km in a thickness.

Thus, on one side, the perturbations of the atmospheric electric field before the strong earthquake favor the formation of a layer with increased concentration of sodium ions and atoms in the D – ionosphere. On the other side, the electric field in this layer, with the increased electron concentration, will heat-up electrons.

We can evaluate the electron temperature in the D–ionosphere layer in the presence of the seismic electric field by using the results [5]. Assuming that the seismic electric field is normal to the geomagnetic field and has an amplitude of the order of $10^{-4} V/cm$, we obtain that the electron temperature is approximately 1000-1300K at an altitude 100-120 km. It is well known that the vibration excitation of nitrogen at this temperature is more efficient, and the vibration temperature of the lowest levels is practically equal to the electron temperature.

The population of the vibration levels in this case differs considerably from the conventional Boltzmann distribution (even a population of the third vibration level is higher by 300 times compared with the corresponding Boltzmann population). Knowing the electron temperature and taking into account that the distribution function in vibration levels has a plateau in the middle range of vibration numbers [6], we can evaluate a number of nitrogen molecules excited on the eighth vibration level by the electron impact. Here, we cite a final result. It says that a number of nitrogen atoms excited on the eighth vibration level is $n_{N_2} \approx 3 \times 10^7 cm^{-3}$.

In conclusion, we give a rough evaluation of the intensity of sodium doublet I, which emerges by virtue to the above discussed mechanism, from unit volume of the ionosphere

$$I = \hbar\omega\sigma v n_{Na} n_{N_2} \qquad (2)$$

where $\hbar\omega = 2{,}1\ eV$ is the energy of sodium transition from the first excited state to the ground that, $\sigma = 5 \times 10^{-15} cm^2$ is the cross-section of the resonant transfer of the nitrogen vibration energy, $v = 2 \times 10^4 cm/s$ is the velocity of sodium atoms (with respect to nitrogen molecules), $n_{Na} \approx 3 \times 10^6 cm^{-3}$ and $n_{N_2} \approx 3 \times 10^7 cm^{-3}$ are the concentrations of sodium atoms and vibration excited nitrogen molecules in the *D-layer*, respectively. To compare this with the intensity of the conventional sodium doublet (200 Rayleigh $\approx 7 \times 10^{-4} erg/(cm^2 s)$), we have to multiply (2) by a factor 1/6 and by a thickness of the *D*-ionosphere layer enriched by sodium atoms $h = 10\ km$. After substitution of the typical numerical values of the parameters, we obtain $Ih/6 \approx 5 \times 10^{-3} erg/(cm^2 s)$ which exceeds almost by one order the conventional radiation of the sodium doublet.

The increasing in the intensity of the sodium doublet in the spectrum of the night ionosphere can be registered by monitoring of the night sky over the seismic dangerous regions and can be considered as a prediction of the coming earthquake.

This work was supported in part by the ISSEP grant № APU 062067.

References

1. E.L. Milne, Sodium atom excitation in nitrogen afterglow, J. Chem. Phys., vol. 52, №10, 53 (1970).

2. L.M. Fishkova, Night radiation of the middle latitude upper earth atmosphere, "METsNIEREBA", Tbilisi (1983).

3. G. Kondo, The variation of the atmospheric electric field at the time of earthquake, Memories of the Kakuoka magnetic observatory, vol.13, №1, 11(1968).

4. V.P. Kim, V.V., V.V.Khegai, and P.V. Illich-Svitych, On the possibility of metal ions layer formation in the E-domain of the night middle latitude ionosphere before a strong earthquake, Geomagnetism and aeronomiya, vol. 33, №5, 114 (1993).

5. A.V. Gurevich, A.B. Shvarzburg, Non-linear theory of electromagnetic waves propagation in the ionosphere, Nauka, M. (1973).

6. V.D. Rusanov, G.V. Sholin, Physics of chemically unequilibrium plasma, NAUKA, M., (1984).

Formation of a new phase nucleus in an excited dipole plasma

G.Eu. Chaika and V.M. Malnev

The Ukrainian Academy of Communication
Taras Shevchenko University
252017, Kyiv, Ukraine

In this communication we consider some properties of a weakly ionized plasma when a considerable part of atoms of its neutral component is excited on the same electronic level by an external pumping. It is well known that in the thermal equilibrium a number of excited atoms in a weakly ionized plasma is small enough. Let an external source of energy (laser radiation, electron beam, and so on) acts on the neutral component of the plasma and stationary excites some amount of atoms. We call such a plasma is an excited dipole plasma. In excited state atoms gain the virtual dipole moment and can interact much stronger than those in the ground state. The operator of interaction between two excited atoms can be obtained in the dipole-dipole approximation considering them as immersed in a medium of the electron-ion plasma. The latter can be taken into account by dividing the operator of dipole-dipole interaction by the plasma dielectric permitting.

The thermodynamic properties of a resonant excited gas of neutral particles with no plasma firstly has been studied in [1] where was shown that even at comparatively small percentage of excited atoms causes strong departure of the gas from perfectness. The thermodynamic functions of a dipole plasma consisting molecules with constant electric dipoles as a neutral component were analyzed in [2].

Density numbers of excited particles n satisfy the following continuity equation with source associated with creation of excited particles from unexcited with the help of the external pumping and their decaying:

$$\frac{\partial n}{\partial t} + div\vec{j} = \alpha - \frac{n - n_0}{\tau}, \qquad (1)$$

where α is a number of excited particles appearing in unit volume of the system per unit time, the coefficient α is determined by the intensity of the external pumping creating excited particles, n_0 is the density number, τ is the time life of exciting particles. The flow density of excited particles can be presented in the form

$$\vec{j} = -D\left[\nabla n - \frac{nF}{T}\right]. \tag{2}$$

Here D is the diffusion coefficient, T is the system temperature. The force F, which acts on an excited particle from the rest of excited particles, is given by the expression

$$\vec{F} = -\nabla \int U(\vec{r}, \vec{r}')\, n(\vec{r}')\, d\vec{r}' \tag{3}$$

where $(\vec{r}, \vec{r}')$ is the effective interaction between excited particles immersed in the electron-ion plasma.

After substitution of (2) in (1) with taking account of the expressions for F, we obtain the nonlinear integro-differential equation which describes the space-time dependence of density numbers of excited particles in the electron-ion plasma:

$$\frac{\partial n}{\partial t} = D\left[\Delta n + \frac{n}{T}\Delta_r \int U(\vec{r}, \vec{r}')\, n(\vec{r}')\, d\vec{r}'\right] + \alpha - \frac{n - n_0}{\tau}, \tag{4}$$

The possible formation of the so called dissipative structures is connected with the nonlinear terms in (4) [3, 4].

A stationary solution of equation (1) corresponds to a uniform distribution of excited n_s=*const* particles:

$$n_s = n_0 + \alpha\tau. \tag{5}$$

We consider now small departures from the stationary uniform distribution of excited particles. Introducing small perturbations of density numbers $n' << n$, we linearize equation (4) and perform the space Fourier transform. As a result, we obtain the first order linear differential equation, which describes the time dependence of the density number perturbation $n_k(t)$, k is a wave number of the Fourier transform. Seeking a solution of this equation in the form $\sim exp(pt)$, we can find the connection between the wave vector k of the Fourier amplitude and the parameter p:

$$p = -k^2 D\left[1 + \frac{(n_0 + \alpha\tau)U(k)}{T}\right] - \frac{1}{\tau}. \tag{6}$$

At a low level of the external pumping $\alpha\tau<<1$, $p<0$, and the small perturbations of the uniform distribution of excited particles decay with time. On increasing the pumping level for negative $U(k)$ (which corresponds to the attractive

interaction between excited particles) the parameter p passes through zero and becomes positive. This means that the uniform distribution of excited particles is unstable.

We have to note that the condition $\frac{(n_0+\alpha\tau)|U(k)|}{T}>1$ can be satisfied only in a dense dipole plasma at high level of the external pumping $\alpha\tau>>1$. This condition can be realized more easy in a solid state plasma.

The typical size of the inhomogeneity λ, that appears at high level of the external pumping, can be evaluated from formula (6) at p=0:

$$\lambda^2 \approx 4\pi^2 D\tau \frac{T}{(n_0+\alpha\tau)|U(k)|}. \qquad (7)$$

Here we assumed that $U(k)$ weakly depends on the wave vector k.

A further analysis needs the solution of the nonlinear integro-differential equation (3), which can be done only by the numerical methods.

We consider now the thermodynamic approach to the problem assuming that at definite level of the external pumping the uniform distribution of excited particles is unstable.

At the same time, two phases with different contain of excited atoms coexist and they are more thermodynamic profitable. Let total numbers of particles in the first and second phases be

$$N_1+N_2=N, \qquad (8)$$

where N_2 relates to excited particles, N is a total number of particles.

We consider two coexisting homogeneous phases and assume that excited and unexcited particles located in these phases are in different quantum states. The probability of realization of the situation when N_1 particles are in the first phase and N_2 – in the second phase is given by the expression

$$P = \frac{N!}{(N-N_1)!N_1!}\cdot\frac{N!}{(N-N_2)!N_2!}\cdot exp[-E], \qquad (9)$$

where the energy of the configuration E is

$$E = wN_2 - \gamma N_2^{2/3}. \qquad (10)$$

Here w is the energy needed to transfer a particle from the phase one to the phase two (we put the energy of a particle in the first phase is equal to zero), the second term in (9) phenomenologycally describes the surface energy of the second phase.

The equilibrium state of the system corresponds to the distribution of excited and unexcited particles which realizes a maximum of probability (9) with taking account of constraint (8). In other words, we have to find an extremum of the functional

$$\Phi = \ln P + \mu(N_1 + N_2) \tag{11}$$

with respect to N_1 and N_2. Even in this simple case, we need the numerical analysis of the obtained formulas. Below we described the main conclusions of the analysis. The conditional probability (9) as a function of $x = \frac{N_2}{N_1 + N_2}$ has two maxim at $x = x_1$ and $x = x_2$. At $0<x<x_1$ and $x_2<x<1$, the uniform distribution of the excited and unexcited particles corresponds to the thermodynamically equilibrium state. If $x_1<x<x_2$, then the uniform distribution is unstable and the system decay in two phases excited and unexcited particles. This situation can be understood if we note that the expression (10) changes its sign at $N_2 = (\gamma / w)^3$. This means that the bulk energy begins to exceed the surface energy and the separated phases of excited and unexcited particles become more energy profitable. The phenomenology parameters can specified comparing the results of the numerical solution of (4) for a particular interaction between excited particles.

This work was supported in part by the ISSEP grant № APU 062067.

References

1. V.N. Malnev and S.I. Pekar, The intermolecular interaction and the equation of state of a highly excited gas, Zhur. Eks. Teor. Fiz., vol.51, 1811 (1966).

2. S. Mulugeta and V.N. Malnev, Thermodynamic properties and waves in a dipole plasma, J. Plasma Physics, vol.30, 475 (1988).

3. H. Haken, Synergetics, Springer, New York (1978).

4. V.I. Sugakov, Introduction to synergetics [in Russian] Izdatel'stvo "Kievskii universitet", Kiev (1992).

The Influence of Electron Trapping on the Propagation of the Electrosound Waves in Plasma

H. Abbasi, M.R. Rouhani

Institute for Studies in
Theoretical Physics And Mathematics
Tehran, Iran
and
Department of Physics
Amir Kabir University
Tehran, Iran

It is known that the charged particles trapped by the longitudinal electic field play an important role in nonlinear wave dynamics in plasma [1, 2, 3]. The consideration of the trapped particles is especialy important for discription of the slow motion of the plasma.The trapped particles not only often determine the property of nonlinear wave, but also the possibility of its existance.

At present the investigation of the interaction of high-ferequency (HF) electromagnetic waves with plasma is one of the urgent problems. Under the action of HF field on plasma the average pondermotive force creates charge separation and exitation of low-ferequency (LF) longitudinal waves, which in turn change the particle distribution in usual space.If the intensity of the excited LF longitudinal waves is sufficiently high, then they can capture the particles and change the distribution of particles in the velocity space as well. Such a nonlinear redistribution of particles leads to the changes in the character of the propagation of HF nonlinear waves in plasma.

By taking into account the trapping of plasma particles in present paper a system of coupled equations , which describe the dynamics of LF longitudinal waves and the amplitude of HF electromagnetic waves, is formulated. The influence of particle trapping on the propagation of nonlinear waves is investigated.

Let us consider the plasma being in a constant magnetic field $\vec{B}_0$ along the z-axis and HF field of circularly polarized electromagnetic wave

$$\vec{E} = (1/2)(\vec{e_x} \mp i\vec{e_y})E_0(z,t)e^{-i\omega t} + c.c. \,, \tag{1}$$

where $\vec{e_x}$ and $\vec{e_y}$ are the unit vectors along the corresponding axes; the signs " $\mp$ " correspond to the left and right polarization of the wave. We neglect the motion of ions in HF field.

For describtion of electron trapping we start from the Velasov' s equation.We can write down this equation in the frame , which oscillates with the ferequency of HF field [4].This kind of transformation is convenient for representation of distribution function in the form of a sum of slowly and rapidly varying parts and for the construction of equations for each part [5]:

$$f_e = < f_e > + \tilde{f}_e \,. \tag{2}$$

In (2) $< f_e >$ is the electron distribution function averaged over one period of HF field, $2\pi/\omega$, and $\tilde{f}_e$ is HF part.In what follows we restrict ourselves to the terms of order not higher than E_0^2. It is clear then that $\tilde{f} \simeq E$. After averaging the kinetic equation for the slowly varying electron distribution function we obtain equation:

$$\frac{\partial < f_e >}{\partial t} + v_z \frac{\partial < f_e >}{\partial z} + \frac{1}{m_e}\frac{\partial}{\partial z}[e\phi_s - \frac{\omega}{\omega \mp \Omega_e}\frac{e^2 \mid E_0 \mid^2}{2m_e\omega^2}]\frac{\partial < f_e >}{\partial v_z} = 0 \ , \qquad (3)$$

where $\Omega_e = eB_0/m_e c$ and ϕ_s is the potential created due to the charge separation under the action of the pondermotive force. Eq.(3) is written down for one-dimentional distribution of electrons. We have neglected the electron thermal velocity as compared to the phase velocity of HF wave and have taken into account the sign of the electron charge, $e = \mid e \mid$.

According to [6] eq.(3) describes the capturing of electrons by nonstationary longitudinal field.One can solve this equation if the potential changes slightly during one oscillation period of electrons when they are performing finite motion in the potential well. Unlike [6] the role of the potential in our case is played by the effective potential

$$\phi_{eff} = \phi_s - \frac{1}{2}\frac{\omega}{\omega \mp \Omega_e}\frac{e \mid E_0 \mid^2}{m_e\omega^2} \ , \qquad (4)$$

which also contains the pondermotive potential (the second term in eq.(4)). Using the solution of eq.(3) for the electron density we obtain:

$$n_e = n_0 e^{\phi_m} N(\phi - \phi_m) \ , \qquad (5)$$

$$N(s) = e^s(1 - \Phi(\sqrt{s})) + \frac{2}{\sqrt{\pi}}\sqrt{s} \ , \qquad (6)$$

where $\phi = e\phi_{eff}/T_e \geq \phi_m$ and T_e is the electron temperature, ϕ_m is the value of the effective potential level, which separates the regions of infinite and finite motions and Φ is the error function

$$\Phi(x) = \frac{2}{\sqrt{\pi}}\int_0^x e^{-t^2}dt \ . \qquad (7)$$

From the Maxwell's equations we can find the following equation for the slowly varing complex amplitude of HF field:

$$2i\omega\frac{\partial E_0}{\partial t} + c^2\frac{\partial^2 E_0}{\partial z^2} + \omega^2 E_0 - \alpha\omega_p^2\frac{n_e(z,t)}{n_0}E_0 = 0 \ , \qquad (8)$$

where $\omega_p^2 = 4\pi e^2 n_0/m_e$ and $\alpha = \omega/(\omega \mp \Omega_e)$.

Eqs.(5),(6) and (8) together with the hydrodynamic equations for ions and Poisson equation form a complete system. It is impossible to solve this system of equations analytically in general case. We represent the results of calculation in special cases.

1. Let us consider the stationary distribution of electric field, $E_0 = E_0(z)$ and assume that the potential ϕ_s connected with charge separation is negligible. Then for $\alpha > 0$ we have $\phi = -\varepsilon$, $\phi_m = -\varepsilon_{max}$,where

$$\varepsilon = \frac{\alpha e^2 \mid E_0 \mid^2}{2m_e\omega^2 T_e} \ . \qquad (9)$$

From eqs. (5), (6) and (8) we obtain

$$(\frac{\partial \varepsilon}{\partial x})^2 + V(\varepsilon) = 0 \ , \tag{10}$$

$$V(x) = -\varepsilon[\varepsilon_{max} - \varepsilon - \frac{\alpha\omega_p^2}{\omega^2} e^{-\varepsilon_{max}} \int_0^{\varepsilon_{max}-\varepsilon} N(s)ds] \ , \tag{11}$$

where $x = 2\omega z/c$ and ε_{max} is determined by the maximum value of the amplitude of HF field, $\varepsilon_{max} = \alpha e^2 \mid E_{max} \mid^2/(2m_e\omega^2 T_e)$. Taking into account the behavior of the error function (7) one can show that the quantity N(s) is monotonously increasing function.For the large values of ε_{max} (it means large amplitude of HF field$\mid E_{max} \mid$ or $\alpha >> 1$.) it is easy to satisfy the condition

$$(\frac{2}{\sqrt{\pi}})(\frac{\alpha\omega_p^2}{\omega^2})\varepsilon_{max} < e^{\varepsilon_{max}} \ , \tag{12}$$

(the case $\alpha\omega_p^2/\omega^2 > 1$ is allowed). Then one can show that the effective potential energy (11) becomes zero at $\varepsilon = 0$ and $\varepsilon = \varepsilon_{max}$.Between these two points $V(\varepsilon) < 0$ and it has only one minimum. It means that ε and simultineously the electron density (5) change periodically. The characteristic lenght of their variation is $\simeq c/\omega$.

It must be noted that for $(\alpha\omega_p^2/\omega^2) > 1$,$\alpha > 0$ the magnetized plasma is untranspar-ent.Our results show that due to the action of the strong pondermotive force HF field can deform the electron density distribution, traps electrons and peneterate the plasma.

2.We now cosider the case for small effective potential, $\phi << 1$, and restrict ourselves to the stationary motion of the plasma, when all quantities depend on $\xi = z - ut$. We assume that the characteristic lenght of the wave amplitude variation is larger than that of ϕ. It means that when ϕ is changing, E_0 can be taken as constant: Using the equations (5) and (6) along with the Poisson and ion-hydrodynamic equations one can find:

$$(\frac{\partial \varphi}{\partial \xi})^2 - (1 - \frac{c_s^2}{u^2})\varphi^2 + \frac{16}{15\sqrt{\pi}}\varphi^{5/2} + 2[\varepsilon\frac{c_s^2}{u^2} - (1 - \frac{c_s^2}{u^2})\phi_{min}]\varphi = 0 \ , \tag{13}$$

where $\phi = e\phi_{eff}/T_e$ again, $\varphi = \phi - \phi_{min}$. ϕ_{min} is the minimum of ϕ and ε is determined by (9). In this case the coefficient α can be both positive and negative. The expansion of the error function (7) was used to obtain eq. (13).If the square brackets in the equation (13) becomes zero then the solution has the form of soliton:

$$\phi = \phi_{min} + (\phi_{max} - \phi_{min})cosh^{-4}(\gamma\xi) \ , \tag{14}$$

where $\gamma = (4/15\sqrt{\pi})(\phi_{max} - \phi_{min})^{1/4}$ and we have the following relations:

$$\frac{u^2}{c_s^2} = 1 + (16/15\sqrt{\pi})\sqrt{\phi}_{max} \ , \phi_{min} = (15\sqrt{\pi}/16)\frac{\varepsilon}{\sqrt{\phi}_{max}} \ . \tag{15}$$

If the square brackets in (13) is not zero then the only possibility for bound solution is a periodic one:

$$\phi = \phi_{min} + [s_- + (\sqrt{\phi}_{max} - s_-)dn^2(\beta\xi, k)]^2 \ , \tag{16}$$

where dn(x) is Jacobi elliptic function,

$$s_{\pm} = \frac{15\sqrt{\pi}}{16(\phi_{max}+2b)}[b \pm \sqrt{b^2 + (32/15\sqrt{\pi})b(\phi_{max}+2b)\sqrt{\phi_{max}}}] , \tag{17}$$

$$b = \varepsilon - (\frac{u^2}{c_s^2} - 1)\phi_{min} \quad , \quad k = \sqrt{\frac{\sqrt{\phi_{max}} - s_+}{\sqrt{\phi_{min}} - s_-}} , \tag{18}$$

$$\beta = r_D\sqrt{\frac{\sqrt{\phi_{max}} - s_-}{16(\phi_{max}+2b)}} \quad , \quad \frac{u^2}{c_s^2} = \frac{\phi_{max} + 2(\varepsilon + \phi_{min})}{\phi_{max} + 2\phi_{min}} , \tag{19}$$

and r_D is the electron debye lenght. These parameters should be chosen in such a way to have $s_+ > 0$.

Thus the potential can have the soliton-like shape above a level which depends on the pumping wave and the amplitude of the soliton depends on this level.

References

[1] I. Bernstein, I. Green, M. Kruskal.Phys. Rev., **108**, 546, 1957.

[2] R. Z. Sagdeev, Review of Plasma Physics, M. A. Leontovich, ed., Consultants Bureau, New York. 1966, vol.4.

[3] V. E. Zakharov, V. I. Karpman, JETP, **43**,490,1962.

[4] V. P. Silin, Introduction in the kinetic theory of gases, ed., Nauka, Moscow, 1971.

[5] L. Stenflo, G. D. Tomaradze, N. L. Tsintsadze, Fizika plazmi, **11**, 111, 1985.

[6] A. V. Gurevich, JETP, **53**, 953, 1967.

IMPROVED FUSION PERFORMANCE IN LOW-q, LOW TRIANGULARITY PLASMAS WITH NEGATIVE CENTRAL MAGNETIC SHEAR*

E.J. Strait, T.N. Casper,† M.S. Chu, J.R. Ferron, C.B. Forest, C.M. Greenfield, A.W. Hyatt, L.L. Lao, R.J. La Haye, E.A. Lazarus,Δ G.A. Navratil,◊ B.W. Rice,† A.C.C. Sips,# F.X. Söldner,# B.W. Stallard,† T.S. Taylor, and A.D. Turnbull

General Atomics, P.O. Box 85608, San Diego, California 92186-9784 USA

The fusion performance in DIII–D low-q single-null divertor discharges has doubled as a result of improved confinement and stability, achieved through modification of the pressure and current density profiles. These discharges extend the regime of neoclassical core confinement associated with negative or weak central magnetic shear to plasmas with the low safety factor ($q_{95} \sim 3$) and triangularity ($\delta \sim 0.3$) anticipated in future tokamaks such as ITER. Energy confinement times exceed the ITER–89P L–mode scaling law by up to a factor of 4, and are almost twice as large as in previous single-null cases with $3 \leq q_{95} \leq 4$. The normalized beta [β (aB/I)] reaches values as high as 4, comparable to the best previous single-null discharges, with no confinement deterioration. The peak fusion power gains of $Q_{DD} = 1.0 \times 10^{-3}$ and D–D neutron rates of 1.4×10^{16} s^{-1} are more than double the previous maximum values for single-null discharges. Although high triangularity allows a larger plasma current, the fusion gain in these low triangularity plasmas is similar to that of high triangularity double-null plasmas at the same plasma current. These results are encouraging for advanced performance operation in ITER and for D–T experiments in JET.

Introduction

Plasmas with negative central shear (NCS) may represent an attractive regime for advanced performance operation in ITER, as well as for D–T fusion experiments in existing devices such as JET. Weak or negative magnetic shear, in combination with E×B flow shear, is predicted to stabilize microinstabilities which may be responsible for energy transport. Indeed, there is clear evidence from DIII–D[1–3] and other tokamaks that transport can be reduced to near-neoclassical levels in a central region of negative magnetic shear. This core "transport barrier," accompanied by a reduction in fluctuation amplitude, results in high central pressure.

Stability to long wavelength magnetohydrodynamic (MHD) modes at high beta is necessary to utilize the improved energy confinement in NCS discharges. Calculation and experiment show that the beta limit is sensitive to the plasma profiles and discharge shape. Highly triangular double-null NCS plasmas in DIII–D with strongly peaked pressure profiles disrupt at $\beta_N = \beta\,(I/aB)^{-1} \approx 2$ while discharges with broader pressure profiles reach $\beta_N \lesssim 5$, consistent with MHD stability calculations. However, the improvement in β_N with broadening of the pressure profile is calculated to be small for circular cross-section discharges. The highest fusion performance in DIII–D[4] has been achieved in high triangularity discharges with a relatively broad pressure profile and weak central magnetic shear, consistent with calculated stability limits.

The purpose of the experiments described here was to determine whether a core transport barrier occurs in NCS plasmas with a lower triangularity, single-null configuration similar to JET or ITER,

*Work supported by the U.S. Department of Energy under Contract Nos. DE-AC03-89ER51114, DE-AC05-84OR21400, and W-7405-ENG-48.

†Lawrence Livermore National Laboratory, Livermore, California, USA.
ΔOak Ridge National Laboratory, Oak Ridge, Tennssee, USA.
◊Columbia University, New York, New York USA.
#JET Joint Undertaking, Abingdon, U.K.

whether stability at high beta can be maintained with relatively low triangularity, and whether these properties extend to the low values of safety factor (q_{95} ~3) anticipated in future tokamaks such as ITER. The results will provide input for development of high performance scenarios with negative shear in JET.[5]

Plasma Formation

The experiments were carried out in DIII–D plasmas similar, except in size, to those planned for "advanced tokamak" experiments in JET. The cross-sectional shape of the DIII–D plasma (Fig. 1) closely reproduces a JET model equilibrium, with elongation $\kappa \approx 1.8$ and triangularity $\delta \approx 0.3$. The aspect ratios differ slightly, with A = 2.75 in DIII–D and A = 3.2 in JET. Figures 1 through 3 describe a 1.8 MA discharge with an edge safety factor $q_{95} \approx 3.5$, but 2.0 MA discharges with $q_{95} \approx 3.0$ were also operated with no special difficulty.

Negative central shear profiles are formed by using low-power neutral beam heating during the plasma current rise to slow the penetration of inductive current,[6] as shown in Fig. 2(a). The q-profile in DIII–D is determined from MHD equilibrium fits which include motional Stark effect (MSE) measurements of the internal magnetic field at the locations shown in Fig. 1. A plasma current ramp rate $dI/dt \approx 0.7$ to 1 MA/s is used in both DIII–D and JET, representing a change in safety factor dq_{95}/dt about twice as fast in DIII–D as in JET. Assuming classical current density diffusion and the same electron temperature in both cases, similar q-profiles should result at the same edge safety factor q_{95}, since the smaller radius of DIII–D is compensated by the more rapid time evolution.

As the heating power increases in the current flattop, an internal transport barrier forms, producing a strong rise in central pressure. Although initially the plasma remains in L–mode, the global energy confinement is about 1.4 times the prediction of the ITER–89P L–mode scaling,[7] as seen in Fig. 2(c). In this phase, a region of negative shear ($dq/dr < 0$) extends over a normalized minor radius $0 < \rho < 0.5$, as shown in Fig. 3(a). Profiles of electron density measured with Thomson scattering and

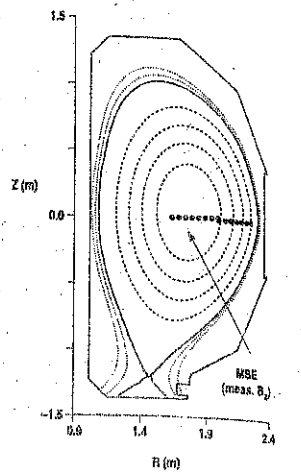


Fig. 1. Cross-section of single-null negative central shear plasma. (Discharge 88964, I_P = 1.8 MA, B_T = 2.1 T).

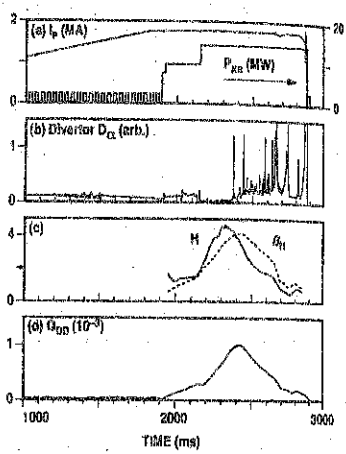


Fig. 2. Time evolution of single-null negative central shear plasma (discharge 88964): (a) plasma current and neutral beam power, (b) D_α emission, (c) energy confinement quality ($H = \tau_E/\tau_{ITER-89P}$) and normalized beta [$\beta_N = \beta\ (I/aB)^{-1}$], and (d) fusion power gain $Q_{DD} = P_{fus}/P_{in}$.

several CO_2 laser interferometer chords, ion temperature measured with charge exchange recombination spectroscopy, and electron temperature measured with Thomson scattering and electron cyclotron emission, shown in Fig. 3, all exhibit strong gradients in the region of weak or negative shear.

Uncontrolled peaking of the pressure profile often leads to disruptions at relatively low beta. Here, an additional increase in beam power at t = 2150 ms ensures an H–mode transition, indicated by the drop in D_α emission in Fig. 2(b), which broadens the pressure profile (Fig. 3) before a stability limit is reached. The confinement quality factor $H = \tau_E/\tau_{ITER-89P}$ rises to a maximum of ~4, as does the normalized beta β_N [Fig. 2(c)], and the fusion power gain Q_{DD} [Fig. 2(d)] reaches a maximum of 1.0×10^{-3} at the end of the ELM-free H-mode phase.

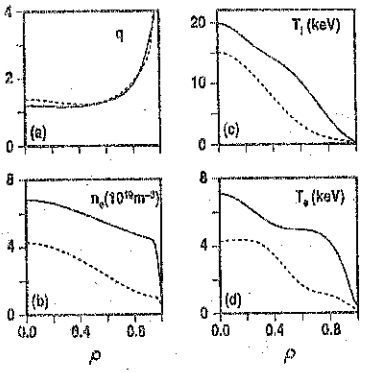


Fig. 3. Profiles of single-null negative central shear plasma during L–mode (broken lines) and H–mode (solid lines): (a) safety factor, (b) electron density, (c) ion temperature, and (d) electron temperature. (Discharge 88964, t = 2.1 and 2.4 s.)

Plasma Performance

The energy confinement in these discharges is significantly better than in other, comparable single-null discharges, as shown in Fig. 4. The H factor in previous low triangularity single-null discharges reaches a maximum of about 3, and diminishes as q_{95} decreases below 4, while the present NCS discharges reach values up to 4, almost twice as large as in previous single-null cases with $3 \leq q_{95} \leq 4$. The improved confinement has resulted in stored energies as high as 3.0 MJ, greater than in any previous low triangularity single-null plasma. Stability limits are similar to those in previous low triangularity single-null discharges, with values of normalized beta up to 4. However, it is noteworthy that even at the highest β_N there is no degradation of energy confinement (see Fig. 5).

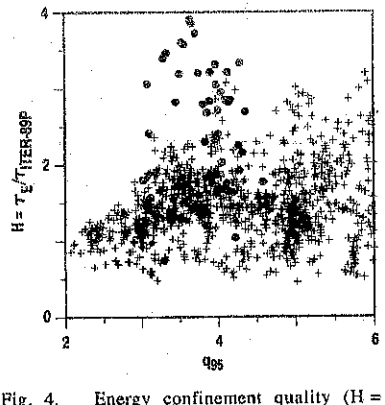


Fig. 4. Energy confinement quality ($H = \tau_E/\tau_{ITER-89P}$) versus q_{95} for low triangularity single-null NCS plasmas (solid circles) compared to the DIII–D confinement data base of single-null plasmas with $1.5 < \kappa < 2$ and $\delta < 0.5$ (crosses).

The combination of internal transport barrier, H–mode edge transport barrier, and stability at high beta leads not only to high global energy confinement but also to higher fusion power gain than in single-null divertor discharges with conventional q profiles. The peak fusion power gains of $Q_{DD} = 1.0 \times 10^{-3}$ (obtained in 1.8 and 2.0 MA discharges) and D–D neutron rates of 1.4×10^{16} s^{-1} (at 2.0 MA) are more than double the previous maximum values for single-null discharges.

The fusion performance of these low triangularity single-null discharges is comparable to that of the best high triangularity double-null plasmas[4] at the same plasma current. This is consistent with the

observation that the two cases have similar normalized energy confinement (H). Since fusion power density varies roughly as the square of the plasma pressure and the energy confinement time scales with the plasma current, the fusion power gain is expected to vary approximately as $Q \sim P_{in}\tau_E^2 \sim P_{in}I_p^2$. As shown in Fig. 6, the measured Q_{DD} does increase as I_p^2, with similar values for high and low triangularity discharges. However, the maximum plasma current is smaller for low triangularity plasmas, restricting them to a smaller maximum fusion power and fusion power gain.

Conclusions

The fusion performance in DIII–D low-q single-null divertor discharges has doubled as a result of improved confinement and stability, achieved through modification of the pressure and current density profiles. These discharges extend the regime of neoclassical core confinement associated with negative or weak central magnetic shear to plasmas with the low safety factor ($q_{95} \sim 3$) and triangularity ($\delta \sim 0.3$) anticipated in future tokamaks. These results are encouraging for advanced performance operation in ITER and for D–T experiments in JET.

[1]Strait, E.J., et al., Phys. Rev. Lett. 75, 4421 (1995).
[2]Lao, L.L., et al., Phys. Plasmas 3, 1951 (1996).
[3]Rice, B.W., et al., Phys. Plasmas 3, 1983 (1996).
[4]Lazarus, E.A., et al., "Higher Fusion Power Production With Pressure Profile Control in Strongly-Shaped DIII–D Tokamak Plasma," submitted to Phys. Rev. Letters.
[5]Söldner, F.X., et al., Contr. Fusion and Plasma Physics (Proc. 22nd EPS Conference) Vol. 19C, Part IV, (1995) 113.
[6]Rice, B.W., et al., Plasma Phys. Contr. Fusion 38 (1996), to be published.
[7]Yushmanov, P.N., Nucl. Fusion 30, 1999 (1990).

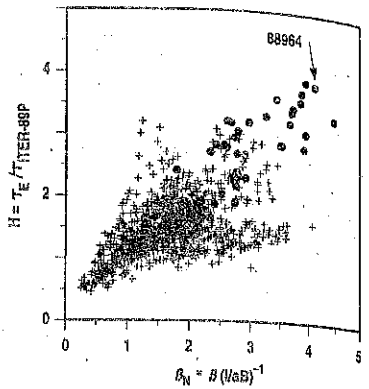


Fig. 5. Energy confinement quality (H) versus normalized beta (β_N) for low triangularity single-null NCS plasmas (solid circles) compared to the DIII–D confinement database of single-null plasmas with $1.5 < \kappa < 2$ and $\delta < 0.5$ (crosses).

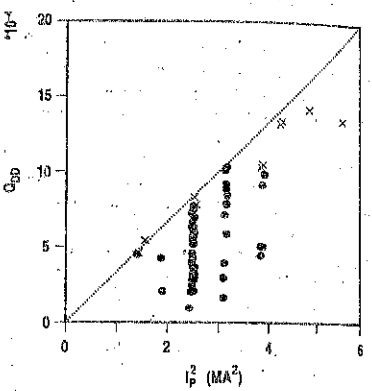


Fig. 6. Fusion power gain ($Q_{DD} = P_{Fusion}/P_{in}$) versus plasma current squared, for low triangularity single-null NCS plasmas (solid circles) and high triangularity double-null NCS plasmas (crosses).

On Channeling of ICRF Minority Tail Energy

J.A. Heikkinen[1], T.P. Kiviniemi[2] and A. Saveliev[3]

[1] *VTT Energy, TEKES-Euratom Fusion Association, P.O. Box 1604, FIN-02044, VTT, Finland*
[2] *Helsinki University of Technology, FIN-02150 Espoo, Finland*
[3] *A.F.Ioffe Physical-Technical Institute, St. Petersburg 194021, Russia*

Abstract: Electrostatic waves can interact with fast minority ions produced by ion cyclotron heating in tokamak plasmas through stochastic Landau damping or cyclotron damping. By two-dimensional Fokker–Planck and fully toroidal Monte Carlo calculations it is shown that power deposition and fast ion confinement are significantly influenced by the radial ion drift induced by electrostatic waves. The possibility of channeling the ICRF power to the LH waves is discussed.

Introduction: During recent years, the interaction of energetic ions with radiofrequency (RF) waves has attracted a great deal of interest, but only little effort has been put into the study of a possible synergy of the ion-cyclotron radio frequency (ICRF) and lower hybrid (LH) waves when launched simultaneously. Because of the different ability to penetrate into the plasma, all the radial diffusion mechanisms are of great interest. It has been also suggested [2] that, in the presence of wave-induced radial diffusion certain geometrical and boundary conditions could alter the direction of power transfer between the wave and the alpha particles. In the present work, these effects are studied by using two-dimensional code, which solves the Fokker–Planck equation as a function of radius r, perpendicular velocity $v_\perp$ and time t.

Numerical model: In the limit of strongly anisotropic velocity distribution and for a cylindrical plasma, Fokker–Planck equation of minority particles can be written in the form

$$\frac{\partial f(v_\perp, r, t)}{\partial t} = C(f) + Q_{IC}(f) + Q_{LH}(f) + Q_{an}(f), \qquad (1)$$

where $C(f)$ is the Coulomb collision term, Q_{IC} and Q_{LH} are the wave diffusion terms for the ICRF and LH waves, respectively, and Q_{an} stands for the radial diffusion mechanisms not originating from the LH or ICRF waves e.g. anomalous diffusion. Expressions for $C(f)$ and Q_{IC} are given in [1]. The LH wave operator in (1) based on the stochastic

Landau interaction of the ions with the wave can be written as [4] $Q_{LH} = (1/r)\mathcal{L}_r D_{LH} \mathcal{L} f$ with [5] $\mathcal{L} = (1/v_\perp)\partial/\partial v_\perp + (k_\eta/\omega\Omega_{ci})\partial/\partial r$. Here, D_{LH} is the diffusion coefficient, ω is the LH wave angular frequency, $k_\eta = k_\theta B_\phi/B - k_\phi B_\theta/B$ is the perpendicular component of the LH wavenumber projected on the magnetic surface. k_θ, k_ϕ B_θ and B_ϕ are the poloidal and toroidal components of the wavenumber and ambient magnetic field, respectively. It is important to note that the present study is based on cylindrical geometry. In toroidal geometry, in the presence of strong ICRF heating, most ions are trapped and the radial coordinate of the reflection points of the trapped ions would be unaffected by the nonradial perpendicular wave propagation. However, the trapped ions are still radially diffused by the finite toroidal momentum exchange between the wave and ions, which can be evaluated from the 2D cylindrical results by exchanging k_η with $-Bk_\phi/B_\theta$ [3].

The ray-tracing code FRTC is used to evaluate the LH wave diffusion coefficient operator averaged over the ray ensemble and parallel refractive index as

$$D_{LH}(r, v_\perp) = \frac{q^2\epsilon^2}{2m^2\omega}\left(\int dn_{L\|} \frac{|E_{L\perp}(n_{L\|})|^2}{(v_\perp{}^2 - (c/n_{L\perp})^2)^{1/2}} \left(\frac{c}{n_{L\perp}}\right)^3\right). \tag{2}$$

for $v_\perp > \omega/|k_{L\perp}|$, and otherwise $D_{LH} = 0$. Here, c is the speed of light, and $n_{L\|}$ and $n_{L\perp}$ denote the refractive index components of the LH wave along the magnetic field and perpendicular to that, respectively. $k_{L\perp} = \sqrt{k_{Lr}^2 + k_\eta^2}$ is the perpendicular wavenumber. k_{Lr} is the radial wavenumber component, and $E_{L\perp}$ is the perpendicular electric field component of the LH wave. For more quantitative analysis, Gaussian prescribed profiles $D = D_0 \exp(-4(\frac{r-r_0}{r_d})^2)$ are used for both D_{IC} and D_{LH}.

Zero-flux boundary conditions [6] are used at small and large perpendicular velocity limits. Similar condition is also applied at the minor axis $r = 0$. Near the plasma edge $r = a$, the distribution is assumed to be Maxwellian with a fixed temperature relevant for local plasma edge conditions. Because of cylindrical approximation, no bounce averaging is applied. As an initial condition, a Maxwellian thermal minority velocity distribution with a radial density and temperature profile of the background plasma is adopted. Plasma density and temperature are assumed to have radial dependencies $n, T = n_0, T_0 \times (1 - r^2/a^2)^{\nu_{n,T}}$, where n_0 and T_0 are the density and temperature on the plasma axis and a is the plasma minor radius. An operator for the anomalous radial diffusion of the fast ions by mechanisms different from those caused by the wave is added with a form

$$Q_{an}(f) = \frac{1}{r}\frac{\partial}{\partial r} r D_{an}\left(1 - \frac{r^2}{a^2}\right)\frac{\partial f}{\partial r} + \frac{1}{r}\frac{\partial}{\partial r}\frac{2r^2\alpha_n D_{an}}{a^2} f \tag{3}$$

to maintain the adopted profile in the absence of RF-induced diffusion. This operator,

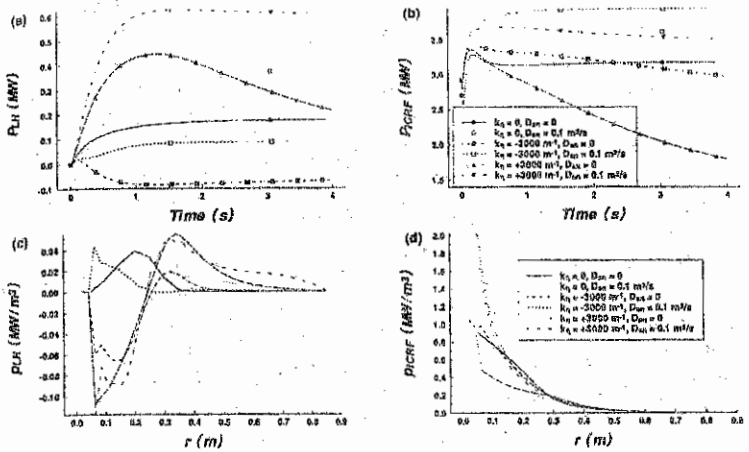


Figure 1: *(a) LH and (b) ICRF power absorption, (c) LH and (d) ICRF power deposition profiles for various values of $k_{\parallel}$ and D_{an}.*

with a constant diffusion coefficient D_{an}, also guarantees the recycling of the centrally heated minorities and thermal minorities produced near the plasma edge.

Results: For the case with low density and low temperature, parameters similar to the JET discharge 33153 are used. Densities of the hydrogen minority ions and background particles on the plasma axis are $n_H(0) = 3.61 \times 10^{17}$ m^{-3}, $n_e(0) = 2.96 \times 10^{19}$ m^{-3}, $n_D(0) = 7.28 \times 10^{18}$ m^{-3} and $n_C(0) = n_{Be}(0) = 2.19 \times 10^{18}$ m^{-3} with the profile constant $\alpha_n = 0.25$. Temperatures for electrons and background ions on the axis are $T_e(0) = 5.88$ keV and $T_i(0) = 2.68$ keV, respectively for each ion species $i = H, D, C, Be$, with the profile constant $\alpha_T = 1.5$. Minor radius is $a = 0.89$ m, and the LH wave absorption on electrons from the ray-tracing is $P_{LH} = 2.4$ MW. Here, in the ray-tracing the real JET geometrical configuration with the ellipticity 1.68 and triangularity 0.1 are used. As the Fokker-Planck calculations are done in the cylindrical geometry with $a = 0.89$ m, the resulting total power absorptions shown in the figures 1(a) and (b) have to be scaled up by a factor 1.68. Fixed value $\sqrt{E_{IC-}^2/E_{IC+}^2} = 4$ for $|E_{IC+}| = 3$ kV/m is used for the relation between right and left-hand circularly polarized wave components.

Figures 1(a)-(d) show the LH and ICRF power absorption as a function of time and time-averaged (over 4 seconds) power deposition profiles for various radial diffusion parameters. When the perpendicular LH wavenumber is radially directed i.e. $k_{L\perp} = k_{Lr}$, the LH

wave within the present model has no influence on the fast ion radial density profile and both LH and ICRF power absorption reach steady-state after the high-energetic tail is formed. When k_η is positive, heated ions are removed from the centre plasma by the LH wave, which can be seen as an negative LH power deposition near the centre in figure 1(c). However, because the particles are diffusing to higher energies, the total power absorption remains positive. This outwards directed movement continues until the particles are transfered to the plasma edge where their are replaced by thermal ions. This can be seen as an strongly decreasing power absorption in Fig. 1(a) after 2 seconds. In Fig. 1(b), ICRF power absorption begins to decrease immediately, when the outwards directed transport begins. In case with $k_\eta = -3000\ m^{-1}$, particles are still diffusing outwards from the centre, because of the extensive ICRF heating, which makes the density along the diffusion path decrease towards lower energies. Here, the rapidly decreasing LH wave-ion velocity interaction regime for increasing radius and the high anisotropy of the ICRF heated ions, as well as the reflecting boundary for the ion diffusion on the axis, play an important role in reversing the direction of power transfer between the ions and the LH wave. This extraordinary situation means that the ICRF power absorbed by the ions, is now found to channel to the LH wave. However, this is the case only when anomalous effects are ignored. Otherwise, anomalous radial diffusion can be assumed to diffuse the ICRF-heated particles outwards in way that prevents the formation of the favourable density gradient meaning that the direction of energy transfer is from the LH wave to particles.

Conclusions: In most cases in this study the LH wave was found to be absorbed. However, in 2D Fokker–Planck calculations net power transfer from the fast minority ions to the LH wave were observed for negative k_η. Unfortunately, this effect disappears when anomalous diffusion is taken into account and was not seen at all in fully toroidal MC calculations. In toroidal calculations, where the large orbit widths of the fast ions make the ions relatively insensitive to the details of the LH wave structure near the plasma centre, positive absorption is observed for both inward and outward directed LH wave-induced radial diffusion.

Acknowledgements: Valuable comments from A. Piliya, L.-G. Eriksson and M.J. Mantsinen are gratefully acknowledged.

[1] T.H. Stix, Nucl. Fusion 15 (1975) 737
[2] N.J. Fisch and J.-M. Rax, Phys. Rev. Lett. 69 (1992) 612
[3] L. Chen, J. Vaclavik, and G.W. Hammett, Nucl. Fusion 28 (1988) 389
[4] C.F.F. Karney, Phys. Fluids 22 (1979) 2188
[5] J.A. Heikkinen and S.K. Sipilä, Physics of Plasmas 2 (1995) 3724
[6] T. Morishita, A. Fukyama, K. Hamamatsu, S.-I. Itoh, and K. Itoh, Nucl. Fus. 27 (1987) 1291

INDEX

Abbasi H. III-pd019
Abel G. I-a143
Adachi K. I-a070
Adamov I.Yu. II-b032
Afanassiev V.I. III-f014, III-f015
Akers R.J. I-a140, III-pd022(*OP8a*)
Akhmetov T.D. II-c017
Akimoto K. III-g018
Aksenov N.N. III-f067
Akulina D.K. II-b039, II-b048, II-b049
Alexander M. I-a001, I-a026
Ali-Arshad S. I-a052, I-a056, I-a058, I-a059, I-a168
Alladio F. I-a133, I-a134
Allen S.L. II-d017
Alper B. I-a051, I-a052, I-a056
Ambrosov S. III-pd005
Amemiya H. II-d011
Anderson D. I-a111
Andrushchenko Zh. II-b014, III-g022
Andryukhina E.D. II-b049
Anikeev A.V. II-c030, II-c031
Anisimov I.O. III-i020, III-i021, III-j021
Anton M. I-a030, I-a032, I-a035(*OP13*), III-f013
Antoni V. II-d001
Antonov V.A. III-j030
Apicella M.L. I-a049
Appel L.C. I-a057
Ardelea A. II-b010
Arsen'ev A.V. II-b032
Arslanbekov R. I-a124(*OP7*), II-e036
Ascasibar E. II-b039, II-b042, II-b043
Atipo A. III-g032
Azarenkov N.A. III-g008
Azizov E.A. I-a106
Babich I.L. III-f002
Bagatin M. II-d001
Bagdasarov A.A. I-a078
Bagryansky P.A. II-c030, II-c031
Bak H.I. III-g012, III-j012
Bak J.G. III-g012, III-j012
Bakos J.S. III-h005
Balakirev V. III-g040
Balbin R. II-b040, II-d046
Baldzuhn J. II-b005(*OP15*), III-f004
Balescu R. I-a129
Balet B. I-a044

Bamford R.A. I-a140
Baranchuk N.S. III-j002
Baranov Y. II-e050
Bardamid A.F. III-pd011
Barnsley R. I-a054
Barry S. I-a035(*OP13*)
Barth C.J. III-f034
Bartirorno R. III-f029
Bashutin O.A. III-f023
Basiuk V. I-a124(*OP7*), III-f035
Batanov G.B. II-b048, II-b049
Bateman G. I-a101
Batha S. I-a011
Becoulet A. I-a124(*OP7*)
Beer M. I-a011
Behn R. I-a030, I-a032, I-a035(*OP13*)
Behringer K. I-a023, III-f007
Beidler C.D. II-b002, II-b004
Belikov V.S. I-a073
Bell R.E. I-a011
Belov A.M. I-a106
Belova N.G. III-h008
Belyakov V.A. I-a071
Bender E.D. II-c017
Berezhetskii M.S. II-b049
Berezhnyj V.L. III-f047
Bergsaker H. II-c022(*OP4*)
Berio S. II-e017
Bernabei S. II-e005
Berroukeche M. I-a171
Bertschinger G. II-d043
Besedin N.T. I-a091, I-a092, II-b025
Bessenrodt-Weberpals M. I-a023, III-f009
Besshou S. II-b012
Beurskens M.N.A. I-a123, III-f034
Bevir M.K. I-a136
Bezborodov V.I. III-f022
Bibet Ph. II-e017
Bindslev H. II-e051
Biskamp D. I-a002(*OP1*)
Blanchard N. I-a143
Bleuel J. II-d006
Boedo J.A. II-d041
Boev A.G. III-i001(*OP24*)
Boeva A.A. III-i008
Bogomolov L.M. II-d025
Bohmeyer W. III-f049
Bolzonella T. II-c002, II-c003, II-c004
Bombarda H. I-a097, I-a099, I-a100
Bondarenko I.S. I-a156
Bondarenko S.P. II-b018
Bondeson A. I-a065
Bonhomme G. III-g032
Booth M. I-a141(*OP20*)
Borba D. I-a042
Borik S. III-pd003
Borrass K. I-a008(*OP6*)
Bosch H.S. I-a019, I-a020

Boucher C. I-a142, II-d036
Boucher I. III-f057, III-f058
Boyd D. II-e042
Bracco G. I-a133, II-e013
Brakel R. II-b008, II-b036
Brambilla M. II-d005
Branas B. III-f004
Bregeon R. I-a130
Briguglio S. I-a176(*OP8*)
Brinkschulte H. II-e008
Brooker P. II-e042
Brooks N.H. II-d019
Bruev A.A. III-j030
Brunsell P. II-c022(*OP4*), II-c023
Bruschi A. II-e013
Brusehaber B. III-g020
Bryzgunov V.A. III-f046
Brzosko J.R. II-c009
Brzosko J.S. II-c009
Brzozowski J.H. II-c022(*OP4*), II-c023
Buchl K. I-a008(*OP6*), III-f009
Budaev V.P. I-a106, II-d022
Budnikov V.N. II-d028, II-e003, II-e004, III-f027
Budny R.V. I-a010, I-a012, I-a014, I-a015, I-a124(*OP7*), III-f054(*OP23*)
Buffa A. II-c001, II-c002
Bugrova A.I. II-c033
Buhlmann H. I-a030, I-a035(*OP13*), III-f013
Bulanin V.V. II-e003
Buratti P. I-a133, II-e013
Burhenn R. II-b008
Burlak G.N. III-h001
Burmasov V.S. III-g043
Burrell K.H. I-a095, I-a134, II-e025
Burri A. I-a035(*OP13*)
Bush C.E. I-a011
Buts V.A. III-g036, III-g037, III-g038
Buttery R.J. I-a001, I-a136, I-a140, III-pd022(*OP8a*)
Bystrenko O.V. III-i027
Buyadgi T. III-pd004
Cairns R. II-e042
Caloutsis A. I-a136
Campell D.J. I-a058, I-a059
Campostrini P. II-c002
Candy J. I-a042
Cardinali A. II-e005
Carlson A. II-d003
Carolan P.G. I-a029, I-a140, I-a141(*OP20*)
Carraro L. II-c004, II-c006
Casarotto E. II-c004
Caspani D. III-g016
Casper T.A. I-a095, I-a096
Casper T.N. III-pd020

Castejon H. II-b038, II-b041, II-b044
Castle G.G. I-a139
Cattanei G. II-b009
Cesario R. II-e040
Chaika G.E. III-j016, III-pd017
Chang Z. I-a014
Chankin A. I-a055
Chareau J.M. I-a126
Chatenet J.H. I-a103
Chavan R. I-a035(*OP13*), III-f013
Chebotarev V.V. II-c033, II-d052, III-f047, III-j032
Chechik E.O. II-d028
Chechkin A.V. II-b018, III-i007
Chechkin V.V. II-b018
Cheetham A. I-a052
Chen H. I-a062
Cheremnych O.K. III-g022
Cherkasov S.V. I-a090
Chernobai A.P. I-a106
Cherubini A. I-a043(*OP19*), I-a045, I-a061
Chitarin G. II-c002
Chmyr T. III-g058
Chodura R. II-d003
Christou C. II-b012, II-e044
Chu C.C. III-f034
Chu M.S. I-a065, I-a134, III-pd020
Chutov Yu.I. III-g001, III-g002, III-j002, III-j003
Cirant S. II-e013
Clairet F. I-a124(*OP7*), I-a130, III-f057, III-f058
Clement S. I-a055, I-a168
Codling D.M. I-a140, III-pd022(*OP8a*)
Coffey I.H. I-a054
Colas L. I-a126, I-a130
Colome J.V. I-a127
Colton A.L. I-a141(*OP20*)
Condea I. I-a142
Conway N.J. I-a029, I-a140, I-a141(*OP20*), III-pd022(*OP8a*)
Cooper W.A. II-b010
Coppi B. I-a097, I-a099, I-a100
Cordey J.G. I-a045
Corrigan G. I-a046, II-d045
Costa S. II-c006
Coster D. II-d038, III-f007
Coster D.P. III-f010
Cote A. I-a143, II-e042
Cote C. I-a142, I-a143, II-e042
Cottrell G.A. I-a060
Counsell G.F. I-a140
Cox M. I-a140
Crisanti F. I-a134
Cristofani P. I-a131

Crotinger J. I-a096
Cunningham G. II-e010(*OP5*), III-f012
Cuthbertson J.W. I-a094
Cyzewski T. III-f056
D'Antona G. I-a058, I-a059
da Cruz D.F. I-a123
Dalla S. III-f030
Dan'ko P.L. III-j002
Den'kov S. III-pd005
Danilkin I.S. II-b049
Das J. III-f005
Daughton W. I-a097
Davies S. I-a055
Davies S.J. I-a168
Davydenko V.I. II-c017
Davydova T.A. III-g004, III-g046
de Baar M.R. I-a118
de Benedetti M. I-a058, I-a059
de Blank H.J. I-a024
De Boo J.C. I-a095
Decoste R. I-a143
de Esch H. I-a042
de Esch H.P.L. I-a045
de Grassie J.S. II-e025
Degtyarev L. III-g006
Deichuli P.P. II-c030, II-c031
de Kloe J. I-a123
Dela Luna E. II-b039
Deliyanakis N. I-a040, I-a052, I-a061
De Luca F. I-a040
Demchenko M.Yu. III-f025
Demchenko V.V. II-e020
Demers Y. II-d029, II-e042
De Michelis C. II-d030
Dendy R.O. I-a135, III-f030
Denner T. II-d041
de Pena Hempel S. I-a020, I-a023, I-a026, III-f007, III-f010
De Ploey A. I-a117
Derepovskij N.T. II-d052
Deschenaux C. I-a035(*OP13*)
Desideri D. II-d001
Detragiache P. I-a099, I-a100
de Vries P.C. I-a102(*OP2*)
Devynck P. I-a124(*OP7*), I-a130
Dimov G.I. II-c017
Diver D.A. III-g034
Dnestrovskij Yu.N. I-a082, I-a090, III-f044
Dobbing J. II-e050
Dodel G. III-f007
Donne A.J.H. I-a102(*OP2*), III-f059
Donskaya N.P. II-b049
Dorn C. III-f007
Dovbakh S.V. III-j021
Dowling J. I-a140
Doyle E.J. I-a095

Drake J. II-c022(*OP4*)
Drake J.F. I-a002(*OP1*)
Duck R.C. II-e010(*OP5*)
Dumbrajs O. II-e051
Duong H.H. I-a012
Durst R.D. I-a095
Dutch M. I-a030
Dutch M.J. I-a032, I-a035(*OP13*), I-a036, III-f013
Duval B.P. I-a030, I-a032, I-a033, I-a034, I-a035(*OP13*), II-d009
Dux R. I-a008(*OP6*), I-a020, I-a023
Dyachenko V.V. II-d028, II-e003, II-e004
Dziubanov D.A. III-i033
Edwards A. I-a056
Edwards A.M. I-a029, I-a058, I-a059
Edwards A.W. I-a051, I-a052
Efba M. I-a043(*OP19*)
Efimov A. III-pd005
Efthimion P.C. I-a011
Ejiri A. I-a070
Ekedahl A. II-e050
Eliseev L.G. I-a156
Elsner A. II-b008, II-b036
Endler M. II-d006
Engsrom L. III-pd013
Enk Th. III-j019(*OP12*)
Erba M. I-a045, I-a061
Erckmann V. II-e007(*OP22*)
Erents S.K. I-a140
Ermak G.P. III-f025, III-f026
Ernst D. I-a011
Esipov L.A. II-d028, II-e003, II-e004, III-f027
Esposito B. I-a063
Esser H.G. II-e012
Estrada T. II-b039
Evans T.E. II-d019
Fahrbach H.-U. III-f010
Fainberg Ya.B. III-g051
Falko O.G. III-i005
Fall T. II-c022(*OP4*), II-c023
Fanack C. III-f057, III-f058
Fasel D. I-a035(*OP13*)
Fasoli A. I-a035(*OP13*), I-a042, I-a116
Faulconer D. II-d054(*OP16*)
Favre A. I-a035(*OP13*)
Fedutenko E. III-g011
Fedyanin O. II-b043
Fedyanin O.I. II-b048, II-b049
Feneberg W. I-a022
Fenstermacher M.E. II-d017, II-d019
Ferron J.R. III-pd020
Fiedler S. II-b005(*OP15*), II-b008, III-f005
Fielding S.J. I-a141(*OP20*)
Filippov N.V. II-c009
Filippova T.I. II-c009

Finken K.H. II-d041, II-d054(*OP16*)
Finkenthal M. III-f029
Fischer B. II-e050
Fishchuk A.I. III-g004
Fisher R.K. I-a012
Fishpool G. I-a052, I-a058, I-a059
Flewin C. I-a062
Fomichov V.V. III-i006
Fomin I.P. III-f047, III-f048
Fontanesi M. III-g016, III-g017
Forest C.B. II-e025, III-pd020
Fournier K.B. III-f029
Frank A. I-a119
Franke S. I-a030, I-a032, I-a035(*OP13*)
Franzen P. I-a021
Frigione D. III-f028
Fu G.-Y. I-a010
Fubmann G. III-f049
Fuchs Ch. I-a008(*OP6*)
Fuchs F. II-e042
Fuchs G. II-d054(*OP16*)
Fuchs J.C. I-a008(*OP6*), I-a020
Fujisawa A. I-a070
Gafert J. III-f007
Galli P. I-a040
Gamberale L. III-g016, III-g017
Garbet X. I-a103, I-a128, I-a130, I-a131
Garcia L. II-b035
Garcia-Cortes I. I-a052, I-a168, II-d046, III-f052(*OP17*)
Garkusha I.E. II-c033, II-d052, III-j032
Garkusha V.V. III-j032
Garzotti L. II-c003, II-c004
Gasparino U. II-e006, II-e041
Gates D. I-a136, I-a139
Gates D.A. I-a029, I-a141(*OP20*)
Gauvreau J.-L. I-a143
Gavrilov N. III-pd003
Gee S.J. II-e010(*OP5*)
Gehre O. I-a004, I-a026
Geiger J. II-b003, II-b007
Geist T. III-f004
Gerasimov O.I. III-j005
Geraud A. I-a131, I-a173
Germanova S.V. II-c024, II-c026
Ghoranneviss M. I-a122
Giannella R. I-a040, I-a043(*OP19*), I-a051, I-a054, I-a061, I-a134, II-d002
Giannone L. II-b008, II-b036, II-d006, II-d046
Gibson K. III-f012

Gibson K.J. II-e010(*OP5*)
Gierszewski P. I-a143
Giesen B. II-d054(*OP16*), II-e012
Gil C. I-a130, I-a131
Gil'varg A.B. III-f046
Gill R.D. I-a051, I-a052
Gimblett C.G. I-a136, I-a137(*OP14*)
Girka I.O. II-e021
Girka V.O. II-d031
Giruzzi G. II-e005
Gladkov G.A. II-b048, II-b049
Glasser A.H. I-a100
Glazunov G.P. II-d016
Glushkov A.V. III-pd003, III-pd004, III-pd005
Gnesotto F. II-c002
Goedbloed J.P. I-a116, I-a117
Golant V.E. I-a071
Goldston R.J. I-a015
Goloborod'ko V.Ya. I-a074, I-a075
Golota V.I. III-j030
Gondhalekar A. III-f030
Goniche M. II-d029
Gordienko I.Ya. II-c013
Gorelenkov N.N. I-a010, I-a012, III-f054(*OP23*)
Gorini G. I-a040
Gormezano C. I-a042, I-a060, II-e050
Gott Yu.V. I-a084, I-a085, I-a088
Goutych I.F. III-g054
Granucci G. II-e013
Grebenshchikov S. II-b040
Grebenshchikov S.E. II-b048, II-b049
Greene J.M. I-a065
Greenfield C.M. I-a095, III-pd020
Greenwald M. I-a097
Gregory B.C. I-a142
Grekov D.L. III-f041
Gresillon D. I-a126, III-f040
Grigor'eva L.I. II-b018
Grigorenko Ye.I. III-i033
Griguli P. II-b008, II-b036
Grimalsky V.V. III-g044, III-h001
Gritzaenko S.V. III-f031
Gross B. III-f061
Grote H. III-f049
Gruber O. I-a008(*OP6*), I-a026
Gryaznevich M. I-a136, I-a140, III-pd022(*OP8a*)
Gubarev V.F. III-f067
Guilhem D. II-d029
Guirlet R. II-d002
Guiziou L. I-a126
Gunn J. II-d036

Gunston T. I-a140, III-pd022(*OP8a*)
Gusakov E.Z. II-e003, III-f027, III-f053, III-g020
Gusev V.K. I-a071
Haas G. I-a008(*OP6*), II-d004, II-d040, III-f010
Habler M. II-d054(*OP16*)
Haddad E. I-a142, I-a143
Hahm T.S. I-a011
Hamada Y. I-a070
Hammett G. I-a011
Han J.M. I-a117, III-g012, III-j012
Harris J.H. II-d029
Hartfuss H.J. II-b008, II-e006, II-e007(*OP22*), III-f004
Hartmann D.A. II-b009
Hastie R.J. I-a135, I-a137(*OP14*)
Hawkes N. I-a061
Hawkes N.C. I-a062
Hedin G. II-c022(*OP4*)
Hedqvist A. II-c022(*OP4*)
Heikkinen J.A. II-e031, II-e051, III-pd023
Heinrich O.P. II-d007, III-f005
Hellblom G. II-c022(*OP4*)
Hellsten T. I-a038
Hender T.C. I-a001, I-a029, I-a057, I-a136, I-a137(*OP14*), III-pd022(*OP8a*)
Herranz J.A. III-f034
Herrmann A. II-b008, II-b036, II-d013, II-d039, II-d040
Herrmann W. I-a024, III-f010
Hernegger F. II-b001
Hess W.R. II-d030
Heuraux S. II-e049, III-f057, III-f058
Heyn M.F. II-b028
Hidalgo C. I-a168, II-b040, II-d046, III-f052(*OP17*)
Hidekuma S. I-a070
Hildebrandt D. II-b008, II-b036
Hirayama T. I-a112
Hirokura S. I-a070
Hirose A. I-a143
Hirsch K. III-f007
Hirsch M. II-b005(*OP15*), III-f004
Hirsch S. II-d040, III-f007
Hirshman S. II-d019
Hoang G.T. I-a124(*OP7*), I-a126, I-a130, II-e005, II-e036
Hobirk J. II-d041
Hoenen F. I-a019, I-a036

Hoerling P. II-c022(*OP4*), II-c023
Hofmann F. I-a030, I-a032, I-a034, I-a035(*OP13*)
Hofmeister F. II-d005
Hogan J.T. II-d029, II-d030
Hogeweij G.M.D. I-a118, I-a123, III-f059
Hohg B.G. I-a117
Hokin S. II-c022(*OP4*)
Hollenstein C. I-a035(*OP13*)
Holties H.A. I-a116
Holzhauer E. II-b005(*OP15*), II-e007(*OP22*)
Hong B.G. I-a132
Hori T. II-b034
Horton L.D. II-d002
Hosotubo M. II-e044
Howard J. III-f059
Howman A. I-a060
Hugill J. I-a140, II-e010(*OP5*)
Humphreys D.A. I-a094
Hunt C. I-a141(*OP20*)
Hutter T. I-a124(*OP7*)
Huysmans G.T.A. I-a057, I-a116
Hwang D. I-a143
Hyatt A.W. I-a094, II-e025, III-pd020
Ida K. I-a070, II-b012
Ignat D. II-e005
Igonkina G. II-d013
Igoshin V.G. II-c017
Iguchi H. I-a070
Ijiri Y. II-b012
Ilgisonis V.I. I-a080
Ingesson C. I-a051, I-a052
Innocente P. II-c003, II-c004
Irie H. III-g018
Isaev M.Yu. II-b016
Ishkabulov K. III-h001
Isler R. II-d019, II-d017
Isoz P-F. I-a035(*OP13*)
Its E.R. II-d028, II-e003, II-e004, III-f027
Ivanov A.A. II-c030, II-c031
Ivchenko V.M. III-pd016
Jacchia A. I-a040
Jackel H.J. I-a040
Jacker H. II-b008
Jacquet P. II-d029
Jaenicke R. II-b005(*OP15*), II-b007
Jarmen A. I-a157
Jaskola M. III-f056
Jaspers R. II-d041
Jenkins I. I-a136, I-a140, III-pd022(*OP8a*)
Jimenez J.A. II-b043
Johner J. I-a127
Johnson L.C. III-f054(*OP23*)
Johnson V. III-f012
Jones J. I-a060
Jones T.T.C. I-a045

JongGu Kwak III-g012, III-j012
Joye B. I-a030, I-a035(*OP13*)
Jupen C. III-pd013
Kabantsev A.A. II-c017, II-e027
Kado S. II-b012
Kaganovich I. I-a164
Kaganskaya N.M. III-g020
Kaiser M. II-b004
Kaita R. II-e005
Kaleck A. II-d054(*OP16*)
Kallenbach A. I-a020, I-a023, II-d037
Kalmykov S.G. I-a115
Kalvin S. III-h005
Kalyuzhnyj N.V. II-b022
Kamelander G. II-e020
Kamenev Yu.E. III-f021, III-f022
Kanda Y. II-e044
Kandaurov I.V. III-g043
Kano Y. I-a070
Kantor M.Yu. III-f039
Karakin M.A. II-c009
Karas' V.I. III-g051, III-h008
Kardaun O. III-f010
Kardon B. III-h005
Karelse F.A. III-f059
Karpushov A.N. II-c031
Karttunen S.J. II-e011
Kasilov S.V. II-b028, II-e023, II-e024, II-e029
Kass T. I-a019
Kastelewicz H. II-d038
Kaufmann M. I-a008(OP6), III-f009
Kavin A.A. I-a071
Kawasumi Y. I-a070
Kazakov O.E. II-d052
Kellman A.G. I-a094
Kelnyk O.I III-i021.
Kernbichler W. II-b028
Kerner W. I-a041, I-a042, I-a116
Keston D.A. III-g034
Khademian A. I-a122
Kharchev N. II-b040
Kharchev N.K. I-a156, II-b049
Kharchevnikov V.K.II-c033
Kholnov Yu.V. II-b049
Khrebtov S.M. I-a156
Khudoleev A.V. III-f014, III-f015
Khutoretsky A. III-f010, III-f044
Khvesyuk V.I.II-c015,II-c016
Khydyntsev M.N. III-j005
Kim S.K. I-a117, I-a132, III-g012, III-j012
Kink I. III-pd013
Kinsey J.E. I-a101
Kirnev G.S.II-d051

Kiseliov V.K. III-f021, III-f022
Kisslinger J. II-b001
Kivganov A. III-pd004
Kiviniemi T.P. III-pd023
Knyaz'kov B.N. III-f021, III-f022
Kobayashi S. II-b012, II-b013
Kobryn A.E. III-g055
Koch R.II-d054(*OP16*), II-e012, II-e049
Kocsis G. III-h005
Kojima M. I-a070
Kolesnichenko Ya.I. I-a073, I-a109, I-a110, I-a111
Kolik L.V. II-b049
Kollermeyer J. I-a154(*OP3*)
Kondakov V.V. II-b029
Kondo K. II-b012, II-e044
Konen L. II-d043
Konkashbaev A.I. III-i006
Konkashbaev I.K. III-i006
Kononenko V.K.III-f021, III-f022
Kononov A.V. III-j011
Konrad Ch. II-b005(*OP15*)
Kontar E.P. III-i002
Kornejew P.III-f049
Korotkov V.A. I-a071
Koslowski H.R. II-d043
Kostrov U.A. I-a071
Kotenko V.G. II-d016
Kotlyarov I.Yu. III-j021
Kotsarenko N.Ya. III-g044, III-h001, III-i025
Kouprienko D.V.III-f039
Koval A.G.III-f031
Kovan I.A. II-e026
Kovrizhnykh L.M. II-b049
Kozin G.I.III-f023
Kozintseva M.V. II-c033
Kozyrev A. III-g011
Kramer M. III-g020, III-j019(*OP12*)
Kramer-Flecken A. I-a102(*OP2*), II-d043
Krasilnikov A.V. III-f054(*OP23*)
Krauz V.I. II-c009
Kravchenko A.Yu. III-g001, III-g002, III-j003
Krejci A. I-a030
Kritz A.H. I-a101
Krlin L. I-a104
Kruglyakov E.P. III-g043
Krupnik L.I. I-a156, III-f052(*OP17*)
Krutko O.B. III-j026
Kryshtal A.N. III-i024
Kubaichuk V. III-i026
Kuhner G. II-b008
Kulaga A.E. II-b032
Kuleshov E.M.III-f021, III-f022

Kulik N.V. III-j032
Kulish V.V. III-j026
Kupschus P. I-a049
Kurnaev V.A. II-d051
Kurzan B.III-f006
Kuvshinov B.N. III-g015(*OP18*)
Kuzmin E.G. I-a071
Kuznetsov G.I. II-c031
Kuznetsov V.D. III-i006
Kuznetsov Yu.K. II-b021, II-b025
Kwon O.J. III-pd022(*OP8a*)
Lachambre J-L. I-a143
Lackner K. I-a019
La Haye R.J. III-pd020
Laing E.W. III-g034
Lanckner K. I-a026
Lang P.T. I-a008(*OP6*), III-f009
Lang R. I-a008(*OP6*)
Lao L.L. I-a065, I-a095, I-a096, I-a134, III-pd020
Lapshin V. III-g011
Lapshin V.I. II-e021
Laqua H. II-e007(*OP22*)
Larionova N.F. II-b049
Larsson D. II-c022(*OP4*)
Lasaar H. II-d054(*OP16*)
Lashkin V.M. III-g047
Lashkul S.I. II-d028
Lasnier C.J. I-a094, II-d017
Lauro-Taroni L. I-a062, II-d002
Laux M. II-d037, II-d040
Laviron C. I-a124(*OP7*), I-a130
Lavrent'ev O.A. II-c024, II-c026
Lawson K.D. II-d002
Lazarev S.L. II-b029
Lazarus E.A. I-a095, III-pd020
Lazzaro E. I-a058, I-a059
Leclert G. I-a130, II-e049, III-f057, III-f058
Lee R.L. I-a094
Lennholm M. II-e050
Leonard A.W. II-d017, II-d019
Lesnyakov G.G. II-b025, II-d015
Letunov A.A. II-b049
Leuterer F. I-a154(*OP3*), II-e008
Levandovskii V.G. III-j016
Levchenko V.D. III-g051
Levinton F. I-a011, I-a016
Levitsky S.M. III-j021
Li J. I-a038
Likin K.M. II-b049
Lingertat J. I-a055, I-a056, I-a168
Lipatov A.S. II-c033
Lisak M. I-a111

Lisitchenko T.E. III-j002
Lisovskiy V.A. III-j014, III-j015
Lister J. I-a042
Lister J.B. I-a034, I-a036
Litaudon X. I-a124(*OP7*), I-a125, I-a130, I-a171, II-e036
Litvinov A.P. II-e029
Litvinov V.A. III-f031
Liu D.H. I-a038
Lizunov G.V. III-j021
Lloyd B. I-a029
Loarte A. I-a055, I-a168
Lok J. I-a123, II-e032
Lomas P. I-a134
Lomas P.J. I-a060
Lopes Cardozo N.J. I-a118
Lopez A. II-b042
Lopez-Fraguas A. II-b039, II-b043
Lotte Ph. III-f035
Luce T.C. I-a064
Luciani J.F. I-a103
Lutsenko V.V. I-a109, I-a110
Lyadina E. I-a051
Lyakhov A.N. II-c015, II-c016
Lyon J.F. II-b009
Lysenko S.E. I-a090
Lysenko V.N. III-i033
Lyssoivan A.L. II-e012, II-e029
Maas A. II-d002
Maas A.C. I-a054
Maassberg H. II-b002, II-b004, II-e006, II-e041
Maget P. I-a130
Maggi C. II-d002
Mai H. I-a143
Mai H.H. I-a142
Mailloux J. II-d029, II-d036
Makhlay V.A. III-j032
Malaquias A. III-f052(*OP17*)
Malijevsky I. I-a104
Malnev V.M. III-pd016, III-pd017
Maltsev S.G. I-a106
Mancuso A. I-a134
Mandl W. II-d030, III-f036(*OP10*)
Manhood S.J. I-a141(*OP20*)
Manickam J. I-a010, I-a137(*OP14*)
Mank G. II-d041, III-h005
Mansfield D.K. I-a012
Manso M.E. III-f006
Mantica P. I-a040
Manuilenko O.V. III-g036, III-g037, III-g038
Maraschek M. I-a001, I-a019
Marchand R. I-a142, II-d036
Marchenko V.S. II-e043
Marcus F. I-a057
Marcus F.B. I-a063
Marletaz B. III-f013
Marmillod P. III-f013

Marrelli L. II-c005
Martin F. I-a143, III-pd022(*OP8a*)
Martin G. I-a125, III-f035
Martin P. II-c005
Martin R. I-a136
Martin T.J. I-a135
Martin Y. I-a030, I-a032, I-a033, I-a036
Martin-Solis J.R. I-a168
Martin-Solis R. I-a063
Martinell J. II-e055
Martines E. II-c002, II-d001
Martini S. II-c002, II-c003, II-c004
Martinson I. III-pd013
Martynov A. III-g006
Martysh Eu.V. III-pd016
Marushchenko N. II-e006, II-e024, II-e041
Maschke E.K. I-a171
Maslov V.A. II-c024, II-c026
Masnavi M. I-a122
Mast F. I-a008(*OP6*), I-a020
Masuzaki M. III-g040
Matsushita K. II-b034
Matthews G.F. I-a168
Mattioli M. I-a131, III-f029, II-d030
Maximov V.V. II-c030, II-c031
Mayer H. II-d038
Mazzucato E. I-a011
McArdle G.J. I-a029
McCarthy K.J. II-b042, III-f055
McCarthy P. III-f009
McChesney J.M. I-a012
McClements K.G. I-a135, III-f030
McCormick K. III-f005
McCune D. I-a015
Medina F. II-b038
Medley S.S. I-a012
Medvedev S. III-g006
Meigs A. III-pd013
Mel'nik V.N. III-i002
Melnichenko V.L. III-j002
Melnikov A.V. I-a156, III-f052(*OP17*)
Mertens V. I-a008(*OP6*), I-a020, I-a021, III-f009
Meshcheryakov A. II-b040
Meshcheryakov A.I. II-b049
Meshkov O.I. III-g043
Meyer W.H. I-a096
Micozzi P. I-a133, I-a134
Migliuolo S. I-a100
Mikhailov M.I. II-b016
Mikkelsen D. I-a011
Miller C.O. I-a015
Minaev V.B. I-a071
Mirnov S.V. I-a106, II-e026
Mironov M.I. III-f014, III-f015, III-pd022(*OP8a*)

Mironov Yu.K. II-d016
Miroshnikov I. III-f009
Misguich J.H. I-a129, III-g013(*OP11*)
Mitina N.I. III-j032
Mizuuchi T. II-b012, II-e044
Moinier-Garbet P. II-d030
Moiseenko V.E. II-b028, II-e028, II-e029
Moller A. II-c022(*OP4*)
Moller J. I-a096
Monakhov I.A. II-e026
Monk R. I-a055
Monk R.D. I-a168
Montvai A. II-d054(*OP16*)
Moravec J. I-a030
Moreau Ph. I-a130
Moret J-M. I-a030, I-a032, I-a033, I-a034, I-a035(*OP13*), I-a036
Morimoto S. II-b034
Morozov A.I. II-c033
Morris A.W. I-a029, I-a139, I-a141(*OP20*)
Motojima O. II-b026, II-b027, II-b030, II-d016
Muir D. I-a042
Mukhin V.V. III-j030
Muller H.W. I-a008(*OP6*), III-f009
Munich M. II-e008
Murakhtin S.V. II-c030, II-c031
Murari A. II-c005
N'guyen F. I-a130
Nagasaki K. II-b012, II-b013, II-e044
Nakamura Y. II-e044
Napiontek B. II-d037, II-d040, III-f007
Narihara K. I-a070
Naujoks D. II-d037
Navratil G. I-a095, III-pd020
Nazarov N.I. II-b018, II-d016, II-e029
Nechaev Yu.I. II-b039, II-b049
Nedzelskij I.S. I-a156, III-f052(*OP17*)
Nemov V.V. II-b019, II-b022
Nesterov P.K. III-f021, III-f022
Neu G. I-a021
Neu R. I-a008(*OP6*), I-a023
Neuhauser J. I-a008(*OP6*), II-d004
Nguyen F. I-a124(*OP7*)
Nicolai A. II-d054(*OP16*)
Niedermeyer H. II-d006, II-d046
Nieswand Ch. I-a030, I-a032
Niethammer M. III-f007
Nightingale M.P.S. III-pd022(*OP8a*)
Nikandrov L.B. III-i006

Nishizawa A. I-a070
Nomura I. I-a070
Noterdaeme J.-M. II-d005
Novik K.M. II-e004
Novokhatsky A.N. I-a071
Nowak S. II-e013
Nozdrachev M.G. II-c024
O'Brien D. I-a056, I-a134
O'Brien M. I-a029
O'Connell R. I-a029, I-a141(*OP20*)
O'Mullane M.G. I-a054, I-a062
Obiki T. II-b034, II-e044
Oboznyi V.P. II-c024
Ochando M.A. II-b038, II-b044
Ocheretenko V.L. III-f047
Ohya K. II-d043
Okabayashi M. II-e005
Okada H. II-b012, II-e044
Okamoto T. II-e044
Olshansky V.V. II-e020
Omel'chenko A.Ya. II-b022
Onishchenko I. III-g040
Oomens A.A.M. I-a118, I-a123
Opanasenko O.V. III-j021
Oraevsky V.N. III-i006
Osborne T.H. I-a134
Ossipenko M.V. I-a081
Ostrikov K.N. III-g008
Ott W. II-b003
Oyabu N. II-d016
Paccagnella R. II-c006
Pacella D. III-f029
Palets D.B. III-j021
Panchenko V.G. II-e018
Pankin A.Yu. III-g046
Pankratov I.M. I-a092, II-b032
Paoletti F. II-e005
Parail V.V. I-a040, I-a043(*OP19*), I-a045, I-a061
Paris P. III-f013
Park C.W. III-g012, III-j012
Parks P.B. I-a012
Pashchenko I.A. III-j030
Pasqualotto R. II-c003
Pastukhov V.P. I-a080
Pattikangas T.J.H. II-e011
Paume M. I-a126, I-a130
Pavlenko I.V. II-d031
Pavlenko V.N. II-e018
Pavlenko V.P. III-j009, III-j010
Pavlichenko O.S. II-b025, II-d016, III-f048
Pavlo P. I-a104
Peacock N.J. I-a062
Pearlstein L.D. I-a096
Pecoul S. II-e049
Pecquet A.L. I-a131
Pedrosa M.A. II-b040, II-d046

Peeters A.G. I-a154(*OP3*), II-e001
Pegoraro F. III-g015(*OP18*)
Pegourie B. I-a173
Penningsfeld F.-P. II-b003
Perelygin S.F. II-b029
Pereverzev G. I-a026
Pericoli-Ridolfini V. II-e050
Peterson B.J. II-b012, II-f018
Petravich G. III-h005
Petrov A.A. III-f028
Petrov A.E. II-b049
Petrov A.V. II-e003
Petrov M.P. I-a010, I-a012
Petrov S. III-pd022(*OP8a*)
Petrov V.G. III-f028
Petrov Yu.V. II-e026
Petty C.C. I-a064, I-a095, II-e025
Peysson Y. I-a124(*OP7*), II-e036, II-e042, III-f037
Philipps V. II-d043
Pierre Th. III-g032
Pietrzyk Z.A. I-a032
Piffl V. I-a030
Pijper F.J. III-f034
Pinos I.B. II-b018, II-b021
Pinsker R.I. II-e025
Piterskii V.V. I-a078
Pitts R. I-a030, II-d009
Plyusnin V. II-b009
Plyusnin V.V. II-b018, II-e029
Podminogin A.A. II-c030, II-c031
Podushnikova K.A. I-a071
Podyachy Yu.I. III-i034
Poedts S. I-a117
Pogozhev D.P. II-b025
Pogutse O. I-a041
Polischuk V. III-pd003
Polman R.W. II-e032
Polozhiy K.I. II-b004
Poltavtsev N.S. II-d052
Polupanov V.N. III-f022
Pomaro N. II-c002
Poperenko L.V. III-pd011
Poritsky P.V. III-j011
Porte L. I-a061
Porte L.P I-a040
Porter G.D. II-d019, II-d020(*OP9*)
Pospieszczyk A. II-d043, III-h005
Poznyak V.I. I-a078
Prater R. II-e025
Prepelitsa G. III-pd004
Pugno R. II-c003
Puiatti M.E. II-c004, II-c006
Pulayev V.A. III-i033
Puppin S. I-a056
Pyatak A.I. II-e023, II-e024
Qin J. II-b043
Quirion B. I-a143

Rachlew-Kallne E. II-c022(*OP4*)
Radford G. II-d045
Raman R. I-a143
Rantamaki K.M. II-e011
Rantsev-Kartinov V.A. I-a087
Rapoport Yu.G. III-g044, III-i025
Rapp J. II-d043
Rasmussen D.A. II-b009
Ratel G. I-a142
Raus J. I-a030
Razumova M.A. III-h003
Redd A.J. I-a101
Redi M.H. I-a010, I-a015
Reimerdes H. I-a004
Reiner H.-D. III-f049
Reiter D. II-d007, II-d038, II-d054(*OP16*), III-f010
Rem J. III-g014
Rettig C.L. I-a095
Reuss J.-D. III-g013(*OP11*)
Reva V.B. II-c017
Revin I.D. III-f025
Reznik S.N. I-a074, I-a075
Rhodes T.L. I-a095
Ribeiro C. I-a136, III-pd022(*OP8a*)
Riccardi C. III-g016, III-g017
Rice B.W. I-a065, I-a095, I-a096, II-e025, III-pd020
Richard N. I-a142, I-a143
Rimini F. II-e050, I-a060
Robinson D.C. I-a141(*OP20*), III-pd022(*OP8a*)
Rodriguez-Rodrigo L. II-b038
Rogal' I. II-d050
Rogers B. I-a014
Rogozin A.I. II-c030
Rohde V. II-d040
Romanelli M. I-a051
Romanyuk L.I. III-j021
Rome M. II-e006, II-e041
Romero J. II-e050
Rommers J.H. II-e032, III-f059
Rookes A. I-a061
Roquemore A.L. III-f054(*OP23*)
Rossi A. I-a049
Rouhani M.R. III-pd019
Rozhansky V. I-a163, I-a164
Rozum I.N. II-e018
Rubakov V.A. II-b018
Rubel M. II-d043
Rubtsov K.S. II-b018, II-b023
Rudakov V.A. II-b023
Rusbridge M.G. II-e010(*OP5*)
Rusbuldt D. II-d014
Ryter F. I-a004, I-a154(*OP3*)
Sabbagh S. I-a010
Sadler G. I-a042
Sadowski M. III-f056

Sagara A. II-b026, II-d016
Saibene G. I-a049
Sakakita H. I-a070
Sakamoto K. II-b012
Sakharov N.V. I-a071
Salas A. II-b042
Salierno M. III-g016
SallanderJ. II-c022(*OP4*)
Salzmann H. I-a008(*OP6*)
Samm U. II-d041, II-d043
Sanchez E. II-d046
Sanchez J. II-b039, III-f004
Sanchez R. I-a063, II-b035
Sandeman J.C. II-e010(*OP5*)
Sandmann W. II-d004
Sanin A.L. III-g043
Sano F. II-b012
Santagiustina A. I-a058, I-a059
Sarichev D.V. II-d051
Sarksyan K.A. II-b049
Sartori F. I-a058, I-a059
Sartori R. I-a055, I-a060
Sasaki K. II-c023
Sato F. II-e044
Sato K.N. I-a070
Sattin F. II-c006
Sauter O. I-a065, II-e040
Seveliev A. III-pd023
Savjolov A.S. III-f023
Savrukhin P. I-a058, I-a059
Sbitnikova I. II-b040
Sbitnikova I.S. II-b049
Scarin P. II-c004, II-c006
Schep T.J. III-g015(*OP18*)
Schevchuk B.A. II-c024, II-c026
Schissel D.P. I-a095
Schittenhelm M. III-f011
Schmidt G.L. I-a016
Schneider R. II-d007, II-d038, III-f010
Schneider W. II-d004, II-d005, III-f009
Schram P.P.J.M. III-g001, III-g002, III-g054, III-g057
Schuller F.C. I-a102(*OP2*), I-a118, I-a119, III-f059
Schumacher U. III-f007
Schunke B. I-a041
Schweer B. II-d043
Schweinzer J. I-a004, I-a008(*OP6*), II-d004, II-d005
Scott B. I-a005
Sebelin E. II-e036
Seki T. I-a070
Selenin V.L. III-g020
Semenov D.V. II-c015
Senju T. II-b012, II-e044
Sequi J.L. I-a130
Sergienko S. II-d014
Serianni G. II-d001
Serra F. III-f006
Shafranov V.D. II-b016

Shakhovetz K.G. I-a071
Shamrai K.P. III-j009, III-j010
Sharapov S. I-a042
Shcherbinina T.E. II-b032, III-i001(*OP24*)
Shikhovtsev I.V. II-c030, II-c031
Shilo S.N. III-j030
Shirai H. I-a112
Shishkin A.A. II-b002, II-b026, II-b027
Shkarofsky I. II-e042
Shkarofsky I.F. II-e036
Shorikov V.Yu. III-f027
Shoucri M. II-e036, II-e042
Shtan' A.V. II-d016
Shurygin V.A. I-a087
Shvidkij A.A. III-i025
Sidorenko D. III-g040
Sidorenko I.N. II-b026, II-b027
Sigov Yu.S. III-g051
Silivra O.A. I-a073
Silva A. III-f006
Silva C. I-a141(*OP20*)
Simard M. II-d036
Simmet E.E. II-b004
Simonetto A. II-e013
Simonini R. I-a046, II-d045
Siomok V.P. III-j016
Sipila S.K. II-e031
Sips A.C.C. III-pd020
Sips G. I-a060
Sitenko A.G. III-f040, III-g053, III-g054, III-j005
Skibenko A.I. III-f047, III-f048
Skiff F. II-e042
Skrynnik B.K. III-f025
Smeulders P. I-a044
Smirnov A.P. III-f044
Smirnov R.D. III-g001
Smirnov V.M. II-b029
Smirnova M.S. II-b020, II-b026
Smith R.T.C. III-pd022(*OP8a*)
Sokoll M. I-a001
Sokolov V.G. II-c017
Soldatov S.V. I-a082, I-a083
Soldner F.X. III-pd020
Solyakov D.G. II-c033, II-d052, III-j032
Sorokovoj E.L. II-b018
Sosenko P. III-f040
Sotnikov G. III-g040
Spzzi C. II-e013
Spence J. I-a046
Speth E. II-b003
Spineanu F. I-a129
Sporov A.E. II-d031
Springmann E. I-a043(*OP19*), I-a046, I-a061
St-Onge M. I-a143

St.John H.E. I-a095
Stallard B.W. I-a096, III-pd020
Stansfield B. II-d036
Starchuk P.D. III-j011
Start D. I-a042
Start D.F.H. I-a060
Stefanovskij A. II-d013
Stepanov A.Yu. II-e004, III-f027
Stepanov K.N. II-e020, II-e021, II-e023, II-e024
Steuer K.-H. I-a020, I-a023
Stober J. I-a004, I-a024, III-f010
Stork D. I-a045
Strait E.J. I-a065, II-e025, III-pd020
Stupishin N.V. II-c030, II-c031
Subbotin A.A. II-b016
Sudo S. II-b012, III-f018, II-e044
Sugiyama L. I-a097
Suprun A.D. III-h003
Suttrop W. I-a004, I-a008(*OP6*), I-a024, I-a026, I-a154(*OP3*), II-d004, III-f006
Suwon Cho III-j012
Sykes A. I-a136, III-pd022(*OP8a*)
Szydlowski A. III-f056
Takizuka T. I-a112
Tanabe T. II-d043
Tanga A. I-a058, I-a059
Tanzi C.P. I-a119
Taran G.V. III-j030
Taranov V.B. III-j009, III-j010
Tarasyan K.N. I-a090
Taroni A. I-a040, I-a043(*OP19*), I-a045, I-a046, II-d045, I-a061
Taskaev S.Yu. II-c017
Taylor P.L. I-a094, III-pd020
Taylor T.S. I-a065, I-a096
Tendler M. I-a163, I-a164
Tennfors E. II-c022(*OP4*), II-c023, II-e028
Tereshin V.I. II-c033, II-d052, III-j032
Theimer G. II-d006
Thoma A. II-d037
Toi K. I-a070
Tokar A. II-d054(*OP16*)
Tokar M.Z. II-d041, II-d043
Tokarchuk M.V. III-g055
Tolstoluzhsky A.P. III-g036, III-g037, III-g038
Toshi K. II-b012
Trevisan F. II-c002
Tribaldos V. II-b039, II-b040, II-b041, II-b042

Trofimenko Yu. III-f052(*OP17*)
Troyon F. III-g006
Trubchaninov S.A. III-j032
Trubnikov B.A. III-i018, III-i019
Tsarenko A.V. III-j032
Tsaun S.V. I-a082
Tsushima A. II-d011
Tsvetkov I.V. II-b029
Tsygankov V.A. II-b049
Tudisco O. I-a133, II-e013, III-f028
Tunklev M. III-pd013
Tur A.V. III-i007
Turnbull A.D. I-a065, III-pd020
Tyntarev M.A. III-f053
Tyupa V.I. II-b021
Uehara K. II-d011
Uguchi S. II-b034
Unterberg B. II-d043
Usenko A.S. II-d012
Uzlov V.S. I-a071
Valisa M. II-c003, II-c004, II-c006
Valovic M. I-a136, I-a139, I-a141(*OP20*)
Van-der Linden R.A.M. I-a041
van-der Meiden H.J. III-f034
Van Houtte D. I-a125
Van Milligen B. II-d046
Van Milligen Ph. II-b041
Van Oost G. II-d043, II-d054(*OP16*), II-e012
van Toledo W. II-d009
Varandas C. III-f052(*OP17*)
Varela P. III-f006
Veklich A.N. III-f002
Verbeek H. II-d007, III-f010
Verbitskij A.P. III-f044
Veres G. III-h005
Veres I. III-h005
Verkhoglyadova O.P. III-i009
Verplancke Ph. II-d005
Vers A.V. II-e003
Vershkov V.A. I-a082, I-a083
Villard L. III-g006
Vinnichenko M.V. III-pd011
Vizgalov I.V. II-d051
Vlad M. I-a129
Vlases G. II-d045
Vlasov V.P. III-i018, III-i019
Voitenko L.M. III-j011
Voitenko Yu.M. II-e053, III-g062
Voitsenya V.S. III-f047, III-pd011
Voitskhovitch I. I-a124(*OP7*)
Volkov E.D. II-b018, II-b025, II-b031(*OP21*), II-b032, II-d016, II-e029
von Goeler S. II-e005
von Hellermann M. I-a062
Voskoboynikov S. I-a163

Voslamber D. III-f036(*OP10*)
Vovchenko E.D. III-f023
Vyacheslavov L.N. III-g043
Wade M.R. I-a093, II-d019
Waidmann G. I-a102(*OP2*)
Wakatani M. II-e044
Walsh M.J. I-a136, I-a140, III-pd022(*OP8a*)
Waltz R.E. I-a128
Warder S.E.V. III-pd022(*OP8a*)
Watanabe K.Y. II-b026, II-b030
Weiland J. I-a101
Weinlich M. I-a008(*OP6*), II-d003, II-d040
Weisen H. I-a030, I-a032, I-a033, II-d009, III-f013
Welander A. II-c022(*OP4*)
Weller A. I-a030, II-b007, II-b008, II-e007(*OP22*)
Wenzel U. II-d037, II-d040
Wesson J. I-a044, I-a051
West W.P. I-a093, II-d017, II-d019
Westerhof E. II-e032, II-e033, III-g014
White R. III-f035
White R.B. I-a010, I-a015, I-a093
Whyte D. I-a142
Whyte D.G. II-d019
Wijnands T. I-a125
Wilson H.R. I-a001, I-a136
Wobig H. II-b001
Wolf G.H. II-d054(*OP16*)
Wolf R. II-b008
Wolf R.C. II-b036
Wood R.D. I-a093, II-d017, II-d019
Woodruff S. II-e010(*OP5*)
Wuerz H. III-j032
Xuantong D. III-g016, III-g017
Yagi Y. II-c002, II-d001
Yaguchi K. II-b012
Yakimenko I.P. III-g057
Yakimov K.I.pd011
Yakovenko I.V. III-j006
Yakovenko V.M. III-j006
Yakovenko Yu.V. I-a109, I-a110
Yakovets A.N. I-a078
Yakovetsky V.S. III-j003
Yamamoto T. II-b034
Yamazaki K. II-b026, II-b030
Yanovsky M.S. III-f021, III-f022
Yanovsky V.V. III-i007
Yavorskij V.A. I-a074, I-a075
Yegorenkov V.D. II-c013, III-j014, III-j015
Yoshida Z. II-c023
Yukhimuk A.K. III-i005
Yukhimuk V.A. III-i005

Yurchenko E.I. I-a084, I-a088
Zagorodny A.G. II-d050, III-g054, III-g058, III-i026, III-i027
Zakharov L. I-a010, I-a014
Zapesochny I.P. III-f051
Zavadsky V.M. III-f039
Zdrazil V. III-f061
Zehetbauer T. I-a021
Zehrfeld H.-P. III-f009
Zeiler A. I-a002(*OP1*)
Zhao Y. I-a010
Zhdanov S.K. III-i018, III-i019
Zhivolup T.G. III-i035
Zhovtyansky V.A. III-f002
Zhuravlev V. III-f004
Zimeleva L.G. I-a156
Zinevych S.M. III-g053
Zohm H. I-a001, I-a004, I-a008(*OP6*), I-a019, III-f009, III-f011
Zoletnik S. III-h005
Zollino G. II-c002
Zolotukhin A.V. II-b001, II-b026
Zou X.L. I-a126, I-a130, III-f057, III-f058
Zurro B. II-b042, III-f055
Zushi H. II-b012, II-b013, II-e044
Zvonkov S. II-d013
Zweben S. I-a074
Zweben S.J. I-a010, I-a015
Zwingmann W. I-a056